UNIVERSITY OF CAPE TOWN
IYUNIVESITHI YASEKAPA • UNIVERSITEIT VAN KAAPSTAD

Accretion Processes in Cataclysmic Variable Stars:

Insights from Optical Transient Surveys

Submitted in academic fulfilment of the requirements for the degree of
Doctor of Philosophy

Mokhine Motsoaledi

Institution
Department of Astronomy
University of Cape Town
November 2023

Supervisors
Prof. Patrick Woudt
Prof. David Buckley
Prof. Brian Warner

Declaration

I, Mokhine Motsoaledi, hereby declare that the work on which this thesis is based is my original work (except where acknowledgements indicate otherwise) and that neither the whole work nor any part of it has been, is being, or is to be submitted for another degree in this or any other university. I authorise the University to reproduce for the purpose of research either the whole or any portion of the contents in any manner whatsoever.

	8 November 2023
Signature	Date

A special thank you to the late Prof. Brian Warner for his fundamental role in fostering my interest in cataclysmic variable stars and for the very interesting general conversations. It is a privilege to have known and been supervised by such an extraordinary person.

Contents

List of Figures

List of Tables

CHAPTER 1

Introduction

Cataclysmic variables (CVs) are close interacting binary stars powered by mass accretion onto a white dwarf (WD), mostly through an accretion disc. CVs are dynamic systems which are continuously varying in optical brightness, sometimes by many magnitudes, over timescales ranging from sub-seconds to millions of years. These observationally rewarding systems have relatively short orbital periods (~ 0.1 to 10 hours) which allow for a variety of different observations over the entire orbital cycle, sometimes even during a single night's observation. CVs radiate across the electromagnetic spectrum, from radio to gamma rays, thus a multi-wavelength observational approach to CVs can reveal the complexities associated with the different components and their interactions.

Accretion discs exist in many astronomical objects on various scales in the universe, from the formation of planets, stars and galaxies, discs in various stellar binary systems to discs surrounding the supermassive black holes in active galactic nuclei at the centre of many galaxies. Many such accretion phenomena present observational challenges, however CVs provide some of the best opportunities for the study of accretion processes because of their apparent brightness, relative proximity in the Galaxy and timescale of variability. The dynamic CV discs allow the study of accretion in optically thick stable-state discs, with high rates of mass transfer, optically thin unstable discs with low mass transfer and the transitions between them due to thermal/tidal instabilities or enhanced mass-transfer.

Despite the extensive studies of CVs through observations and modelling, the physics behind disc accretion is yet to be fully understood. Helium disc accretion remains even more elusive as fewer helium-accreting binaries have been discovered and investigated compared to less evolved hydrogen-accreting systems. AM Canum Venaticorum (AM CVn) stars are ultra-compact helium-accreting binary stars with a degenerate (or partially degenerate) donor star, arising from one of three formation channels. The accretion of helium onto a compact object, compared with hydrogen, affects processes associated with the donor star, accretion disc, accreting star, and the overall evolution of the binary.

AM CVns provide unique opportunities to study the later stages of binary evolution and help improve constraints on the poorly understood common envelope phase, as most AM CVns are thought to arise from two common envelope phases. With orbital periods less than 70 min, these ultra-compact binaries are believed to be steady sources of low-frequency gravitational wave radiation.

AM CVn stars evolve to longer orbital periods with different evolutionary stages of long-term outburst properties. An increase in the number of optical synoptic and transient surveys over the last decade has resulted in a significant increase in the known AM CVn systems. This allows for improved understanding of the relation between the orbital period, the long-term outburst properties, and the influence of the nature of the donor star. Recently discovered systems have challenged the findings of earlier studies based on long-term outburst properties of smaller group samples. In this work, I have followed up AM CVn stars discovered from different optical transient surveys photometrically and spectroscopically, with a focus on determining the orbital period and long-term outburst properties.

Many observational and evolutionary aspects of CVs are influenced or determined by magnetism, whether in the accretion process or interactions between the component stars. For example, the loss of angular momentum (and decrease in orbital separation) is a result of interactions between the stellar wind and magnetic field of the donor star, which governs their evolution: magnetic turbulence in the accretion disc induces the viscosity needed to explain their formation and structure; the decrease in the mass transfer rates are due to magnetised stellar spots on the donor star; and the strong magnetic fields from the accreting white dwarf change the accretion mechanism. In the latter case, the accretion disc is partially or completely disrupted as infalling mass is redirected out of the orbital plane along the magnetic field lines.

A CV accretion disc behaves as a reservoir for transferred mass before settling on the WD, therefore the absence of an accretion disc in magnetic CVs (polars) allows for the study of mass accretion from the donor as changes in the donor star would be reflected as immediate variations in the accretion luminosity, which is mostly emitted in the accretion column and its surroundings.

With the efforts of amateur astronomers, some individual magnetic CVs have continuously been monitored for decades. However, the long-term photometric properties and thus the long-term high and low accretion state variations of the global population of magnetic CVs have not been so well studied until the advent of long-term surveys, for example the Catalina Real-Time Survey (CRTS; which is the main survey I have exploited in my thesis), ASAS-SN, Kepler/K2 and TESS.

I used the photometry database from the CRTS to investigate the long-term photometric variations in a sample of ~ 80 previously-known magnetic CVs of the polar subclass. In addition, new polar candidates were selected from the light curves of CVs identified by the CRTS, based on their long-term photometric variations, which I then observed photometrically and spectroscopically to confirm their nature and improve my selection criteria for polars from transient surveys.

Having investigated both CV subclasses, AM CVns and magnetic CVs, I assess the lack of magnetic AM CVn systems compared to the high fraction of magnetic CVs, highlighting two magnetic AM CVn candidates.

This chapter introduces the geometry and evolution of CVs, and expands on the literature of the fundamental accretion disc properties in CVs (§ 1.1). Overviews of AM CVn stars and magnetic CVs (polars in particular) can be found in § 1.2 and § 1.3, respectively. As this work focuses on CVs from specific optical transient surveys, § 1.4 elaborates on these transient surveys as well as other optical surveys which have made significant contributions to the discovery of magnetic and helium-dominated CVs.

1.1 CATACLYSMIC VARIABLES

A cataclysmic variable consists of a WD star and a low-mass main sequence star, usually a red dwarf of K-M spectral type. Due to the close proximity of the stars, the more massive white dwarf exerts a significant gravitational force on the main sequence star. The geometry of the binary and the gravitational interaction provide the conditions for the WD to accrete mass from the main sequence donor star (see Fig. 1.1). A crucial process for the formation of a CV is a common envelope (CE) phase in which the more massive star of the detached CV progenitor system, evolving at a faster rate than its main sequence companion star, becomes a red giant and envelopes the distant companion star such that both stars are in the shell of one star. During the common envelope phase, the stars are accelerated to closer orbital separations as they experience frictional drag within the envelope due to angular momentum loss (Paczynski, 1976; Iben and Livio, 1993; Taam and Sandquist, 2000; Ivanova et al., 2013). The angular momentum is transferred to the envelope which is expelled away from the binary, resulting in a white dwarf + main sequence binary.

The boundary of constant and equal gravitational potential surrounding both stars is known as the critical equipotential surface, or sometimes the Roche lobe[1]. The Roche lobe resembles a figure "8" or "∞", with each star situated at the centre of their respective lobe. This is the largest closed equipotential within which mass remains gravitationally bound to each star. The sizes of the Roche lobes are determined by the orbital separation (a) and mass ratio q ($q = M_2/M_1$, where M_1 is the mass of the primary accreting star and the M_2 is the mass of the secondary donor star). The inner Lagrangian (L1) point is the meeting point of both Roche lobes. When the donor star fills its Roche lobe, the mass situated at the L1 point spills through the L1 point into the Roche lobe of the WD as a result of its gravitational attraction.

The L1 point moves in a circular motion with the binary orbit which causes the stream of mass to flow past the WD instead of radially towards the WD due to the conservation of angular momentum. In the absence of a strong magnetic field, the stream circles around the WD and makes contact with itself, settling into a ring within the WD Roche lobe whose angular momentum is the same as that of the material leaving the L1 point. The ring slowly widens to form a permanent disc due to the effects

[1] Strictly speaking the Roche solution applies to point masses, so does not account for real stars with changing density as a function of radius.

of viscosity and conservation of angular momentum (Lynden-Bell and Pringle, 1974). Fig. 1.2 illustrates this disc formation process. Mass flowing through the disc eventually drains onto the WD. The impact region between the stream of mass and the edge of the accretion disc is heated and radiates a substantial amount of energy identified as a bright spot. When the accretion disc activity is low, during quiescence, the bright spot may be the brightest component of the binary system optically.

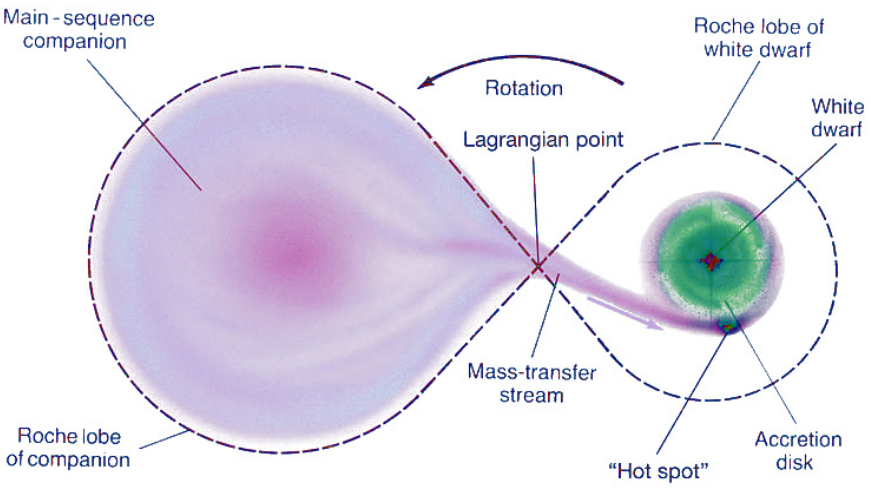

FIGURE 1.1 – Schematic diagram of a cataclysmic variable showing the stellar components, disc, stream and bright/hot spot reproduced from Pearson Prentice Hall, Inc. Note: The Roche lobe in this figure is not a true representation of the Roche lobes in CVs as the accreting WD is more massive thus the WD has a larger lobe than the donor star.

In order for mass transfer to take place continuously, the donor star must maintain contact with the Roche lobe. Considering the radius of the donor star decreases as it loses mass, the donor Roche lobe decreases as well. The orbital separation, and thus the orbital period, decreases due to angular momentum loss driven by magnetic braking (Verbunt and Zwaan, 1981) and gravitational radiation (Paczyński, 1967; Faulkner et al., 1972). During the former, ionised material from the stellar wind from the donor star gets coupled with its magnetic field, forcing it to co-rotate with the donor which slows the donor down. Since the system is tidally locked, angular momentum is lost from the binary orbit. Gravitational radiation results in energy loss and hence angular momentum loss, particularly at small orbital separations for short-period systems.

The orbital periods of CVs are observed to lie between $\sim 2\,\mathrm{d}$ and $\sim 78\,\mathrm{min}$ for hydrogen-accreting systems with non-degenerate companion stars. In order for the system to be stable, mass is required to be transferred from the less massive to the more massive star, implying that the mass of the donor star (M_2) is lower than that of the WD (M_1), which is below the Chandrasekar limit of $1.4\,\mathrm{M}_\odot$. The system only begins to transfer mass when the binary separation is small such that the donor Roche lobe is close enough to the WD, and thus small enough to be filled by the low-mass main sequence donor star. Therefore the low-mass companion stars lead to short orbital periods observed in CVs.

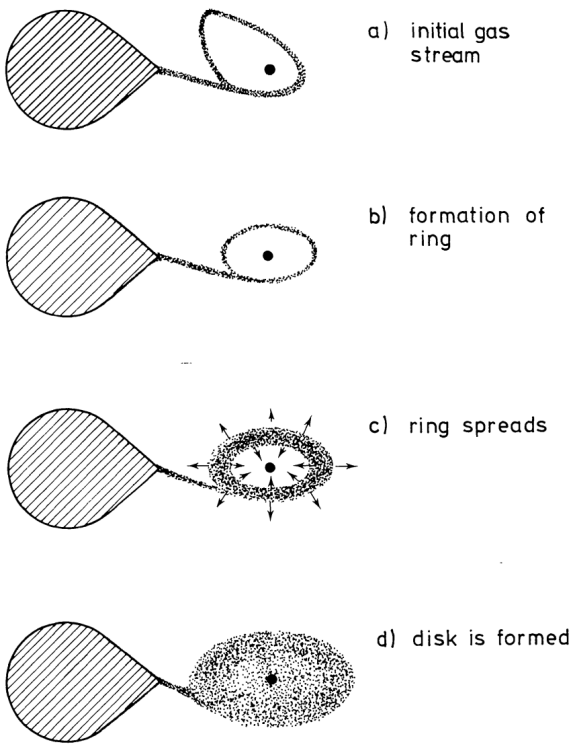

FIGURE 1.2 – Schematic diagram showing disc formation in CVs. Reproduced from Verbunt (1982).

When a CV reaches an orbital period ($P_{\rm orb}$) of ~ 2.8 h, the donor star with a radiative core is thought to become fully convective and contracts. Therefore the effect of continued mass loss will eventually mean the donor detaches from the Roche lobe, temporarily discontinuing mass transfer. The convection leads to diminished stellar winds, which results in a decrease in the main angular momentum loss mechanism, magnetic breaking. Due to angular momentum loss through gravitational radiation, the binary separation continues to decrease and at $P_{\rm orb} \sim 2.2$ h the Roche lobe shrinks to the size of the donor and mass transfer resumes. This interval of a detached phase is known as the period gap, where the number of interacting non-magnetic CVs diminishes. It is thought that magnetic braking is the dominant angular momentum loss mechanism before the donor becomes fully convective at $P_{\rm orb} \sim 2.8$ h (as the radiative energy transfer layer disappears), thereafter gravitational radiation takes over for the remaining lifetime. The mass of the donor star eventually becomes so low that it behaves like a degenerate star, increasing in radius as it loses mass, thus increasing the orbital separation and orbital period (Paczynski and Sienkiewicz, 1981). This turning point occurs at a period minimum of ~ 78 min (e.g. Kolb and Baraffe, 1999; Knigge, 2006; Gänsicke et al., 2009; Knigge et al., 2011) after which the system evolves to longer periods. The evolutionary path of CV can be seen in Fig. 1.3 showing the relation between the orbital period and mass of the donor star.

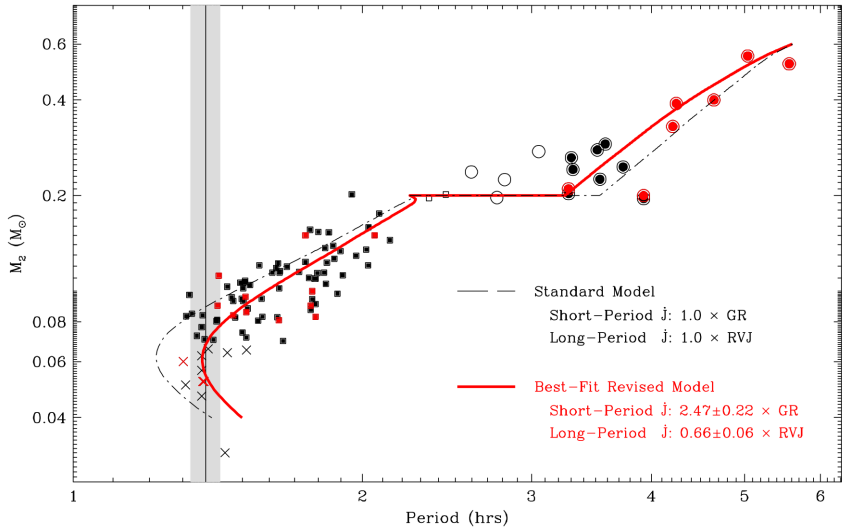

FIGURE 1.3 – The period-mass relation of CVs reproduced from Knigge et al. (2011). The points represent observational data of CVs. The black line is the standard model for CV evolution. The red line is the best-fit model.

1.1.1 *Accretion discs*

Mass from the donor star reaches the surface of the accreting WD through various processes, many of which take place in the accretion disc surrounding the WD. The mass entering the differentially rotating accretion disc, governed by Keplerian motion, embarks on a complex journey before reaching the surface of the WD star. Such discs display properties of steady state discs characterised by steady mass flow within and out of the disc. Most of the accretion disc physics is based on the assumption of steady state accretion.

One of the properties of a steady accretion state disc is a "thin disc" approximation. Stream and disc activity both occur in the orbital plane preventing a significant amount of gas from being flung out beyond the orbital plane at the point of impact, thus hydrostatic equilibrium determines the "thin disc" nature. A CV accretion disc is approximated to "thin disc" because the disc radius far exceeds the scale height (H) of the disc ($H \ll r$). For $r \gg R_1$, where R_1 is the radius of the accreting WD,

$$\frac{H}{r} \propto \alpha^{-\frac{1}{10}} r^{\frac{1}{8}}. \tag{1.1}$$

$\frac{H}{r}$ increases with increasing r, resulting in the concave structure seen in Figure 1.4. For a definition of α, refer to the discussion below.

Disc accretion is a result of the outward transfer of angular momentum in the disc. The exact nature of the mechanism transporting the disc angular momentum is uncertain but is related to a dissipative process known as viscosity. Viscosity comes in different scales and forms. It is theorised that the effective viscosity in an accretion disc is driven by hydrodynamic turbulence and magnetic stresses (Shakura and Sunyaev, 1973). Molecular viscosity is too small to have an effect on disc accretion. Viscosity from

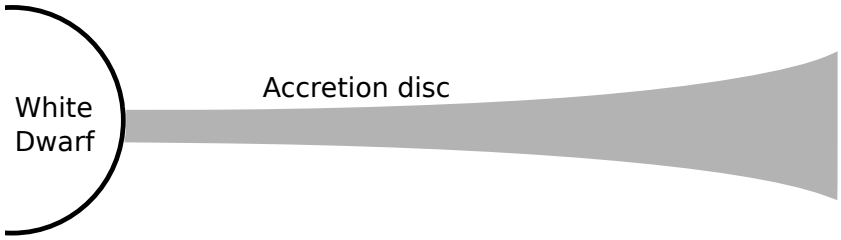

FIGURE 1.4 – Schematic diagram of thin disc, with concave and flaring structure, surrounding a white dwarf star (not to scale).

convection is applicable to cooler accretion discs than those in most close binaries (such as CVs) or quasars.

Shakura and Sunyaev (1973) introduced the α-prescription as the "efficiency of the mechanism of angular momentum transport" due to insufficient understanding of the physics of the viscosity in rotating accretion discs. This parametrisation of effective viscosity is expressed as a dimensionless parameter

$$\alpha = \left(\frac{r}{H}\right)^2 \frac{1}{t_\nu \Omega_k} \tag{1.2}$$

where t_ν is the time the system takes to move between different states, and Ω_k is the Keplerian angular velocity. α can be obtained from observable parameters $r/H, t_\nu$ and Ω_k.

Balbus and Hawley (1991); Hawley and Balbus (1991); Balbus and Hawley (1998) proposed the widely accepted magneto-rotational instability MRI, or otherwise known as the Balbus-Hawley instability, to explain accretion disc viscosity, with the condition of strong coupling between ionised material and magnetic fields within the disc. Two blobs of material at adjacent annuli would be travelling at their respective orbital velocities, resulting in a stretched magnetic field as the inner blob moves faster than the outer one. The inner blob slows down, decreasing its angular momentum, as the outer blob is sped up, which increases its angular momentum. The outward transfer of angular momentum causes the inner blob to move inwards and the outer blob to move further outwards, thus strengthening the magnetic field line.

Verbunt (1982) found that observational data implied non-steady CV accretion discs have $\alpha \approx 0.01 - 1$ depending on the type of accretion disc. The value of α for an outbursting CV accretion disc been narrowed down to $\approx 0.1 - 0.3$ (e.g. Smak, 1998; Cannizzo, 2001b,a; Balman and Revnivtsev, 2012; Coleman et al., 2016). A discrepancy is evident between numerical simulations of MRI yielding α for outbursting CVs as low as 0.01 (e.g. Hirose et al., 2009), however observational data (Smak, 1999; Kotko and Lasota, 2012) indicate α is likely greater than 0.1.

The kinematic velocity, v_k, of the mass travelling circularly in a differentially rotating thin disc is Keplerian. This is shown to be supersonic in the following equation:

$$v_k = \frac{r}{H} c_s \tag{1.3}$$

where c_s is the isothermal sound velocity. Radial drift velocity, $v_{\rm rad}$, is the velocity of particles as they diffuse radially inward, towards the accretor, while angular momentum is transported outward in the disc. The radial drift velocity,

$$v_{\rm rad} \sim \alpha \left(\frac{H}{r}\right) c_s, \tag{1.4}$$

is subsonic, contrary to kinematic velocity. The instability driving viscosity is able to increase until radial drift velocity becomes trans-sonic (Shakura and Sunyaev, 1973), beyond which the fundamental nature of the turbulence changes, which serves as a limitation to the strength of the turbulence (Martin et al., 2019).

This radial transport of mass and angular momentum is also responsible for the conversion of orbital kinetic energy to heat in the disc. The effective disc temperature within radius r is given by

$$T_{\rm eff}(r) = T_* \left(\frac{R_1}{r}\right)^{3/4} \left(1 - \left(\frac{R_1}{r}\right)^{1/2}\right)^{1/4}, \tag{1.5}$$

where

$$T_* = \frac{3Gm_1\dot{M}}{8\pi\sigma R_1^3}. \tag{1.6}$$

For $r \gg R(1)$,

$$T_{\rm eff}(r) \approx T_* \left(\frac{R_1}{r}\right)^{3/4}, \tag{1.7}$$

where $\dot{M}$ is the mass transfer rate and σ is the Stefan-Boltzmann constant. I have defined m_1 as the mass of the accreting WD in g and $M_1 = m_1/{\rm M}_\odot$, and similarly for m_2. This shows that a steady state accretion disc has the highest effective temperature closest to the WD, which decreases with increasing radius. An accretion disc with a typical mass transfer rate emits at ultraviolet (UV) wavelengths nearest to the WD and at infrared wavelengths in the cooler outer regions. If the disc is optically thick, it radiates almost as a blackbody. If the disc is optically thin, gas emissivity is lower than a blackbody thus the gas temperature would be required to be higher than the optically thick case.

CVs are ideal for observing accretion discs because their luminosity is dominated by the disc as the donor star is usually small, faint and cool compared to the disc. The disc luminosity is given by

$$L_{\rm disc} = \frac{Gm_1\dot{M}}{2R_1} = \frac{1}{2}L_{\rm acc}, \tag{1.8}$$

which only constitutes half of the total accretion luminosity, $L_{\rm acc}$. The other half of the accretion luminosity comes from a small area of the disc called the boundary layer. This implies that the boundary layer is of comparable importance as the accretion disc, energetically. Given the Keplerian orbital velocities of the disc, the largest velocities are found towards the inside of the disc while the surface of the accreting WD rotates at significantly lower angular velocities. The boundary layer is the transition between these close in proximity but vastly differing velocity regions (e.g. Sunyaev and Shakura, 1986; Narayan and Popham, 1993; Popham and Narayan, 1995). The velocity in the boundary layer is significantly lower than the rest of the disc, eventually matching that of the

surface of the WD (e.g. Frank et al., 2002). To ensure a quick and smooth deceleration of mass onto the WD surface, a large amount of energy is released as heat and radiated in soft X-ray and extreme UV wavelengths during outburst (optically thick) (e.g. Córdova et al., 1980; Jones and Watson, 1992; Suleimanov et al., 2014). During quiescence, the boundary layer is optically thin and observed at hard X-rays (e.g Pandel et al., 2003, 2005; Takeo et al., 2021). An alternative model is a spreading layer which is radially smaller but spreads out latitudinally onto the surface of the accretor (e.g. Inogamov and Sunyaev, 1999; Piro and Bildsten, 2004). According to Philippov et al. (2016), the efficiency of the mixing of the matter in the spreading layer with the surface of the WD is more efficient further away from the equatorial.

1.1.2 *Dwarf nova outbursts*

The most common type of non-magnetic CVs are dwarf novae (DNe) which experience dwarf nova outbursts (see Warner (1995a) and Frank et al. (2002) for reviews on dwarf nova outbursts), observed as short-lived, usually recurrent, brightenings with amplitudes generally up to five magnitudes, typically lasting over approximately 3 – 10 days. The source of the additional luminosity is attributed to changes in the accretion disc, primarily. During a DN outburst, the accretion disc is in a state of increased effective temperature and viscosity, eventually resulting in enhanced accretion of mass onto the WD (Osaki, 1974; Hōshi, 1979; Meyer and Meyer-Hofmeister, 1981).

Each annulus in the differentially rotating accretion disc rotates at its angular velocity dictated by Keplerian rotation, with inner annuli rotating at higher velocities than outer annuli. A change in the state of the disc begins as a local instability on an annulus at some radius from the centre. To become a global instability, the instability spreads throughout the disc as unstable annuli trigger adjacent annuli into the same instability. Referring to a thermal instability in the disc, the most accepted model for dwarf novae outbursts is the disc instability model (DIM, Meyer and Meyer-Hofmeister, 1981; Smak, 1982; Cannizzo et al., 1982), extended upon foundational work developed by Osaki (1974); Hōshi (1979). During quiescence, the surface density in the disc lies below the cold critical value $\Sigma_{\rm max}(r)$ and increases gradually throughout the disc with time through the inflow of mass from the donor star, until a disc annulus reaches (and exceeds) $\Sigma_{\rm max}(r)$, triggering the start of a DN outburst as the disc transitions into a hot state. Due to an increase of the scaleheight H at a given radius, this annulus experiences increased viscosity in an accretion disc decreasing the velocity of the inner annulus and increasing the outer annulus velocity, in an attempt to equalise the rotation rate of adjacent annuli. This causes an outward transfer of angular momentum. The hot state conditions of the triggered annulus are transferred to adjacent annuli like a domino effect which propagates outward and inward heating fronts in the disc.

The relationship between the disc surface density and effective temperature ($\Sigma - T_{\rm eff}$) for each disc annulus is given by an S-shaped thermal equilibrium curve (refer to Fig. 1.5, Meyer and Meyer-Hofmeister, 1981). $T_{\rm eff,\,crit1}$ and $T_{\rm eff,\,crit2}$ are, respectively, the effective temperatures below and above which a disc annulus is thermally stable, with corresponding mass transfer rates, $\dot{M}_{\rm crit1}$ and $\dot{M}_{\rm crit2}$. Effective temperatures and mass transfer rates between the critical values are thermally unstable. A random perturbation of a disc annulus at point P in Fig. 1.5, in the unstable region, causes the annulus to

increase in temperature until it reaches the hot stable branch. The surface density Σ decreases as the mass in the disc is transferred to the accreting WD at a rate higher than it is transferred onto the disc from the donor star. When the temperature reaches $T_{\text{eff, crit2}}$, the annulus is cooled to the lower cool stable branch, returning to a quiescent state where Σ increases as more mass enters the disc than leaves. A DN outburst is, therefore, the transitioning of the disc between cool and hot states of thermal stability via unstable conditions. Meyer and Meyer-Hofmeister (1981) found that the thermal instability occurs when the disc's effective temperature is hot enough to partially ionise the hydrogen disc (at $T_{\text{eff, crit2}}$). The outburst cycle is thus the transition of the disc between the cold neutral hydrogen stable state and the hot ionised hydrogen stable state.

Critical disc surface densities for hydrogen accretion discs are given by Cannizzo et al. (1988):

$$\Sigma_{\max}(r) = 11.4 r_{10}^{1.05} M_1^{-0.35} \alpha_{\text{C}}^{-0.86} \ \text{g cm}^{-2}, \tag{1.9}$$

$$\Sigma_{\min}(r) = 8.25 r_{10}^{1.05} M_1^{-0.35} \alpha_{\text{H}}^{-0.8} \ \text{g cm}^{-2}, \tag{1.10}$$

where α_{C} and α_{H} is the viscosity parameter α for a cold disc and a hot disc, respectively, and $r_{10} = r/10^{10}$ cm. The disc viscosity parameter α varies with the binary system states, in order to obtain the high amplitude outbursts observed in CVs. The hot α_{H} during outburst is larger than the α_{C} during the cool quiescent state by ~ 10 (Smak, 1984a; Meyer and Meyer-Hofmeister, 1984).

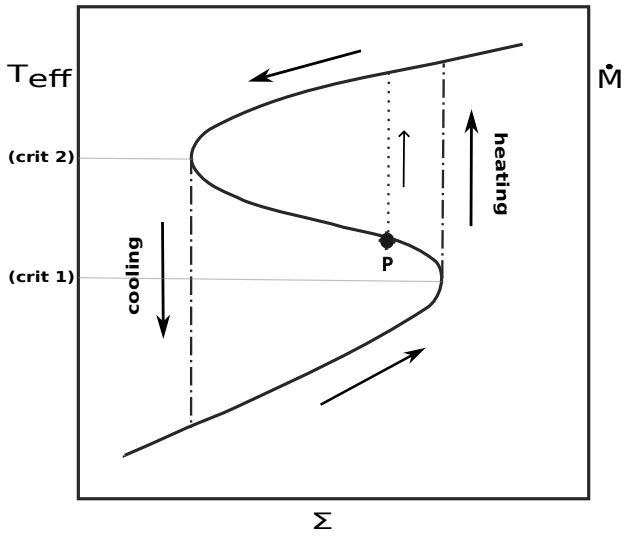

FIGURE 1.5 – The thermal-equilibrium curve for accretion discs. The disc surface density and effective temperature relationship ($\Sigma - T_{\text{eff}}$) in the CV accretion disc given by a so-called, S-curve for a given radius. The relationship describes changes within an accretion disc between quiescence and DN outbursts. The region between $T_{\text{eff, crit1}}$ and $T_{\text{eff, crit2}}$ is considered thermally unstable. A point P in this thermally unstable region which triggers a DN outburst and moves along the direction of the arrows until the disc reaches a cool stable state.

In the DIM model, $\Sigma_{\min}$ and $\Sigma_{\max}$ are not constant throughout the disc. $\Sigma_{\max}(r)$ increases and $\Sigma_{\min}(r)$ decreases as the radius increases. Therefore, it is more difficult

to reach $\Sigma_{\rm max}(r)$ at outer regions while $\Sigma_{\rm min}(r)$ is easily attainable at the outer disc. An inward heating front is able to maintain surface density above $\Sigma_{\rm max}(r)$, whilst an outward heating front may not reach $\Sigma_{\rm max}(r)$ at the outer regions. The surface density of a disc in hot state gradually decreases until an annulus, usually towards the outer edge of the disc, reaches $\Sigma_{\rm min}$. This triggers a cooling front, which sweeps through the disc from larger radii. Unlike the heating front, a cooling front only travels inward because $\Sigma(r)$ decreases with increasing r, as $\Sigma(r) \propto r^{-3/4}$ (Warner, 1995a) in the outburst state, and $\Sigma_{\rm min}(r)$ increases with increasing r. If $\Sigma_{\rm min}(r)$ is reached during the propagation of the heating front, the cooling front is triggered immediately and sweeps inward, therefore the outburst may be interrupted before spreading through the entire disc.

An outburst that starts from the inner disc and propagates mostly outward is known as an inside-out outburst. One that starts towards the outer disc and travels mostly inward is an outside-in outburst. The overall duration of inside-out outbursts are generally longer than outside-in outbursts because the rise time $t_{\rm r}$ of the former is longer (Smak, 1984a). A heating front moving outwards travels slower than a heating front moving inwards because an increase in surface density with increasing radius makes it increasingly difficult for angular momentum to be removed as the front spreads out. The decline time $t_{\rm d}$ is always approximately the same duration because the cooling front always moves inward from the outer edge of the disc, unless disrupted.

The inflowing mass in the accretion disc is essentially stored in the disc during quiescence, with little to no mass transfer, and drained out onto the accreting WD during outbursts. Significant accretion onto the WD occurs over the specific interval of the outburst, beginning when the heating front arrives at the inner disc and ending when the cooling front reaches the inner edge of the disc (Warner, 1995a).

The non-static disc not only varies during outbursts, but continuously fluctuates at all states. A cold disc during quiescence contracts due to the addition of mass from the donor star via a stream with specific angular momentum lower than the edge of the disc; and the tidal removal of angular momentum by the donor star from the disc. During DN outbursts, however, angular momentum is transported to the outer parts of the disc as mass is accreted onto the WD from the disc, resulting in an expansion of the disc (Smak, 1971, 1984b). Observations by Smak (1984c); O'Donoghue (1986) of accretion discs during outburst and quiescence support these DIM predictions.

The mass transfer rate from the donor ($\dot{M}_2$) also contributes to the overall outburst behaviour. A low $\dot{M}_2$ leads to longer outburst intervals and outbursts that are triggered from the inner disc. High $\dot{M}_2$ systems are more inclined to have shorter recurrence times and begin towards the outer edge of the disc because mass does not have enough time spread inwards before reaching the inner disc (Smak, 1984a; Mineshige and Osaki, 1985). However, Buat-Ménard et al. (2001) show that outside-in outbursts can occur for low $\dot{M}_2$ with the presence of other heating mechanisms such as stream impact and tidal-torques. An essential condition for DNe is that $\dot{M}_2 < \dot{M}_{\rm DN}$, where $\dot{M}_{\rm DN}$ is the mass transfer rate onto the accretor during a DN outburst (Frank et al., 2002).

1.1.3 *Superoutbursts*

Similar to dwarf novae outbursts, superoutbursts arise from instabilities in the disc resulting in larger outburst amplitudes and longer outburst durations (∼ weeks) than DN outbursts. The duration from one superoutburst to the next is known as a supercycle. Superoutbursts generally erupt less frequently than DN outbursts, which may occur numerous times per supercycle. While the DIM is consistent with the observations of DN outbursts, it cannot be extended to superoutbursts. In addition to thermal instabilities in the discs, accretion discs undergo tidal instabilities during superoutbursts (Whitehurst, 1988; Hirose and Osaki, 1990). Thus Osaki (1989) proposed the thermal-tidal instability (TTI) model based on the DIM (refer to Fig. 1.6), where the accretion disc transitions between states of thermal and tidal stability, via unstable conditions.

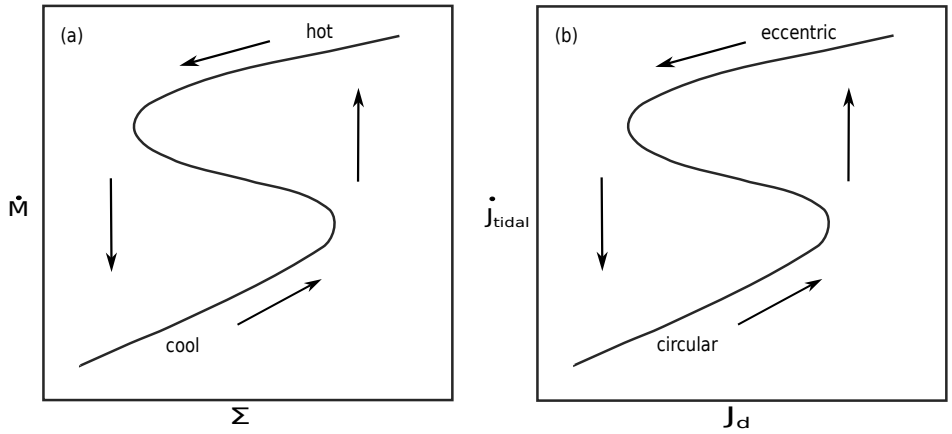

FIGURE 1.6 – (a) The tidal–torque relaxation oscillation in the disc given by the S-curve, similar to (b) the Σ –$T_{\rm eff}$ relationship.

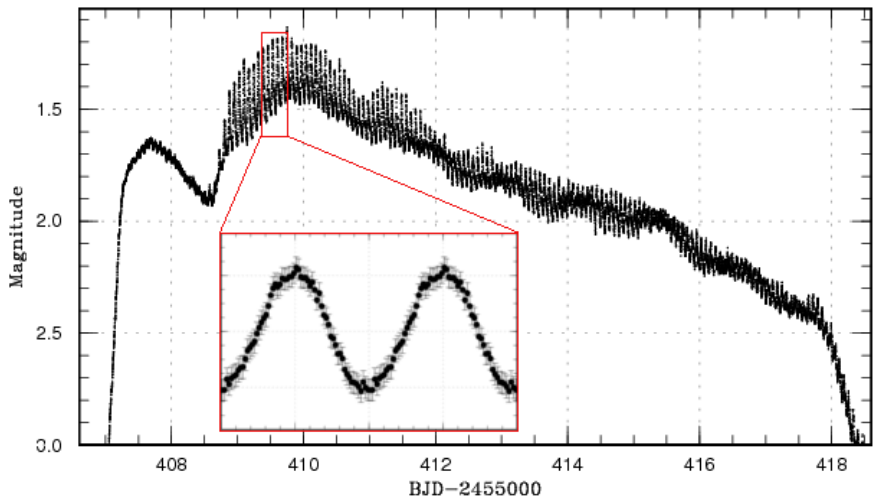

FIGURE 1.7 – The light curve of a superoutburst of V1504 Cygni reproduced from Osaki and Kato (2013). The inset shows the averaged light curve of superhump profiles which appear as vertical lines in the main figure.

As mass is transferred from the donor star, mass accumulates in the disc, therefore increasing the angular momentum. A superoutburst is triggered by a precursor DN outburst that facilitates the expansion of the disc to a critical radius, triggering a tidal instability. The circular disc becomes elliptical when the accretion disc reaches a critical radius for 3:1 resonance (when a point in the elliptical disc travels around the accretor in precessing elliptical motions which repeat every third orbit). The elliptical disc precession is due to the disc orbiting quicker/slower than the binary stars while being gravitationally pulled by the donor star. This results in brightness variations called superhumps where the superhump period $P_{\rm SH}$ is slightly shorter/longer than the orbital period $P_{\rm orb}$.

Superhumps were originally thought to appear at the start of (or shortly before) superoutburst maxima (Semeniuk, 1980). However, Kato et al. (2012a) later determined that, in many cases, the superhumps develop during the rising branch, at the maximum or shortly after the precursor outburst (Kato and Osaki, 2013a,b). This suggests that superhumps lead to superoutbursts and not the other way around, in agreement with the TTI model.

The TTI model is able to reproduce superhumps and their periods, however Smak (1996, 2000) identified inconsistencies with the data. This includes the condition that the 3:1 resonance holds only for $q_{\rm crit} < 0.25$, yet superhump systems with larger $q_{\rm crit}$ have been observed. Furthermore, superhump simulations produce superhumps with amplitudes 4 – 10 times lower than observed (Smak, 2009c).

An alternative model for superoutbursts is the enhanced mass-transfer (EMT) model (Osaki, 1985; Lasota et al., 1995; Hameury et al., 2000; Smak, 2008). The EMT model attributes superoutbursts to enhanced mass transfer from the donor star. In this model, the increased mass transfer increases the disc radius which triggers the 3:1 resonance after the initiation of the superoutburst, in contrast with the TTI model.

Superoutburst light curves are characterised by a rapid incline and a plateaued region beginning at maximum amplitude with gradual decline until a rapid decline (see Fig 1.7). A defining feature of systems undergoing superoutbursts is the presence of low amplitude superhumps, usually visible in the light curve profile (Vogt, 1974; Warner, 1975).

Kato et al. (2009) conducted a large continuous survey of period variations of superhumps, spanning several years (e.g. Kato et al., 2009, 2012a, 2014a, 2016). One of the initial and most important findings was that superhump periods vary systematically throughout the duration of the superoutburst. Three distinct stages were observed: an early Stage A, middle stage B and final stage C (as seen in Fig. 1.8 comparing the observed superhump periods with the calculated superhump periods). Stage A superhumps are growing (in amplitude) with longer $P_{\rm SH}$. The fully developed superhumps in stage B vary systematically, decreasing and then increasing until stage C where $P_{\rm SH}$ is shortest and remains roughly constant.

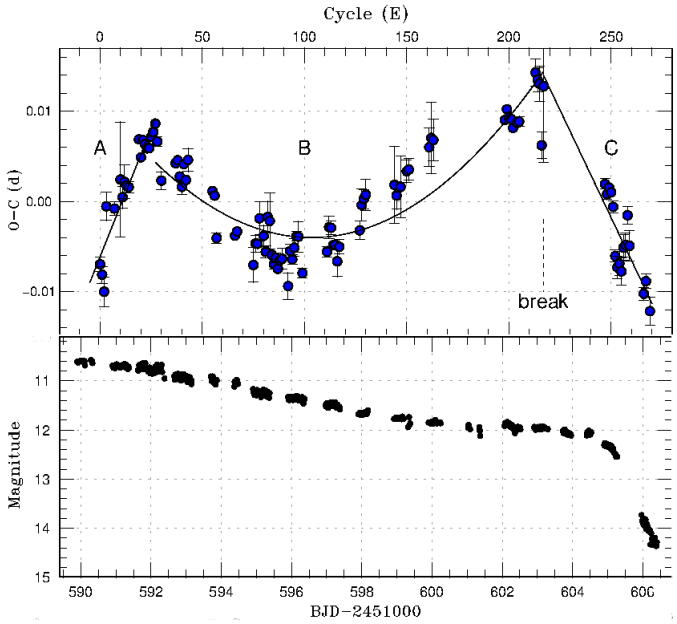

FIGURE 1.8 – Top: The O-C diagram showing three superhump stages of SW UMa reproduced from Kato and Osaki (2013b). Stage A: developing superhumps with long, increasing superhump period. B: fully developed superhumps with systematic variation. C: shortest, roughly constant superhump period. Bottom: Light curve of corresponding SW UMa superoutburst.

1.2 AM CVN STARS

AM CVn stars are a sub-class of ultra-compact CVs powered by helium accretion. The donor star is one of three helium-rich stars: 1) a white dwarf (Paczyński, 1967; Faulkner et al., 1972); 2) a non-degenerate helium star (Savonije et al., 1986; Iben and Tutukov, 1987); 3) an evolved MS star which has lost its outer hydrogen layer (Tutukov et al., 1985; Podsiadlowski et al., 2003). The three types of donor stars arise from three slightly different formation channels (Nelemans, 2005; Nelemans et al., 2010). They all undergo a first common envelope (CE) phase as described in § 1.1 after which the white dwarf (future accretor) is formed. The product of this CE phase determines the outcome of the pending AM CVn.

If, after the first CE phase, the secondary star (future donor) has a mass below 2.3 $M_\odot$ (Iben and Tutukov, 1986), the binary system undergoes a second CE phase and evolves into a helium WD, as seen in the left branch of Fig. 1.9. In the second evolutionary track, the secondary star, with $2.3 \lesssim M_2 \lesssim 5\,M_\odot$ (Savonije et al., 1986; Iben and Tutukov, 1987) after the first CE phase, evolves into a semi-degenerate helium star after a second common envelope phase. This helium star channel is represented in the right branch of Fig. 1.9. The arrow labelled 'a' in Fig. 1.9 indicates that if the secondary depletes its helium before mass transfer takes place, the helium star may evolve into a hybrid WD (with a C/O core, a thick He-C-O mantle and some hydrogen in the outer layer) and joins the WD evolutionary track (Yungelson et al., 2002). The third evolutionary track requires very specific conditions. If the donor star has initial mass $0.85 \lesssim M_2 \lesssim 1.25\,M_\odot$ (Tutukov et al., 1985) and a core hydrogen abundance < 0.4 (Podsiadlowski et al., 2003), it may evolve to a closer separation, into a long-period hydrogen AM CVn. If the

separation of the stars is too large for a second CE phase, it becomes a standard CV. The three evolutionary tracks are shown in Fig. 1.10.

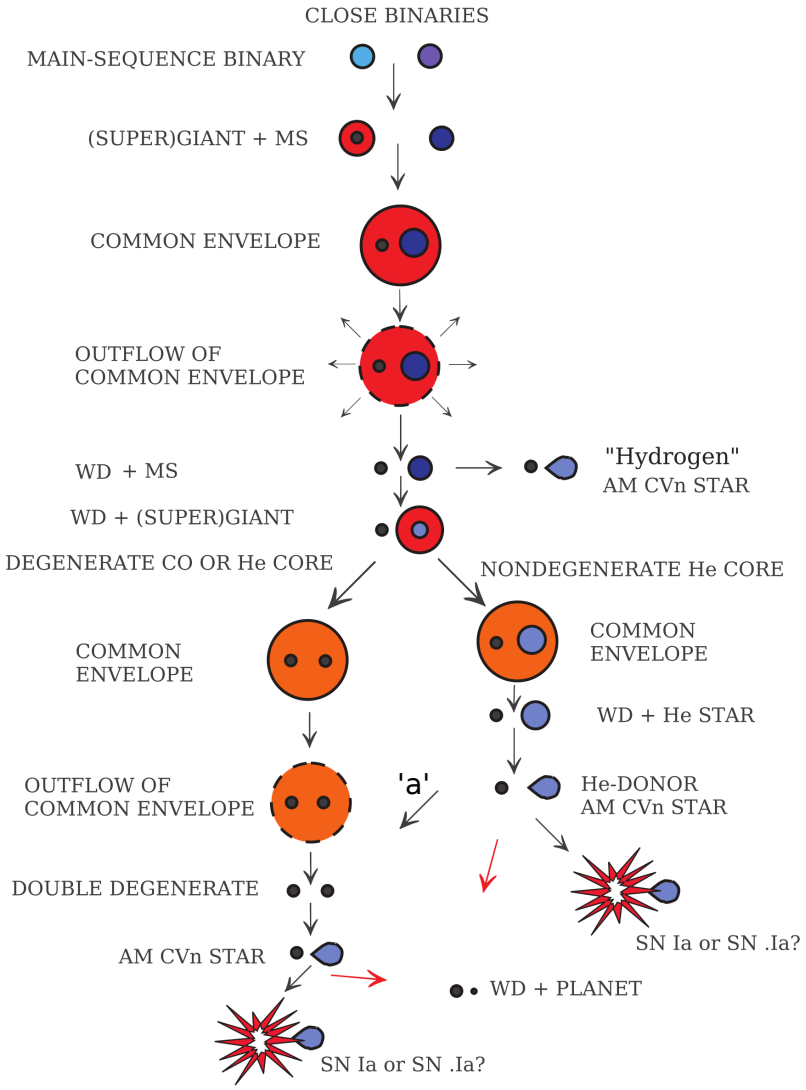

FIGURE 1.9 – A schematic of formation and evolution of the three AM CVn channels from detached binaries reproduced from Solheim (2010) and prepared by L. Yungelson.

1.2.1 *Donor star channels*

White dwarf channel: Stable mass transfer begins when $0.13 \lesssim M_2 \lesssim 0.3\,\mathrm{M}_\odot$ (Tutukov and Yungelson, 1996). During the direct-impact phase, the binary separation is so small that a disc is unable to form and the accretion stream falls directly on the surface of the accretor. Using certain assumptions regarding the stability of the initial mass transfer rate and the donor mass, Nelemans et al. (2001) found that the white dwarf channel always begins with direct-impact accretion before the formation of the disc at larger orbital separations. In the absence of a disc, stable mass transfer is dependent on the efficiency of tidal coupling between both stars in which the spin and orbital periods

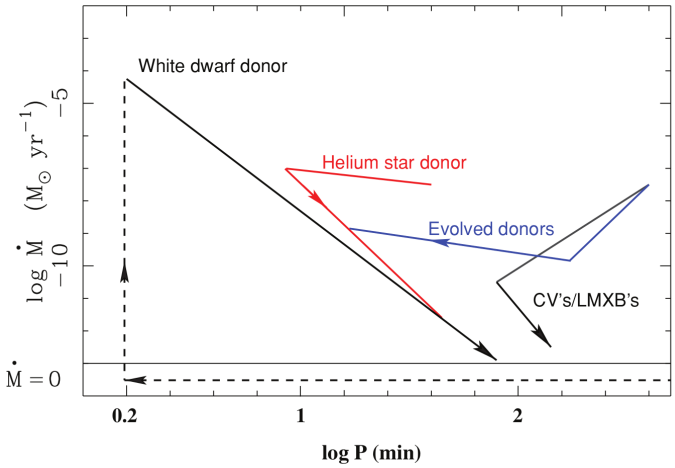

FIGURE 1.10 – The formation and evolution tracks of the three AM CVn channels represented by mass transfer rate as a function of orbital period, reproduced from Nelemans (2005); Nelemans et al. (2010). The white dwarf channel is shown in black, the helium star donor channel in red, and the hydrogen star channel in blue. The non-generate donor CVs and low mass X-ray binaries (LMXB) channel is also included in black.

synchronise. The sensitivity to the synchronisation timescale of the accretor from the start of mass transfer is crucial for the formation of stable AM CVns. Inefficient tidal coupling could lead to a merger of the stellar components. The system parameters have been found to oscillate during the first few orbits before stabilising (Gokhale et al., 2007).
The three evolutionary phases of the white dwarf channel (Deloye et al., 2007a,b) begin with the turn-on phase when the mass transfer rate reaches a maximum as R_2 contracts, and thus the orbital separation/period decreases. In the next phase, R_2 increases adiabatically as the donor loses mass. During the third and longest phase, the donor loses entropy and R_2 decreases until it becomes fully degenerate. This occurs when the mass loss timescale drops below the thermal timescale of the donor.

Helium-star channel: The helium star donor is initially non-degenerate and the mass ratio is required to be $\lesssim 1.2$ (Tutukov and Fedorova, 1989; Ergma and Fedorova, 1990). The orbital separation decreases with angular momentum loss and a disc always forms at the onset of mass transfer. When the mass transfer rate peaks at $P_{\rm orb} \sim 10$ min and the mass of the helium star is below $\sim 0.2\,M_\odot$, it becomes semi-degenerate and thereafter the orbital separation increases as mass transfer decreases. The degeneracy increases until the orbital period reaches $\sim 35-40$ min and the donor may become a fully degenerate hybrid WD if the mass transfer timescale exceeds the thermal timescale of the donor. At this stage, the system joins the WD channel.
During the early stage of mass transfer, the high accretion rate of helium onto the WD may lead to the destruction of the system in a supernova or a non-destructive nova (Bildsten et al., 2007). During this rapid accretion phase of the helium channel, the mass transfer rates of $> 10^{-7}\,M_\odot\,{\rm yr}^{-1}$ onto a carbon-oxygen WD, may cause the nova ignition(s) of the helium shell on the WD (Taam, 1980). The final outburst as the accretion rate decreases is the most violent, given the amount of accumulated helium by

the end of the outburst series (Fujimoto and Sugimoto, 1982; Bildsten et al., 2007). For the white-dwarf channel, maximum mass transfer rates of $\sim 10^{-6}\,M_\odot\,yr^{-1}$ ignite helium flashes/novae on the surface of the accreting WD (Tutukov and Yungelson, 1996). Another cause for helium nova eruptions on $\sim 0.6-1\,M_\odot$ WD accretors is the accumulation of $\sim 0.15-0.3\,M_\odot$ of helium (Iben and Tutukov, 1987, 1991).

Hydrogen-star channel: This channel is thought to only undergo one CE phase (see Fig. 1.9). The minimum orbital period, before it evolves to longer periods, is between ~ 10 and 80 min (Tutukov et al., 1985; Podsiadlowski et al., 2003). Unlike the other two channels, the donor still contains a low percentage of hydrogen in the envelope before it reaches the minimum period. The degeneracy and helium content increase as the system evolves. It was shown that angular momentum loss via gravitational wave radiation and (modified) magnetic breaking may only lead to the formation of hydrogen-rich AM CVns under very specific conditions (van der Sluys et al., 2005), thus Nelemans et al. (2004) showed that hydrogen-rich donor stars are expected to be ~ 50 times less common in our Galaxy than the WD and helium donors combined. The minimum orbital period, before it evolves to longer periods, is between ~ 10 and ~ 80 min (Tutukov et al., 1985; Podsiadlowski et al., 2003). Unlike the other two channels, the donor still contains a low percentage of hydrogen in the envelope before it reaches the minimum period. The degeneracy and helium content increase as the system evolves. It was shown that angular momentum loss via gravitational wave radiation and (modified) magnetic breaking may only lead to the formation of hydrogen-rich AM CVns under very specific conditions (van der Sluys et al., 2005), thus Nelemans et al. (2004) showed that hydrogen-rich donor stars are expected to be ~ 50 times less common in our Galaxy than the WD and helium donors combined.

1.2.2 *Direct impact accretion*

HM Cnc (Israel et al., 1999; Burwitz and Reinsch, 2001; Ramsay and Cropper, 2002b) and V407 Vul (Motch and Haberl, 1995; Motch et al., 1996; Cropper et al., 1998) have the shortest observed AM CVn periods with $P_{\rm orb} = 5.36$ min and 9.49 min, respectively. During the initial years of discovery, different models were proposed to explain their behaviour including intermediate polar (Motch and Haberl, 1995; Israel et al., 1999), polar (Cropper et al., 1998), unipolar inductor (Wu et al., 2002; Dall'Osso et al., 2007) models. The direct impact model (Marsh and Steeghs, 2002) best explained the observed data (Roelofs et al., 2010).

Marsh and Steeghs (2002) proposed that direct impact accretion occurs under the condition that the ballistic stream of mass from the centre of mass of the accretor is shorter than the radius of the accretor, as is the case with Algol binary stars with a main sequence star accretor. It was suggested that these direct-impact AM CVn stars are white dwarf analogues of Algol binaries.

ES Cet (Warner and Woudt, 2002) has an orbital period of $P_{\rm orb} = 10.33$ min, less than a min longer than V407 Vul, although it accretes via a disc and does not display the same observed features as the other two shorter period systems (e.g. the X-ray light curves trail behind the photometric light curve by 0.2 cycles and soft X-rays are detectable for only half of a cycle giving it an on/off X-ray profile). Recent observations of ES Cet

by Bąkowska et al. (2021) confirm accretion via a disc and show evidence for eclipses making ES Cet an eclipsing AM CVn star with the shortest orbital period.

1.2.3 *Chemical composition*

The transferred mass from the donor is stripped from the outer layers inwards. The chemical composition of the disc thus reveals the nature of the donor star, possibly indicating the AM CVn channel and its evolutionary status. The three channels show different spectral properties and CNO abundance ratios. The abundance patterns of the white dwarf channel are an indicator of the mass of the main-sequence progenitor. The abundance patterns for the helium star channel reflect the binary period after the common envelope phase. The presence of hydrogen indicates that it most likely belongs to the hydrogen star channel.

The N/C ratio can help differentiate between the white dwarf and helium star channels. For a helium star, Nelemans et al. (2010) found that the N/C ratio is significantly lower than that of helium white dwarfs, which is usually ~ 100. N/O and N/He ratios further reveal information on the mass of the main sequence progenitor of the white dwarf and helium star.

The abundances in the helium star channel vary throughout the evolution of the binary and are dependent on the amount of helium in the donor star at the start of mass transfer. In the early stages, the abundances are similar to helium white dwarfs, with lower N/C ratios because of their higher initial mass. This ratio decreases as more helium is depleted in the core (Nelemans et al., 2010). If the mass transfer begins when helium in the core is exhausted then the donor may later transfer carbon-oxygen mixture (Ergma and Fedorova, 1990).

1.2.4 *Long-term outbursting behaviour*

Unlike their hydrogen accreting analogues, AM CVn stars evolve to longer orbital periods. As the (semi-)degenerate donor star loses mass, the donor radius increases, which increases the orbital separation. Observational evidence suggests that AM CVns can be divided into four different groups according to accretion rate and disc properties (Bildsten et al., 2006; Ramsay et al., 2012; Levitan et al., 2015):

1. Direct impact systems, found at the lowest AM CVn orbital periods, accrete directly onto the surface of the accretor without the presence of a disc.
2. High state systems within $10 \lesssim P_{\rm orb} \lesssim 20$ min are known to be in continuous high or outburst state with high mass transfer rates. These systems are thermally stable but tidally unstable. Their spectra, dominated by an optically thick disc, generally show broad helium absorption lines with a hot blue continuum.
3. Low state systems are found at $P_{\rm orb} \gtrsim 40$ min. These long-period systems are known to be in permanent low state or quiescence with optically thin discs. They have low mass transfer rates. These systems are tidally and thermally stable. Low state spectra display helium emission lines with a hot blue continuum.
4. Outbursting systems are analogous to hydrogen DN, at orbital periods between high and low state AM CVns. Their discs are thermally unstable and exhibit (super)outbursts. As they transition from outburst to quiescence, their spectra

change from absorption to emission lines, briefly displaying an almost continuous spectrum.

Smak (1983) and Tsugawa and Osaki (1997) predicted that outbursting systems would lie between ∼ 20 and ∼ 40 min. Observational studies have been done on samples of outbursting AM CVn binaries by Ramsay et al. (2012) and Levitan et al. (2015) where they found that known outbursting AM CVns lie at orbital periods $24 \lesssim P_{\rm orb} \lesssim 44$ min (see Fig. 1.11). They further subdivided the outbursting systems into three groups according to outburst behaviour. Those with $P_{\rm orb} \lesssim 28$ min, which have just transitioned from stable high states, spend most of their time in high state, with semi-regular short (1-2 d) outbursts during the short quiescent intervals. Systems with $28 \lesssim P_{\rm orb} \lesssim 37$ min are predominantly in quiescence with regular (super)outburst behaviour. Longer period systems with $37 \lesssim P_{\rm orb} \lesssim 44$ min experience rare outbursts with short superoutburst duration (15-20 d) compared to shorter period outbursting systems. The transitions between the outburst behaviour as a function of $P_{\rm orb}$ appear to be gradual. The outburst recurrence time was found to be increasing and the outburst amplitudes decreasing by the following relations (Levitan et al., 2015):

$$P_{\rm recur} = (1.53 \times 10^{-9} P_{\rm orb}^{7.35}) + 24.7 \tag{1.11}$$

$$\Delta{\rm mag} = 0.13\, P_{\rm orb} - 0.16 \tag{1.12}$$

where $P_{\rm orb}$, in minutes, gives $P_{\rm recur}$ in days.

More recently, the division between outbursting and stable low state AM CVn stars is becoming increasingly vague as more outbursting AM CVn systems with orbital periods much larger than expected are being discovered, e.g. Gaaia14aae ($P_{\rm orb}$ =49.7 min, Campbell et al., 2015; Green et al., 2018b), MOA 2010-BLG-087 ($P_{\rm orb} \sim 50$ min, Green et al., 2020), SDSSJ0807+4852 ($P_{\rm SH}$ =53.3 min, Kong et al., 2018; Kupfer et al., 2019) and ASASSN-21au ($P_{\rm orb} \sim 58$ min, Isogai et al., 2021; Rivera Sandoval et al., 2022).

1.2.5 *Helium accretion discs*

The small size of helium-rich discs significantly affects the physical processes taking place. Outbursting AM CVns experience different types of high mass transfer rates. The outbursts analogous to hydrogen-rich DN outbursts have a short 1-2 day duration. These outbursts could easily be missed by short cadence surveys. More common AM CVn outbursts have longer durations and extended high state intervals. Warner (1995b) proposed thermal instabilities in such small discs cannot sustain the high states at shorter periods over such long durations. Instead he suggested that they exhibit VY Scl-type behaviour and are most likely powered by irradiation of the donor star by the close disc.

The standard DIM (Osaki, 1989; Tsugawa and Osaki, 1997) does well in explaining DN outbursts in hydrogen-rich CVs but fails in explaining the dominant superoutbursts in AM CVn stars. Modified versions of the DIM were proposed to account for superoutbursts (Lasota et al., 2008; Kotko et al., 2010). The tidal-thermal instability (TTI) model (Osaki, 1989) is more successful in modelling superoutbursts but does not completely agree with observations (e.g. Schreiber et al., 2004; Buat-Ménard and Hameury, 2002; Smak, 2009a,b,d). Another model proposed to explain superoutbursts

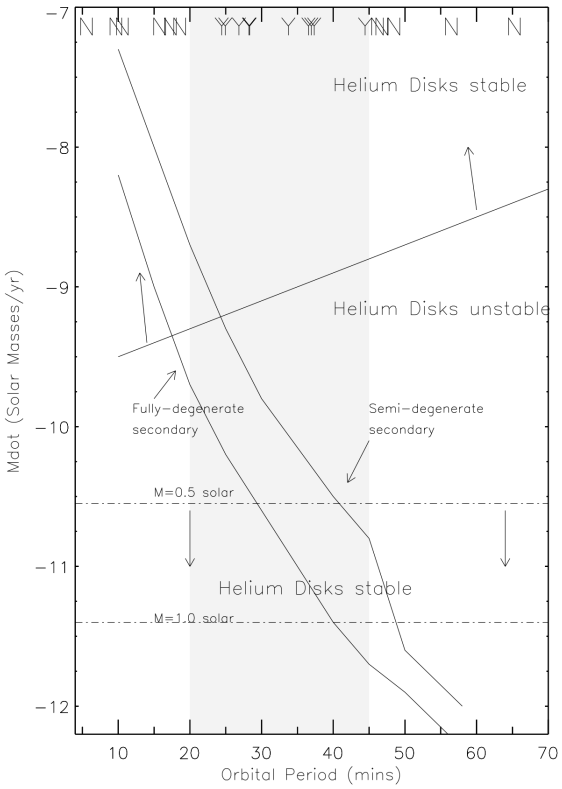

FIGURE 1.11 – Figure showing the stable and unstable regions of helium AM CVns reproduced from Ramsay et al. (2012), which include the updated models of the orbital period as a function of mass transfer rate derived by Tsugawa and Osaki (1997) for fully and semi-degenerate AM CVns. Above the solid straight line is the hot stable region. The cool stable region is situated below the dashed straight lines depending on the mass of the donor. Between the straight lines is the unstable region.

is the enhanced mass-transfer (EMT) model which appears to best support the data (Kotko et al., 2012; Smak, 2013; Rivera Sandoval et al., 2021). A possible explanation for the mass enhancement is the irradiation of the donor star by the nearby accretion disc, considering the close proximity of the system components (Warner, 1995b, 2015). Given that the long-term behaviour of AM CVns is dominated by superoutbursts, it is important to understand the physical processes powering these extended outbursts. The chemical composition, smaller discs, short orbital periods and low mass ratios of helium discs contribute to the differences between helium and hydrogen accretion.

The critical temperature of a helium-rich disc is the temperature at which helium ionisation/recombination occurs. The temperature for the ionisation of the first electron of neutral helium is $T_{\mathrm{He\,II}} \sim 28\,500\,\mathrm{K}$. which is twice that of hydrogen. The effective critical temperature of a hot steady-state pure helium accretion disc is above (Lasota et al., 2008)

$$T_{\mathrm{eff,crit,hot}} = 13100\alpha_{0.1}^{-0.01} r_{10}^{-0.08} M_1^{0.03}\mathrm{K}. \tag{1.13}$$

The effective temperature of a cool steady-state pure helium accretion disc is below

$$T_{\mathrm{eff,crit,cold}} = 9700\alpha_{0.1}^{-0.01} r_{10}^{-0.09} M_1^{0.03}\mathrm{K}, \tag{1.14}$$

where $\alpha_{0.1} = \alpha/0.1$ and $r_{10} = r/10^{10}$ cm.

The ionisation temperature for the second helium electron is $T_{\mathrm{He\,III}} \sim 63\,000$ K. The presence of two electrons allows for multiple combinations of states between ionised and excited electrons. The high temperatures in helium discs also ionise other elements, such as carbon and oxygen, which increases free electrons thus influencing the opacity in the disc. These additional electrons affect the cooling and heating mechanisms in helium discs (Kotko et al., 2012).

The mass accretion rate above (below) which a hot (cool) pure stable helium disc exists is (Lasota et al., 2008)

$$\dot{M}_{\mathrm{crit,hot}} = 1.01 \times 10^{17} \alpha_{0.1}^{-0.05} r_{10}^{2.68} M_1^{-0.89}\,\mathrm{g\,s^{-1}} \tag{1.15}$$

and

$$\dot{M}_{\mathrm{crit,cold}} = 3.17 \times 10^{16} \alpha_{0.1}^{-0.02} r_{10}^{2.66} M_1^{-0.89}\,\mathrm{g\,s^{-1}}. \tag{1.16}$$

For stable equilibrium, these should apply throughout the entire disc. $\dot{M}_{\mathrm{crit,cool}}$ is 12 times higher for helium discs than hydrogen-rich accretion discs.

1.3 MAGNETIC CATACLYSMIC VARIABLES

Magnetic cataclysmic variables (mCVs) have magnetic fields strong enough to affect the trajectory of the stream of mass falling towards the accretor. Just as the non-magnetic counterpart, magnetic CVs are usually composed of a white dwarf accretor and a low mass main sequence donor star. With a range of observed magnetic field strengths, mCVs are divided into two groups known as polars and intermediate polars. Polars have strong observed magnetic field strengths of $\sim 7 - 230$ MG (Ferrario et al., 1995; Schmidt et al., 1996) which prevent disc formation as mass from the donor star is directed out of the orbital plane and channelled along the magnetic field lines. Accretion onto the WD takes place near the magnetic poles. With observed orbital periods ranging from ~ 80 to 480 min, the magnetic moment of the white dwarf ($\mu_1 \gtrsim 10^{34}\,\mathrm{G\,m^3}$) in polars is high enough to force the spin period into synchronous rotation with the orbital period, with some exceptions known as asynchronous polars, although the degree of asynchronism in these is typically only a few percent. Intermediate polars (IPs) have magnetic field strengths between non-magnetic CVs and polars, that are too weak to prevent the formation of an accretion disc, but strong enough to truncate the inner accretion disc and direct the accreted material along the magnetic field lines (see Fig. 1.12). See Mukai (1988), Cropper (1990) and Warner (1995a) for full reviews.

A standard accretion model for polars (e.g. Hōshi, 1973; Lamb and Masters, 1979) can be described as uniform accretion and densities in a vertically extended cylindrical accretion column and surrounding region, located at the magnetic poles. While the fundamental principles of the standard accretion model remain valid, there were inconsistencies that were later discovered with the increased number of known mCVs and multi-wavelength observations. An inhomogeneous accretion model (e.g. Stockman and Lubenow, 1987), adapted from the standard model, was developed to better fit the observational data. The inhomogeneous model presents an accretion region with a linearly extended accretion arc, slightly offset from the magnetic pole(s), and non-uniform

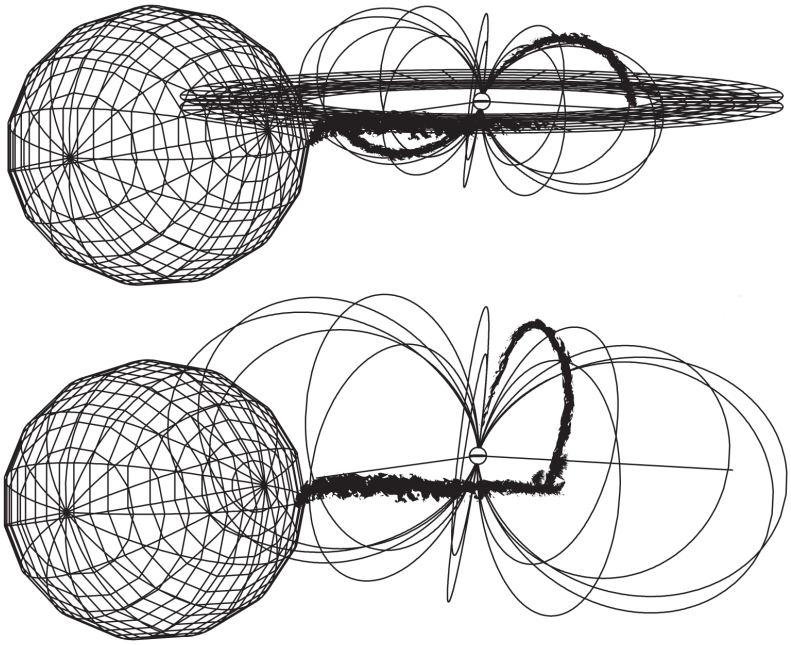

FIGURE 1.12 – Schematic diagrams from Cropper et al. (2002) of magnetic cataclysmic variables displaying accretion via strong magnetic fields. Single pole accretion of an intermediate polar is displayed at the top and a polar at the bottom.

densities and emission rates. Some observational considerations of the inhomogeneous accretion model include soft X-ray excess (e.g. Kuijpers and Pringle, 1982, see § 1.3.2), non-radial and two-pole accretion (e.g. Cropper, 1989; Piirola et al., 1990), cyclotron emission peaking at red and infrared wavelengths (instead of ultraviolet) (e.g. Wickramasinghe and Ferrario, 1988; Wu and Chanmugam, 1988), quasi-periodic oscillations (e.g. Tuohy et al., 1981; Patterson et al., 1981) and no (or weak) correlation between the flickering of hard and soft X-rays (e.g. Szkody et al., 1980; Watson et al., 1987)

1.3.1 *Magnetic accretion*

If the radius of the magnetosphere, where the magnetic pressure of the field lines is close to the ram pressure and gas pressure of the stream (r_μ), reaches or exceeds the radius of the WD accretor's Roche lobe, i.e. close to the distance to the inner Lagrangian point ($R_{1,L1}$), the stream of mass attaches to the magnetic field lines of the WD as it leaves the L1 point. If $r_\mu < R_{1,L1}$, then the stream follows the same ballistic trajectory as a non-magnetic CV and is only affected when it reaches r_p, where the magnetic pressure of the field lines exceeds the thermal pressure of the stream (which is less than r_μ). From r_p, only the shape and density of the stream are affected while it continues on the same trajectory. Eventually, the subsonic stream is unable to adjust to the increasing magnetic pressure, breaking it up into large fragments. Multiple processes then break the large fragments into smaller blobs before reaching r_μ. At r_μ the small blobs are threaded onto the magnetic field lines while the larger blobs manage to penetrate even further before being threaded as well. The trajectory of the stream leaves the orbital plane as it spirals along the magnetic field lines towards the surface of the accretor, increasing in velocity.

(Warner, 1995a)

The now supersonic stream falls into the atmosphere of the accretor and forms a shock front. The heated gas ahead of the front expands and pushes the shock further away from the accretor. The equilibrium height of the column is determined by the efficiency of the gas to cool to the temperature of the accretor and transition from supersonic (before the shock) to subsonic velocities (below the shock to the photosphere of the WD). The velocity decreases, and density increases, by a factor of four while being cooled by three mechanisms, namely bremsstrahlung emission, cyclotron emission and Compton cooling. (Warner, 1995a)

Bremsstrahlung emission is radiated as hard X-rays. These hard X-rays are emitted essentially isotropically, so about half the hard X-ray flux is intercepted by the WD. While some that flux is reflected, the rest is absorbed and reprocessed within the WD, emitting approximately as a hot black body at soft X-ray and EUV wavelengths. Cyclotron emission, which is produced by electrons in the stream spiralling along the magnetic field lines, is radiated mostly in optical to IR wavelengths. At lower cyclotron harmonics, the emission is optically thick and becomes optically thin as the harmonic number increases. Higher energy electrons peak at higher harmonics. (Warner, 1995a)

Three cooling regions are identified in the $B - \log L/f$ plane where L is the local accretion luminosity and f is the fraction of accretion area on the WD surface shown in Fig. 1.13 (Lamb and Masters, 1979). Bremsstrahlung dominates in the first zone where the ions and electrons have similar temperatures and the plasma is treated as a single fluid. In the second and third zones, cyclotron cooling dominates. The electrons are cooled more effectively than the ions in zone two so treated as a two-temperature fluid. In the third zone, cyclotron cooling is even more effective at cooling the ions that velocity distribution becomes non-Maxwellian (non-hydrodynamic) and the shock structure collapses (Masters, 1978; Lamb and Masters, 1979).

1.3.2 *Observations*

The spectra of high accretion rate magnetic CVs typically display prominent Balmer, He I and He II emission lines with a continuum that rises towards longer wavelengths. A characteristic spectral feature is a strong He II 4686 line, comparable with that of H_β, arising from the accretion column (Mukai, 1988; Warner, 1995a, p. 372).

The emission lines of high accretion rate magnetic CVs seen in high-resolution spectra typically consist of multiple components (Cowley and Crampton, 1977). These include a broad base component associated with the accretion column; a narrow component thought to originate from the surface of the donor star (which may have been irradiated by the accretor); a medium-velocity component is thought to arise along the stream further away from the accretor and a high-velocity component from the curved ballistic part of the stream (Rosen et al., 1987; Schwope et al., 1997a; Gänsicke et al., 1998). The spectral contributions from the donor star, consisting of both absorption and emission lines, are more visible during low accretion rates.

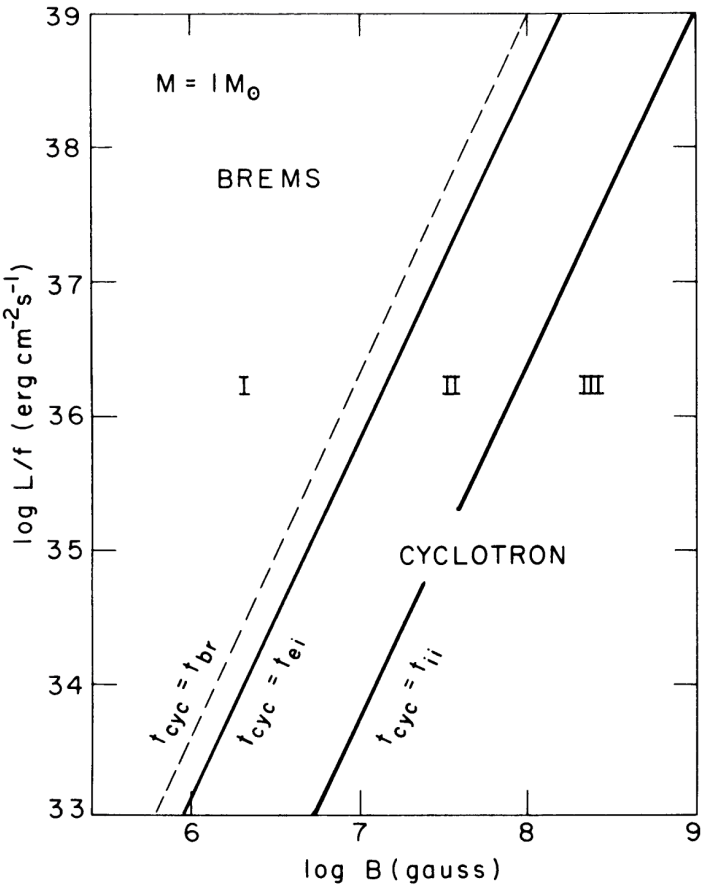

FIGURE 1.13 – The magnetic field – specific luminosity plane for a $1M_{\odot}$ WD from Lamb and Masters (1979). Three cooling regions of the $B - \log L/f$ plane: Region I is dominated by bremsstrahlung cooling; Region II and III are dominated by cyclotron radiation; In region III, the cyclotron radiation is so effective that the shock collapses.

Optical line profiles, varying over the orbital cycle, commonly have asymmetric peaks with steeper declines which indicates an extended emission region along one direction. This further supports the inhomogeneous accretion model (e.g. Schwope et al., 2003; Thomas et al., 2012; Oliveira et al., 2020).

X-ray and optical light curves are known to display flickering and oscillations on timescales of sub-seconds to minutes. A strong correlation between the optical and hard X-ray variations indicates a shared (accretion) region of origin, while soft X-rays usually have little or no correlation with other wavelengths (e.g. Szkody et al., 1980; Stella et al., 1986; Beuermann et al., 1987; Bernardini et al., 2014). Hard and soft X-rays originate from the main accreting pole but soft X-rays are mostly detected from the second pole and their light curve profiles are usually out of phase with each other. The soft X-ray profiles may vary between different epochs of various time scales and have been observed to switch between phases for some two/multi-pole systems (Heise et al., 1985; Schwope et al., 2020). The phase reversal has little to no effect on the optical light curve (Mazeh et al., 1986).

Multi-wavelength light curves vary for observed one- and two-pole accreting systems. Many two-pole systems have magnetic field strengths that differ for each pole (Meggitt and Wickramasinghe, 1989), posing additional challenges for resolving each pole when both poles are simultaneously in view. Some systems have been identified as likely quadrupole magnetic systems, with even more complexities (e.g. Cropper, 1989; Schwope et al., 1995; Beuermann et al., 2007, 2020).

For a two-pole system, the observationally dominant pole accretes more gas but has the weaker magnetic field, with about half the strength of the stronger pole (e.g. Ferrario et al., 1989; Wickramasinghe et al., 1989; Schwope et al., 1990; Reimers and Hagen, 2000; Schwarz et al., 2002). This magnetically weaker pole points most towards the donor star (Wickramasinghe and Wu, 1991) and is usually closest to the orbital plane. At times, the emission from the magnetically stronger (fainter) pole is visible from the far-red to infrared, however, it may not be detected at other wavelengths.

The blackbody, bremsstrahlung and cyclotron energy balance equation is

$$\frac{L_{\rm BB}}{(L_{\rm brem}+L_{\rm cyc})} = \frac{1-\alpha_x}{1+\alpha_x} \approx 0.56 \tag{1.17}$$

where α_x is the albedo and $L_{\rm BB}$, $L_{\rm brem}$ and $L_{\rm cyc}$ are the blackbody, bremsstrahlung and cyclotron luminosities, respectively. Early observations appeared not to be in agreement with Eq. 1.17 as the observed soft X-rays usually exceeded the expected value, known as the soft X-ray 'puzzle' (e.g. Lamb, 1985). Kuijpers and Pringle (1982) suggested that the additional soft X-rays come from large dense blobs in the accretion column which penetrate the donor's atmosphere. They argued that the resulting shock (hard X-rays) is thermalised within the atmosphere and re-radiated as a blackbody-like component (soft X-rays). Ramsay et al. (1994) and Beuermann and Schwope (1994) showed that the weakest fields have little or no soft X-ray excess whereas stronger magnetic fields produce the right conditions for the presence of denser blobs in the accretion region. Since 2004, XMM-Newton satellite[2] has found an increasing number of polars with soft X-ray components well below the expected level (e.g. Ramsay and Cropper, 2004b, see § 2.2.1), resembling intermediate polar X-ray spectra. When polars transition to lower accretion rates, they may be observed as hard X-ray sources as the temperature of the heated soft X-ray region decreases (Ramsay et al., 2004; Schwope et al., 2020).

The magnetic field strength and temperature of the donor star can be approximately calculated from the observed cyclotron spectrum by fitting the spacing of cyclotron harmonics. These harmonic features are not always visible and vary throughout the orbital cycle as the visibility of the accretion region varies (e.g. Schwope and Beuermann, 1990; Burwitz et al., 1996; Thomas et al., 2012; Hakala et al., 2022). In theory, the requirements for observing cyclotron humps in a spectrum are high signal-to-noise and a wide wavelength coverage (e.g. Cropper, 1986, 1990), however, systems with low field strengths may have spectra with blended cyclotron harmonics that appear as a single hump continuum (Schwope et al., 1995; Fuchs et al., 2016; Littlefield et al., 2018).

[2] https://www.cosmos.esa.int/web/xmm-newton

The spectra of CVs with stronger magnetic fields may display Balmer lines with detectable Zeeman splitting originating from different sources (Schmidt et al., 1996, 2001), which can also be used to determine the magnetic field strength. Balmer emission lines from the halo surrounding the accretion region display Zeeman splitting during high accretion state (Achilleos et al., 1992; Schwope et al., 1995). During low accretion states, the Zeeman splitting from Balmer absorption lines arise from the WD photosphere (Wickramasinghe and Martin, 1985; Ferrario et al., 1992; Schwope et al., 1995). The magnetic field strength determined through Zeeman features from the accretion halo is comparable to the field strength determined by cyclotron harmonics. However, these differ from the magnetic field strength derived from photospheric Zeeman lines because they are detected from different locations.

1.3.3 *Polarisation*

As the name suggests, polars (and intermediate polars) are polarised in optical to near-infrared wavelengths. The radiation from spiralling of the electrons along the ordered magnetic field lines, producing cyclotron emission, is polarised linearly or circularly, depending on the orientation of the accretion column along the line of sight. The strengths of the polarisation vary periodically according to the rotation of the white dwarf. Linear polarisation and cyclotron radiation are observed with maximum variations when the magnetic field lines are oriented perpendicularly to the line of sight. On the other hand, maximum variations from circular polarisation are seen when viewing along (i.e. parallel to) the magnetic field lines. In one orbital cycle, the linear polarisation peaks during the bright phase and circular polarisation peaks twice, just before and after the bright phase, coinciding with the minimum viewing angles.

In some rare cases, e.g. AR UMa (Schmidt et al., 1996) and V884 Her (Schmidt et al., 2001), emission lines from polarisation spectra can be used to determine the sources of emission (Schmidt et al., 1996, 2001) but such spectra can only be obtained for systems with strong magnetic fields. The polarisation spectra have revealed that most of the emission from an mCV mostly originates from the accretion region and the threading region (Ferrario et al., 2002).

1.3.4 *Low states in magnetic CVs*

MCVs are known to undergo changes in mass transfer rates. Higher mass transfer rates are referred to as “high state" and similarly lower mass transfer rates are called “low state". These states exist mainly in magnetic CVs but can be seen in some non-magnetic systems. High states are driven by normal or enhanced Roche-lobe overflow and low states are thought to be due to a significant decrease in the amount of mass being transferred through the L1 point. “Off” states, the cessation of mass transfer, are also categorised as low states. During low states, variations in the measured flux can still be seen while “Off” states fluxes are not variable.

It is easier to determine when mass transfer ceases in disc-less CVs because they do not have a reserve of material stored in discs which could continue to drain into the WD after mass transfer is disrupted. Discs are also able to change the mass accretion rate which could be misleading. This makes polars ideal for studying individual stellar

components. Numerous studies suggest that the magnetic activity on the donor star is responsible for the low states. It has been thought that low states occur when star spots on the surface of the donor star pass through the inner Lagrangian L1 point. Instead, accretion occurs via stellar wind at a rate of $\leq 10^{-12}\,M_{\odot}\ yr^{-1}$ (e.g. Hessman et al., 2000). The star-spot model by Livio and Pringle (1994) is the most accepted explanation for low states.

The spectra of some low state mCVs may differ from those of high state mCVs, apart from the obvious reduced flux. The Hα emission line was found to contain two satellite components (Kafka et al., 2008, 2010). Doppler tomography indicates that one or both of the satellite components may arise from magnetic loop "prominence-like" material on the surface of the donor star similar to those found in rapidly rotating single stars (Collier Cameron et al., 1990; Collier Cameron and Woods, 1992). These slingshot prominences result from magnetic activity on the donor star and once they reach the L1 ridge line, they get pulled towards the WD and matter flowing through the field lines collects at the tip of the loop. The clump of matter, situated between both stars, gets illuminated by the stars and produces emission (Steeghs et al., 1996; Hessman, 2000).

It is thought that these structures identified in binaries are stabilised and kept in place longer than those in single stars by the binary potential (Steeghs et al., 1996) and/or the interaction of the magnetic field lines on both stars (Kafka et al., 2010). Hessman et al. (2000) showed, through modelling, that the surface of the AM Her donor (at least at/around the L1 point) would need to be very spotted in order to produce its long-term light curve (Fig. 1.14). It is possible that the spottiness on the donor star is not uniform across the surface but that the Roche potential attracts prominences from other locations on the star.

A large X-ray study revealed that almost 50 % of polars were found in a low state, which suggests that they spend about half of the time in high/low state (Ramsay and Cropper, 2004a; Ramsay et al., 2004). It was also found that there was no correlation between the orbital period and the accretion state, although those which are "off" are biased towards shorter orbital periods. Soft X-rays, often detected in high state systems, were not found in the low state systems of the study. The reprocessed radiation is thought to be cooler than during the high state implying that it may be radiating at UV (or extreme UV) wavelengths (Ramsay and Cropper, 2002a,b). This is supported by UV observations of mCVs in their low state (Ramsay et al., 2004)

A small fraction of known polars remain in extended low state and are termed pre-polars, or low accretion rate polars (LARP, Schwope et al., 2002b; Schmidt et al., 2005b). They are believed be detached post-common-envelope binaries in the phase before mass transfer via Roche lobe overflow (Webbink and Wickramasinghe, 2005). In addition to being faint with no long-term photometric brightening, other observational identifiers include strong cyclotron humps, weak X-ray emission, and optical and near-infrared emission from the donor star (Webbink and Wickramasinghe, 2005).

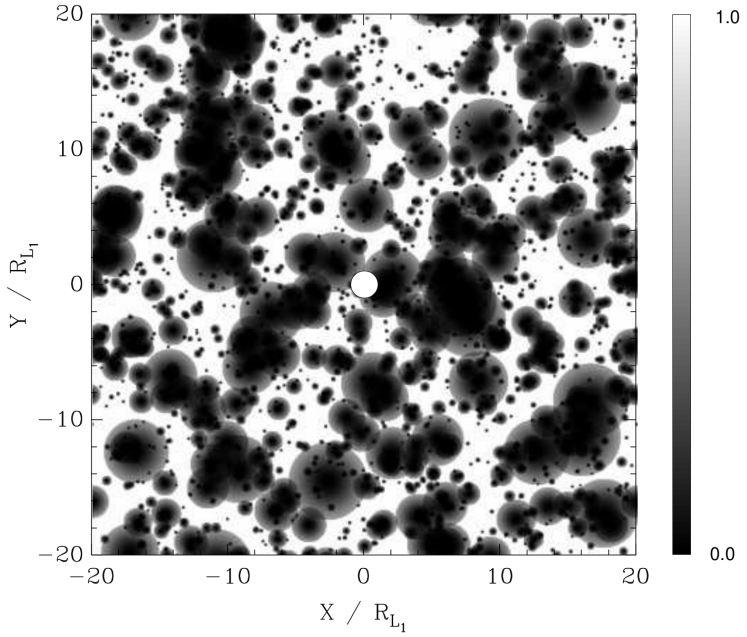

FIGURE 1.14 – A simulated image of the surface of the donor star in AM Her, produced from Hessman et al. (2000).

1.4 TRANSIENT AND SYNOPTIC SURVEYS

In this section, I describe different optical surveys which have made a significant contribution to the discovery of CV, particularly AM CVn stars and magnetic CVs which are the focus of my work. The discoveries of these CVs are summarised in §2.1.1, 2.1.2 and 2.2.1.

1.4.1 *Catalina Real-time Transient Survey*

The Catalina Real-time Transient Survey (CRTS; Drake et al., 2009) began in 2004 as the smaller Catalina Sky Survey, detecting near-Earth objects (NEOs), including asteroids and comets. As part of NASA's Near-Earth Objects Observations Program, the CSS made a significant contribution to the number of known NEOs at the time. It is only from November 2007 that it began processing its data for the detection and characterisation of transients until 2023. The CRTS consisted of a combination of three sub-surveys, namely the Catalina Sky Survey (CSS), Mt. Lemmon Survey (MLS), both in the northern hemisphere, and the Siding Spring Survey (SSS), in the south. Each survey used a wide-field telescope, equipped with an unfiltered 4000×4000 pixel CCD. CSS used a 0.68 m telescope in USA (Mt. Bigelow, Arizona), with the widest field of view of 8.2 deg^2 and sky coverage to -80°declination with 30 s exposures. MLS used a 1.5 m telescope in USA (Arizona). With the smallest field of view of 1.1 deg^2, it took 30-40 s exposures and only covered the section along the ecliptic of ±10°. MLS detected fainter objects than the other surveys with magnitude limits of V=21.5 for MLS, V=19 for SSS, V=19.5 for CSS. SSS, discontinued in July 2014, used a 0.5 m telescope in Australia (Siding Spring) with 4.0 deg^2 field of view. SSS surveyed the sky at declinations of -80°≤ Dec ≤0°using

20 s exposures.

The telescopes observed over 21 nights per lunation on clear nights with a cadence of one to four observations per lunation. The whole survey covered a total of $\sim 33\,000\,\mathrm{deg}^2$ of sky between -75 °and +65 °declination, excluding the densely populated Galactic plane. On average, each observation consisted of four images taken ten minutes apart over 30 min, which filtered out asteroids and artefacts, although some artefacts still manage to get through the filtering process (Mahabal et al., 2011). The latest observations were compared with older catalogues of the same field by co-adding at least 20 past images to detect differences in brightness above a threshold. Co-added images have a higher signal-to-noise ratio than a single constituent image. Additionally, higher resolution catalogues from other surveys (e.g. Palomar-Quest survey and Sloan Digital Sky Survey) were used as well. Alternatively, a high signal-to-noise template image was used for image differencing (Drake et al., 2009). Objects were identified as transients if they differ in magnitude by ≥ 0.65 from the co-added image and $\geq 3\sigma$ flux difference within the CRTS light curve (Drake et al., 2014; Coppejans et al., 2016b). This threshold was changed from the original selection criteria of ≥ 2 mag difference (Drake et al., 2009). The identified transient should also have been present in three of the four images per observation. After filtering out artefacts and classifying the candidates, the optical transients cutout images, light curves and the additional metadata were immediately posted online[3] where they are accessible to the public[4].

Approximately 13 % of the CRTS discoveries are CVs (Breedt et al., 2014) and the CV candidates were identified with >95 % accuracy (Drake et al., 2014). CRTS has discovered ~ 1513[5] CV candidates. There is a bias towards CVs that show photometric variations, i.e. outbursting and magnetic CVs. Along with outbursts, eclipses may be visible from light curves. CRTS was strictly a photometric survey but follow-up spectra were obtained (or collected) for 85 candidate CVs by Breedt et al. (2014) and others by Thorstensen and Skinner (2012); Thorstensen et al. (2016); Oliveira et al. (2017, 2020). The CRTS CVs with X-ray counterparts in the ROSAT catalogue were found to be non-magnetic systems (Drake et al., 2014).

The survey, likely, did not detect all outbursts due to its low cadence. The discovery rate of CVs from the CRTS peaked in earlier years, discovering most systems with high accretion rates and frequent outbursts, and then slowly decreased in the later years. Further discoveries of outbursting CVs would likely be those with longer outburst recurrence times (Breedt et al., 2014). The orbital period distribution is more concentrated at shorter periods (fainter systems), as the population uncovered by CRTS traces a fainter distribution than those discovered in previous surveys (Wils et al., 2010; Woudt et al., 2012a; Drake et al., 2014).

1.4.2 *All-Sky Automated Survey for SuperNovae*

The All-Sky Automated Survey for SuperNovae (ASAS-SN; Shappee et al., 2014) is an automated photometric transient survey primarily in search of supernovae and other

[3] http://crts.caltech.edu/
[4] http://nesssi.cacr.caltech.edu/DataRelease/
[5] http://crts.caltech.edu/

bright transients. The programme began in April 2013 with one station in Haleakala Observatory in USA (Hawaii). It currently consists of five stations, the other four located in Cerro Tololo International Observatory (CTIO) in Chile, McDonald Observatory in USA (Texas) and the South African Astronomical Observatory (SAAO) in South Africa. The stations are hosted and run by the Las Cumbres Observatory. Each station consists of four 14 cm Nikon telescopes on a common mount. Each telescope has a field of view of 4.47 $\deg^2$ with the combined overlapping field of view of $\sim 360\,\deg^2$ for all stations. At the start of the programme, the first station covered 10 000 $\deg^2$ per clear night. Currently, all five stations cover 48 000 $\deg^2$ per clear night (Kochanek et al., 2017), with a high cadence of 2-3 days (Holoien et al., 2017). Having multiple sites decreases the effects of bad weather.

ASAS-SN is limited to bright nearby sources of $V \leq 17$ mag. Each observation entails dithering three 90 s exposures. The data are reduced in real-time and candidate transients are selected using an automated difference image pipeline. The data have been made available to the public[6] and, until recently, light curves too[7] (Jayasinghe et al., 2018).

1.4.3 *Sloan Digital Sky Survey*

The Sloan Digital Sky Survey (SDSS; York et al., 2000) is a synoptic survey operating since May 2000 at the Apache Point Observatory (APO) in USA and designed to meet multiple science goals through photometry and multi-object spectroscopy. The survey uses a 2.5 m telescope, with a mosaic CCD and a pair of multi-fibre spectrographs, and a 0.5 m auxiliary telescope for photometric calibration. The imaging camera consists of 30 2048×2048 pixel CCDs (Gunn et al., 1998). Each row contains five CCDs of r', i', u', z', g' filters, respectively. The telescope, with a 3 $\deg^2$ field of view (Gunn et al., 2006), continuously scans the sky in lines that form great circles. Each filter passes through every observed field for 54.1 s (5.7 min altogether). The survey covers mostly the North Galactic Cap and extends to a small area of South Galactic Cap between. The PHOTO pipeline reduces and calibrates the photometric data, then identifies and characterises objects.

The spectroscopic survey is in operation during unfavourable photometric conditions and seeing however the spectroscopic footprint is smaller than the photometric footprint. Some targets are flagged by the pipeline as not suitable for spectroscopic observations. Spectroscopic targets are selected from images which have been identified photometrically and classified as point or extended sources. Different survey projects have different criteria for spectroscopic follow-up regarding colour spaces, redshift, flux, surface brightness and star-galaxy separation (Eisenstein et al., 2001; Strauss et al., 2002; Richards et al., 2002). Spectroscopic targets should be bright enough to yield decent quality spectra.

The science telescope has an intricate system in place for changing between instruments and fibre cartridges in the spectrograph. It is possible to obtain 1000 spectra simultaneously (increased from 640) with a total wavelength coverage of 3600-10 400 Å.

[6] http://www.astronomy.ohio-state.edu/asassn/index.shtml
[7] http://www.astronomy.ohio-state.edu/asassn/transients.html

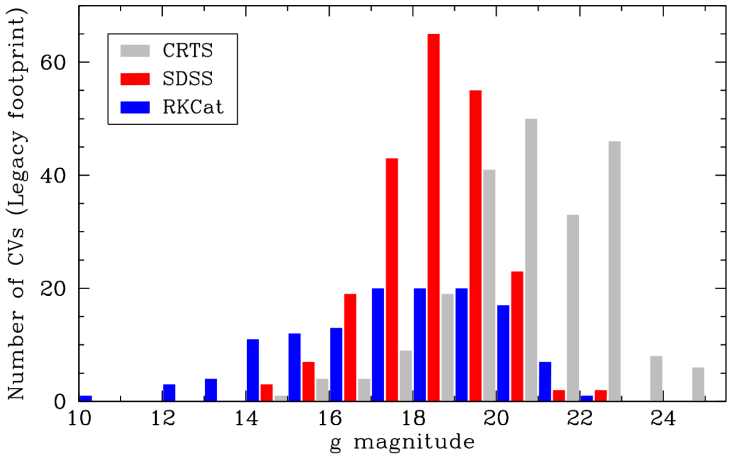

FIGURE 1.15 – The *g – band* magnitude distribution of CVs from SDSS (red), CRTS (grey) and Ritter-Kolb catalogue (blue) reproduced from Breedt et al. (2014).

The spectrograph has a dichroic beam splitter centred at 6000 Å to split the incoming light into the blue and red cameras with a spectral resolution 1560-2270 in the blue channel and 1850-2650 in the red channel (Smee et al., 2013). Each observation consists of a series of 15 min exposures with a combined signal-to-noise ratio per resolution element exceeding a certain threshold depending on the brightness of the targets. This is usually a total of 45 min under good observational conditions (Strauss et al., 2002).

The SDSS-discovered population of CVs was mostly identified through the quasar projects as CVs lie within the same colour spaces as quasars (e.g. Szkody et al., 2002, 2003b, 2004, 2005). Approximately 23% of SDSS CVs were identified through CRTS as well. When comparing the g-band magnitude distribution of SDSS CVs with CRTS CVs, Breedt et al. (2014) found that CRTS CVs were concentrated at fainter magnitudes than SDSS CVs (Fig. 1.15). Many of the SDSS population which were undetected by CRTS did not meet the CRTS transient criteria due to low photometric variability. Thorstensen and Skinner (2012) suggests a bias by the CRTS towards large amplitude outbursting CVs. The SDSS selection criteria are unaffected by low photometric variability. CRTS, on the other hand, is able to detect fainter CVs than SDSS.

1.4.4 *Palomar Transient Factory*

The Palomar Transient Factory (PTF; Rau et al., 2009; Law et al., 2009) saw first light in 2009 and operated until 2016. Situated at the Palomar Observatory in USA (California), this photometric synoptic survey consisted of a 48 inch telescope (P48) for surveying and a 60 inch (P60) telescope for follow-up observations. The P48 camera surveyed the sky, roughly the same sky territory as SDSS, in search of candidate transients. The camera consists of 12 CCDs of 2000×4000 pixels each with field of view of 7.26 deg^2. It observes with the R and SDSS g' filters for optimum detection during full moon and dark-sky conditions, respectively. P48 is limited to magnitudes brighter than R≈20.6 and $g' \approx 21.3$ with 60 s exposures. The P60 camera is a 2048×2048 pixel CCD with g', r', i', z' filters down to magnitudes of $g' \approx 21.4$, $r' \approx 21.2$, $i' \approx 20.9$, $z' \approx 19.8$. A single

120 s exposure was taken for classification.

The allocated time was divided between different survey programmes. The 5-day cadence experiment (5DC) had a five day median cadence, as the name suggests. It is primarily dedicated to finding supernovae although other Galactic and extragalactic transients were detected in the process (Rau et al., 2009). Two 60 s exposures were taken every hour as the sky was scanned. The dynamic cadence project (DyC) had a shorter dynamic cadence, between 1 min and 5 days, targeting fast and/or short-lived transients. The Orion Field project was allocated 40 consecutive nights per year for three years to monitor the Orion star-forming region in search of Jupiter-sized planets orbiting young stars. This project took continuous 30 s exposures for high-precision differential photometry. The Deep Hα Sky survey was a 3π sr sky survey in Hα. Narrowband filters (Hα, H$\alpha_{\rm off}$ and [O III]) are used for observations taking place during full moon for three nights per lunation (Law et al., 2009).

The data from P48 went through two data reduction pipelines. The first was the real-time transient differencing pipeline which subtracts the P48 image from the reference image. Any sources identified as transient candidates were forwarded to the Transients Classification Pipeline which identified and classified transients in real-time. The pipeline classifies candidate transients by identifying several features to determine the most likely science class. This rapid-response pipeline offered basic classification. At the end of each night, the data were sent through the Infrared Processing and Analysis Center (IPAC) pipeline for robust point-source photometry. After the data were sent through the reduction pipelines, the positions of candidate transients were sent to the P60 observation queue. Sources identified as new transient candidates had been detected at least twice by the P48. The P60 observations were used for transient confirmation and further colour classification. The Follow-up Marshal monitored the new transients for further follow-up studies/programmes (Law et al., 2009).

1.4.5 *Zwicky Transient Facility*

The Zwicky Transient Facility (ZTF; Bellm et al., 2019; Graham et al., 2019) is an optical transient/time-domain survey which transitioned from the PTF (and intermediate PFT) in 2017. The ZTF uses the wide-field camera on the Palomar 48 inch telescope (P48) and the integral field unit spectrograph (IFUS) on the Palomar 60 inch telescope (P60). Each field is observed with r and g filters at least 30 min apart within a night (with a brightness limit is $r = 20.7$ for a 60 s exposure). The allocated time is divided between public surveys (40 %), partnership observations (40 %) and Caltech programmes (20 %). The public survey has a general all-sky cadence of, now, two days and only one day in the Galactic plane.

An image differencing pipeline identifies candidate transients and variables which vary in brightness and position. Public alerts are sent, in near-real time to community brokers, namely Arizona-NOAO Temporal Analysis and Response to Events System (ANTARES; Narayan et al., 2018), Automatic Learning for the Rapid Classification of

Events (ALeRCE)[8] Lasair[9], and Las Cumbres Observatory[10]. Nightly alerts are also released by ZTF[11]

1.4.6 *Mobile Astronomical System of TElescope Robots*

The Mobile Astronomical System of TElescope Robots (Master; Lipunov et al., 2010) project is a network of optical telescopes in search of transients and variables. Initially located in Russia, outside Moscow, it has expanded to San Juan (Argentina), Tenerife (Spain), Caucasus (Russia), Ekaterinburg (Russia), Irkutsk (Russia) Blagoveschensk (Russia) and Sutherland (South Africa) (Buckley et al., 2015). The telescopes have dual 40 cm cameras which observe in different modes: aligned cameras with different filters (U, B, V or I) or polarisers (Stokes Q or U); or misaligned cameras which double the sky coverage (Buckley et al., 2015). Each observation consists of consecutive 3×60 s exposures (during grey/bright moon) or 3×180 s exposures (during dark moon). The general cadence for all nodes is 10-15 days with a typical limiting magnitude of 19-20. The observing schedule is prompted by either survey, alert or special mode.

After difference subtraction, objects detected in three consecutive images with at least a 2 magnitude difference (negative and positive) from the reference images and those which are absent from catalogues, are considered potential transients (Kornilov et al., 2012). Objects moving along the same trajectory over repeat observations are considered asteroid candidates.

1.5 STUDY AND THESIS OVERVIEW

My thesis focus is on CV subclasses, namely AM CVn stars and magnetic CVs discovered from optical transient surveys. The increasing number of optical and X-ray surveys has led to a significant increase of both populations. Despite both existing under the CV umbrella, AM CVn stars and magnetic CVs display extensive differences and thus are identified from surveys through various multiple approaches. I study individual AM CVn stars and magnetic CVs selected from optical transient surveys, as well as the larger magnetic CV population. Subsequently, I consider if these significantly differing subclasses can be represented within a common magnetic AM CVn system.

I identify the sample of AM CVns for follow-up observations from the CRTS and ASASSN based on post-outburst alerts and colour selection. The selection criteria used to identify the AM CVns and the magnetic CVs are discussed in Chapter 2. A common feature of magnetic CVs is the transitions between high and low states of mass transfer over timescales of days to years. These variations are identifiable in long-term light curves from CRTS and used, in this work, as a magnetic CV indicator. Exploring the light curves of previously known magnetic CVs reveals additional long-term behavioural patterns which I use to characterise the previously known magnetic CVs. I have developed a set of criteria which can be applied to long-term optical light curves of CVs to identify magnetic CV based on their long-term light curve properties. This has been tested on

[8] http://alerce.science/
[9] https://lasair-ztf.lsst.ac.uk/
[10] https://mars.lco.global/
[11] https://ztf.uw.edu/alerts/public/

CRTS light curves and success rate of the classification is discussed in Chapter 2.

Through further analysis, in Chapter 2, of the long-term CRTS light curves, the periods of the previously known magnetic CVs are determined through Lomb-Scargle periodograms and compared with those found in literature. The orbital phase-folded light curves (using either the original period from the literature or the Lomb-Scargle period) are used to reveal the nature of the orbital modulations and confirm eclipse identifications from the long-term light curves. I present follow-up photometric and spectroscopic data of individual AM CVns in Chapter 3, and magnetic CV candidates in Chapter 4, including descriptions of the observation procedures and data reduction methods. The results and data analyses confirm the nature of the systems.

In Chapter 5, I discuss the contribution of optical transient surveys towards the AM CVn and magnetic CV populations. I compare the sample of AM CVns and magnetic CVs in this work with the entire population in the literature and review my selection criteria, taking into consideration the biases and limitations. Having investigated AM CVns and magnetic CVs as individual CV subclasses, and the long-term photometric properties of the magnetic CV population, I assess the absence of magnetic AM CVn systems, highlighting two (ambiguous) magnetic AM CVn candidates, SDSS J080449.49+161624.8 and Gaia14aae. The thesis summary and future outlook are presented in Chapter 6.

CHAPTER 2

Sample selection and analysis of long-term CRTS light curves

In this Chapter, I summarise the survey discoveries of AM CVn stars and magnetic CVs, specifically polars, and detail my selection criteria for samples to follow up through photometric and/or spectroscopic observations. I analyse the long-term CRTS light curves of previously known polars to better understand the CRTS light curves. I discuss my characterisation of the long-term light curves of previously known polars and use the light curves of known polars and dwarf novae to eliminate dwarf novae and identify new candidate polars from CRTS.

2.1 AM CVn stars

2.1.1 *AM CVn stars from synoptic surveys*

By 2007, six AM CVn systems had been serendipitously discovered from the SDSS (Anderson et al., 2005; Roelofs et al., 2005; Anderson et al., 2008), which was largely targeted at finding quasars and galaxies (Eisenstein et al., 2011). At this time, this was a significant increase to the 12 known AM CVn stars at the time. The SDSS systems were identified by their helium emission line spectra and lack of hydrogen from the large SDSS spectroscopic database.

Using this sample of only six AM CVn systems from the SDSS, Roelofs et al. (2007c) derived observed local space densities of $1 - 3 \times 10^{-6}$ pc^{-3}, while different population synthesis models from Nelemans et al. (2001) and Nelemans et al. (2004) produced a lower limit on the space density of 6×10^{-6} pc^{-3} and an upper limit space density of 3×10^{-5} pc^{-3}. However, Roelofs et al. (2007c) predicted the photometric database of SDSS Phase I should contain at least 50 AM CVn stars down to limiting magnitude

$g = 21$, but with high uncertainties due to the small sample size. The study showed that the previously known homogeneous sample AM CVn stars from SDSS occupied a $(u-g, g-r)$ colour space very close to the blackbody cooling track and above the DA white dwarf model cooling sequence (see Fig. 2.1).

In 2009, the same team reported on their observing programme to uncover more AM CVn stars using multiple telescopes (Roelofs et al., 2009). They selected a photometric sample from SDSS using colour information from nine known helium-emission-line AM CVns with SDSS photometry from the Data Release 6 (DR6) database, six of which were discovered from the SDSS spectroscopic database. The criteria included restrictions in the $u-g$, $g-r$ and $r-i$ colour spaces. To decrease contamination from DA and DB white dwarfs, the portion of the sample parallel to the blackbody track to the left of the black dashed line of the $(u-g, g-r)$ colour space in Fig. 2.1 (left) was removed. Previously identified objects (predominantly in the brighter section of the sample) were also removed. It was expected that the sample of 1523 candidates would contain ~ 40 new emission-line AM CVn stars, assuming a completeness of 90 %. The sample provided a sample for spectroscopic follow-up. One new AM CVn with a peculiar spectrum was reported by Roelofs et al. (2009). The SDSS programme was biased towards longer period systems of $P_{\rm orb} > 35$ min with helium accretion-line spectra and cooler temperatures as observed with the initial six AM CVns upon which the search was based.

Four new AM CVn systems were announced by Rau et al. (2010) as part of the SDSS AM CVn programme. Carter et al. (2013a) added new constraints to the sample selection criteria of the above-mentioned SDSS observing programme in an attempt to increase the AM CVn detection efficiency. The colour space cuts were extended beyond the SDSS bands by cross-matching the SDSS colour-selected sample with *GALEX* catalogue[1] which covers near-ultraviolet (NUV) and far-ultraviolet (FUV) bands. The SDSS sample was also cross-matched with UKIRT (United Kingdom Infrared Telescope) Infrared Deep Sky Survey (UKIDSS) catalogue[2] which images in Y, J, H and K broad-band filters. They were able to separate most DB white dwarfs from the sample using $(\mathrm{NUV}-u, r-i)$ colour space. This updated study, which included the latest SDSS DR7 data, led to an observed space density of $(5 \pm 3) \times 10^{-7}$ pc^{-3} and predicted the SDSS sample contained 18 AM CVns down to magnitude $g = 20.5$.

The constraints were later revised to allow for a larger sample selection after finding two new systems outside of the specified $u-g$ colour space while searching through candidate white dwarf spectra (Carter et al., 2014a). Applying the new constraints to the SDSS DR10 increased the sample selection to 5728 objects. The spectra were visually inspected and no further AM CVns were identified. Two new additional AM CVn systems from the SDSS were serendipitously discovered by a separate team (Anderson et al., 2008). SDSS J120841.96+355025 was selected because of its colour properties during a search for DQ white dwarfs and then identified by its helium emission-line spectrum, while SDSS J204739.4+000840.3 was identified from time-domain imaging data from the SDSS-II supernova survey. Fontaine et al. (2011) later reported a new AM CVn from the SDSS which was initially identified as a potential compact pulsator

[1] https://galex.stsci.edu/GR6/
[2] http://www.ukidss.org/index.html

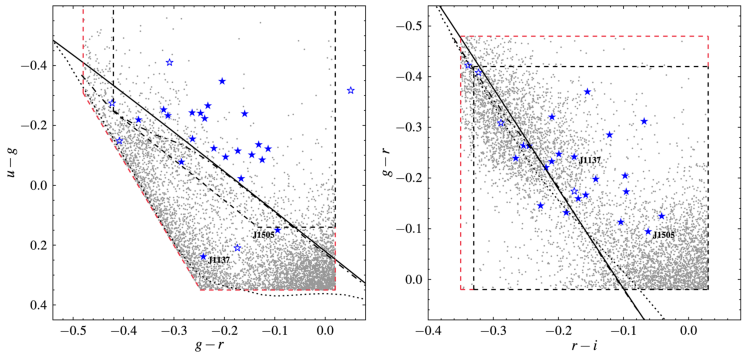

FIGURE 2.1 – Colour space diagrams taken from Carter et al. (2014a). The blue stars represent known AM CVn stars with *ugri* photometry. The grey dots are the sample of candidates from SDSS. The solid line represents the blackbody cooling track; the dotted and dot-dashed lines are the DA and DB model cooling sequences respectively. The black dashed lines are the colour-cuts from Roelofs et al. (2009) and the red dashed lines are the new colour-cuts.

based on its colour. It was then included in a short cadence *Kepler* survey which revealed multi-periodic variations. Further optical spectroscopic data revealed a He-dominated spectrum.

2.1.2 *AM CVn stars from transient surveys*

The PTF had a programme in search of outbursting AM CVn stars, called the PTF AM CVn System Key Project (Levitan et al., 2013). Five[3] AM CVns were initially identified as supernovae via the so-called 'transient' pipeline, which processes data within a few hours using difference imaging photometry for rapid discoveries (Levitan et al., 2011, 2013). Another three AM CVns were identified by searching through light curves for outbursts (Levitan et al., 2013, 2014). The 'photometric' pipeline takes longer to process data more accurately using aperture photometry. Candidates had outbursts with amplitudes of at least 2 mag above the median magnitude and a second measurement at least a day later that was 5σ brighter than the median. Follow-up identification spectra were used to identify the AM CVns. Unlike the SDSS programme, this programme, and others using transient surveys, is biased towards outbursting AM CVns.

Only four AM CVn stars have been discovered from the CRTS. Breedt et al. (2014) spectroscopically followed up 72 CV candidates with the addition of spectra for 13 more CRTS CV candidates obtained from SDSS and Public ESO Spectroscopic Survey for Transient Objects (PESSTO)[4] (Smartt et al., 2015). Amongst those, three were identified as AM CVn stars by their spectra. One of them had already been identified as an AM CVn from PTF (Levitan et al., 2013). The fourth AM CVn was discovered by Aungwerojwit et al. (in prep.). The only other CRTS-discovered AM CVns are part of the work done in this thesis. CXOGBS J175107.6-294037 is an X-ray source identified by *Chandra* in the Galactic Bulge Survey (Jonker et al., 2011, 2014). Optical observations were reported as

[3]Five systems were first identified as AM CVn stars through PTF, although two of those, CSS090219:043518+002941 (Kato et al., 2012b) and CSS110507:163229+351108, were initially discovered as CVs through the CRTS

[4]https://www.pessto.org/

part of the optical catalogue in Wevers et al. (2016a). It was identified as an AM CVn following optical spectroscopic observations (Wevers et al., 2016b).

Since ASAS-SN has been operational, a number of AM CVn stars have been discovered. ASASSN-14cc was found because of its 62 % outburst duty cycle and the short photometric period, suggesting an AM CVn (Kato et al., 2015). Gaia14aae was initially discovered as ASASSN-14cn from ASAS-SN during outburst. It was discovered as a transient, two months later, during the following outburst by the *Gaia* Science Alerts project[5]. Follow-up optical observations confirmed it is an eclipsing AM CVn (Campbell et al., 2015; Green et al., 2018b). ASASSN-14ei was confirmed as an AM CVn shortly after identification by ASAS-SN (Prieto et al., 2014b,a; Green et al., 2020), followed by ASASSN-14mv (Green et al., 2020), ASASSN-14fv Wagner et al. (2014), ASASSN-15kf (Kato et al., 2016) and ASASSN-16mg Phillips et al. (2016); Prieto (2016). More recently, at least 8 more AM CVn stars have been discovered through ASAS-SN (Aydi et al., 2021; Isogai et al., 2021; Kato and Kojiguchi, 2021). Only two other *Gaia* AM CVns, Gaia16all (Pichardo Marcano et al., 2021) and Gaia22ayj (Kato, 2022), are currently known.

More recently, nine AM CVn stars were discovered through the Zwicky Transient Facility (ZTF). van Roestel et al. (2021) cross-matched outbursting stars from ZTF with Gaia and Pan-STARRS for colour selections. High priority ZTF candidates were restrained within the colour spaces $-0.6 < BP-RP < 0.3$, $g-r < 0.1$ and $g-r < 0.1$. A further five eclipsing AM CVns were discovered through ZTF for which system parameters were determined (van Roestel et al., 2022). A list of known AM CVns can be found in table 2.1.

Amateur astronomers have made a large contribution towards the study of CVs (Shears, 2017). Even though amateur astronomers have relatively small telescopes, they tend to have better access, unlike professional astronomers on very large telescopes who are usually restricted to allocated time slots (although SALT is a counter-example, as are most queue-scheduled telescopes), and transient surveys which scan the same patch of sky weekly or monthly. Data from amateur astronomers are most useful for long-term daily monitoring of a target. A number of new AM CVn stars, discovered from transient surveys, have been followed up by amateur astronomers. Not all surveys make photometric data available to the public, so the monitoring of AM CVn stars by amateurs helps professionals keep track of behaviour of these systems. Professional astronomers use this data to trigger observing campaigns with larger telescopes which provide more detailed observations with improved time resolution. AM CVn stars discovered by ASAS-SN have been monitored with the help of amateur astronomers[6]. I report on some of these systems in section 3.7

[5] http://gsaweb.ast.cam.ac.uk/alerts/home
[6] https://www.aavso.org/visionmission

TABLE 2.1 – Known AM CVn stars with their orbital periods and outburst status.

AM CVn system	$\mathbf{P_{orb}}$ (min)	**Outburst status**	**References**
HM Cnc	5.4	SHS	*1*
V407 Vul	9.5	SHS	*2, 3, 4*
ES Cet	10.3	SHS	*5*
SDSS J1351-0643	15.7	SHS	*6*
AM CVn	17.1	SHS	*7, 8*
SDSSJ1908+3940	18.2	SHS	*9, 10*
HP Lib	18.4	SHS	*11*
PTF1J1919+4815	22.5	O	*12*
MGAB-V240	22.8 (*sh*)	O	*13*
CX361	22.9	SHS	*14*
ASASSN-14cc	22.5 (*sh*)	O	*15*
CR Boo	24.5	O	*16*
KL Dra	25.0	O	*17*
V803 Cen	26.6	O	*18, 19*
PTF1J0719+4858	26.8	O	*20*
ASASSN-15kf	27.67 (*sh*)	O	*21,81,* ***32***
PTF1J2219+3135	∼ 28.	O	*22, 23, 24*
YZ Lmi (SDSSJ0926+3624)*	28.3	O	*25, 26*
CP Eri	28.5	O	*27*
SDSSJ1043+5632	28.7 (*p*)	O	*28, 23*
CRTSJ0910-2008	29.7 (*sh*)	O	*29*
Gaia16all	∼ 30.	O	*24, 30*
PTF1J0943+1029	30.4	O	*22*
CSS0105+1903	31.6	O	*31,* ***32***
PTF1J1632+3511	32.7 (*p*)	O	*22, 23*
CRTSJ0744+3254	33. : (*p*)	O	*33, 23*
V406 Hya	33.8	O	*34, 35, 36*
PTF1J0435+0029	34.3	O	*22, 33*
SDSSJ1730+5545	35.2	NO	*37*
ZTFJ0407-0007*	35.4	O	*38*
V558 Vir (2QZ J1427-01)	36.6 (*sh*)	O	*39,* ***32***
SDSSJ1240-0159	37.4	O	*40*
ZTFJ2252-0519*	37.4	O	*38*
NSV1440	37.5 (*sh*)	O	*41*
V744 And (SDSSJ0129+3842)	37.6	O	*25, 42, 23*

Notes: Objects highlighted in bold are presented in this work. '*c*' denotes a candidate AM CVn system, 'SHS' represents systems in stable high state, 'O' denotes systems with observed outbursts and 'NO' represents systems with no recorded outbursts and possibly in stable low state. '*sh*' indicates a superhump period. * indicates an eclipsing system. Orbital periods marked with '*p*' are predicted by Levitan et al. (2015) according to the system outburst properties. ':' denotes an uncertain value.

(Continued on next page)

Table 2.1 – continued from previous page

AM CVn system	P_{orb} (min)	Outburst status	References
SDSSJ1721+2733	38.1	O	*43*, *23*
ASASSN-21br	38.6(*sh*)	O	*44*,*45*
V493 Gem (ASASSN-14mv)	40.8(*sh*)	O	*46*, *47*, ***32***
OX Eri (ASASSN-14ei)	43.(*sh*)	O	*48*, *49*, *50*, *51*, *46*, ***32***
SDSSJ1525+3600	44.3	O	*43*, *42*
SDSSJ0804+1616	44.5	NO	*52*
SDSSJ1411+4812	46.0	O	*25*, *53*
GP Com	46.5	NO	*54*, *55*, *56*
CSS0450-0931	47.3	O	*57*, *58*, ***32***
SDSSJ0902+3819	48.3	O	*43*, *59*
Gaia14aae*	49.7	O	*60*, *61*
MOA 2010-BLG-087	∼ 50	O	*46*
ASASSN-17fp	51.0(*sh*)	O	*62* ***32***
SDSSJ1208+3550	52.6	NO	*63*, *42*
SDSSJ0807+4852	53.3(*sh*)	O	*64*, *65*
ZTFJ0220+2141*	53.3	NO	*38*
SDSSJ1642+1934	54.2	NO	*43*, *42*
SRGeJ045359.9+622444*	55.1	NO	*66*
ZTFJ0003+1404*	55.5	NO?	*38*
SDSSJ1552+3201	56.3	NO	*25*, *67*
ASASSN-21au	∼ 58	O	*68*, *69*
SDSSJ1137+4054	59.6	NO	*70*
ZTFJ1637+4917*	61.5	NO	*38*
V396 Hya	65.1	NO	*71*
SDSSJ1319+5915	65.6	NO	*72*, *73*
ASASSN-16mg		NO	*74*, *75*
CRTSJ0844-0128		NO	*33*
PTF1J0857+0729		NO	*22*, *23*
SDSSJ1505+0659		NO	*70*
PTF1J1523+1845		NO	*22*, *23*
PU Aqr (SDSSJ2047+0008)		NO	*63*
ASASSN-14fv		NO	*76*
ZTFJ2128+6325		O	*77*, *78*
ZTFJ1329-1216		O	*78*
ZTFJ0449+0251		O	*78*
ZTFJ1918+4449		O	*78*

Notes: Objects highlighted in bold are presented in this work. '*c*' denotes a candidate AM CVn system, 'SHS' represents systems in stable high state, 'O' denotes systems with observed outbursts and 'NO' represents systems with no recorded outbursts and possibly in stable low state. '*sh*' indicates a superhump period. * indicates an eclipsing system. Orbital periods marked with '*p*' are predicted by Levitan et al. (2015) according to the system outburst properties. ':' denotes an uncertain value.

(Continued on next page)

Table 2.1 – continued from previous page

AM CVn system	P_{orb} (min)	Outburst status	References
ZTFJ2108-1349		O	*78*
ZTFJ0820+6804		O	*78*
ZTFJ1325-1452		O	*78*
ZTFJ0701+5023		O	*78*
ASASSN-20eq (*c*)		O	*79*
ASASSN-20gx (*c*)		O	*79*
ASASSN-20jt (*c*)		O	*79*
ASASSN-20ke (*c*)		O	*79*
ASASSN-20la (*c*)		O	*79*
ASASSN-20lr (*c*)		O	*79*
Gaia22ayj* (*c*)	9.4	O	*80*

Notes: Objects highlighted in bold are presented in this work. '*c*' denotes a candidate AM CVn system, 'SHS' represents systems that are stable in high state, 'O' denotes systems with observed outbursts and 'NO' represents systems with no recorded outbursts and possibly stable in low state. '*sh*' indicates a superhump period. * indicates an eclipsing system. Orbital periods marked with '*p*' are predicted by Levitan et al. (2015) according to the system outburst properties. ':' denotes an uncertain value.

References: [*1*] Ramsay and Cropper (2002a), [*2*] Cropper et al. (1998), [*3*] Marsh and Steeghs (2002) , [*4*] Ramsay and Cropper (2002b), [*5*] Espaillat et al. (2005), [*6*] Green et al. (2018a), [*7*] Smak (1967), [*8*] Warner and Robinson (1972), [*9*] Fontaine et al. (2011), [*10*] Kupfer et al. (2015), [*11*] O'Donoghue et al. (1994), [*12*] Levitan et al. (2014), [*13*] Kato (2023), [*14*] Wevers et al. (2016b), [*15*] Kato et al. (2015), [*16*] Wood et al. (1987), [*17*] Wood et al. (2002), [*18*] Elvius (1975), [*19*] O'Donoghue et al. (1987), [*20*] Levitan et al. (2011), [*21*] VSNET-alert #18669., [*22*] Levitan et al. (2013), [*23*] Levitan et al. (2015), [*24*] Pichardo Marcano et al. (2021), [*25*] Anderson et al. (2005), [*26*] Copperwheat et al. (2011), [*27*] Abbott et al. (1992), [*28*] Carter et al. (2013a), [*29*] Aungwerojwit et al. (in prep.), [*30*] Breedt et al. (in prep.), [*31*] Thorstensen and Skinner (2012), [*32*] this work, [*33*] Breedt et al. (2014), [*34*] Wood-Vasey et al. (2003), [*35*] Chornock and Filippenko (2003), [*36*] Woudt and Warner (2003), [*37*] Carter et al. (2014b), [*38*] van Roestel et al. (2022), [*39*] Woudt et al. (2005), [*40*] Roelofs et al. (2005), [*41*] Isogai et al. (2019), [*42*] Kupfer et al. (2013), [*43*] Rau et al. (2010),[*44*] Aydi et al. (2021), [*45*] Motsoaledi et al. (2021), [*46*] Green et al. (2020), [*47*] VSNET-alert #18124, [*48*] Prieto et al. (2014b), [*49*] Prieto et al. (2014a), [*50*] VSNET-alert #17575, [*51*] Isogai et al. (2015), [*52*] Roelofs et al. (2009), [*53*] VSNET-alert #22174, [*54*] Burbidge and Strittmatter (1971), [*55*] Nather et al. (1981), [*56*] Marsh (1999), [*57*] Drake et al. (2012), [*58*] Woudt et al. (2013), [*59*] Kato et al. (2014b), [*60*] Campbell et al. (2015), [*61*] Green et al. (2018b), [*62*] Marsh et al. (2017), [*63*] Anderson et al. (2008), [*64*] Kong et al. (2018), [*65*] Kupfer et al. (2019), [*66*] Rodriguez et al. (2023), [*67*] Roelofs et al. (2007b), [*68*] Isogai et al. (2021), [*69*] Rivera Sandoval et al. (2022), [*70*] Carter et al. (2014a), [*71*] Ruiz et al. (2001), [*72*] Kepler et al. (2015), [*73*] Kupfer et al. (in prep.), [*74*] Phillips et al. (2016), [*75*] Prieto (2016), [*76*] Wagner et al. (2014), [*77*] Szkody et al. (2020), [*78*] van Roestel et al. (2021), [*79*] Kato and Kojiguchi (2021), [*80*] Kato (2022), [*81*] Kato et al. (2016)

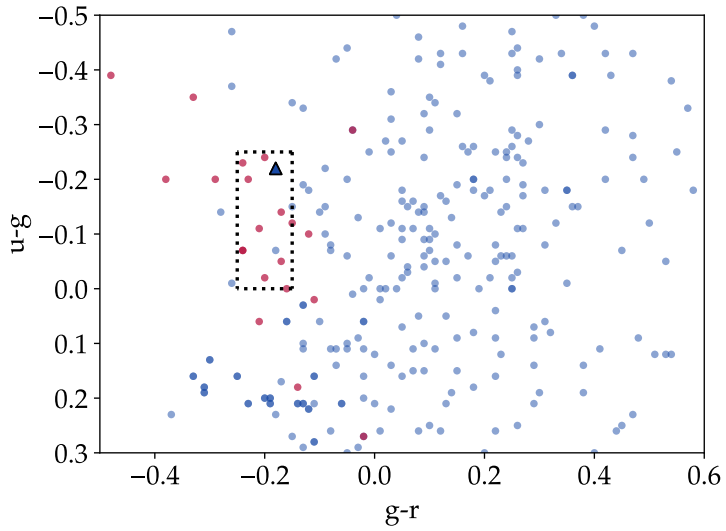

FIGURE 2.2 – Colour–colour diagrams of AM CVn stars overplotted on CVs from CRTS with SDSS colours. The blue dots represent transients in CRTS which have been cross-matched with transients that have SDSS photometry. The red dots represent the known AM CVns. The blue triangle is one of the CRTS transients, CSS0105+19, which falls within the dotted box constraining the tight group of AM CVns.

2.1.3 *Selection criteria for my sample*

One of the targets in this work from the CRTS, CSS0105+19, was colour-selected. The candidate CVs from the CRTS were cross-matched with the SDSS multi-filter photometric data. Those with SDSS *ugriz* photometry were plotted on a $(u-g, g-r)$ colour diagram. Among the CRTS candidate CVs in blue in Fig. 2.2) were previously confirmed AM CVns (in red). I constrained a small group of known AM CVns within a small box with parameters: $-0.25 < u-g < 0.0$ and $-0.25 < g-r < -0.15$. The size of the box was determined by the area with the highest concentration of AM CVns. CSS0105+19 (blue triangle), along with two other CRTS CVs, was found inside the box. One of those, CSS090219:043518+002941 or PTF1J0435+0029, was later discovered to be an AM CVn through PTF (Levitan et al., 2013; Breedt et al., 2014). The other object is CSS120421:124719+013843.

The other CRTS targets were followed up after superoutbursts were detected. CSS0450-09 was identified as a candidate AM CVn after being reported to be dominated by helium and lack of hydrogen lines (Drake et al., 2012), very shortly after the superoutburst. CSS2333-15 was identified as an eclipsing DN with an orbital period below the period minimum (Woudt and Warner, 2011). V558 Vir was identified as a candidate blazar by the 2dF QSO Redshift Survey. Its helium-dominated spectra qualified it as a candidate AM CVn (Croom et al., 2004) The selection through colour alone is subject to contamination by quasers and DA/DB white dwarfs but the combination of colour and outburst behaviour strengthens the selection of AM Cvn candidates as some of the objects sharing

the same colour space do not experience outbursts.

My remaining sample was selected from ASAS-SN, including ASASSN-14ei, ASASSN-14mv, ASASSN-15kf and ASASSN-17fp, all of which were identified during superoutburst and identified as AM CVns after spectroscopic confirmation, via publication/alert services ATel, VSNET-alert or CBA:news. ASSASN-14mv and ASASSN-15kf were previously identified as candidate CVs from CRTS but were only identified as candidate AM CVns after identification by ASAS-SN. They were, and continue to be, monitored through the American Association of Variable Star Observers (AAVSO[7]) during and after outburst activity.

2.2 MAGNETIC CATACLYSMIC VARIABLES

2.2.1 *Discoveries of magnetic cataclysmic variables*

The increasing number of multi-wavelength surveys with improving sensitivity has enhanced the study of magnetic CVs. In this section, I detail mCV discoveries over the past decades, with the most contributions from X-ray surveys/telescopes in the earlier decades. Contributions from optical surveys increased in more recent years.

ROSAT was an X-ray telescope observing at soft X-ray (0.1-2.4 KeV: 100-5 Å) and extreme ultraviolet (0.025-0.2 KeV: 500-60 Å) wavelengths (Truemper, 1982; Kent et al., 1990). In survey mode, *ROSAT* scanned a specific field of view for 25 seconds every 96 minutes over a period of several days. In pointed mode, *ROSAT* was capable of viewing a single source for over two days, enabling the detection of variability. CVs were initially identified by cross-matching the *ROSAT* data with existing CV catalogue positions. This led to the identification of soft X-ray counterparts of 77 % of magnetic CVs, 66 % of dwarf novae and 24 % of novae and novalike variables (Beuermann and Thomas, 1993).

To identify potential magnetic CVs from *ROSAT* All Sky Survey (RASS), the sources were required to be significantly variable and soft X-ray or extreme ultraviolet emitters (Voges et al., 1999). Prior to *ROSAT*, serendipitous discoveries led to 17 known polars (see Warner, 1995a; Cropper, 1990). *ROSAT* uncovered at least 27 new polars to due soft X-ray excess thought to be a defining characteristic of all (or most) polars (e.g. Buckley et al., 1993; Singh et al., 1995; Schwope et al., 2002a). Just as many polars were discovered through previous soft X-ray sensitive telescopes/surveys, namely EINSTEIN[8], EXOSAT[9], and EUVE[10] (sensitive to ~ 0.18 keV in the extreme UV).

Operating at soft and hard X-ray wavelengths, *XMM-Newton* consists of three co-aligned X-ray telescopes, altogether spanning energy band $0.2 - 12$ keV with the 2XMM survey, covering ~ 1 % of the sky (Watson et al., 2009). Due to its small field of view and non-survey nature, the *XMM-Newton* has made very few serendipitous discoveries of magnetic CVs (e.g. Vogel et al., 2008; Ramsay et al., 2009; Bernardini et al., 2017; Webb et al., 2018). Bernardini et al. (2017) reported on seven new CVs selected by their

[7] https://www.aavso.org/visionmission
[8] https://heasarc.gsfc.nasa.gov/docs/einstein/heao2.html
[9] https://heasarc.gsfc.nasa.gov/docs/exosat/exosat.html
[10] https://heasarc.gsfc.nasa.gov/docs/euve/euve.html

hard X-rays. Using *XMM-Newton* and other telescopes, they confirmed 5 as IPs and 1 as a polar, contributing to the small number of polars (less than 15) discovered by their hard X-rays. The population of magnetic CVs detected by hard X-ray telescopes/surveys is predominantly intermediate polars (IPs), a few polars and even less non-magnetic CVs. Findings by Falanga et al. (2019) of hard X-ray systems detected by *INTEGRAL* and *Swift* and followed up by *XMM-Newton* are in agreement with Bernardini et al. (2017), with the highest number of systems being intermediate polars. Falanga et al. (2019) also found that 10 % of known polars were significant hard X-rays emitters, which is higher than expected.

The *XMM-Newton*-MSSL survey (Ramsay and Cropper, 2004b) is a follow-up survey of 39 polars, targeting known and candidate magnetic CVs. Ramsay and Cropper (2004b) found that almost half of their observed sample of polars were in low or reduced accretion rates and undetected by RASS. While reviewing the total number of polars at the time, they found that more than half of the polars undetected by RASS were in low accretion states, which is may be the reason they were missed by the RASS scans initially. Despite the significant increase in known polars from the RASS, (Ramsay and Cropper, 2004b) also showed that many polars do not exhibit the expected soft X-ray excess. Along with the previously known magnetic CVs, very few (if any) polars with soft X-ray excess have been discovered with *XMM-Newton* (e.g. Vogel et al., 2008; Ramsay et al., 2009; Bernardini et al., 2017; Webb et al., 2018). It may be that the missing soft X-ray component is due to the peak of the emission moving into the extreme UV regime (Worpel and Schwope, 2015; Worpel et al., 2016).

XMM-Newton has also played an important role in the investigation of the X-ray properties of SDSS-selected magnetic CV candidates. SDSS optical spectroscopy confirmed the magnetic nature of CVs identified in the shared colour-colour space of CVs, quasars, single white dwarfs, white dwarf M-star binaries and hot blue stars (Szkody et al., 2002, 2003b, 2004, 2011). The *XMM-Newton* telescope was used for further X-ray follow-up of magnetic CVs from the SDSS. Due to the optical sensitivity of SDSS, the emerging magnetic CVs are mostly faint optical and X-ray sources, some of which are low accretion rate polars (LARPs Schwope et al., 2002a) or pre-polars (Schmidt et al., 2005b, 2008). These magnetic systems exist below the detection threshold of RASS.

Another optical survey which has made a large contribution to the known CVs is the CRTS (Breedt et al., 2014). Follow-up observations have enabled the determination of the nature of the CVs, some of which are magnetic CVs, discovered serendipitously (e.g. Schwope and Thinius, 2012; Szkody et al., 2014, 2018). In a targeted search for magnetic CVs, Oliveira et al. (2017, 2020) spectroscopically followed up on candidate magnetic CVs, predominantly from the CRTS. They visually inspected the long-term light curves of CVs from CRTS and selected those that adhered to either of the following criteria: (i) transitions between different brightness levels, indicating accretion state changes, (ii) intrinsic flux variability (larger than observational error expected for mean magnitude), indicating possible accretion processes, and (iii) zero to barely any outbursts, to minimise the number of dwarf novae. Optical identification spectra were obtained with Southern Astrophysical Research (SOAR) 4.1 m telescope in Chile and the Perkin-Elmer 1.6 m telescope in south-east Brazil. From a total of 71 CVs, Oliveira et al. (2017, 2020)

reported 30 mCVs (polars and IPs) of which 19 were new classifications.

Most recently, Gabdeev et al. (2020) use mid-band filters to identify candidate polars. They use the Edmund Optic colours filters, within which the diagnostic HeII λ 4686 line lies. The criteria used to identify candidate polars are (i) a combination of colour-colour limits and (ii) the colour variation of an object should be three times higher than the average error in measuring colour indices (Gabdeev et al., 2020). The application of these criteria with the MMPP polarimeter on the Zeiss-1000 telescope of SAO RAS was 75 % successful at detecting known polars. The intention is to expand the method to candidate CVs in the CRTS database to identify new candidate polars.

Within the first year of the ZTF, Szkody et al. (2020) found 2 candidate magnetic CVs (one likely an intermediate polar) from a sample of 218 candidates. Rodriguez et al. (2022) cross-matched *eROSITA* (extended ROentgen Survey with an Imaging Telescope Array) X-ray data with ZTF photometry which led to the discovery of two polars. Li et al. (2022) systematically targeted short-period CVs from ZTF by searching for periods of 1 – 2 hr from the ZTF light curves resulting in the discovery of at least 50 CVs, although the magnetic CVs from the sample are yet to be confirmed.

The selection effects within surveys highlight various characteristics of magnetic CV populations. *eROSITA* is a recent X-ray telescope array (on board the Spektrum-Röntgen-Gamms (SRG) satellite) observing from soft to hard X-rays in the 0.3-10keV energy range (Merloni et al., 2012; Schwope, 2012). *eROSITA* is $\sim$ 30 times more sensitive than *ROSAT* within its soft spectral band and is the most sensitive hard X-ray all sky survey to date. It is revealing a faint X-ray population of magnetic CVs, below the detection limit of *ROSAT* and *XMM-Newton*. This will lead to improved population density calculations and bring light to some unanswered evolutionary questions.

2.3 LONG-TERM PHOTOMETRIC LIGHT-CURVES OF POLARS

This section details the different long-term photometric behavioural patterns that I observed from the light curves of previously known polars.

I analysed the light curves of previously confirmed polars from the Ritter and Kolb catalogue (RKcat, Ritter and Kolb, 2003) by eye. From looking at the long-term light curves available in CRTS data release 2, it became evident that the photometric behaviour of mCVs is more complicated than expected. The high and low states of mCVs and the transitions between them are very clearly represented in light curves spanning over years, along with additional characteristics. The long-term light curves were grouped according to their photometric behavioural patterns in order to statistically analyse the properties of each group. Systems which displayed the properties of multiple groups were categorised accordingly. Eclipsing systems had high potential of being identified from these long-term light curves as the eclipsing data points usually fell below the overall mean light curve levels. A number of polars were excluded from the study, either because they did not fall within the coverage range of the CRTS, or they had too few data points to get any definitive results.

Two states

The more obvious and expected behaviour which was observed in the long-term light curves was the distinct transitions between the low and high states. This was represented as the system becoming fainter and brighter as it transitioned. I describe the behaviour of systems that spend more time in low state as low-to-high, and vice versa as high-to-low. Some systems spend a fairly equal amount of time in both states (e.g. V358 Aqr and IW Eri in Fig. 2.5). It is evident that systems display a range of changes in magnitude between the states. Warner (1999) showed that there is a trend between the orbital period and change in magnitude (Δm) between high and low states (Fig. 2.3). Systems with longer orbital periods tend to have smaller changes in magnitude. Warner (1999) explained that, at low states, the stellar components contribute the most to the brightness of the system. For systems with larger orbital periods, Δm is smaller because the donor star is larger/brighter and so the overall low state brightness is higher. At smaller orbital periods, the donor star has a smaller contribution to the system brightness so the low state brightness is lower resulting in larger Δm.

I have updated this figure based on the CRTS light curves of RKcat polars in Fig2.4 which does not consistently show the same relation found in Fig. 2.3 with the addition of systems in the bottom left quadrant. Without the systems in the bottom left quadrant, one could infer that the change in magnitude between states decreases with increasing orbital period. The triangle points with the largest amplitude changes are what I have defined as three-state systems using only the high and low state data and dismissing the intermediate states (see explanation of three-state systems in the following paragraph). It is worth noting that Warner (1999) determines larger amplitude changes in magnitudes between states, even when comparing AM Her for which I determine a 1.4 magnitude difference using CRTS data and the Warner (1999) figure shows a value larger than 3 magnitudes.

Three states

In addition to the common high and low state transition, some polars have an intermediate state which lies somewhere between the high and low. They are less numerous than the other groups, totalling only five systems with three distinct states from the sample of 78 systems (e.g. FL Cet and HU Aqr in Fig. 2.6). Within the observation time frame (i.e $\sim$9 seasons/years), HU Aqr initially appeared to have only two states until the final years of observations, where it surpassed the brightness of the previously known "high" state. This led to re-classifying the previously termed "high" state to an intermediate state (e.g. Fig. 2.6, right). It is known that some systems with two-pole accretors can switch between one or two actively accreting pole e.g. AM Her (Heise et al., 1985; Schwope et al., 2020), MT Dra (Schwarz et al., 2002), QS Tel (Rosen et al., 1996, 2001) and BM CrB (Kolbin et al., 2023). A possible explanation for three states is if a two-pole accreting polar changes to a single pole accretor and at other times experiences low accretion rates due to a decrease in mass transfer.

Slightly variable

Some systems show variations in the long-term light curves which are not as prominent as two-state systems but also not as constant as stable systems. Such systems have small amplitude variations although they do not have clear a distinction between different

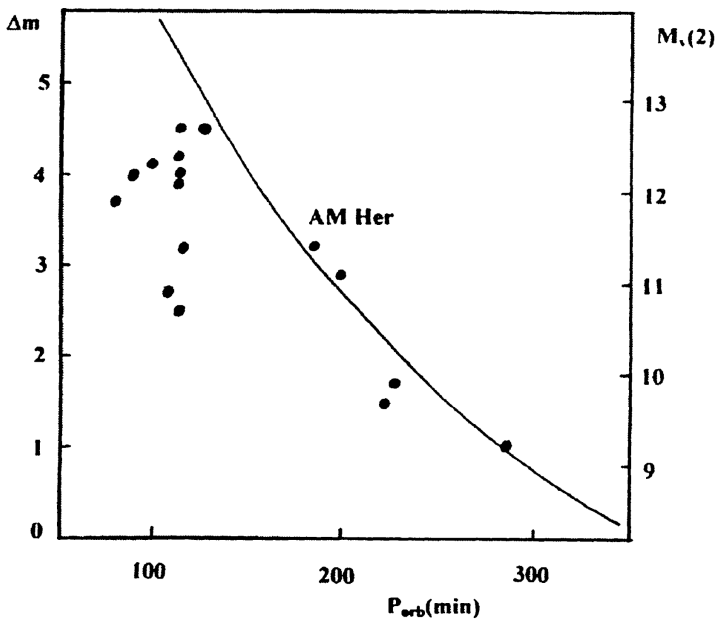

FIGURE 2.3 – The change in magnitude between states (Δm) plotted against orbital period of mCVs taken from Warner (1999).

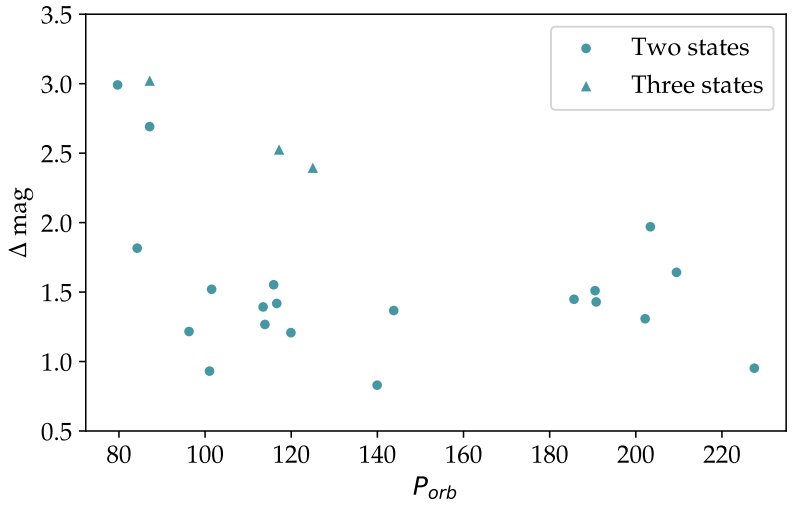

FIGURE 2.4 – The updated figure showing the change in magnitude between states (Δ mag) plotted against orbital period of magnetic CVs using CRTS data.

states. I define these systems as slightly variable with variations not large enough to transition between different states (e.g. PW Aqr and V1189 Her in Fig. 2.7).

Large scatter

In some instances, polars display large amplitude variations over a short period of time. These large amplitude variations occur over a single 30 min observation or from month

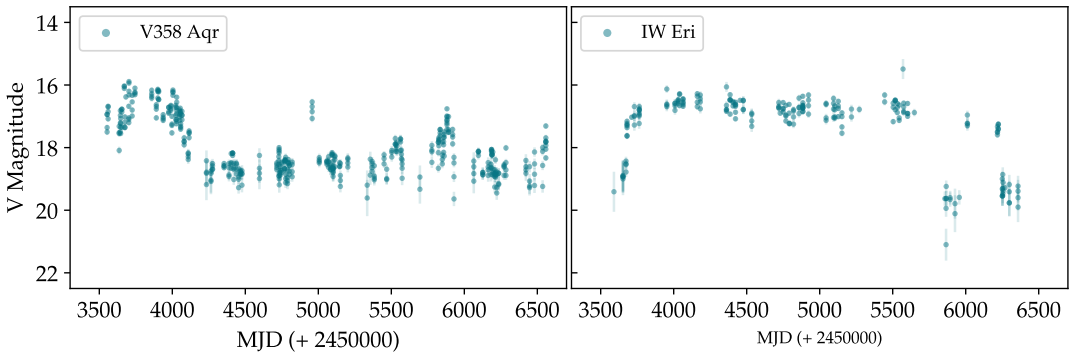

FIGURE 2.5 – CRTS long-term light curves of V358 Aqr (low-to-high) and IW Eri (high-to-low) showing two distinct states.

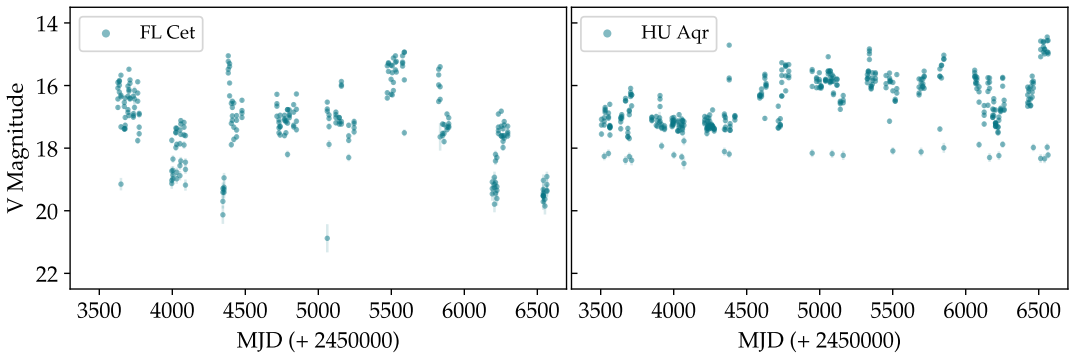

FIGURE 2.6 – CRTS long-term light curves of FL Cet and HU Aqr showing three states.

to month. The large scatter is an indication of large amplitude orbital modulation. The data points are spread over at least two magnitudes for sections of the light curve or the entire light curve (e.g. FR Lyn and J1344+2044 in Fig. 2.8).

Stable

The most unexpected behaviour is that of the stable systems. Over the 8 – 9 years of monitoring, they do not exhibit any obvious photometric variability. These systems remain constant for extended periods of time. It would be impossible to classify these systems as polars based solely on their long-term light curves (e.g. HS 0922+1333 and V379 Vel in Fig. 2.9). The literature of most of the previously known stable systems reveals that they are, in fact, low accretion rate polars or pre-polars (e.g. HS 0922+1333 (Reimers and Hagen, 2000), V379 Vel (Schmidt et al., 2005a; Linnell et al., 2010), MQ Dra (Szkody et al., 2003a), J1514+0744 (Breedt et al., 2012a) and J1250+1549 (Breedt et al., 2012a)), so with little accretion driven variability.

2.4 ANALYSIS OF LONG-TERM LIGHT CURVES OF CONFIRMED POLARS

This section describes the results of the period analysis of the CRTS long-term light curves of previously known polars. The photometric periods are compared with ex-

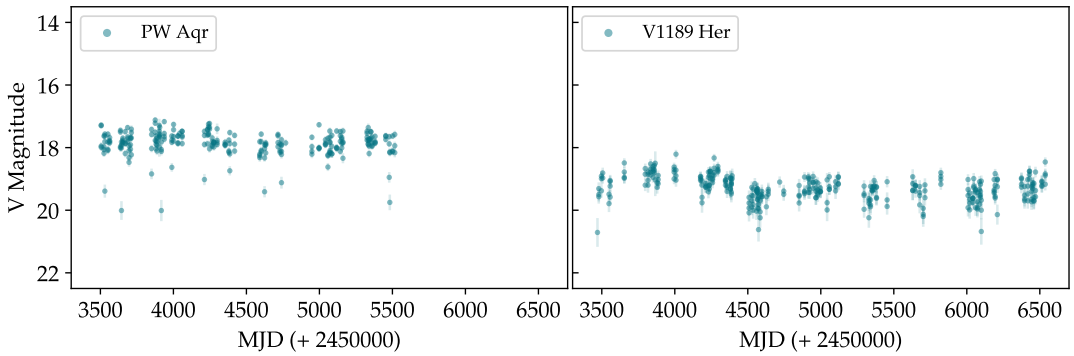

FIGURE 2.7 – CRTS long-term light curve of PW Aqr and V1189 Her showing slightly variable photometric behaviour.

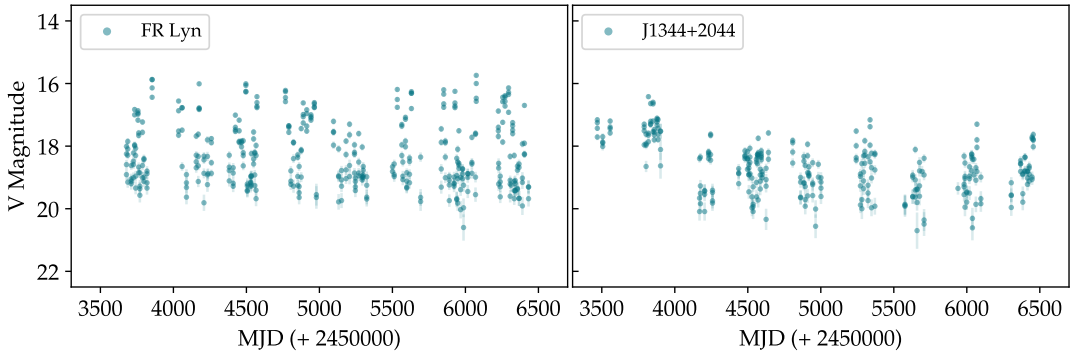

FIGURE 2.8 – CRTS long-term light curve of FR Lyn and J1344+2044 showing large scatter.

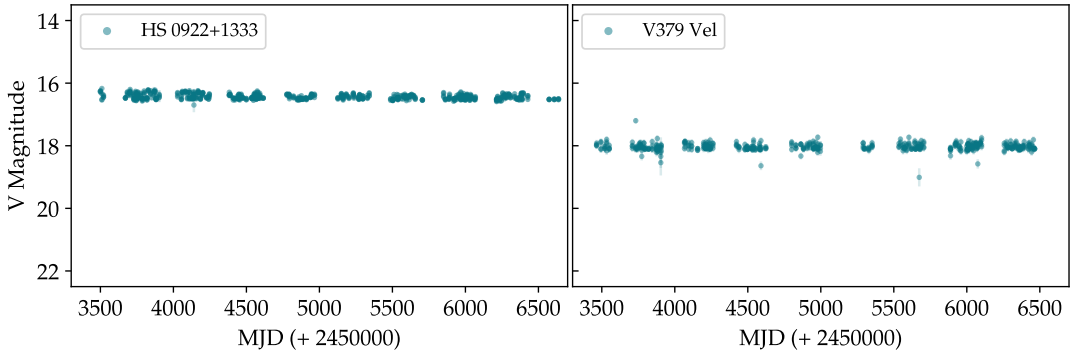

FIGURE 2.9 – CRTS long-term light curve of stable systems, HS 0922+1333 and V379 Vel.

isting values from literature and resulting orbital modulations are discussed. The periodograms referred to in this section can be found in the appendix A.2

2.4.1 *Orbital periods derived from long-term CRTS data*

Many of the phase-folded light curves (phase plots) produced by folding the CRTS data over known orbital periods from literature, appear noisy and without any indication

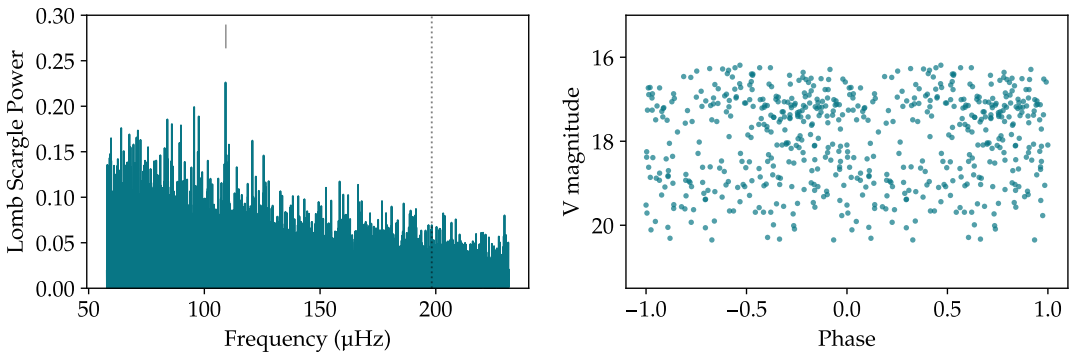

FIGURE 2.10 – Lomb Scargle periodogram of BM CrB on the left. The dotted line indicates the orbital period from the literature the arrow marks the highest peak in the periodogram. To the right is the CRTS light curve folded over the Lomb Scargle period given by the highest Lomb Scargle peak.

of orbital structure or modulation. In an attempt to obtain orbital periods that are consistent over the 8 – 9 year CRTS baseline, a Lomb-Scargle analysis was applied to the long-term data from the CRTS of the previously known polars (refer forward to § 3.3.2 for a description of a Lomb-Scargle analysis). The previously reported orbital periods in the literature have more commonly been derived from data taken over days or weeks of observations, with observation lengths on the order of an hour and integration times of seconds to minutes. Additional epochs of data may be combined to refine the derived orbital periods. The long-term CRTS data differ in time resolution and baseline/length. Each observation consists of four snapshots over 30 minutes with 10 minute intervals. Observations are taken between two and four weeks apart during active observing times. The 8 – 9 year baselines of the CRTS data may compensate for large gaps between observations, sometimes resulting in orbital periods that are consistent throughout long baselines.

Using the known orbital periods from the literature assists in narrowing the range over which to search for a period in the Lomb-Scargle periodogram. For many systems, the Lomb-Scargle periodogram of the CRTS data failed to produce any significant peaks close to the previously known orbital period from the literature. Of the peaks that are identified in the periodograms, many do not correspond with the existing literature orbital periods or show any orbital modulation when folded upon such values (refer to Fig. 2.10, more examples from tables 2.2 and 2.3 in appendix A.2.

The orbital periods derived from this work with Lomb-Scargle periodograms for most of the systems in table 2.2 have a reasonable overlap, given the uncertainties, with the orbital periods from the literature. It is only for EG Lyn that the orbital period derived using the Lomb-Scargle method differs slightly in the last few decimal places from the literature value (table 2.2). When folding the long-term period over the literature orbital period, an initially noisy and structureless phase plot transforms to show minor or significant improvement with visible orbital modulations in a phase plot when using the slightly modified Lomb-Scargle value. In such instances, the long-term data could be used to refine an existing orbital period value. The orbital period derived from the

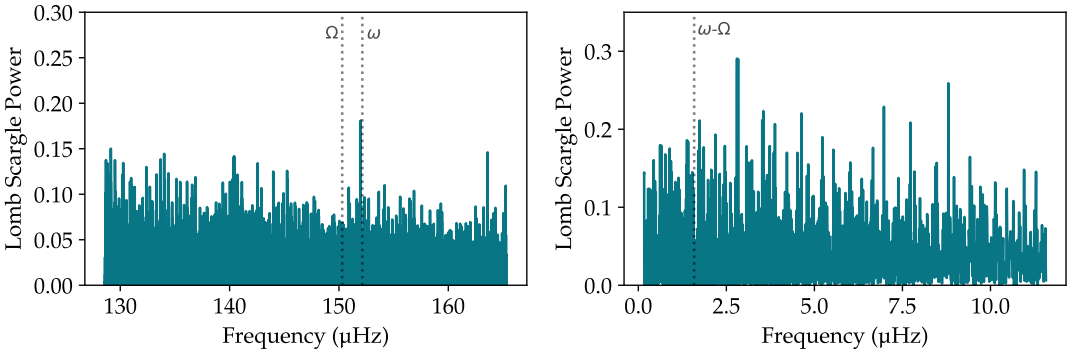

FIGURE 2.11 – Lomb-Scargle periodogram of CD Ind. The dashed lines in the left plot represent the orbital and spin periods from the literature. The dashed line in the right plot represents the beat period from the literature.

CRTS data of J2319+2615 (0.125456(2) d) is an improvement on the value obtained from the literature (0.12544(3) d) based on the phase-folded light curves produced for both periods with the phase plot folded over the orbital period derived from the long-term data showing clear orbital modulations (Fig. 2.13). There are periods found through the CRTS data for only a few systems which do not correspond closely with the existing literature orbital period, but show orbital modulations in the light curves folded on the revised CRTS-derived orbital periods (namely J0733+2619, J1007-2017, RS Cae and V1237 Her in table 2.3). It is uncertain what the nature of these periods are, or even if they are strictly periodic. The Lomb Scargle periodograms of the CRTS light curves of polars in tables 2.2 and 2.3 and the light curves folded over the corresponding Lomb Scargle periods can be found in the appendix A.2.

Asynchronous polars are polars with spin and orbital periods that are not synchronised. Only two confirmed asynchronous polars have corresponding long-term CRTS data, namely CD Ind and V1432 Aql. CD Ind has a known orbital period of 0.077006944 d (Vennes et al., 1996; Schwope et al., 1997a) and a spin period of 0.076076389 d (Vennes et al., 1996; Myers et al., 2017). The only identifiable peak from the Lomb-Scargle periodogram of CD Ind in the vicinity of the orbital/spin periods is 0.076150 d, which is closest to the spin period as seen in Fig. 2.11. Multiple low amplitude peaks are seen in the Lomb-Scargle periodogram of V1432 Aql, although none correspond with the 0.140235812 d orbital period (Patterson et al., 1995; Littlefield et al., 2015) or the 0.140585 d spin period (Patterson et al., 1995; Bonnardeau, 2012) (refer to Fig. 2.12. A beat period is a period corresponding to the beat frequency ($\omega - \Omega$), where the beat frequency is the difference between the spin (ω) and orbital frequency (Ω). In the Lomb-Scargle periodograms, peaks are seen at larger periods, although neither corresponds with the known beat periods of CD Ind and V1432 Aql.

2.4.2 *Orbital structures and eclipses of confirmed polars derived from CRTS light curves*

When viewed by eye, the long-term light curves from the Catalina Real-time Transient Survey (CRTS) may provide insightful indicators of individual cataclysmic variable systems, and the collective characteristics of a group of similar systems. One may infer if

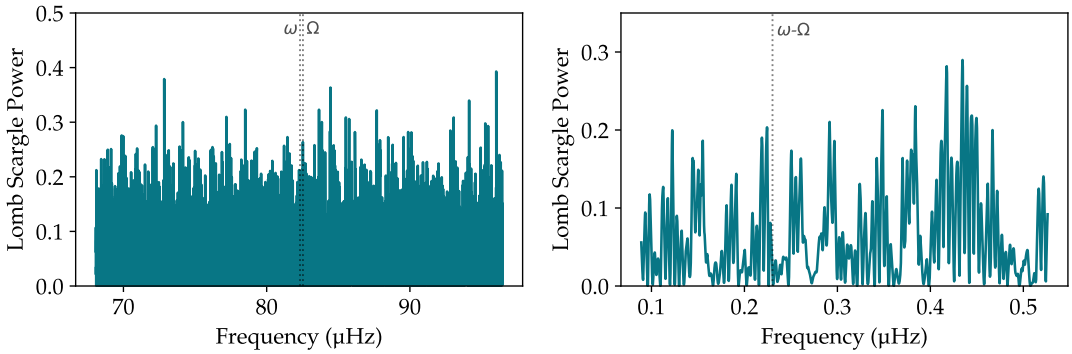

FIGURE 2.12 – Lomb-Scargle periodogram of V1432 Aql. The dashed lines in the left plot represent the orbital and spin periods from the literature. The dashed line in the right plot represents the beat period from the literature.

TABLE 2.2 – Table of orbital periods of previously known polars.

Polar	**Literature P_{orb}** (d)	**LS P_{orb}** (d)	**% difference**	**Reference (Literature P_{orb})**
HS0922+1333	0.16831231(15)	0.168312(4)	0	Vogel et al. (2011)
EG Lyn	0.06901389(200)	0.0689941(8)	0.029	Schwope et al. (2002a)
EK UMa	0.0795440225(24)	0.079544(1)	0.0	Beuermann et al. (2009)
J0328+0522	0.0847(63)	0.084768(1)	0.080	Szkody et al. (2007)
J1333+1437	0.0917(42)	0.088117(3)	3.907	Schmidt et al. (2008)
J2218+1925	0.08996	0.090099(1)	0.155	Thorstensen and Halpern (2013)
J2319+2615	0.12544(3)	0.125456(2)	0.013	Shafter et al. (2008)
MQ Dra	0.182985(5)	0.182987(5)	0.001	Szkody et al. (2008)
V1189 Her	0.093056(1400)	0.092756(1)	0.322	Gänsicke et al. (2009)
V393 Pav	0.06862456(14)	0.0686249(9)	0.0	Thomas et al. (1996)

Notes: P_{orb} = orbital period. LS = Lomb Scargle. The second column and fifth columns are the periods obtained from literature and the corresponding references. The third column has the periods obtained from the Lomb Scargle periodogram of the long-term CRTS data. The fourth column is the percentage difference between the literature and LS periods. The table lists only the polars where the Lomb Scargle period is the same as the original period from literature, or an improved value. The improvement is determined by the structure and coherence of the phase-folded light curves from both periods. The Lomb Scargle periodograms of the CRTS light curves can be found in the appendix A.2.

TABLE 2.3 – Table of previously known polars with LS periods different from orbital periods from literature.

Polar	**Literature P** (d)	**LS P_{orb}** (d)	**% difference**	**Reference (Literature P_{orb})**
J0733+2619	0.1390950(2)	0.093085(1)	33.078	Gabdeev (2015)
J1007-2017	0.144863923(36)	0.101688(1)	29.804	Thomas et al. (2012)
RS Cae	0.0709	0.097644(2)	37.721	Traulsen et al. (2014)
V1237 Her	0.08080175(8)	0.096498(1)	19.426	Homer et al. (2005)

Notes: P_{orb} = orbital period. LS = Lomb Scargle. The second column and fifth columns are the periods obtained from literature and the corresponding reference. The third column has the periods obtained from the Lomb Scargle periodogram of the long-term CRTS data. The fourth column is the percentage difference between the literature and LS periods. The LS periods listed are different from the orbital periods from the literature. The Lomb Scargle periodograms of the CRTS light curves can be found in the appendix A.2.

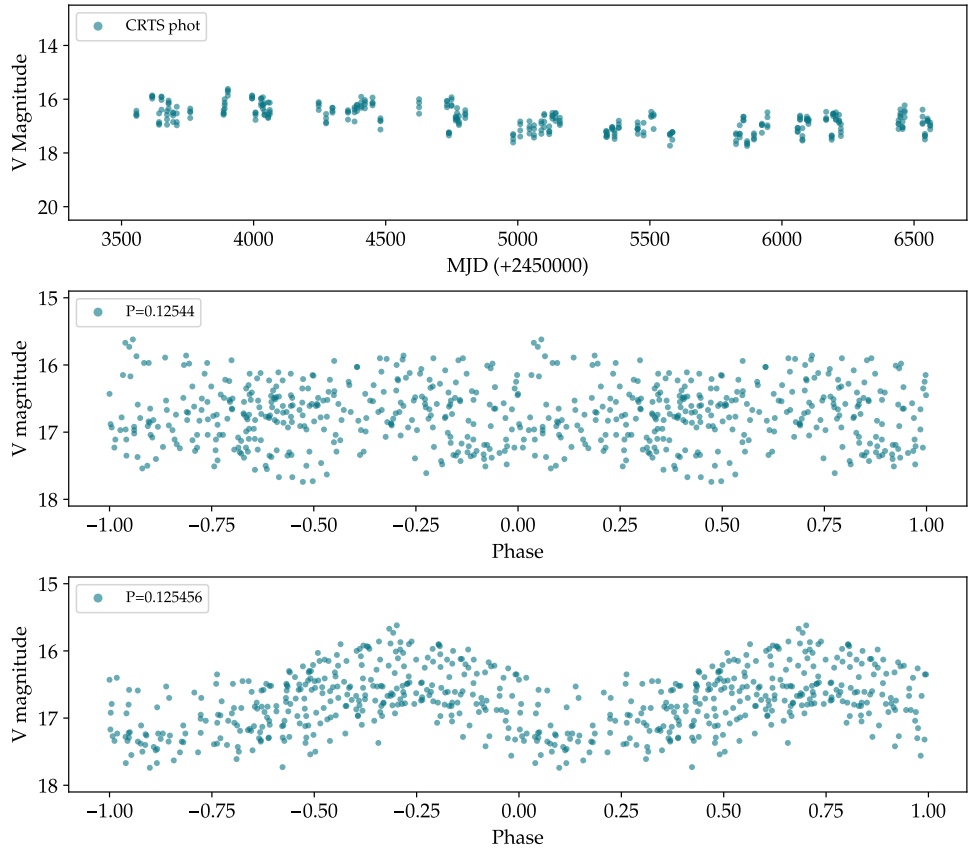

FIGURE 2.13 – Top: Long-term light curve of J2319+2615 from CRTS. Middle: Phase plot folded over the orbital period, 0.12544 d, from literature. Bottom: Phase plot folded over an orbital period of 0.125456 d, derived from the CRTS data.

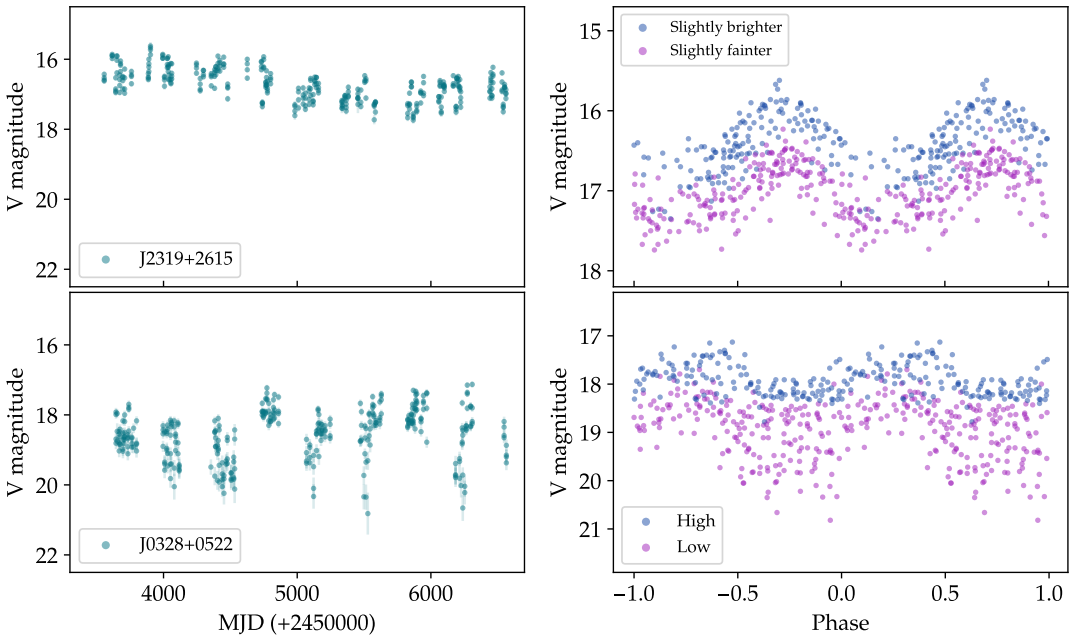

FIGURE 2.14 – Left: The long-term light curve of J2319+2615 and J0328+0522 from CRTS. Right: Phase plots of J2319+2615 and J0328+0522. Blue and purple represent high and low states, respectively.

a system is outbursting, eclipsing, has high/low accretion states or large orbital modulations. Additionally, a phase plot can be produced by folding the long-term data over the orbital period, where each data point constitutes a fraction of the orbital phase between zero and one. If consistent, the orbital structure may be seen in the phase-folded light curve using the entire dataset.

An assessment of the phase-folded long-term data of known polars reveals some expected and unexpected behaviours. For multi-state systems, as is the case for most polars, it may be necessary to evaluate states separately. To assist in interpretation, I have colour-coded the phase plots by state the phase plot at different magnitudes. Purple is assigned to low states and blue to high states. The phase plot of HU Aqr (Fig. 2.15), with three accretion states, is divided by blue, orange and purple to represent high, intermediate and low states, respectively.

Interestingly, V379 Tel, V519 Ser and V834 Cen (Fig. 2.16) show similar orbital features where an orbital hump-like structure is seen in high state (blue) and a constant stable signal in low state (purple). It is evident that the long-term light curves of V379 Tel and V519 Ser both show larger scatter in high state than in low but differ in the low/high state duty cycle. V379 Tel is observed mostly at low state at first and remains predominantly in high state after transitioning, however, V519 Ser transitions frequently between high and low states. In contrast, some systems show orbital modulations in high state as well as low state e.g. J0328+0522 (Fig. 2.14) HU Aqr (Fig. 2.15), J0227+1306 (Fig. 2.18, bottom), MN Hya (Fig. 2.19).

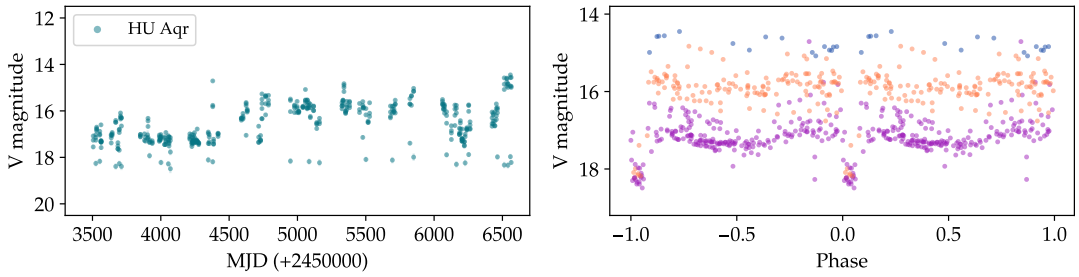

FIGURE 2.15 – Left: The long-term light curve of HU Aqr from CRTS. Right: Phase plot of HU Aqr. Blue, orange and purple represent high, intermediate and low states, respectively.

Systems with no state changes are less complicated to phase, as the orbital structure is expected to remain fairly constant in brightness and phase. HS 0922+1333 shows a stable long-term light curve characteristic of a low accretion rate polar (LARP). Tovmassian and Zharikov (2007) found evidence of a faint accretion stream in HS 0922+1333. The phase-folded light curve in this work shows distinct low amplitude (< 0.5 magnitude) orbital modulations as seen in Fig. 2.17. In comparison, orbital modulations greater 1 magnitude are seen in the R_c filter light curve from Tovmassian and Zharikov (2007).

The presence of eclipses, and their approximate depths, can be identified in long-term light curves. With enough data, a phase-folded light curve reveals the width of the eclipse profile, indicating the absence/presence of an accretion disc. The factors affecting the detection of eclipses in the long-term light curves include the orbital period, inclination of the system, eclipse depth, eclipse duration and observing cadence. Eclipses are often detected in the long-term light curves of HU Aqr (Fig. 2.15), PW Aqr (Fig. 2.18, top) and J0227+1306 (Fig. 2.18, bottom). Although a coherent orbital structure is not seen in the phase plots of PW Aqr and J0227+1306, well-aligned narrow eclipses are distinguishable.

In contrast, the eclipsing system MN Hya has $P_{\rm orb}$ = 3.39 h and deep but narrow (lasting just 4 % of the orbit) eclipses (Buckley et al., 1998; Wang et al., 2018). Eclipses are rarely seen in the long-term CRTS light curve and unidentifiable in the phase-folded light curve (Fig. 2.19, top). DP Leo is a well-sampled eclipsing system. Despite having a short orbital period of ∼ 1.5 h (Pandel et al., 2002), evidence of eclipses is only seen in the last two seasons of the long-term light curve (Fig. 2.19, bottom). These could be interpreted as outliers with large errors as they are not consistent throughout the light curve. The alignment of the four faint detections as part of an eclipse profile in the phase plot reveals the eclipsing nature of this system.

2.5 SELECTION CRITERIA FOR MY SAMPLE OF POLARS

The initial selection of my sample of potential polars was through the visual inspection of the long-term light curves of CVs discovered by CRTS. Having visually analysed the light curves of previously known polars, I selected 27 objects which had similar light curves properties to the previously known polars. Refer to § 2.3 for characterisations of polar light curves. Follow-up observations began in December 2013, independently of

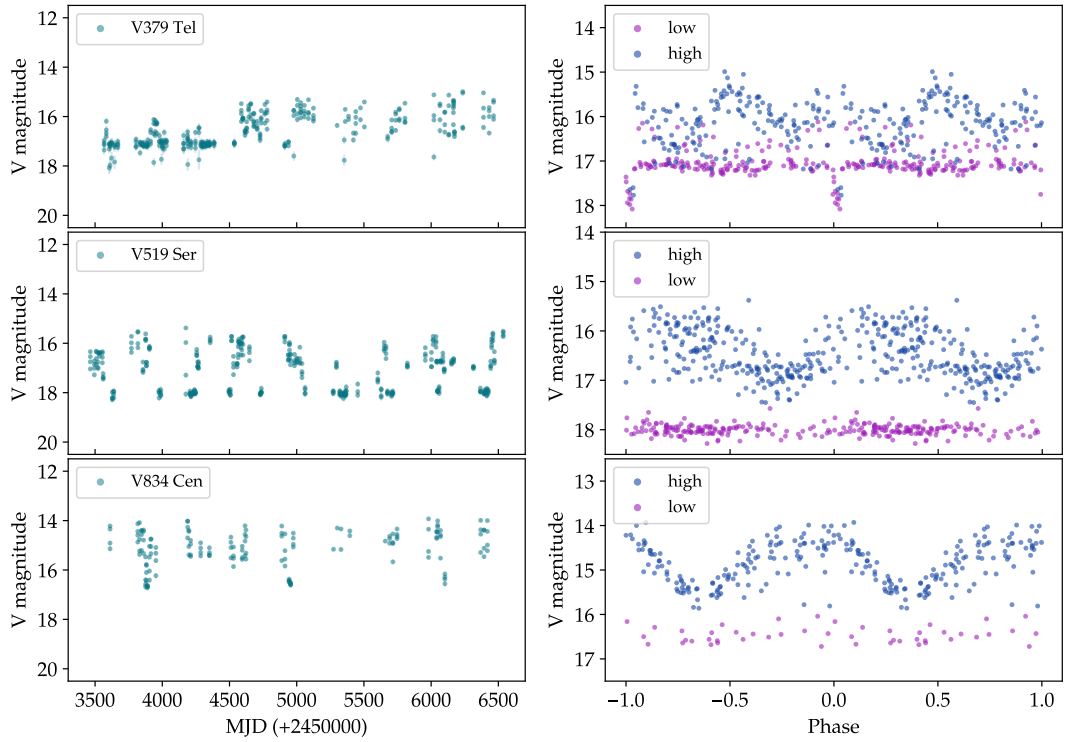

FIGURE 2.16 – Left: The long-term light curves of V379 Tel, V519 Ser and V834 Cen from CRTS (in the blue-green colour, teal). Right: Phase plots of V379 Tel, V519 Ser and V834 Cen, respectively. Dark blue indicates high state and purple indicates low state.

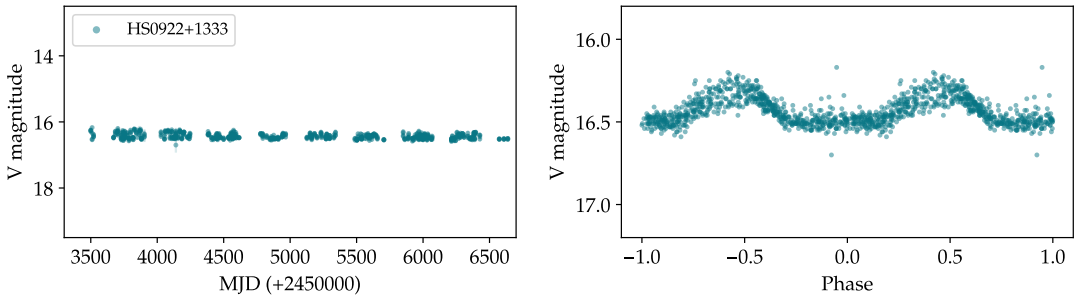

FIGURE 2.17 – Left: The long-term light curve of HS 0922+1333 from CRTS. Right: Phase plot of HS 0922+1333.

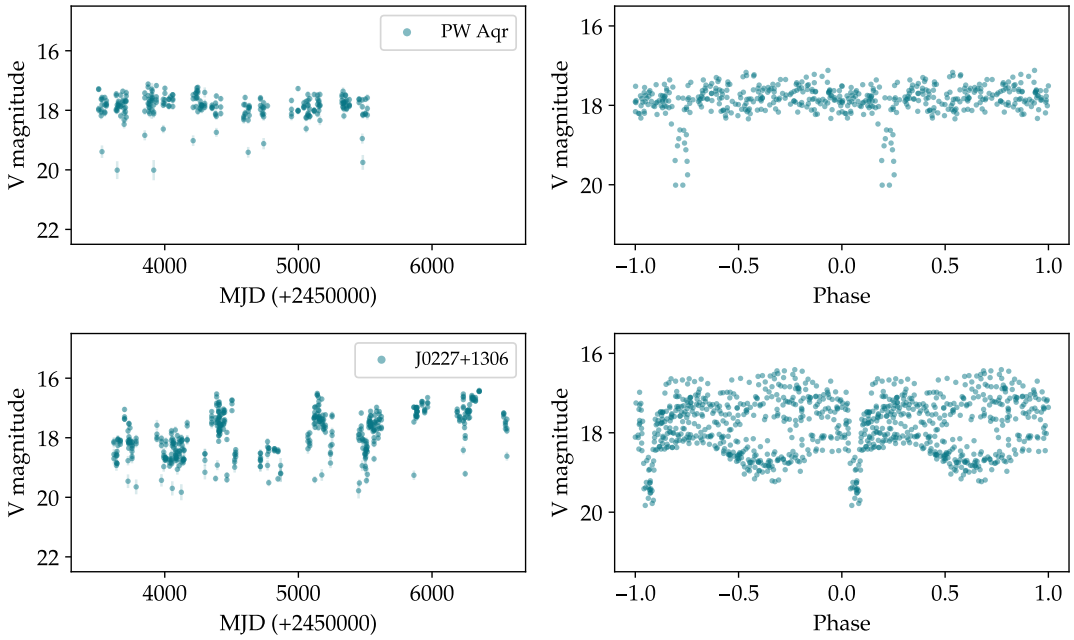

FIGURE 2.18 – Left: The long-term light curves of PW Aqr and J0227+1306 from CRTS. Right: Phase plots of PW Aqr and J0227+1306, respectively.

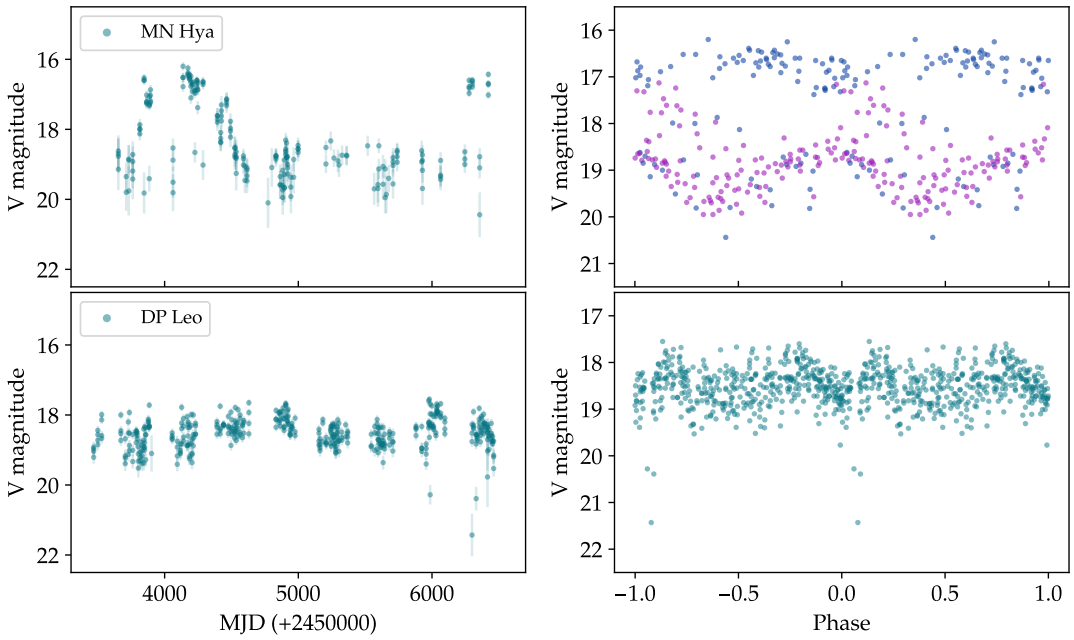

FIGURE 2.19 – Left: The long-term light curves of MN Hya and DP Leo from CRTS (in the colour teal). Right: Phase plots of MN Hya and DP Leo, respectively. Dark blue indicates high state and purple indicates low state.

Oliveira et al. (2017, 2020) who also searched for CRTS through visual inspection. A list of objects and the results from follow-up observations can be found in chapter 4.

2.6 AUTOMATED CHARACTERISATION OF LONG-TERM LIGHT CURVES OF POLARS

The long-term photometric variations of polars are not well studied or characterised. Having identified different characteristics of the long-term light curves of polars in § 2.3, I systematically analysed the properties of long-term light curves of the previously known polars, according to the different characterisations. This was done with the objective of understanding the long-term photometric behaviour of polars and developing an automated method to identify candidate polars and characterise the long-term light curves of polars from current and future transient surveys. The following sections detail my approach to the analysis of the long-term CRTS light curves of known polars, using them as a training set for the characterisation of the light curves of polars.

The magnitude peaks are extracted from the long-term light curves for each year of observations assigned a season. The outbursting CVs, mostly dwarf novae, are identified and removed from the sample, with potential polars remaining. Bright and faint outlier peaks are removed from the main peaks of the remaining sample to prevent flares and eclipses from being included in the characterisation. The divisions between different states are then defined and objects are characterised based on which states are occupied and how frequently, with respect to the long-term light curve. The characterisation process is represented as a flow diagram in Fig. 2.20. More details to follow in subsequent subsections.

2.6.1 *Systematic analysis of long-term light curves of confirmed polars*

The CRTS provides long-term light curves, with 8 – 9 years of coverage, which I divide into annual seasons of 365 days. Each season consists of CRTS observations taken over the months that the target is visible to the survey telescopes within a year (see fig. 2.21). Some of the seasons may be less sampled than other seasons, so I have added the condition that any season with less than eight data points is removed. Each observation consists of four snapshots taken 10 minutes apart. Thus eight data points represent two epochs of observations, if observations are complete.

Histograms of the data are produced, with 0.2 magnitude bins for each season, as well as the entire dataset, and represented as density plots and Gaussian Mixture models of the histograms (see Fig. 2.22), which are now described. A density plot is a smooth and continuous approximation of a histogram distribution. It estimates the general overall distribution of the data by smoothing out the noise. The density plots for the long-term dataset and seasonal magnitudes are fit using a Gaussian kernel density estimation (kde)[11], which produces the distribution by combining Gaussian distributions from each histogram point. A required parameter is the *density covariance factor*, a bandwidth factor that determines the smoothness of the distribution. Each individual season is assigned its own *density covariance factor*. A single peaked narrow

[11] https://docs.scipy.org/doc/scipy/reference/generated/scipy.stats.gaussian_kde.html

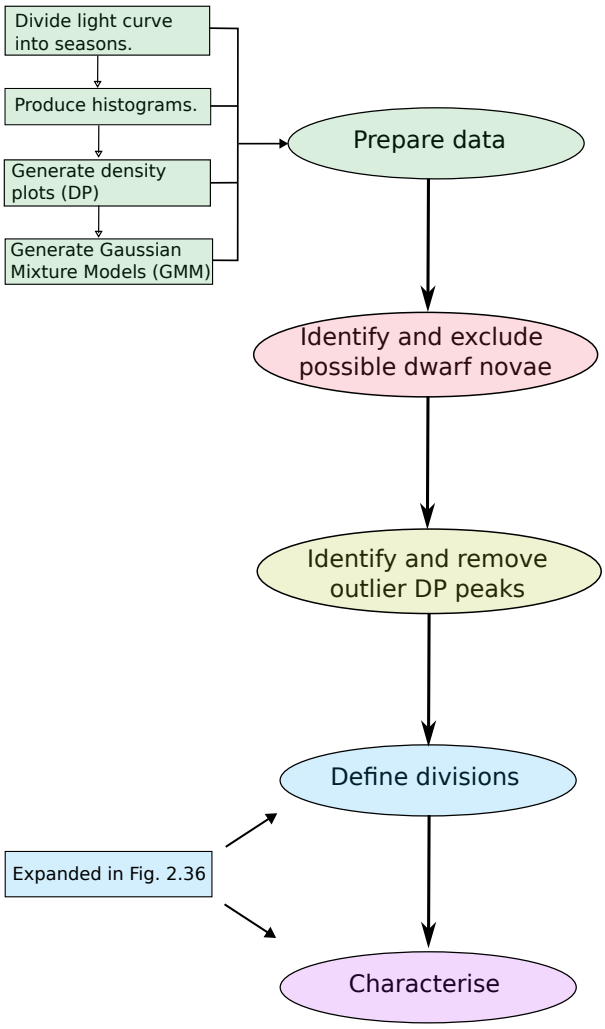

FIGURE 2.20 – A flow chart showing a summary of the quantitative process for characterising the long-term light curves of polars.

histogram requires a larger *density covariance factor* to prevent an overestimation of the modes. A wide (and possibly multi-modal) histogram requires a smaller *density covariance factor* to prevent over-smoothing. The *density covariance factor* is determined using the following empirical relation, dependent on the magnitude range:

$$dcf = \left(\frac{mr + 3.5}{mr + 0.8} + 2.05\right) \times 10^{-1} \tag{2.1}$$

where *dcf* is the *density covariance factor* and *mr* is the magnitude range. This relation that I derived from the data gives a good estimate of the histogram distribution.

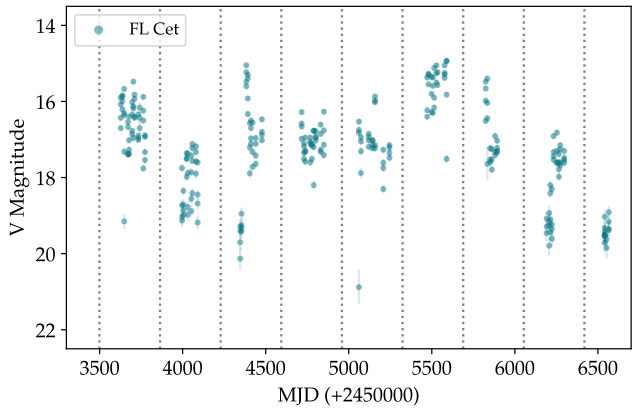

FIGURE 2.21 – The long-term light curve of FL Cet from CRTS. The dotted vertical lines show the divisions between seasons.

When determining the magnitude range of the long-term data for the *density covariance factor*, it is only necessary to include the magnitude range for the main/bulk distribution, i.e. without outliers. The double median absolute deviation (MAD, Hampel, 1974; Huber, 1981) algorithm is used to remove outlying data (eclipses, flares, brightenings and outliers) from the long-term light curve. The double MAD for asymmetric univariate distributions is an adaptation of median absolute deviation (MAD) for symmetric univariate distributions, where outliers are determined using the positive distances of each point from the median. The magnitude range of the data without outliers is used in equation 2.1 to determine the *density covariance factor*.

With the production of seasonal and long-term density plots, the magnitude of the peaks of the density plot distributions are determined. These peaks indicate the highest density magnitudes of each group/clump of data and therefore provide a good representation of the underlying magnitude distribution.

In addition to the density plot, a Gaussian Mixture Model (GMM, Nemec and Nemec, 1991; Krishnan et al., 1996) is fit to the seasonal and long-term data. A GMM is an algorithm that identifies various clusters (or groups) of data and fits a Gaussian distribution to each cluster. Each Gaussian is composed of three parameters: 1) The mean/centre of the Gaussian which is the peak of that distribution cluster; 2) the covariance that defines the width of the Gaussian and 3) a mixing probability that defines the size and weight of the Gaussian in relation to the others in the distribution. The sum of the mixing probabilities always equals one. GMMs are convenient because initial guesses for fit parameters are not required.

The *number of components* (i.e. peaks) is a required parameter for the GMM. As this is an automated method with no prior information on the distribution, the value for the *number of components* is obtained from the number of density plot peaks previously determined. The one-dimensional magnitude data are reshaped to meet the GMM requirement of a two-dimensional input dataset. The GMM is fit to the data using the

sklearn.mixture.GaussianMixture()[12] Python function. As with the density plot, the peaks are obtained. Additionally, the mean, covariance and mixing probability of individual peaks are determined.

An advantage of density plots is that they are positioned more accurately with respect to the magnitudes of the histogram peaks (i.e. the peak magnitudes), but they fall short at representing the heights of the histograms. The density plot heights are usually lower than the histograms. The benefit of GMMs is that they give more accurate peak height. In trying to fit Gaussian distributions to the histograms which are not exact Gaussians, the GMMs may have a larger difference in the positions of the peak magnitudes from the data. These differences are seen in Fig. 2.22, an example of the eclipsing polar, FL Cet. More examples of histograms of polars with other characterisations are presented in appendix B.1. The histograms, DPs and GMMs are normalised which means the area of the histograms and the areas under the DPs and GMMs are equal to one.

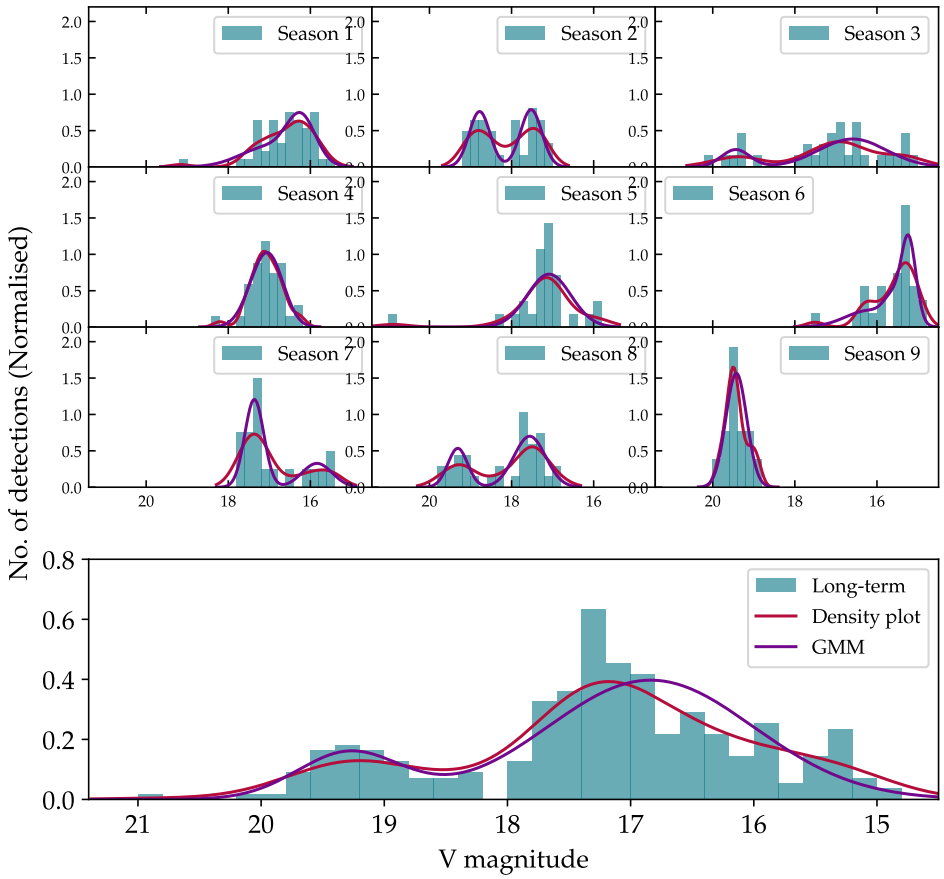

FIGURE 2.22 – The histogram (teal), density plot (red) and Gaussian Mixture model (purple) of the FL Cet magnitudes from the CRTS light curve (Fig. 2.21). The top panel is seasonal and the bottom panel is long-term.

[12] https://scikit-learn.org/stable/modules/generated/sklearn.mixture.GaussianMixture.html

2.6.2 *Identifying outbursting Dwarf Nova CVs*

Before characterising the long-term photometric behaviour of potential polars, it is necessary to discard the light curves of the non-magnetic CVs. Most non-magnetic CVs exhibit outbursts of some form, namely dwarf novae outbursts, superoutbursts and echo-outbursts/rebrightenings. The duration and duty cycles of these events vary for different CV subclasses. Using this common behaviour, detected outbursts from long-term light curves can be used to identify most non-magnetic CVs. Other observable behaviour of non-magnetic CVs is constant mean brightness as observed in i) Nova-like variables with stable hot accretion discs transferring mass at high rates, which may sporadically switch to states of low mass transfer (i.e. VY Scl subclass), ii) very short period AM CVs stars in permanent high states of mass transfer, iii) long period AM CVn systems with stable discs in permanent quiescent state, and iv) WZ Sge CVs with very long outburst recurrence times.

Outbursting systems are identified by evaluating the brightness histograms and corresponding density plot peaks of seasonal and long-term light curves. Two criteria are defined for identifying outbursting systems: criterion 1 is based on a defined outburst amplitude and criterion 2 incorporates outliers. Each criterion consists of one or more conditions. If all conditions are met then the system is flagged as outbursting based on the corresponding criterion. An outbursting system need not be limited to one criterion and may meet the conditions of both criteria. If any, or both of the criteria are met then the system is flagged as outbursting. Despite the number of outbursts occurring per season, only a single outburst is flagged per season. Only the brightest detected magnitude of that season is considered as the potential outburst, if it meets other conditions. Other fainter outburst detections may exist in the same season but are not considered.

2.6.2.1 Criterion 1 - Large amplitude outburst

A potential outburst is identified as the brightest detection in each season over 1 or 2 histogram bins (0.2 or 0.4 magnitudes) with at least one empty adjacent bin (0.2 magnitudes). Each season is searched for a potential outburst. If the magnitude of the potential outburst is 2.5 magnitudes brighter than the magnitude of the highest density plot peak for that season, then the first criterion is met and the system is classified as an outbursting system. A visual representation of these conditions of the first criterion is seen in Fig. 2.23.

2.6.2.2 Criterion 2 - Outlier detection

To identify outbursts with amplitudes less than 2.5 magnitudes from the highest density plot peak, stricter restrictions are applied to avoid classifying polars with sporadic low amplitude flares/brightenings as outbursting dwarf nova systems (e.g. Fig. 2.26). As mentioned, the potential outburst is required to span one or two bins (0.2 or 0.4 magnitudes) and be at least 0.2 magnitudes (one bin size) from the next faintest detection. A 0.2 magnitude gap may seem low considering outbursts have larger amplitudes, but this gap also applies to other outburst detections in the season which may lie close in brightness to the potential outburst (e.g. Fig. 2.24). In addition, more than one detection

at the potential outburst magnitude is required, because outbursts usually rise quickly (but not as quick as flares) and can be observed at/around the same maximum/peak brightness for at least a few hours to days (e.g. Fig. 2.25). In contrast, many flares/brightenings in polars do not usually stay at one observed brightness because they are typically fast and short-lived, they increase or decrease in brightness during a single observation of four snapshots over 30 minutes (see Fig. 2.26).

The histogram of the long-term light curve gives a representation of the magnitude distribution of the complete long-term monitoring by CRTS. While seeking outbursts in individual seasons, the brightness of the outbursts is compared to the magnitude distribution of the long-term light curve. Outliers within the distribution are removed, using the double MAD method, in order to remove outbursts and derive a quiescent brightness limit (brightest magnitude for quiescent brightness). True outburst magnitudes are expected to be brighter than the long-term quiescent brightness limit. This criterion works well for identifying outbursts if the system has less frequent outbursts (e.g. Fig. 2.27). In comparison, the first criterion is loosely constrained and less limiting than the second criterion. A visual representation of these conditions is seen in Fig. 2.28, with a detailed description in the caption. If outbursts occur more frequently, they would not be identified as outliers (e.g. Fig. 2.29).

The second criterion is as follows: The potential outburst is as defined previously. If the potential outburst has more than one detection at the same magnitude and if the potential outburst magnitude is brighter than the long-term quiescent brightness limit then the system is classified as an outbursting system. This means that the potential outburst is brighter than the general observed brightness.

2.6.3 *Determining the amplitude outburst limit for first criterion by evaluating different outburst amplitudes*

To obtain a limit for the outburst amplitude applied to the first criterion, a sample of known polars and dwarf novae from the Ritter-Kolb Catalogue (RKcat, Ritter and Kolb, 2003) and CRTS are evaluated. The total sample consists of 78 polars from RKcat with sufficient CRTS data, 34 randomly selected outbursting CVs from RKcat (mostly dwarf novae) and 36 randomly selected RKcat dwarf novae discovered by CRTS. Of the 34 outbursting CVs from RKcat, two light curves display no recorded outbursts by CRTS (see Fig. 2.30, top) as well as two of the 36 dwarf novae from CRTS (see Fig. 2.30, bottom), although CSS1626-1255 is under-sampled. Using the 70 outbursting CVs (from RKcat and CRTS), the amplitude of 197 observed outbursts from the magnitude of the brightest density plot peak for the corresponding season are recorded. An amplitude limit of 2.5 magnitudes includes 75% of all observed outbursts in the sample, 80% of outbursts have outburst amplitudes > 2.31 magnitudes and 90% of outbursts have outburst amplitudes > 2.07 magnitudes.

When applying the first criterion: 62% of RKcat outbursting CVs, 86% of CRTS dwarf novae and 10% of polars are flagged as outbursting, using an amplitude of 2.5 magnitudes; 68% of RKcat outbursting CVs, 86% of CRTS dwarf novae and 15% of polars are flagged as outbursting, using an amplitude of 2.31 magnitudes; 74% of RKcat

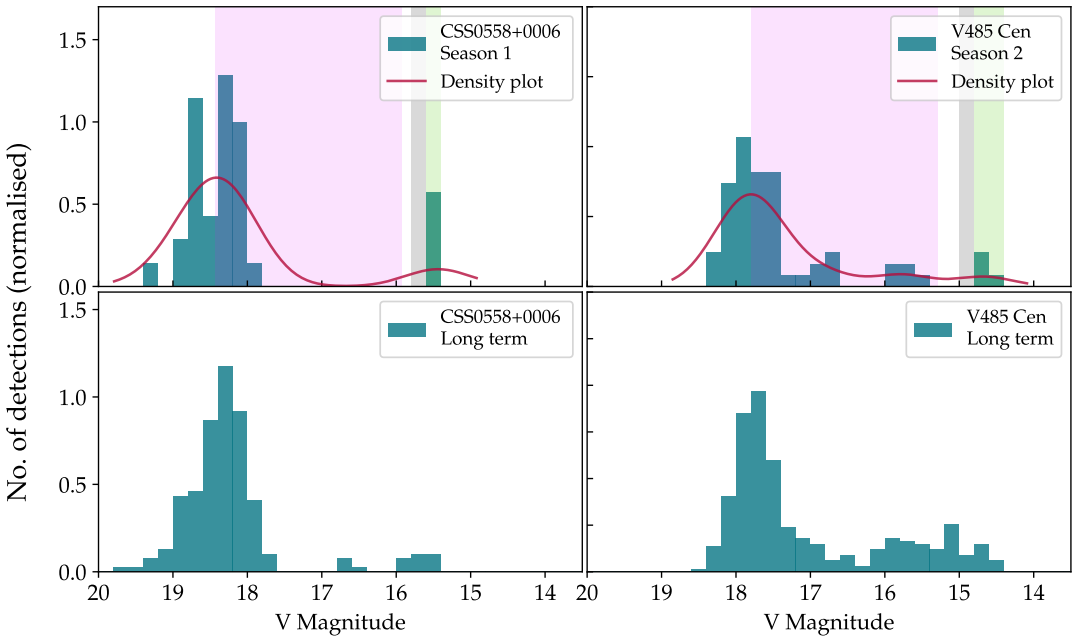

FIGURE 2.23 – A visual representation of the first criterion for identifying outbursting CVs, i.e. dwarf novae. The seasonal (top) and long-term (bottom) histograms in teal of CSS0558+0006 and V485 Cen are seen left and right, respectively. The corresponding red density plots overlay the seasonal histograms. The magnitude range of the potential outbursts of 0.2 or 0.4 magnitude width is filled in light green. The grey represents the area of 0.2 magnitudes, adjacent to the potential outburst, without any detections at that magnitude. The pink area is the outburst amplitude limit of 2.5 magnitudes. The potential outburst would be brighter than this limit.

outbursting CVs, 86 % of CRTS dwarf novae and 17 % of polars, are flagged as outbursting, using an amplitude of 2.07 magnitudes. When applying the second criterion: 59% of RKcat outbursting CVs, 81 % of CRTS dwarf novae and 4 % of polars are flagged as outbursting (refer to table 2.4 for quantities relating to percentages.).

When applying both criteria, the total number of systems flagged as outbursting is as follows: 82 % of RKcat outbursting CVs, 91 % of CRTS dwarf novae and 14 % of polars for an amplitude limit of 2.5 magnitudes for both criteria; 85 % of RKcat outbursting CVs, 92 % of CRTS dwarf novae and 18 % of polars for an amplitude limit of 2.31 magnitudes for the first criterion; 91 % of RKcat outbursting CVs, 92 % of CRTS dwarf novae and 20 % of polars for an amplitude limit of 2.07 magnitudes for the first criterion (see table 2.5).

Table 2.4 shows that there is a 6 % increase from 2.5 to 2.31 mag amplitude limits and 6 % increase from 2.31 to 2.07 mag amplitude limits, for RKcat outbursting CVs flagged as outbursting. For polars, there is a 5 % increase between 2.5 and 2.31 mag amplitude limits and 1 % increase between 2.31 and 2.07 mag amplitude limits. There is no difference between all criterion 1 amplitude limits for CRTS dwarf novae. Criterion 2 is most effective at identifying CRTS dwarf novae. When reviewing CVs identified as outbursting by both criteria together in table 2.5, there is a 3 % increase from 2.5 to 2.31 mag amplitude limits for RKcat outbursting CVs and 4 % increase between 2.5 and 2.31

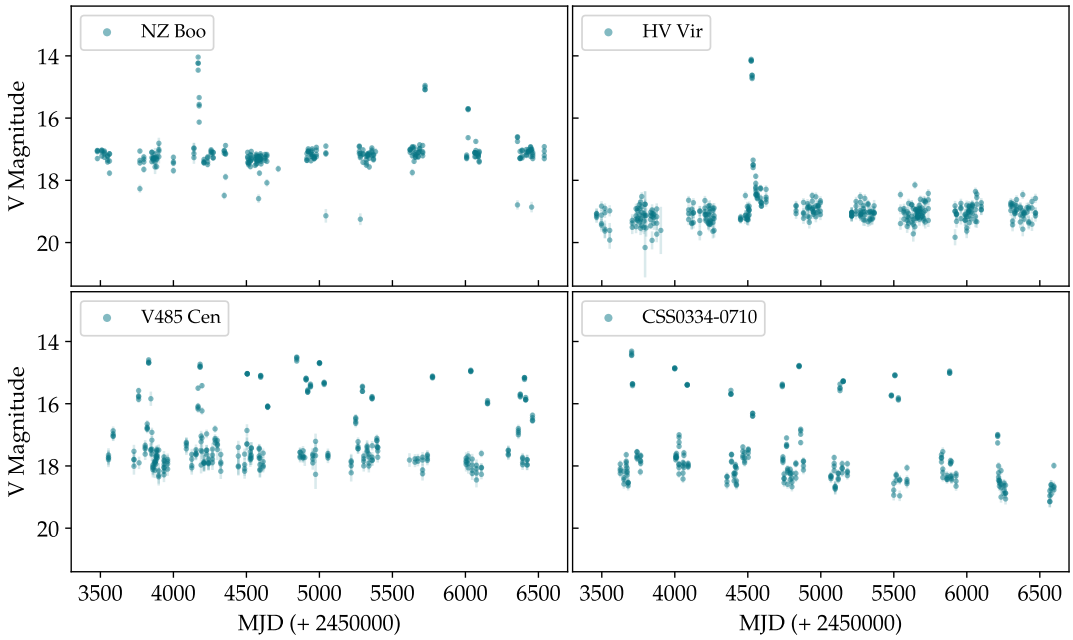

FIGURE 2.24 – The long-term light curves from CRTS of outbursting CVs; namely NZ Boo, HV Vir, V485 Cen, CSS0334-0710, respectively. Multiple detections per outburst or multiple outbursts per season can be seen in the light curves.

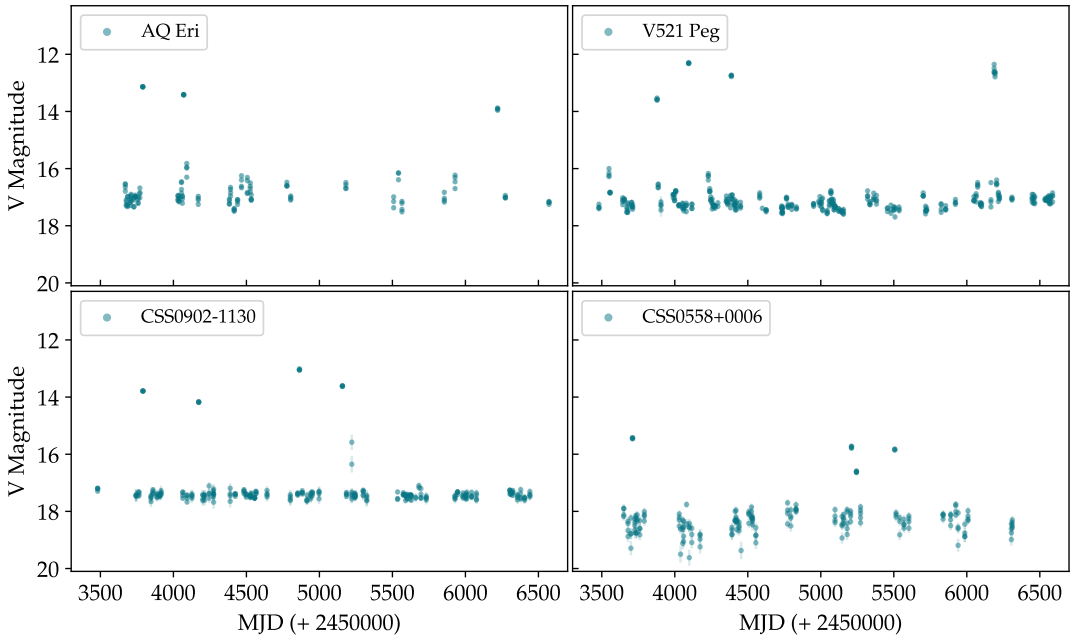

FIGURE 2.25 – The long-term light curves from CRTS of outbursting CVs; namely AQ Eri, V521 Peg, CSS0902-1130 and CSS0558+0006, respectively.

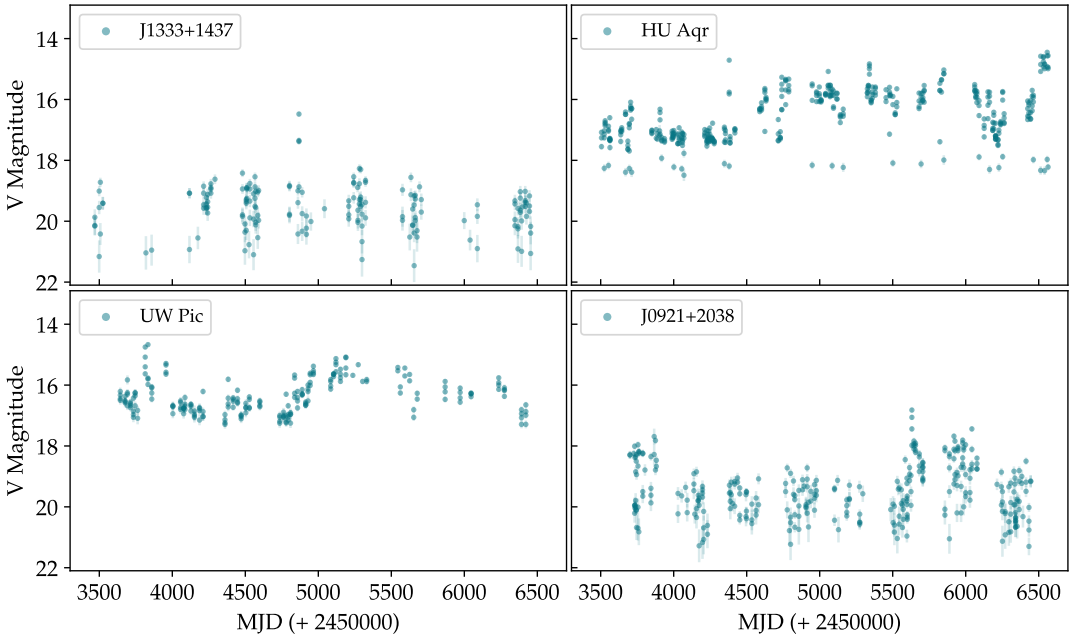

FIGURE 2.26 – The long-term light curves from CRTS of polars; namely J1333+1437, HU Aqr, UW Pic, J0921+2038, respectively. Brightenings/flares can be seen in each light curve.

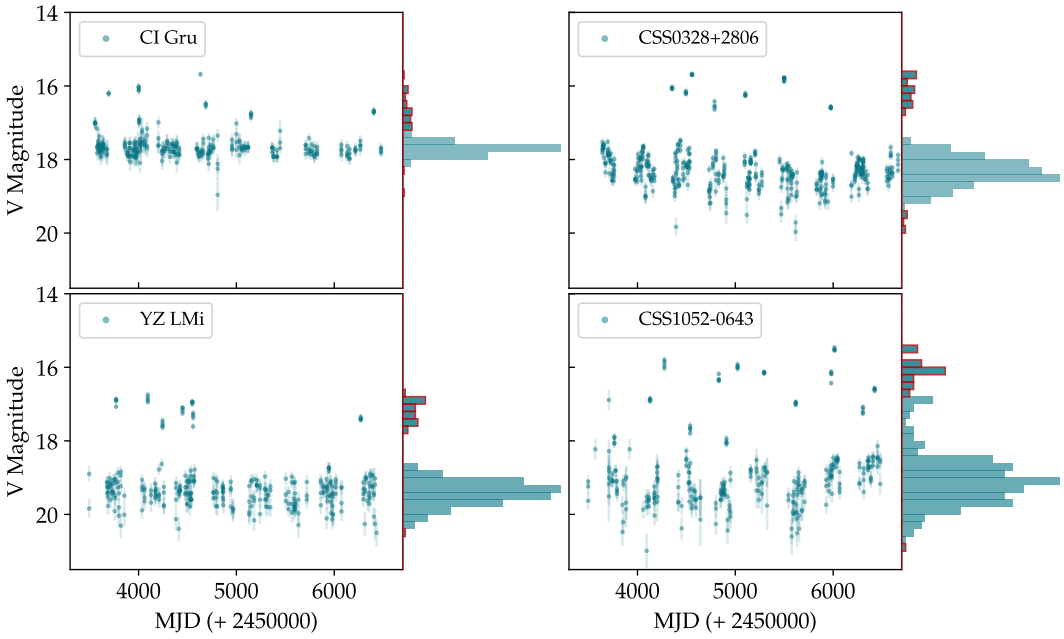

FIGURE 2.27 – The long-term light curves from CRTS of dwarf novae; namely CI Gru, CSS0328+2806, YZ LMi, CSS1025-0643, respectively. The side panels are histogram representations of the magnitude distribution. Histogram magnitudes with a red outline represent outlier magnitudes, as determined by the Median Absolute Deviation method.

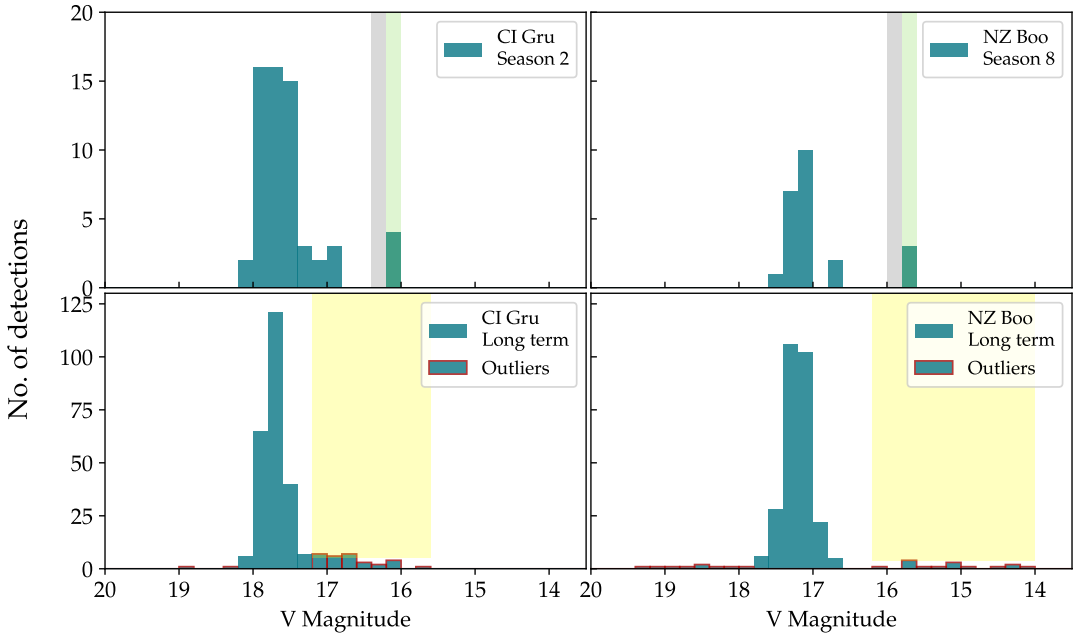

FIGURE 2.28 – A visual representation of the second criterion. The seasonal(top) and long-term (bottom) histograms in teal of CI Gru (left) and NZ Boo (right) are seen in columns 1 and 2, respectively. The magnitude area of the potential outbursts of 0.2 magnitude width is filled in light green. The grey represents the area of 0.2 magnitudes, adjacent to the potential outburst, without any detections at that magnitude. The yellow area in the bottom panels displays the location of the outliers in the long-term light curves, which are outlined in red. The potential outburst would lie with this area.

mag amplitude limits for polars.

In an effort to maximise the DN and minimise the polars flagged as outbursting, an outburst amplitude of 2.5 mag is selected. The benefit of a 2.5 mag amplitude limit outweighs the benefit of 2.31 mag amplitude limit as the increase in polars are flagged as outbursting from 2.5 to 2.31 mag amplitude limits is greater than that of outbursting RKcat CVs (when taking the contribution from both criteria into consideration). At 82 % of RKcat outbursting CVs, 92 % of CRTS dwarf novae and 15 % of polars flagged as outbursting, the dwarf novae that are missed by criterion 1, have a chance to be flagged as outbursting by criterion 2, meanwhile, the polars misflagged as outbursting would be reduced.

2.6.4 *Removing eclipses, flares/brightenings and outliers*

After the light curves of the possible outbursting systems are removed, the remaining light curves are evaluated by first removing outliers. Going forward, the light curves are evaluated as density plot (DP) peaks for each season which are peak magnitudes for the seasonal density plots. Refer to the top panel of Fig. 2.31 which corresponds with the seasonal histograms and density plots of FL Cet (Fig. 2.22). Eclipses, flares/brightenings and isolated outliers are usually represented as small DP peaks at either the bright or faint end of the magnitude range (see seasonal brightness plots with eclipses in Fig. 2.22,

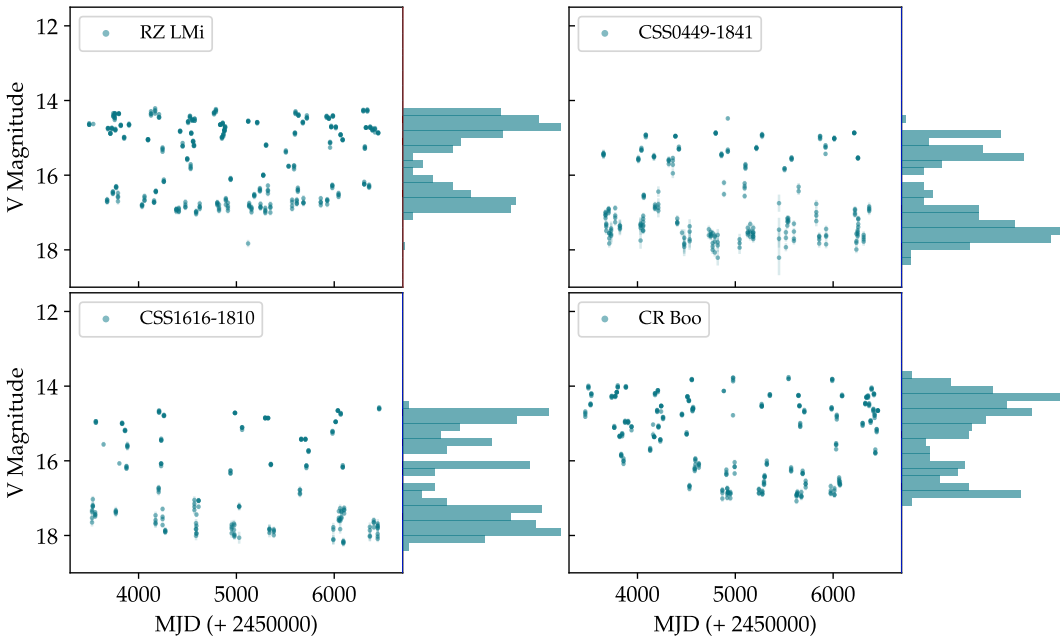

FIGURE 2.29 – The long-term light curves from CRTS of dwarf novae; namely RZ LMi, CSS0449-1841, CSS1616-1810, CR Boo, respectively. The side panels are histogram representations of the magnitude distribution. There are no outliers, as determined by the Median Absolute Deviation (MAD) method.

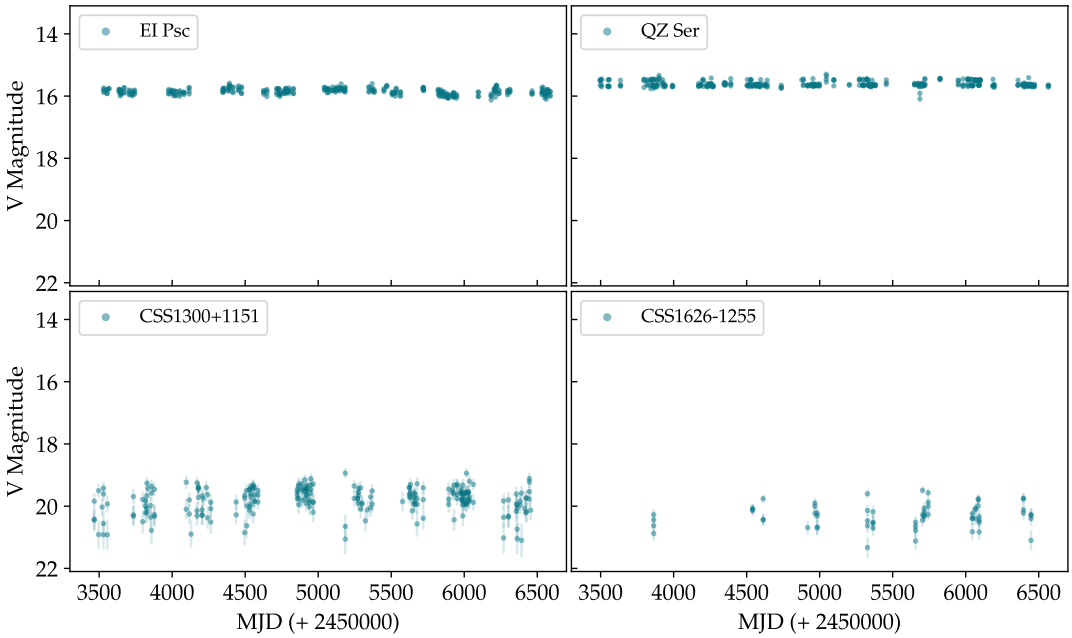

FIGURE 2.30 – Top: The long-term light curves from CRTS of RKcat dwarf novae, EI Psc and QZ Ser. Bottom: The long-term light curves from CRTS of dwarf novae from CRTS, CSS1300+1151 and CSS1626-1255 (which is undersampled). These light curves show no obvious observed outbursts.

TABLE 2.4 – Comparison of the effectiveness of outbursting criterion 1 (using outburst amplitudes 2.5, 2.31 or 2.07 mag) and criterion 2.

Sample	**Total**	**C1** (2.5)	**C1 %** (2.5)	**C1** (2.31)	**C1 %** (2.31)	**C1** (2.07)	**C1 %** (2.07)	**C2**	**C2 %**
RKcat OB	34	21	62	23	68	25	74	20	59
CRTS DN	36	31	86	31	86	31	86	29	81
RKcat mCVs	78	8	10	12	15	13	17	3	4

Notes: The outbursting criteria are tested on a sample of known outbursting CVs from RKcat, known DN from CRTS and known mCVs from RKcat. C1 = criterion 1, C2 = criterion 2; OB = outbursting CV; The limits in parentheses indicate the outburst amplitude limit used for criterion 1.

TABLE 2.5 – Comparison of the effectiveness of outbursting criterion 1 (using outburst amplitudes 2.5, 2.31 or 2.07 mag) and criterion 2 combined.

Sample	**C1+C2** (2.5)	**C1+C2 %** (2.5)	**C1+C2** (2.31)	**C1+C2 %** (2.31)	**C1+C2** (2.07)	**C1+C2 %** (2.07)
RKcat OB	28	82	29	85	31	91
CRTS DN	33	92	33	92	33	92
RKcat mCVs	11	14	14	18	16	21

Notes: C1+C2 is the total flagged as outbursting for each sample. The outbursting criteria are tested on a sample of known outbursting CVs from RKcat, known DN from CRTS and known mCVs from RKcat. C1 = criterion 1, C2 = criterion 2; OB = outbursting CV; The limits in parentheses indicate the outburst amplitude limit for criterion 1, used to determine the total flagged as outbursting.

e.g. season 1. The outlier DP peaks are removed from the bulk data to prevent them from interfering with the brightness positions of the states and the interpretation of the long-term characterisation of the system. The second panel of Fig. 2.31 shows the DP peaks of FL Cet without the eclipse outliers. Eclipse and flare/brightening information is recorded aside as the overall long-term trend is analysed.

To identify and remove outliers with large errors from the list of density plot peaks per season, the following steps are taken:

1. Each season in the list of the density plot peak magnitudes is searched.
2. If any season has more than one DP peak, the individual peaks are evaluated and the height of the lowest peak is compared to the highest peak. The highest peak would represent the bulk of the data or one of the states in that season.
3. If the lowest peak height is at least 3.4 times (refer below to the last paragraph of this subsection for a discussion of the determination of the 3.4 limit) less than the height of the highest peak, the magnitudes and corresponding errors of individual data points within the lowest DP peak distribution are assessed.

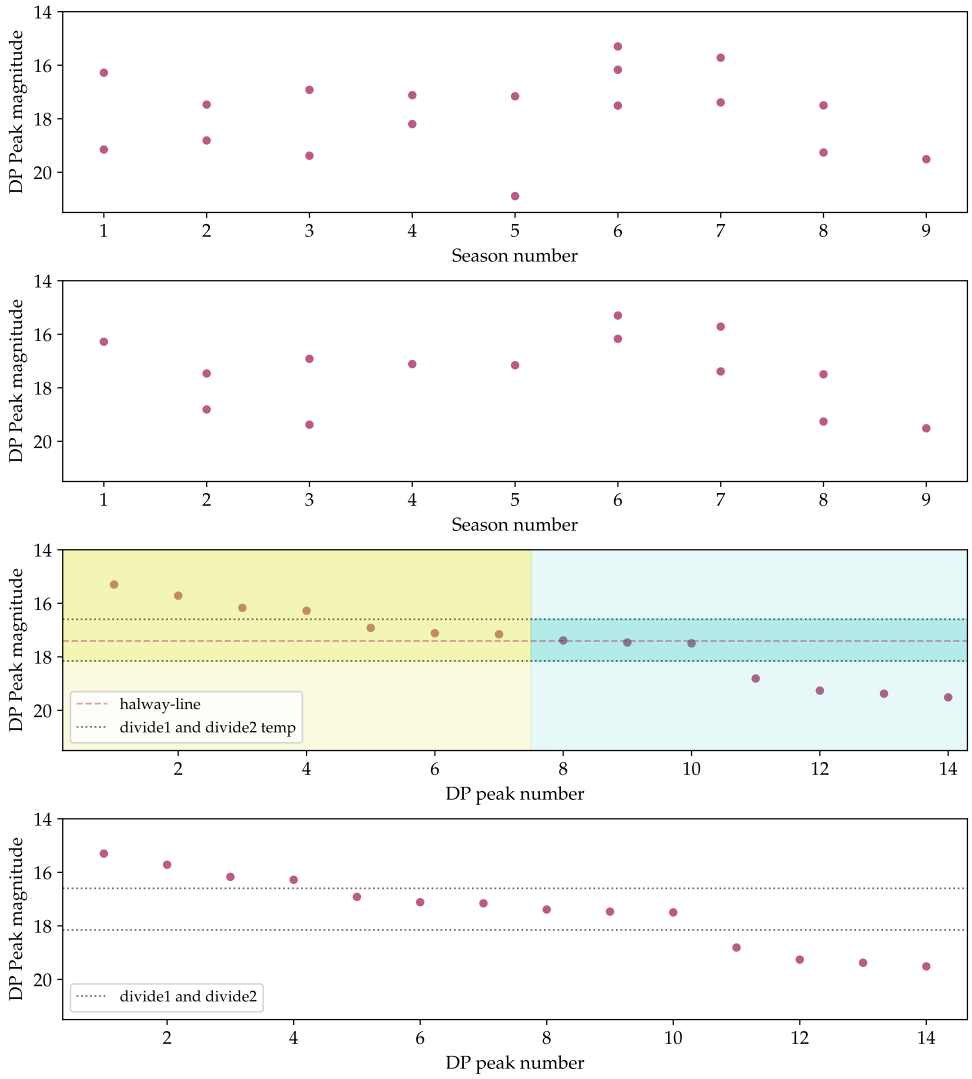

FIGURE 2.31 – The density plot peaks corresponding to histograms of FL Cet in Fig. 2.22. In the top panel are the density plot peaks in each season. The second panel has the same density plot peaks but with the bright and faint outliers (i.e. flares and eclipses) removed. The third panel shows the density plot peaks, without outliers, sorted in order of brightest to faintest magnitude. When determining where to place the divisions between states, the system is assessed and compared temporarily as a two-state system (yellow across the full x-axis) and three-state system (cyan across the full x-axis). The bottom panel shows sorted density plot peaks. The dotted lines represent the lines *divide1* and *divide2* separating high and intermediate states as well as intermediate and low states.

4. If the magnitude error is large enough to place the data point in the adjacent DP peak distribution then the lowest DP peak magnitude is removed from the list of peak magnitudes for that season.
5. Steps 1-4 are repeated for all seasons.

Similar steps are taken to identify and remove eclipses and remaining outlier peaks from the total list of peaks with the exception of the previous steps 3 and 4.

1. Each season in the list of the DP peak magnitudes is searched.
2. If any season has more than one DP peak, the individual peaks are evaluated and the height of the lowest peak is compared to the highest DP peak. The highest DP peak would represent the bulk of the data or one of the states in that season.
3. If the lowest DP peak height is at least 3.4 times less than the height of the highest DP peak and if the lowest DP peak magnitude is fainter than the magnitude of the highest DP peak, the lowest DP peak is considered an eclipse point or faint outlier.
4. The eclipse and outlier magnitudes, the corresponding seasons and the index of the eclipse DP peaks are placed into new lists.
5. The eclipse index is used to remove the DP peak associated with the eclipse from the list of seasonal DP peak magnitudes.
6. This process is continued as long as the season contains more than one peak and the lowest DP peak is 3.4 times less than the highest DP peak. The loop is broken if/when the magnitude of the lowest DP peak value is brighter than the magnitude of the highest peak value.
7. Steps 1-6 are repeated for all seasons.

The same process is repeated for identifying and removing brightenings/flares or bright outliers. The difference is in step 3) If the lowest DP peak height is at least 3.4 times less than the height of the highest peak and if the lowest peak magnitude is brighter than the magnitude of highest peak, the lowest peak is considered a flare or bright outlier. Step 6 also differs by not needing to break the loop as fainter outliers would have already been removed.

The 3.4 limit for outliers, eclipses and flares is obtained by considering all observed outliers, eclipses and flares detected by CRTS in the long-term light curves of the sample of previously known polars from RKcat. An evaluation of the ratio of the highest DP peak heights and the lowest DP peak heights from each season shows that if the lowest DP peak height is at least 3.4 times less than the height of the highest DP peak then the lowest DP peak height is likely an outlier, eclipse or flare. The lowest ratio value found for an outlier, eclipse or flare from the sample is 3.47.

2.6.5 *Determine states (define divisions)*

Groups of brighter and fainter data points indicate high and low accretion states, respectively. To distinguish between states, a magnitude value is defined where the brighter high state lies above and the fainter low state lies below, called the *dividing-line*. This magnitude value is represented as a line separating high and low states throughout the long-term light curve. For some systems, there is a clear division between states (e.g. EV UMa in Fig. 2.32, left), while the light curves of other systems appear ambiguously divided between states (e.g. EG Lyn in Fig. 2.32, right).

When defining different states, the DP peak values are evaluated, instead of Gaussian Mixture Model peaks, because density plot peaks are more accurately positioned/aligned

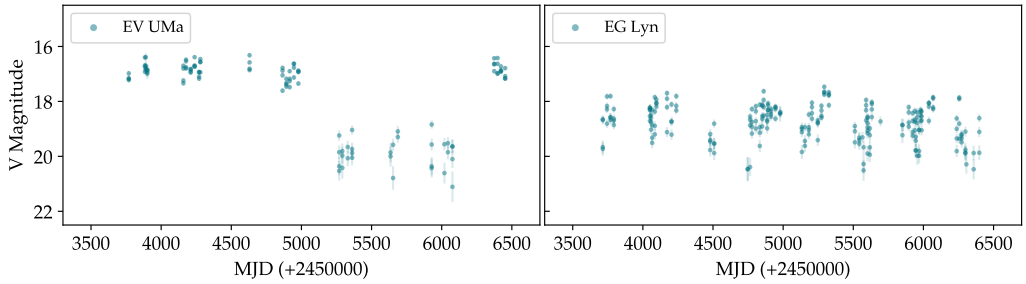

FIGURE 2.32 – The long-term light curve of EV UMa (left) showing high and low states, and the light curve of EG Lyn (right) without clearly distinguishable states.

with the original data peak magnitudes. The magnitude values for the density plot peaks, for each individual season, are placed into a single list, in seasonal order. The list is then rearranged in order of brightest to faintest magnitude values, called the *sorted-peaks* seen in the third and fourth panels of Fig. 2.31. Consecutive DP peak magnitude values are subtracted from each other (i.e. peak[i+1] - peak[i]) to obtain the magnitude gap widths between consecutive peaks. Intuitively, the DP peaks within the same state are expected to group together with larger gaps between the states.

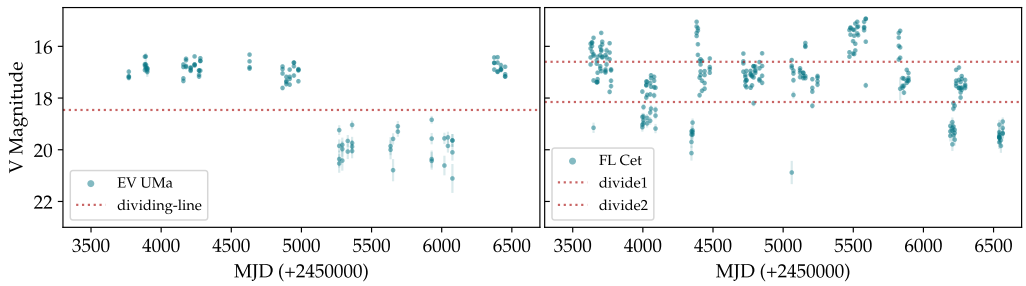

FIGURE 2.33 – Left: The long-term light curve of EV UMa. The red dotted line indicates the *dividing-line*. Right:The long-term light curve of FL Cet. The red dotted lines mark *divide1* and *divide2*.

A *halfway-line* is defined as the mid-point between the first peak and the last peak of the *sorted-peaks*. All systems are assessed as both temporary two-state systems and temporary three-state systems unless they are classified as stable or slightly variable, in order to best determine how many states a system has and where to place the states on a magnitude scale. Temporary dividing lines and states were assigned in order to assess different scenarios. The centres/midpoints of the two largest consecutive peak gaps are assigned *divide1-temp* and *divide2-temp*, where *divide1-temp* is the smaller gap value and *divide2-temp* is the larger gap value. The temporary *dividing-line* (*dividing-line-temp*) is assigned the value of *divide1-temp* or *divide2-temp*, closest to the *halfway-line*. Simply allocating the *halfway-line* as the *dividing-line* may be inadequate if the high and low states are not equally sized. See an example of assessment with temporary lines and states in the third panel of Fig. 2.31. The darker yellow area represents the temporary high state and light yellow is the temporary low state of a temporary two-state system. The top and bottom light cyan areas represent the temporary high and low states and the

darker cyan area represents the temporary intermediate state of a temporary three-state system. Except for stable and slightly variable systems, all systems are evaluated as both temporary two- and three-state systems. The following process is represented as a summarised flow diagram in Fig. 2.36.

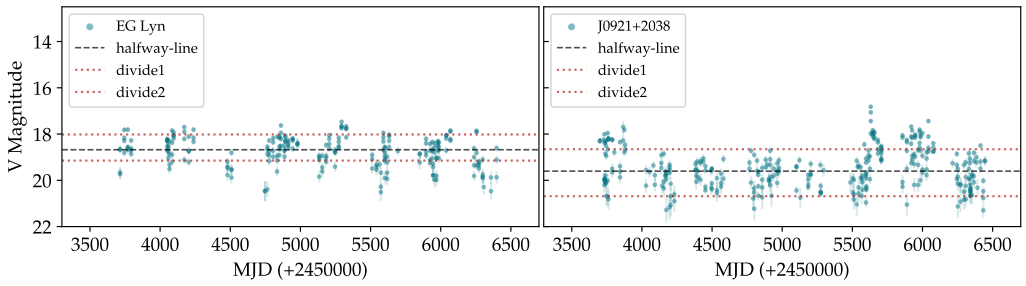

FIGURE 2.34 – Left: The long-term light curve of EG Lyn. The red dotted lines indicate *divide1* and *divide2*. The black dashed lines show the *halfway-line*. Right: The long-term light curve of J0921+2038. *divide1* and *divide2* are represented by the red dotted lines and the *halfway-line* is shown as the black dashed line.

No *dividing-line* is defined for a stable system, all DP peaks are considered to be in the same high or low state. Although, the system is most likely in an extended low state on the basis that most of the stable systems of the confirmed mCVs were identified as low accretion rate polars or pre-polars (e.g. HS0922+1333, V379 Vir, MQ Dra). A system is characterised as stable if a system meets the following two criteria:

1. all differences between consecutive DP peak magnitudes are less than 0.3 magnitudes
2. the standard deviation of the DP peaks in *sorted-peaks* is less than 0.1.

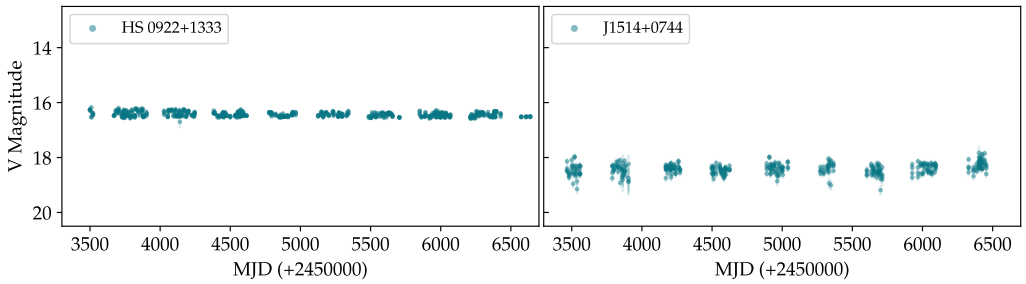

FIGURE 2.35 – The long-term light curve of stable systems, HS 0922+1333 and J1514+0744.

No *dividing-line* is defined for a slightly variable system, as variability is not large enough to separate high and low states. A system is considered slightly variable if the standard deviation of all the DP peaks from the combined seasons is between 0.1 and 0.5.

During the assessment as temporary two- and three-state systems, the following definitions are used. *2s-high-temp* is the list of DP peaks in the temporary high state of a temporary two-state system, with the DP peak magnitudes brighter than the *dividing-line-temp*. *2s-low-temp* contains the DP peak magnitudes in the temporary low state of a

two-state system, positioned fainter than the *dividing-line-temp*. Similarly, *3s-high-temp* contains DP peak magnitudes in the temporary high state of a temporary three-state system, containing DP peaks brighter than *divide1-temp*; *3s-int-temp* is the temporary intermediate state with DP peak magnitudes that lie between *divide1-temp* and *divide2*; *3s-low-temp* contains the DP peak magnitudes in the temporary low state of a temporary three-state system, with peaks fainter than the *divide2-temp*.

divide1-temp and *divide2-temp* have varying roles, depending on the status of the system. In the case of a two-state system, either *divide1-temp* or *divide2-temp* becomes the *dividing-line* separating the low and high states. For three-state systems, *divide1-temp* becomes *divide1* and *divide2-temp* becomes *divide2*, which separate high, intermediate and low states (refer to the bottom panel of Fig. 2.31 for the three-state characterisation of FL Cet).

The standard deviation of the combined peak values in the *2s-high-temp* list and the standard deviation of the peak values in the *2s-low-temp* list are determined. The ratio of the standard deviation of the DP peaks in the state with the highest standard deviation and the standard deviation of the DP peaks in the state with the lowest standard deviation is also used to determine the status of the system.

Some systems with two states have overlapping states or very gradual transitions between the states. At times *divide1-temp* and *divide2-temp* may lie a large distance from the *halfway-line*, closer to the bright and faint ends of the light curve. In such cases, the *halfway-line* is a better representation of the *dividing-line* than either *divide1-temp* or *divide2-temp* (see Fig. 2.34, right). The criteria for using the *halfway-line* as the *dividing-line* is:

1. The standard deviation of the DP peak magnitudes in *2s-high-temp* or *2s-low-temp* with the highest standard deviation is at least 2.5 times larger than the standard deviation of the temporary state with the lowest standard deviation.
2. The standard deviation of the DP peak magnitudes in *3s-int-temp* is larger than both the standard deviations of the DP peak magnitudes in *3s-low-temp* and *3s-high-temp*.

If a system is classified as a three-state system, it has two divisions. The markers for *divide1* and *divide2* for FL Cet, are seen in the bottom panel of Fig. 2.31. The following criteria are required for the system with three states:

1. Not classified as a two-state system with the *halfway-line* as the *dividing-line*.
2. The difference between the faintest and brightest DP peak magnitudes of the entire *sorted-peaks* is greater than 2 magnitudes. A large magnitude range prevents overlap between high and low states with additional room for an intermediate state.
3. The standard deviation of the DP peak magnitudes in *2s-high-temp* or *2s-low-temp* with the highest standard deviation is at least 2.5 times larger than the standard deviation of the temporary state with the lowest standard deviation.

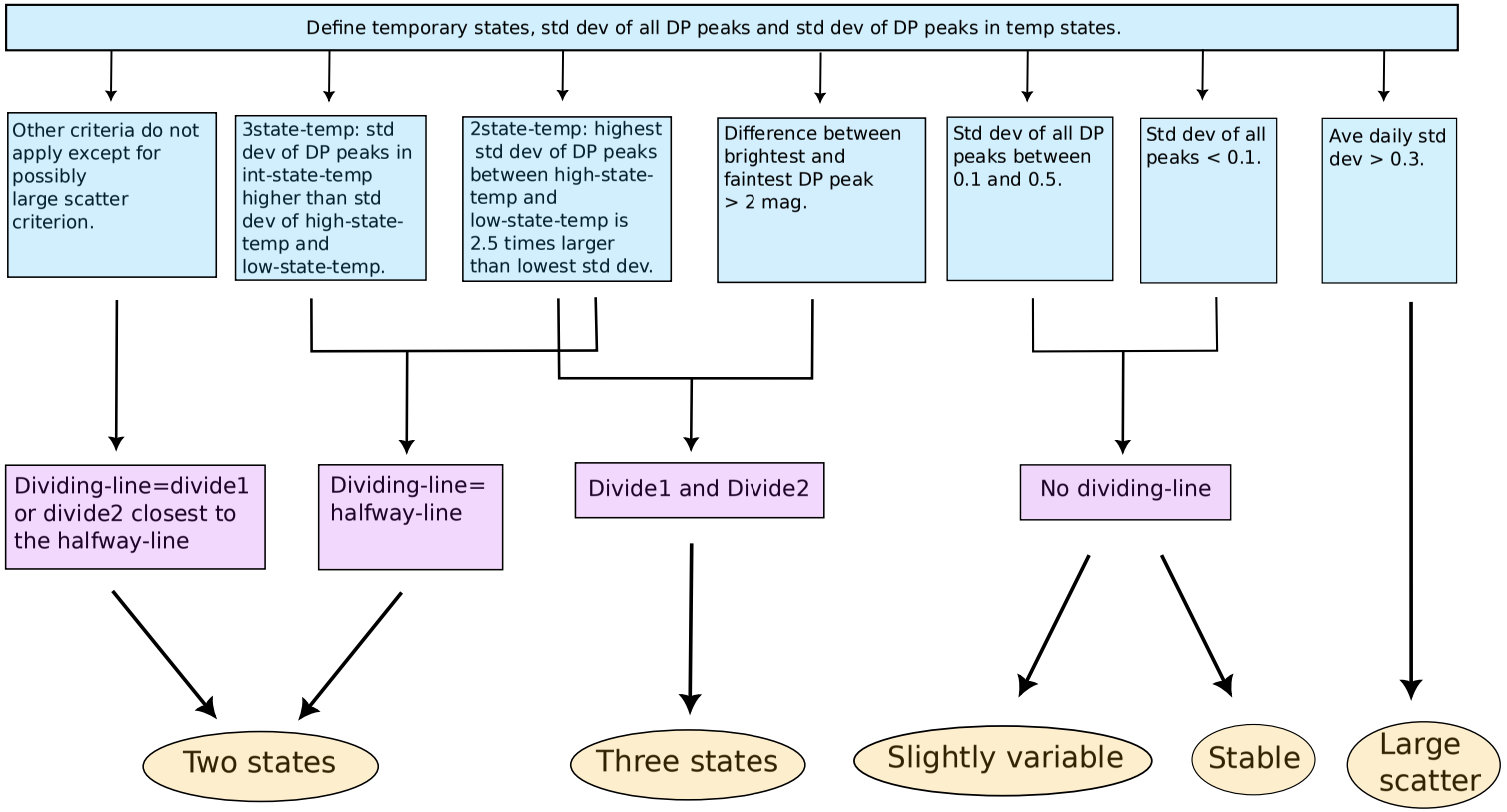

FIGURE 2.36 – An expansion of the last two steps of Fig. 2.20 describing the criteria used for defining the divisions between states and characterising the systems.

2.6.6 *Characterising polars*

Two-state systems are classified as either low-to-high, high-to-low or high=low. Low-to-high is defined as having 60 % of the total peaks in low state. High-to-low is defined as having 60 % of the total DP peaks in high state. If 40-60 % of the DP peaks are in high state and 40-60 % of the DP peaks are in low state, the system is classified as high=low.

If an intermediate state is identified, the system is characterised as a three-state system. Three-state systems are further classified as either three-state (low-to-high), three-state (high-to-low), three-state (high=low) and three-state (predominantly intermediate). Three-state (low-to-high) is classified when the number of DP peaks in low state exceeds the number DP peaks in high state, and similarly for three-state (high-to-low). If the three-state system has an equal number of DP peaks in high state as in low state, it is classified as three-state (high=low). If the number of DP peaks in the intermediate state exceeds those in both high and low states, the system is classified as a three-state (predominantly intermediate).

Systems found to have all DP peaks in high state or all DP peaks in low state are considered to be stable if 1) all differences between consecutive DP peak magnitudes is less than 0.3 magnitudes, and 2) the standard deviation of the *sorted-peaks* is less than 0.1.

Systems found to have all DP peaks in high state or all DP peaks in low state are considered to be slightly variable if the standard deviation of all the DP peaks from the combined seasons is between 0.1 and 0.5.

Systems are classified as having large scatter if the average standard deviation of the data taken in each day is greater than 0.3 and all peaks are in the same state.

Fig. 2.20 is a summarised visual representation in the form of a flow chart of the process of characterising the light curves from the division of the long-term CRTS light curves into seasons. The last two steps in Fig. 2.20 are expanded in Fig. 2.36.

A comparison of the characterisation of the previously known polars by eye with the quantitative method using the aforementioned criteria is seen in table 2.37. The crosses represent my characterisation by eye with question marks where I am unsure between different characterisations. The shade blocks are the characterisations using the systematic method. Ideally, both methods would align with an overlap between crosses and shaded blocks e.g. J0921+2038 in table 2.37, although some systems may not have mismatching characterisations e.g. EQ Cet in table 2.37. The two-state characterisations are in good agreement, having most mismatches with the slightly variables. Mismatches in the stable systems were mostly with the slightly variables as well. This may be an indication that the characterisations are not finite but rather transitional, so the characterisation parameters are more gradual and gradient-like. The large scatter systems are not characterised as well as the other characterisations, with 7 mismatches out of 12 systems. A more detailed table of the results of the quantitative analysis of the previously known polars from RKcat is given in appendix B.2, table B.1.

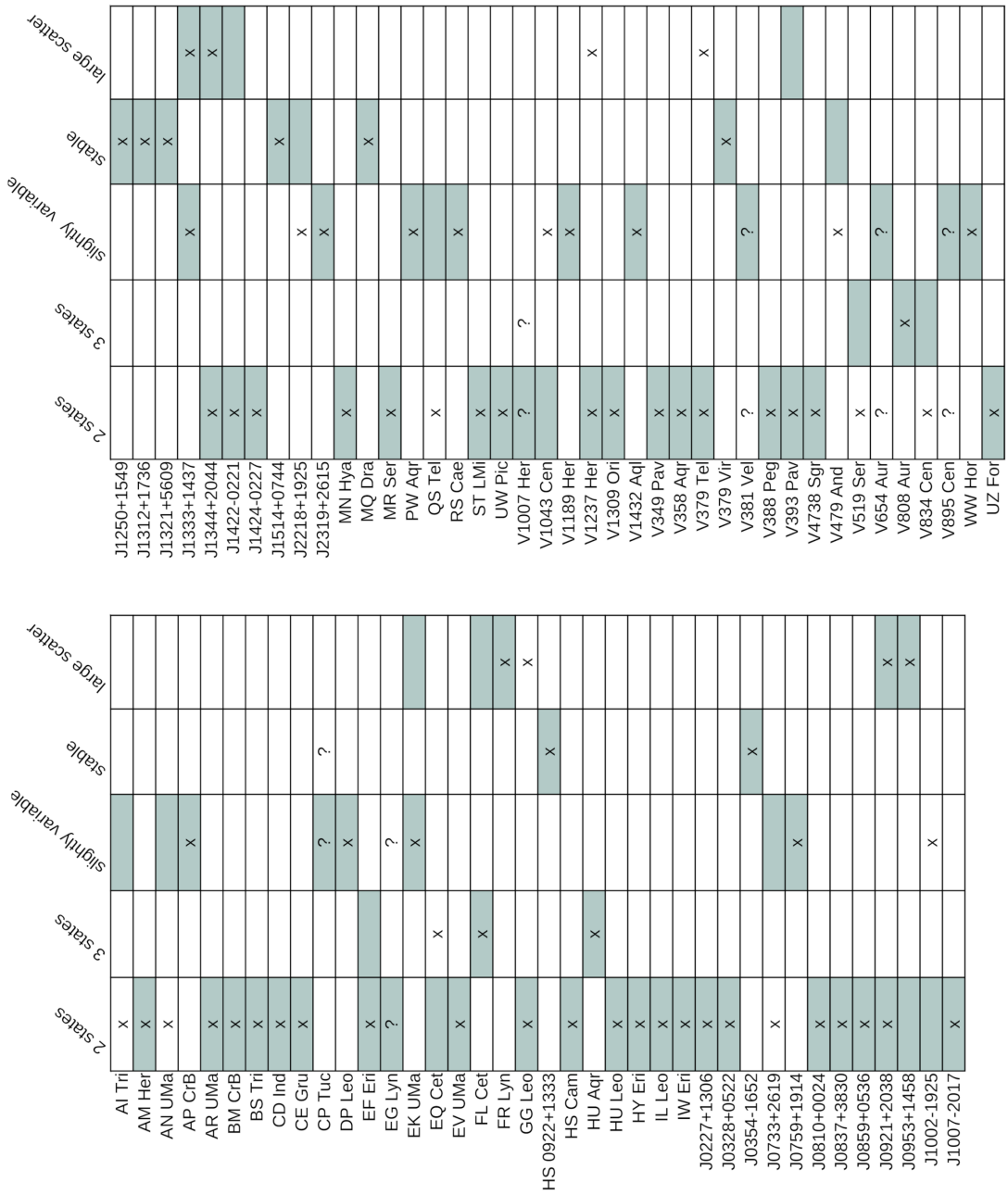

FIGURE 2.37 – A table comparing characterisations of previously known polars by eye (crosses) with the quantitative method developed using the aforementioned criteria (shaded blocks).

CHAPTER 3

AM CVn stars from optical transient surveys

In this chapter, I present my observations of AM CVn stars and a helium-rich dwarf nova selected mostly from CRTS and ASAS-SN. I give a detailed description of the photometric and spectroscopic observational processes, the data reduction processes and the processes for analysing the data. Detailed logs of photometric and spectroscopic observations of individual objects are provided. I discuss the photometric and spectroscopic results and analysis of these individual objects and conclude with a summary section and a tabulated summary of the results of the individual objects. The AM CVn stars in this work are all outbursting systems with orbital periods ranging from 31.65 to 54.78 min, four of which have orbital periods larger than 40 min. All AM CVn light curves show single or multiple humps per orbital cycle. The helium-rich dwarf nova, CSS2333-15, with a 61.70 min orbital period, is the only system with detectable hydrogen in the spectrum.

3.1 Photometric observations

All photometric observations were taken with either the 1.9-m Radcliffe telescope[1] or the 1.0-m Elizabeth telescope[2] at the South African Astronomical Observatory (SAAO) site in Sutherland. Mounted on these telescopes was the Sutherland High-speed Optical Camera (SHOC) CCD (Gulbis et al., 2011; Coppejans et al., 2013), for most of the observations, consisting of an Andor iXon X3 888 UVB camera. SHOC has a field of view of 1.92×1.92 arcmin^2 on the 1.9-m telescope and 2.85×2.85 arcmin^2 on the 1.0-m telescope. SHOC was used in frame-transfer mode in 1 MHz conventional mode with a preamplifier gain of 2.4. The University of Cape Town (UCT) CCD (O'Donoghue, 1995; Koen and O'Donoghue, 1995) was used for two of the observations taken in 2005 in frame-transfer mode. No filters were used in order to maximise the photon density for

[1] https://www.saao.ac.za/astronomers/1-9m/
[2] https://www.saao.ac.za/astronomers/1-0m/

all observations.

The observing procedure remained fairly constant for each target. If the orbital/superhump period was known, then I aimed for observing run lengths exceeding those periods. If observing a target for which the orbital/superhump period was unknown, the initial observing run was 3-4 hours (weather permitting) and subsequent runs were adjusted accordingly. Targets were observed for days at a time and sometimes observed again months or years later. The observing log is given in table 3.1, representing a total of 209.66 hours of photometric observations.

TABLE 3.1 – Observing log of photometric observations of AM CVn stars and a helium-rich DN.

Object	**Run No.**	**Date of obs.** (start of night)	**HJD of first obs.** (+2450000.0)	**Length** (h)	$t_{\rm in}$ (s)	**Tel.**	***r*** (mag)
CSS0105+19	S8206	2012 Sep 19	6190.44294	3.33	40	1.9-m	19.3
	S8212	2012 Sep 22	6193.46106	2.00	60	1.9-m	19.4
	S8214	2012 Sep 24	6195.44909	2.00	45	1.9-m	19.4
	S8217	2012 Sep 25	6196.42106	3.61	50	1.9-m	19.5
CSS0450-09	S8254	2013 Jan 08	6301.29106	5.15	60	1.9-m	19.0
	S8256	2013 Jan 10	6303.32149	2.00	60	1.9-m	19.1
	S8257	2013 Jan 11	6304.31005	7.22	30, 50	1.9-m	19.2
	S8259	2013 Jan 12	6305.29331	5.00	30, 60	1.9-m	19.1
	S8261	2013 Jan 13	6306.41206	4.17	30, 60	1.9-m	19.1
	S8263	2013 Jan 14	6307.29564	5.00	80	1.9-m	18.9
	S8265	2013 Jan 15	6308.29682	2.00	60	1.9-m	18.9
CSS2333-15	S8114	2011 Oct 19	5854.31250	1.28	15	1.0-m	17.0
	S8115	2011 Oct 20	5855.23215	4.06	20, 40	1.0-m	18.0
	S8132	2011 Dec 15	5911.28395	2.08	60	1.9-m	19.8
	S8134	2011 Dec 16	5912.28705	2.08	60	1.9-m	19.8
	S8137	2011 Dec 17	5913.34156	2.08	60	1.9-m	19.8
	S8139	2011 Dec 18	5914.28411	1.12	60	1.9-m	19.7
	S8141	2011 Dec 20	5916.28843	2.00	60	1.9-m	19.1
	S8215	2012 Sep 24	6195.52027	1.80	60	1.9-m	19.9
	S8335	2013 Oct 09	6575.40008	2.78	60	1.9-m	19.8
V558 Vir	S7646	2005 May 15	3506.42704	1.97	60	1.9-m	17.3
	S7647	2005 May 16	3507.28100	5.01	90	1.9-m	17.3
	S8274	2013 Mar 11	6363.58940	1.67	40	1.9-m	19.1
	S8277	2013 Mar 12	6364.54308	2.78	40	1.9-m	19.1
	S8316	2013 May 10	6423.44171	4.08	10	1.9-m	19.0
	S8318	2013 May 11	6424.50067	2.83	60	1.9-m	18.7
ASASSN-14ei	S8458	2014 Sep 07	6908.48258	4.40	5	1.0-m	15.6
	S8461	2014 Sep 08	6909.50874	3.74	5	1.0-m	15.6
	S8464	2014 Sep 09	6910.50808	3.70	5	1.0-m	15.0
	S8467	2014 Sep 10	6911.52971	3.16	5	1.0-m	13.8
	S8471	2014 Sep 12	6913.50871	3.00	20	1.0-m	15.7
	S8474	2014 Sep 13	6914.53661	3.00	10	1.0-m	15.8
	S8476	2014 Sep 14	6915.50859	3.59	10	1.0-m	15.9
	S8480	2014 Oct 17	6948.38387	3.00	2	1.9-m	15.6
	S8483	2014 Oct 18	6949.40510	2.50	2	1.9-m	15.7
	S8486	2014 Oct 19	6950.46260	2.00	2	1.9-m	13.0
	S8489	2014 Oct 20	6951.40523	2.50	3	1.9-m	15.1

Abbreviations: obs = observation, Tel = Telescope and $t_{\rm in}$ = integration time.

(Continued on next page)

Table 3.1 – continued from previous page

Object	Run No.	Date of obs. (start of night)	HJD of first obs. (+2450000.0)	Length (h)	t_{in} (s)	Tel.	$\bar{r}$ (mag)
	S8492	2014 Oct 21	6952.39418	2.50	3	1.9-m	15.9
	S8525	2014 Nov 30	6992.27257	7.51	8	1.9-m	15.9
	S8532	2015 Jan 10	7033.27633	2.00	10	1.9-m	16.1
	S8557	2015 Feb 20	7074.26713	2.48	10	1.0-m	16.3
	S8762	2015 Oct 16	7312.52914	2.50	5	1.0-m	16.4
	S8764	2015 Oct 17	7313.43615	2.00	5	1.0-m	16.3
	S8769	2015 Oct 19	7315.44432	4.53	5	1.0-m	16.2
	S8805	2016 Jul 31	7601.59010	1.99	30	1.0-m	16.4
	S8809	2016 Sep 03	7604.55883	3.34	5	1.0-m	16.4
	S8811	2016 Sep 04	7605.54726	3.41	5	1.0-m	16.5
	S8813	2016 Sep 05	7606.55289	3.45	5	1.0-m	16.4
	S8815	2016 Sep 06	7607.56147	2.57	20	1.0-m	16.4
	S8819	2016 Sep 08	7609.51783	4.01	5	1.0-m	16.3
	S8821	2016 Sep 09	7610.68648	4.02	5	1.0-m	16.1
ASASSN-14mv	S8530	2015 Jan 09	7032.40309	3.01	5	1.9-m	15.1
	S8533	2015 Jan 10	7033.37375	4.01	5	1.9-m	14.2
	S8536	2015 Jan 11	7034.36697	4.05	2, 1	1.9-m	14.3
	S8539	2015 Jan 12	7035.36610	3.48	5	1.9-m	15.3
	S8541	2015 Jan 13	7036.44958	2.04	10	1.9-m	15.3
	S8542	2015 Jan 14	7037.40449	0.83	5	1.9-m	15.1
	S8545	2015 Jan 16	7039.38270	1.51	3	1.9-m	13.8
	S8548	2015 Jan 18	7041.36966	2.00	5	1.9-m	15.4
	S8594	2015 Feb 22	7076.26394	2.08	5	1.9-m	16.0
ASASSN-15kf	S8674	2015 Jun 11	7185.27365	1.00	5	1.0-m	16.1
	S8683	2015 Jun 14	7188.39042	3.00	10	1.0-m	16.1
	S8686	2015 Jun 17	7191.36202	3.00	15	1.0-m	18.0
	S8689	2015 Jun 18	7192.33302	3.50	15	1.0-m	18.4
	S8692	2015 Jun 19	7193.37111	3.50	15	1.0-m	18.7
ASASSN-17fp	S8869	2017 May 13	7887.42333	6.40	60	1.0-m	19.0
	S8872	2017 May 14	7888.42526	6.25	60	1.0-m	19.0

Abbreviations: obs = observation, Tel = Telescope and t_{in} = integration time.

3.2 PHOTOMETRIC DATA REDUCTION

The photometric data were displayed with the visualisation tool for astronomical data `SAOImageDS9` (Joye and Mandel, 2003), and reduced with `IRAF` (Tody, 1986) using standard `IRAF` tasks. The raw data output from SHOC is a data cube containing a series of photometric images taken at intervals of the set exposure time. The original cube contains the UTC-OBS header set to universal time at the end of the first exposure which corresponds to the start of the exposure. Using *imslice*, the 3-dimensional cube was split into separate 2-dimensional images which are all given the same header as the data cube by default.

The cube containing the sky-flats consists of images taken at the minimum exposure time for a given binning. The sky-flats were taken during evening twilight over a small window period when the SHOC read a count rate between 20 000 and 30 000 counts. The sky-flats cube was spliced to produce individual images which were used to create a

master flat. The master flat is the normalised average of all the sky-flats. I then applied the flat-field correction to the science images by dividing them by master flat. This corrects for any image artifacts due to instrumental imperfections such as pixel-to-pixel sensitivity variations of the detector or shadows cast by dust particles. The FITS-file image headers were edited to contain the correct information including the object name, its coordinates, epoch, date of observation, time of observation, observatory and filter. Each image was assigned its own individual time stamp corresponding to the start of each exposure. These were all the necessary steps taken for the preparation of the images for photometric reductions.

The DS9 frame was flipped on its x-axis to match the orientation of the finder chart, to identify the target. To locate the bright stars in the field, the standard deviation of the mean noise level was determined and used in the data parameters for *daofind*, which was used to find the x and y pixel positions of the stars that met the set requirements/-parameters, without identifying galaxies or other extended astronomical objects and cosmic rays (Stetson, 1987). Differential aperture photometry was done using aperture photometry task *phot* in the DAOPHOT package. It performs simple aperture photometry within a circular annulus with a given radius centred on the peak of the stellar profile (Stetson, 1987; Artusi et al., 2016). For images without drifting, i.e. the x-y positions of the stars in the frame remain relatively constant throughout the data cube, the photometry was done using the positions of the selected bright stars from the first exposure. The aperture had the freedom to move by a few pixels from its previous position if slight drifting occurred. If there was significant drifting, the positions of the selected stars from each exposure were used, so the apertures were placed in the exact positions of the selected stars for each frame.

Ten or more apertures were selected with radii ranging from smaller than the target and comparison stars to larger. The photometry was done on all the previously selected stars from the *daofind* output file(s), using all the listed apertures. The aperture corrections were computed with *mkapfile* in the PHOTCAL package. This task subtracts the sky background from the computed magnitudes from the previous step for each aperture. *mkapfile* computes the instrumental magnitude of the selected stars using the growth-curve method (Stetson, 1990). A growth curve displays the mean magnitude difference between the brightness through two consecutive apertures, over a range of 10 or more apertures with increasing radii. The curve of growth steeply increases for apertures smaller than the star in the field and then gradually increases as the apertures exceed the radius of the star (Fig. 3.1), if the curve converges. The gradual increase is predominantly due to random and local systematic errors, contributing to the total noise, which increases with increasing aperture radii. The asymptotic value where $R_{\text{aperture}} = \infty$ gives the optimum aperture with maximum signal-to-noise ratio and corresponding instrumental magnitude.

One or more comparison stars can be used for differential aperture photometry. I used one star close to the apparent size of the target and derived the mean value of the comparison star magnitude. Any deviations of the comparison star were subtracted from the mean and the corresponding offsets were applied to the instrumental magnitude of the target for the same exposure frame. Differential photometry corrects for the changes in the effects of the Earth's atmosphere or the instrument. All calibrations were made

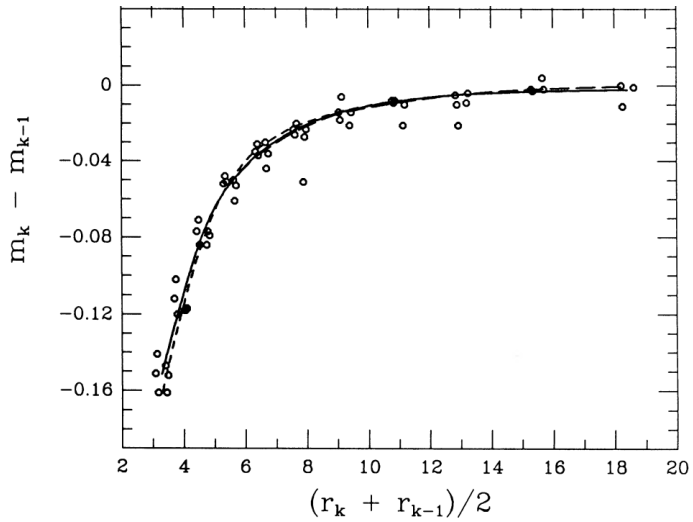

FIGURE 3.1 – An example of a curve of growth from Stetson (1990). The data points are observed magnitude differences for increasing consecutive apertures. The long dashed line is an empirical curve of growth from averaging the data points. The solid line is a compromise between the empirical curve and a best-fitting analytical curve of growth (short dashed line).

using the SDSS photometry of comparison stars (Sloan r photometric system). It was found that, for stars with a magnitude in the range of $g - r = 0.2 - 1.0$, there is a stable zero-point offset between V and SDSS r of 1.2 ± 0.05 on a clear photometric night (Woudt et al., 2012b). This is consistent with the photometric transformation in Jester et al. (2005). If an observed target was not covered by the SDSS, then the calibrated offset of another observed target from that same night was used.

3.3 PHOTOMETRIC ANALYSIS PROCESS

This section describes the different period analysis techniques used for determining the periods from light curve data. Fourier analysis and phase dispersion minimisation were both used for analysing the data from the observing runs. They both usually yielded the same results in § 3.7 and § 4.6, 4.7 & 4.8 but sometimes the results were not in agreement. Lomb Scargle analysis was used in § 2.4 to find periods from the long-term CRTS data.

3.3.1 *Fourier analysis and phase dispersion minimisation*

The periodicities for the light curves were determined by Fourier analysis and phase dispersion minimisation (PDM). Fourier analysis decomposes the original periodic signal into its constituent sine and cosine waves, making it ideal for finding the period of sinusoidal data. The equation for the Fourier Transform (FT) is

$$\mathcal{F}(\nu) = \int_{-\infty}^{\infty} e^{(i2\pi\nu t)} dt, \tag{3.1}$$

which is solved numerically because real data, represented by g_n, is not an analytical function. The complex exponential function, where ν is the test frequency, is multiplied by the observed measurement and the time difference between each point. Then all the

measurements are summed over. The classic periodogram of the discrete FT for discrete data points can be derived from the analytical FT as:

$$\mathcal{P}(\nu) = \frac{1}{N}\left|\sum_{n=1}^{N} g_n e^{-i2\pi\nu t_n}\right|^2 \tag{3.2}$$

$$= \frac{1}{N}\left(\left(\sum_n g_n \cos(-2\pi\nu t_n)\right)^2 + \left(\sum_n g_n \sin(-2\pi\nu t_n)\right)^2\right), \tag{3.3}$$

where g_n is the observed function, ν is frequency, t_n is the observing time for the n-th data point. The function g_n is evaluated repeatedly for every test frequency within the given range. This method is ideal for uniformly sampled data with periodicity parameters that remain constant. In this work, the FT analysis was performed with Eagle software developed by Darragh O'donoghue on the multiple nights of SHOC data.

PDM is minimisation of the "variance of the data with respect to the mean light curve" (Stellingwerf, 1978). The variance of the whole data set is

$$\sigma^2 = \frac{\Sigma(x_i - \bar{x})^2}{N-1}, \quad (i = 1,...,N), \tag{3.4}$$

where N is the total number of data points. The variance within each bin is

$$s_j^2 = \frac{\Sigma(x_{kj} - \bar{x}_j)s_j^2}{n_j - 1}, \quad (j = 1,...,M), \tag{3.5}$$

where n_j is the number of data points in the j-th bin, M is the number of phase bins and . The overall variance of all phase bins j is

$$s^2 = \frac{\Sigma(n_j - 1)s_j^2}{\Sigma n_j - M}, \quad (j = 1,...,M). \tag{3.6}$$

The scatter is evaluated using the statistic

$$\Theta_{PDM} = \frac{s^2}{\sigma^2}. \tag{3.7}$$

PDM works by folding the data over a test period to obtain a phased mean light curve. The phase is divided into bins and the overall variance of the binned data is compared to the overall variance of the unbinned data. The period that gives the lowest ratio of the binned variance to the total unbinned variance, i.e. the minimum value for Θ_{PDM}, is taken as the true period. The PDM method finds the period with the minimum scatter of the observed light curve from the mean light curve. Unlike Fourier analysis, PDM is suitable for data that is non-sinusoidal, contains gaps or has poor coverage. The PDM analysis in this work was performed using a Python program written and adapted by Deanne Coppejans. Both Fourier analysis and PDM were used to analyse all SHOC data in order to compare for the best results.

3.3.2 *Lomb-Scargle Periodogram*

The Lomb-Scargle periodogram (Lomb, 1976; Scargle, 1982) was developed from the classical periodogram associated with the discrete FT, for detecting periodicities within non-uniformly sampled data. Scargle (1982) generalised the classic periodogram of the discrete FT as follows:

$$\mathcal{P}(\nu) = \frac{A^2}{2}\left(\sum_n g_n \cos(-2\pi\nu(t_n-\tau))\right)^2 + \frac{B^2}{2}\left(\sum_n g_n \sin(-2\pi\nu(t_n-\tau))\right)^2, \tag{3.8}$$

where A,B and τ are arbitrary functions of frequency ν. The LS periodogram is expressed as

$$\mathcal{P}_{LS}(\nu) = \frac{1}{2}\left(\frac{(\sum_n g_n \cos(-2\pi\nu(t_n-\tau)))^2}{\sum_n \cos^2(-2\pi\nu(t_n-\tau))} + \frac{(\sum_n g_n \sin(-2\pi\nu(t_n-\tau)))^2}{\sum_n \sin^2(-2\pi\nu(t_n-\tau))}\right), \tag{3.9}$$

where the time-shift τ is calculated from

$$\tan(4\pi\tau) = \left(\frac{\sum_n \sin(4\pi\nu(t_n)}{\sum_n \cos(4\pi\nu(t_n)}\right) \tag{3.10}$$

to ensure the periodogram solution remains constant with a time-shift.

When observations are sampled uniformly, the Lomb-Scargle periodogram reduces to classical FT periodogram. The LS periodogram is equivalent to least-squares fitting of sin waves and unaffected by global time shifts in the data. The Lomb-Scargle analysis was performed on the long-term CRTS light curves which are not uniformly sampled using GATSPY[3] (VanderPlas and Ivezić, 2015)

3.4 SPECTROSCOPIC OBSERVATIONS

Various telescopes and instruments were used to obtain spectra for the objects in this chapter, including the SAAO segmented 11 m Southern African Large Telescope (SALT[4]), the 3.58 m European Southern Observatory (ESO) New Technology Telescope (NTT[5]), ESO's Very Large Telescope (VLT[6]), the 11 m Hobby-Eberly Telescope (HET[7]) at the McDonald Observatory and the Roque de los Muchachos Observatory (ORM) 2.56 m Nordic Optical Telescope (NOT[8]). The phase-resolved spectra for ASASSN-14ei, ASASSN-14mv and ASASSN-17fp have a total length of the observation larger than or equal to the orbital period, comprised of multiple spectra with shorter integration times over the orbital phase.

Doppler tomography (see § 3.6.1) was performed on ASASSN-14ei which has well-defined spectral lines in the individual spectra. The spectra for CSS0105+19, CSS2333-15 are classification spectra with a total of one or two spectra. See table 3.2 for the detailed observing log, representing a total of 10.56 hours of spectroscopic observations.

[3] https://www.astroml.org/gatspy/
[4] https://www.salt.ac.za/telescope/
[5] https://www.eso.org/public/teles-instr/lasilla/ntt/
[6] https://www.eso.org/public/teles-instr/paranal-observatory/vlt/
[7] https://mcdonaldobservatory.org/research/telescopes/HET
[8] http://www.not.iac.es/instruments/

TABLE 3.2 – Observing log of spectroscopic observations of AM CVn stars and a helium-rich DN.

Object	**Date of obs.** (start of night)	**Length** (s)	$t_{\rm in}$ (s)	**Tel.**	**Instrument**
CSS0105+19	2018 Jan 01	2400	1200	NTT	EFOSC
V558 Vir	2005 May 31	2700	2700	HET	LRS
ASASSN-14ei	2014 Oct 10	2727	97	VLT	FORS2
ASASSN-14mv	2015 Jan 13	3000	60	NOT	ALFOSC
	2015 Jan 14	3000	60	NOT	ALFOSC
	2015 Jan 16	3000	60	NOT	ALFOSC
ASASSN-17fp	2017 May 07	6000	150	SALT	RSS
	2017 May 16	6200	200	SALT	RSS
CSS2333-15	2011 Oct 28	2580	215	SALT	RSS
	2011 Dec 15	2310	330	SALT	RSS
	2011 Dec 18	990	330	SALT	RSS
	2012 Sep 24	1900	1900	SALT	RSS
	2016 Jun 19	1200	1200	VLT	FORS2

Abbreviations: obs = observation, Tel. = Telescope and $t_{\rm in}$ = integration time.

3.5 SPECTROSCOPIC DATA REDUCTION

The following section details spectroscopic data reduction process of SALT RSS spectra. The reduction of spectra from other telescopes are similar to the detailed process.

The raw SALT spectra were partially reduced using `PySALT` (Crawford et al., 2010) before receiving it, including gain and cross-talk correction, bias subtraction (only overscan correction), removing detector cosmetic defects and amplifier mosaicing, to create the product data. Further spectroscopic reductions on the product data were performed using SAOImageDS9 and basic `IRAF` tasks from the `TWODSPEC` package. Laplacian Cosmic Ray Identification software (`L.A. Cosmic`; (van Dokkum, 2001) was used to remove the cosmic rays from the product spectra using a Laplacian edge detection algorithm. The FITS spectrum was then trimmed along the top and bottom to make it easier to correct for the curvature along the y-axis.

The corresponding Argon or Xenon arc lamp was used to identify the spectral lines and find a dispersion solution with `IRAF` tasks *identify* and *reidentify*. Individual lines were selected across the pixel range to assign wavelengths according to the arc lamp plot with the corresponding grating and grating angle. It was only necessary to mark the wavelengths of a small number of emission lines across the arc lamp image after which they were checked using the wavelength fit as a function of pixels and the residuals of the fit. I aimed for low RMS values by removing outliers. *identify* would then correctly mark the remaining lines according to the dispersion solution obtained from fitting the first set of markings. Again, outliers were removed from the wavelength fit and the residuals fit. *reidentify* used that dispersion solution to reidentify the lines along every row in the image and trace the curvature of the lines. `IRAF` task, *fitcoords*, was used to create a transformation function from pixels to wavelengths for the arc image.

transform then applied the transformation to the science image resulting in a wavelength-calibrated image with vertically straight lines provided the dispersion correction and transformation function were correct.

Using *background*, the background signal was selected along the y-axis from a cross section void of any emission/absorption lines and fitted to the cross section of the spectrum. The background was subtracted from the science image resulting in an image with very low (almost zero) background noise and removed sky lines. To extract the primary aperture, the position and size of the aperture were selected and adjusted according to the position and width of the signal from a cross section while running *apall* from the APEXTRACT package. The aperture was traced in the velocity direction. Outlying points were deleted for lower RMS values and a fit was applied to the trace to extract the primary aperture. Two science images were taken during observation, one after the other for every target. When satisfied with the reduced spectra, the science images were combined using *scombine* to produce a mean spectrum to increase the overall signal-to-noise ratio.

Spectrophotometric standard stars were used for relative flux calibrations. Accurate absolute flux calibrations cannot be done due to SALT's design in which the segmented, under-filled entrance pupil constantly varies in movement (Buckley et al., 2018). A subdirectory within onedstd$ directory contains standard star calibrations listing the wavelength, width of bandpass, and magnitude of the standard star. If the standard star in use was not one of the pre-saved standards, then a calibration file was downloaded online. The selected standard star was observed as close as possible to the science spectra with the same instrument settings. The product standard spectrum was reduced using the same process as the science image. The cosmic ray artifacts were removed and the image was trimmed to the same specifications as the science images. The same wavelength transformation as the science image was applied to the standard image and the spectrum was extracted using *apall*.

The parameters (eg. the directory and name of the calibrations file, observatory, airmass and exposure time) for the *standard* task were set according to the specific standard star in use. This task produces a list of the observed counts within each bandpass and the standard star fluxes by integrating the standard spectrum over the calibration bandpasses and dividing by the exposure time. Next, *sensfunc* was executed which interactively fits the sensitivity function as a function of wavelength to the *standard* output. Finally, *calibrate* transformed the science spectra using the sensitivity function.
A guide[9] by Massey, Valdes and Barnes for the reduction of slit spectra details the full IRAF reduction process.

3.6 SPECTROSCOPIC DATA ANALYSIS

3.6.1 *Doppler tomography*

Doppler tomography is the translation of the emission line variations over a single phase/orbit into a velocity map (Marsh and Horne, 1988). Each point source of emission

[9] https://iraf.net/irafdocs/spect.pdf

in a binary can be defined by a velocity amplitude and phase. The orbital motion of the point source, assumed to be moving parallel to the orbital plane, would map out a sinusoid or an S-wave along the mean velocity of the binary over a single orbital cycle as seen to the left of Fig. 3.4. The emission lines in the phased CV spectra belong to different components of the CV, Doppler tomography helps to separate these components by imaging the different regions of a specific element according to the velocities relative to the inertial frame (not the rotating frame).

A tomogram is represented by velocity coordinates which are projected in the x and y directions. The x-axis is the direction from the white dwarf to the donor star and the y-axis is the direction of motion of the donor star. The donor star is assumed to be co-rotating with the binary as a solid body thus maintaining its shape in velocity coordinates. It is rotated by 90° and ends up on the positive y-axis with the stream of mass flowing from the L1 point increasing in velocity as it approaches the white dwarf. Since the accretion disc is in Keplerian rotation, the outside of the disc which is the slowest is located toward the inside of the tomogram. Conversely, the high-velocity inner part of the disc is located at the outer edge of the tomogram. The white dwarf is located at the centre of the accretion disc although it is not often visible (refer to Fig. 3.2). At phase 0.0 the donor star is closest to the observer, and furthest away at phase 0.5. The translation from polar velocity coordinates to polar position coordinates is seen in Fig. 3.3

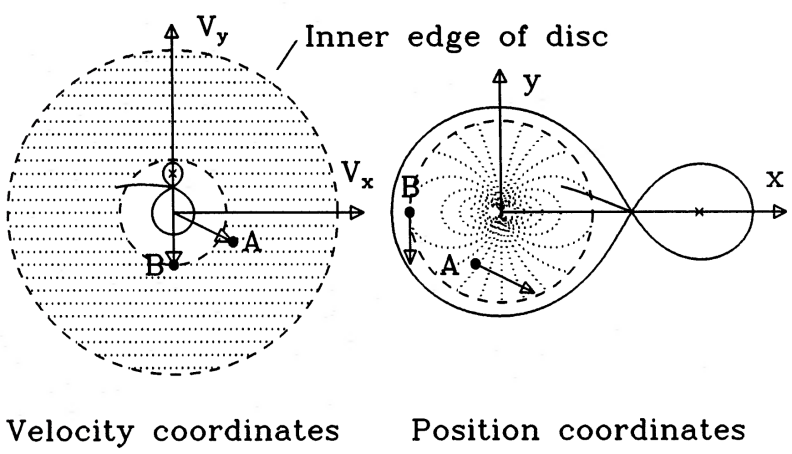

FIGURE 3.2 – The figure shows the translation of velocity coordinates to position coordinates reproduced from Marsh and Horne (1988). Dotted lines represent regions of equal radial velocity. The Roche lobes, stream of mass, A and B are equivalent to one another.

There are two common methods of computing Doppler tomograms, filtered back-projection and maximum entropy inversion. Filtered back-projection is a linear method in which each spectrum is filtered in velocity. Each filtered profile is smeared along the direction of the corresponding phase in order to construct the original image (refer to Fig. 3.4). This process can be thought of as working backwards from the observed profiles to the projection. This method is fast but not using enough spectra over an orbital cycle could cause linear artifacts. Maximum entropy inversion uses χ^2 to obtain a desired goodness-of-fit to construct images in velocity space. The image with the

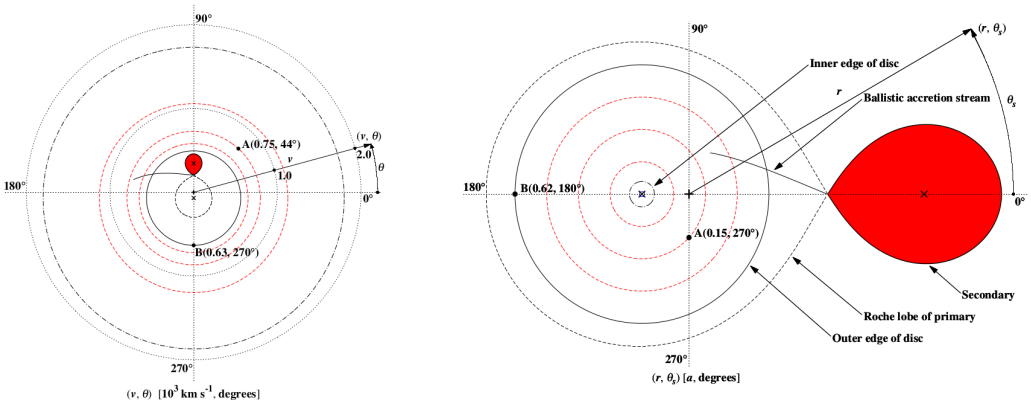

FIGURE 3.3 – The figure shows the translation of polar velocity coordinates to polar position coordinates reproduced from Kotze et al. (2015).

highest entropy is selected. The advantage of this method is that a model fit can be reconstructed and compared with the original data as a check.

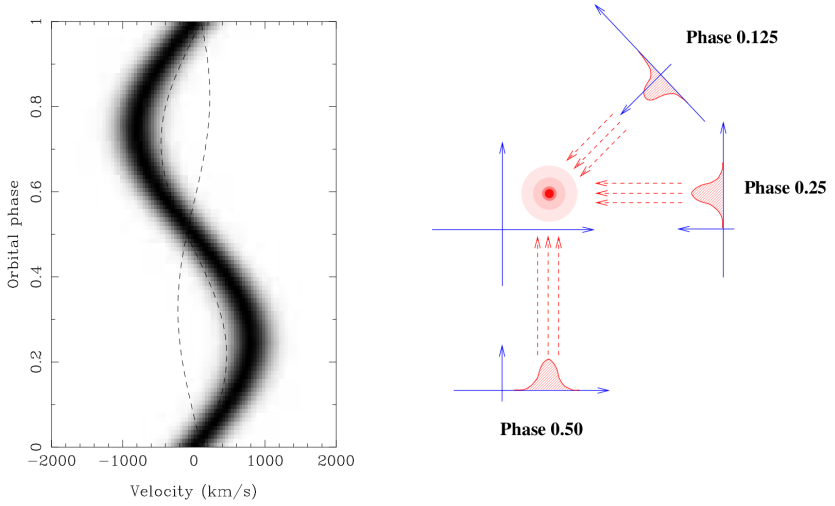

FIGURE 3.4 – To the left is a trail spectrum over a single orbital cycle. The right side is an example of back-projection. The profiles at different phases are used to create the image in the centre. From Marsh (2001).

3.7 INDIVIDUAL SYSTEMS

In this section, I report the results of the individual objects, including AM CVn stars and a Helium-rich dwarf nova. The data are presented together in a figure with the long-term light curves from CRTS or AAVSO (Kloppenborg, 2023) at the top and the SHOC photometry and the spectrum (if available) below. I also present the photometric periods and periodograms determined via the FT and PDM. The SHOC light curves in this section are the average light curves from the individual observations phase-folded

over the photometric period. The light curves of the individual observation can be found in the appendix C.

3.7.1 *CSS0105+19 (CSS091016:010550+190317)*

CSS0105+19, which was discovered as a candidate CV by CRTS on 16 October 2009, has an average brightness of V ∼ 19.6 mag and an outburst amplitude of V ∼ 4 mag. As described in § 2.1, CSS0105+19 was selected for follow-up because it has multi-filter SDSS photometry which places it within a constrained $(u-g, g-r)$ colour space occupied by other previously known AM CV stars. CSS0105+19 was observed with the 1.9-m telescope over four nights from 19 to 25 September 2012.

The ephemeris for maximum light is given by

$$HJD_{\max} = 2456190.46100 + 0.021978(2)\,E, \tag{3.11}$$

where HJD is the heliocentric Julian day and E is the cycle number.

Light curves display small amplitude orbital modulations seen as single peak humps (see appendix C, Fig. C.0.1). Fig. 3.5 (middle) shows the average light curve of all the runs folded on a period of 31.648(2) min. The Fourier transform in Fig. 3.6 clearly shows the fundamental frequency at 526.63(3) μHz with the first harmonic of the orbital frequency at 1053.30(9) μHz and the second harmonic displayed at 1580.38(19) μHz.

The spectrum of CSS0105+19 was taken in January 2018. The faintness of the target resulted in a low signal-to-noise spectrum without clear emission/absorption lines (Fig. 3.5, bottom). The common emission/absorption lines are indicated by vertical dashed lines. The continuum peaks towards blue wavelengths and decreases gradually with increasing wavelength. The interpretation of the spectrum is inconclusive.

3.7.2 *CSS0450-09 (CSS121123:045020-093113)*

With an average brightness of V ∼ 20.5, CSS0450-09 was identified as a CV candidate by CRTS on 23 November 2012 after it had gone into a superoutburst with an amplitude exceeding 5 magnitudes. This is the first and only recorded outburst by the CRTS. CSS0450-09 was observed spectroscopically during quiescence, by Drake et al. (2012) with the Keck-I+LRIS on 16 December 2012. The emission line spectrum contained helium and nitrogen with no indication of the presence of hydrogen, classifying it as an AM CVn candidate. We followed it up photometrically, shortly after the superoutburst in January 2013 over two nights, confirming CSS0450-09 as an AM CVn, likely analogous to a WZ Sge-type DN (Woudt et al., 2013), i.e. dwarf novae with long (super)outburst recurrence times.

The average light curve of all the runs of CSS0450-09 folded on a period of 47.245(3) min is seen in Fig. 3.7 (middle). The orbital modulation is represented as a single hump profile. The ephemeris for maximum light is

$$HJD_{\max} = 2456301.32162 + 0.032809(2)\,E \tag{3.12}$$

The Fourier transform in Fig. 3.8 clearly shows the orbital frequency at 352.77(2) μHz with the second harmonic of the orbital frequency at 1058.16(1) μHz. The first harmonic is not clearly visible.

The spectrum of CSS0450-09 reported by Drake et al. (2012) shows a blue continuum and broad emission lines. The identifiable lines are He I (λ 3889, 4121, 4471, 4922, 5016, 5876, 6678, 7065), He II (λ 4686, 6560, 4541?, 4686, 5412) and N I (λ 8200, 8700).

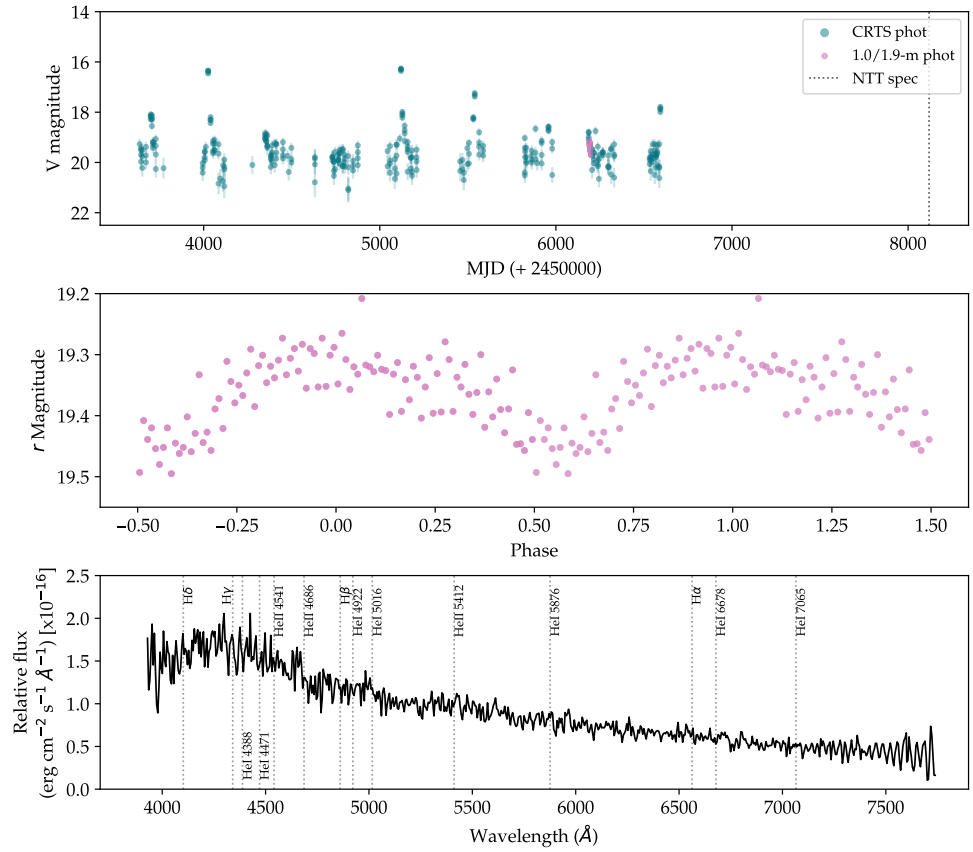

FIGURE 3.5 – Light curves and spectrum of CSS0105+19. Top: Long-term light curve of CSS0105+19 from CRTS in teal. The pink points are all of the follow-up photometric observations. The black dashed line represents the date of the follow-up spectroscopic observation. Middle: An average phase-folded light curve of the follow-up observations with SHOC CCD. The complete set of individual light curves can be found in appendix C (Fig. C.0.1). Bottom: A single spectrum taken with the ESO New Technology Telescope (NTT), courtesy of Elme Breedt. The common emission/absorption lines are indicated by vertical dashed lines.

3.7.3 *V558 Vir*

In 2003, V558 Vir was classified as a possible blazar in the 2dF QSO Redshift Survey by Veron-Cetty and Veron. Almost two years later, in Jan 2005, it was observed in superoutburst by ROTSE-III sky-patrol at a magnitude of R = 15.1. Spectroscopy obtained in quiescence by Croom et al. (2004) and in outburst by Rykoff et al. (IAUC 8531)[10] reveal a strong presence of helium. Three outbursts have been recorded since 2005 by the CRTS. We observed V558 Vir on 15 and 16 May 2005 during superoutburst using the UCT CCD O'Donoghue (1995) on the 1.9-m telescope and followed up almost 8 years later in March and May 2013 during quiescence using SHOC CCD.

The superoutburst light curves display small amplitude orbital modulations with a single peak while the light curves during quiescence show no variations (see appendix C, Fig. C.0.3). The non-variations cannot be attributed solely to the faintness of V558 Vir during quiescence because S8316 is very well sampled but still remains relatively

[10] http://www.cbat.eps.harvard.edu/iauc/08500/08531.html

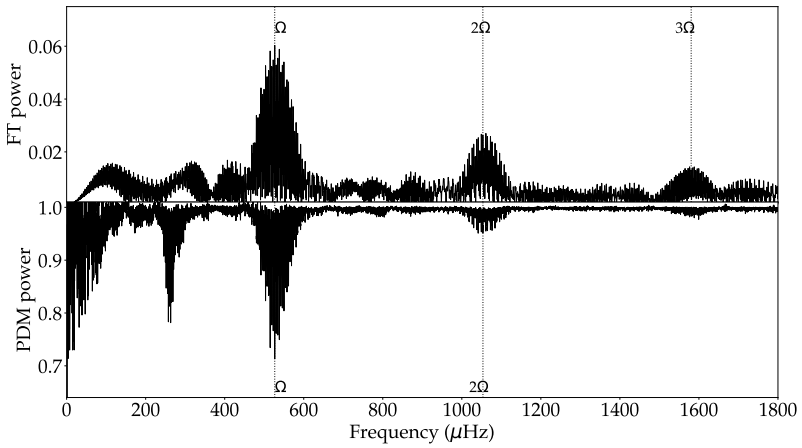

FIGURE 3.6 – The Fourier transform of all of the combined light curves of CSS0105+19 at the top. The vertical dotted lines indicate the fundamental frequency (Ω), the first harmonic (2 Ω) and second harmonic (3 Ω) of the fundamental frequency. The PDM periodogram at the bottom. The vertical dotted lines indicate the fundamental frequency (Ω) and first harmonic (2 Ω) frequency.

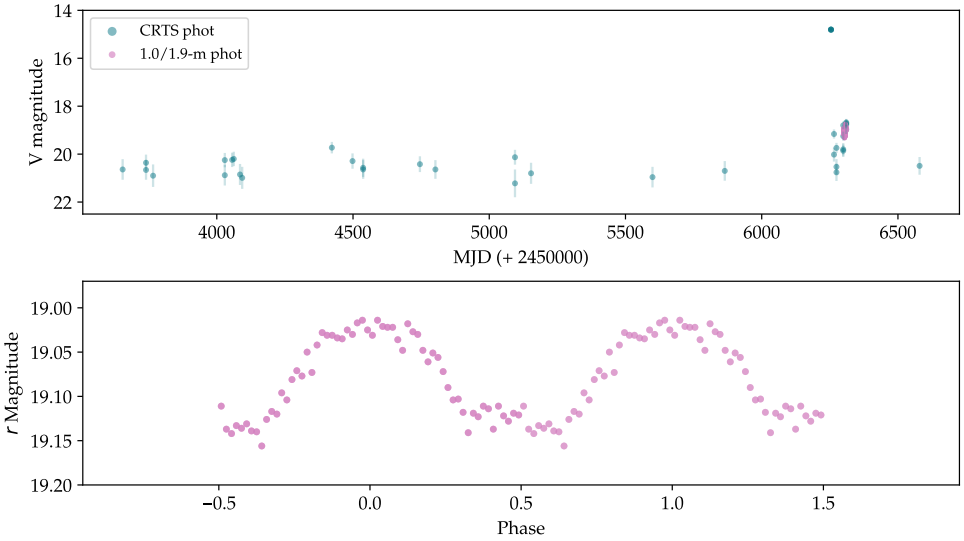

FIGURE 3.7 – Top: Long-term light curve of CSS0450-09 from CRTS in teal. The pink points are all follow-up photometric observations. Bottom: An average phase-folded light curve from the follow-up observations with SHOC CCD. The complete set of individual light curves can be found in appendix C (Fig. C.0.2).

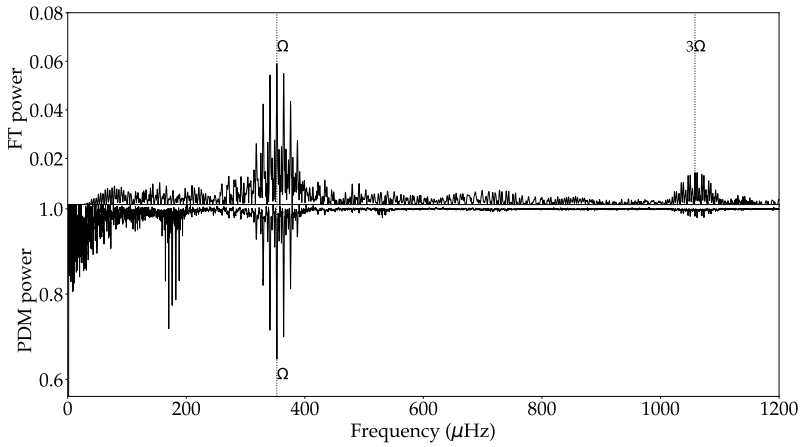

FIGURE 3.8 – The figure at the top is the Fourier transform of the all of combined runs of CSS0450-09. The vertical dotted lines indicate the fundamental frequency (Ω) and the second harmonic (3 Ω) frequency. The figure at the bottom is the PDM periodogram of the all of combined runs of CSS0450-09. The vertical dotted line indicates the fundamental frequency (Ω).

constant. Fig. 3.9 (middle) shows the average light curve V558 Vir of runs S7646 and S7647 during superoutburst folded on 34.78(5) min. The FT of those observations gives a photometric (likely superhump) frequency of Ω = 479.9(6) μHz and the first harmonic frequency 2 Ω = 957.4(7) μHz. The light curves from 2013 during quiescence show no photometric variability and the FT also does not detect any frequencies from those observations. The ephemeris for maximum light is

$$HJD_{\max} = 2453506.44996 + 0.02411(3)\,E \tag{3.13}$$

The HET spectrum of V558 Vir is dominated by helium emission lines with a blue continuum. Specific lines seen are He I (λ 4388, 4471, 4922, 5016, 5876, 6678, 7065, 7281, 9210), He II (λ 4686) and possibly N I (λ 8700). Most lines are double-peaked indicating the presence of a disc.

3.7.4 *ASASSN-14ei = OX Eri*

ASASSN-14ei was discovered on 21 July 2014 during a superoutburst by ASAS-SN (Prieto et al., 2014b). The long-term photometric light curve of ASASSN-14ei from AAVSO shows 12 consecutive echo outbursts since the first detection taking place over ∼ 6 months (Fig. 3.11, top). It has a photometric period of ∼ 42.9 min. He I and He II lines were found in follow-up optical spectra taken with the du Pont 2.5-m telescope at Las Cumbres Observatory on 28 July 2014 and 01 August 2014 (Prieto et al., 2014a) which were obtained during the extended intermediate state. Green et al. (2020) presented optical light curves and spectra of ASASSN-14ei. Our photometric observations were taken over September to November 2014, and then revisited in 2015 and 2016. The ephemeris for maximum light is

$$HJD_{\max} = 2456913.52492 + 0.029807(2)\,E \tag{3.14}$$

The average light curve of the September 2014 observations of ASASSN-14ei (taken between echo-outbursts) is folded on a period of 42.923(2) min (Fig. 3.11, second panel).

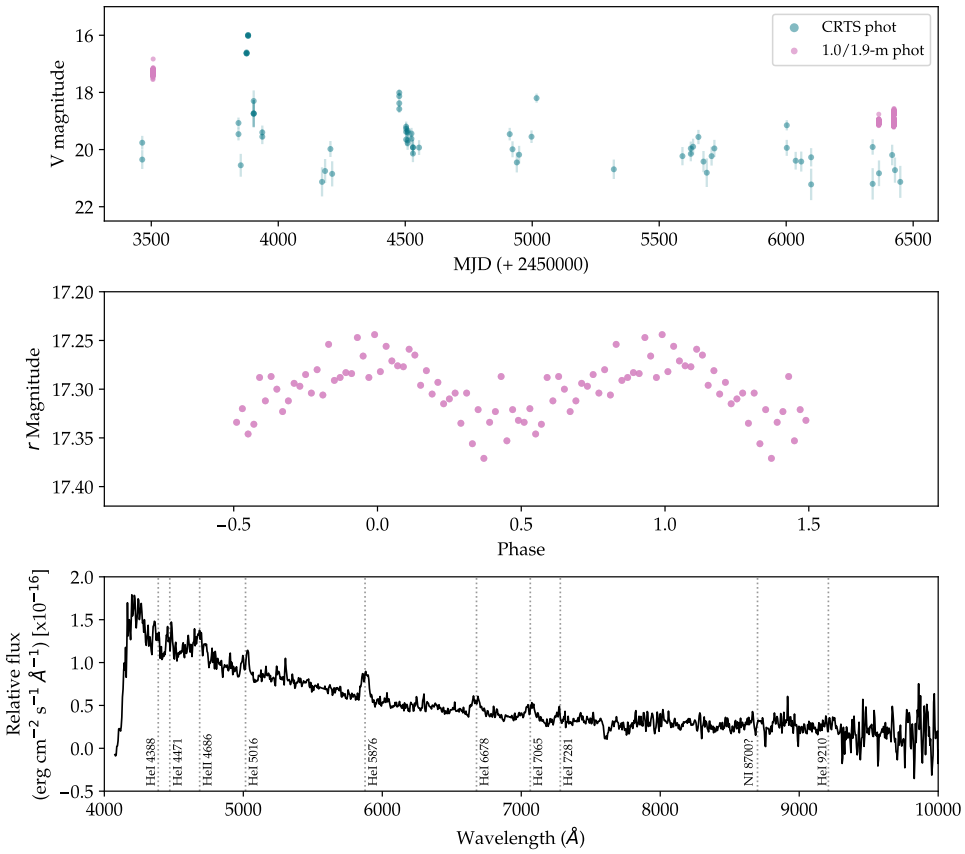

FIGURE 3.9 – Top: Long-term light curve of V558 Vir from CRTS in teal. The pink points are all follow-up photometric observations. Middle: An average phase-folded light curve from follow-up observations with the UCT CCD. The complete set of light curves can be found in appendix C (Fig. C.0.3). Bottom: A single spectrum with marked emission/absorption lines taken with the HET telescope.

S8464 and S8467, which took place during echo-outbursts, were excluded. This phase-folded light curve displays a double-humped profile. The Fourier transform in Fig. 3.12 clearly shows the following frequencies: Ω = 388.30(2) μHz; 2 Ω = 776.90(2) μHz; 3 Ω = 1165.59(5) μHz; 4 Ω = 1553.96(4) μHz and 7 Ω = 2719.7(1) μHz.

The average light curve of observations taken 2016 during quiescence folded over a slightly different period of 42.854(3) min (Fig. 3.11, third panel) varies from the 2014 light curve, with at least one additional peak in the orbital phase. While periodograms of the 2016 data do not contain a second harmonic, the orbital frequencies are very similar to those obtained from the 2014 data, with Ω = 388.92(3) μHz; 2 Ω = 777.79(3) μHz; 4 Ω = 1555.45(4) μHz. Both 2014 and 2016 photometric periods are very likely associated with the orbital period, as the 2016 data were taken during a quiescent state and both periods are only slightly larger than the orbital period range of 41-42.5 min from Green et al. (2020).

Phase-resolved VLT spectrum of ASASSN-14ei (Fig. 3.11, bottom) show was taken on 10 October 2014. The broad emission lines can be seen in individual spectra. The emission lines that can be identified are He I (λ 3820, 3888, 4026, 4143, 4388, 4471, 4481, 4922) and He II 4686. In comparison with Green et al. (2020), Ca II H+K are

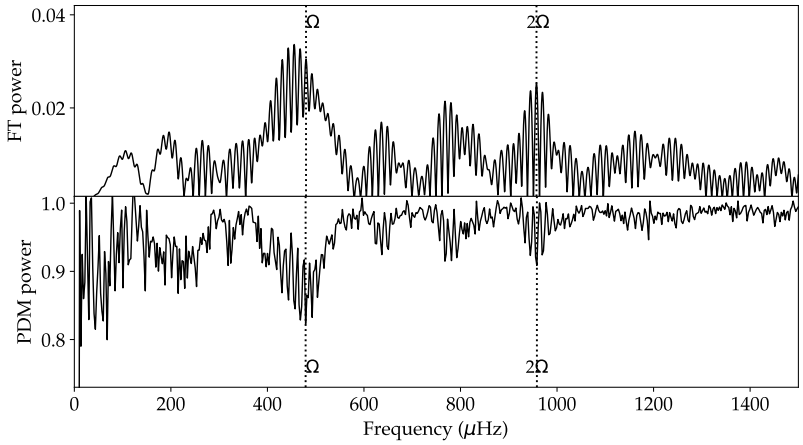

FIGURE 3.10 – The Fourier transform of V558 Vir of the combined light curves of S7647 and S7648 during superoutburst at the top. The vertical dotted lines indicate the fundamental frequency (Ω) and first harmonic (2 Ω) frequency. The PDM periodogram of the combined runs of S7647 and S7648 during superoutburst at the bottom. The vertical dotted lines indicate the fundamental frequency (Ω) and first harmonic (2 Ω) frequency.

identified in both spectra and additional lines seen beyond the wavelength coverage of our spectra are Mg I (λ 5167, 5172, 5183), Na I λ 5890, Si II λ 6347, N I (λ 8200, 8700).

For the Doppler tomography of ASASSN-14ei, the average of the known parameter values for eclipsing AM CVn stars from table 3 from van Roestel et al. (2022), $M_1 = 0.83$ $M_\odot$, $q = 0.15$, were used, as the actual values for ASASSN-14ei are not known. We assessed inclinations of both 40° and 50° based on the average value and the light curve profile. We settled on 40°, which aligned better with the velocity model. We used the 2014 period of 42.923 min which overlaps with the time the the spectra were taken. Figures 3.15, 3.14 and 3.16 refer to the Doppler tomography of He I λ 4388, 4921 and He II λ 4686 with the tomograms to the left and the input and reconstructed trailed spectra to the right. The inner disc radius (marked by a solid inner circle in the tomograms) was determined using Eq. 2.81 from Warner (1995a) and the outer disc radius (marked by the dashed outer circle in the tomograms) for $q \leq 0.3$ with a 3:1 resonance was determined using Eq. 3.39 from Warner (1995a), otherwise the Eq. 2.61 from Warner (1995a) was used. The details of the velocity models and the code used for the Doppler tomography maps can be found in Kotze et al. (2015). We took a qualitative approach to phasing the tomograms as phase 0 from the light curve, associated with the brightest light, did not position the system components in alignment with the velocity model, thus we adjusted the phasing to line up with the velocity models.

The Doppler tomography of He I λ 4921 in Fig 3.14 shows the source of the emission from the disc is evident and the brightest emission, likely from the bright spot, is in the position where the solid stream line crosses the inner disc radius. For He I λ 4388 in Fig 3.15, the emission is primarily in the disc and possibly the bright spot which does not appear much brighter than the disc. The Doppler tomography of He II λ 4686 in Fig 3.16 reveals emission from the disc and the centre, likely associated with the accreting WD, although the strongest emission is off-centre. This off-centre source is peculiar and may originate from close to the surface of the WD. When compared to the Doppler tomography of ASASSN-14ei presented by Green et al. (2020) using data taken

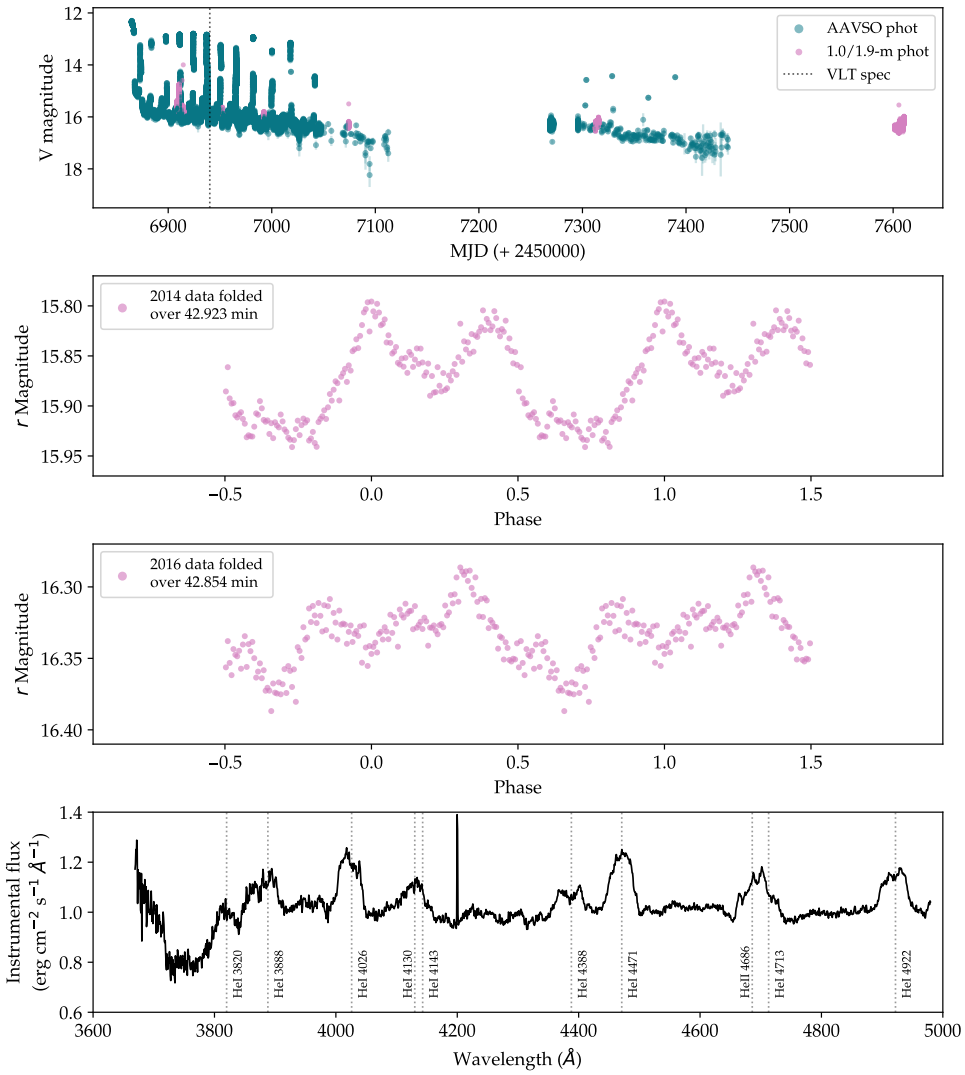

FIGURE 3.11 – Top: Long-term light curve of ASASSN-14ei from AAVSO in teal. The pink points are all follow-up photometric observations. The black dotted line represents the date of the follow-up spectroscopic observation. Second: An average phase-folded light curve from 2014 follow-up observations with SHOC CCD. Third: An average phase-folded light curve from 2016 follow-up observations with SHOC CCD.The complete set of light curves can be found in appendix C (Fig. C.0.4 and Fig. C.0.5). Bottom: A phase-resolved spectrum with marked emission lines taken with VLT, courtesy of Gavin Ramsay.

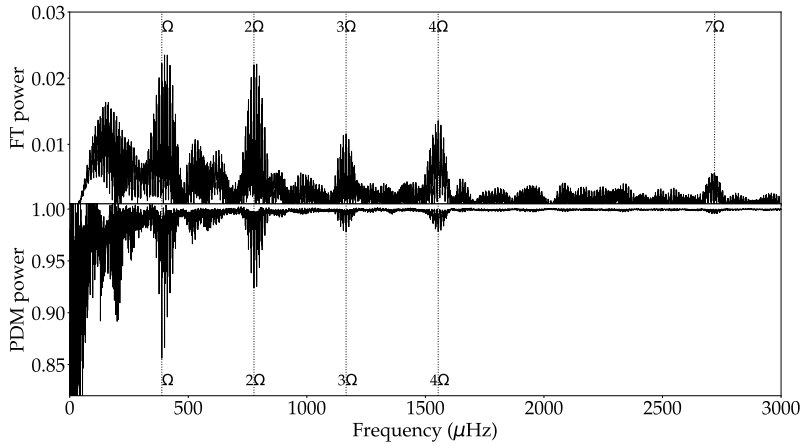

FIGURE 3.12 – The top figure is the ASASSN-14ei Fourier transform of the combined runs of observations taken during the quiescent phase between the echo-outbursts in September 2014. The vertical dotted lines indicate the photometric frequency (Ω), the first harmonic ($2\,\Omega$), second harmonic ($3\,\Omega$), third harmonic ($4\,\Omega$) and sixth harmonic ($7\,\Omega$). At the bottom is the PDM periodogram of the combined runs of the observations taken during quiescence in September 2014. The vertical dotted lines indicate the orbital frequency (Ω), the first harmonic ($2\,\Omega$), second harmonic ($3\,\Omega$) and the third harmonic ($4\,\Omega$).

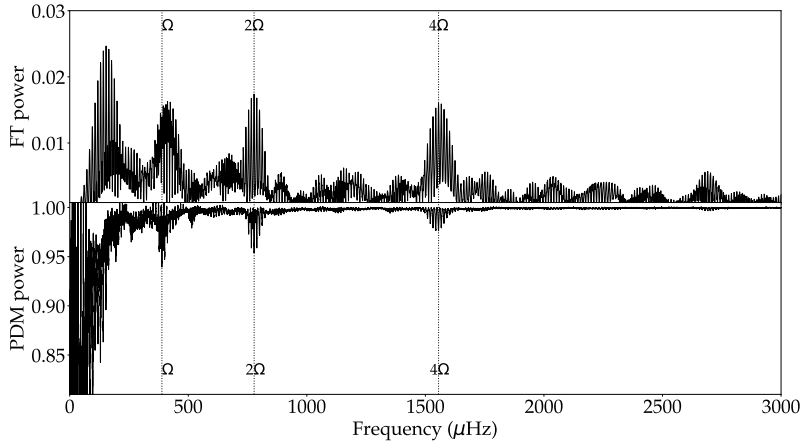

FIGURE 3.13 – The top figure is the ASASSN-14ei Fourier transform of the combined runs of observations taken during the quiescence in August 2016. The vertical dotted lines indicate the photometric frequency (Ω), the first harmonic ($2\,\Omega$) and the third harmonic ($4\,\Omega$). At the bottom is the PDM periodogram of the combined runs of the observations taken during quiescence in August 2016. The vertical dotted lines indicate the orbital frequency (Ω), the first harmonic ($2\,\Omega$), second harmonic ($3\,\Omega$) and the third harmonic ($4\,\Omega$).

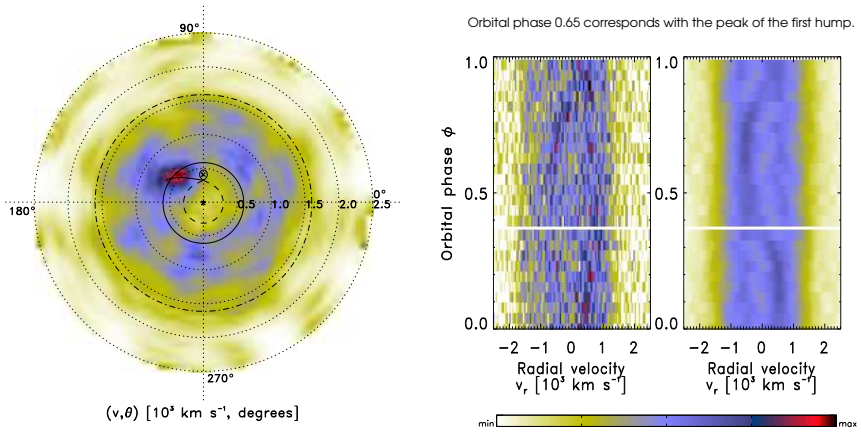

FIGURE 3.14 – Doppler tomography of ASASSN-14ei for He I λ 4921 emission line. Left: Doppler tomogram with velocity models. Right: Input and reconstructed trailed spectra.

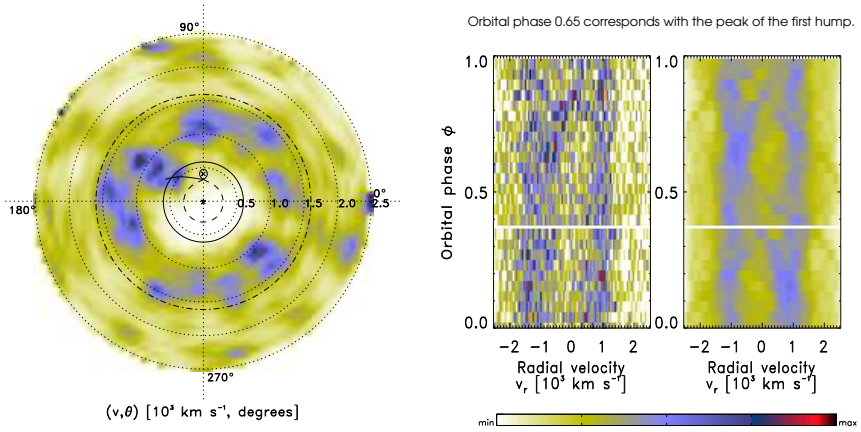

FIGURE 3.15 – Doppler tomography of ASASSN-14ei for He I λ 4388 emission line. Left: Doppler tomogram with velocity models. Right: Input and reconstructed trailed spectra.

about 10 months after the data in this work, the He II λ 4686 tomogram appears similar, with a disc component and central components however the brighter emission is more central and generally associated with the WD (i.e. has a lower radial velocity). Green et al. (2020) also evaluate the He I λ 4713 line which is not resolvable in this spectrum as it may be blended with the He II λ 4686 emission.

3.7.5 *ASASSN-14mv = V493 Gem*

ASASSN-14mv was first caught in superoutburst by MASTER-Tunka in January 2011 and CRTS, as MLS J071327.3+205553, but it was not until December 2014 that it was identified as a CV candidate by ASSAS-SN after a superoutburst (Denisenko et al., 2014). Shortly afterwards, it experienced 11 consecutive echo-outbursts over almost three months, exhibiting very similar behaviour to ASASSN-14ei. As seen in the AAVSO light curve in Fig. 3.17 (top) the recurrence time of the echo-outbursts increases with

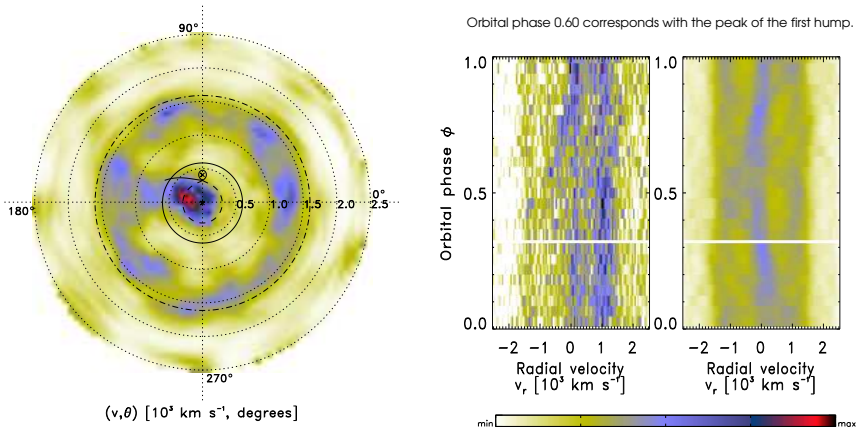

FIGURE 3.16 – Doppler tomography of ASASSN-14ei for He I λ 4686 emission line. Left: Doppler tomogram with velocity models. Right: Input and reconstructed trailed spectra.

each echo-outburst. The ∼ 41 min orbital period and helium-dominated spectrum were confirmation of its status as an AM CVn (*vsnet*-alerts 18124, 18135, 18160, Breedt, 2015; Hardy et al., 2017). Green et al. (2020) presented optical light curves and spectra of ASASSN-14mv. Our photometric observations were taken in January and February 2015, most of which were during the early echo-outbursts shortly after the superoutburst with one observation taken towards the end of the echo-outbursts.

The light curves were taken at different stages of the echo-outbursts resulting in dissimilar profiles. The brightest light curves taken during outburst show the smaller variations. The average light curve of ASASSN-14mv in Fig. 3.17 (second panel) was determined using observations from the extended intermediate phase with the defined superhumps. The superhump structure appears to be one large main peak and two smaller side peaks. The ephemeris for peak brightness is

$$HJD_{\max} = 2457032.41080 + 0.028305(1)\,E \tag{3.15}$$

The average light curve (Fig. 3.17 (middle), has been folded over the photometric period of 40.760(1) min. The following frequencies from the Fourier transform are indicated in Fig. 3.18: $\Omega = 408.90(1)$ μHz; $2\,\Omega = 817.57(2)$ μHz; $3\,\Omega = 1226.24(2)$ μHz; $4\,\Omega = 1635.18(5)$ μHz.

The phased resolved spectra from NOT taken on 13, 14 and 16 January 2015, courtesy of Pasi Hakala, have low signal-to-noise ratios without distinct features therefore the mean spectra are used here. The mean spectra from 13 and 14 January have a close resemblance with each other (see Fig. 3.17, third panel), with strong Ca II H+K and most helium lines in absorption. Identifiable lines are He I (λ 3820, 3888, 4026, 4388, 4436, 4471, 4481, 4713, 4922), He II (λ 4541, 4686, 4859) and Mg II 4481. The mean spectrum from 16 January was taken during an echo-outburst (Fig. 3.17, bottom). Although the features are weaker than the previous spectra, many lines are emission or emission lines within wider absorption features. The previously strong Ca II H+K absorption features are no longer visible.

The spectrum of ASASSN-14mv from Green et al. (Fig. 4, 2020), taken during quiescence with emission lines, has a small wavelength overlap at lower wavelengths with

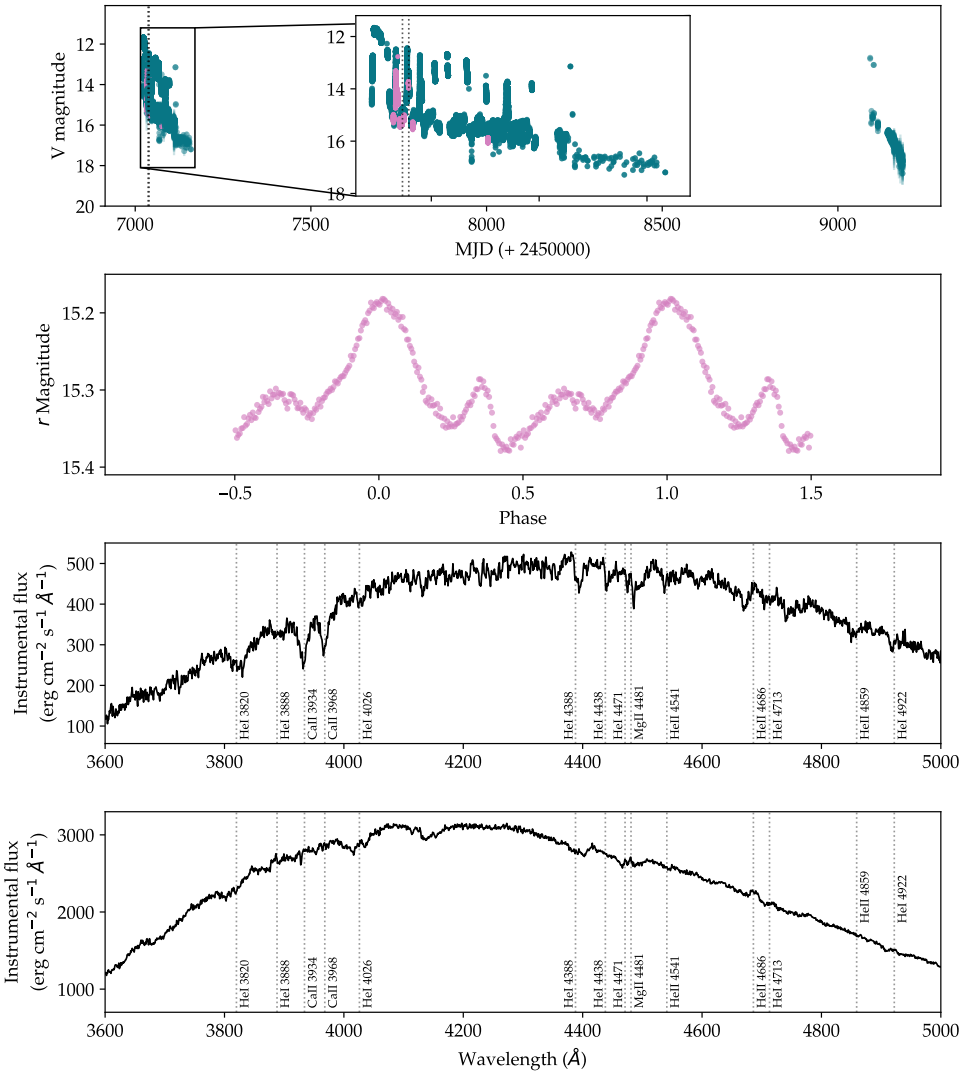

FIGURE 3.17 – Top: Long-term light curve of ASASSN-14mv from CRTS in teal. The pink points are all follow-up photometric observations. The black dotted line represents the date of the follow-up spectroscopic observation. Second: An average phase-folded light curve from follow-up observations with SHOC CCD. The complete set individual of light curves can be found in appendix C (Fig. C.0.6). Third: A mean spectrum with NOT from 13 January 2015 during quiescence, courtesy of Pasi Hakala. Bottom: A mean spectrum with NOT from 16 January 2015 during outburst, courtesy of Pasi Hakala.

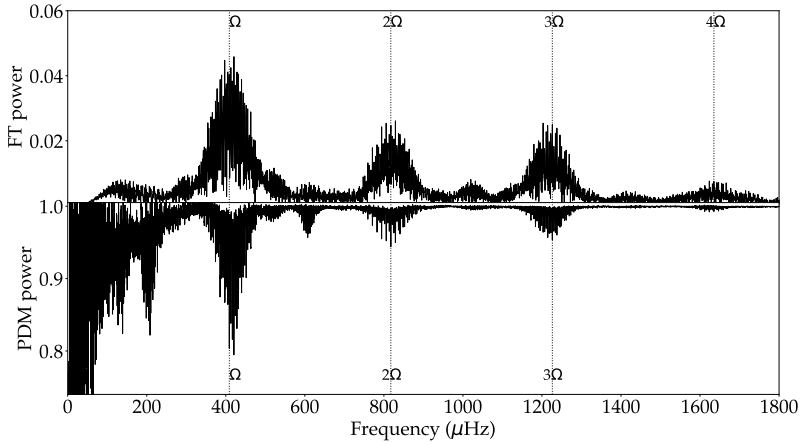

FIGURE 3.18 – Above is the Fourier transform of ASASSN-14mv using the data taken during the quiescent phase between echo-outbursts. The vertical dotted lines indicate the fundamental frequency (Ω) and first (2 Ω), second (3 Ω) and third (4 Ω) harmonic frequencies. The PDM periodogram of the same runs at the bottom. The vertical dotted lines indicate the fundamental frequency (Ω) and first harmonic (2 Ω) frequency.

Ca II H+K and He I lines seen in both spectra. The aforementioned He II lines would be located within a large gap (>1000 Å) in the Green et al. (2020) spectrum, however Si II, N I and Ca II lines are seen above 6000 Å. As Si II λ 4541 is detected in Green et al. (2020), it is likely that the line at λ 4130 in our spectrum is also Si II.

3.7.6 *ASASSN-15kf*

ASASSN-15kf, also known as SSS J153838.3-303549 (Drake et al., 2009), was reported as an AM CVn candidate in a *vsnet*-alert 18712[11] and *vsnet*-alert 18724[12] in June 2015 during and after a superoutburst. Our photometric observations were taken shortly after the alert. The light curves taken during the superoutburst peak display very low amplitude modulations while the light curves during the decline of superoutburst display well-defined orbital peaks (Refer to appendix C, Fig. C.0.7). The ephemeris for maximum light is

$$HJD_{\max} = 2457192.34274 + 0.038040(8)\,E \tag{3.16}$$

Our determined photometric period of 54.78(2) min is most likely the superhump period of ASASSN-15kf. This is almost double the previously reported period of 27.68 min (refer to table 2.1) as a double-peaked hump profile can easily be mistaken for a single peak profile with insufficient data and/or if the data were taken when individual humps are comparable. The average light curve of S8689 and S8692, folded over this period, is displayed in Fig. 3.19 (bottom). The Fourier transform in Fig. 3.20 marks the fundamental frequency Ω = 304.26(7) μHz and the following harmonic frequencies: 2 Ω = 608.33(3) μHz; 4 Ω = 1216.93(14) μHz; 5 Ω = 1522.59(18) μHz and 6 Ω = 1824.41(18) μHz.

[11] http://ooruri.kusastro.kyoto-u.ac.jp/mailarchive/vsnet-alert/18712
[12] http://ooruri.kusastro.kyoto-u.ac.jp/mailarchive/vsnet-alert/18724

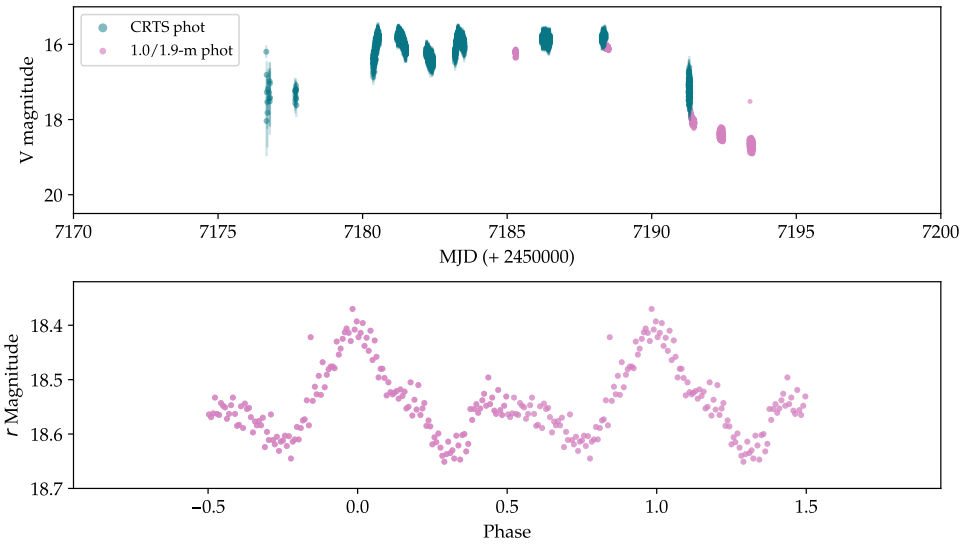

FIGURE 3.19 – Top: Long-term light curve of ASASSN-15kf from CRTS in teal. The pink points are all follow-up photometric observations. Bottom: An average phase-folded light curve from follow-up observations with SHOC CCD. The complete set of individual light curves can be found in appendix C (Fig. C.0.7).

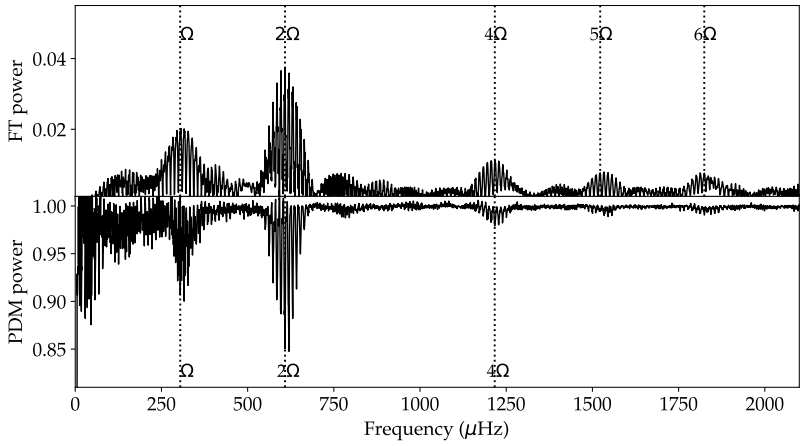

FIGURE 3.20 – The top figure is the Fourier transform of ASASSN-15kf using all observations except S8674. The vertical dotted lines indicate the fundamental frequency(Ω), first (2 Ω), third (4 Ω), fourth (5 Ω) and fifth (6 Ω) harmonic frequencies. Below is the PDM periodogram of the combined runs of S8686, S8689 and S8692 where the vertical dotted lines indicate the fundamental (Ω), first harmonic frequencies (2 Ω) and second harmonic frequencies (3 Ω).

3.7.7 *ASASSN-17fp*

ASASSN-17fp was discovered by ASASSN on 28 April 2017 with magnitude V= 16.2 during outburst and identified as a possible AM CVn star by the extended Public ESO Spectroscopic Survey for Transient Objects (ePESSTO; Smartt et al., 2015) after the spectrum taken post-outburst revealed the absence of H absorption and the presence of He I (Cartier et al., 2017). A week later Marsh et al. (2017) reported a periodic variation of 51.0 min confirming it as an AM CVn. J. Patterson reported that Berto Monard found a period of 51.4 min in cba:news. It was reported in outburst again (either echo-outburst or a successive superoutburst) on 16 May 2017 by E. Breedt (Waagen, 2017). We observed ASASSN-17fp target photometrically on 13 and 14 May 2017, shortly after the superoutburst and before the echo-outburst. The ephemeris for peak brightness is

$$HJD_{\rm max} = 2457887.49069 + 0.03569(5)\,E \tag{3.17}$$

A single hump profile is seen in the average light curve (Fig. 3.21 middle), which has been folded over the photometric period of 51.39(7) min. This period is likely a superhump period as it was derived between two consecutive outbursts, implying the modulations are superhumps. The photometric frequencies from the Fourier transform in Fig. 3.22 are: Ω = 324.33(43) μHz; 2 Ω = 648.55(55) μHz; 3 Ω = 973.59(59) μHz.

The SALT phase-resolved spectra were obtained on 7 and 16 May 2017. A total of 40 spectra were taken on 7 May however the signal in the individual and the combined spectra is too low to see clear emission/absorption lines. On 16 May, 31 spectra were taken with improved signal-to-noise ratios in individual and combined spectra. The mean spectrum lacks hydrogen and a combination of weak and broad helium emission and absorption lines are seen. Identifiable lines include He I (λ 4143, 4388, 4471, 5016, 5047, 5876, 6678, 7065) and He II λ 4686. Some lines appear to be emission and others absorption. This suggests that the system was observed during a transition into or out of outburst. The shallow double-peaked profile seen in some lines suggests the presence of a disc. The spectrum looks similar to the spectra of prototype AM CVn (Fig. 1, Roelofs et al., 2006) and V803 Cen (Fig. 1, Roelofs et al., 2007a), in outburst.

An attempt was made to derive the radial velocities from the phase-resolved SALT spectra through cross-correlation using the `RVSAO` package (Kurtz and Mink, 1998) from `IRAF`. Cross-correlation is defined as multiplying the Fourier transform of each object spectrum with the conjugate of the Fourier transform of the template spectrum, where the template spectrum is the sum of the individual spectra. The signal-to-noise ratios for the individual spectra were insufficiently low to determine realistic radial velocities over the orbital cycle.

3.7.8 *CSS2333-15 (CSS111019:233313-155744)*

Photometric observations from 2011 reveal CSS2333-15 as an eclipsing DN with an orbital period of ∼61 min and a superhump period of ∼63 min (Woudt and Warner, 2011). Further follow-up photometric observations were taken later in 2011 during superoutburst and quiescence, and again 2012 and 2013.

The 2011 light curve profiles are unusual and dissimilar with a wide eclipse during superoutburst and slanted humps without eclipses in the second light curve in Fig. C.0.9 in appendix C. The light curves in 2012 and 2013 during quiescence have symmetric humps with very narrow eclipses which are not detected at every cycle. Fig. 3.23,

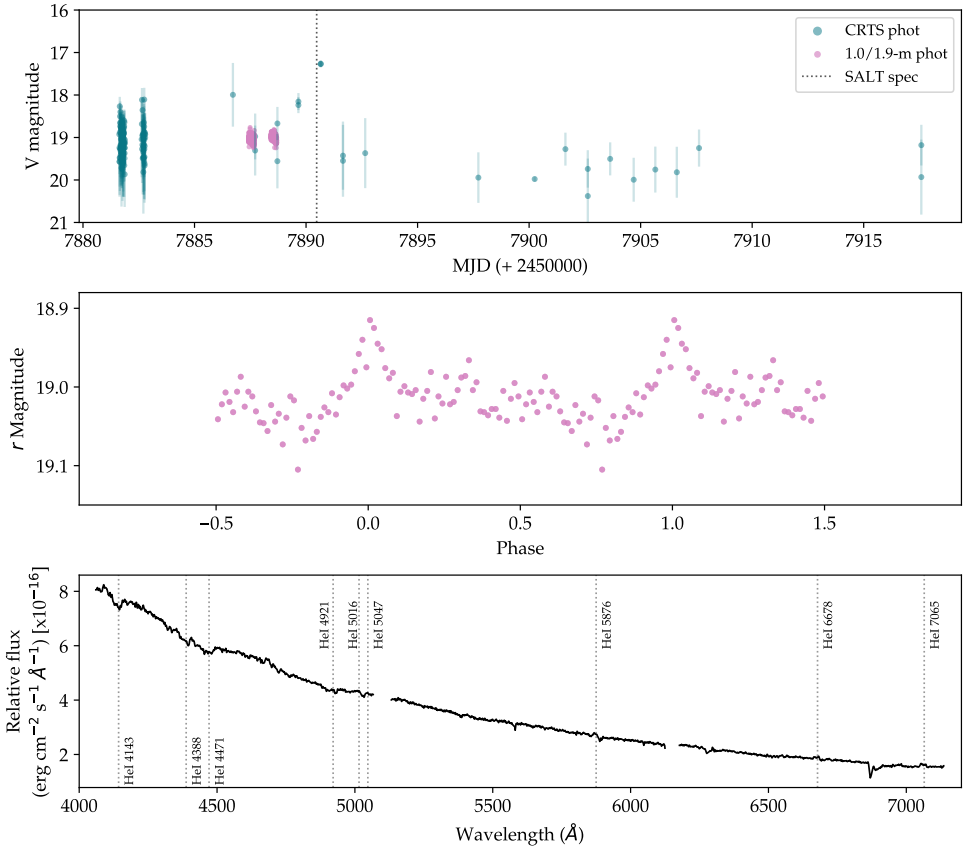

FIGURE 3.21 – Light curves and spectrum of ASASSN-17fp. Top: Long-term light curve of ASASSN-17fp from CRTS in teal. The pink points are follow-up photometric observations. The black dotted line represents the date of the follow-up spectroscopic observation. Middle: An average phase-folded light curve from follow-up observations with SHOC CCD. The complete set of individual light curves can be found in appendix C (Fig. C.0.8). Bottom: A mean spectrum from one night of observations with SALT.

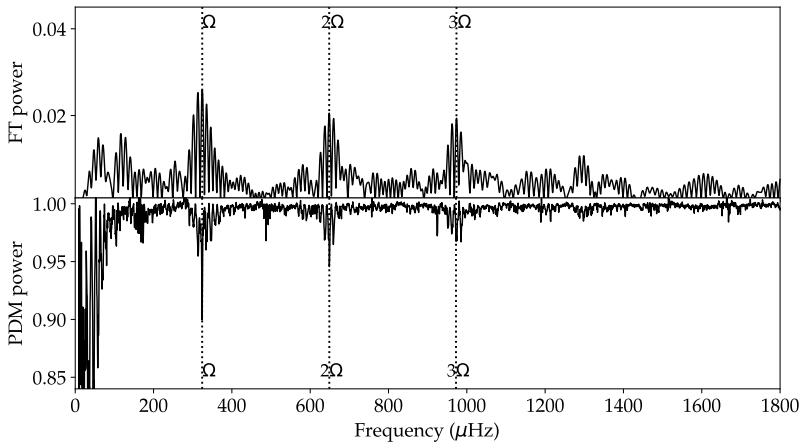

FIGURE 3.22 – The Fourier transform of ASASSN-17fp on top with vertical lines marking the fundamental, first and harmonic frequencies. The PDM is below, marked with the same vertical lines as the FT.

(middle), is the average light curve of all quiescent runs folded on 61.7(3) min. This displays clear double-peaked humps per orbital cycle. Shallow and narrow eclipses are seen in the average light curve of CSS2333-15. The ephemeris for minimum light is

$$HJD_{\rm min} = 2455911.28763 + 0.04282(2)\,E \tag{3.18}$$

The fundamental frequency determined by PDM for the runs in December 2011 during quiescence is $\Omega = 270.14 \pm 1.3$ μHz and first harmonic is $2\,\Omega = 539.97 \pm 2.2$ μHz. The perceived fundamental frequency determined by FT is double that of the PDM i.e. $(2\,\Omega)$ at 540.29(5) μHz. There is no peak frequency in the FT which corresponds to half of the main FT peak frequency. The FT does not differentiate between the individual humps in the orbital cycle therefore only identifying a peak frequency double that of the actual photometric/orbital frequency (Refer to Fig. 3.24).

Spectroscopic observations of CSS2333-15 were taken in October, December 2011 and August 2012 with SALT and additionally in June 2016 with VLT, courtesy of Elme Breedt. The VLT emission line spectrum, taken during quiescence, shows the presence of both hydrogen and helium (Fig. 3.23, bottom). The strongest lines are hydrogen Balmer emission lines (Hα, Hβ, Hγ, Hδ), followed by He I (λ 4471, 4922, 5016, 5876, 6678, 7065). There is a trace of a weak He II λ 4686 emission line. The double-peaked emission lines suggest the presence of a disc which is in a quiescent state. The orbital/photometric period below the CV period minimum and the presence of hydrogen suggest that the system is a helium-rich dwarf nova (DN). The He I (5876)/Hα ratio is found to be higher for the few Helium-rich DNe than typical DNe (Breedt et al., 2012b; Carter et al., 2013b). The He I λ 5876/Hα ratio for CSS2333-15 is $\sim$ 0.82, which is higher than typical values of $\sim$ 0.2-0.4 for common hydrogen DNe (e.g. Szkody, 1981; Williams and Ferguson, 1982; Thorstensen and Taylor, 2001). Most of the SALT spectra are taken during quiescence (see overlap with the long-term light curve in Fig. 3.23, top), and show no signal above the noise level. The spectrum taken on 28 October 2011, was taken during the decline of a (super)outburst. The spectrum has a 1.9×10^{-16} erg cm^{-2}s^{-1}Å^{-1} flux offset for visual convenience and is limited to bluer wavelengths, compared to the VLT spectrum. Although the SALT spectrum has a low signal, it is evident that stronger lines show absorption within emission lines and there is a notable increase in strength of the He II (λ 4686) line from the quiescent state, relative to the other spectral lines (see inset in Fig. 3.23, bottom).

3.8 SUMMARY OF INDIVIDUAL SYSTEMS

CSS0105+19 is among many CRTS CV candidates with SDSS multi-filter photometry. It was discovered as an AM CVn through a targeted approach by constraining previously known AM CVn stars within a tight $(u-g, g-r)$ colour space. The remaining AM CVns and He dwarf nova were identified for follow-up observations in this work after post-outburst discoveries through transient surveys and public alerts of periodic or spectral significance. Since the initial discoveries, long-baseline transient surveys like CRTS and amateur astronomer networks like AAVSO have been useful at monitoring outburst behaviour.

As seen in the long-term light curves, every system has been detected at least once in outburst by CRTS or AAVSO. The orbital period range for this sample of AM CVn stars

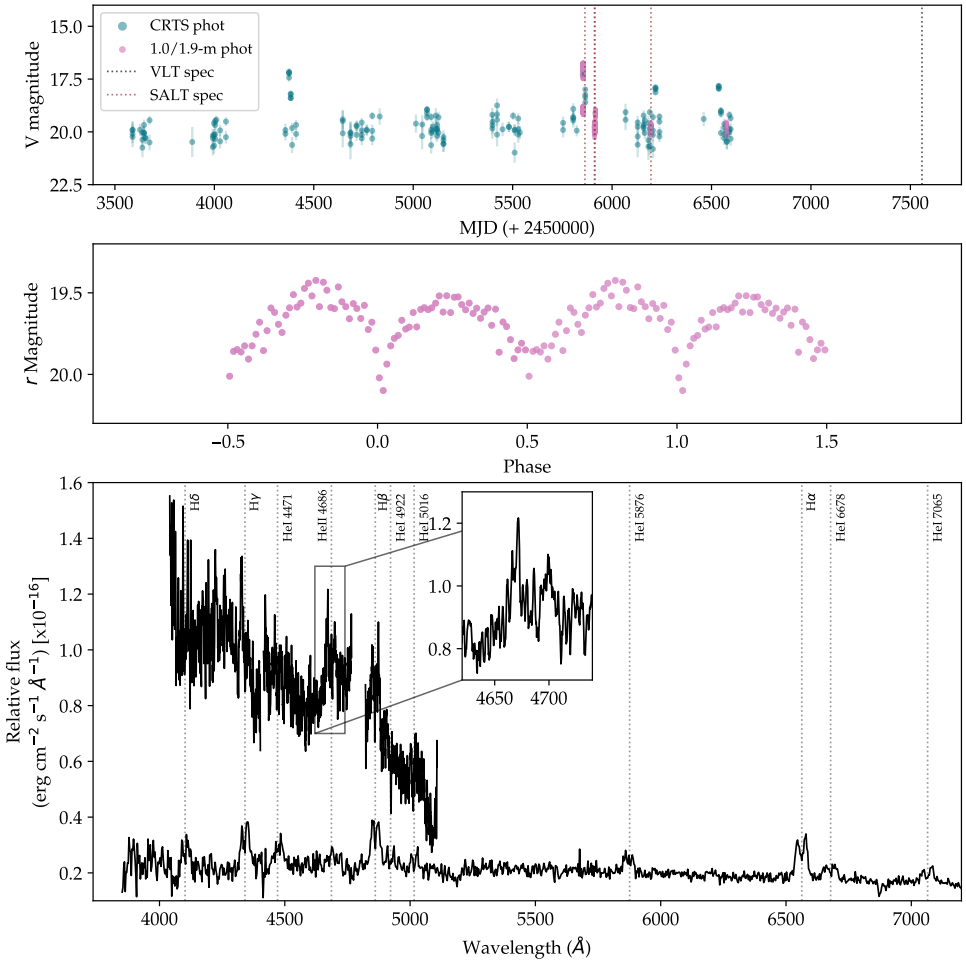

FIGURE 3.23 – Light curves and spectra of CSS2333-15. Top: Long-term light curve of CSS2333-15 from CRTS in teal. The pink points are follow-up photometric observations. The red dotted line represents the date of the follow-up SALT spectroscopic observations and the black dotted line for the VLT spectroscopic observation. Middle: An average phase-folded light curve from follow-up observations with SHOC CCD. The complete set of light curves can be found in appendix C (Fig. C.0.9). Bottom: Above is a single SALT spectrum taken during the decline of an outburst, with a vertical offset. Below is a single spectrum taken with VLT during quiescence, courtesy of Elme Breedt.

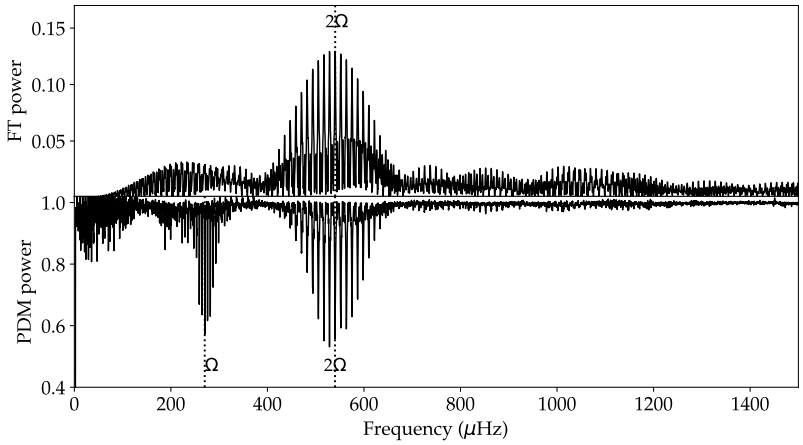

FIGURE 3.24 – The CSS2333-15 Fourier transform of the combined runs of S8132, S8234, S8137, S8139 and S8141 during quiescence at the top. The top figure is the PDM periodogram of those runs. The vertical dotted lines indicate the fundamental frequency (Ω) and first harmonic (2 Ω) frequency.

is 31.65 – 54.78 min and the period of the helium dwarf nova, CSS2333-15, is 61.70 min. With a period of 47.25 min, CSS0450-09 was the first long-period AM CVn (longer than 40 min) reported in (super)outburst and has only been detected once in outburst. Thereafter, numerous long-period AM CVn systems have been observed in outburst, including SDSSJ0902+3819 ($P_{\rm orb}$ =48.3 min, Rau et al., 2010; Kato et al., 2014b), Gaia14aae ($P_{\rm orb}$ =49.7 min, Campbell et al., 2015; Green et al., 2018b), SDSSJ1525+3600 ($P_{\rm orb}$ =44.3 min, Rau et al., 2010; Kupfer et al., 2013), SDSSJ1411+4812 ($P_{\rm orb}$ =46.0 min, Anderson et al., 2005), Gaia14aae ($P_{\rm orb}$ =49.7 min, Campbell et al., 2015; Green et al., 2018b), MOA 2010-BLG-087 ($P_{\rm orb}$ ∼ 50 min, Green et al., 2020), SDSSJ0807+4852 ($P_{\rm SH}$ =53.3 min, Kong et al., 2018; Kupfer et al., 2019) and ASASSN-21au ($P_{\rm orb}$ ∼ 58 min, Isogai et al., 2021; Rivera Sandoval et al., 2022), many of which were identified as outbursting years after their initial discoveries as AM CVn stars. ASASSN-15kf was initially reported to have $P_{\rm orb}$ = 27.67 min, however I determine a photometric period almost double that value, at 54.78 min. ASASSN-14ei and ASASSN-14mv lie within what was thought to be the boundary between long-period and outbursting AM CVns and exhibiting unusual outburst behaviour. Following a superoutburst, several echo-outbursts/rebrightenings were detected over the succeeding months. Since the initial outburst events, ASASSN-14ei has been detected in several brief outbursts over the subsequent years and ASASSN-14mv has been observed in outburst at least once almost six years later.

ASASSN-14ei and ASASSN-14mv are the brightest in the sample with quiescent magnitudes brighter than V∼ 18, while the rest are fainter than V∼ 18. All light curves show low amplitude orbital modulations (< 4 mag), with CSS0105+19, CSS0450-09, V558 Vir, ASASSN-17fp displaying a single hump profile per orbit. ASASSN-14ei and CSS2333-15 show double humps and ASASSN-14mv have triple humps (a main hump and smaller side humps).

Unlike other CV subclasses, all of the AM CVn spectra studied here have the absence of hydrogen in common. Neutral helium is most abundant in the spectra followed by

ionised helium. Ca II H+K is found in ASASSN-14mv and N I in CSS0450-09. Helium dwarf nova CSS2333-15 is dominated by strong double-peaked Balmer emission lines and neutral helium. The Doppler tomography of ASASSN-14ei shows He I emission from the disc and the bright spot. He II λ 4686 is also seen in the disc with strong emission arising from the central component associated with the WD. It is peculiar that the strongest emission is located slightly off-centre.

A summary of the individual systems in this chapter is found in table 3.3.

TABLE 3.3 – Summary of individual systems helium-accreting systems.

Object	**Type**	$P_{\mathbf{orb}}/P_{\mathbf{sh}}$ (min)	**Photometry**	**Spectroscopy**
CSS0105+19	AM CVn	31.648(2)	Sinusoidal	Blue continuum, no clear lines
CSS0450-09	AM CVn	47.245(3)	Single hump profile	He I, He II, N I emission *
V558 Vir	AM CVn	34.78(5)	Too faint. Variations only during outburst	Double peaked emission, He I, He II, possible N I
ASASSN-14ei	AM CVn	42.923(2)	Double hump profile	He I, He II, emission
		42.854(3)		
ASASSN-14mv	AM CVn	40.760(1)	Main hump and side humps	Emission and absorption, He I, He II, Ca II
ASASSN-15kf	AM CVn	54.78(2)	Double hump profile	-
ASASSN-17fp	AM CVn	51.39(7)	Single hump profile	Double peaked, emission, absorption, He I, He II
CSS2333-15	He DN	61.7(3)	Double humps, shallow eclipses	Double peaked H and He emission lines

Notes: DN = dwarf nova. A question mark indicates a lack of information or certainty. An asterisk indicates the information is obtained from the literature discussed in the relevant subsections.

CHAPTER 4

Magnetic cataclysmic variable candidates from optical transient surveys

In this chapter, I present my observations of 27 candidate magnetic cataclysmic variables from the CRTS. The detailed descriptions of the photometric observations, reductions and analysis have been described in the previous AM CVn observational chapter. I describe the spectroscopic observational, reduction and analysis processes. I include detailed logs of photometric and spectroscopic observations. Photometric and/or spectroscopic results for individual objects are discussed and then summarised in a table. The individual objects were classified as follows: The objects are classified as follows: 8 polars + 1 polar candidate, 7 DN + 4 DN candidates, 1 nova-like CV, 1 RR Lyr, 2 AGNs and 3 unknown. Two polars were observed spectroscopically over both high and low states showing differences in the emission lines visible in the spectra. The AGN and nova-like CV long-term light curves resemble the long-term features of polars which highlight the importance of follow-up observations.

4.1 Photometric observations

The photometric observation process is described in section 3.1. The observing runs are listed in Table 4.1, representing a total of 278.7 hours of photometric observations.

TABLE 4.1 – Observing log of photometric observations of CV candidates from CRTS.

Object	Run No.	Date of obs. (start of night)	HJD of first obs. (+2450000.0)	Length (h)	t_{in} (s)	Tel.	r (mag)
CSS0109-27	S8346	2013 Dec 25	6652.27788	2.00	60	1.9-m	19.1
	S8349	2013 Dec 26	6653.27806	2.50	60	1.9-m	18.8
	S8354	2013 Dec 29	6656.27892	1.15	60	1.9-m	19.0
	S8417	2014 Jul 30	6869.54591	3.00	30	1-m	17.3
	S8419	2014 Jul 31	6870.54523	3.50	40	1-m	18.0
	S8422	2014 Aug 01	6871.54823	2.78	40	1-m	18.3
	S8438	2014 Aug 30	6900.66394	2.50	15	1-m	17.9
	S8441	2014 Aug 31	6901.49919	4.00	5	1-m	17.0
	S8444	2014 Sep 01	6902.52284	3.38	10	1-m	18.0
	S8447	2014 Sep 02	6903.56564	2.25	25	1-m	18.6
	S8450	2014 Sep 03	6904.55090	2.74	40	1-m	18.9
	S8453	2014 Sep 04	6905.54543	2.79	50	1-m	19.0
CSS0357+10	S8363	2014 Jan 24	6682.37259	1.50	20	1.9-m	17.3
	S8366	2014 Jan 25	6683.29243	3.00	10	1.9-m	17.2
	S8369	2014 Jan 26	6684.28607	3.00	10	1.9-m	17.3
	S8372	2014 Jan 27	6685.28543	3.00	10	1.9-m	17.3
	S8374	2014 Jan 29	6687.29777	2.50	10	1.9-m	17.2
	S8375	2014 Jan 30	6688.28361	2.75	10	1.9-m	17.2
	S8380	2014 Feb 02	6691.29220	1.00	10	1.9-m	17.2
MLS0720+17	S8352	2013 Dec 27	6654.42911	4.00	60	1.9-m	18.1
	S8552	2015 Feb 18	7072.36246	2.33	50	1-m	18.6
	S8555	2015 Feb 19	7073.37489	1.65	70	1-m	18.3
	S8587	2015 Feb 20	7074.26862	2.65	30	1.9-m	18.3
	S8561	2015 Feb 21	7075.40719	0.88	60	1-m	-
	S8567	2015 Feb 23	7077.35533	1.11	45	1-m	18.4
SDSS0804+16	S8379	2014 Feb 01	6690.40183	3.72	40	1.9-m	18.4
	S8381	2014 Feb 02	6691.35338	3.26	30	1.9-m	18.6
	S8382	2014 Feb 03	6692.39172	2.50	20	1.9-m	18.4
	S8383	2014 Feb 04	6693.38652	3.50	40	1.9-m	19.2
CSS0812+04	S8364	2014 Jan 24	6682.45982	1.55	20	1.9-m	18.4
	S8367	2014 Jan 25	6683.43171	1.72	20	1.9-m	18.5
	S8370	2014 Jan 26	6684.42414	2.50	20	1.9-m	18.5
	S8373	2014 Jan 27	6685.55586	1.24	30	1.9-m	18.6
	S8376	2014 Jan 30	6688.44167	1.73	30	1.9-m	18.4
	S8405	2014 Mar 20	6737.25748	2.00	30	1-m	18.5
	S8409	2014 Mar 21	6738.25493	2.00	30	1-m	18.5
SSS1012-18	S8553	2015 Feb 18	7072.47486	3.87	70	1-m	18.7
	S8658	2015 May 06	7149.22393	3.09	70	1-m	18.9
	S8661	2015 May 07	7150.21925	4.00	80	1-m	18.9
	S8664	2015 May 08	7151.20740	4.00	80	1-m	18.9
	S8670	2015 May 11	7154.20495	3.58	70	1-m	18.7
SSS1020-33	S8161	2012 Feb 28	5986.34529	4.00	30	1-m	17.7
	S8198	2012 May 01	6049.21715	2.10	30	1-m	17.5
	S8573	2015 Feb 26	7080.49488	1.83	30	1-m	17.9
CSS0910+16	S8409	2014 Mar 21	6738.36147	1.54	40	1-m	17.4
	S8412	2014 Mar 22	6739.26938	2.65	60	1-m	17.3
	S8666	2015 May 09	7152.23354	3.00	60	1-m	18.7
	S8668	2015 May 10	7153.20179	3.15	60	1-m	18.7

Abbreviations: obs = observation, Tel = Telescope and t_{in} = integration time.

(Continued on next page)

Table 4.1 – continued from previous page

Object	Run No.	Date of obs. (start of night)	HJD of first obs. (+2450000.0)	Length (h)	t_{in} (s)	Tel.	r (mag)
	S8671	2015 May 12	7155.20022	3.00	60	1-m	18.6
CSS1127-05	S8362	2014 Jan 23	6681.51762	2.50	20	1.9-m	18.7
	S8365	2014 Jan 24	6682.53760	2.00	30	1.9-m	18.9
	S8368	2014 Jan 25	6683.51213	2.50	30	1.9-m	18.8
	S8371	2014 Jan 26	6684.53774	2.00	15	1.9-m	18.7
CSS1307-20	S8659	2015 May 06	7149.46159	2.77	40	1-m	18.2
	S8662	2015 May 07	7150.45285	2.32	40	1-m	18.2
	S8665	2015 May 08	7151.38615	3.90	10	1-m	18.3
	S8667	2015 May 09	7152.39740	4.13	15	1-m	18.3
	S8669	2015 May 10	7153.35376	3.75	10	1-m	18.3
CSS1455-11	S8695	2015 Jun 20	7194.37191	2.94	70	1-m	20.2
	S8698	2015 Jun 21	7195.35054	2.56	80	1-m	20.3
	S8701	2015 Jun 22	7196.28601	3.26	90	1-m	20.3
MLS1525-03	S8672	2015 May 12	7155.38649	4.44	2	1-m	16.3
	S8675	2015 Jun 11	7185.33693	2.81	5	1-m	16.4
	S8678	2015 Jun 12	7186.38865	2.78	10	1-m	16.4
	S8706	2015 Jun 23	7197.30773	3.05	10	1-m	16.3
CSS1619+13	S8415	2014 Jul 30	6869.26364	2.72	10	1-m	16.9
	S8420	2014 Aug 01	6871.26478	2.62	30	1-m	17.0
	S8423	2014 Aug 02	6872.22786	3.42	10	1-m	17.0
	S8427	2014 Aug 06	6876.28788	1.83	10	1-m	17.1
	S8435	2014 Aug 29	6899.24197	1.41	10	1-m	17.2
	S8436	2014 Aug 30	6900.24436	3.00	15	1-m	17.2
	S8439	2014 Aug 31	6901.22840	1.66	10	1-m	17.2
SSS1935-53	S8416	2014 Jul 30	6869.40120	3.00	15	1-m	16.7
	S8418	2014 Jul 31	6870.39887	2.93	30	1-m	-
	S8421	2014 Aug 01	6871.39006	3.50	30	1-m	17.7
	S8425	2014 Aug 03	6873.39614	3.50	40	1-m	18.7
	S8440	2014 Aug 31	6901.32107	4.00	40	1-m	18.8
	S8443	2014 Sep 01	6902.39131	3.00	30	1-m	18.9
SSS1944-42	S8446	2014 Sep 02	6903.39021	3.50	20	1-m	17.2
	S8449	2014 Sep 03	6904.39000	3.50	25	1-m	17.9
	S8452	2014 Sep 04	6905.45226	1.83	20	1-m	17.5
	S8475	2014 Sep 14	6915.36263	3.00	60	1-m	17.0
	S8478	2014 Sep 15	6916.38145	2.90	90	1-m	18.1
CSS2042-09	S8748	2015 Aug 12	7247.41157	3.00	50	1-m	19.0
	S8749	2015 Aug 14	7249.40708	3.00	40	1-m	19.4
	S8752	2015 Aug 15	7250.37046	2.10	40	1-m	19.7
SSS2046-31	S8687	2015 Jun 17	7191.52455	4.00	80	1-m	19.2
	S8690	2015 Jun 18	7192.48669	5.00	80	1-m	19.2
	S8693	2015 Jun 19	7193.52563	4.06	70	1-m	19.2
CSS2154+15	S8700	2015 Jun 21	7195.61570	1.86	5, 10	1-m	17.6
	S8705	2015 Jun 22	7196.61248	2.08	10	1-m	17.6
	S8753	2015 Aug 15	7250.46334	2.08	10	1-m	17.7
	S8757	2015 Aug 17	7252.42348	3.00	15	1-m	17.4
CSS2335+12	S8426	2014 Aug 03	6873.55089	0.80	20	1-m	18.3
	S8437	2014 Aug 30	6900.42142	3.00	40	1-m	19.0
	S8482	2014 Oct 18	6949.28649	2.50	10	1.9-m	18.5

Abbreviations: obs = observation, Tel = Telescope and t_{in} = integration time.

(Continued on next page)

Table 4.1 – continued from previous page

Object	Run No.	Date of obs. (start of night)	HJD of first obs. (+2450000.0)	Length (h)	t_{in} (s)	Tel.	r (mag)
	S8485	2014 Oct 19	6950.34302	2.50	25	1.9-m	18.4
	S8488	2014 Oct 20	6951.26950	3.00	30	1.9-m	18.7
	S8491	2014 Oct 21	6952.26092	3.00	30	1.9-m	18.5
	S8750	2015 Aug 14	7249.54853	2.52	40	1-m	18.8
	S8754	2015 Aug 15	7250.55669	2.32	40	1-m	18.8
	S8758	2015 Aug 17	7252.55905	2.37	15	1-m	18.3

Abbreviations: obs = observation, Tel = Telescope and t_{in} = integration time.

4.2 PHOTOMETRIC DATA REDUCTION

The photometric observation process is described in section 3.2 of the previous observation chapter.

4.3 PHOTOMETRIC ANALYSIS PROCESS

The photometric observation process is described in section 3.3.

4.4 SPECTROSCOPIC OBSERVATIONS

Due to the faint nature of my targets, all of the spectroscopic data taken to classify the magnetic CV candidates were taken with the Robert Stobie Spectrograph (RSS; Burgh et al., 2003; Kobulnicky et al., 2003; Smith et al., 2006) on the segmented 11 m Southern African Large Telescope (SALT) situated at SAAO. The RSS is a prime focus spectrograph with many capabilities including low to medium resolution spectroscopy with a wavelength range of 3200-9000.

For the purpose of this study, RSS was used in long-slit spectroscopy mode with a slit width of 1.5", giving R=933 at the central wavelength. The RSS Simulator (version 4.1.0 and 4.2.1) along with the input spectrum of known polar, HU Leo, enabled us to find the optimum configuration to ensure meeting my scientific goals. PG0900 grating in faint, slow readout mode gives the desired signal-to-noise per resolution element (S/N_{pre}) for individual exposures. The initial grating angle of 14° was used for the PG0900 grating for first semester targets for a spectral coverage of 3800-6800 but it was later discovered that the first chip gap was too close to the Hα wavelength which resulted in Hα emission/absorption lines being partially obstructed. The grating angle was changed to 14.75° for the second semester. Most of the targets were observed for 2×660 s. For very bright/faint targets, the exposure time was adjusted accordingly. Second semester targets were observed four times at separate epochs in an observing semester in order to identify radial velocity variations. Observations are listed in Table 4.2, representing a total of 10.29 hours of spectroscopic observations.

TABLE 4.2 – Observing log of spectroscopic observations of CRTS CVs.

Object	**Date of obs.** (start of night)	**Length** (*s*)	**Grating angle** (°)
CSS0105-08	2015 Aug 06	2×660.2	14.00
CSS0109-27	2015 Jul 05	2×660.2	14.00
SSS0617-36	2015 Dec 09	2×690.2	14.75
	2015 Dec 14	2×690.2	14.75
	2016 Mar 13	690.2+551.1	14.75
	2016 Apr 08	2×690.2	14.75
CSS0812+04	2016 Jan 04	2×690.2	14.75
	2016 Jan 05	2×690.2	14.75
	2016 Feb 10	2×690.2	14.75
	2016 Mar 01	2×690.2	14.75
CSS0919-05	2016 Jan 13	2×690.2	14.75
	2016 Feb 27	2×690.2	14.75
	2016 Mar 08	2×690.2	14.75
SSS1012-18	2015 May 19	2×660.2	14.00
MLS1115+05	2015 May 20	2×660.2	14.00
MLS1137+00	2016 Mar 31	2×690.2	14.75
	2016 Apr 07	2×690.2	14.75
	2016 Apr 10	2×690.2	14.75
	2016 Apr 12	2×690.2	14.75
MLS1247-04	2015 May 19	2×720.2	14.00
SSS1440-22	2015 May 19	2×750.2	14.00
CSS1455-11	2015 May 20	3×660.2	14.00
MLS1525-03	2015 May 20	2×660.2	14.00
SSS1955-30	2016 Apr 02	2×690.2	14.75
	2016 Apr 09	2×592.2	14.75
	2016 Apr 10	2×690.2	14.75
MLS2044-16	2015 May 19	2×500.2	14.00

4.5 SPECTROSCOPIC DATA REDUCTION

The spectroscopic data process is described in section 3.5.

4.6 INDIVIDUAL SYSTEMS WITH HIGH-SPEED PHOTOMETRY AND SPECTROSCOPY

In this section, and the following two sections, I report the results of the individual objects which were selected for follow-up observations. The data are presented together in a figure with the long-term light curves from CRTS above and the SHOC photometry and/or the SALT spectrum below. Instead of displaying the average light curves as in the previous chapter, the most detailed single example of the individual SHOC light curves is used because many of the polar light curves show mostly random flickering which is diminished when averaging the light curves. The light curves of the individual observations can be found in the appendix D. I also present the photometric periods and periodograms determined via the FT and PDM.

4.6.1 *CSS0109-27 (CSS131015:010946-274524)*

The long-term light curve of CSS0109-27 (Fig. 4.1, top) displays occasional brightenings/outbursts and the second half of the long-term light curve appears to have less scatter than the first half. Follow-up photometric observations took place over 12 nights between December 2013 and September 2014 with the 1-m and 1.9-m telescopes. These follow-up photometric observations were taken at varying states, during quiescent state as well as ascending into or descending from outburst (as seen in red in Fig. 4.1).

The follow-up light curves of CSS0109-27 (Fig. 4.1, middle) show varying behaviour. The quiescent light curves display flickering variations. During outburst, the light curves taken show smoother, wave-like transitions on longer time scales than the flickering. Nothing conclusive can be said about the orbital structure. I was unable to determine a photometric period for this system.

The RSS spectrum of CSS0109-27 is noisy with weak emission lines (Fig. 4.1, bottom). The emission lines are broad hydrogen Balmer lines (Hα, Hβ, Hγ, Hδ, Hϵ, Hζ). The continuum is flat, decreasing in noise with increasing wavelength.

CSS0109-27 is classified as a dwarf nova based on the presence of outbursts in the long-term light curve, the follow-up light curve in outburst, and the spectrum containing only broad hydrogen Balmer lines.

4.6.2 *CSS0350+32 (CSS091218:035011+323230)*

I identified CSS0350+32 as a candidate magnetic CV and possibly eclipsing through its long-term CRTS light curve (Fig. 4.2, top, courtesy of Paul Mason). As a northern target, it was followed up photometrically and spectroscopically by our collaborator Mason et al. (2019), after which we confirmed it as an eclipsing polar. The light curve (Fig. 4.2, middle, courtesy of Paul Mason) is relatively flat with constant flickering. A narrow, deep eclipse is preceded by a pre-eclipse dip due to absorption of the light from the accretion region by the matter in the accretion stream near the white dwarf.

The emission line spectrum (Fig. 4.2, bottom, courtesy of Paul Mason) is dominated by strong hydrogen Balmer lines (Hα, Hβ, Hγ, Hδ, Hϵ, Hζ, Hη) and strong He II λ 4686

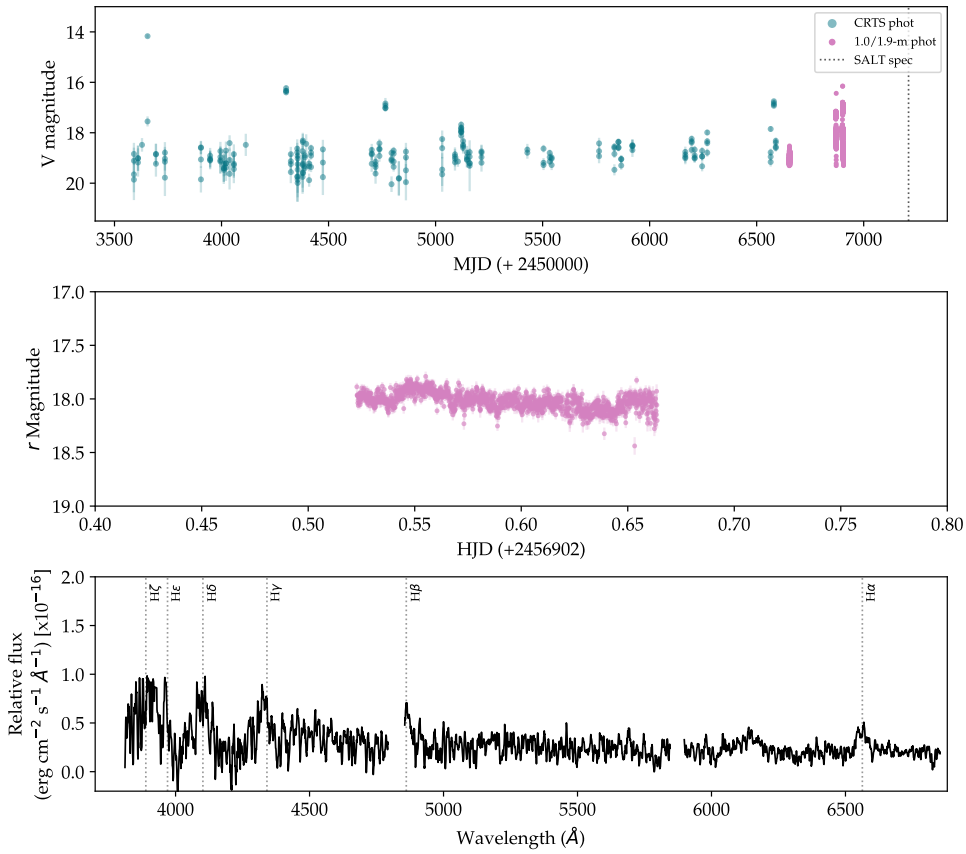

FIGURE 4.1 – Light curves and spectrum of CSS0109-27. Top: The long-term light curve of CSS0109-27 from the CRTS. The teal data points are from the CRTS database. The pink data points are all follow-up photometric observations taken with SHOC CCD on the SAAO telescope(s). The black dotted line is the corresponding JD of the follow-up SALT spectroscopic observations. Middle: A single light curve of CSS0109-27 from follow-up observations with SHOC CCD in pink. The complete set of light curves can be found in appendix D (Fig. D.1.1). Bottom: Mean SALT spectrum of CSS0109-27 with identifiable emission lines indicated by grey dotted lines.

comparable with Hβ. The weaker emission lines include He I (λ 4922, 5016, 6678, 7065). We reported an orbital period of 142.30 min along with multiple system parameters determined by eclipse timing and modeling (see table 6 from Mason et al., 2019)).

4.6.3 *CSS0357+10 (CSS091109:035759+102943)*

CSS0357+10 was classified as a candidate polar by Schwope and Thinius (2012) based on photometry and archival X-ray observations, with a period of 114 min. Thorstensen et al. (2016) present spectroscopy with the strength of He II λ 4686 shy of Hβ strength, and large velocity amplitudes which confirm the magnetic nature. CSS0357+10 has clear distinctions between the low and high states in the long-term light curve (Fig. 4.3, top). The system frequently changed between high and low states during the first half of long-term monitoring after which the system dipped to intermediate state and returned to high state. Follow-up photometric observations of CSS0357+10 took place during

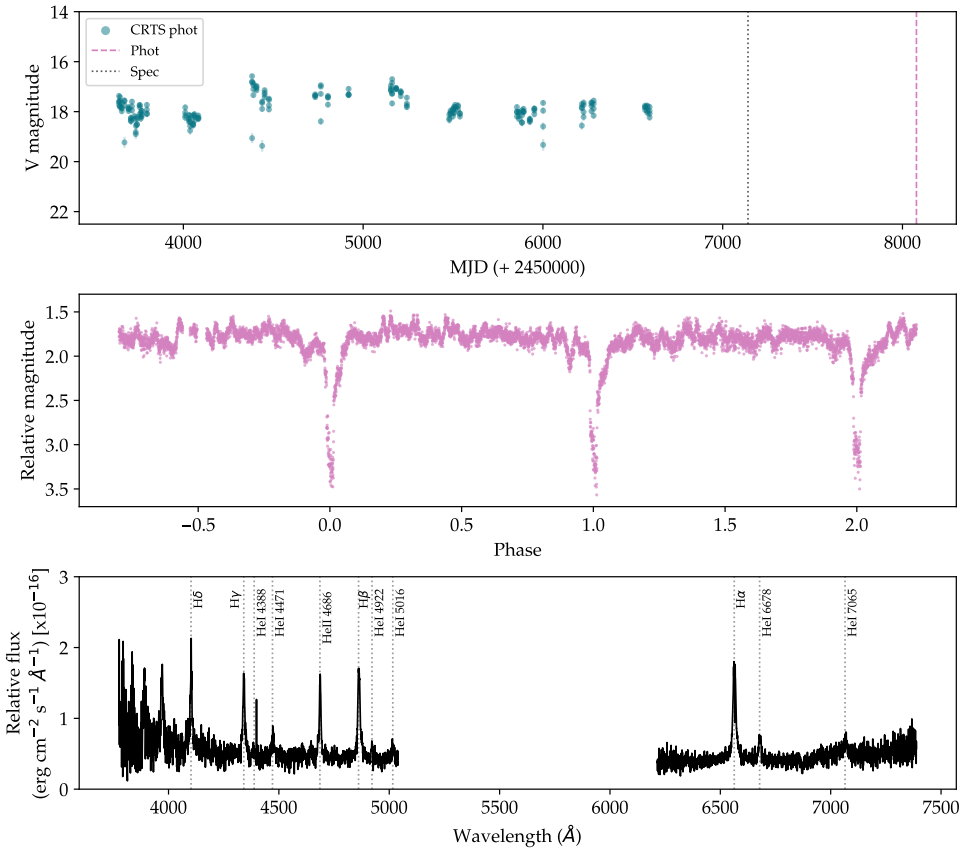

FIGURE 4.2 – Light curves and spectrum of CSS0350+32. Top: The long-term light curve of CSS0350+32 from the CRTS. The teal data points are from the CRTS database. The pink dashed line corresponds to the date of the photometric observations taken with the 2.1-m telescope at the McDonald Observatory. The black dotted line is the corresponding JD of the follow-up SALT spectroscopic observations. Middle: A single light curve of CSS0350+32 from follow-up observations from the 2.1-m telescope in pink, courtesy of Paul Mason. Bottom: Mean spectrum of CSS0350+32 with identifiable emission lines indicated by grey dotted lines was taken with the Apache Point Observatory 3.5-m telescope, courtesy of Paul Mason.

the high state (as seen in red in Fig. 4.3). I observed it over seven nights in January and February 2014 with the 1.9-m telescope.

$$HJD_{\max} = 2456683.29672 + 0.07918(27)\,E \tag{4.1}$$

The follow-up light curves of CSS0357+10 display random flickering throughout (Fig. 4.3, bottom). Although the orbital structure is constant from cycle to cycle, the intensities and finer structures differ. There is a hump, followed by a shallow, narrow dip and continuous flickering.

The phase-folded light curve Fig. D.1.3 in appendix D is folded over a period of 114.0(4) min, corresponding to a PDM fundamental frequency of $\Omega = 146.2(5)\,\mu$Hz. The first and second harmonic frequencies are $2\,\Omega = 292.3(6)\,\mu$Hz, $3\,\Omega = 438.3(6)\,\mu$Hz, respectively.

At first glance, the dip appears to correspond with the orbital period, implying an eclipse (or partial eclipse), but further investigation reveals that the dip timing

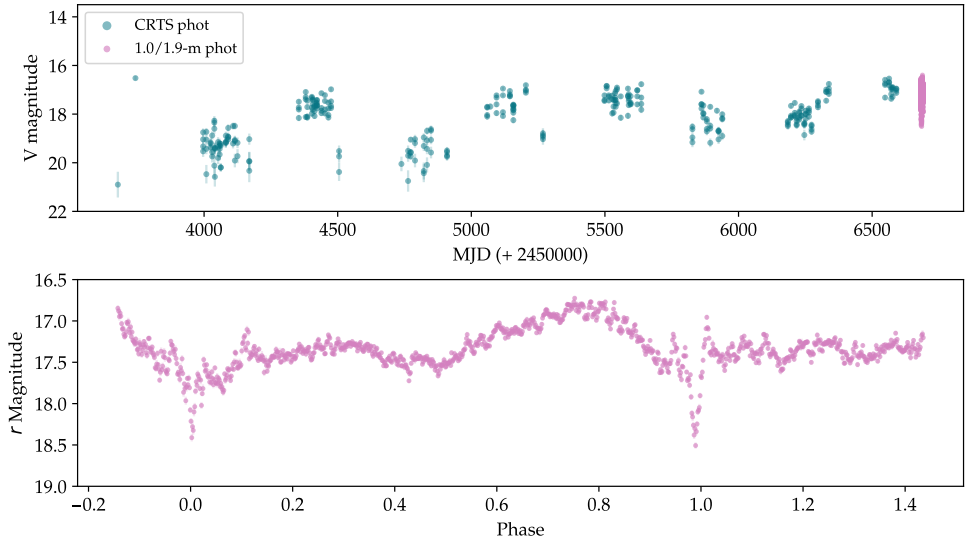

FIGURE 4.3 – Light curves of CSS0357+10. Top: The long-term light curve of CSS0357+10 from the CRTS. The teal data points are from the CRTS database. The pink data points are all follow-up photometric observations taken with SHOC CCD on the SAAO telescope(s). Bottom: A single light curve of CSS0357+10 from follow-up observations with SHOC CCD in pink. The complete set of light curves can be found in appendix D (Fig. D.1.2).

varies slightly around the orbital period as seen in Fig. 4.4. The small fluctuations in the dip timings around the orbital period suggest that the dip is associated with the accretion stream which is less stable than an eclipse. The position (and thus timing) of the accretion stream with respect to the orbital cycle is influenced largely by the accretion rate. Two scenarios are possible: 1) The accretion stream obscures the accretion region as the far-field stream transits the accretion region, similar to AR UMa (Szkody et al., 1999), HU Aqr (Schwope et al., 1998; Harrop-Allin et al., 1999) and UZ For (Sirk and Howell, 1998) (although HU Aqr and UZ For have eclipses following the stream dips). As we do not see any evidence of an eclipse by the secondary star, this scenario would only apply to a very small inclination range. 2) A small (top or bottom) segment of the secondary star eclipses the accretion stream as the secondary star travels past the accretion stream blocking emission from the stream, seen at the start of the eclipses of HU Aqr (e.g. Hakala, 1995; Bridge et al., 2002), EP Dra (e.g. Bridge et al., 2003) and MASTER J061451.70-272535.5 (Breytenbach et al., 2019). Phase-resolved spectra would allow further constraints on the geometry of the binary system.

CSS0357+10 is classified as a polar, in agreement with Schwope and Thinius (2012) and Thorstensen et al. (2016), based on distinct high and low states in the long-term light curves and flickering features in the follow-up light curves.

4.6.4 *SSS0617-36 (SSS100511:061754-362655)*

Woudt et al. (2012b) reported a photometric period of 0.143 days for SSS0617-36. A spectrum presented by Oliveira et al. (2020) shows strong evidence of a hot, optically thick disc during DN outburst. SSS0617-36 show slight variations in the quiescent state in the long-term light curve as well as short-lived brightenings/outbursts (Fig. 4.5, top). SSS0617-36 was observed photometrically on 28 and 29 November 2014.

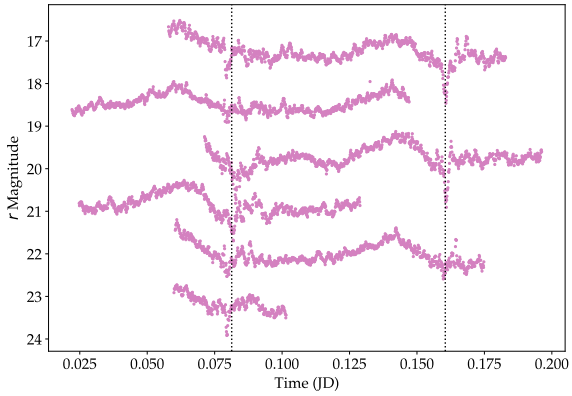

FIGURE 4.4 – Individual light curves of CSS0357+10 aligned along the orbital period.

The two follow-up light curves of SSS0617-36 (Fig. 4.5, middle) differ very slightly. Both are increasing in brightness, during outburst, with small high-frequency variations. At higher brightness, the variations are clearer and more structured. I was unable to determine any photometric periods.

The follow-up spectra were taken over a timescale of four months. All three spectra of SSS0617-36 have high signal-to-noise ratios (Fig. 4.5, bottom and Fig. D.2.1 in appendix D). The first spectrum taken on 9 December 2015 shows broad absorption lines, namely hydrogen Balmer lines (Hα, Hβ, Hγ, Hδ) and He I (λ 4471, 4922). Within the broad absorption lines of Hα, Hβ, are narrow emission lines. The ratio of emission to absorption is stronger with Hα, compared to Hβ. The spectrum from 13 March 2016 contains emission lines. The strongest lines are the hydrogen Balmer lines. Absorption is seen in addition to emission in Hβ, Hγ, Hδ, where absorption strength decreases with increasing wavelength. The weaker lines include He I (λ 4922, 5016, 5876), some of which may be double-peaked. The spectrum taken on 08 April 2016 displays strong double-peaked hydrogen Balmer emission lines and weaker He I emission lines (λ 4471, 4922, 5016, 5876). At low state, this spectrum has the lowest signal-to-noise ratios.

According to the sequence of spectra, the first spectrum was taken during outburst, the second spectrum was taken while transitioning into or out of outburst and the last spectrum was during the faint quiescent state. The continua of all three spectra are blue, with the steepest decline during outburst, indicative of a hot disc, and the most gradual decline in quiescence.

SSS0617-36 is indeed a DN (most likely a U Gem binary) based on 1) the long-term light curve showing frequent outbursts, 2) the light curves during outburst and 3) the three spectra in quiescence and outburst with strong, double-peaked emission lines, broad Balmer emission lines and strong blue continua.

4.6.5 *MLS0720+17 (MLS101226:072033+172437)*

The light curve of MLS0720+17 was first reported by Hardy et al. (2017) to display eclipses with disc properties. Conversely, Oliveira et al. (2017) suggest that MLS0720+17 is a polar based on a Goodman identification spectrum with a blue continuum, He II 4686 , Bowen blend C III/N III and narrow He I emission lines. In Paterson et al. (2019),

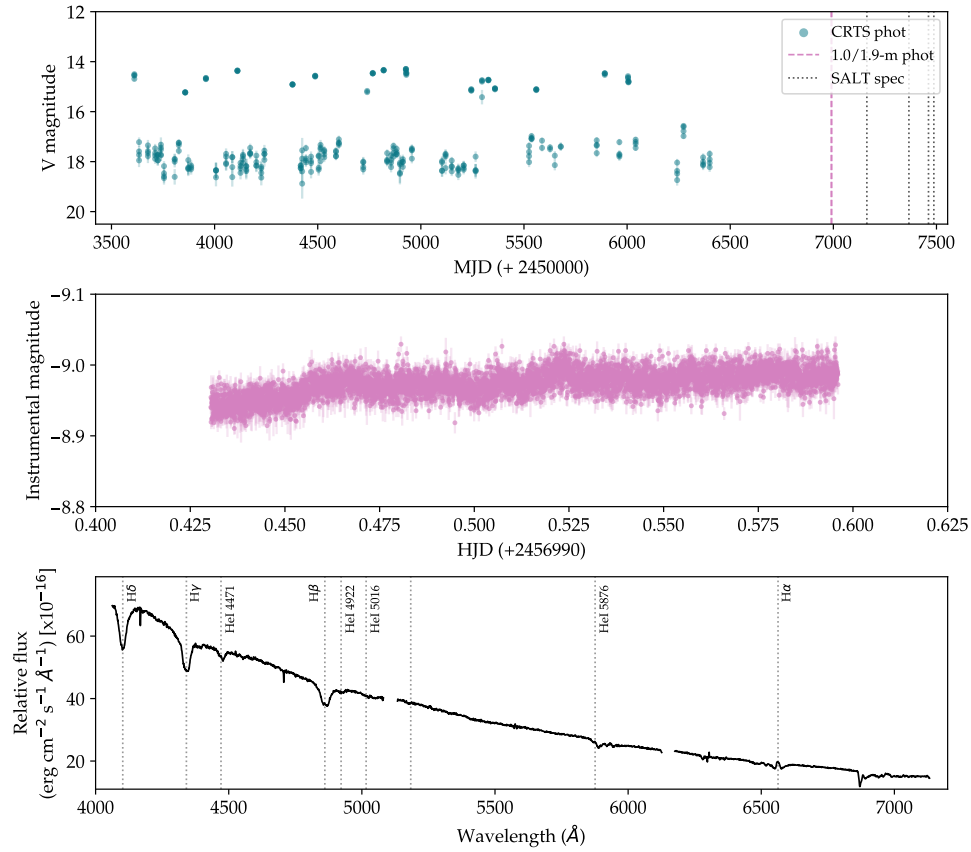

FIGURE 4.5 – Light curves and spectrum of SSS0617-36. Top: The long-term light curve of SSS0617-36 from the CRTS. The teal data points are from the CRTS database. The pink dashed lines are follow-up photometric observations taken with SHOC CCD on the SAAO telescope(s). The black dotted line is the corresponding JD of the follow-up SALT spectroscopic observations. Middle: A single light curve of SSS0617-36 from follow-up observations with SHOC CCD in pink. The complete set of light curves can be found in appendix D (Fig. D.1.4). Bottom: One of the mean SALT spectra of SSS0617-36 with identifiable emission lines indicated by grey dotted lines.

we showed that MLS0720+17 is likely an SW Sex (nova-like) CV based on photometry and spectroscopy presented in this subsection.

MLS0720+17 has a sparsely sampled long-term light curve (Fig. 4.6, top). There appear to be low and high states. Most data lies in the high state with one transition to the low state and evidence of eclipses. MLS0720+17 was observed during the high state (as seen in pink in Fig. 4.6, middle). Follow-up photometric light curves contain deep and wide v-shaped eclipses which are indicative of the presence of an accretion disc surrounding a white dwarf. (Fig. 4.6). The ephemeris for minimum light is

$$HJD_{\rm min} = 2457072.40892 + 0.150408(7)\,E \tag{4.2}$$

which corresponds to $P_{\rm orb} = 3.61$ h.

The average phase-resolved spectrum of MLS0720+17 (Fig. 4.6, bottom, courtesy of John Thorstensen) displays a blue continuum populated by emission lines. Visible lines include strong hydrogen Balmer lines (Hα, Hβ, Hγ), He I (λ 4471, 4922, 5876, 6678,

7065) and He II λ 4686. The relative strength of the Balmer lines decreases towards longer wavelengths. The radial velocities are fit to a sinusoid of

$$v(t) = \gamma + Ksin(2\pi(t - t_0)/P) \tag{4.3}$$

using linear least squares, with constant P derived from eclipse timing. The fit produced the following values: $\gamma = 88(\pm19)\,\mathrm{km\,s^{-1}}$, velocity half-amplitude $K = 299(\pm23)\,\mathrm{km\,s^{-1}}$ and t_0 =HJD$_0$ = 2457141.698(±0.003).

The radial velocity fit in Paterson et al. (2019) (Fig. 5) is offset from the eclipse phase by 0.175(±0.031), which is characteristic of SW Sex stars. The Balmer radial velocities lag behind the white dwarf motion due to complex emission structures. This is observed in eclipsing systems as the Balmer radial velocities return to the mean value following the eclipse. Other observed SW Sex features include an S-wave absorption component within Hα emission and orbital periods above the period gap within the range P_{orb} = 3–4 h (Rodríguez-Gil et al., 2009). Compared to Hβ, He II λ 4686 is relatively weak but its presence along with that of the Bowen blend and single-peaked emission lines further support the classification of MLS0720+17 as an SW Sex/nova-like CV.

4.6.6 *CSS0812+04 (CSS080228:081210+040352)*

Spectroscopy presented by (Oliveira et al., 2020) with a blue continuum, emission lines and a high He II/Hβ ratio, strongly suggests that CSS0812+04 is a polar. Complimentary results by us from (Thorstensen et al., 2020) are presented in this subsection. The long-term light curve of CSS0812+04 (Fig. 4.7, top) shows general large scatter on long timescales and also over single 30 minute observations. The overall brightness of the system remains relatively constant while occasional dips provide evidence for eclipses. CSS0812+04 was observed over seven nights in January and March 2014 with the 1.9-m and 1-m telescope, respectively. These observations can be seen in pink in Fig. 4.7 (middle).

The non-defined follow-up light curves of CSS0812+04 (Fig. 4.7, middle) contain low amplitude flickering. A shallow and narrow dip which aligns in every orbital cycle is likely a partial eclipse and preceded by smaller non-periodic dips. The eclipse and pre-eclipse dips are not visible in all of the light curves due to low time resolution. The orbital (or photometric) period could not be obtained using the photometric data. Using the orbital period of $P_{\mathrm{orb}} = 162\pm0.3$ min, determined from phase-resolved spectroscopic data through a radial velocity curve, the phase-folded light curve (Fig. D.1.7 in appendix D) was obtained. The phase-folded light curve reveals a clear orbital partial eclipse but no phased pre-eclipse dips, as well as a broader low amplitude orbital hump structure. The velocity half-amplitude $K = 131 \pm 14\,\mathrm{km\,s^{-1}}$ is much smaller than most polars, which are observed to have higher radial velocities than other CVs due to magnetically influenced accretion flow which can reach free-fall velocities, typically higher than most parts of an accretion disc (Rosen et al., 1987; Schwope et al., 1997b).

The spectra of CSS0812+04 (Fig. 4.7, bottom and Fig. D.2.2 in appendix D) were taken over almost two months. The first spectrum, taken on 05 January 2016, shows emission lines. It contains strong hydrogen Balmer lines (Hα, Hβ, Hγ, Hδ), strong He II λ 4686 and weaker He I (λ 4388, 4471, 4922, 5016, 5876, 6678, 7065) and He II (λ 4541, 5412). During bright phases, the Bowen blend C III/N III is visible at the base of He II λ 4686. The spectrum taken on 10 February 2016 shows the same lines as those in the first spectrum but not as strong. The weaker lines are almost drowned out by the noise.

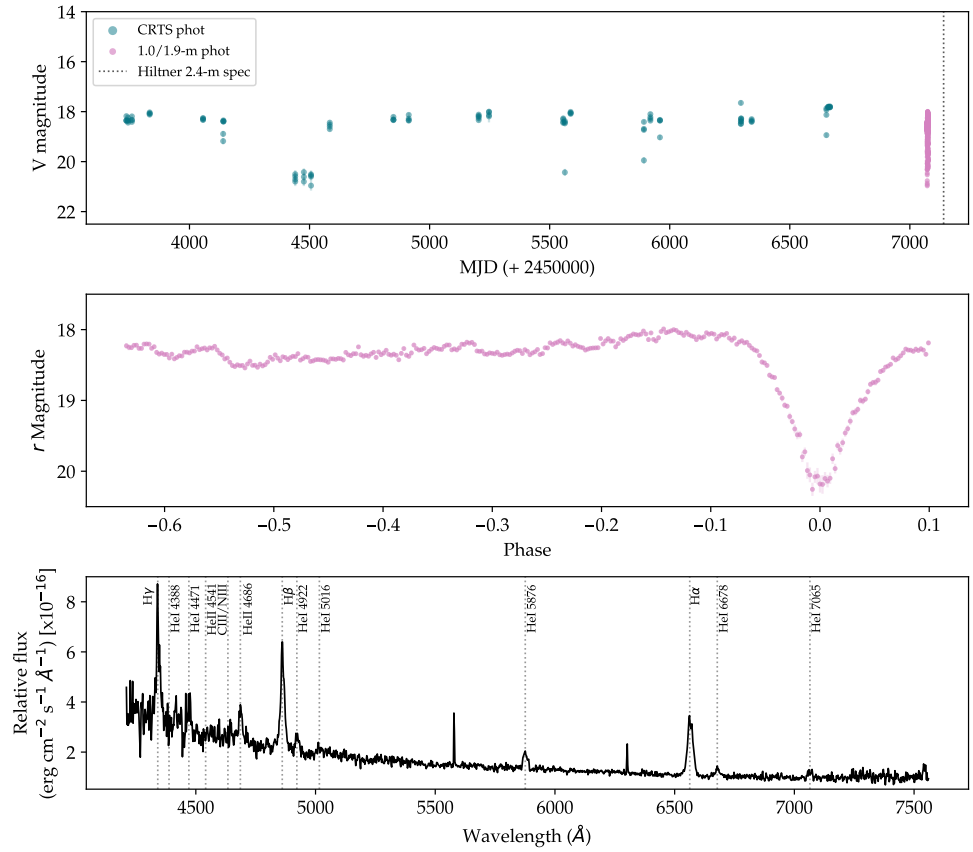

FIGURE 4.6 – Light curves and spectrum of MLS0720+17. Top: The long-term light curve of MLS0720+17 from the CRTS. The teal data points are from the CRTS database. The pink data points are all follow-up photometric observations taken with SHOC CCD on the SAAO telescope(s). The black dotted line is the corresponding JD of the follow-up SALT spectroscopic observations. Middle: A single light curve of MLS0720+17 from follow-up observations with SHOC CCD in pink. The complete set of light curves can be found in appendix D (Fig. D.1.5). Bottom: A mean spectrum of MLS0720+17, courtesy of John Thorstensen, with identifiable emission lines indicated by grey dotted lines.

The spectrum on 12 February 2016 is mostly noise but the strongest lines, hydrogen Balmer lines and He II λ 4686, are visible. The weaker lines are barely visible above the noise level. The spectrum from 01 March 2016 was taken during high state and has the strongest signal. He I (λ 5016) and He II (λ 4541) are visible in addition to the lines from the first spectrum on 10 February. The helium lines are more prominent in this spectrum and also appear to be double-peaked. The relative strength of He II λ 4686 compared to Hβ varies for the different spectra. The He II λ 4686 line is either larger than, or roughly the same strength as Hβ across the spectra. The continua are all similar, gradually increasing towards blue wavelengths. According to the sequence of spectra, CSS0812+04 begins and ends in high state. Over the two months in between, the system transitions to and from a lower state to high again.

The presence of He II lines, the Bowen blend and the strong presence of He II λ4686 line in spectra taken in both high and low states indication of a polar, in agreement with Oliveira et al. (2020), despite the low velocity half-amplitude.

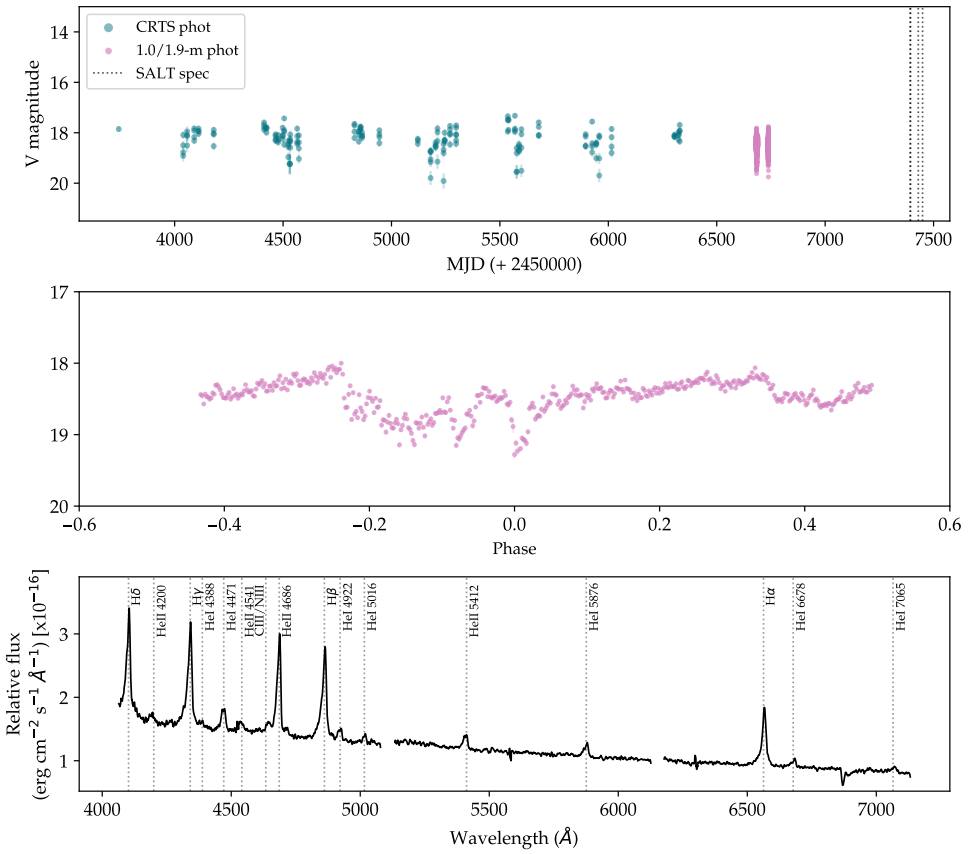

FIGURE 4.7 – Light curves and spectrum of CSS0812+04. Top: The long-term light curve of CSS0812+04 from the CRTS. The teal data points are from the CRTS database. The pink data points are follow-up photometric observations taken with SHOC CCD on the SAAO telescope(s). The black dotted line is the corresponding JD of the follow-up SALT spectroscopic observations. Middle: A single light curve of CSS0812+04 from follow-up observations with SHOC CCD in pink. The complete set of light curves can be found in appendix D (Fig. D.1.6). Bottom: One of the mean SALT spectra of CSS0812+04 with identifiable emission lines indicated by grey dotted lines.

4.6.7 *CSS0910+16 (CSS140218:091002+164819)*

CSS0910+16 was first discovered as a CV through SDSS (Szkody et al., 2009) and later reported to exhibit multiple superoutbursts with a superhump period of 0.0734 d (Kato et al., 2017). The long-term light curve of CSS0910+16 (Fig. 4.8, top) shows large short-term scatter throughout the light curve and slight variations in the brightness of the system. There are two large amplitude brightenings, most likely outbursts, and constant shallow dips. My photometric observations took place during possible bright and faint states (as seen in red in Fig. 4.8). CSS0910+16 was observed over five nights in March 2014 and May 2015.

The follow-up light curves of CSS0910+16 (Fig. 4.8) display random flickering. The large-scale structure in the light curve is not consistent throughout the light curves. The large amplitude variations in the quiescent state in the long-term light curve are observed in the follow-up light curves. There is over one magnitude difference between

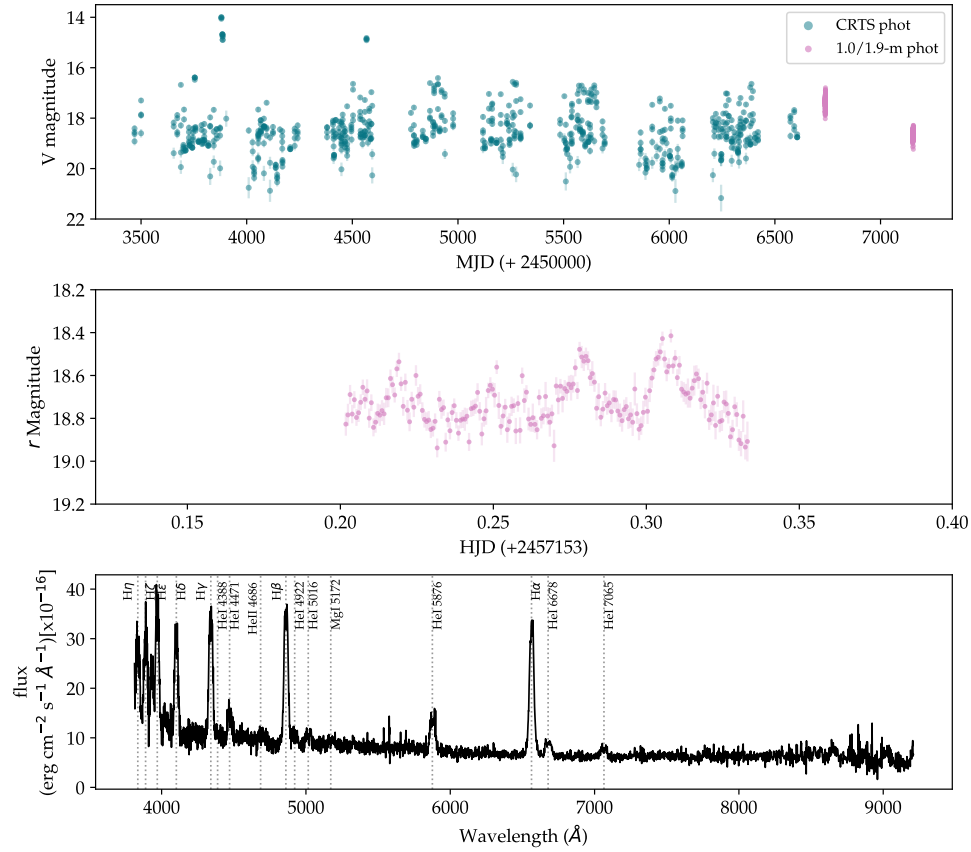

FIGURE 4.8 – Light curves and spectrum of CSS0910+16. Top: The long-term light curve of CSS0910+16 from the CRTS. The teal data points are from the CRTS database. The pink data points are follow-up photometric observations taken with SHOC CCD on the SAAO telescope(s). Middle: A single light curve of CSS0910+16 from follow-up observations with SHOC CCD in pink. The complete set of light curves can be found in appendix D (Fig. D.1.8). Bottom: A mean spectrum of CSS0910+16 from SDSS with identifiable emission lines indicated by grey dotted lines.

the average data from 2014 and 2015. The data are insufficient for period determination using the FT or PDM. The high signal-to-noise spectrum from SDSS has a slight blue continuum populated by emission lines. Strong hydrogen Balmer lines (Hα, Hβ, Hγ, Hδ, Hϵ, Hζ, Hη) dominate the spectrum, accompanied by weaker double peaked He I (λ 4471, 4922, 5016, 5876, 6678, 7065) lines and He II λ 4686.

Based on two detected outbursts in the long-term light curve and the SDSS spectrum with strong Balmer emission lines and the double-peaked He I lines, CSS0910+16 is a dwarf nova observed during quiescence, in agreement with Kato et al. (2017).

4.6.8 *SSS1012-18 (SSS110203:101217-182411)*

Coppejans et al. (2016a) classified SSS1012-18 as a DN based on three outbursts recorded in the CRTS database. A spectrum presented in Oliveira et al. (2017) corresponding to quiescent brightness is similar to other intermediate polars. The spectrum contains a blue continuum, broad He I and Balmer lines, stronger Hβ than Hα and the presence

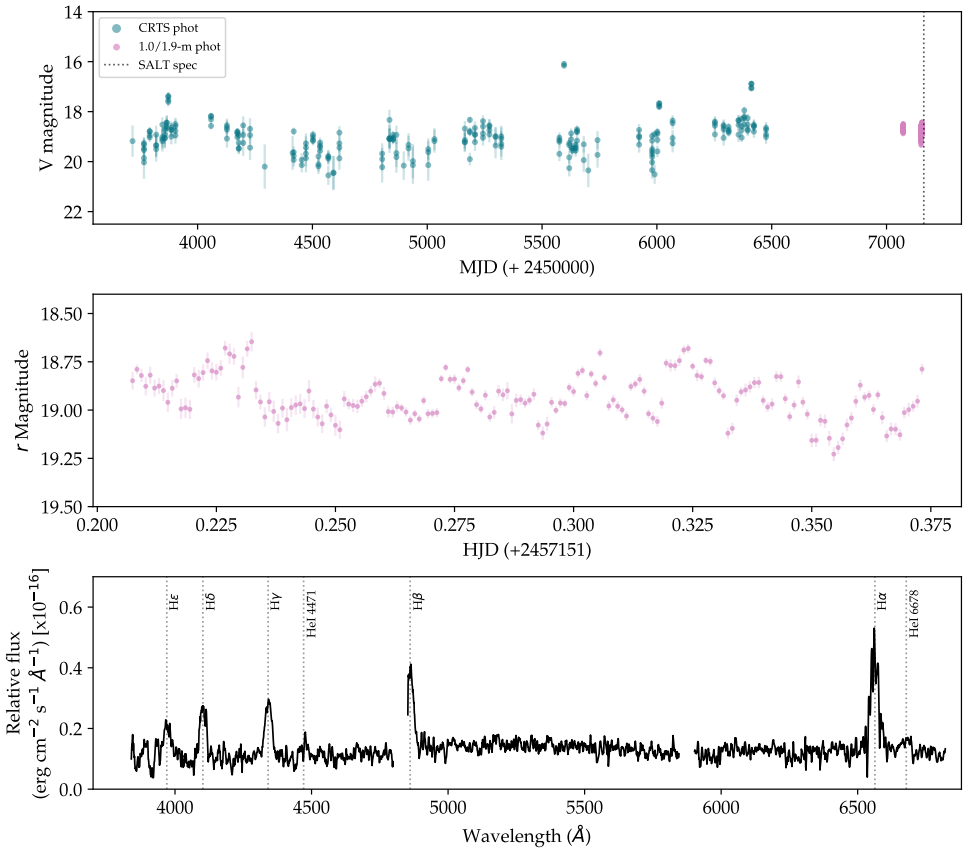

FIGURE 4.9 – Light curves and spectrum of SSS1012-18. Top: The long-term light curve of SSS1012-18 from the CRTS. The teal data points are from the CRTS database. The pink data points are follow-up photometric observations taken with SHOC CCD on the SAAO telescope(s). The black dotted line is the corresponding JD of the follow-up SALT spectroscopic observations. Middle: A single light curve of SSS1012-18 from follow-up observations with SHOC CCD in pink. The complete set of light curves can be found in appendix D (Fig. D.1.9). Bottom: Mean SALT spectrum of SSS1012-18 with identifiable emission lines indicated by grey dotted lines.

of He II (λ 4686). The long-term light curve of SSS1012-18 (Fig. 4.9, top) displays a slightly variable quiescent state with occasional brightenings/outbursts. Follow-up photometric observations took place over five nights in February and May 2015 with the 1-m telescope.

The follow-up light curves of SSS1012-18 (Fig. 4.9, middle) show constant brightness variability with random flickering across the light curves. The variations in the orbital structure are subtle such that the overall appearance of the light curves is level. A photometric period could not be determined.

The spectrum of SSS1012-18 shows broad emission lines (Fig. 4.9, bottom). The most prominent lines are hydrogen Balmer lines (Hα, Hβ, Hγ, Hδ, Hϵ, Hζ). The weaker emission lines within the noisy continuum, namely He I (λ 4471, 6678), appear to be double-peaked. The continuum is roughly flat across the observed spectrum.

The 2-3 recorded outbursts in the long-term light curve and the spectrum dominated by broad double-peaked Balmer emission lines are indicative of a dwarf nova, in agreement with Coppejans et al. (2016a) and Oliveira et al. (2017).

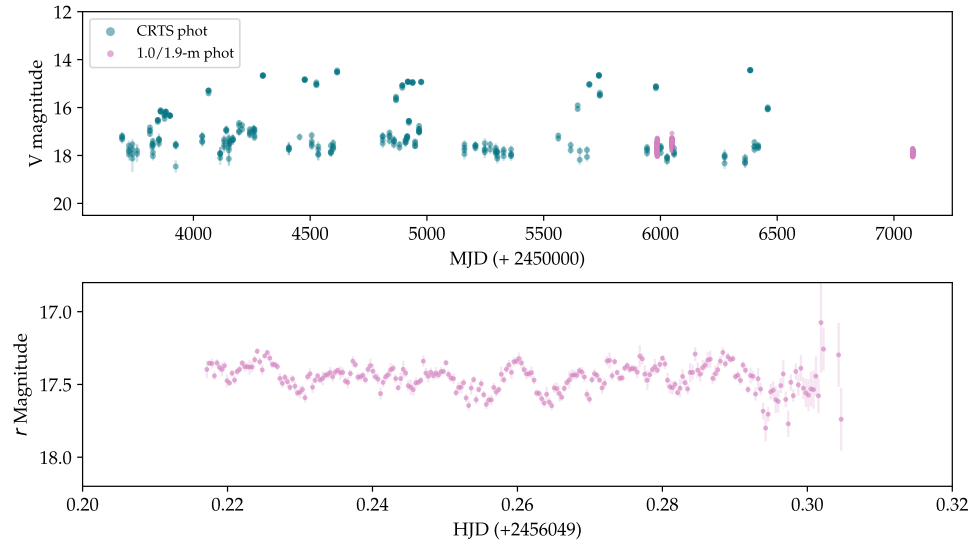

FIGURE 4.10 – Light curves of SSS1020-33. Top: The long-term light curve of SSS1020-33 from the CRTS. The teal data points are from the CRTS database. The pink data points are all follow-up photometric observations taken with SHOC CCD on the SAAO telescope(s). Bottom: A single light curve of SSS1020-33 from follow-up observations with SHOC CCD in pink. The complete set of light curves can be found in appendix D (Fig. D.1.10).

4.6.9 *SSS1020-33 (SSS120215:102042-335002)*

Oliveira et al. (2020) presented a spectrum of SSS1020-33 with evidence of a hot disc and the development of broad Hydrogen Balmer lines, confirming a DN in outburst. The long-term light curve of SSS1020-33 (Fig. 4.10, top) shows numerous high amplitude outbursts. Follow-up photometric observations for SSS1020-33 were taken with the 1-m telescope three years apart, in 2012 and 2015.

The follow-up light curves of SSS1020-33 (Fig. 4.10, bottom) contain constant random flickering with no general orbital structure. No periodicity was found.

4.6.10 *CSS1127-05 (CSS110225:112749-054234)*

Despite a weak He II λ 4686 emission line compared to Hβ, Oliveira et al. (2017) suggest a likely polar nature for CSS1127-05 based on high and low-brightness states. They do not rule out the possibility of an IP. Despite the first half of the long-term light curve being sparsely sampled with only five separate observations, the light curve is well sampled over the second half (Fig. 4.11, top). The early data points may belong to a low state as they appear to be below the brightness levels recorded in the second half.

Follow-up photometric observations of CSS1127-05 appear to be taken during high state, over four consecutive days in January 2014. The light curves contain high-frequency fluctuations but lack orbital structure. A photometric period could not be determined.

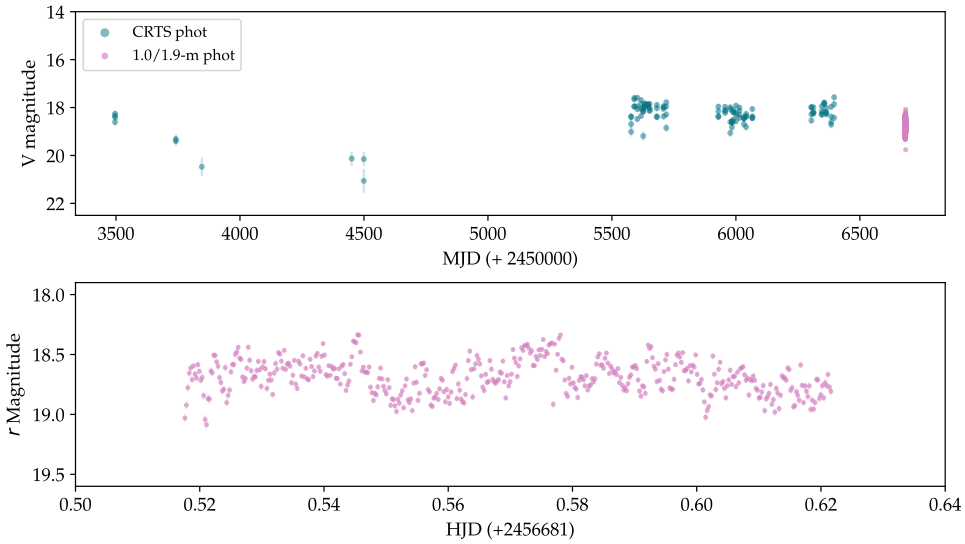

FIGURE 4.11 – Light curves of CSS1127-05. Top: The long-term light curve of CSS1127-05 from the CRTS. The teal data points are from the CRTS database. The pink data points are all follow-up photometric observations taken with SHOC CCD on the SAAO telescope(s). Bottom: A single light curve of CSS1127-05 from follow-up observations with SHOC CCD in pink. The complete set of light curves can be found in appendix D (Fig. D.1.11).

4.6.11 *CSS1455-11 (CSS120303:145555-111957)*

According to the long-term light curve (Fig. 4.12, top), the brightness of CSS1455-11 is predominantly in stable quiescent state, with two outbursts. The second outburst appears to be a superoutburst, after which the quiescent brightness increased, before settling to a fainter quiescent brightness. Follow-up photometric observations of CSS1455-11 took place over three nights in June 2015, with the 1-m telescope.

Due to the faintness of CSS1455-11 during quiescent state, the follow-up light curves (Fig. 4.12) are undefined. These light curves are mostly noise, and very little signal. The spectrum of CSS1455-11 displays defined double-peaked emission lines (Fig. 4.12), indicative of the presence of a disc and high inclination. The most obvious lines are hydrogen Balmer lines with Hα and Hβ being the strongest. The signals for Hγ and Hδ are just above the noise level. The continuum increases slightly and gradually decreases towards the red end of the spectrum. The two recorded outbursts in the long-term light curve and the spectrum showing only broad double-peaked Balmer lines are suggestive of a DN-type CV.

4.6.12 *MLS1525-03 (MLS120517:152507-032655)*

MLS1525-03 was briefly discussed as an eclipsing CV and polar candidate, as part of a large photometric study of 74 CVs by Hardy et al. (2017). Gabdeev et al. (2019) confirmed that 1RXS J152506.9-032647, the X-ray counterpart of MLS1525-03, is a polar through photometry, spectroscopy and Doppler tomography.

The long-term light curve of MLS1525-03 (Fig. 4.13, top) shows clear low, high and intermediate states. During the first half of CRTS monitoring, this system spent most of its time in low state with a brief jump to intermediate during the low state. There

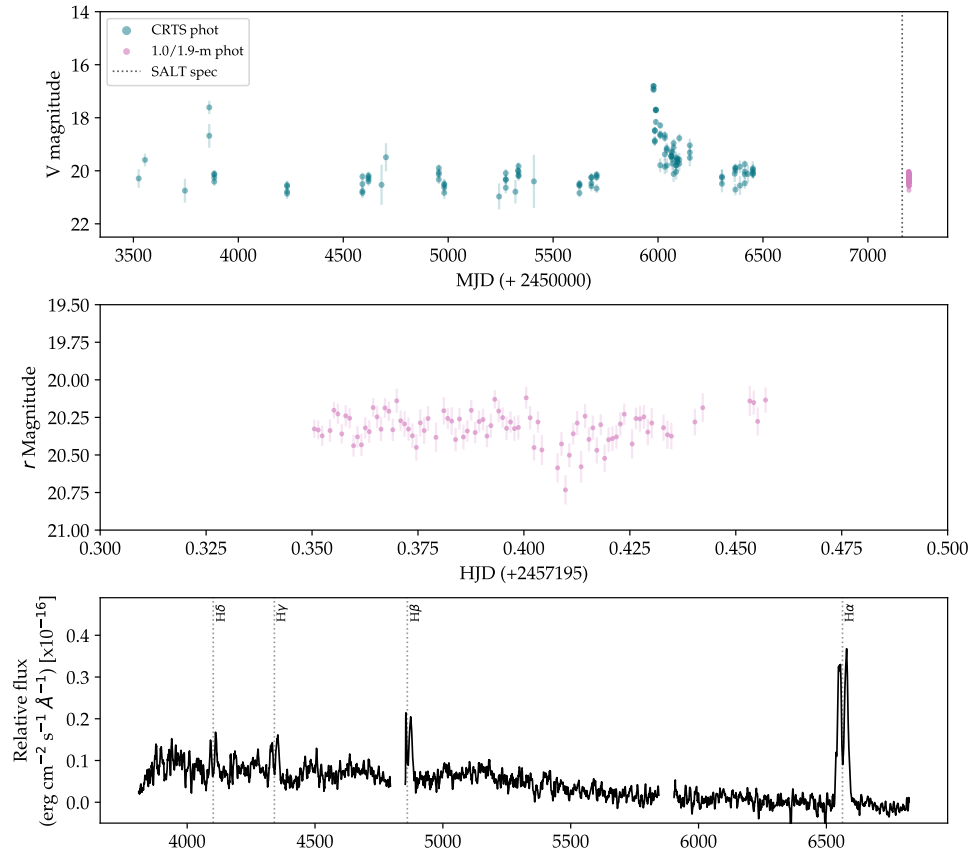

FIGURE 4.12 – Light curves and spectrum of CSS1455-11. Top: The long-term light curve of CSS1455-11 from the CRTS. The teal data points are from the CRTS database. The pink data points are follow-up photometric observations taken with SHOC CCD on the SAAO telescope(s). The black dotted line is the corresponding JD of the follow-up SALT spectroscopic observations. Middle: A single light curve of CSS1455-11 from follow-up observations with SHOC CCD in pink. The complete set of light curves can be found in appendix D (Fig. D.1.12). Bottom: Mean SALT spectrum of CSS1455-11 with identifiable emission lines indicated by grey dotted lines.

is evidence of deep eclipses during the low states. It then increased substantially to high state, where it experienced a slow continuous decline. I observed MLS1525-03 during the decline (as seen in red in Fig. 4.13). MLS1525-03 was observed with the 1-m telescope over four nights during two separate observing runs. The first observation was taken on 12 May 2015 and further follow-up took place a month later on 11, 12 and 23 June 2015 (see table. 4.1).

The follow-up light curves of MLS1525-03 show great detail (Fig. 4.13). There is constant flickering throughout the light curves which is more evident in S8672 and S8675 because of their shorter exposure times of 2 s and 5 s, respectively. The flickering appears to be random as it was not identified through period analysis. The light curves contain general structural modulations which are repetitive over the orbital cycles. Although the general orbital structure is constant, it is not identical over each orbital cycle. Some dips (or peaks) are deeper (or higher) than those from different cycles. There are deep eclipses that take place on a peak inclination. These eclipses are over four

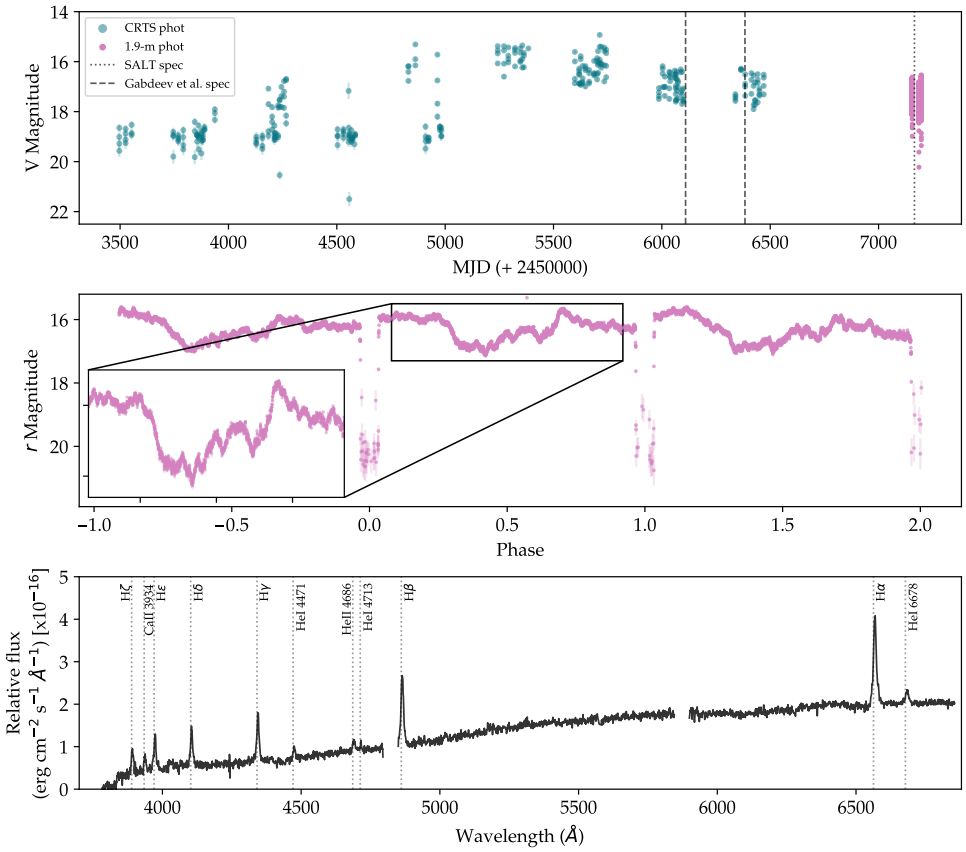

FIGURE 4.13 – Light curves and spectrum of MLS1525-03. Top: The long-term light curve of MLS1525-03 from the CRTS. The teal data points are from the CRTS database. The pink data points are follow-up photometric observations taken with SHOC CCD on the SAAO telescope(s). The black dotted line is the corresponding JD of the follow-up SALT spectroscopic observations. The black dashed lines are the JDs associated with the spectra from Gabdeev et al. (2019) taken in July 2012 and April 2013. Middle: A single light curve of MLS1525-03 from follow-up observations with SHOC CCD in pink. The complete set of light curves can be found in appendix D (Fig. D.1.13). Bottom: Mean SALT spectrum of MLS1525-03 with identifiable emission lines indicated by grey dotted lines.

magnitudes deep and with a ~ 10 min duration. The deep narrow eclipses are indicative of the absence of an accretion disc, as the white dwarf is eclipsed.

The ephemeris for minimum light is

$$HJD_{\rm min} = 2457155.44497809 + 0.06438159(3)\,E \tag{4.4}$$

The orbital period determined by eclipse timing is 92.70950(5)m̈in which is very close to that of the FT. A linear regression was fit to the mid-eclipse times of the observations to determine the ephemeris with the error in the orbital period calculated from the standard error in the gradient.

The spectrum of MLS1525-03 has a high signal-to-noise ratio with emission lines (Fig. 4.13). The strongest lines are hydrogen Balmer lines (Hα, Hβ, Hγ, Hδ, Hϵ, Hζ). The weaker lines are He I (λ 4471, 4713, 6678), He II λ 4686 and Ca II λ 3934. The continuum gradually increases in flux with increasing wavelength, as does the strength

of the Balmer lines. This indicates that there may be a high contribution to the total flux from the companion. The red continuum and weak He II λ 4686 are uncharacteristic of magnetic CVs. Gabdeev et al. (2019) obtained spectra on July 2012 and April 2013 with stronger He II λ 4686 lines compared to Hβ (see top panel of Fig. 4.13 for comparison of my data with the collection of the Gabdeev et al. (2019) spectra). They note that in the phase near the eclipse, the He II λ 4686 line disappears due to the associated region being eclipsed by a cold star.

Photo-polarimetric observations were taken over two nights in July 2020. In Fig. 4.14 from 20 July and Fig. 4.15 from 21 July, the photometric light curves (top) are seen with simultaneous circular (second) and linear (third) polarisation curves, with the corresponding position angles (bottom). The light curve in Fig. 4.15 shows more definition and variation in the orbital structure and flickering than in Fig. 4.14 which indicates a higher photometric signal in Fig. 4.15. The circular and linear polarisation profiles are not consistent between both observations suggesting a variation in accretion. Although the profiles differ, it is evident that both show clockwise and anti-clockwise (positive and negative) circular polarisation between 10 and 20 % which indicates accretion occurs near two poles.

The negative circular polarisation is associated with the bright phase and peaks during the largest photometric peak. The maximum positive circular polarisation percentage is seen during the fainter phase, shortly before the smaller photometric peak during the bright phase. The circular polarisation is negative for a larger fraction of the orbital phase implying that it is associated with the more prominent accretion pole in the upper hemisphere. The upper hemisphere may be in view for all or most of the orbital phase, and possibly simultaneously in view with the pole in the lower hemisphere, corresponding to the positive circular polarisation. Thus the percentage of positive circular polarisation from the lower hemisphere may be higher than the resulting value obtained, as the resulting value may be a combination of positive and negative circular polarisation from both poles. The polarisation from both poles cannot be disentangled which complicates the interpretation of the polarisation curves.

The high percentage of linear polarisation (for a polar) is comparable with the circular polarisation percentage. A two-pulse linear profile is more evident in Fig. 4.15, where each peak corresponds with a sign reversal of circular polarisation indicating the appearance or disappearance of a pole from the limb of the white dwarf. Given the entanglement of the polarisation contribution of each pole, the values for the polarisation angles are a combination from both poles, and without further information about the geometry and phasing of the accretion regions (which may be obtained through phase-resolved spectro-polarimetric observations), it is difficult to extract any meaningful information.

The distinct two-state long-term light curve, the follow-up light curves displaying narrow eclipses and continuous flickering, and the relatively high circular and linear polarisation percentages are strongly indicative of a polar, despite the unusual spectrum.

4.6.13 *CSS1619+13 (CSS090416:161909+135146)*

CSS1619+13 was studied spectroscopically by Thorstensen et al. (2015) and classified as a DN due to emission lines typically found in DNe spectra and the presence of absorption lines during outburst. The long-term CRTS light curve shows frequent outburst brightenings and gradual variations in the quiescent brightness.

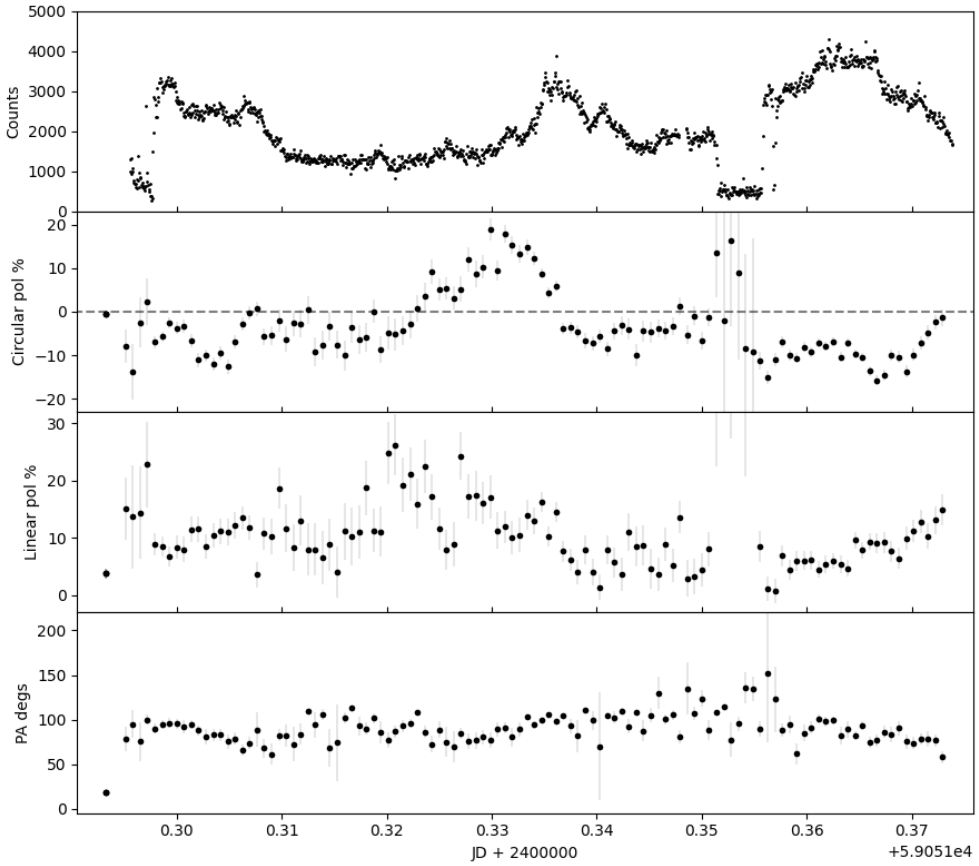

FIGURE 4.14 – Simultaneous light and polarisation curves of MLS1525-03 from 20 July 2020. Top: A light curve of MLS1525-03 from 20 July 2020. Second: Simultaneous percentage of circular polarisation. Third: Simultaneous percentage of linear polarisation. Bottom: The position angle associated with the linear polarisation.

Follow-up photometric observations were taken in July and August 2014 during outburst and quiescence as seen in the top panel of Fig. 4.16. The follow-up light curves do not show orbital modulation but rather flickering throughout the orbit (e.g. bottom panel of Fig. 4.16). Our photometry during outburst and quiescence supports the DN classification.

4.6.14 *SSS1944-42 (SSS100805:194428-420209)*

SSS1944-42 was classified as a polar by Coppejans et al. (2014) based on photometric observations during bright state with $P_{\rm orb} = 0.06358$ d. The identification spectrum by Oliveira et al. (2017) confirms that classification with blue continuum, narrow single peaked Balmer, He I and He II λ 4686 lines, the intensity of Hα > Hβ and extended red wings alongside Balmer and He II lines. The long-term light curve of SSS1944-42 (Fig. 4.17, top) shows two distinct states without overlap. In addition, at least two brightenings are seen.

Follow-up photometric observations were taken in September 2014, during high state (as seen in red in the top panel of Fig. 4.17). All light curves have orbital hump-like

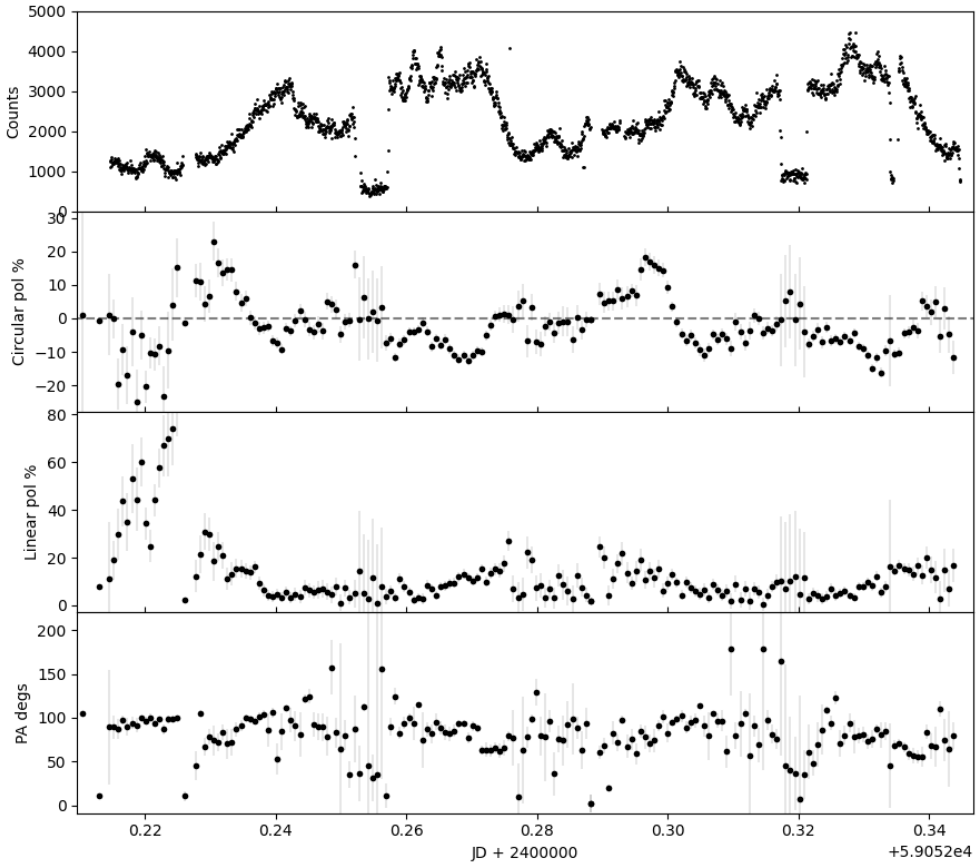

FIGURE 4.15 – Simultaneous light and polarisation curves of MLS1525-03 from 21 July 2020. Top: A light curve of MLS1525-03 from 21 July 2020. Second: Simultaneous percentage of circular polarisation. Third: Simultaneous percentage of linear polarisation. Bottom: The position angle associated with the linear polarisation.

structures, which differ slightly for each orbital phase, with an amplitude of ∼1 magnitude. Higher time resolution light curves display clearer defined flickering structures (Fig. 4.17, middle).

The noisy spectrum (Fig. 4.17, bottom) shows narrow and weak hydrogen Balmer lines (Hα, Hβ, Hγ, Hδ, Hϵ, Hζ). The continuum is generally flat with higher noise levels towards the bluer wavelengths. Due to the lack of additional spectral features, it is assumed that the spectrum was taken during low state.

The clearly-defined two states in the long-term light curves, the flickering variations and large amplitude orbital humps in the follow-up light curves support the polar classification by Coppejans et al. (2014) and Oliveira et al. (2017). The low state spectrum shows no indication of the presence of the He II λ 4686 line, unlike the seemingly high state spectrum presented by Oliveira et al. (2017).

4.6.15 *MLS2044-16 (MLS111021:204455-162230)*

MLS2044-16 was first classified as an RR Lyrae star along with 837 RR Lyrae stars through the Lowell Observatory Near Earth Objects Survey Phase I (LONEOS-I) survey by Miceli et al. (2008). Oliveira et al. (2017) reclassified MLS2044-16 as an RR Lyr star,

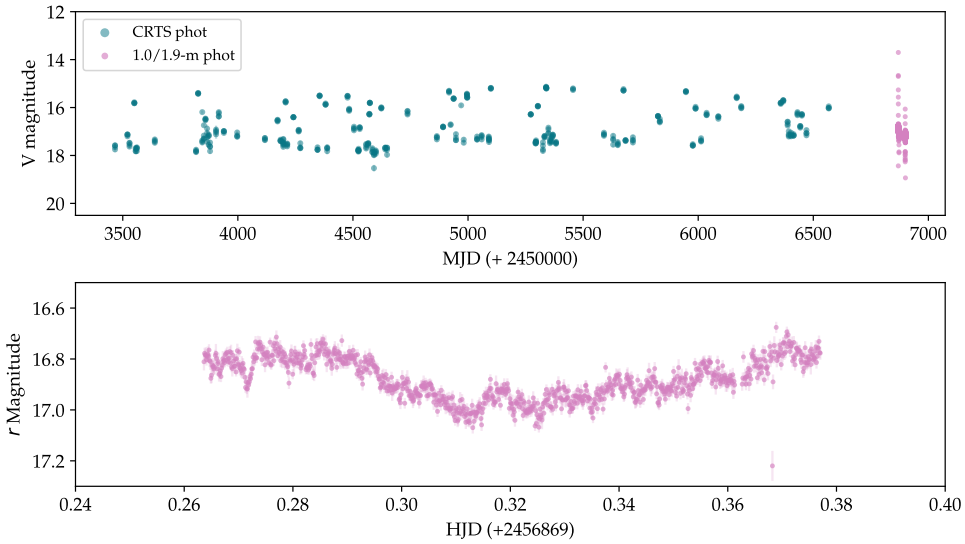

FIGURE 4.16 – Light curves and spectrum of CSS1619+13. Top: The long-term light curve of CSS1619+13 from the CRTS. The teal data points are from the CRTS database. The pink data points are all follow-up photometric observations taken with SHOC CCD on the SAAO telescope(s). Bottom: A single light curve of CSS1619+13 from follow-up observations with SHOC CCD. The complete set of light curves can be found in appendix D (Fig. D.1.14).

in search of magnetic CVs from CRTS, based on a blue continuum with absorption lines consistent with an A or F star and a 0.535 d photometric period. The long-term light-curve of MLS2044-16 (Fig. 4.18, top) is stable in magnitude. This bright system shows no evidence of brightenings/outbursts. Follow-up photometric observations were taken over five days in May and June 2015.

The follow-up light curves show different sections of the orbital phase, although neither displays a complete orbital phase. Observations vary in length from 2.4 to 4.5 hours which is less than half the orbital period. The orbital hump-shaped structure increases gradually to peak magnitude, with a steeper decrease (Fig. 4.18, middle). This is a typical profile of an RR Lyr light curve.

The spectrum of MLS2044-16 has strong signal (Fig. 4.18, bottom). It is composed of absorption lines which include hydrogen Balmer lines (Hα, Hβ, Hγ, Hδ),Ca II (λ 3934, 3968). At short wavelengths, the continuum increases steeply and then gradually, peaking at roughly 5400Å. Gradually, it decreases towards higher wavelengths. MLS2044-16 is certainly not a CV. The follow-up light curve profile and the strong calcium presence in the blue continuum absorption spectrum are in accordance with the RR Lyra classification by Oliveira et al. (2017).

4.7 INDIVIDUAL SYSTEMS WITH HIGH-SPEED PHOTOMETRY ONLY

4.7.1 *MLS1247-04 (MLS140518:124709-040758)*

Oliveira et al. (2020) classify MLS1247-04 as an AGN at redshift $z = 2.765$ based on the presence of Lyα, O I λ 1304, Si II λ1307, C IV λ1549, He II λ 1640 in emission. The long-term light curve of MLS1247-04 (Fig. 4.19, top) takes a small dip and then increases in brightness. The transitions are small and gradual so the light curve appears to gently

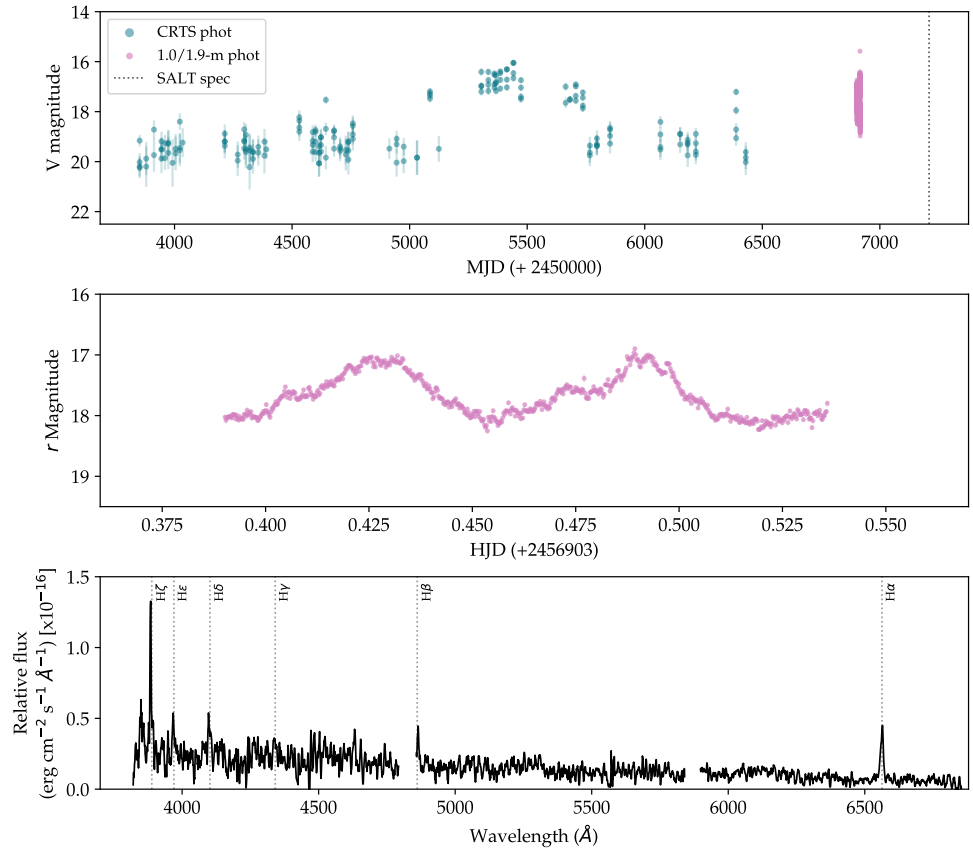

FIGURE 4.17 – Light curves and spectrum of SSS1944-42. Top: The long-term light curve of SSS1944-42 from the CRTS. The teal data points are from the CRTS database. The pink data points are all follow-up photometric observations taken with SHOC CCD on the SAAO telescope(s). The black dotted line is the corresponding JD of the follow-up SALT spectroscopic observations. Middle: A single light curve of SSS1944-42 from follow-up observations with SHOC CCD. The complete set of light curves can be found in appendix D (Fig. D.1.15). Bottom: Mean SALT spectrum of SSS1944-42 with identifiable emission lines indicated by grey dotted lines.

curve. Due to its faint nature, even during the bright state, only two observations were taken with the 1-m telescope on 12 and 14 June 2015.

The follow-up light curves of MLS1247-04 show barely any brightness variations over timescales on the order of hours (Fig. 4.19, bottom). It is impossible to identify features in the light curves which is expected for observations of this faint nature taken with the 1-m telescope.

MLS1247-04 was spectroscopically observed but a spectrum could not be obtained as there was no signal above the noise level in the data. Due to the faint nature of MLS1247-04, all follow-up data are inconclusive. The spectrum by Oliveira et al. (2020) shows a stronger signal from which the AGN nature of MLS1247-04 was determined.

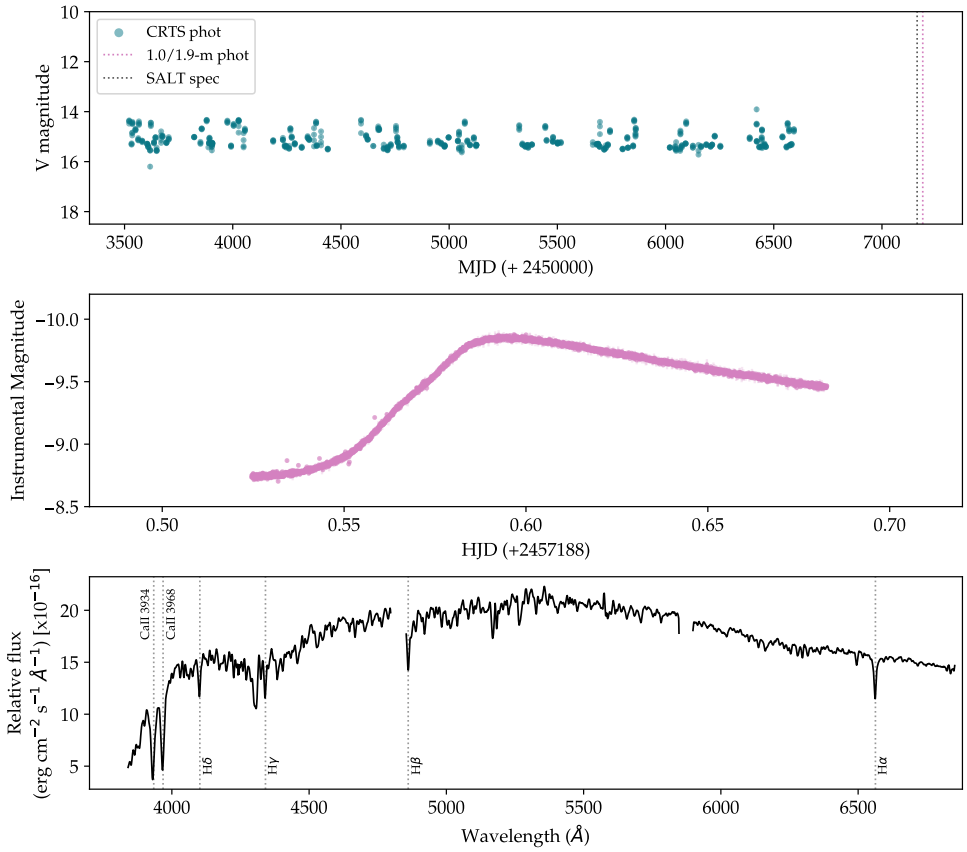

FIGURE 4.18 – Light curves and spectrum of MLS2044-16. Top: The long-term light curve of MLS2044-16 from the CRTS. The teal data points are from the CRTS database. The pink dotted line marks the date of the follow-up photometric observations taken with SHOC CCD on the SAAO telescope(s). The black dotted line is the corresponding JD of the follow-up SALT spectroscopic observations. Middle: A single light curve of MLS2044-16 from follow-up observations with SHOC CCD in pink. The complete set of light curves can be found in appendix D (Fig. D.1.16). Bottom: Mean SALT spectrum of MLS2044-16 with identifiable emission lines indicated by grey dotted lines.

4.7.2 *SSS1935-53 (SSS110624:193511-531746)*

The long-term light curve of SSS1935-53 (Fig. 4.20, top) displays a slightly variable quiescent state and common outburst brightenings. Follow-up photometric observations SSS1935-53 over 6 nights July, August and September 2014.

The follow-up light curves of SSS1935-53 display random flickering (Fig. 4.20, bottom). The quiescent observations appear to have subtle general orbital structure along with flickering variations. During outburst, light curves show smoother, subtle wave-like variations, without flickering. I was unable to obtain an orbital (or photometric) period. The common outbursts seen in the long-term light curves and the follow-up light curves, taken during outburst and quiescent, suggest SSS1935-53 is likely a dwarf nova.

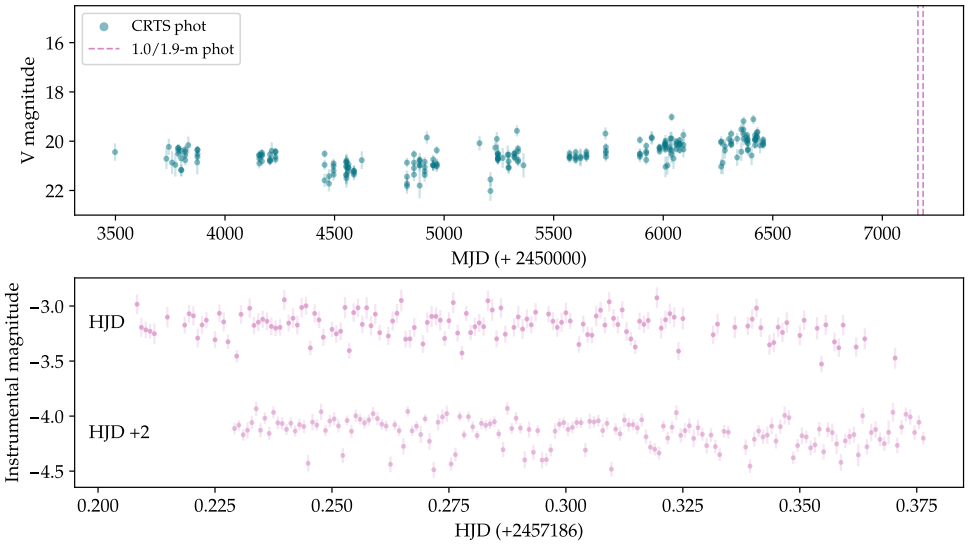

FIGURE 4.19 – Light curves of MLS1247-04. Top: The long-term light curve of MLS1247-04 from the CRTS. The teal data points are from the CRTS database. The pink dashed lines are follow-up photometric observations taken with SHOC CCD on the SAAO telescope(s). Bottom: Light curves of MLS1247-04 from follow-up observations with SHOC CCD in pink. The bottom pink light curve was taken 2 days after the top pink light curve.

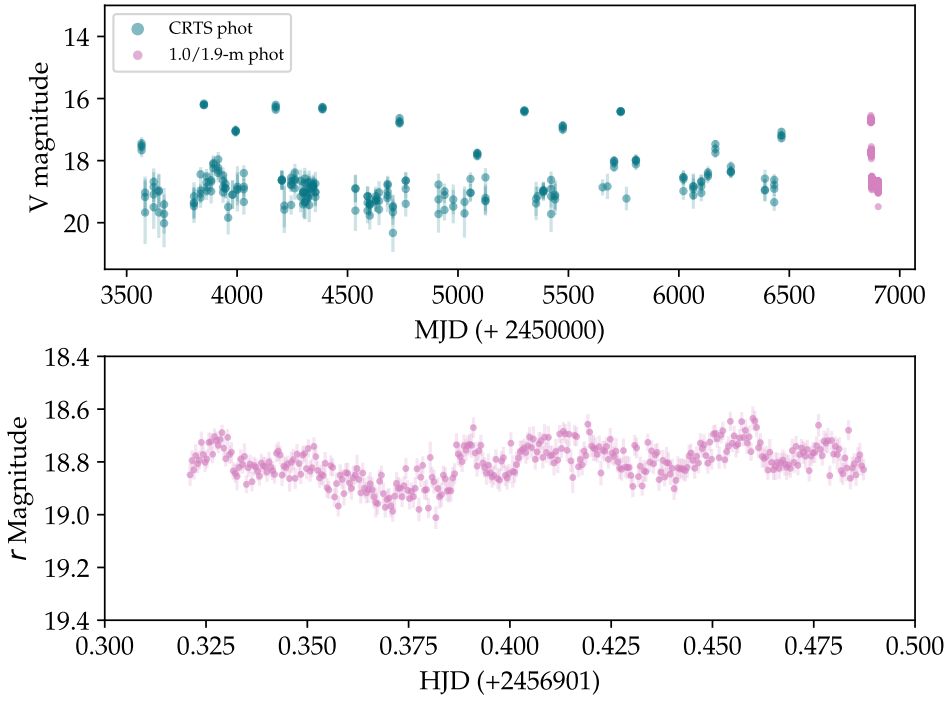

FIGURE 4.20 – Light curves of SSS1935-53. Top: The long-term light curve of SSS1935-53 from the CRTS. The teal data points are from the CRTS database. The pink data points are all follow-up photometric observations taken with SHOC CCD on the SAAO telescope(s). Bottom: A single light curve of SSS1935-53 from follow-up observations with SHOC CCD in pink. The complete set of light curves can be found in appendix D (Fig. D.1.17).

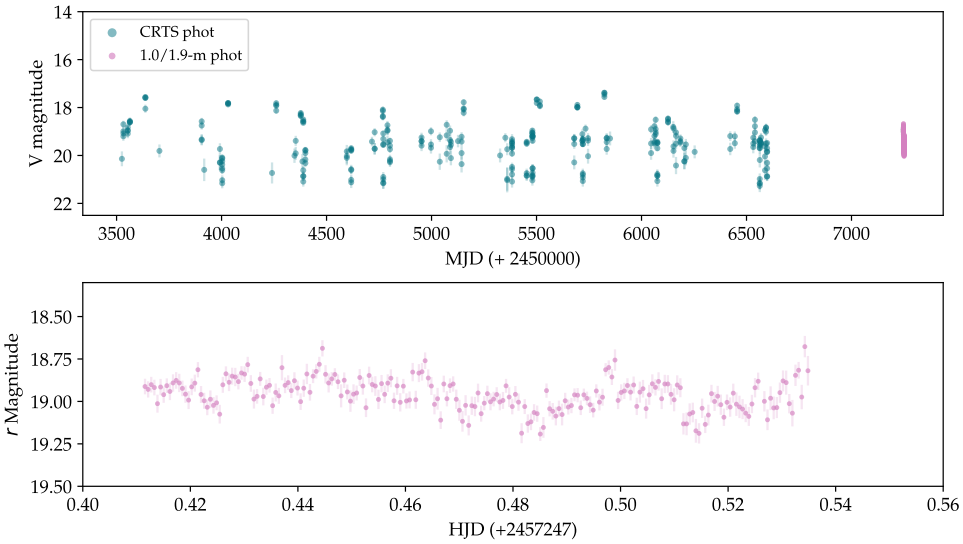

FIGURE 4.21 – Light curves of CSS2042-09. Top: The long-term light curve of CSS2042-09 from the CRTS. The teal data points are from the CRTS database. The pink data points are all follow-up photometric observations taken with SHOC CCD on the SAAO telescope(s). Middle: A single light curve of CSS2042-09 from follow-up observations with SHOC CCD in pink. The complete set of light curves can be found in appendix D (Fig. D.1.18).

4.7.3 *CSS2042-09 (CSS150708:204247-095351)*

The spectrum presented by (Oliveira et al., 2020) shows Balmer emission lines and He I but is inconclusive as to the nature of the CV. The long-term light curve of CSS2042-09 (Fig. 4.21, top) shows large long-term variations of almost four magnitudes with frequent switches between maximum and minimum brightness. There appear to be low amplitude brightenings/outbursts occurring one to three times per season. Follow-up photometric observations for CSS2042-09 took place with the 1-m telescope on the nights of 12, 14 and 17 August 2015.

The low signal-to-noise light curves of CSS2042-09 have subtle variations which may be interpreted as flickering (Fig. 4.21, bottom). There may be orbital structure but it is too subtle to identify by eye and the FT/PDM methods fail to determine a photometric period. A spectral observation failed to produce a spectrum with a signal above the noise level.

The odd long-term light behaviour, the faint spectrum without a signal above the noise and the vague follow-up light curves are insufficient, thus the nature of CSS2042-09 is inconclusive.

4.7.4 *SSS2046-31 (SSS110413:204618-312128)*

The long-term light curves of SSS2046-31 (Fig. 4.22, top) show gradual variations in the faint/quiescent state. There are four large amplitude brightenings/outbursts. The system was followed up photometrically while quiescent, over three consecutive nights in June 2015 the 1-m telescope.

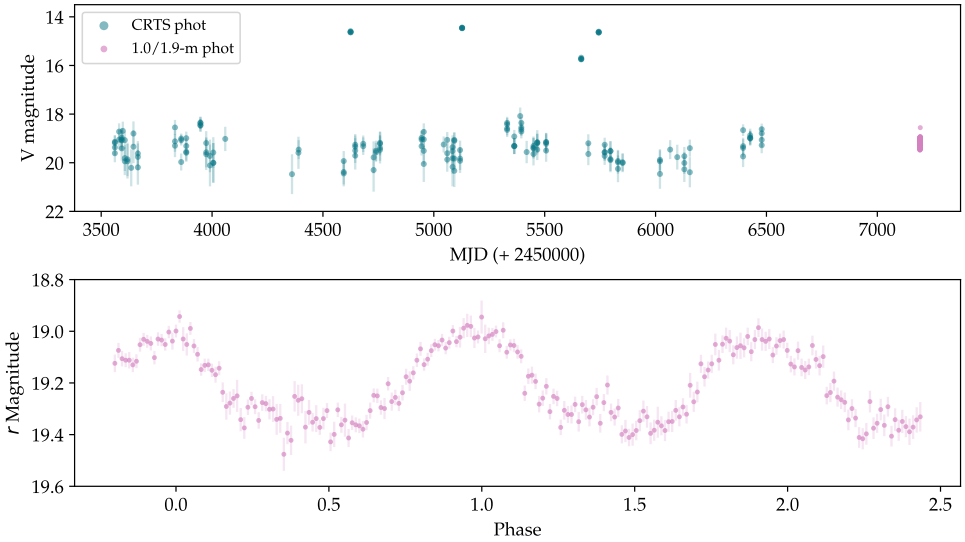

FIGURE 4.22 – Light curves of SSS2046-31. Top: The long-term light curve of SSS2046-31 from the CRTS. The teal data points are from the CRTS database. The pink data points are all follow-up photometric observations taken with SHOC CCD on the SAAO telescope(s). Bottom: A single light curve of SSS2046-31 from follow-up observations with SHOC CCD in pink. The complete set of light curves can be found in appendix D (Fig. D.1.19).

The follow-up light curves of SSS2046-31 (Fig. 4.22, bottom) display clear orbital humps with ∼0.3 magnitude amplitude. There appears to be a flattening at minimum between peaks. The FT and PDM show corresponding peaks at the fundamental frequency Ω=146.95(7) µHz. The first harmonic frequency is $2\,\Omega$ =294.2(4) µHz in Fig. 4.23. SSS2046-31 has an orbital period of 113.42(5)ṁin.

The ephemeris for maximum light is

$$HJD_{\max} = 2457191.55326 + 0.07876(4)\,E \tag{4.5}$$

The large amplitude outbursts in the long-term light curve would suggest that SSS2046-31 is a dwarf nova.

4.7.5 *CSS2154+15 (CSS130604:215427+155714)*

CSS2154+15 was reported as a polar based on the 1.5 magnitude amplitude hump feature in light-curve with 96.9 min period (*vsnet*-alert 15803, Kato, 2013; Szkody et al., 2014). This was accompanied by phase-resolved spectra with a strong He II line and large K (velocity) amplitudes. Furthermore, Doppler tomography and polarimetry are presented by Borisov et al. (2017). The long-term light curve of CSS2154+15 (Fig. 4.24, top) shows large short-term scatter with distinctions between low and high states, although overlapping. This system spent most of its time in high state, smoothly transitioned to low state during the second half of monitoring and made a quick jump to high state again. Follow-up photometric observations were taken during high state (as seen in red in Fig. 4.24, top). I observed CSS2154+15 with the 1-m telescope over four nights in June and August 2015.

The follow-up light curves of CSS2154+15 have a distinct orbital structure (Fig. 4.24, middle). The orbital phase is dominated by a hump with an amplitude of almost 1.5

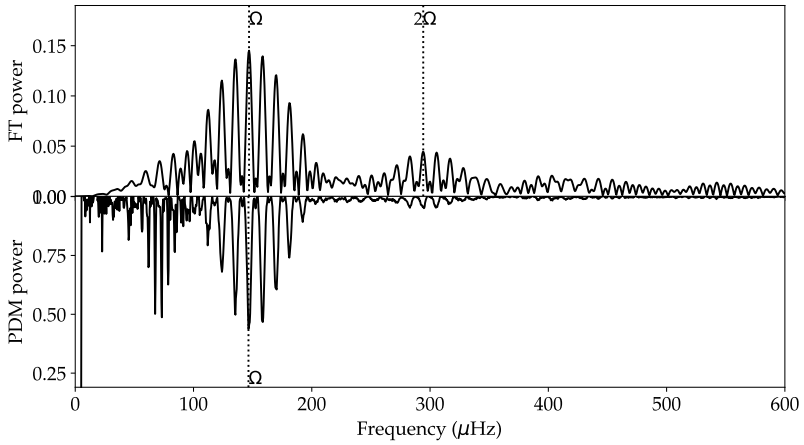

FIGURE 4.23 – FT and PDM of the light curves of SSS2046-31. The figure at the top is the Fourier transform of all of the combined light curves. The vertical dotted lines indicate the fundamental frequency (Ω) and the first harmonic ($2\,\Omega$) frequency. The figure at the bottom is the PDM periodogram of the all of combined runs of SSS2046-31. The vertical dotted line indicates the fundamental frequency (Ω).

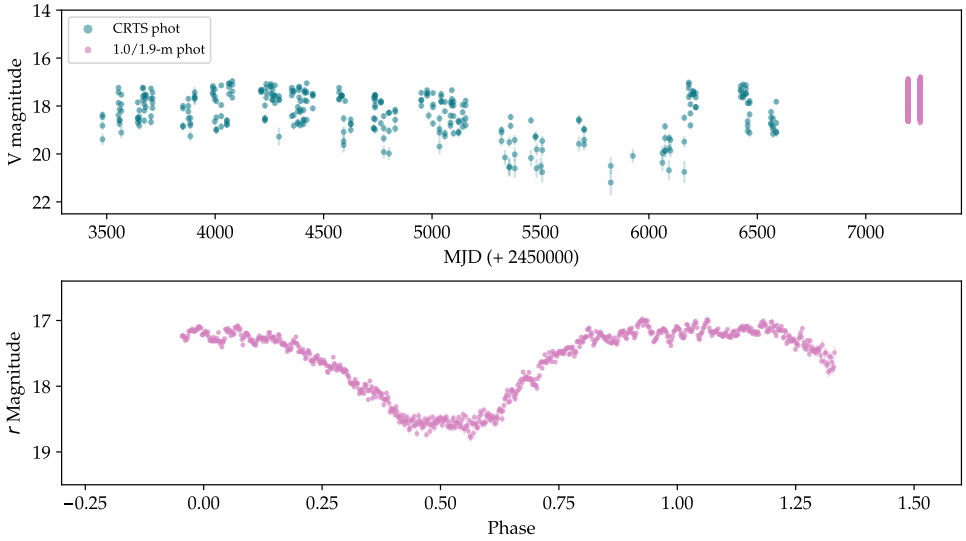

FIGURE 4.24 – Light curves of CSS2154+15. Top: The long-term light curve of CSS2154+15 from the CRTS. The teal data points are from the CRTS database. The pink data points are all follow-up photometric observations taken with SHOC CCD on the SAAO telescope(s). Bottom: A single light curve of CSS2154+15 from follow-up observations with SHOC CCD in pink. The complete set of light curves can be found in appendix D (Fig. D.1.20).

magnitudes. The base of the hump is flattened and flickering occurs which increases in intensity with increasing brightness, as the barely-visible flickering in the fainter flat sections intensifies at the peaks of the humps.

The ephemeris for maximum light is

$$HJD_{\max} = 2457195.66914 + 0.06729(4)\,E \tag{4.6}$$

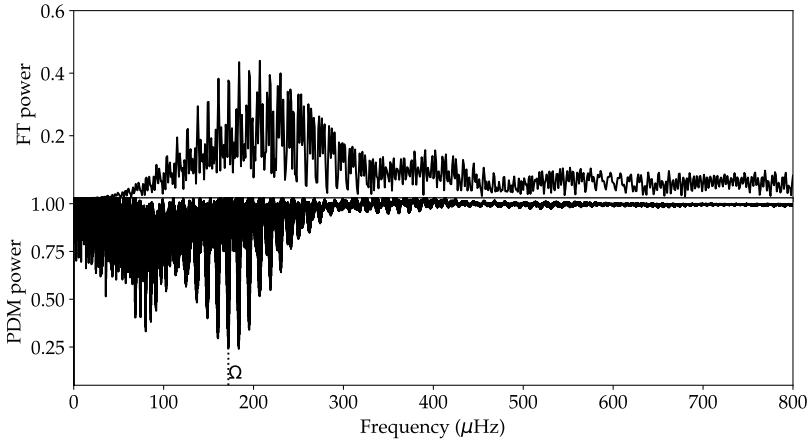

FIGURE 4.25 – FT and PDM of the light curves of CSS2154+15. The figure at the top is the Fourier transform of all of the combined light curves. The vertical dotted lines indicate the fundamental frequency (Ω) and the first harmonic (2 Ω) frequency. The figure at the bottom is the PDM periodogram of the all of combined runs of CSS2154+15. The vertical dotted line indicates the fundamental frequency (Ω).

The peaks of the FT and PDM are slightly offset from each other(Fig. 4.25). The PDM profiles peak at slightly shorter frequencies and produce the most coherent phase-folded light curve folded over a PDM period of 96.89(6) min in Fig. D.1.21, appendix D. The orbital frequency produced by the PDM is Ω=172.0(1) μHz. This PDM peak was selected because it was closest to the literature value of 96.9 min. The period determined by the Lomb Scargle periodogram of the CRTS data is also 96.9 min. The peak for the first harmonic is not frequency is not dominant enough to narrow down the selection of the PDM fundamental frequency.

The observed orbital structure is similar to that of magnetic novae V351 Pup (Camilleri et al., 1992; Woudt and Warner, 2001) and V1500 Cyg (Honda et al., 1975; Schmidt et al., 1995; Pavlenko et al., 2018). CSS2154+15 seems to show a total eclipse (flat-bottomed) lasting about 18 min, which is too long for a WD-only eclipse. It could be the eclipse of an accretion disk, however the evidence of flickering which disappears during eclipse, supports the observed similarity to the light curve of magnetic novae. The long-term light curves showing two states, the large amplitude hump feature in the follow-up light curves and the lack of outbursts are in agreement with the polar classification by Szkody et al. (2014) and (Borisov et al., 2017).

4.7.6 *CSS2335+12 (CSS131214:233546+123448)*

Thorstensen et al. (2016) presented phase-resolved spectra with strong He II λ4686 line relative to Hβ, broad based narrow emission lines and P_{orb} = 3.884 hr indicating the polar nature of CSS2335+12. The long-term light curve of CSS2335+12 (Fig. 4.26, top) shows overlapping low, intermediate and high states. The system spends most of the observed time in intermediate state, with occasional rises and dips to high and low states, respectively. Follow-up photometric observations were taken during intermediate and low states (as seen in Fig. 4.26). This object was observed over 8 nights in 1 year. I observed on 3 and 30 August 2014 with the 1-m telescope, followed by 18-21 October

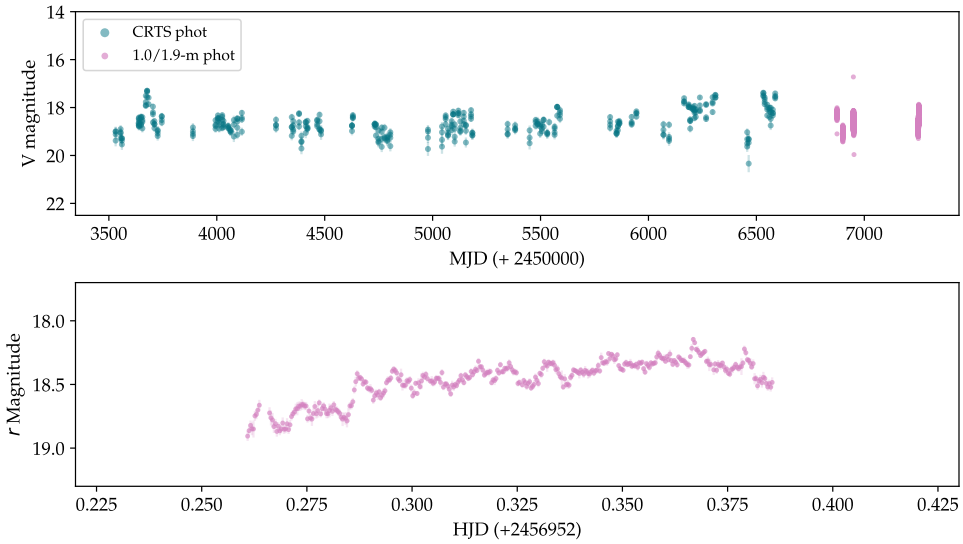

FIGURE 4.26 – Light curves of CSS2335+12. Top: The long-term light curve of CSS2335+12 from the CRTS. The teal data points are from the CRTS database. The pink data points are all follow-up photometric observations taken with SHOC CCD on the SAAO telescope(s). Bottom: A single light curve of CSS2335+12 from follow-up observations with SHOC CCD in pink. The complete set of light curves can be found in appendix D (Fig. D.1.22).

2014 with the 1.9-m telescope. The last observations were taken on 14, 15 & 17 August 2015 with the 1-m telescope.

The follow-up light curves of CSS2335+12 (Fig. 4.26) taken with the 1.9 telescope, with higher time resolution, display clear flickering across the observations. The observations, taken with the 1-m telescope, do not display the flickering detail. There appears to be a repetitive orbital structure with humps seen in all of the light curves although neither light curve completes an orbital cycle. The data are not sufficient for the determination of an orbital (or photometric) period. The high and low states in the long-term light curve and flickering are consistent with a polar classification by Thorstensen et al. (2016).

4.8 INDIVIDUAL SYSTEMS WITH SPECTROSCOPY ONLY

4.8.1 *CSS0105-08 (CSS120104:010558-085437)*

The long-term light curve of CSS0105-08 (Fig. 4.27, top) has two states. The system spent the majority of its observed time in low state with three transitions to high state. At the end of the light curve, the transitions between low and high state are visible. A possible flare is seen near MJD=2455600 days.

An identification spectrum for CSS0105-08 displays a weak signal just above the noise level (Fig. 4.27, bottom). The only lines visible are Hydrogen Balmer emission lines. Hα, Hγ, Hϵ and Hζ are clearly visible. Hβ is positioned within the first chip gap. Usually (in spectra with the same wavelength coverage), there is an indication of the presence of Hβ to the right of the first chip gap, which is missing in this spectrum. The continuum is almost flat with the highest noise level at the lowest wavelengths. The noise decreases, becoming thinner towards the red end of the spectrum. The long-term light

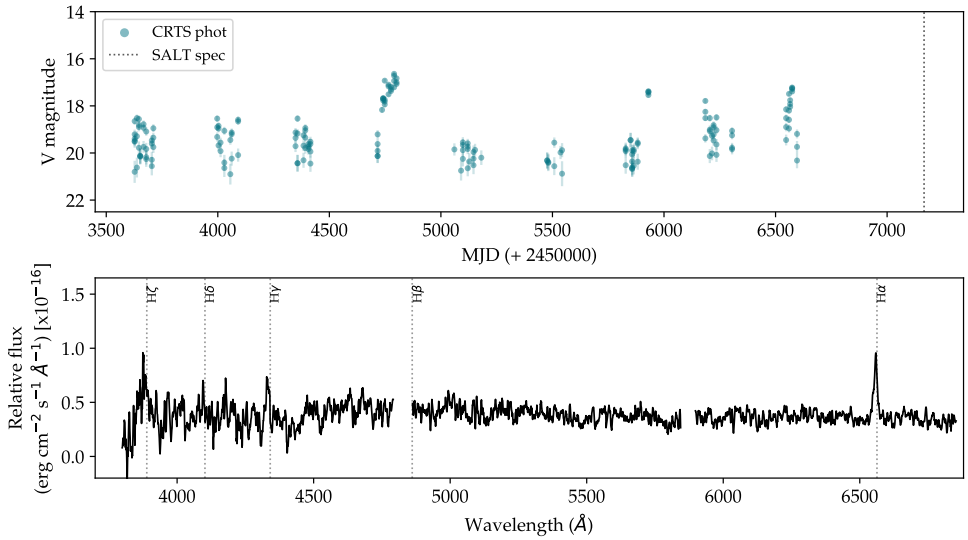

FIGURE 4.27 – Light curve and spectrum of CSS0105-08. Top: The long-term light curve of CSS0105-08 from the CRTS. The teal data points are from the CRTS database. The black dotted line is the corresponding JD of the follow-up SALT spectroscopic observations. Bottom: SALT spectrum of CSS0105-08 with identifiable emission lines indicated by grey dotted lines.

curve is unlike dwarf novae and identification spectra with Balmer lines exclusively make it difficult to determine the nature of this object. Follow-up photometry and spectroscopy in the brighter phase would be useful for further identification.

4.8.2 *CSS0919-05 (CSS110114:091937-055519)*

A spectrum of CSS0919-05 suggests a polar nature (Oliveira et al., 2020). The spectral features include strong Balmer emission lines, high He II/Hβ ratio and a C III/N III Bowen complex. The long-term light curve of CSS0919-05 (Fig. 4.28, top) has clear three states. Most time was spent in low state during the first half of the light curve. The system jumped to a much brighter high state and then decreased to intermediate state where it further dropped to low state over one observation and then increased to intermediate state. It was last recorded in high state following the intermediate state.

The spectra of CSS0919-05 (Fig. 4.28 middle and bottom; and Fig. D.2.3 in appendix D) vary in signal strength over almost 2 months. The spectra taken on 13 January and 27 February 2016 are very similar in appearance. They are taken during high state and display strong emission lines that are well above the noise level. The observed lines are hydrogen Balmer lines (Hα, Hβ, Hγ, Hδ), He I (λ 4471, 4922, 5016, 5876, 6678, 7065), He II (λ 4541, 4686, 5412) and Bowen blend C III/N III alongside He II λ 4686. The spectrum taken on 08 March 2016 was taken during low state or intermediate state and has a lower signal-to-noise ratio. The clearly visible lines are hydrogen Balmer lines and He II λ 4686. Weaker He I emission lines are buried within the noise. The relative strength of Hβ to He II λ 4686 varies across the spectra but remains consistently strong. The continua are either roughly flat or decrease very gradually with increasing wavelength. In strong agreement with Oliveira et al. (2020), multiple features indicate polar nature of CSS0919-05, namely: the multiple state long-term light curve, strong

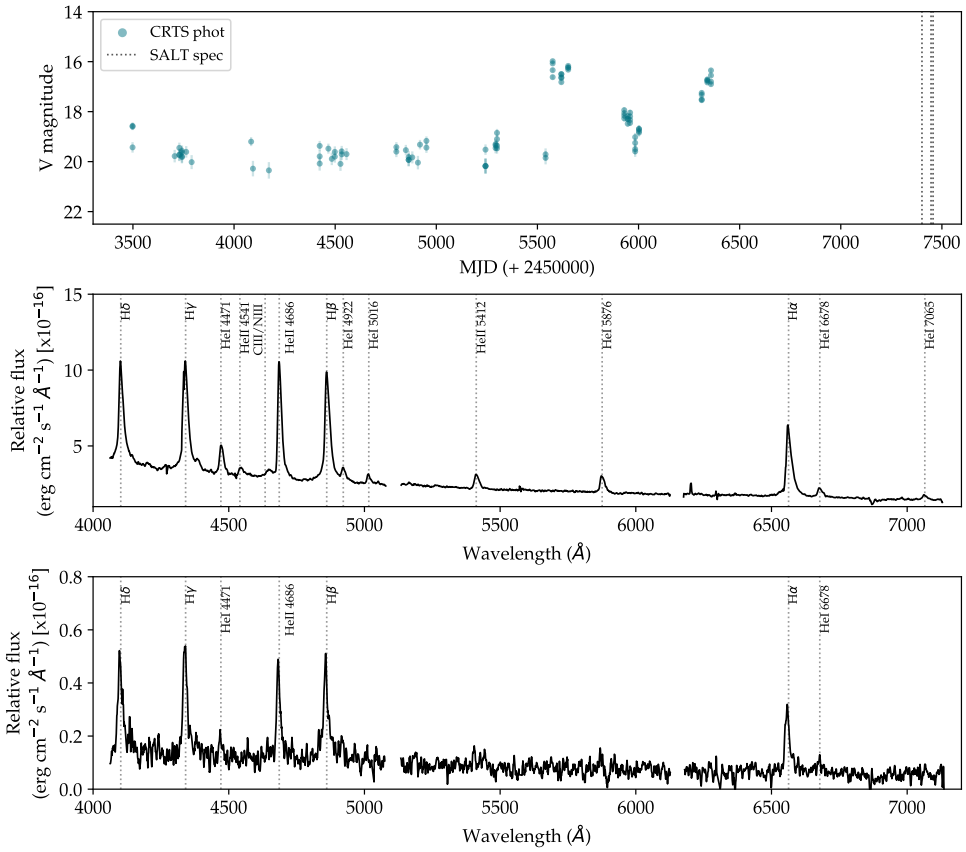

FIGURE 4.28 – Light curve and spectrum of CSS0919-05. Top: The long-term light curve of CSS0919-05 from the CRTS. The teal data points are from the CRTS database. The black dotted line is the corresponding JD of the follow-up SALT spectroscopic observations. Middle: Mean spectrum of CSS0919-05, taken on 27-02-2016, with identifiable emission lines indicated by black dotted lines. Bottom: Mean SALT spectrum of CSS0919-05, taken on 08-03-2016, with identifiable emission lines indicated by grey dotted lines.

emission He II λ 4686 lines in both high and low state spectra, other He II lines and the Bowen blend in high state spectra.

4.8.3 *MLS1115+05 (MLS130313:111537+051002)*

The general brightness of MLS1115+05 varies by almost 2 magnitudes and two brightenings/outbursts are observed in the long-term light curve (Fig. 4.29, top). The spectrum of MLS1115+05 (Fig. 4.29, bottom) has a weak signal dominated by emission lines. The strongest emission lines are hydrogen Balmer (Hα, Hβ, Hγ, Hδ, Hϵ, Hζ), which are broad and appear to be double-peaked, indicating the presence of a disc. He I (λ 4471, 6678) is barely visible above the noise. The continuum is generally flat. The nature of this object is inconclusive, but most likely has an accretion disc.

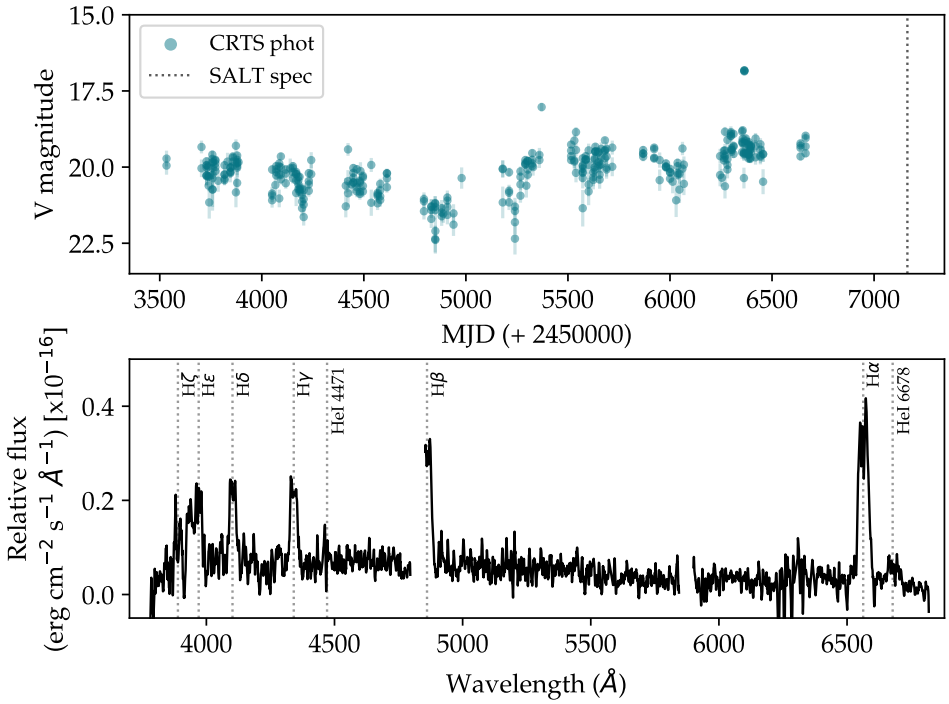

FIGURE 4.29 – Light curve and spectrum of MLS1115+05. Top: The long-term light curve of MLS1115+05 from the CRTS. The teal data points are from the CRTS database. The black dotted line is the corresponding JD of the follow-up SALT spectroscopic observations. Bottom: Mean SALT spectrum of MLS1115+05 with identifiable emission lines indicated by grey dotted lines.

4.8.4 *MLS1137+00 (MLS121203:113751+004218)*

Despite the long-term light curve of MLS1137+00 classified amongst other CVs in the CRTS database, Oliveira et al. (2020) suggested MLS1137+00 is a Type I AGN at $z = 0.99$ based on a spectrum, with broad Mg II λ 2798 and blended UV Fe II multiplets. Over the years of monitoring by CRTS, the long-term light curve of MLS1137+00 (Fig. 4.30, top) shows the system gradually increasing in brightness. At the fainter state, the scatter is larger than the brighter state, which has very smaller short-term (daily) variations.

The spectra of MLS1137+00 (Fig. 4.30, bottom) remain consistent over the two months of observations. With spectral coverage similar to (Oliveira et al., 2020, Fig 1.) shifted slightly to shorter wavelengths, two very broad emission lines are visible from the low signal-to-noise spectrum. The identifiable lines are Mg II λ 2798 and likely C IVλ 1549. The continuum remains flat throughout all identification spectra. Based on these spectra, MLS1137+00 is certainly not a stellar object, as indicated by the AGN classification by Oliveira et al. (2020).

4.8.5 *SSS1440-22 (SSS100504:144038-221409)*

The long-term light curve (Fig. 4.31, top) shows SSS1440-22 in quiescent/low state for most of the monitoring. There are two brief observed brightenings/outbursts. The system also spent extended periods in outburst, most likely superoutbursts. The last recorded superoutburst peaks at MJD=2455306 decline to a minimum (at MJD=2455338)

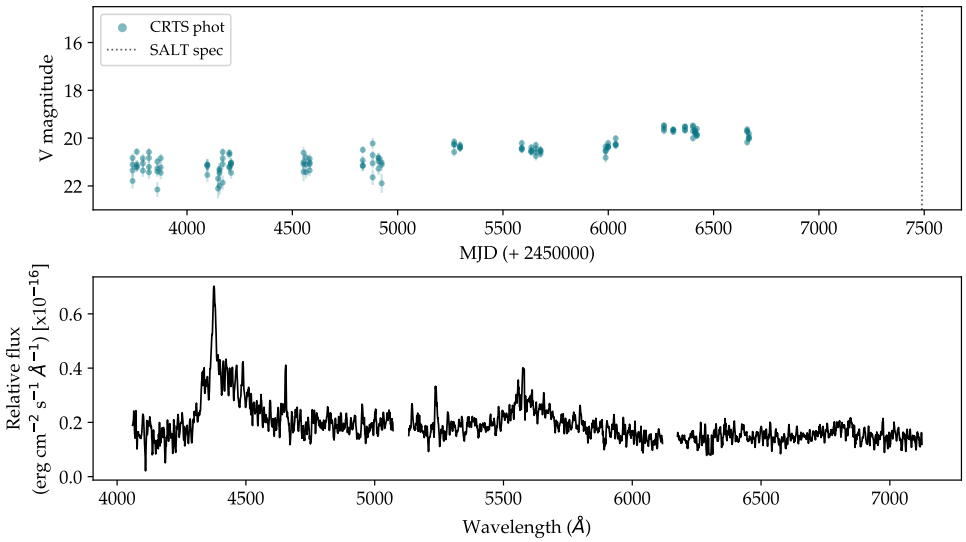

FIGURE 4.30 – Light curve and spectrum of MLS1137+00. Top: The long-term light curve of MLS1137+00 from the CRTS. The teal data points are from the CRTS database. The black dotted line is the corresponding JD of the follow-up SALT spectroscopic observations. Bottom: Mean SALT spectrum of MLS1137+00.

and brighten to an intermediate brightness (at MJD=2455354). Due to a gap in the data thereafter, it is unknown if the increase to intermediate brightness is part of the superoutburst or if it develops separately as an echo-outburst.

The spectrum of SSS1440-22 has a moderate signal-to-noise ratio with broad emission lines (Fig. 4.31, bottom). The strong lines present are hydrogen Balmer lines (Hα, Hβ, Hγ, Hδ, Hϵ, Hζ). The weaker lines are He I (λ 4471 and He I λ 6678). The continuum is roughly flat. The weak He I lines, strong Balmer lines and lack of He II λ 4686 may suggest a DN-type CV. The long-term light curve suggests superoutburst behaviour.

4.8.6 *SSS1955-30 (SSS100514:195555-303601)*

There is low coverage of SSS1955-30 in the long-term light curve (Fig. 4.32, top) but appears to have at least two states and spend more of the observed time in bright state than faint states.

The spectra of SSS1955-30 (Fig. 4.32, bottom) were taken seven days apart with very little difference between them. A broad Hα emission line can be seen from the continuum of the spectrum. No other lines can be seen due to the low signal-to-noise ratio. The noisy continuum decreases towards longer wavelengths. The nature of SSS1955-30 is inconclusive due to a lack of data.

4.9 SUMMARY OF INDIVIDUAL SYSTEMS

The objects identified for photometric or spectroscopic follow-up observations were selected by eye from their CRTS light curves. Any light curve that displayed any magnetic CV characteristics was selected for follow-up based on as wide as possible selection

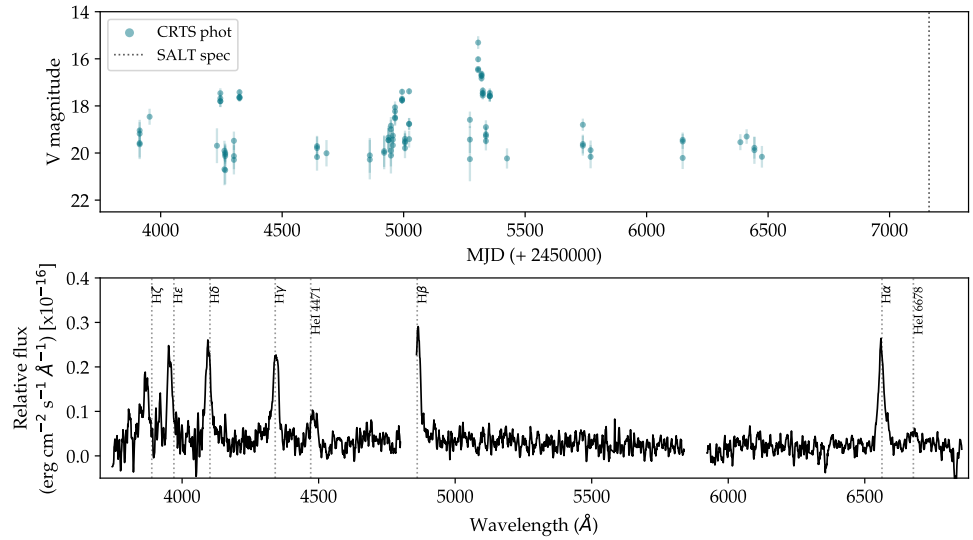

FIGURE 4.31 – Light curve and spectrum of SSS1440-22. Top: The long-term light curve of SSS1440-22 from the CRTS. The teal data points are from the CRTS database. The black dotted line is the corresponding JD of the follow-up SALT spectroscopic observations. Bottom: Mean SALT spectrum of SSS1440-22 with identifiable emission lines indicated by grey dotted lines.

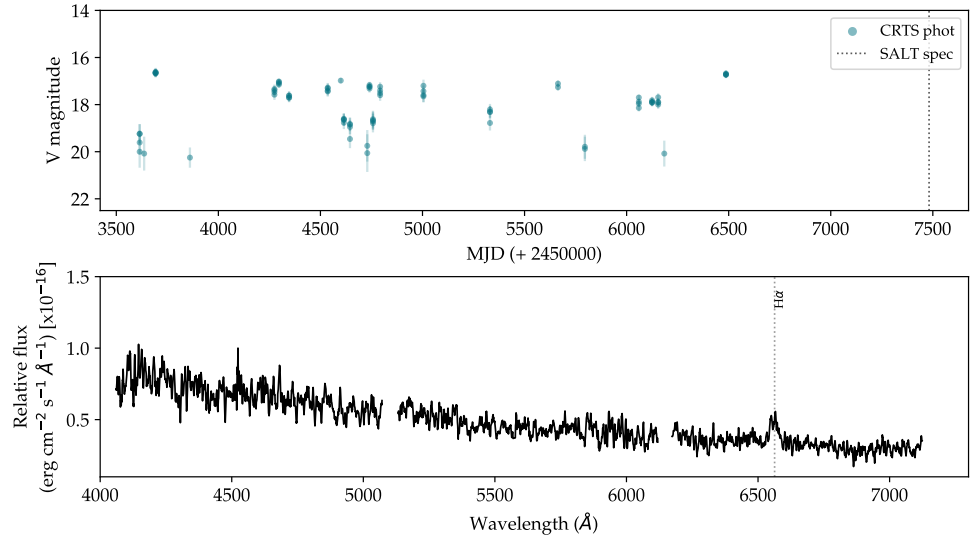

FIGURE 4.32 – Light curve and spectrum of SSS1955-30. Top: The long-term light curve of SSS1955-30 from the CRTS. The teal data points are from the CRTS database. The black dotted line is the corresponding JD of the follow-up SALT spectroscopic observations. Bottom: Mean SALT spectrum of SSS1955-30 with identifiable emission lines indicated by grey dotted lines.

criteria (restricted to objects observable from the South African Astronomical Observatory telescopes in Sutherland). In an attempt to find as many AM Her-type CVs (polars) from the CRTS database, this approach has led to the follow-up observations of a variety of CVs and astronomical objects. The objects are classified as follows: 8 polars + 1 polar candidate, 7 DN + 4 DN candidates, 1 nova-like CV, 1 RR Lyr, 2 AGNs and 3 unknown (see a summary of all individual systems in table 4.3). There are 11 objects which are reported here or in publications by us for the first time, including CSS0109-27, CSS0350+32 (Mason et al., 2019), CSS0812+04 (Thorstensen et al. 2020, roughly the same time as Oliveira et al. 2020), CSS1455-11, SSS1935-53, SSS2046-31, CSS0105-08, MLS1115+05, SSS1440-22, SSS1955-30. The photo-polarimetry of MLS1525-03 is presented here for the first time, showing high percentages of circular and linear polarisation when compared to other polars. A total of 278.7 hours of photometric data was collected for CRTS CVs in Chapter 4 which contributes towards the previously unknown photometry of 6 objects for which only spectroscopic data had previously been published. These objects are CSS0812+04, SSS1020-33, CSS1127-05, CSS1127-05, CSS2042-09, MLS2044-16, CSS2335+12.

Outbursts and superoutbursts are detected in long-term light curves of the dwarf novae and several of which, including MLS1115+05 and SSS2046-31, display variations in the quiescent brightness. The CRTS light curve of nova-like MLS0720+17 could easily be mistaken for a magnetic CV due to the lack of outbursts and the temporary transition to low state. The most common long-term behaviour of the magnetic CVs is transitioning between high and low states. Magnetic CV, CSS2154+15, shows large scatter as well.

Eclipses are also identified in the CRTS light curves. Both MLS0720+17 and MLS1525-03 have deep eclipses with a wide v-shaped eclipse of MLS0720+17 indicating the presence of an accretion disc and a narrow eclipse of MLS1525-03 suggesting the lack of an accretion disc. Shallow dips are seen CSS0812+04 and CSS0357+10 light curves. The phase of the dip found in CSS0357+10 light curves varies slightly over each orbital cycle. This implies the dip is associated with the non-stable accretion stream as the stream either eclipses the accretion region or the donor star eclipses the stream. Possible eclipses are seen in the CRTS light curves of CSS0910+16, CSS2042-09 and MLS1115+05, however, no eclipses are detected through our follow-up observations, most likely due to lack of coverage.

Common features of magnetic CV light curves are flickering and large amplitude orbital modulations which are seen in confirmed AM Her-type CVs CSS0357+10, CSS2154+15, MLS1525-03, SSS1944-42 and CSS2335+12. Flickering is seen in CSS1127-05, however, the amplitude of the orbital modulations is smaller at ~ 0.5 magnitudes. Due to the faintness of many systems, their light curve profiles are undefined. SSS2046-31 is the only DN light curve with defined but low-amplitude orbital modulations. The light curves with orbital modulations and eclipses were used to obtain photometric periods although the period of CSS0812+04 was determined through spectroscopic radial velocities.

We were able to obtain high and low state spectra of CSS0812+04 and CSS0919-05. Only the strongest Balmer lines, the comparably strong He II 4686 line and weaker He I

emission lines are seen in the low state spectra. During high state, weak He I, He II lines and C III/N III Bowen blend are visible above the noise level. Although the light curve of MLS1525-03 presents typical magnetic CV characteristics, the spectrum is rather unlike that of a magnetic CV. The weak He II 4686 emission line compared to Hβ and the red continuum would suggest a possible spectral contribution from the donor star. Most of the spectra of the remaining objects have low signal-to-noise double-peaked Balmer emission lines which indicate the likely presence of an accretion disc. If these are DN spectra then they were likely taken during a faint quiescent state, given the emission lines. The spectrum of SSS0617-36 with absorption features and blue continuum is that of a DN in outburst.

Misidentified CV candidates by CRTS include RR Lyr star, MLS2044-16, and AGNs, MLS1137+00 and MLS1247-04. CRTS uses the long-term data to classify newly discovered objects. The long-term light curves of the AGNs gradually change their brightness over years which could be mistaken for a gradual increase/decrease magnetic CV. The light curve of MLS2044-16 and the spectrum of MLS1137+00 are not characterised by magnetic CV features.

As I was unable to determine photometric periods for most of the objects using the follow-up SHOC data, I applied the same Lomb Scargle analysis to the long-term CRTS light curves as done in § 2.4 with the previously known polars. Unlike the previously known polars in § 2.4, this method was not successful in determining an orbital period from the long-term CRTS data. I only determined a period for two of the CRTS objects, namely CSS2154+15 and MLS2044-16, the RR Lyr star. I determined a period of 96.9 min for CSS2154+15, in agreement with Kato (2013); Szkody et al. (2014) and a period of 0.535125 d which is in agreement with the orbital period of 0.535 d from Oliveira et al. (2017) determined using the long-term CRTS data.

TABLE 4.3 – Summary of CV candidates from CRTS.

Object	Type	P_{orb} (min)	Photometry	Spectroscopy
CSS0105-08	Unknown	–	-	Balmer emission lines
CSS0109-27	DN	–	Constant brightness, faint	Balmer emission lines
CSS0350+32	AM Her	142.3	Flickering, pre-eclipse dip, narrow and deep eclipse	Balmer and He I emission lines, strong He II 4686
CSS0357+10	AM Her	114.03	Flickering, hump preceding misaligned eclipses	Large velocity amplitudes, strong He II 4686*
SSS0617-36	DN	205.9*	constant brightness, faint	Balmer and He I absorption lines, Hα emission
MLS0720+17	SW Sex	216.6	Wide and deep eclipses	H, He I, He II 4686, C II/N II emission lines*
CSS0812+04	AM Her	162	Hump and dip preceding a shallow eclipse	Two states, emission, H, He I, He II, C II/N II, strong He II 4686
CSS0910+16	DN	105.7(*sh*)*	Low amplitude modulations	Double peaked emission lines, H, He I, He II, Mg I, weak He II 4686*
CSS0919-05	AM Her	–	-	Two states, emission, H, He I, He II, C II/N II, strong He II 4686
SSS1012-18	DN	–	Low amplitude modulations	Double-peaked H and He I emission
SSS1020-33	DN	–	Low amplitude modulations	Balmer absorption, He II 4686 emission, in outburst*
MLS1115+05	DN?	–	-	Double-peaked Balmer emission lines
CSS1127-05	AM Her?	–	Flickering? Low amplitude modulations	Emission line spectrum, weak He II 4686 line*
MLS1137+00	AGN	–	-	Redshifted emission and very broad lines, unlike CV spectrum
MLS1247-04	AGN	–	Constant brightness, faint	Lyα, O I 1304, Si II 1307, C IV 1549, He II 1640 emission lines*

Notes: DN = dwarf nova. A question mark indicates a lack of information or certainty. An asterisk indicates the information is obtained from the literature discussed in the relevant subsections. A superhump period is represented by *(sh)*.

(Continued on next page)

Table 4.3 – continued from previous page

Object	Type	P_{orb} (min)	Photometry	Spectroscopy
SSS1440-22	DN?	–	-	Double-peaked Balmer emission lines
CSS1455-11	DN	–	Faint, unclear	Double-peaked Balmer emission
MLS1525-03	AM Her	92.71	Flickering, deep narrow eclipses, large amplitude orbital modulations	H and He I emission, weak He II 4686, red continuum
CSS1619+13	DN	–	Outbursts, flickering	Emission (quiescence), absorption (outburst)*
SSS1935-53	DN?	–	Low amplitude modulations	-
SSS1944-42	AM Her	91.56*	Flickering, large amplitude (∼ 1 mag) orbital modulations	H Balmer emission lines
SSS1955-30	Unknown	–	-	Only double-peaked Hα emission line, low S/N ratio
MLS2044-16	RR Lyr	770.4	Bright, slanted orbital hump	H and Ca II H+K absorption lines
CSS2042-09	Unknown	–	Low amplitude modulations	-
SSS2046-31	DN?	113.42	Low amplitude orbital modulations	-
CSS2154+15	AM Her	90.78	Flickering, large amplitude orbital modulations with flat base	Large velocity amplitudes, strong He II 4686*
CSS2335+12	AM Her	233.04*	Flickering and ∼ 1 mag orbital modulations	

Notes: DN = dwarf nova. A question mark indicates a lack of information or certainty. An asterisk indicates the information is obtained from the literature discussed in the relevant subsections. A superhump period is represented by *(sh)*.

CHAPTER 5

Discussion

5.1 AM CVn stars and magnetic CVs in optical transient surveys

Optical transient surveys identify transients through their photometric variability, which may occur over a range of timescales for a subclass of objects. The science goals of transient surveys influence the survey specifications, including the observing cadence. With a sufficient cadence, the light curve can reveal system properties beyond transient identification such as eclipses, outburst duty cycles, orbital modulations and other periodicities, such as superhumps and spin periods.

AM CVn stars display various characteristics and physical processes which are strongly related to the orbital separation (and therefore period). The effect of these physical processes can be observed photometrically as brightness variations, in which the highest accretion rate systems are found at the shortest orbital periods and the lowest accretion rate systems at the longest orbital periods (Bildsten et al., 2006). In between the highest and lowest accretion rate systems are quiescent systems that undergo superoutbursts. These outbursting systems are the subset of AM CVn systems detected by transient surveys.

AM CVn outbursts and superoutbursts have durations of days to weeks. Varying (super)outburst cycles implies that frequently outbursting AM CVns are identified sooner than those with long (super)outburst cycles. Higher cadence transient surveys allow for higher detection rates of outbursting systems with long recurrence times and improved determination of the outburst duty cycles. High cadence transient surveys may not be as necessary for magnetic CVs as they seem to stay in the same state for longer intervals of weeks to years based on the CRTS data. However Duffy et al. (2022) report short-duration low and high states in polars lasting a few days up to 50 days. Using higher cadence ZTF and TESS (Ricker et al., 2015), they find that short-lived low states were relatively common and short-lived high states were uncommon in their study sample.

The CRTS cadence is usually at least once once per lunation. An analysis of the CRTS data reveals an average cadence range of $\sim 16-35$ days. CRTS observes any given field every 10 min a over 30 min interval. This 30 min interval can give an indication of the orbital and short-term variability, including eclipses. A brief flare in brightness can be differentiated from a dwarf nova outburst or superoutburst over the 30 min, as flares rise or decline on shorter timescales than outbursts (i.e. within the 30 min span).

Many AM CVns and magnetic CVs are faint during quiescence. In an attempt to increase the baseline of the CRTS long-term light curves of my sample, I added more recent data from the Asteroid Terrestrial-impact Last Alert System (ATLAS, Tonry et al., 2018a,b) to the CRTS light curves. ATLAS observes the same field of the sky every two days and each observation consists of four exposures over one hour. Due to a 19.5 magnitude limit during good observing conditions, a manual cut-off of 19 magnitudes was applied to the ATLAS data of both broad band red and blue filters. The higher ATLAS cadence allows for the identification of outbursts at a higher rate than CRTS for SSS0617-36 and SSS1020-33 (Fig. 5.1), assuming relatively constant outburst rates. The scatter of most systems appears larger in ATLAS data than CRTS (see Fig. 5.2) which may be due to the 0.5 m ATLAS telescope diameter which is the same as the SSS telescope but smaller than the CSS (0.68 m) and MLS (1.5 m) telescopes. MLS1525-03 is an eclipsing system which may explain the extension to fainter magnitudes, although it is difficult to differentiate between eclipses and the data of the main orbital structure. MLS2044-16 is a bright RR Lyr star, without eclipses, which explains the scatter seen in the ATLAS data. In contrast, the ATLAS light curve of the faint CV, CSS2042-09, is not as well sampled as CRTS due to the ATLAS magnitude threshold (refer to Fig. 5.3).

A large majority of AM CVn systems discovered since the beginning of the CRTS and SDSS era, have been discovered through optical surveys. The optical survey, SDSS, is not a transient survey, per se, but deserves a mention in this section because of its significant contribution to the discovery of AM CVns, although not as many as expected (refer to § 2.1.1). In search for AM CVn stars, the $(u-g, g-r)$ and $(NUV-u, r-i)$ colour spaces, shared by AM CVn stars and DA/DB white dwarfs, were targeted in SDSS. Multiple-filter observations are useful for distinguishing between astronomical objects by narrowing the search options. In this work, a combination of CRTS single-filter data and SDSS multi-filter data led to the discovery of CSS0105+19 (§ 2.1.3) combining colour information with known outburst behaviour. Targeted searches for CVs from SDSS focused on a colour-colour space occupied by CVs, quasars, single white dwarfs, white dwarf M-star binaries and hot blue stars. Follow-up observations of these systems have led to the discovery of magnetic CVs (§ 2.2.1).

With enough data, periods of light curves from optical transient surveys may be determined. The periods of at least 19 % of the previously known magnetic CVs determined through Lomb Scargle periodograms are the same as, or improved on, the orbital periods found in the literature. When folded on the correct orbital period (whether from the literature or revised), the resulting phase plots display coherent orbital modulations and aligned eclipses. An interesting finding in the phase-folded light curves of magnetic CVs, V379 Tel, V519 Ser and V834 Cen is single or double-peaked modulations in high state and a constant stable signal in the low state. In comparison, orbital modulations are seen in the slightly high and low states of J0328+0522, MN Hya and HU Aqr (see § 2.4).

The spin periods and beat periods of known asynchronous polars are indeterminable through Lomb Scargle periodograms of the CRTS light curves, due to the close spacing of the orbital/spin frequencies.

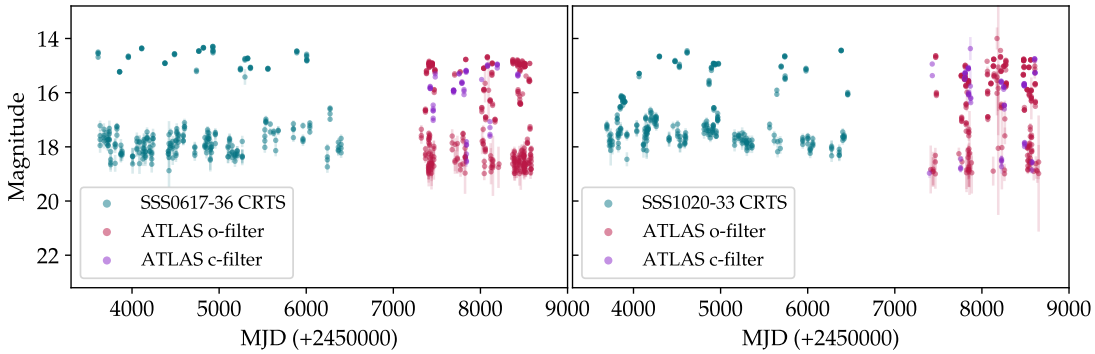

FIGURE 5.1 – Left: The long-term light curves of SSS0617-36 and SSS1020-33. CRTS data is displayed in teal, ATLAS o-filter data in purple and c-filter data in red.

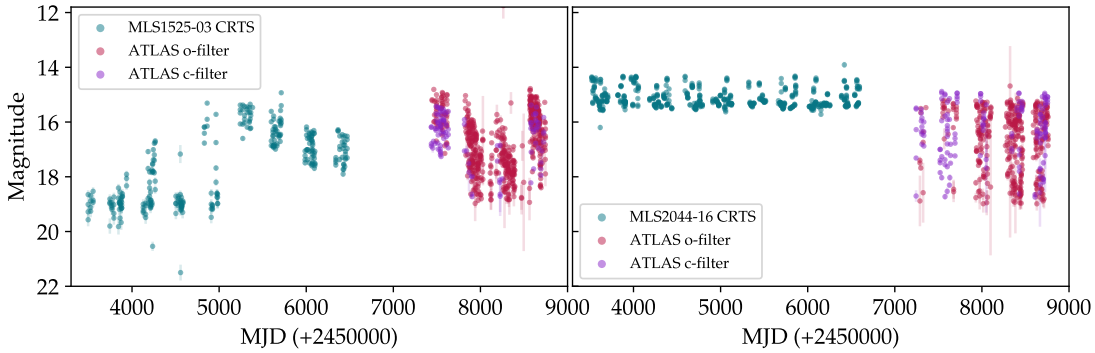

FIGURE 5.2 – Left: The long-term light curves of MLS1525-03 and MLS2044-16. CRTS data is displayed in teal, ATLAS o-filter data in purple and c-filter data in red.

5.2 SAMPLE DISCUSSION: MY SAMPLE VERSUS KNOWN SYSTEMS

5.2.1 *AM CVn stars*

Outbursting AM CVns are observed as most frequently outbursting at shorter orbital periods, with increasing superoutburst recurrence times at longer orbital periods. While the full observed orbital period range of known AM CVn systems is between 5 and 68 min (Green et al., 2020), my outbursting sample of 7 AM CVn stars lies between 31.65 and 54.78 min. Outbursting AM CVns with longer periods in my sample have long recurrence times, with approximately one or two observed superoutbursts in almost a decade. ASASSN-14ei and ASASSN-14mv, with orbital periods between 40 and 43 min, exhibit similar long-term AM CVn behaviour. Following an extended quiescent phase, superoutbursts are succeeded by multiple rebrightenings over several months.

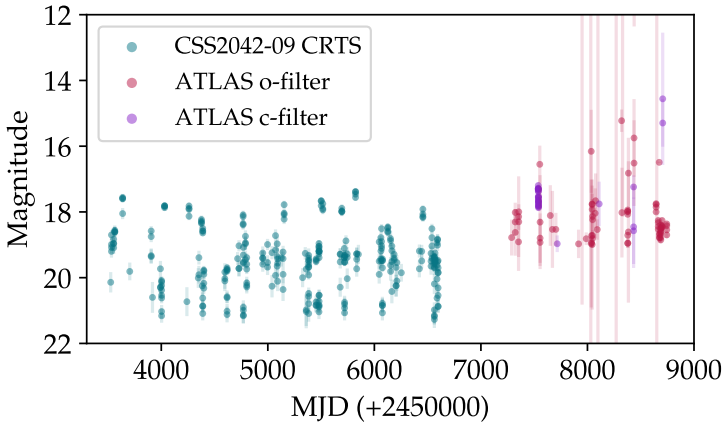

FIGURE 5.3 – Left: The long-term light curves of CSS2042-09. CRTS V-filter data is displayed in teal, ATLAS o-filter data in purple and c-filter data in red.

Prior to large optical surveys like CRTS and SDSS, the known AM CVn population totalled 13 and are distributed as follows: 38.5 % in stable high state; 46 % outbursting; and 15 % with no detected outbursts. Most of those are brighter than V=17. With the advancement of transient surveys (e.g. ZTF), the peak of the distribution of discoveries of new systems has shifted even further towards outbursting AM CVns. They have been discovered at a higher frequency than stable high-state and stable low-state AM CVns, due to the selection bias of transient surveys, most of which are fainter than V=17. With over 70 known AM CVn systems, the current distribution is as follows: 11 % in stable high state; 72 % outbursting; and 17 % in stable low state (with no detected outbursts). With initially almost as many stable high-state systems as the outbursting systems, before large surveys, the stable high-state systems have the lowest relative increase in discoveries through current surveys, e.g. OmegaWhite (Macfarlane et al., 2015, 2017; Kupfer et al., 2017).

The helium-rich dwarf nova CSS2333-15 has a larger orbital period, at 61.7 min, than of the AM CVn sample in this study. With only 15 known Helium-rich dwarf nova systems ranging in orbital periods from 52.1 min to 79.5 min (Green et al., 2020), these rare helium-rich dwarf novae are believed to have evolved beyond the CV period minimum and towards the AM CVn subclass, via the evolved CV channel (Breedt et al., 2012b). The orbital period of CSS2333-15 falls within the range of the other helium-rich dwarf novae, in which all are below the CV period minimum, on the upper end of the AM CVn $P_{\rm orb}$ range. The discovery of more helium-rich dwarf novae may help in understanding and constraining the evolved CV channel.

5.2.2 *Magnetic CVs*

The Ritter and Kolb catalogue (RKcat) contains a continuously updated list of CVs, including the various sub-classes, from which the test sample of previously known magnetic CVs was obtained for this work. This sample was reduced to those that have sufficiently sampled long-term light curves in the CRTS database. Without taking other properties into account, the previously known polar sub-class of magnetic CVs

were characterised in this study according to their long-term photometric behavioural patterns, namely two-state, three-state, slightly variable, large scatter and stable. The CRTS-discovered polar candidates are characterised according to these markers established in this work. A polar displaying long-term photometric behaviour that deviates from previously observed group behaviour may not be characterised accordingly.

Despite the small number of previously known polars showing stable long-term behaviour (11.8 % of the RKcat sample with CRTS light curves), unidentified polars showing such behaviour would remain undetected by CRTS, due to the lack of photometric variability. Furthermore, relying solely on the optical light curve, the long-term stability could have multiple implications and cannot be used as the only diagnostic for identifying polars. Thus this method of identifying polars via long-term photometry would overlook stable pre-polars and low accretion rate polars.

The long-term behavioural distribution of the candidate sample compared with the known polars with long-term CRTS light curves has been summarised in table 5.1. The candidate sample suggests that the CRTS, and likely other transient surveys, have a selection biased towards photometrically variable polars therefore stable polar would not be identified, which constitute almost 12 % of the known polars. My selection criteria discard outbursting CVs (i.e. dwarf novae) which may include some magnetic CVs, like intermediate polars or occasionally flaring polars. Similar to known systems, the majority of the CRTS sample has two states and less systems that are slightly variable or have large scatter. The CRTS sample of known polars has no three-state systems, compared to 6 % of known polars.

MLS1137+00 and MLS1247-04 are incorrectly identified by CRTS as CVs, which leads to further misclassification as candidate polars. Due to the lack of outbursts and overall high/low variations in the long-term light curves, these systems are easily mistaken for polar candidates. The redshifted spectral lines from follow-up observations are an indication of the AGN nature of MLS1137+00 and MLS1247-04.

Many previously known polars were discovered through X-ray observations. Three of the nine CRTS discovered polar candidates have X-ray counterparts, namely CSS0357+10, CSS0919-05 and MLS1525-03. With a magnitude range of V≈16-21, these optically faint magnetic CV candidates may be fainter in X-rays than the detection threshold of current X-ray survey telescopes, as observed with many of the magnetic CVs discovered by SDSS (§ 2.2.1).

Other factors influencing the population of polars discovered by CRTS are the location and brightness of the targets. Polars fainter than the detection threshold of the CRTS telescopes (V= 19 – 21.5 magnitudes depending on the telescope) would not be detected by CRTS. Polars brighter than V≈ 12 magnitudes would also remain undetected by CRTS due to CCD saturation limits of V≈ 12 magnitudes (Breedt et al., 2014). While the brightest known polar is AM Her with V≈ 12 magnitudes in high state and the faintest known RKcat systems have low state brightness of V≈ 21 magnitudes, most of the previously known systems lie in the V= 17 – 18.9 magnitude range. My CRTS-discovered candidate polar population is slightly fainter, with the brightest system at V≈ 16 magnitudes during high state and the majority at V= 18 – 19.9 magnitudes. It

TABLE 5.1 – The distribution of the various long-term photometric behavioural patterns of known polars with long-term CRTS data compared with the CRTS candidate polars. Some systems may display multiple characteristics.

Long-term behaviour	**Known polars**		**CRTS sample**	
	(count)	(%)	(count)	(%)
Two states	42	55.3	7	77.8
Three states	5	6.6	0	0
Slightly variable	19	25.0	2	22.2
Stable	9	11.8	-	-
Large scatter	12	15.8	2	22.2

Notes: Percentages calculated using a total of 78 known polars and 9 CRTS candidate polars.

appears that very few bright polars, if any, would be undetected by the CRTS as the brightest known polar in high state lies at the brightness threshold of CRTS. There may be a hidden population of undetected faint polars to be revealed by more sensitive surveys (e.g. ZTF and the Rubin Observatory's LSST).

The CRTS telescopes do not observe within 10-15° of the Galactic Plane (Drake et al., 2009). The Galactic Plane is avoided because the crowded plane leads to increased false detections and greater uncertainties In addition, regions above ∼70° and below ∼-80° exceed the survey declination limits. Roughly a third (at least 40) of previously known polars lie outside of the CRTS coverage i.e. there is no CRTS data available for these objects. Of those, at least 10 are located very close to the Galactic Plane, with nine systems found at coordinates RA=17h51m, Dec=-29° and one other system at RA=17h45m, Dec=-29° (Muno et al., 2003; Hong et al., 2012). Despite being an all-sky survey, the positional restrictions of CRTS are more limiting than the brightness restrictions, as a significant number of the previously known polars are excluded due to their positions.

5.3 REVISION OF SELECTION CRITERIA

5.3.1 *AM CVn stars*

The AM CVn stars and helium-rich DN in this work were not selected by a common systematic method. Some systems were previously established as having helium-dominated spectra. Other systems were followed up after (super)outburst alerts from ATel, VSnet or cba:news. Having access to SAAO telescopes during rare outbursts was key to successful follow-up observations.

CSS0105+19 is the only system found via a targeted search for AM CVn stars by restricting a specific colour-colour space ($-0.25 < u - g < 0.0$ and $-0.25 < g - r < -0.15$), occupied by other previously known AM CVns. This is similar to the thorough

SDSS approach using strictly colour restrictions (§ 2.1.1, references therein) and the approach by van Roestel et al. (2021) through the Zwicky Transient Facility using colour restrictions of outbursting CVs. AM CVn stars occupy the same colour space as DA and DB white dwarfs. By restricting the search to CRTS-discovered outbursting CV candidates, contamination from other astronomical objects is reduced or avoided.

5.3.2 *Polars*

Note to reader: Concepts and definitions are repeated from Chapter 2, § 2.6 is repeated in this subsection in order for the reader to understand the text without referring back to § 2.6.
Using a sample of 78 long-term CRTS light curves of previously known polars, I characterised the long-term photometric behaviour of polars into 5 groups. Two-state systems have a clear high state and low state with a visible difference in brightness. Three-state systems have an additional intermediate state between the high and low states. Slightly variable systems have differences in brightness but no clear distinctions between high and low states. Stable systems have stable and constant brightness throughout the light curve and the literature shows that they are mostly likely low accretion rate polars. Systems with large scatter have large amplitude variations over short timescales of hours to days. Examples of these characterisations can be seen in Fig. 5.4. The characterisations are subject to the observing baseline and may differ if selected over a longer/shorter baseline or over a different long-term timebase (e.g. 8 – 9 years, as in the CRTS sample).

The initial sample of candidate polars from CRTS was selected by visually inspecting light curves from the CSS, MLS and SSS CV candidates, based on the long-term light curves of polars. This initial selection is based on as wide as possible selection criteria, even with a possibility for contamination by non-magnetic CVs, to maximise the potential to discover new polar candidates. This sample is therefore significantly contaminated by dwarf novae with quiescent state behaviour similar to polars. After a revision of the selection criteria, more stringent and systematic restrictions were applied.

The long-term light curves of a sample of 78 previously known polars and 70 previously known outbursting CVs (i.e. dwarf novae, including 35 discovered from CRTS) were used to apply a more systematic approach to eliminating dwarf novae and selecting candidate polars using the long-term CRTS light curves. The long-term light curves from CRTS, with 8 – 9 year observing baselines, are divided into annual groupings (seasons) and assessed both seasonally and over the whole long-term light curve. Density plots and Gaussian mixture models (GMMs) are used to approximate the distribution of the light curve, seasonally and long-term. The pros and cons of both approximations were discussed in § 2.6.

The light curves of possible dwarf novae are flagged and eliminated to remove the irrelevant CVs (in terms of this study) from my CRTS sample of assorted CV light curves. The remaining light curves are considered potential polars and characterised accordingly. A distinction between outbursts and flares is necessary to prevent the flagging of flaring polars as possible dwarf novae. This is done by defining outbursts as 1) 2.5 magnitudes brighter than the density plot peak of the bulk seasonal brightness or 2) is least 0.2 magnitudes from the next fainter detection and stays at the approximate outburst brightness for at least 10 minutes. A total of 50 % of previously known

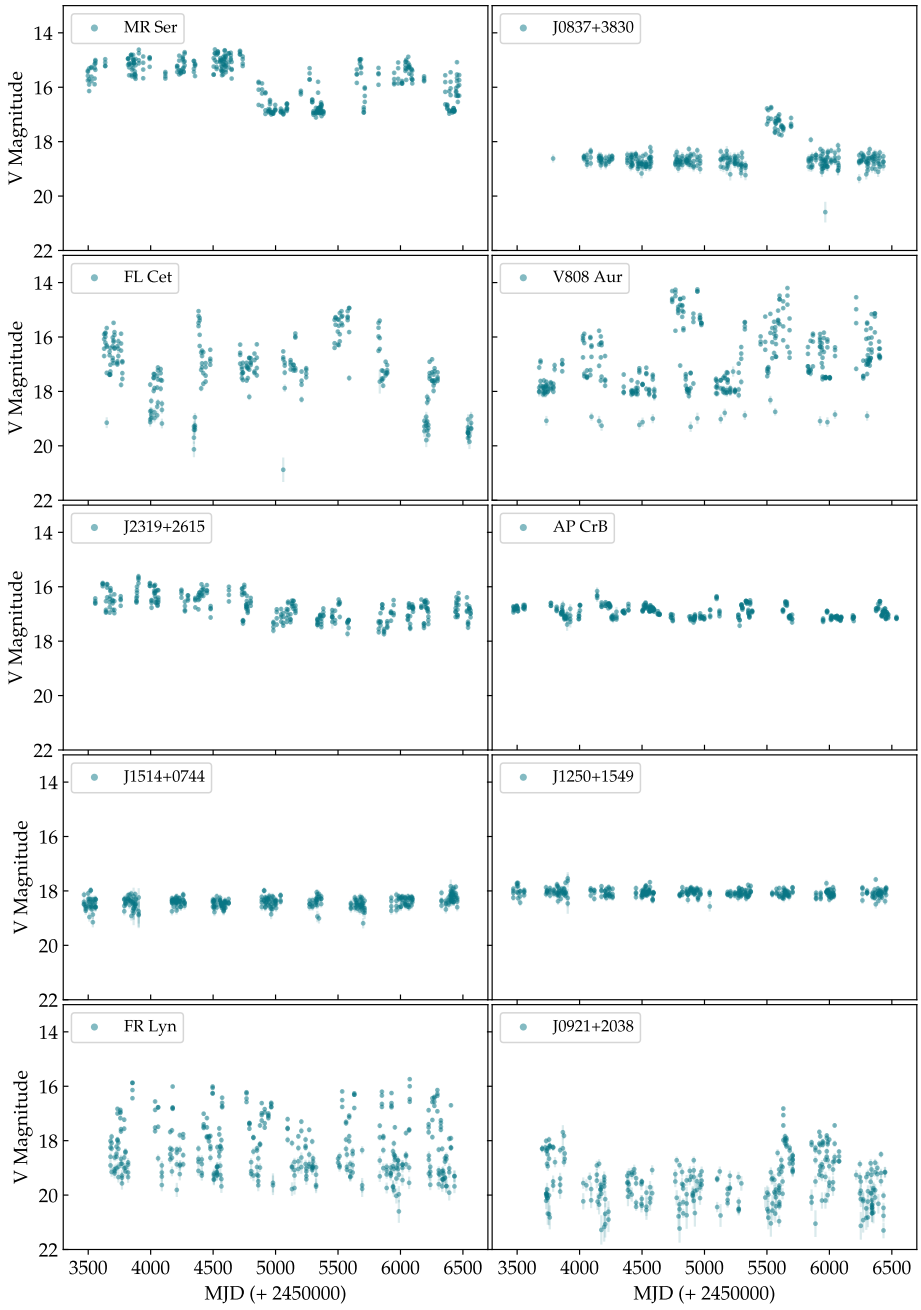

FIGURE 5.4 – Examples of polar characterisations of light curves. There are two examples in each row of two-state systems (MR Ser and J0837+3830 in the first row), three-state systems (FL Cet and V808 Aur in the second row), slightly variable systems (J2319+2615 and AP CrB in the third row), stable systems (J1514+0744 and J1250+1549 in the fourth row) large scatter systems (FR Lyn and J0921+2038 in the bottom row).

dwarf novae are identified with both criteria simultaneously. Approximately 74 % of previously known dwarf novae are identified by criterion 1 and 61 % are identified by criterion 2. Of the previously known polars, 14 % are identified as outbursting, selected primarily by criterion 1. Dwarf Novae with high outburst rates, where some

systems spend roughly the same amount of time in outburst as in quiescence, may not be identified as outbursting, thus appearing as two-state magnetic CV through the seasonal density plots (see examples in Fig. 5.5).

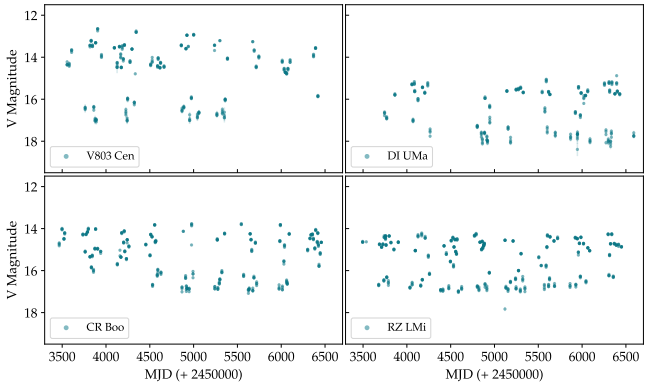

FIGURE 5.5 – Examples of DNe with high outburst rates that are not identified as potential DNe.

The systems not flagged as possible dwarf novae (i.e. with detected outbursts) are considered potential polars. These light curves are further assessed for characterisation by representing them as the density plot peaks for each season (see the light curves of FL Cet in Fig. 2.21 and corresponding density plots in Fig. 2.22 and density plot peaks in the top panel of Fig. 5.6, as an example).

To avoid mis-characterisation due to interference by bright and faint outliers (including flares and eclipses, respectively), outliers are removed. Outliers are defined as a density plot peak 3.4 times less than the largest density plot peak magnitude of each season. If present, outliers were initially removed only once per season but this was revised to repeatedly remove them until none remained. This revision improves the characterisation for systems with multiple detected outliers in a season (e.g. PW Aqr in Fig. A.1.26 with many detected eclipses per season). Outliers with large errors that fall within the DP curve of the bulk data for each season are also removed. Fig. 5.6 shows the DP peaks of the CRTS light curve of FL Cet (top) for every season and the DP peaks with the eclipse outliers removed (second panel).

Without the outliers, the bulk/general behaviour of each system can subsequently be characterised. All systems are assessed as temporary two-state systems and temporary three-state systems unless they are classified as stable or slightly variable, in order to best determine how many states a system has and where to place the states on a magnitude scale. The peak magnitudes of the density plot from all seasons are ordered in ascending order (i.e. from brightest to faintest). The *halfway-line* is defined by the mid-point between the highest and lowest peak magnitude. Every consecutive density plot (DP) peak magnitude is subtracted from the previous peak magnitude to determine the gap widths between consecutive DP peak magnitudes. A temporary *divide1* (*divide1-temp*) and temporary *divide2* (*divide2-temp*) are the mid-gap positions of the two largest gap widths between ordered DP peaks. A temporary dividing-line (*dividing-line-temp*) is assigned to the *divide1-temp* and *divide2-temp* value closest to the *halfway-line* value. Thereafter the system will be characterised based on meeting certain criteria listed

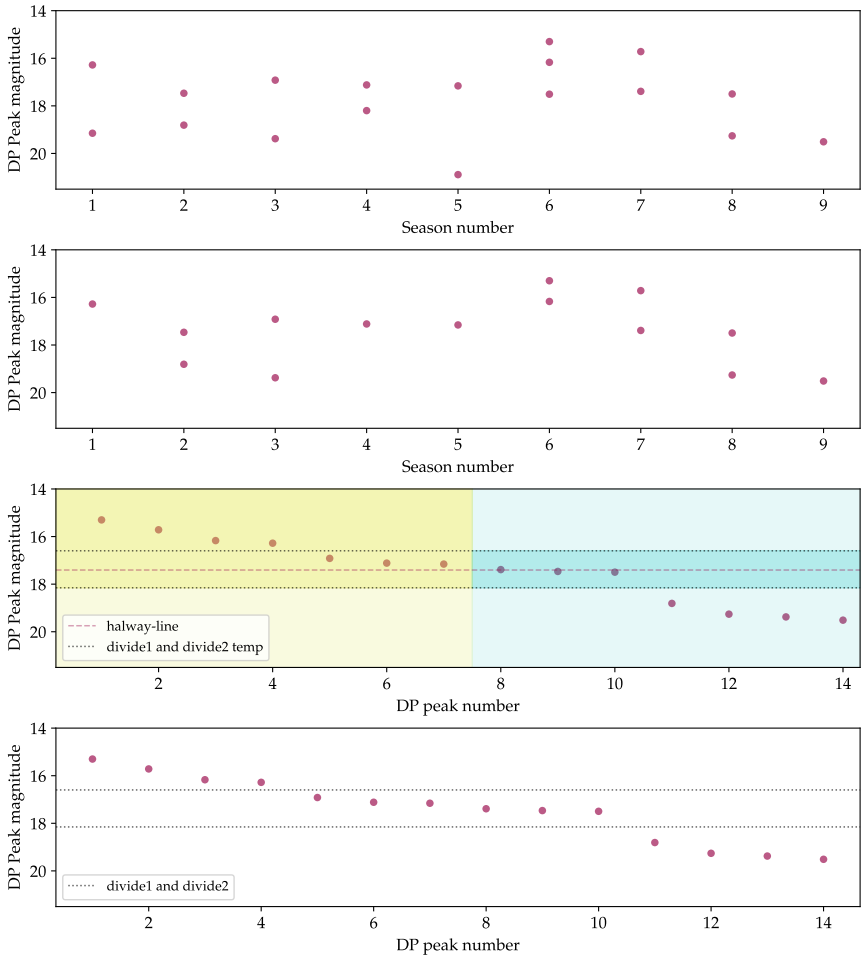

FIGURE 5.6 – The density plot peaks corresponding to histograms of FL Cet in Fig. 2.22. In the top panel are the density plot peaks in each season. The second panel has the same density plot peaks but with the bright and faint outliers (i.e. flares and eclipses) removed. The third panel shows the density plot peaks, without outliers, sorted in order of brightest to faintest magnitude. When determining where to place the divisions between states, the system is assessed and compared temporarily as a two-state system (yellow across the full x-axis) and a three-state system (cyan across the full x-axis). The bottom panel shows sorted density plot peaks. The dotted lines represent the lines *divide1* and *divide2* separating high and intermediate states as well as intermediate and low states.

below, where the *dividing-line* is assigned either the *divide1-temp* or *halfway-line* value for a two-state system and for the three-state system, the lines separating the high state from the intermediate state and the intermediate state from the low states, *divide1* and *divide2*, are assigned the values of *divide1-temp* and *divide2-temp*. See an example of assessment with temporary lines and states in the third panel of Fig. 5.6 and an example of characterisation of three-state system after assessing temporary states at the bottom of Fig. 5.6. Positioning the states correctly lays the foundation for characterisation.

The following criteria define each status:

- The system has no state changes, as the long-term brightness is constant and stable, and therefore no dividing line if 1) all differences between consecutive peak magnitudes are less than 0.3 magnitudes and 2) the standard deviation of the DP peaks is less than 0.01.
- The system has no state changes, as it varies slightly in the long-term brightness, and therefore no dividing line if the standard deviation of the DP peaks is between 0.01 and 0.5 magnitudes.
- A system has two states with the *dividing-line* assigned to *divide1-temp* or *divide2-temp* closest to the *halfway-line*.
- The *dividing-line* of a two-state system is assigned the value of the *halfway-line* if 1) The standard deviation of the peaks in the temporary state with the highest standard deviation, is 2.5 times larger than the state with the lowest standard deviation of the temporary two-state system and 2) The standard deviation of the peak magnitudes in the temporary intermediate state is larger than both the standard deviations of the DP peak magnitudes of the temporary high and low states of the temporary three-state system.
- A system with three states with *dividing1* and *dividing2* assigned to *divide1-temp* and *divide2-temp* if 1) does not have the *halfway-line* defined as the *dividing-line* for a two-state system, 2) the brightest and faintest DP peak are at least 2 magnitudes apart and 3) the standard deviation of the DP peaks in the temporary state with the highest standard deviation, is 2.5 times larger than the state with the lowest standard deviation of the temporary two-state system.

Polars are characterised as follows:

- Stable systems show no state change and have all peaks in one state.
- Slightly variable systems have a standard deviation of the combined density plot peaks between 0.1 and 0.5 magnitudes.
- Two-state systems are further divided into 3 sub-groups: 1) low-to-high have at least 60 % of total density plot peaks in low state; 2) high-to-low have least 60 % of total peaks in high state; and 3) high=low have 40-60 % of total peaks in both states.
- Three-state systems can be sub-divided into 1) high-to-low where most density plot peaks are in the high state; 2) low-to-high where most density plot peaks are in the low state; 3) high=low where there are an equal number of peaks in high and low state; 4) predominantly intermediate where the majority of the peaks are found in the intermediate state.
- Systems with large scatter have an average standard deviation of the daily data points greater than 0.3.

The long-term light curves of some magnetic CVs are almost indistinguishable from those of very active dwarf novae. The polars FR Lyn, GG Leo, J0953+1458 and V519 Ser (see Fig. 5.8) are flagged as outbursting CVs because of their obvious similarities to the light curves of dwarf novae. Although the phase-folded light curves of GG Leo and J0953+1458 are weakly in phase, it is evident that they, along with V519 Ser in high state, show large amplitude orbital modulations. The orbital modulations of FR Lyn cannot be confirmed as neither the literature values, nor the period derived in this work (from Lomb-Scargle power spectrum) values of the orbital periods produce coherent phase-folded light curves from the CRTS. Interestingly, the weakly phased

phase-folded light curve of J0953+1458, looks very similar to the unusual light curve of FR Lyn (J0854+3905) in figure 1 from Dillon et al. (2008).

The long-term light curves of the later-confirmed dwarf novae, from the initial selection by visual inspection, have characteristics resembling the light curves of polars. Most of the light curves of the later-confirmed dwarf novae show slightly variable behaviour during the quiescent phase. Two light curves have large scatter during quiescence. Various outburst frequencies are observed.

	Polar	DN	Other
CSS0105-08			
CSS0109-27		x	
CSS0350+32	x		
CSS0357+10	x		
SSS0617-36		x	
MLS0720+17			x
CSS0812+04	x		
CSS0910+16		x	
CSS0919-05	x		
SSS1012-18		x	
SSS1020-33		x	
MLS1115+05		?	
CSS1127-05	?		
MLS1137+00			x
MLS1247-04			x
SSS1440-22		?	
CSS1455-11		x	
MLS1525-03	x		
CSS1619+13		x	
SSS1935-53		?	
SSS1944-42	x		
SSS1955-30			
CSS2042-09			
MLS2044-16			x
SSS2046-31		?	
CSS2154+15	x		
CSS2335+12	x		

FIGURE 5.7 – A table comparing the observation results of the CRTS CV (crosses) with the systematic classification based on the criteria established in this work (shaded blocks).

Fig. 5.7 shows a comparison between the observation results of the CRTS CV (represented by crosses) with the systematic classification based on the criteria established in this work (seen as shaded blocks). The programme selects outbursting systems well as all but two of the DN (SSS1440-22 and CSS1619+13) were identified as outbursting

CVs. As the code only makes a distinction between outbursting CVs and potential polars, the remaining objects were identified as potential polars, including all polars, the unclassified (likely) CVs (CSS2042-09, SSS1955-30 and CSS0105-08), the nova-like MLS0720+17 and two AGN (MLS1137+00 and MLS1247-04) and RR Lyr MLS2044-09. With an additional step of determining the orbital period from the long-term light curves, the MLS2044-09 would have been excluded from the selection. The nova-like, AGNs and RR Lyr were also selected as part of Oliveira et al. (2017, 2020) samples.

The identification of polar candidates through long-term photometric behaviour should only be used as an indicator. There appears to be a small overlap in the long-term photometric behaviour where dwarf novae and polars lie. Follow-up optical spectroscopic and/or polarimetric observations should be used for confirmation, maybe coupled with X-ray observations. Checking the long-term light curves for coherent periods could further remove the outliers (e.g. RR Lyr, § 4.9).

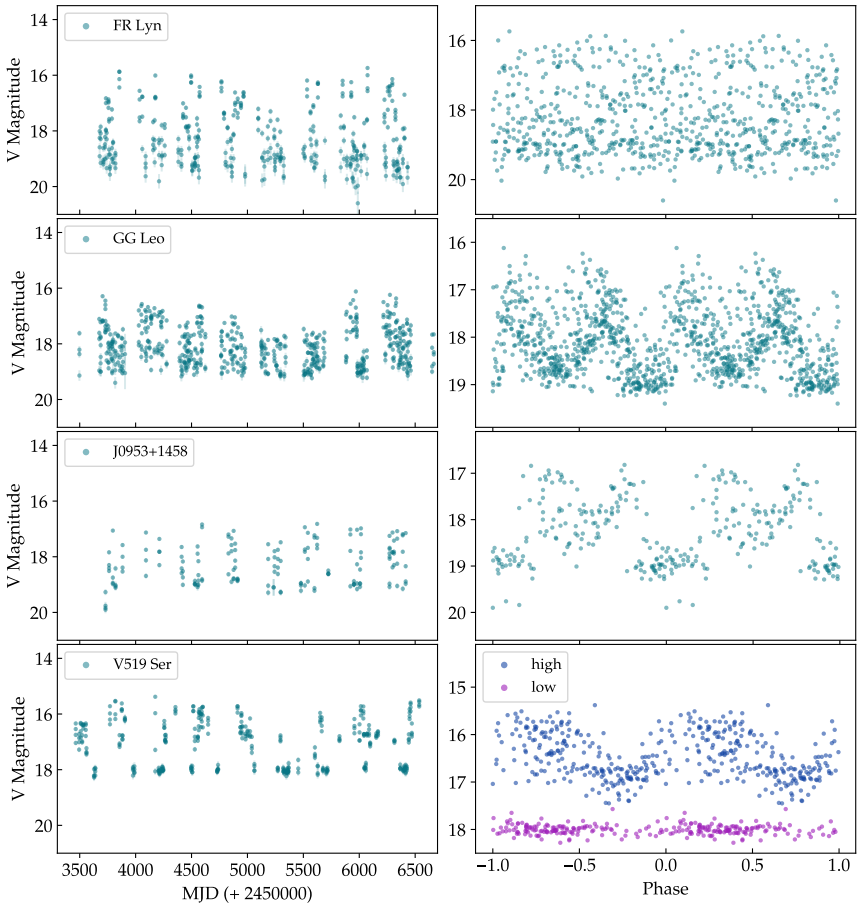

FIGURE 5.8 – The long-term light curves and corresponding phase-folded light curves of polars FR Lyn, GG Leo, J0953+1458 and V519 Ser which resemble DNe.

5.4 LACK OF MAGNETIC AM CVN SYSTEMS

Astronomers have been successful at discovering magnetic CVs, mostly through X-ray surveys. Polarised radiation, Zeeman line splitting from the halo surrounding the accretion shock or white dwarf photosphere, or polarized cyclotron radiation are all strong indicators of magnetic accretion. Astronomers have also made significant progress at finding AM CV stars from optical surveys, through brightness variations, colour selections, lack of hydrogen in their spectra, specific spectral features and ultra-short periods. With established criteria for magnetic CVs, particularly polars, and AM CVn stars, one would expect the subsequent detections of magnetic AM CVn stars. The lack of confirmed magnetic AM CVns would imply that either magnetic AM CVn stars do not display the observable characteristics of polars or AM CVn stars; they are too faint for detection with current instruments; or they do not exist. There are currently two ambiguous candidate magnetic AM CVn stars with periods in the AM CVn period range. SDSS J080449.49+161624.8 (Roelofs et al., 2009) is a peculiar candidate AM CVn star and Gaia14aae, an eclipsing and outbursting AM CVn star with an orbital period close to 50 min.

SDSS J080449.49+161624.8 (SDSS J0804+1616) is classified as a candidate AM CVn star with $P_{\rm orb}$ = 44.5 min. Roelofs et al. (2009) report the presence of strong ionised helium and nitrogen and a lack of carbon and oxygen in the spectrum. The resulting high N/C and N/O ratios suggest that the helium burning phase did not occur during formation and thus excludes the helium star formation channel. Unlike the common double- or triple-peaked emission line spectra (e.g. Marsh, 1999; Ruiz et al., 2001; Morales-Rueda et al., 2003; Roelofs et al., 2005; Zhang et al., 2018) of AM CVn stars, the SDSS J0804+1616 spectrum was observed with broad single-peaked emission lines. The broadness of the lines indicates that the single-peaked lines are not attributed to inclination effects.

Gaia14aae (Kato et al., 2014b; Campbell et al., 2015) is an eclipsing AM CVn with an orbital period of 49.7 min. As a long period outbursting AM CVn (also exhibiting likely echo-outbursts), this system falls outside of the expected period range for outbursting AM CVns. Despite an inferred accretion rate by Campbell et al. (2015) within the limits for outbursting systems according to disc instability models for the system parameters, Maccarone et al. (2023) suggest that the presence of outbursts at this period and the higher luminosity, are an indication of an enhanced mass transfer rate, referring to magnetic breaking as a possible cause. According to Green et al. (2018b), the mass–radius relation of Gaia14aae suggests that Gaia14aae could have formed via either the WD or the He star channel.

Maccarone et al. (2023) reported that SDSS J0804+1616 has X-ray luminosity ~ 50 times brighter than AM CVn systems with roughly the same orbital period, and inferred that both SDSS J0804+1616 and Gaia14aae have accretion rates larger than expected for AM CVn systems with their orbital periods for the evolving under standard AM CVn binary models, which they attribute to the influence of stronger WD magnetic fields. Maccarone et al. (2023) identified X-ray pulse modulations over the spin period of the accretor for SDSS J0804+1616 and Gaia14aae. They reported that the single-peaked X-ray pulse of SDSS J0804+1616 suggests that the accretion disc is truncated further

away from the white dwarf by an inferred magnetic field of at least $\sim 10^5$ G. The double-peaked X-ray pulse of Gaia14aae is reported to suggest the truncation of the accretion disc near the white dwarf by a weaker magnetic field of $\sim 10^{3-4}$ G.

To explore the plausibility of a magnetic AM CVn subclass, I investigated the magnetospheres of WDs in polars. The magnetospheric radius where the magnetic pressure of the white dwarf magnetosphere equals the ram pressure of the infalling matter is called the Alfvén radius (when applied to spherical accretion) or the coupling radius (R_μ). This is the radius where the infalling mass from the donor star begins to follow the trajectory of the magnetic field lines out of the orbital plane. Assuming a dipole and centred magnetic field, the magnetic moment, μ, is given by $\mu = BR(1)^3$. The coupling radius of such a magnetic field, when interacting with the accretion stream, is determined by

$$R_\mu = 1.45 \times 10^{10}\, \mu_{34}^{4/11} \sigma_9^{4/11} M_1^{-1/11} \dot{M}_{16}^{-2/11} \text{cm}, \tag{5.1}$$

(Mukai, 1988; Warner, 1995a, pg. 309) where μ_{34} is μ in units of 1×10^{34} G cm^3, $\dot{M}_{16}$ is $\dot{M}$ is the mass transfer rate in units of 1×10^{16} g s^{-1} and σ_9 is the radius of the stream, σ, in units of 1×10^9 cm. According to Lubow and Shu (1975), σ_9 is ~ 1.

I use parameters of well-studied eclipsing magnetic CVs (table 5.2) to determine R_μ for each system (table 5.3). The sample is limited to eclipsing systems which yield the most accurate system parameters through eclipse modelling. Most parameter values from table 5.2 are found in the literature (see references therein) however $\dot{M}$ is unavailable for DP Leo, FL Cet and V2301 Oph. The accretion luminosity, L_{acc}, for X-ray sources is used to determine $\dot{M}(\text{M}_\odot\,\text{yr}^{-1})$ using the relation

$$L_{\text{acc}} = \frac{G m_1 \dot{M}}{R_1}. \tag{5.2}$$

The values for $\dot{M}$ derived from the accretion luminosity are indicated by * in table 5.2. R_μ is given in units of cm and the orbital separation, a, in table 5.3. The orbital separation is determined by the equation

$$P_{\text{orb}}^2 = \frac{4\pi^2 a^3}{G(m_1 + m_2)}, \tag{5.3}$$

according to Kepler's Law. For comparison, I also display the circularisation radius, R_{circ}, the radius at which the the accretion disc would begin to form for a system with those parameters.

The sample of eclipsing magnetic CVs is limited to magnetic field strengths of less than 65 MG. This is well below the highest observed CV magnetic field strength of 230 MG, which would extend the coupling radius further away from the WD. The mass transfer rates range over four orders of magnitude (refer to table 5.2). The large difference is due to the high and low state of mass transfer occurring in magnetic CVs. Such vast differences can have a significant effect on the coupling radius where, it decreases with increasing mass transfer rate. For systems with the lowest mass transfer rates of the order of 10^{-13} - 10^{-12} M$_\odot$ yr^{-1}, the coupling radius extends to 1.15 a. The remaining systems, with higher mass transfer rates of the order 10^{-11} - 10^{-9} M$_\odot$ yr^{-1}, have coupling

radii well within the orbital separation, situated less than half of the orbital separation away from the WD.

In an attempt to determine R_μ for AM CVn stars, certain assumptions are implemented. I investigate over the range of the magnetic field strengths observed in known polars, namely 7-230 MG. Intermediate polars generally have lower magnetic field strengths with a slight overlap with polars (Ferrario et al., 2015), although relatively few have well-determined field strengths. In table 5.5, field strengths of 10 MG minimum, 200 MG maximum and the mean magnetic field strength for polars, 38 MG (Ferrario et al., 2015), are considered. For consistency, the parameters of eclipsing AM CVns are used (table 5.4). The recent eclipsing Zwicky Transient Facility (ZTF) AM CVn stars reported in (van Roestel et al., 2022) have no determined mass accretion rates or accretion luminosities. Therefore $\dot{M}$ is estimated using Fig. 4 in Ramsay et al. (2018) with the predicted $\dot{M}$ of Bildsten et al. (2006) as a function of $P_{\rm orb}$ for AM CVn stars. The function for a hot donor is used as the AM CVn $\dot{M}$ values in Ramsay et al. (2018) which lie on or above the function. These estimated $\dot{M}$ values are indicated within square parentheses.

As the coupling radius is dependent on the mass transfer rate, the coupling radius would contract to shorter radii during AM CVn outbursts and becomes larger during quiescence. The orbital periods of the eclipsing AM CVns are spread across mid- to high-range, namely 28 – 61 min. For a minimum magnetic field of 10 MG, all coupling radii lie within the orbital separation at 0.31 – 0.63 a, as displayed in table 5.5. At 200 MG the coupling radii are close to or beyond the orbital separation, ranging between 1.41 – 1.87 a. Although higher, the R_μ values for AM CVns reflect what is observed in polars in table 5.3, with respect to the orbital separation. At 10 MG and 38 MG, R_μ is within the orbital separation. R_μ extends to 1.87 a for 200 MG. Despite the 61 MG limitation for eclipsing polars, the large increase may indicate that R_μ may lie closer to the orbital separation, if not beyond, for high field polars, which are not as common as low field systems. Considering magnetic field strengths alone, the existence AM CVn stars of magnetic nature would appear plausible, especially in the low field range. This would be expected for ultra-compact AM CVn binaries.

There are multiple models on the formation of strong WD magnetic fields in CVs which either under- or overpredict the number of magnetic CV systems (e.g. Tout et al., 2004; Wickramasinghe and Ferrario, 2005; García-Berro et al., 2012; Belloni and Schreiber, 2020). According to a model by Isern et al. (2017) and Schreiber et al. (2021), the formation of the WD's magnetic field is attributed to the crystallisation of the white dwarf's core together with a rotation-driven dynamo. The crystallisation takes place when the WD's C/O core cools and the rotation-driven dynamo is generated by the spinning up of the white dwarf when accretion takes place leading to spin and orbital period synchronisation. This model explains the high percentage of known magnetic CVs (approximately 30 %) and the comparatively low number of known magnetic WDs in detached non-degenerate binaries.

According to models by Wong and Bildsten (2021) on the thermal evolution of the accreting WDs in AM CVn stars with He WD donors, the accreting WDs experience reheating after period minimum. The high mass transfer rates at the start of mass transfer

in the WD channel lead to the temporary heating up of the envelope of the accreting WD and eventually the core. As a result, crystallisation is delayed and predicted to start at $P_{\rm orb} \approx 50\,{\rm min}$, and thus a younger WD cooling age than expected. Taking into consideration the requirements for the formation of a strong magnetic field in CVs, a possible explanation for the lack of magnetic AM CVn stars is the disruption of the WD cooling process at the beginning of mass transfer may prevent the formation of a strong WD magnetic field through the combination of core crystallisation and rotation induced dynamo (M. Green, priv. comm.). It is important to note that this model by Wong and Bildsten (2021) only considers AM CVn stars arising from the WD channel.

TABLE 5.2 – The system parameters of eclipsing polars.

Polar	$P_{\mathbf{orb}}$ (hr)	M_1 ($M_\odot$)	M_2 ($M_\odot$)	R_1 ($\times 10^8$ cm)	$\dot{M}$ ($\times 10^{-11}\,M_\odot\,yr^{-1}$)	B (MG)	**Refs**
V2301 Oph	1.883	0.85	0.22	7	*1.3	7	*1*, *2*, *3*, *4*
FL Cet	1.452	0.5	0.07	8.9	*0.43	29	*5*, *6*, *7*
V1432 Aql	3.366	0.85	0.22	8.9	13	30	*8*, *9*, *10*, *11*
HU Aqr	2.084	0.8	0.18	7.3	29	34	*12*, *13*, *14*, *15*, *16*
V808 Aur	1.953	0.86	0.18	7.7	0.015	38	*17*, *18*, *19*
HY Eri	2.855	0.42	0.24	9.5	140	40	*20*, *21*
MN Hya	3.39	0.58	0.22	8.8	360	40	*22*, *23*, *24*
DP Leo	1.497	0.6	0.14	8	0.34	59	*25*, *26*, *27*
V1309 Ori	7.983	0.7	0.46	8	54	61	*28*, *29*, *30*, *31*

Notes: The * indicates $\dot{M}$ values derived from $L_{\rm acc}$. Refs=references. [*1*] Barwig et al. (1994), [*2*] Silber et al. (1994), [*3*] Ferrario et al. (1995), [*4*] Ramsay and Cropper (2007), [*5*] Wiehahn et al. (2004), [*6*] Schmidt et al. (2005a), [*7*] O'Donoghue et al. (2006), [*8*] Geckeler and Staubert (1997), [*9*] Mukai et al. (2003) [*10*] Wang et al. (2021), [*11*] Staubert et al. (2003), [*12*] Schwope et al. (1993), [*13*] Hakala et al. (1993), [*14*] Heerlein et al. (1999), [*15*] Schwope et al. (2011), [*16*] Schwope et al. (2003), [*17*] Schwope et al. (2015), [*18*] Borisov et al. (2016), [*19*] Kolbin et al. (2019), [*20*] Burwitz et al. (1999), [*21*] Beuermann et al. (2020), [*22*] Buckley et al. (1998), [*23*] Ramsay and Wheatley (1998), [*24*] Wang et al. (2018), [*25*] Schwope et al. (2002c), [*26*] Stockman et al. (1994), [*27*] Cropper and Wickramasinghe (1993), [*28*] Garnavich et al. (1994), [*29*] Buckley and Shafter (1995), [*30*] Shafter et al. (1995), [*31*] Harrop-Allin et al. (1997)

TABLE 5.3 – R_μ and R_{circ} determined for eclipsing polars in table 5.2.

Polar	R_{circ}		R_μ	
	($\times 10^{10}$ cm)	(a)	($\times 10^{10}$ cm)	a
V2301 Oph	8.30	0.15	1.38	0.25
FL Cet	7.36	0.20	3.86	1.04
V1432 Aql	1.22	0.15	2.00	0.25
HU Aqr	9.16	0.16	1.45	0.26
V808 Aur	9.23	0.17	6.37	1.15
HY Eri	6.66	0.11	1.65	0.27
MN Hya	9.48	0.13	1.24	0.17
DP Leo	6.59	0.16	4.54	1.10
V1309 Ori	1.50	0.10	1.81	0.12

Notes: R_μ and R_{circ} are given in cm and a fraction of the orbital separation, a.

TABLE 5.4 – The system parameters of eclipsing AM CVn stars.

AM CVn	P_{orb} (hr)	M_1 ($M_\odot$)	M_2 ($M_\odot$)	R_1 ($\times 10^8$ cm)	$\dot{M}$ ($\times 10^{-11}\, M_\odot\, y^{-1}$)	**Refs**
Gaia14aae	0.828	0.87	0.025	6.4	1.4	*1, 2*
YZ LMi	0.472	0.85	0.035	6.75	9.8	*3, 4*
ZTFJ1637+49	1.025	0.9	0.023	6.21	[0.25]	*5*
ZTFJ0003+14	0.925	0.79	0.017	7.37	[0.58]	*5*
ZTFJ0220+21	0.892	0.83	0.014	6.95	[0.7]	*5*
ZTFJ2252-05	0.623	0.76	0.026	6.95	[3.7]	*5*
ZTFJ0407-00	0.59	0.79	0.019	6.95	[6.0]	*5*

Notes: The $\dot{M}$ values in square parentheses are derived from Ramsay et al. (2018) and Refs=references. [*1*] Campbell et al. (2015), [*2*] Green et al. (2018b), [*3*] Anderson et al. (2005), [*4*] Copperwheat et al. (2011), [*5*] van Roestel et al. (2022)

TABLE 5.5 – R_μ and R_{circ} determined for eclipsing AM CVn stars in table 5.4.

AM CVn	$\mathbf{R_{circ}}$		$\boldsymbol{R_\mu}$**(10 MG)**		$\boldsymbol{R_\mu}$**(38 MG)**		$\boldsymbol{R_\mu}$**(200 MG)**	
	(10^{10} cm)	(a)	(10^{10} cm)	(a)	(10^{10} cm)	(a)	(10^{10} cm)	(a)
Gaia14aae	1.15	0.28	1.41	0.48	3.42	0.77	4.19	1.41
YZ LMi	6.78	0.36	1.05	0.52	2.53	0.84	3.11	1.53
ZTFJ1637+49	1.41	0.35	1.85	0.54	3.01	0.87	5.50	1.60
ZTFJ0003+14	1.36	0.30	1.94	0.63	3.15	1.02	5.76	1.87
ZTFJ0220+21	1.49	0.30	1.75	0.57	2.84	0.93	5.20	1.70
ZTFJ2252-05	8.49	0.28	1.30	0.55	2.12	0.90	3.87	1.65
ZTFJ0407-00	9.60	0.41	1.19	0.52	1.93	0.85	3.53	1.55

Notes: R_μ and R_{circ} are given in cm and a fraction of the orbital separation, a, for 10 MG, 38 MG and 200 MG.

CHAPTER 6

Summary and future outlook

6.1 Thesis summary

This work has focused on the detection and study of AM CVn stars and magnetic CVs (polars). I investigated the long-term photometric properties of the global population of previously known polars in order to search for new examples from the CRTS, as well as photometrically and spectroscopically observed individual AM CVns and magnetic CV candidates. This study has shown that long-term photometric behaviour is more complicated than simple high-low state transitions.

The AM CVs stars selected for follow-up observations were identified through post-outburst alerts, with the exception of CSS0105+19. This object was selected by cross-correlating the CRTS CVs with their SDSS colours and constrained within a colour space occupied by other previously known AM CVn stars. The studied AM CVns have orbital periods from 31.65 to 54.78 min, while the helium-rich dwarf nova CSS2333-15 has a larger orbital period of 61.7 min. With an orbital period of 47.2 min, CSS0450-09 is an outbursting AM CVn which falls within the AM CVn long-period range. ASASSN-14ei and ASASSN-14mv, with orbital periods of 40 min and 43 min, respectively, were observed in superoutburst followed by multiple echo-outbursts over several months. Photometric orbital modulations are seen in all AM CVn light curves.

In this optical study, Polars are observed to transition between high and low states of mass transfer. Together with the lack of outbursts in polars, I have used these photometric variations as an indicator for the identification of polar candidates through their long-term CRTS optical light curves. I have developed a systematic method for eliminating outbursting CVs (hydrogen and helium dwarf novae) from the CVs discovered by the CRTS. Intermediate polars observed in outburst would also be identified as outbursting, and thus eliminated. From the sample of general dwarf novae from RKcat, 82.4 % are identified as outbursting, 91.7 % of the sample of CRTS-discovered dwarf novae and 13.9 % of the sample RKcat polars are identified as outbursting.

The long-term photometric behaviour of previously known polars is characterised, in this work, as two states (high-to-low, low-to-high and high=low), three states (predominantly high, predominantly low high=low), slightly variable, stable and large scatter. Two states, three states, slightly variable and stable are mutually exclusive, while the large scatter classification may exist with all other classifications except stable. The previously known sample of polars is characterised as follows: 55.3 % two states, 6.6 % three states, 25.0 % slightly variable, 11.8 % stable and 15.8% large scatter.

Having familiarised myself with the long-term light curves of previously known polars, a sample of polar candidates was initially selected by eye for follow-up observations. Following the development of a method for identifying outbursting CVs, they were removed from the initial sample. As stable systems are too ambiguous to be classified using only their long-term light curves, they would also be eliminated. The remaining systems were considered candidate polars. Using the criteria for identifying outbursting CV and characterising polars, 11 systems were identified as DN/outbursting and the remaining 16 non-outbursting systems are characterised as polars as follows: 10 two states, 1 three states, 3 slightly variable, 2 large scatter and 2 have insufficient data to be characterised. From the sample selected the eye, the follow-up observations revealed 8 polars + 1 polar candidate, 7 DNe + 4 DN candidates, 1 nova-like CV, 1 RR Lyr, 2 AGNs and 3 unknown systems (See full summary in table 4.3).

In analysing the long-term CRTS light curves, Lomb Scargle periodograms of the CRTS data were used to determine the periods of the previously known polars and compared with the orbital periods found in the literature. Folding over the correct orbital period reveals orbital structure/modulation for some systems. The large scatter seen in the light curves is often a result of the large amplitude orbital modulation, common in polars. In some systems, the high state shows orbital modulations while the low state remains unexpectedly constant. I also confirmed that the faint outliers are most often eclipses which are well-aligned when folded over the correct orbital period. The profiles of the eclipses give further insights into the presence/absence of an accretion disc, with narrow or step-wise eclipses indicative of polars.

I compared my sample of AM CVns and polars with the population of known AM CVns. My sample of AM CVns shows that more outburst activity is observed in lower orbital period systems. The majority of the sample of polars in this work ($18 \leq$ V mag < 18.9) is approximately 1 magnitude fainter than the majority of known polars ($17 \leq$ V mag < 17.9). Only four of my polar sample of nine have X-ray counterparts, which could be attributed to being fainter than the threshold for existing X-ray telescopes, including eRosita. As found with the previously known polars, most of my sample of polars are two-state systems. There is also an absence of stable polars from my sample as they would not be identified as transients by the CRTS.

I highlighted two ambiguous magnetic AM CVns candidate systems: SDSS J0804+1616 and Gaia14aae are AM CVn stars reported to have strongly magnetic WDs. Both objects require further follow-up observations to confirm their nature. I investigated the possibility of the existence of magnetic AM CVn stars by comparing the coupling radii (the magnetospheric radii where the infalling mass begins to follow the trajectory of the magnetic field) of known eclipsing polars with the possible coupling radii of existing

eclipsing AM CVn stars if they had comparable magnetic fields. Although the coupling radii for AM CVns are found to be generally higher than those of magnetic CV, they are still positioned within the orbital separation of the binaries for lower magnetic fields of less than 40 MG. It is unclear why there are so few identified magnetic AM CVn stars but future X-ray and optical telescopes with improved capabilities may reveal this hidden population or shed light on their absence.

6.2 FUTURE OUTLOOK

The Vera C. Rubin Observatory Legacy Survey of Space and Time (LSST) (LSST Science Collaboration et al., 2009; Ivezić et al., 2019), previously referred to as the Large Synoptic Survey Telescope, is a 10-year synoptic survey expected to start in 2024/25. The telescopes will observe in u, g, r, i, z, y filters with single image 5σ magnitude depths of 23.9, 25.0, 24.7, 24.0, 23.3, 22.1, respectively. With 1×30 s or 2×15 s observations for the main survey, pairs of filters will be observed 22 min apart per night with the following filter combinations $u+g$, $u+r$, $g+r$, $r+i$, $i+z$, $z+y$, or $y+y$ (Jones et al., 2021). One of the four main science themes of the LSST is to explore the transient optical sky and it is predicted to release millions of alerts per night.

The LSST Science Requirements Document[1] requires that each field is visited an average of 825 times over the 10 year survey baseline. This would be accomplished with an average cadence of 3 days, although an optimised cadence(s) is yet to be determined through an ongoing multi-phase process. Currently in the final phase, the recently assembled Survey Cadence Optimization Committee[2] are tasked with making the cadence recommendation within various survey and science constraints. Simulated strategies seen in figure 2 from Bianco et al. (2022) imply an overall cadence (including all filters) higher than the current CRTS cadence, which I determine as approximately 16 – 28 days, on average, based on the CRTS light curves. Most polars remain in an accretion state over timescales of months to years while some very low accretion rate CVs outburst on timescales of decades lasting ~days to ~weeks. Considering that identifying outbursting CVs is an integral part in magnetic CV identification and characterisation in this work, a minimum cadence would be optimal to reduce the possibility of missing outbursts, especially those with the longest outburst cycles. Any cadence less than that of CRTS may lead to improved results for the identification of outbursting CVs.

Compared with the strictly long-term photometric variations the CRTS uses to discover and distinguish between various astronomical transients, the LSST multi-filtered observations over a long-term baseline will include an additional colour component to refine targeted searches. AM CVn systems have been successfully discovered through SDSS by targeting specific colour–colour spaces. Combining colour space searches with the light curves of CVs, as done in this work with CSS0105+19, may prove to be an efficient technique to discover AM CVns through the LSST.

In preparation for the influx of data expected from future large transient or synoptic surveys like LSST, machine learning algorithms for automated classification of

[1] https://ls.st/srd

[2] https://www.lsst.org/content/charge-survey-cadence-optimization-committee-scoc

discoveries are in development. The Supernova Photometric Classification Challenge (SNPhotCC, Kessler et al., 2010) followed by the Photometric LSST Astronomical Time-Series Classification Challenge (PLAsTiCC, Hložek et al., 2020) were competitions for classifying supernovae and later various astronomical transients and variables, respectively, using simulated light curves from LSST-like conditions. PLAsTiCC attracted over 1000 entries to classify galactic and extragalactic sources including tidal disruption events, kilonovae, active galactic nuclei, RR Lyr, eclipsing binaries, M-dwarf flares, with a large focus on the supernovae subclasses. The magnetic CV characterisations I have developed may provide a foundation for machine learning algorithms to identify and characterise magnetic CV candidates within a diverse pool of CVs. Characterising the polars discovered by LSST would provide an opportunity to study a larger, more complete population of polars with emphasis on the accretion state duty cycles.

Acknowledgements

I would like to thank the following people who have contributed towards my PhD:

My supervisors, *Patrick Woudt* and *David Buckley*, for your all-round academic support, for you being available to discuss work, for your patience, for your professional and academic guidance, for being understanding and accommodating during a tough period.

My supervisor, *Brian Warner*, for your wealth of knowledge on CVs and imparting it whenever I had questions, for the interesting and diverse conversations during our trips to Sutherland, for being willing to drive us to Sutherland, for the best cataclysmic variables course lectures.

The National Research Foundation for the financial support throughout my studies.

I acknowledge with thanks the variable star observations from the AAVSO International Database contributed by observers worldwide and used in this research.

Marissa Kotze for your mentorship and friendship. I valued all our moments together.

Sally and *Deanne* for showing the ropes w.r.t. observing and reducing data, *Deanne Coppejans* for your PDM code and discussions on CRTS data of magnetic CVs vs dwarf novae.

Sally, *Hannes* and *Kerry* for observing some of my targets during your observing runs.

Enrico Kotze for the Doppler tomography analysis of ASASSN-14ei spectra and the follow-up discussions.

Elme Breedt for the spectra of CSS0105+19 and CSS2333-15.

John Thorstensen for the collaboration on targets I identified for follow-up, MLS0720+17 and CSS0812+04.

Paul Mason for the collaboration on CSS0350+32 which I identified for follow-up.

Steve Potter for the photo-polarimetric data of MLS1525-03 and the discussion regarding the interpretation of the data.

Kurt van Heyden for financial support during the last leg of my PhD.

My mother for your unconditional personal support and patience throughout my entire academic journey, even when you were unsure of what my career choice entails.

Uncle Ben for supporting and encouraging me in my decision to pursue a career in astronomy as a young teenager.

Uncle Khomotso for generously extending your home to me.

Itumeleng, *Sulona* and *Elias* for your PhD camaraderie. It was reassuring having friends going through what I was going through and trusting each other enough to open up about our struggles. Also for the many great times we had hanging out and enjoying life.

Lennart for your constant personal and academic support, for your attention to detail and for making it possible for me to meet my thesis submission deadline. I appreciate you.

Tshiamiso and *Reikanseone* for your friendship within and outside of the astronomy department, especially when I needed friends nearby.

Roz, *Nicky* and *Carol* for tending to my departmental needs, and the corridor conversations.

Linda for the meaningful conversations and for looking out for me during a tough time in my life.

Salsa for igniting a passion within me and for enhancing the quality of all of my international academic trips thus far.

APPENDIX A

Long-term CRTS light curves and Lomb Scargle periodograms

A.1 Long-term CRTS light curves

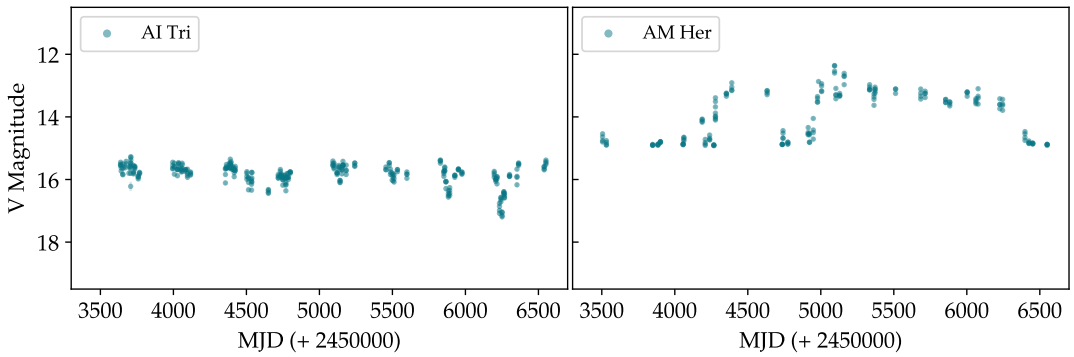

Figure A.1.1 – Long-term CRTS light curve of AI Tri and AM Her.

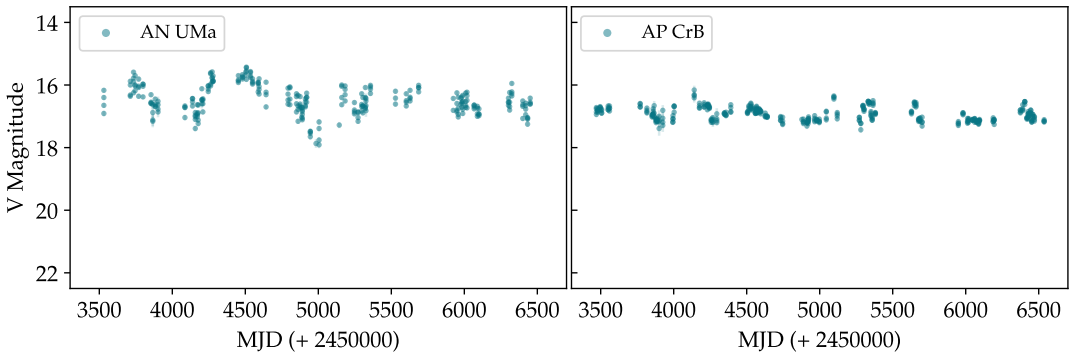

FIGURE A.1.2 – Long-term CRTS light curve of AN UMa and AP CrB.

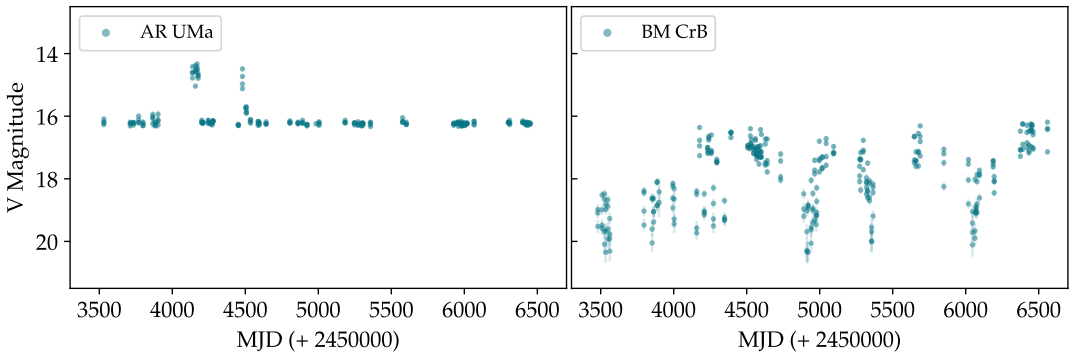

FIGURE A.1.3 – Long-term CRTS light curve of AR UMa and BM CrB.

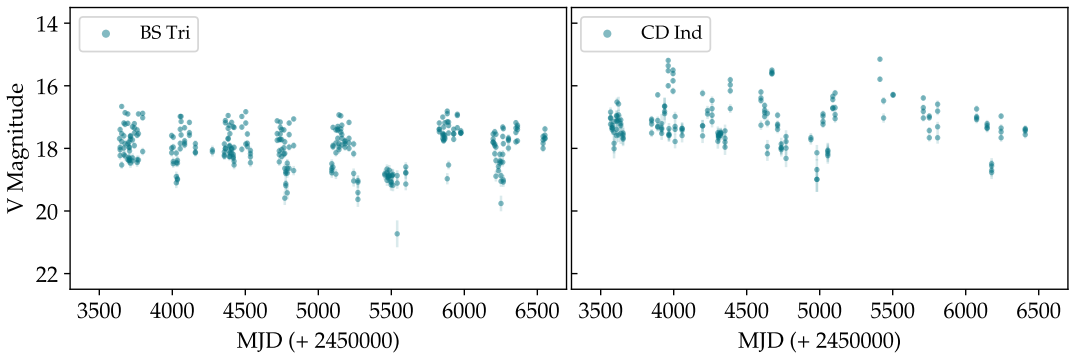

FIGURE A.1.4 – Long-term CRTS light curve of BS Tri and CD Ind.

A.2 LOMB SCARGLE PERIODOGRAMS

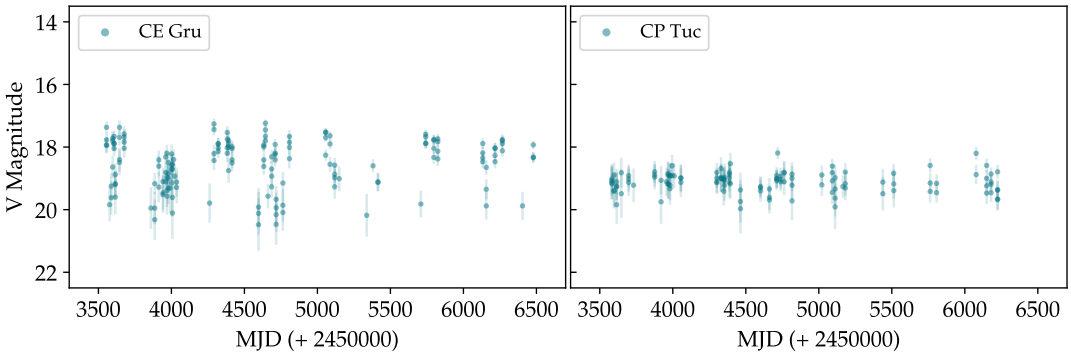

FIGURE A.1.5 – Long-term CRTS light curve of CE Gru and CP Tuc.

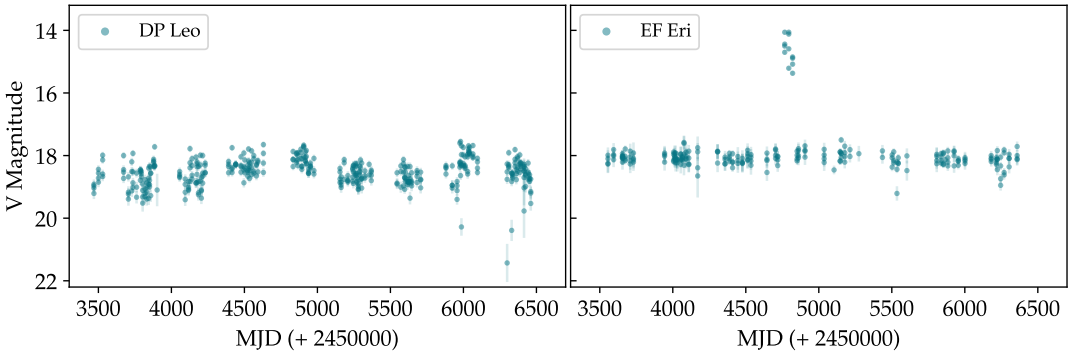

FIGURE A.1.6 – Long-term CRTS light curve of DP Leo and EF Eri.

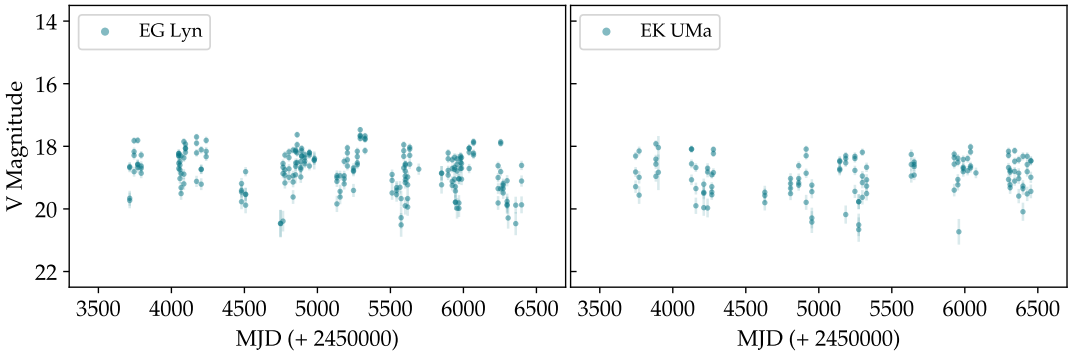

FIGURE A.1.7 – Long-term CRTS light curve of EG Lyn and EK UMa.

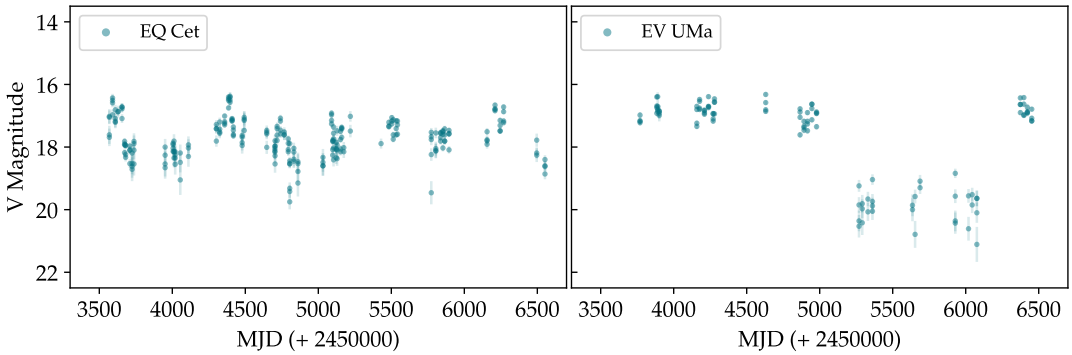

FIGURE A.1.8 – Long-term CRTS light curve of EQ Cet and EV UMa.

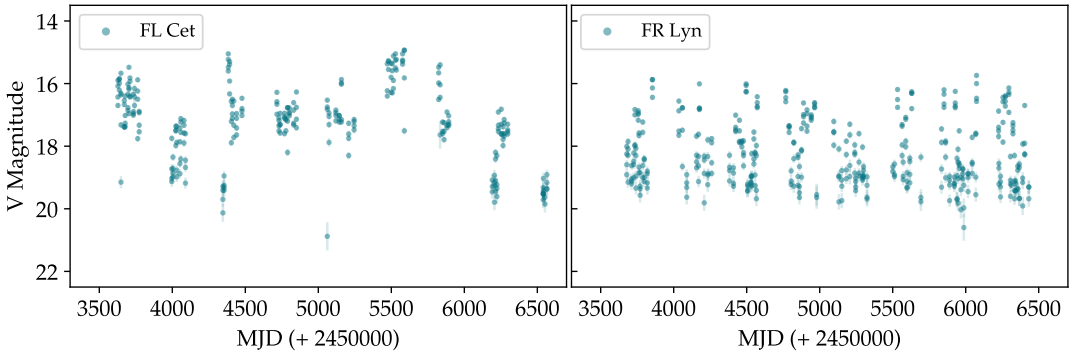

FIGURE A.1.9 – Long-term CRTS light curve of FL Cet and FR Lyn.

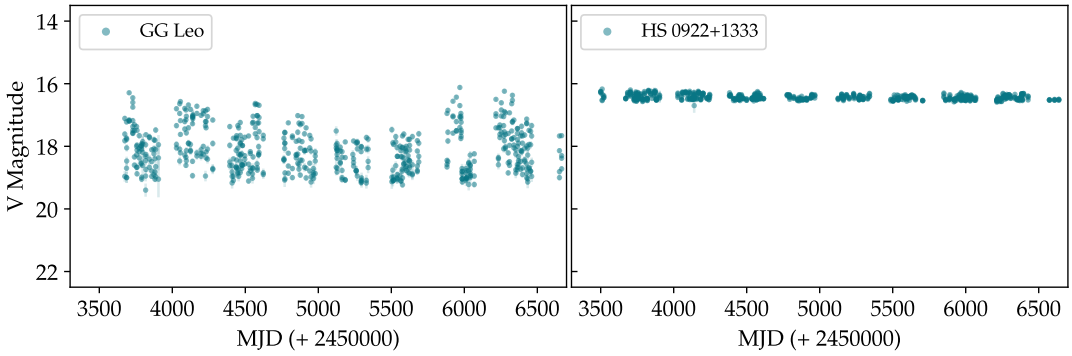

FIGURE A.1.10 – Long-term CRTS light curve of GG Leo and HS 0922+1333.

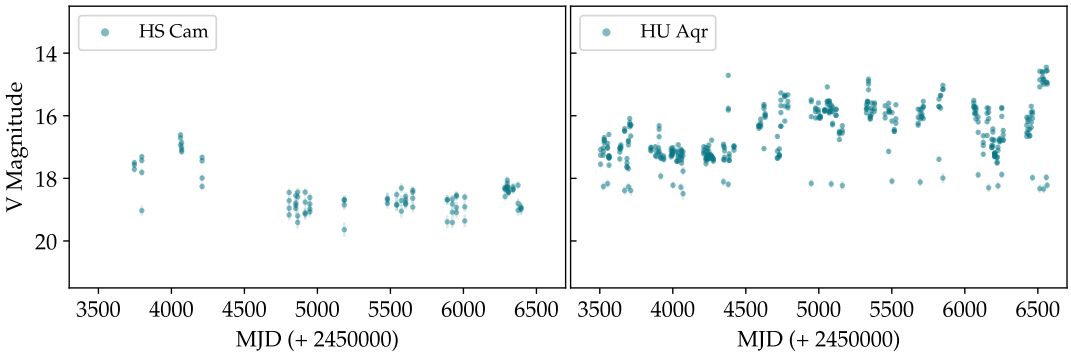

FIGURE A.1.11 – Long-term CRTS light curve of HS Cam and HU Aqr.

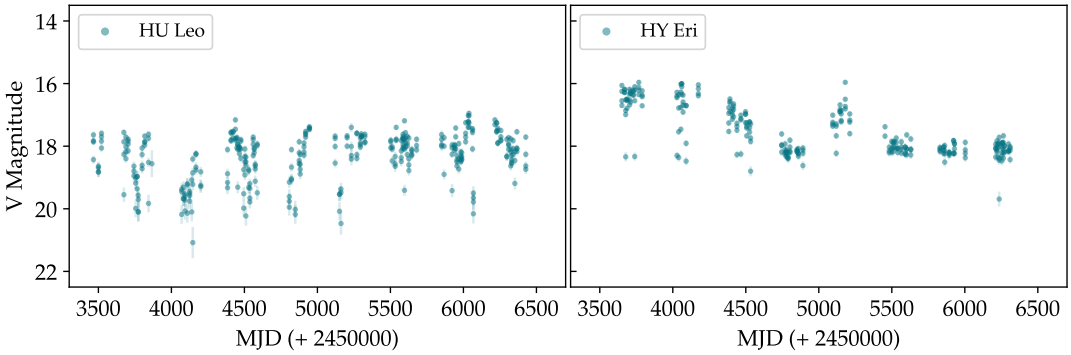

FIGURE A.1.12 – Long-term CRTS light curve of HU Leo and HY Eri.

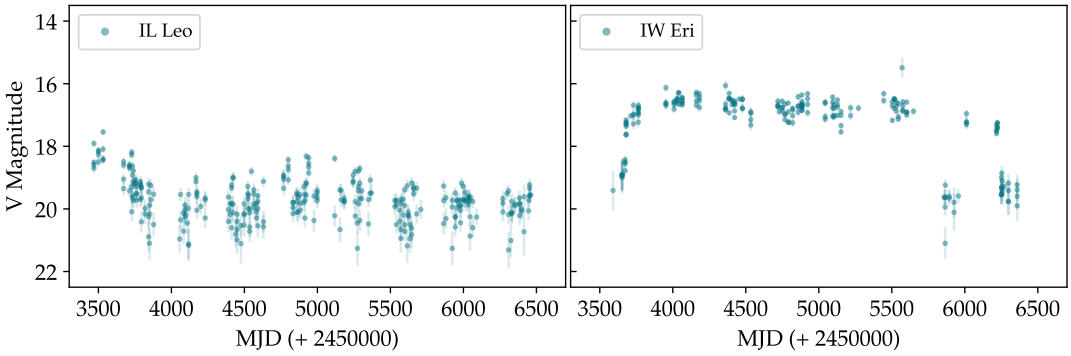

FIGURE A.1.13 – Long-term CRTS light curve of IL Leo and IW Eri.

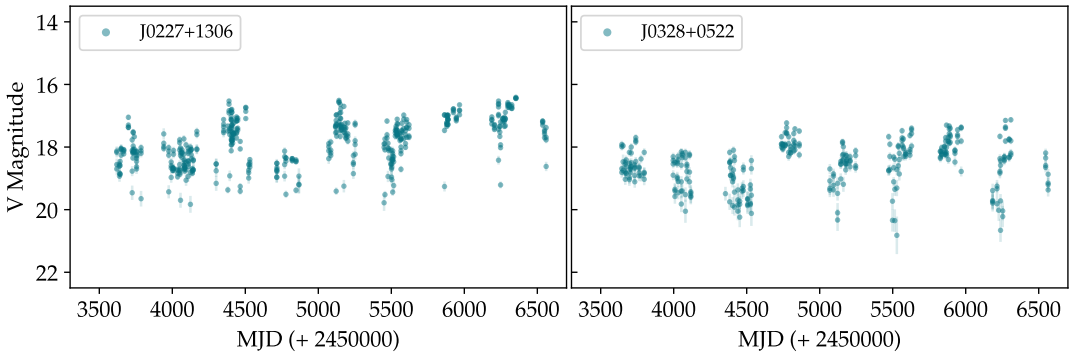

FIGURE A.1.14 – Long-term CRTS light curve of J0227+1306 and J0328+0522.

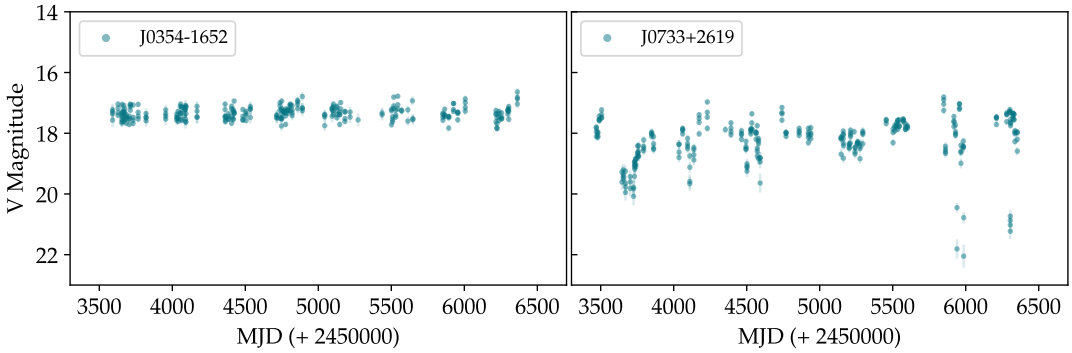

FIGURE A.1.15 – Long-term CRTS light curve of J0354-1652 and J0733+2619.

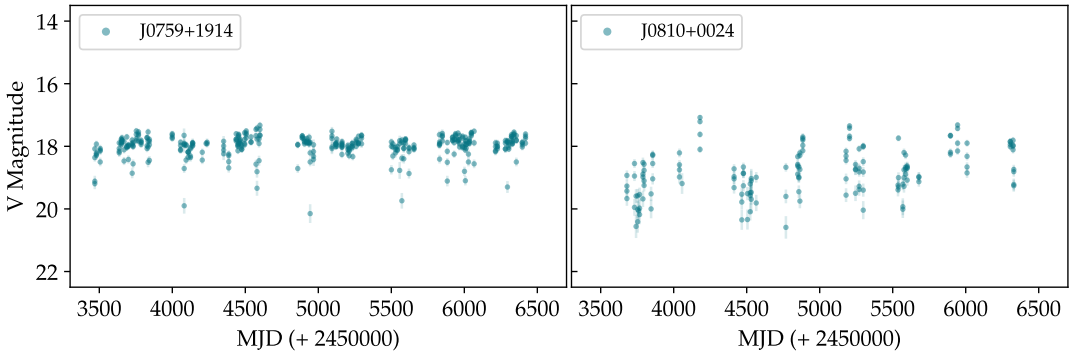

FIGURE A.1.16 – Long-term CRTS light curve of J0759+1914 and J0810+0024.

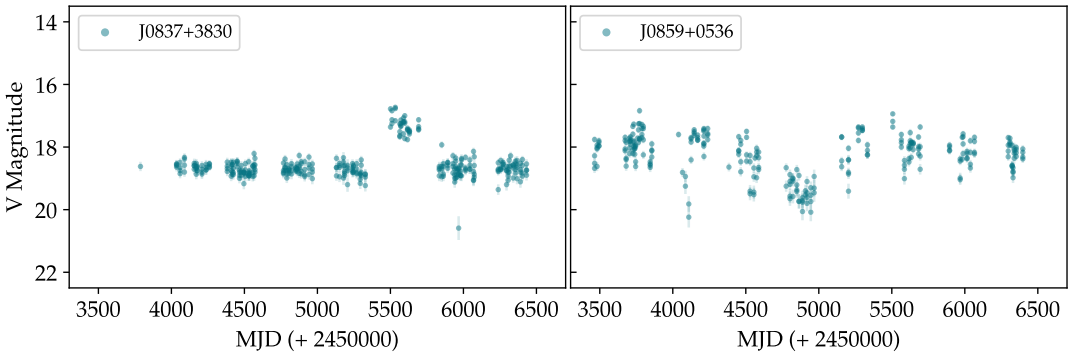

FIGURE A.1.17 – Long-term CRTS light curve of J0354-1652 and J0733+2619.

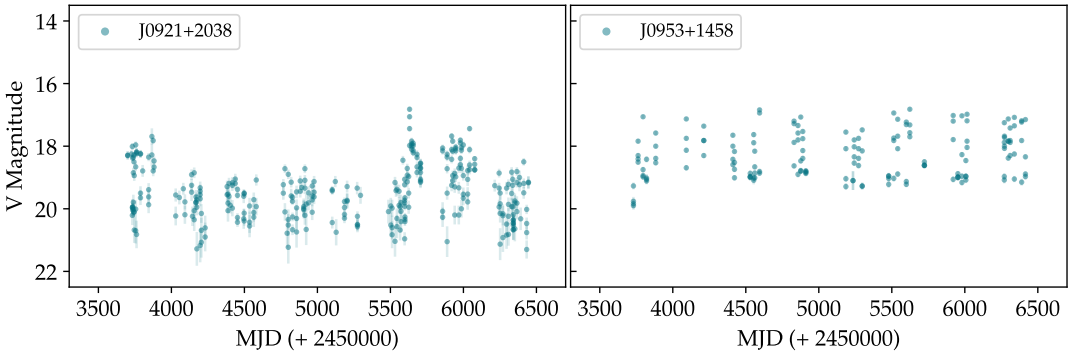

FIGURE A.1.18 – Long-term CRTS light curve of J0354-1652 and J0733+2619.

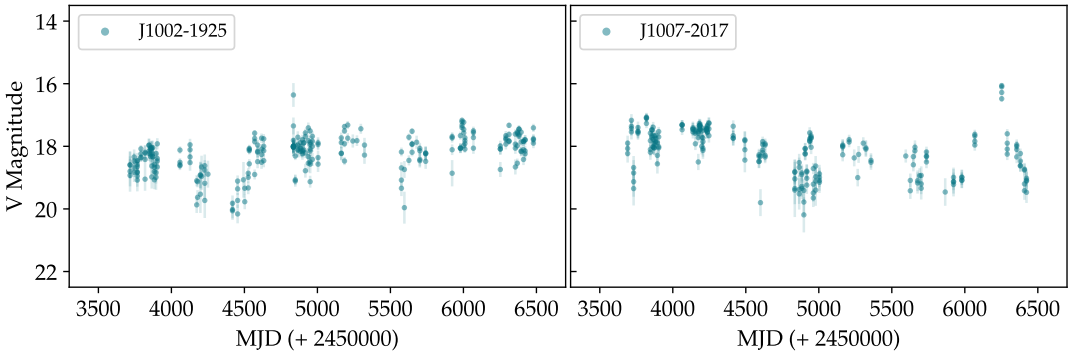

FIGURE A.1.19 – Long-term CRTS light curve of J1002-1925 and J1007-2017.

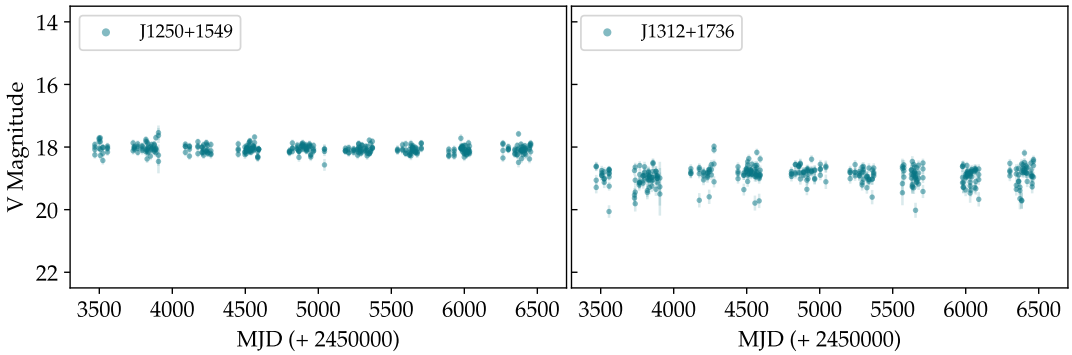

FIGURE A.1.20 – Long-term CRTS light curve of J1250+1549 and J1312+1736.

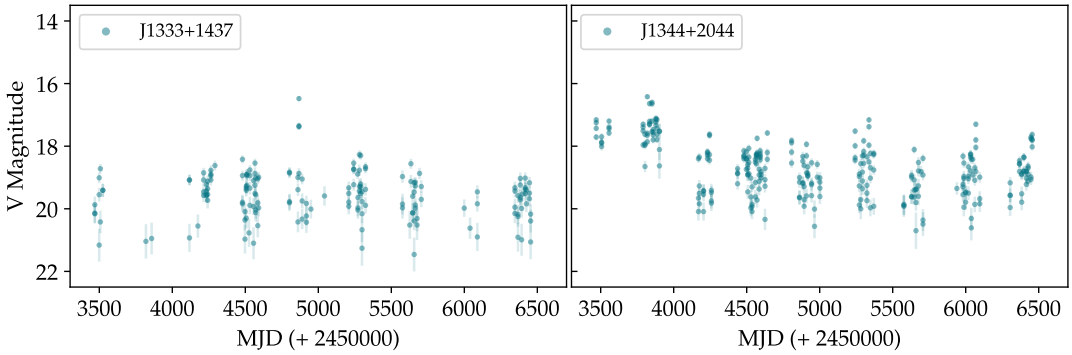

FIGURE A.1.21 – Long-term CRTS light curve of J1333+1437 and J1344+2044.

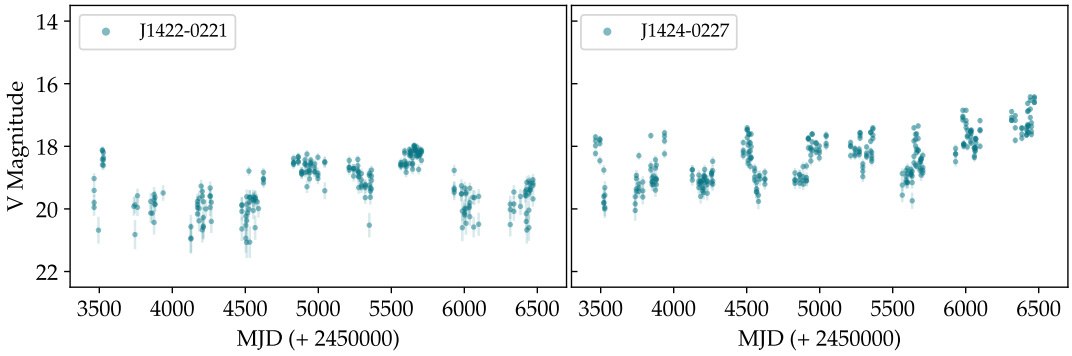

FIGURE A.1.22 – Long-term CRTS light curve of J1422-0221 and J1424-0227.

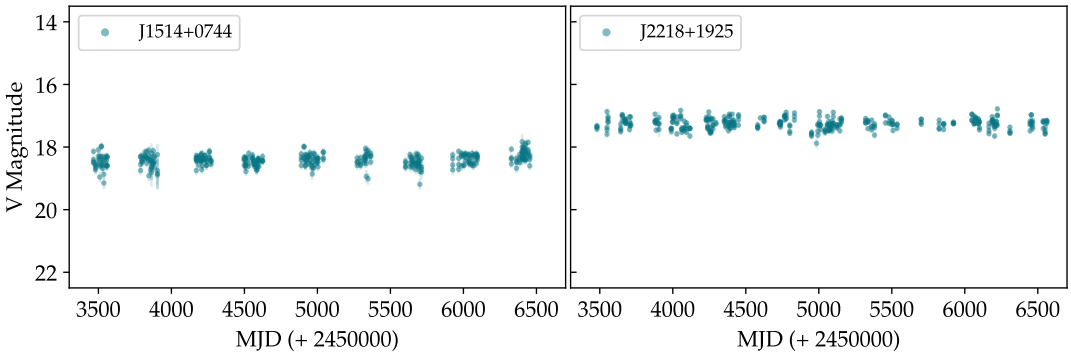

FIGURE A.1.23 – Long-term CRTS light curve of J1514+0744 and J2218+1925.

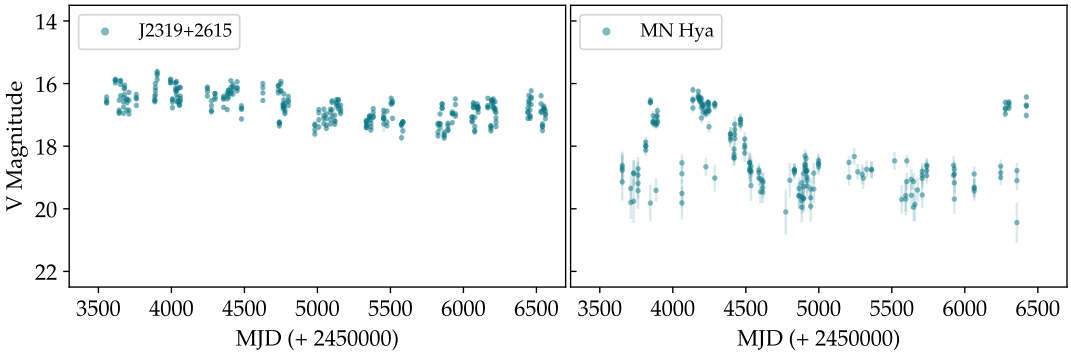

FIGURE A.1.24 – Long-term CRTS light curve of J2319+2615 and MN Hya.

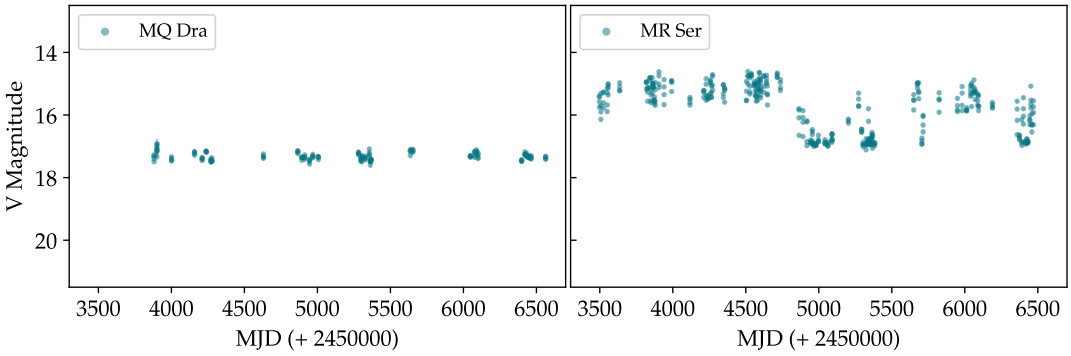

FIGURE A.1.25 – Long-term CRTS light curve of MQ Dra and MR Ser.

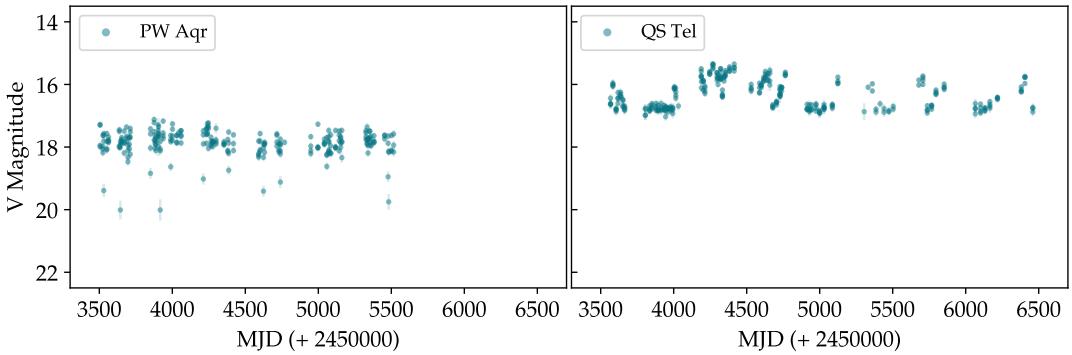

FIGURE A.1.26 – Long-term CRTS light curve of PW Aqr and QS Tel.

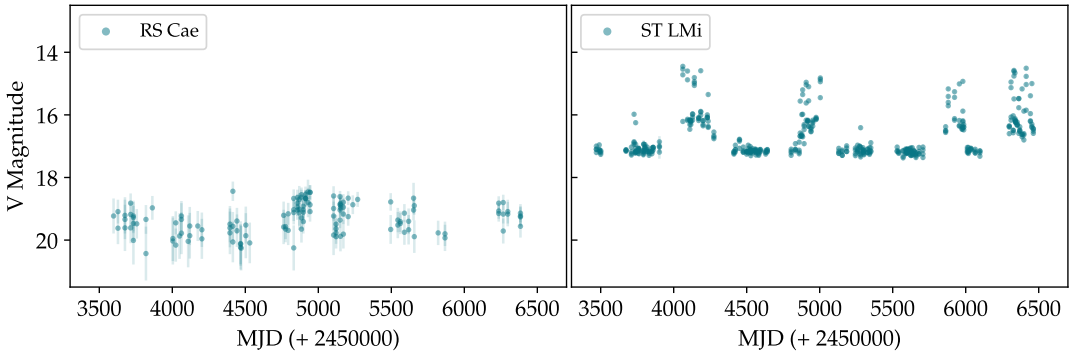

FIGURE A.1.27 – Long-term CRTS light curve of RS Cae and ST LMi.

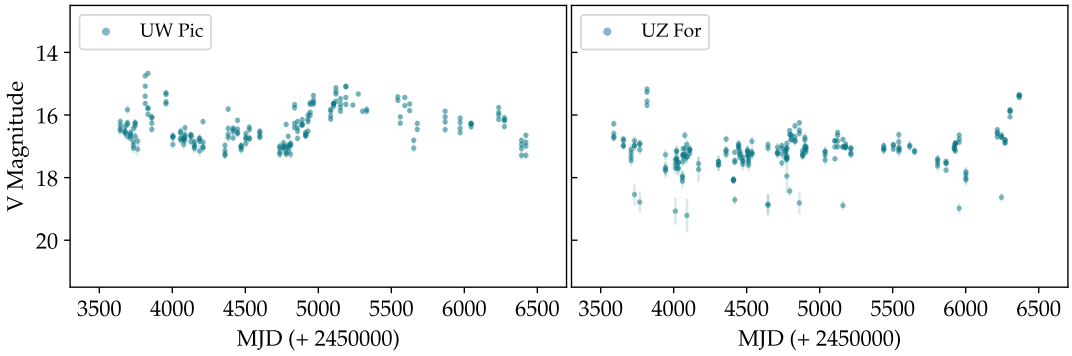

FIGURE A.1.28 – Long-term CRTS light curve of UW Pic and UZ For.

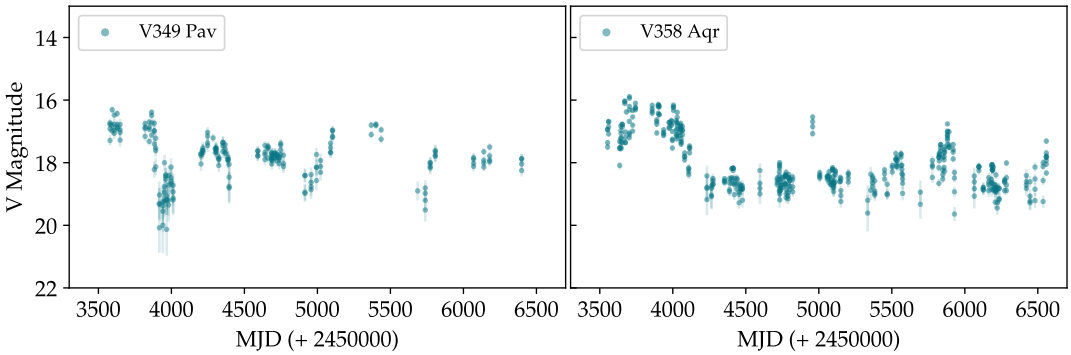

FIGURE A.1.29 – Long-term CRTS light curve of V349 Pav and V358 Aqr.

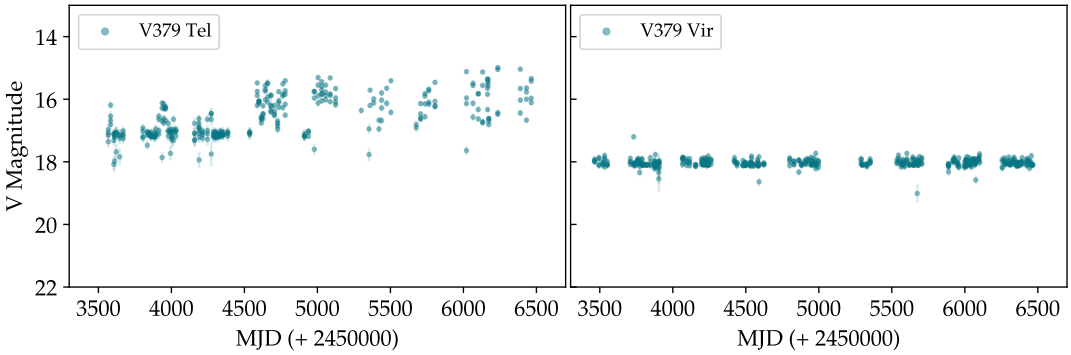

FIGURE A.1.30 – Long-term CRTS light curve of V379 Tel and V379 Vir.

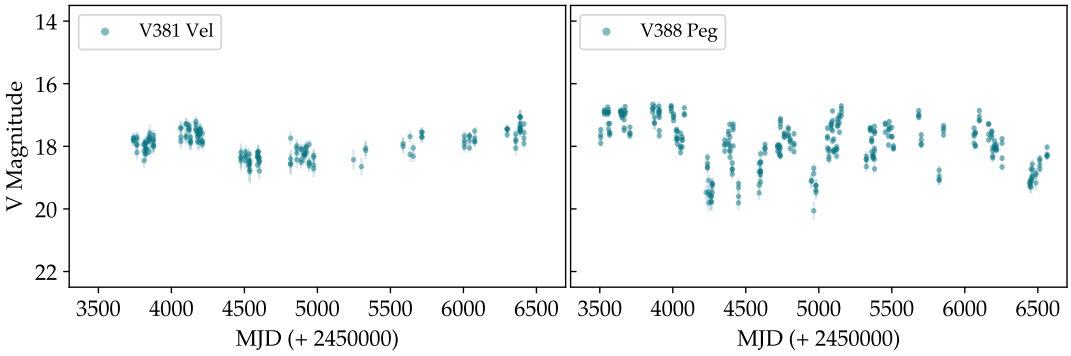

FIGURE A.1.31 – Long-term CRTS light curve of V381 Vel and V388 Peg.

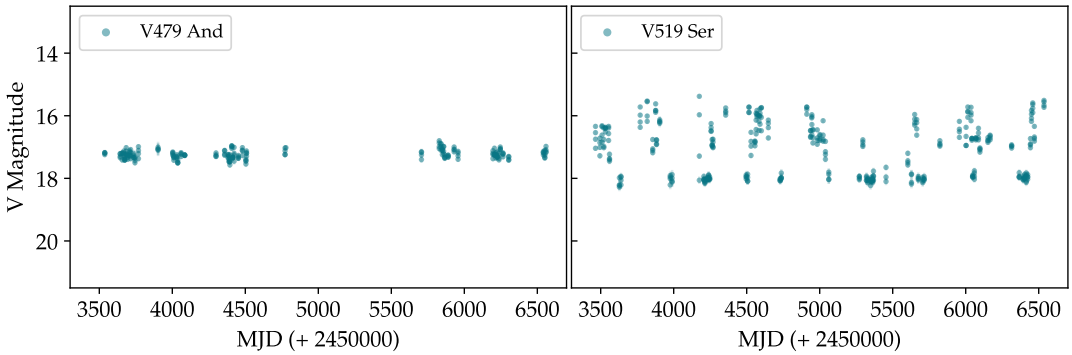

FIGURE A.1.32 – Long-term CRTS light curve of V479 And and V519 Ser.

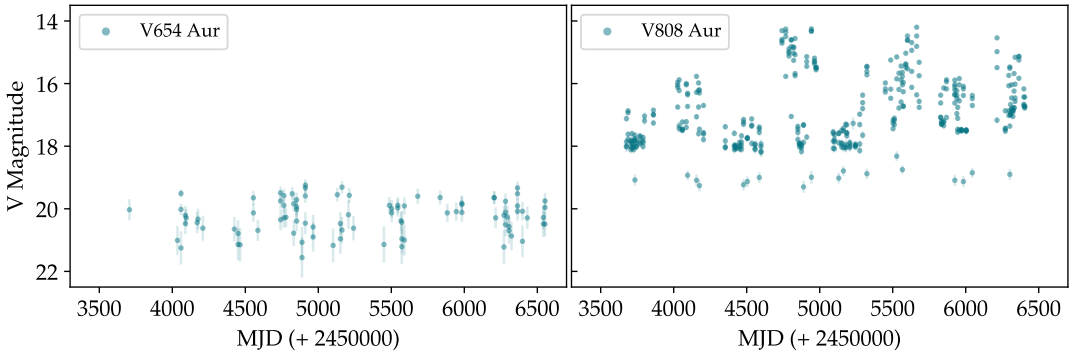

FIGURE A.1.33 – Long-term CRTS light curve of V654 Aur and V808 Aur.

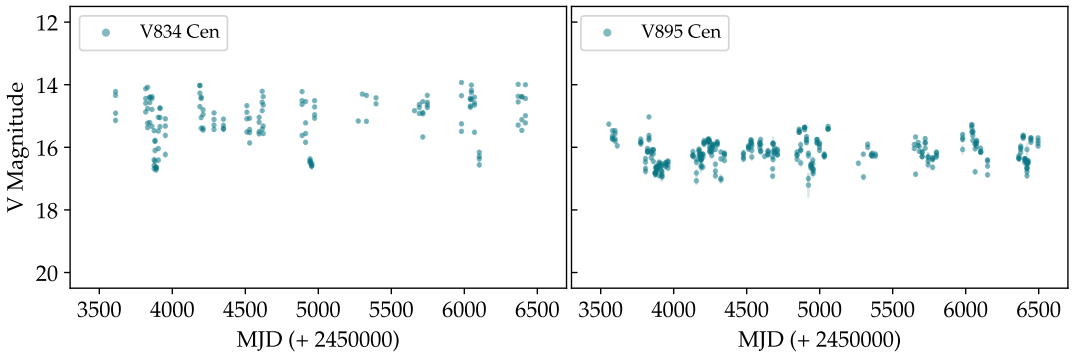

FIGURE A.1.34 – Long-term CRTS light curve of V834 Cen and V895 Cen.

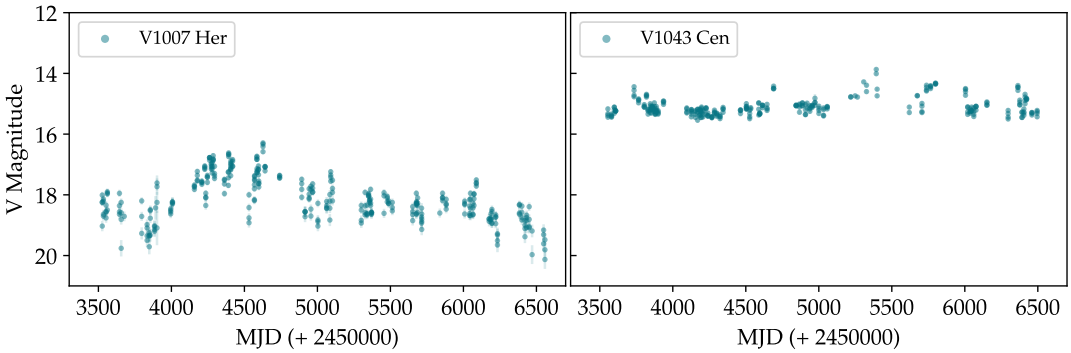

FIGURE A.1.35 – Long-term CRTS light curve of V1007 Her and V1043 Cen.

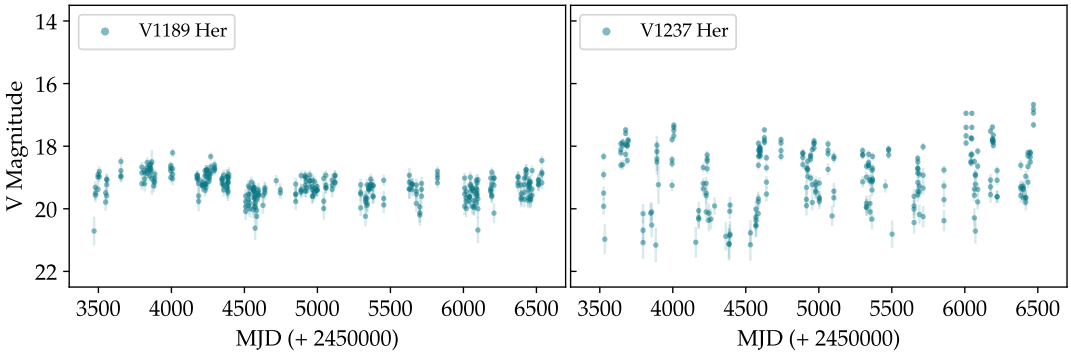

FIGURE A.1.36 – Long-term CRTS light curve of V1189 Her and V1237 Her.

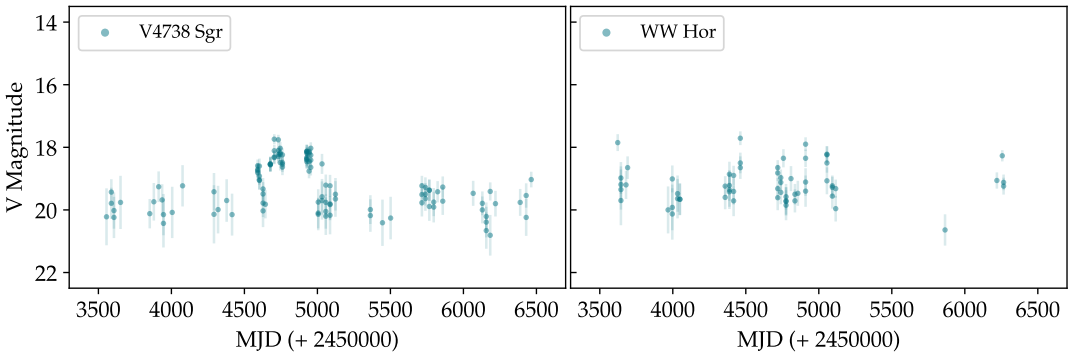

FIGURE A.1.37 – Long-term CRTS light curve of V4738 Sgr and WW Hor.

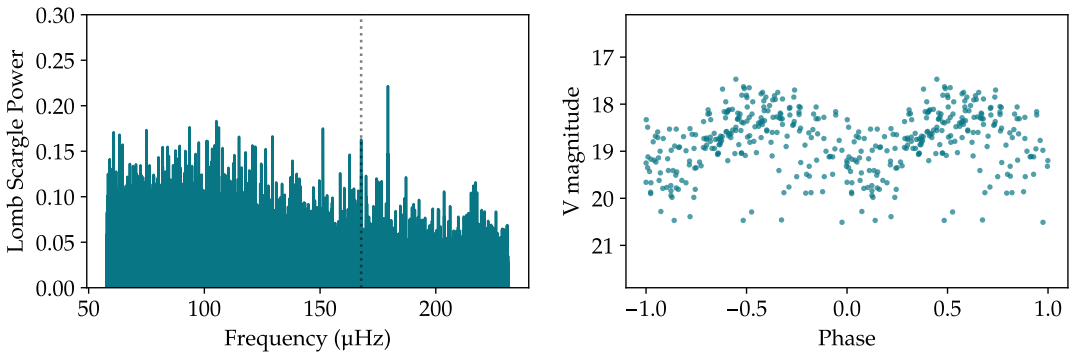

FIGURE A.2.1 – EG Lyn: Lomb Scargle periodogram (left) and CRTS light curve folded over the Lomb Scargle period of 0.0689941 d (right).

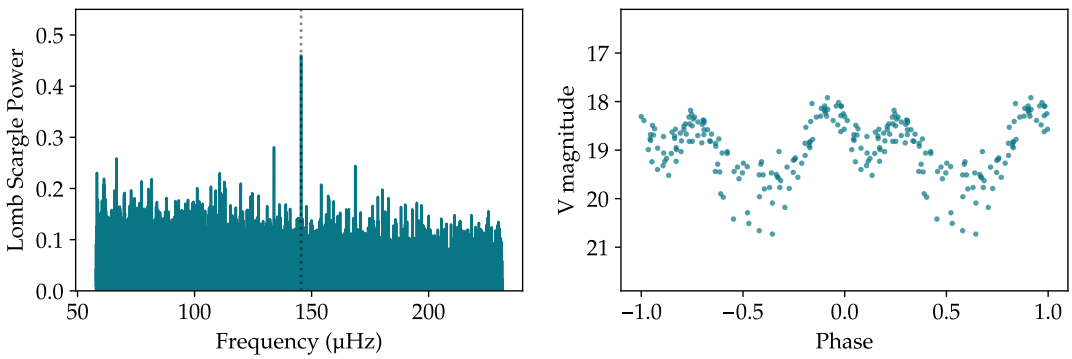

FIGURE A.2.2 – EK UMa: Lomb Scargle periodogram (left) and CRTS light curve folded over the Lomb Scargle period of 0.079544 d (right).

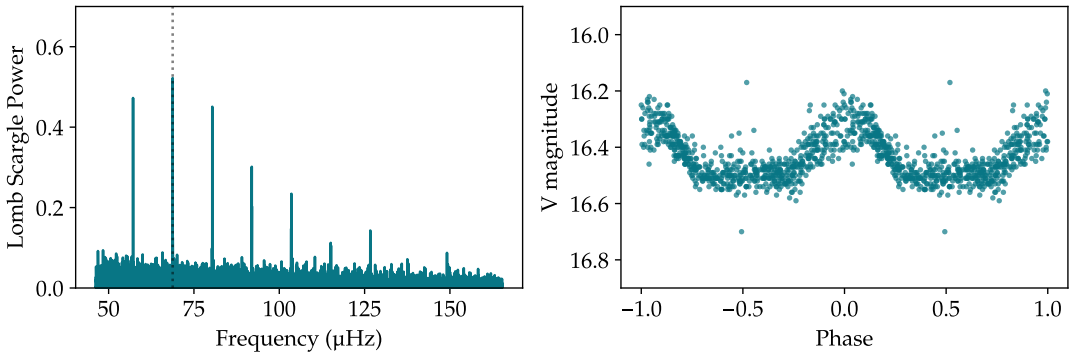

FIGURE A.2.3 – HS0922+1333: Lomb Scargle periodogram (left) and CRTS light curve folded over the Lomb Scargle period of 0.168312 d (right).

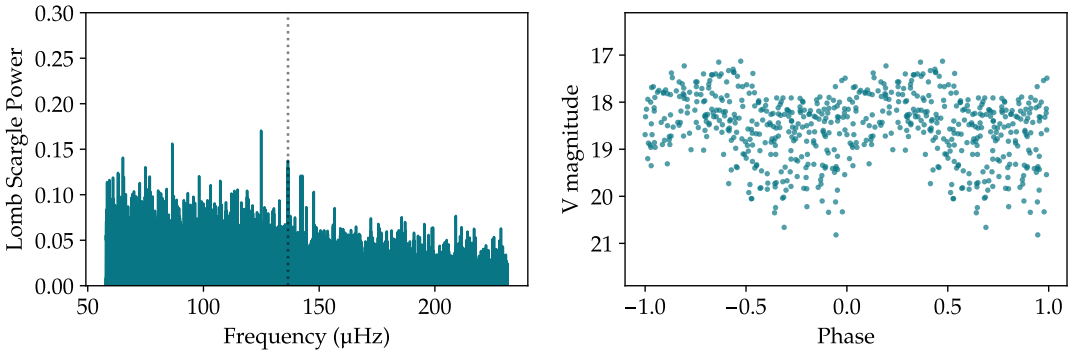

FIGURE A.2.4 – J0328+0522: Lomb Scargle periodogram (left) and CRTS light curve folded over the Lomb Scargle period of 0.084768 d (right).

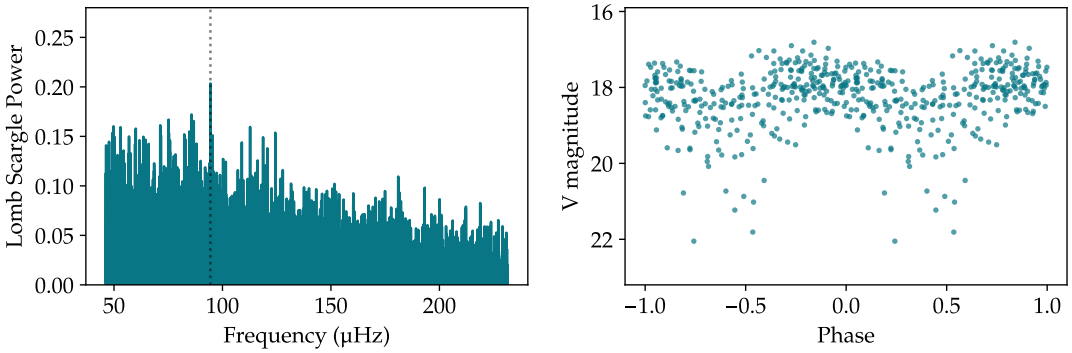

FIGURE A.2.5 – J0733+2619: Lomb Scargle periodogram (left) and CRTS light curve folded over the Lomb Scargle period of 0.093085 d (right).

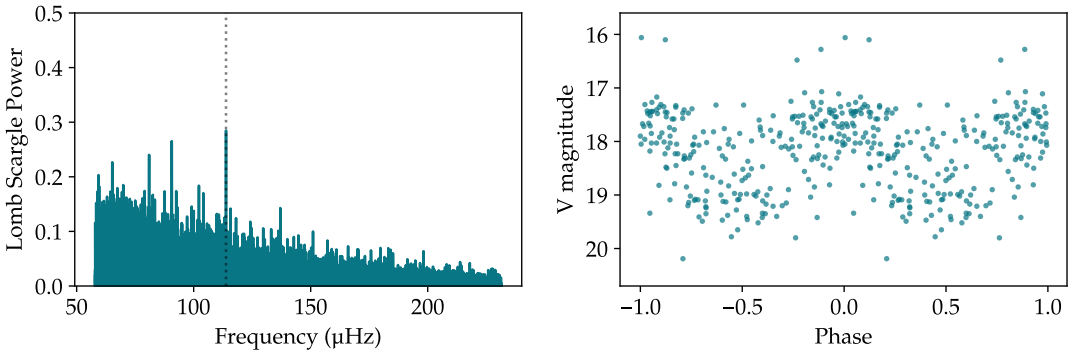

FIGURE A.2.6 – J1007-2017: Lomb Scargle periodogram (left) and CRTS light curve folded over the Lomb Scargle period of 0.101688 d (right).

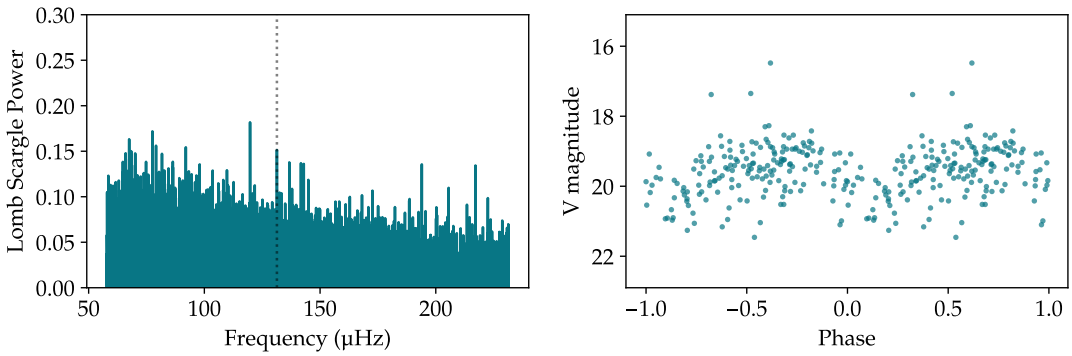

FIGURE A.2.7 – J1333+1437: Lomb Scargle periodogram (left) and CRTS light curve folded over the Lomb Scargle period of 0.088117 d (right).

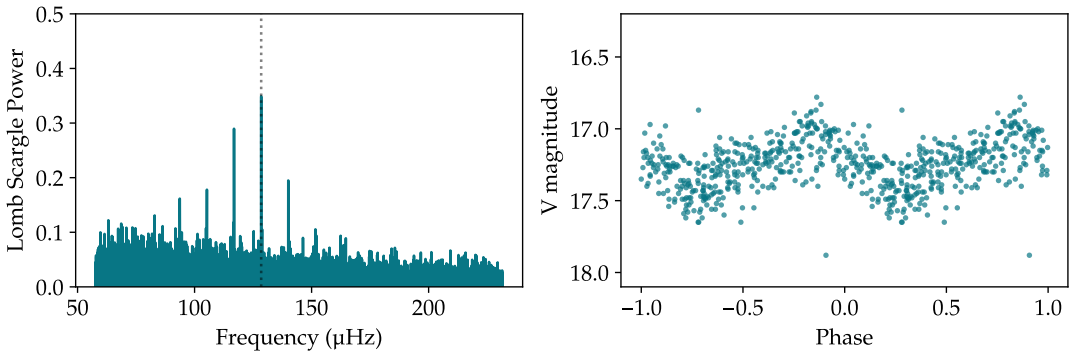

FIGURE A.2.8 – J2218+1925: Lomb Scargle periodogram (left) and CRTS light curve folded over the Lomb Scargle period of 0.090099 d (right).

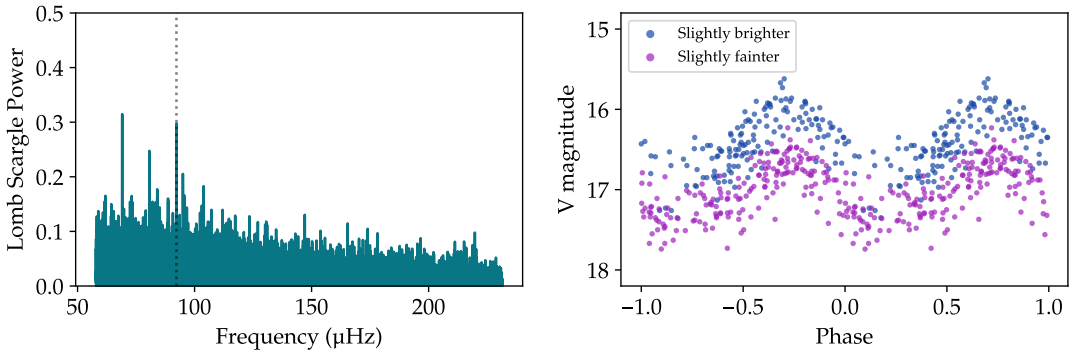

FIGURE A.2.9 – J2319+2615: Lomb Scargle periodogram (left) and CRTS light curve folded over the Lomb Scargle period of 0.125456 d (right).

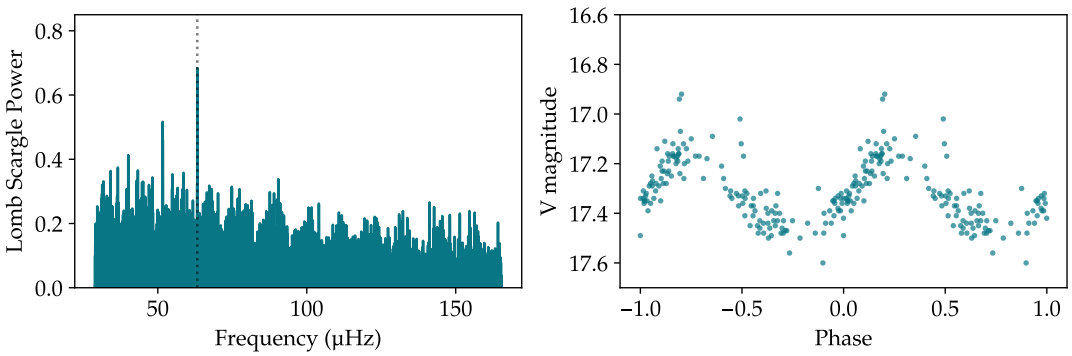

FIGURE A.2.10 – MQ Dra: Lomb Scargle periodogram (left) and CRTS light curve folded over the Lomb Scargle period of 0.182987 d (right).

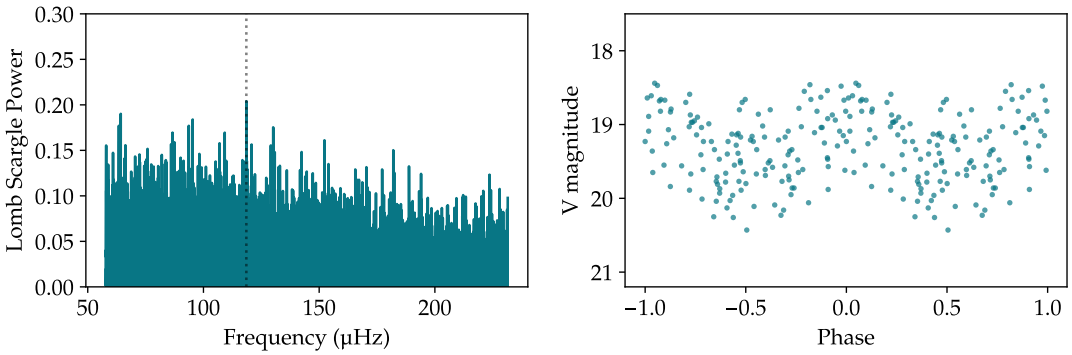

FIGURE A.2.11 – RS Cae: Lomb Scargle periodogram (left) and CRTS light curve folded over the Lomb Scargle period of 0.097644 d (right).

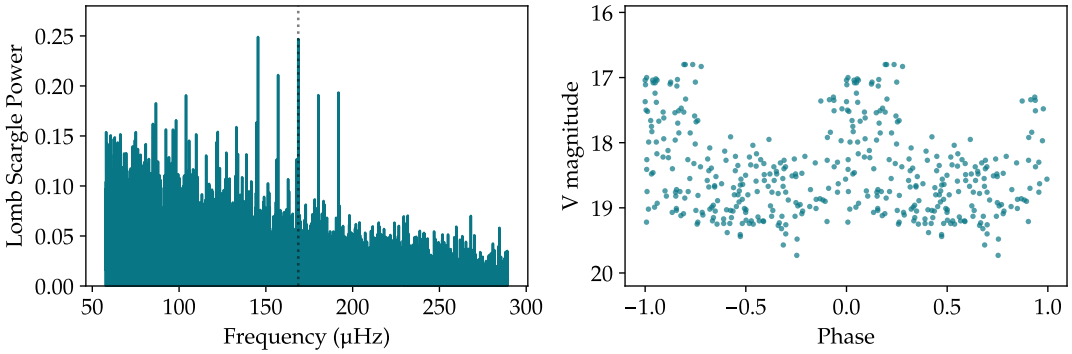

FIGURE A.2.12 – V393 Pav: Lomb Scargle periodogram (left) and CRTS light curve folded over the Lomb Scargle period of 0.0686249 d (right).

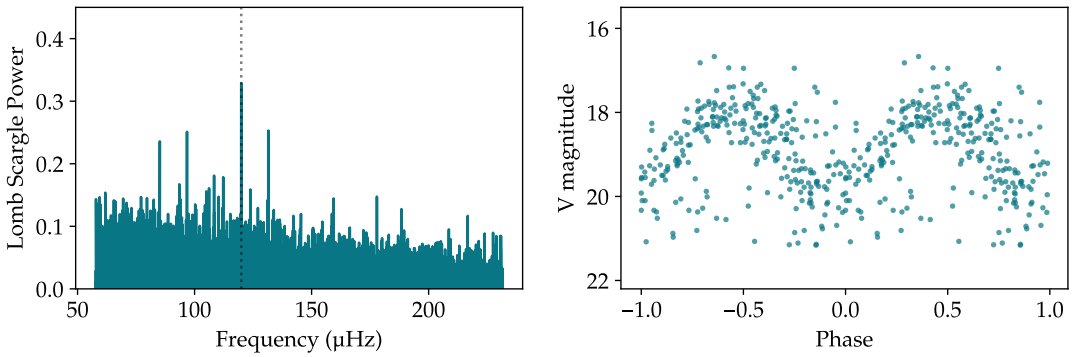

FIGURE A.2.13 – V1237 Her: Lomb Scargle periodogram (left) and CRTS light curve folded over the Lomb Scargle period of 0.096498 d (right).

APPENDIX B

Analysis of long-term polar light curves for characterisation

B.1 Histograms for the different characterisations

This section contains the histograms of previously known polars from RKcat. The seasonal histograms are in the top 9 subplot and the larger histogram of the magnitudes of the long-term light curve is below. Density plots and Gaussian mixture models are presented with each histogram. Two examples are shown for two-state, three-state, slightly variable, stable and large scatter systems, respectively.

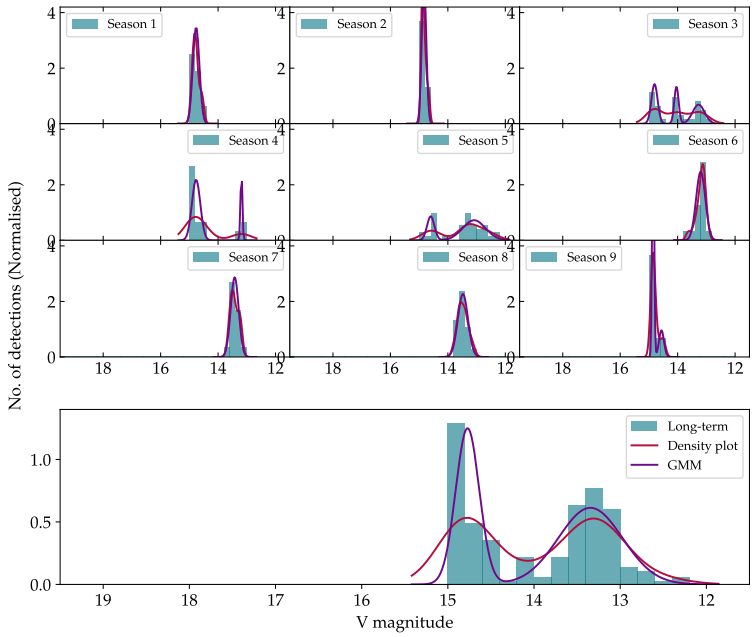

FIGURE B.1.1 – The histogram (teal), density plot (red) and Gaussian Mixture model (purple) of AM Her magnitudes with two states from the CRTS light curve. The top smaller plots are seasonal and the bottom panel is long-term.

B.2 RESULTS FROM QUANTITATIVE ANALYSIS OF THE POLARS TEST SAMPLE

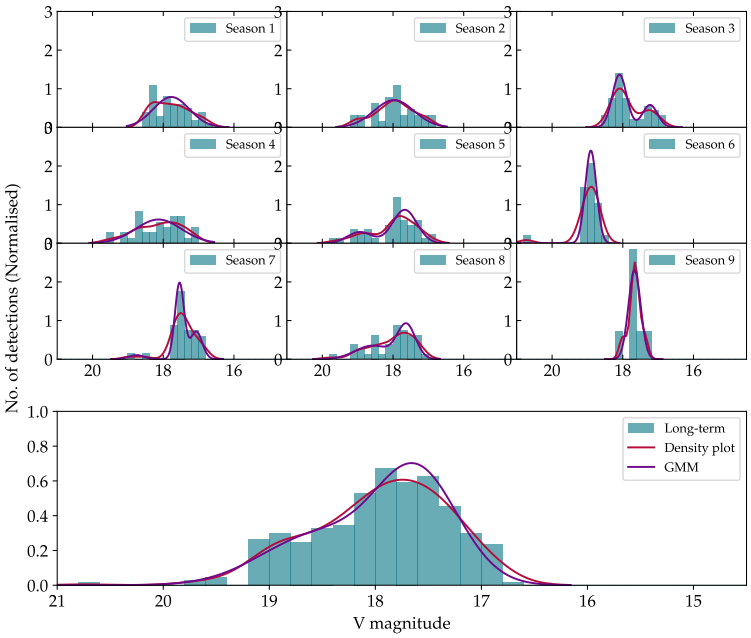

FIGURE B.1.2 – The histogram (teal), density plot (red) and Gaussian Mixture model (purple) of the BS Tri magnitudes with two states from the CRTS light curve. The top smaller plots are seasonal and the bottom panel is long-term.

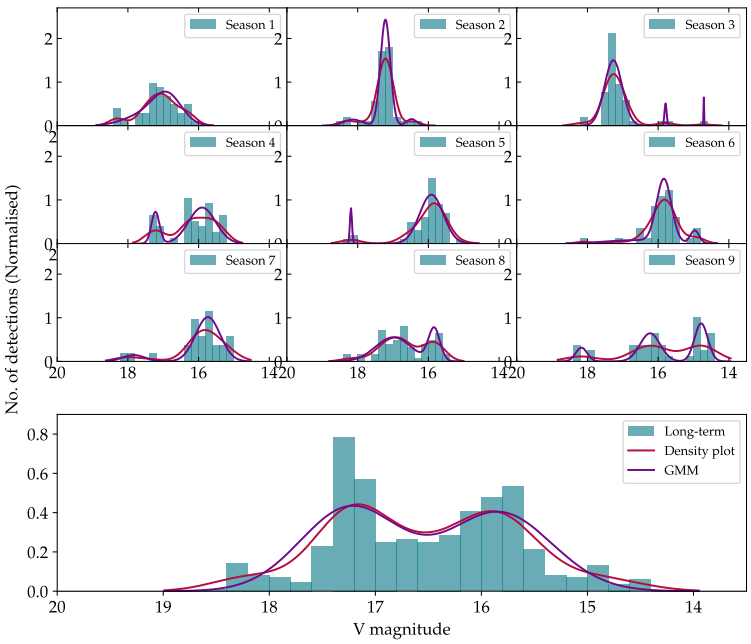

FIGURE B.1.3 – The histogram (teal), density plot (red) and Gaussian Mixture model (purple) of the HU Aqr magnitudes with three states from the CRTS light curve. The top smaller plots are seasonal and the bottom panel is long-term.

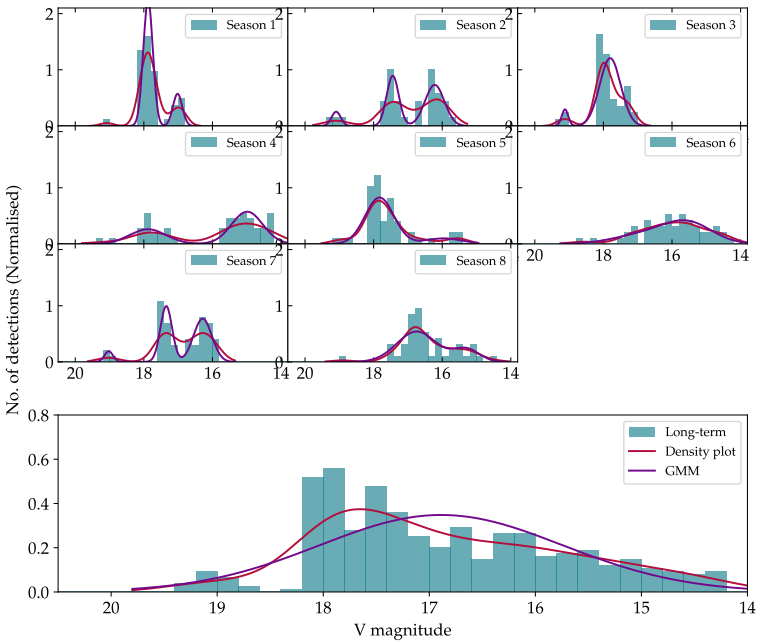

FIGURE B.1.4 – The histogram (teal), density plot (red) and Gaussian Mixture model (purple) of V808 Aur magnitudes with three states from the CRTS light curve. The top smaller plots are seasonal and the bottom panel is long-term.

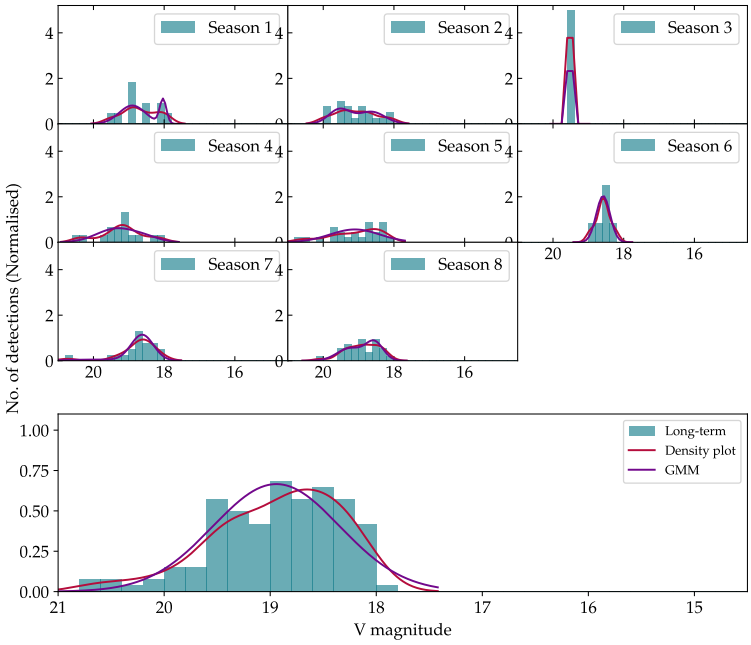

FIGURE B.1.5 – The histogram (teal), density plot (red) and Gaussian Mixture model (purple) of slightly variable EK UMa magnitudes from the CRTS light curve. The top smaller plots are seasonal and the bottom panel is long-term.

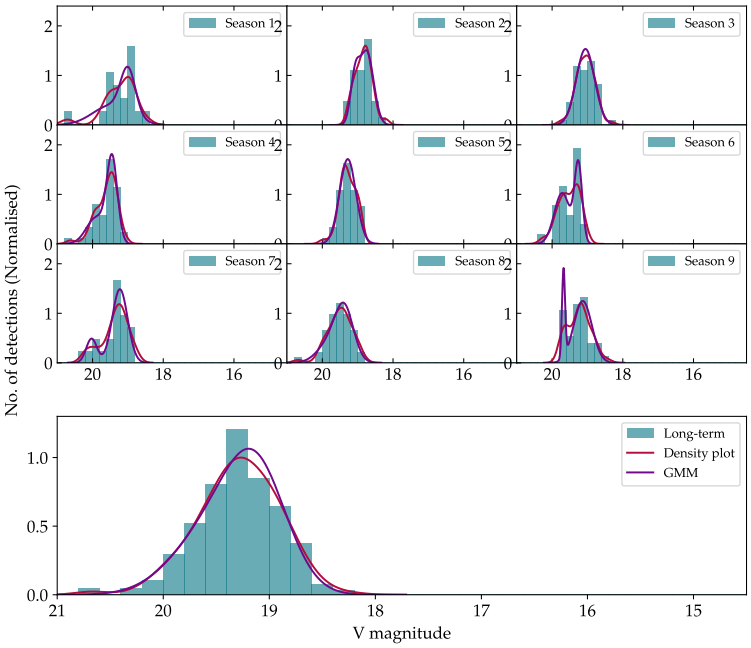

FIGURE B.1.6 – The histogram (teal), density plot (red) and Gaussian Mixture model (purple) of slightly variable V1189 Her magnitudes from the CRTS light curve. The top smaller plots are seasonal and the bottom panel is long-term.

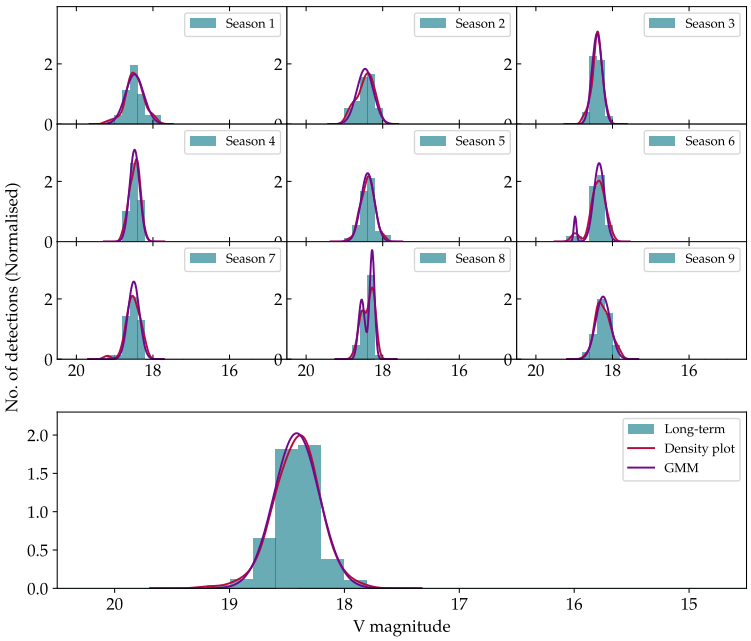

FIGURE B.1.7 – The histogram (teal), density plot (red) and Gaussian Mixture model (purple) of stable J1514+0744 magnitudes from the CRTS light curve. The top smaller plots are seasonal and the bottom panel is long-term.

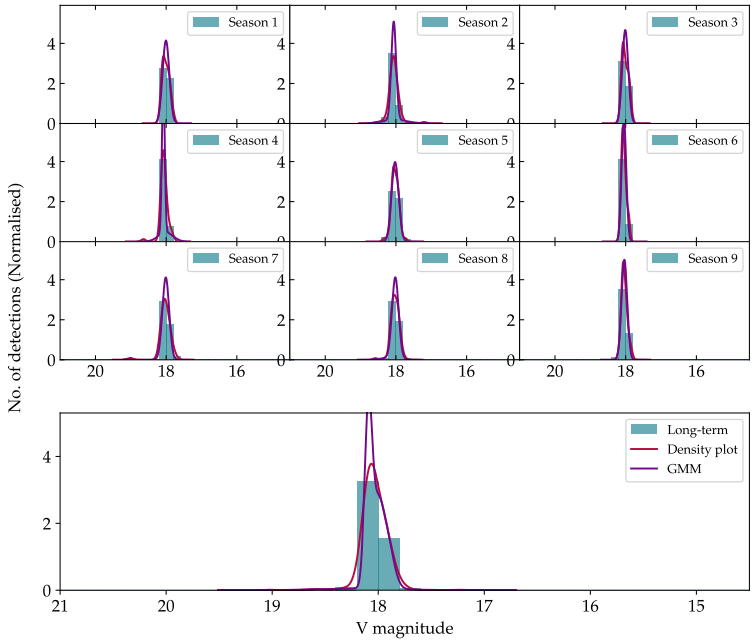

FIGURE B.1.8 – The histogram (teal), density plot (red) and Gaussian Mixture model (purple) of stable V379 Vir magnitudes from the CRTS light curve. The top smaller plots are seasonal and the bottom panel is long-term.

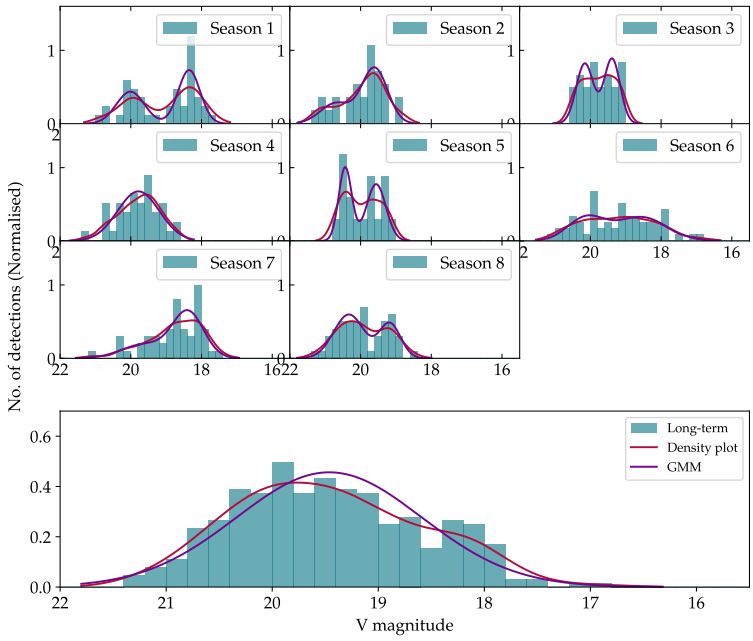

FIGURE B.1.9 – The histogram (teal), density plot (red) and Gaussian Mixture model (purple) of J0921+2038 magnitudes with large scatter from the CRTS light curve. The top smaller plots are seasonal and the bottom panel is long-term.

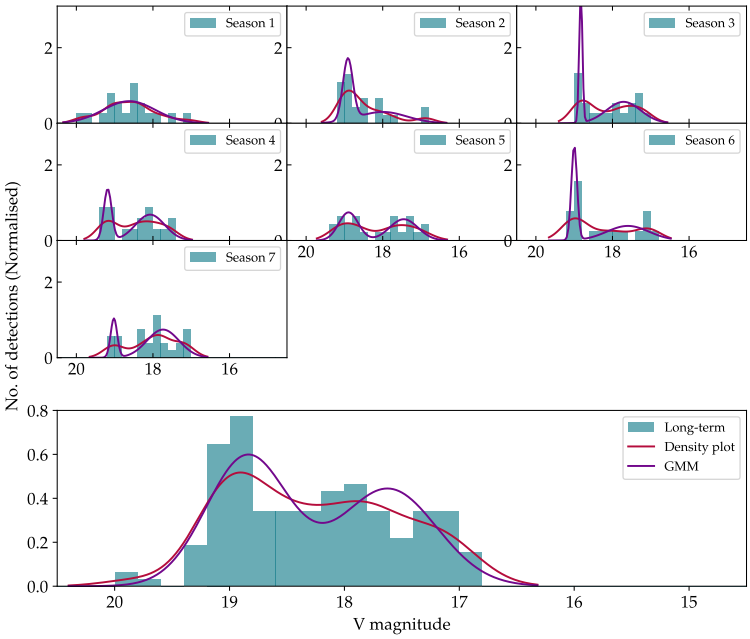

FIGURE B.1.10 – The histogram (teal), density plot (red) and Gaussian Mixture model (purple) of J0953+1458 magnitudes with large scatter from the CRTS light curve. The top smaller plots are seasonal and the bottom panel is long-term.

TABLE B.1 – Results from quantitative analysis of previously known RKcat polars.

Polar	**Characterise1**	**Detail**	**Characterise2**	**Eclipses**	**State division(s)** (mag)	**High-low ratio** high:[int.]:low	**Long-term std deviation**	**Mean seasonal std deviation**
AI Tri	Slightly variable			✗			0.33	0.23
AM Her	Two states	High=low		✗	13.8	0.50:0.50	0.76	0.70
AN UMa	Slightly variable			✗			0.46	0.33
AP CrB	Slightly variable			✗			0.22	0.18
AR UMa	Two states	Low-to-high		✗	15.4	0.12:0.88	0.47	0.22
BM CrB	Two states	High=low		✗	17.6	0.45:0.55	1.08	0.66
BS Tri	Two states	High-to-low	Large scatter	✓	18.1	0.60:0.40	0.64	0.53
CD Ind	Two states	Low-to-high		✗	17.1	0.30:0.70	0.71	0.62
CE Gru	Two states	High-to-low		✗	18.6	0.60:0.40	0.79	0.58
CP Tuc	Slightly variable			✓			0.31	0.31
DP Leo	Slightly variable			✓			0.43	0.36
EF Eri	Three states	Low-to-high		✗	16.3,18.0	0.11:0.11:0.78	0.79	0.38
EG Lyn	Two states	High=low		✓	18.7	0.56:0.44	0.64	0.54
EK UMa	Slightly variable		Large scatter	✓	18.7	0.43:0.57	0.60	0.57
EQ Cet	Two states	Low-to-high		✓	17.1	0.27:0.73	0.61	0.43
EV UMa	Two states	High-to-low		✗	18.5	0.67:0.33	1.39	0.33
FL Cet	Three states	Predom int	Large scatter	✓	15.7,18.2	0.23:0.46:0.31	1.20	0.72
FR Lyn	Two states	High=low	Large scatter	✗	17.6	0.43:0.57	1.04	1.00
HS 0922+1333	Stable			✗			0.08	0.07
HS Cam	Two states	Low-to-high		✗	17.8	0.25:0.75	0.64	0.36
HU Aqr	Three states	Low-to-high	Large scatter	✓	15.3,16.6	0.08:0.50:0.42	0.85	0.65
HU Leo	Two states	High-to-low		✓	19.0	0.73:0.27	0.75	0.63
HY Eri	Two states	High=low		✓	17.6	0.50:0.50	0.77	0.36
IL Leo	Two states	Low-to-high		✗	19.4	0.22:0.78	0.67	0.51
IW Eri	Two states	High-to-low		✗	18.1	0.73:0.27	1.06	0.53

Notes: The results in this table are determined by the programme based on criteria described in Chapter 2. The results may not reflect the true nature of the object. Predom int = Predominantly intermediate, std=standard.

(Continued on next page)

Table B.1 – continued from previous page

Polar	**Characterise1**	**Detail**	**Characterise2**	**Eclipses**	**State division(s)** (mag)	**High-low ratio** high:[int.]:low	**Long-term std deviation**	**Mean seasonal std deviation**
J0227+1306	Two states	High-to-low		✓	17.9	0.67:0.33	0.72	0.49
J0328+0522	Two states	High-to-low		✗	19.1	0.73:0.27	0.72	0.49
J0354-1652	Stable			✗			0.21	0.21
J0733+2619	Slightly variable			✓			0.79	0.57
J0759+1914	Slightly variable			✓			0.35	0.34
J0810+0024	Two states	High-to-low	Large scatter	✗	19.3	0.70:0.30	0.75	0.56
J0837+3830	Two states	Low-to-high		✗	18.0	0.14:0.86	0.49	0.21
J0859+0536	Two states	High-to-low		✗	18.4	0.73:0.27	0.65	0.45
J0921+2038	Two states	High-to-low	Large scatter	✗	19.6	0.50:0.50	0.87	0.69
J0953+1458	Two states	High=low	Large scatter	✗	18.4	0.46:0.54	0.73	0.65
J1002-1925	Two states	High-to-low		✓	18.5	0.78:0.22	0.58	0.45
J1007-2017	Two states	High=low		✓	18.3	0.60:0.40	0.73	0.53
J1250+1549	Stable			✗			0.14	0.14
J1312+1736	Stable			✓			0.29	0.28
J1333+1437	Slightly variable		Large scatter	✓			0.74	0.71
J1344+2044	Two states	High=low	Large scatter	✗	18.6	0.50:0.50	0.84	0.60
J1422-0221	Two states	Low-to-high		✗	19.1	0.40:0.60	0.77	0.44
J1424-0227	Two states	High=low		✗	18.2	0.42:0.58	0.44	0.20
J1514+0744	Stable			✗			0.20	0.18
J2218+1925	Stable			✗			0.17	0.16
J2319+2615	Slightly variable			✗			0.45	0.32
MN Hya	Two states	Low-to-high		✗	18.3	0.40:0.60	1.10	0.72
MQ Dra	Stable			✗			0.12	0.09
MR Ser	Two states	High-to-low		✗	16.0	0.60:0.40	0.75	0.37
PW Aqr	Slightly variable			✓			0.40	0.39
QS Tel	Slightly variable			✗			0.46	0.29

Notes: The results in this table are determined by the programme based on criteria described in Chapter 2. The results may not reflect the true nature of the object. Predom int = Predominantly intermediate, std=standard.

(Continued on next page)

Table B.1 – continued from previous page

Polar	**Characterise1**	**Detail**	**Characterise2**	**Eclipses**	**State division(s)** (mag)	**High-low ratio** high:[int.]:low	**Long-term std deviation**	**Mean seasonal std deviation**
RS Cae	Slightly variable			✗			0.47	0.36
ST LMi	Two states	Low-to-high		✗	15.8	0.31:0.69	0.69	0.36
UW Pic	Two states	High=low		✗	16.3	0.44:0.56	0.56	0.41
UZ For	Two states	Low-to-high		✓	16.8	0.12:0.88	0.62	0.51
V1007 Her	Two states	Low-to-high		✗	18.0	0.30:0.70	0.74	0.43
V1043 Cen	Two states	Low-to-high		✗	14.6	0.18:0.82	0.29	0.22
V1189 Her	Slightly variable			✓			0.39	0.31
V1237 Her	Two states	High=low		✗	18.7	0.47:0.53	0.97	0.86
V1309 Ori	Two states	High-to-low		✓	15.8	0.82:0.18	0.43	0.30
V1432 Aql	Slightly variable			✗			0.40	0.30
V349 Pav	Two states	High-to-low		✗	17.9	0.67:0.33	0.75	0.46
V358 Aqr	Two states	Low-to-high		✗	17.4	0.22:0.78	0.86	0.44
V379 Tel	Two states	High=low		✓	16.3	0.55:0.45	0.65	0.45
V379 Vir	Stable			✓			0.12	0.11
V381 Vel	Slightly variable			✗			0.40	0.22
V388 Peg	Two states	High-to-low		✗	18.6	0.67:0.33	0.76	0.53
V393 Pav	Two states	Low-to-high	Large scatter	✗	18.1	0.36:0.64	0.69	0.50
V4738 Sgr	Two states	High=low		✗	18.9	0.50:0.50	0.77	0.52
V479 And	Stable			✗			0.14	0.12
V519 Ser	Three states	Low-to-high		✗	16.4, 17.4	0.25:0.31:0.44	0.83	0.73
V654 Aur	Slightly variable			✗			0.54	0.51
V808 Aur	Three states	Low-to-high	Large scatter	✓	16.5, 17.1	0.09:0.36:0.55	1.15	0.82
V834 Cen	Three states	High-to-low		✗	15.0, 15.9	0.46:0.31:0.23	0.73	0.61
V895 Cen	Slightly variable			✗			0.40	0.33
WW Hor	Slightly variable			✗			–	–

Notes: The results in this table are determined by the programme based on criteria described in Chapter 2. The results may not reflect the true nature of the object. Predom int = Predominantly intermediate, std=standard.

APPENDIX C

SHOC light curves of individual AM CVn systems and helium dwarf novae

The individual SHOC light curves of AM CVn stars and helium DN are presented in Appendix B. The figures show all the light curves from follow-up observations taken over different nights. They appear in the order that they appear in Chapter 3.

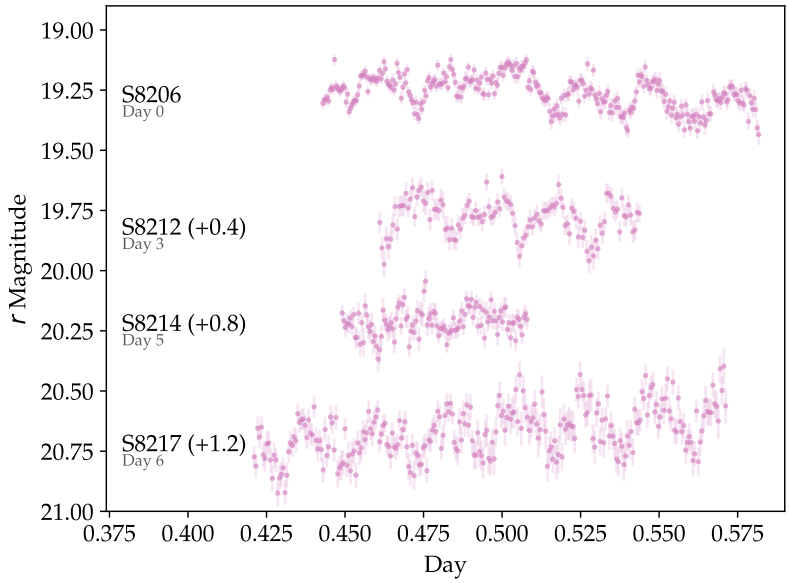

FIGURE C.0.1 – SHOC observations of CSS0105+19 over different nights. The observing run numbers are indicated next to the corresponding light curve. Vertical offsets, indicated by parentheses, are applied to some light curves for visual convenience. The first observation for CSS0105+19 is labelled as Day 0 and the following observations are labelled with respect to Day 0.

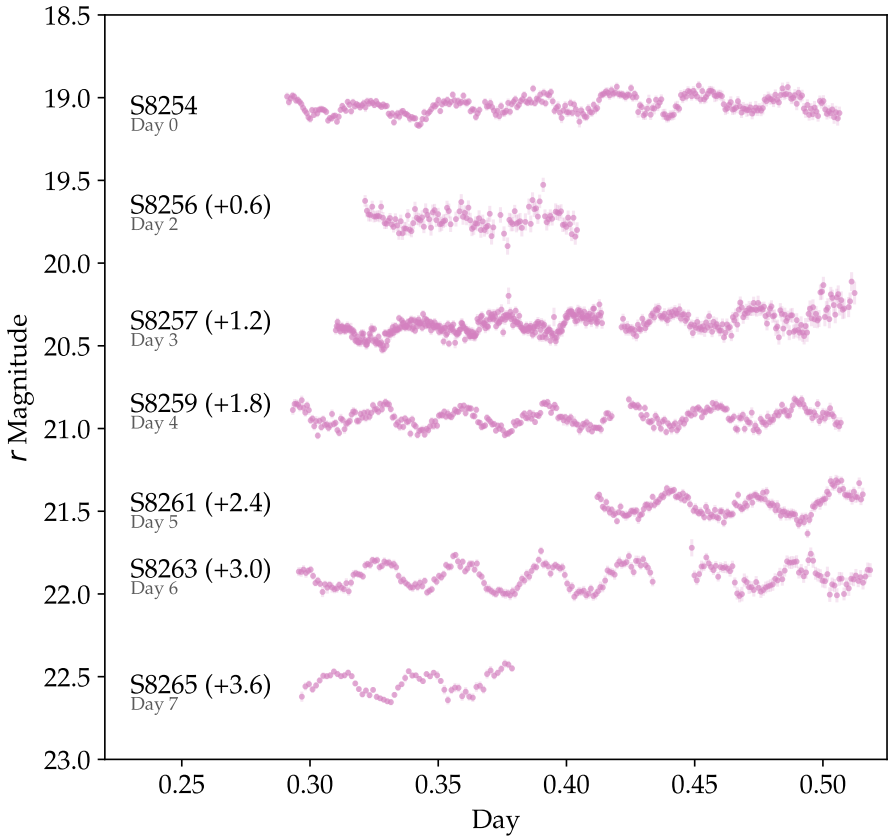

FIGURE C.0.2 – SHOC observations of CSS0450-09 over different nights. The observing run numbers are indicated next to the corresponding light curve. Vertical offsets, indicated by parentheses, are applied to some light curves for visual convenience. The first observation for CSS0450-09 is labelled as Day 0 and the following observations are labelled with respect to Day 0.

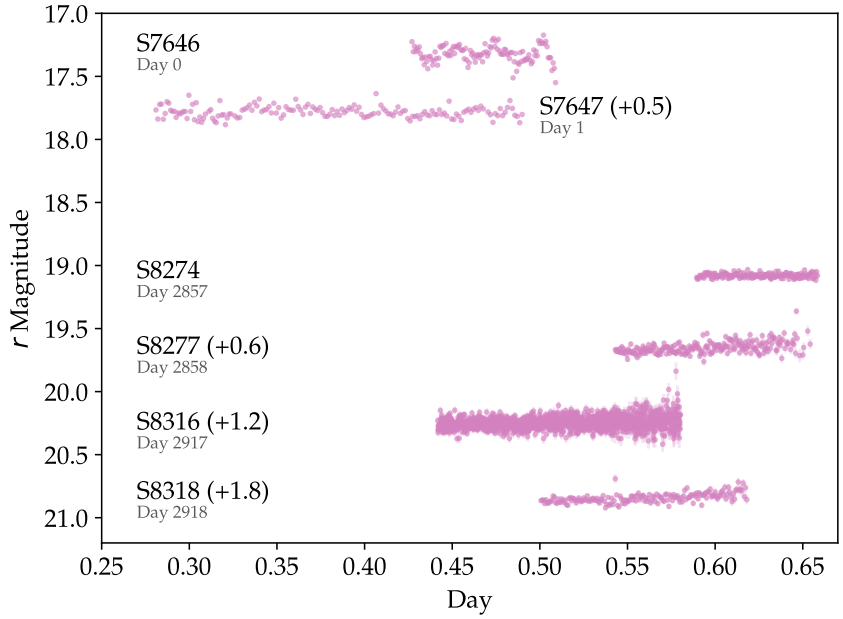

FIGURE C.0.3 – SHOC observations of V558 Vir over different nights. The observing run numbers are indicated next to the corresponding light curve. Vertical offsets, indicated by parentheses, are applied to some light curves for visual convenience. The first observation for V558 Vir is labelled as Day 0 and the following observations are labelled with respect to Day 0.

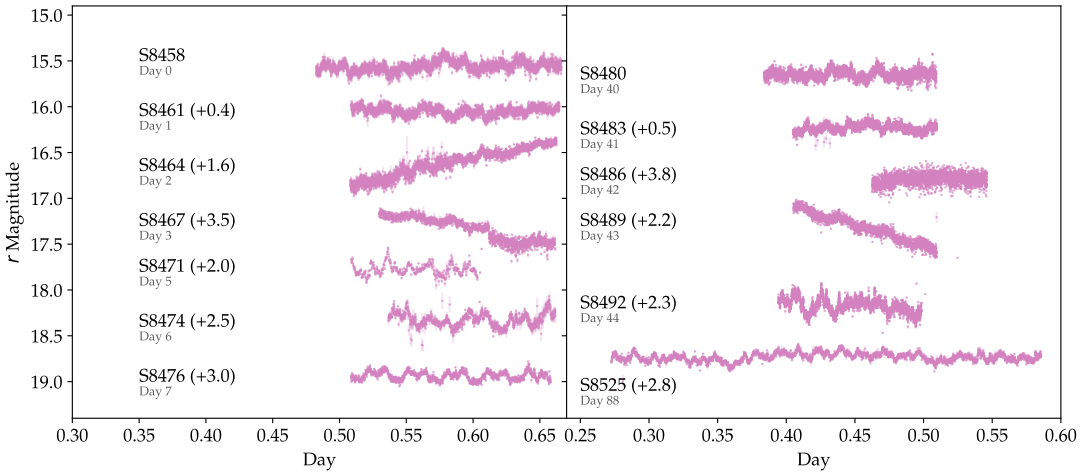

FIGURE C.0.4 – SHOC observations of ASASSN-14ei over different nights. The observing run numbers are indicated next to the corresponding light curve. Vertical offsets, indicated by parentheses, are applied to some light curves for visual convenience. The first observation for ASASSN-14ei is labelled as Day 0 and the following observations are labelled with respect to Day 0.

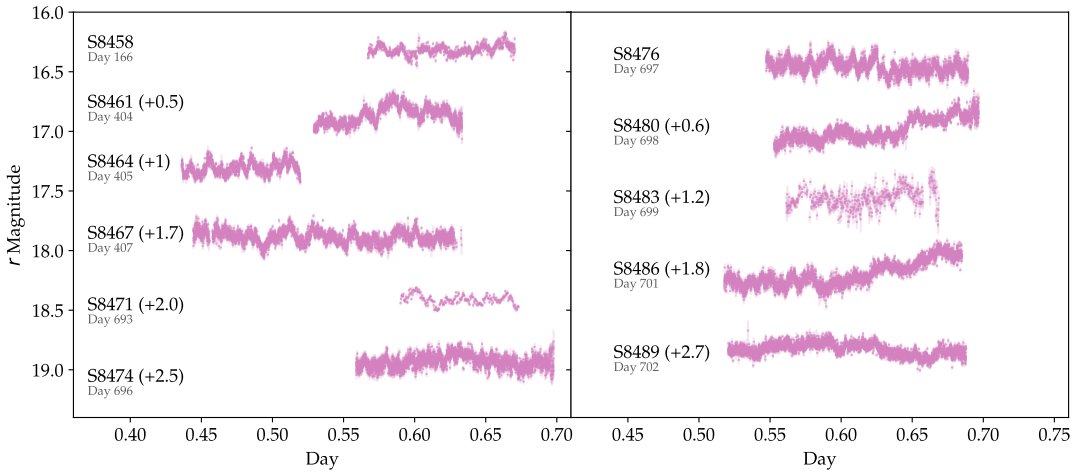

FIGURE C.0.5 – Further SHOC observations of ASASSN-14ei over different nights. The observing run numbers are indicated next to the corresponding light curve. Vertical offsets, indicated by parentheses, are applied to some light curves for visual convenience. The first observation for ASASSN-14ei is labelled as Day 0 and the following observations are labelled with respect to Day 0.

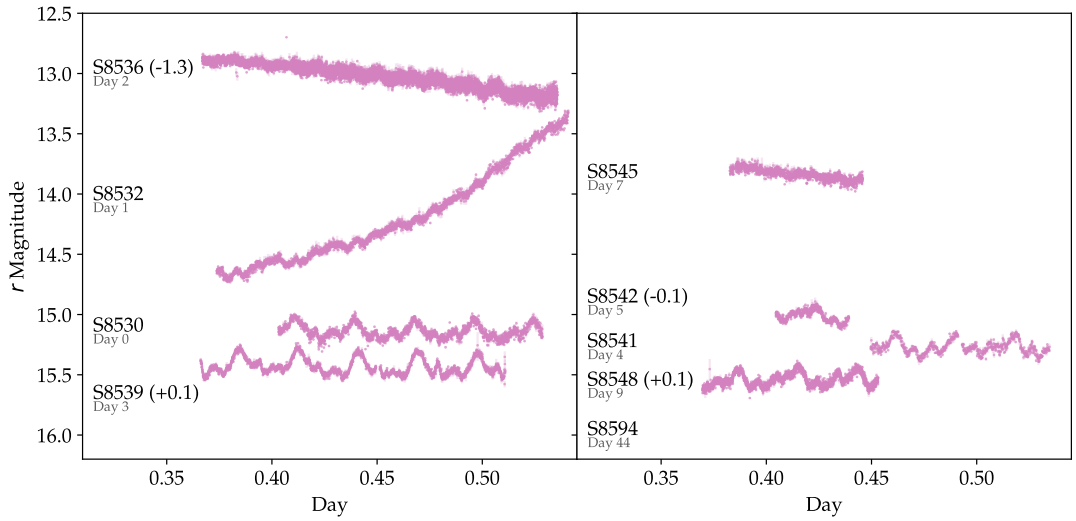

FIGURE C.0.6 – SHOC observations of ASASSN-14mv over different nights. The observing run numbers are indicated next to the corresponding light curve. Vertical offsets, indicated by parentheses, are applied to some light curves for visual convenience. The first observation for ASASSN-14mv is labelled as Day 0 and the following observations are labelled with respect to Day 0.

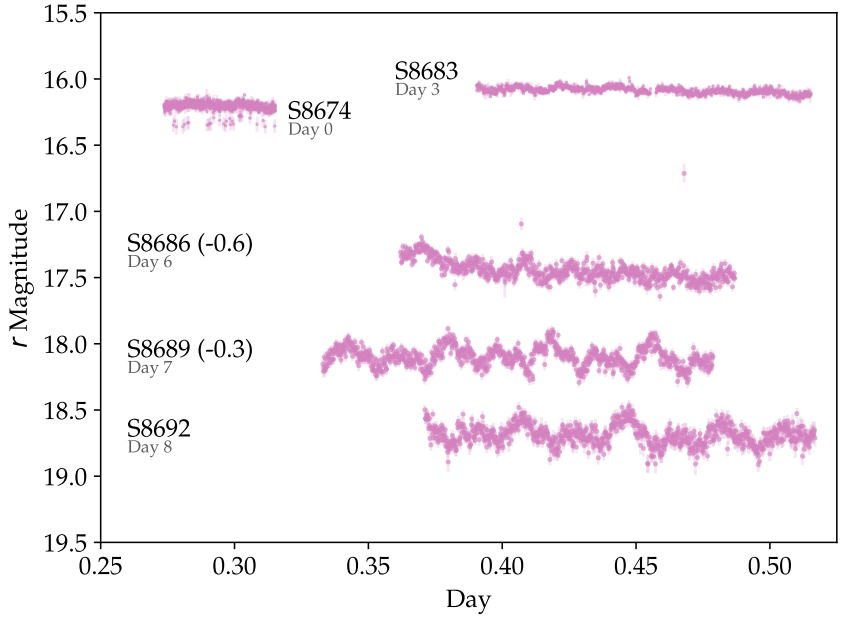

FIGURE C.0.7 – SHOC observations of ASASSN-15kf over different nights. The observing run numbers are indicated next to the corresponding light curve. Vertical offsets, indicated by parentheses, are applied to some light curves for visual convenience. The first observation for ASASSN-15kf is labelled as Day 0 and the following observations are labelled with respect to Day 0.

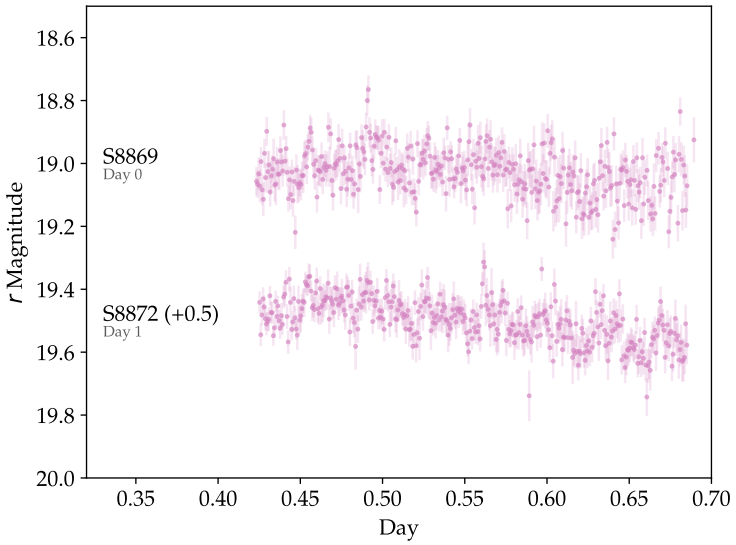

FIGURE C.0.8 – SHOC observations of ASASSN-17fp over different nights. The observing run numbers are indicated next to the corresponding light curve. Vertical offsets, indicated by parentheses, are applied to some light curves for visual convenience. The first observation for ASASSN-17fp is labelled as Day 0 and the following observations are labelled with respect to Day 0.

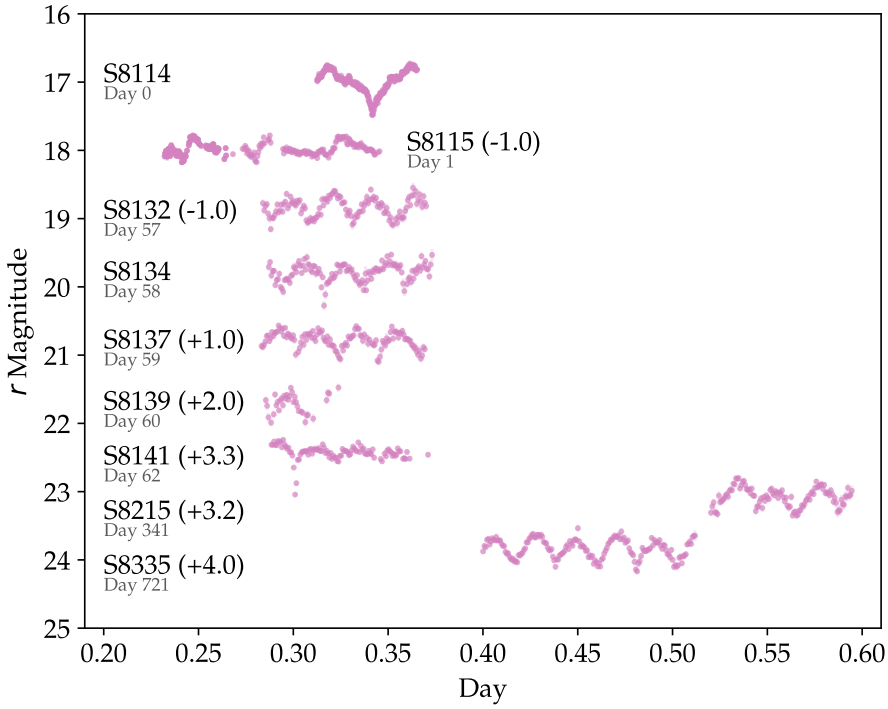

FIGURE C.0.9 – SHOC observations of CSS2333-15 over different nights. The observing run numbers are indicated next to the corresponding light curve. Vertical offsets, indicated by parentheses, are applied to some light curves for visual convenience. The first observation for CSS2333-15 is labelled as Day 0 and the following observations are labelled with respect to Day 0.

APPENDIX D

SHOC light curves and SALT spectra of candidate polars and other CVs

D.1 SHOC light curves of CRTS CVs

The individual SHOC light curves of CRTS CVs are presented in Appendix C. The figures show all the light curves from follow-up observations taken over different nights. They appear in the order that they appear in Chapter 4.

D.2 Objects with multiple SALT spectra

In this section, I present the SALT spectra of objects taken over multiple nights.

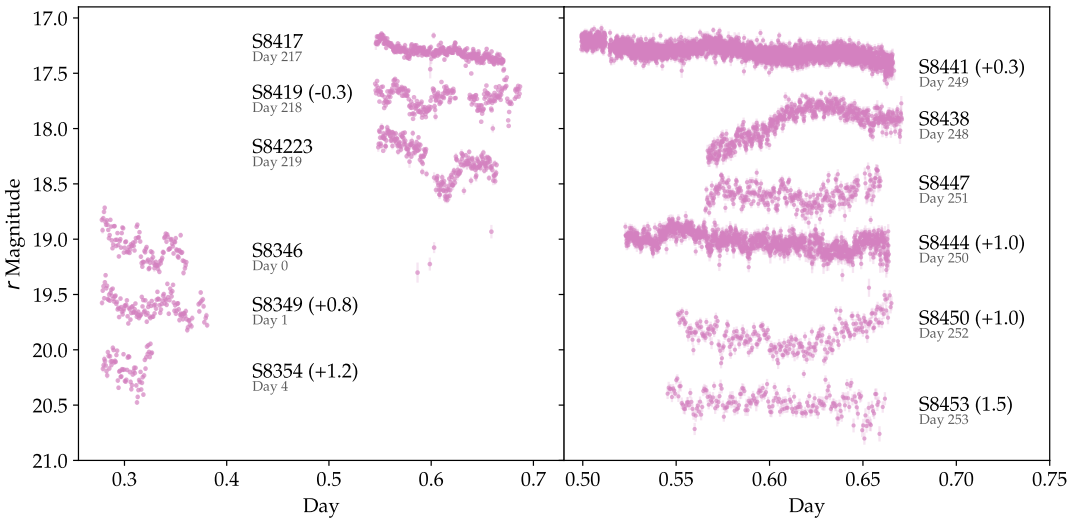

FIGURE D.1.1 – SHOC observations of CSS0109-27 over different nights. The observing run numbers are indicated next to the corresponding light curve. Vertical offsets, indicated by parentheses, are applied to some light curves for visual convenience. The first observation for CSS0109-27 is labelled as Day 0 and the following observations are labelled with respect to Day 0.

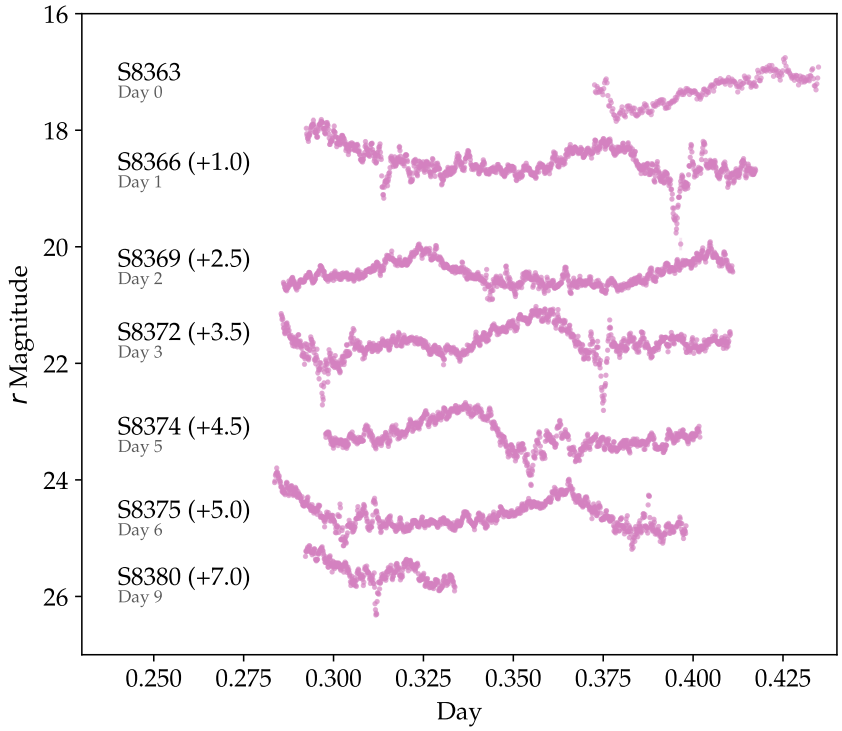

FIGURE D.1.2 – SHOC observations of CSS0357+10 over different nights. The observing run numbers are indicated next to the corresponding light curve. Vertical offsets, indicated by parentheses, are applied to some light curves for visual convenience. The first observation for CSS0357+10 is labelled as Day 0 and the following observations are labelled with respect to Day 0.

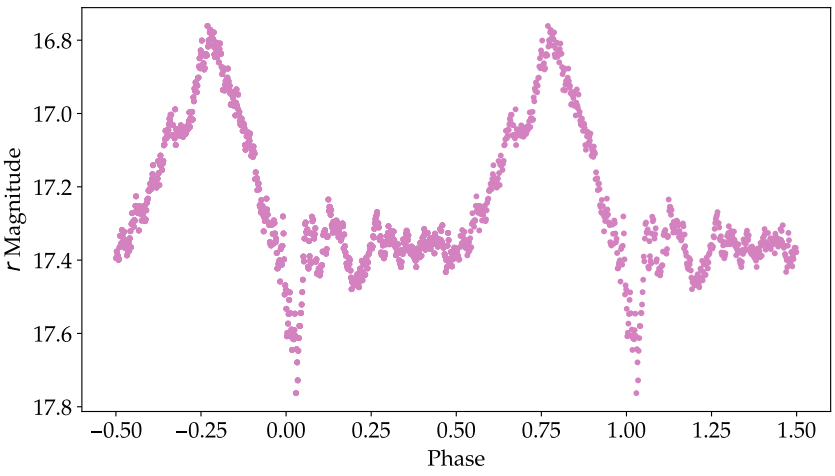

FIGURE D.1.3 – Average phase-folded light curve of CSS0357+10.

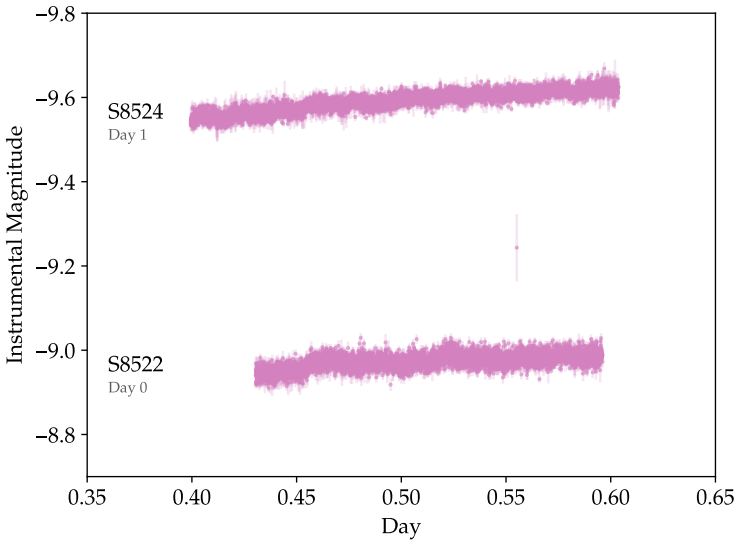

FIGURE D.1.4 – SHOC observations of SSS0617-36 over different nights. The observing run numbers are indicated next to the corresponding light curve. Vertical offsets, indicated by parentheses, are applied to some light curves for visual convenience. The first observation for SSS0617-36 is labelled as Day 0 and the following observations are labelled with respect to Day 0.

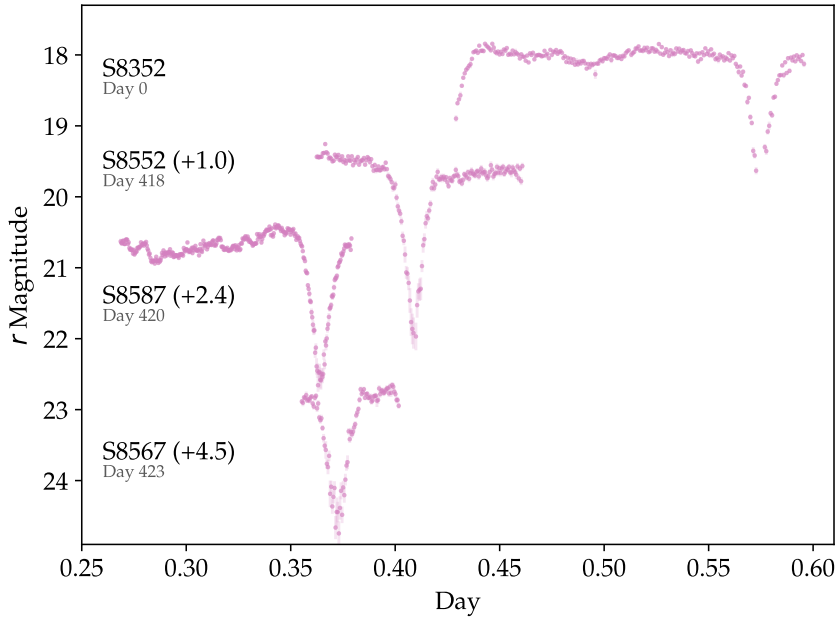

FIGURE D.1.5 – SHOC observations of MLS0720+17 over different nights. The observing run numbers are indicated next to the corresponding light curve. Vertical offsets, indicated by parentheses, are applied to some light curves for visual convenience. The first observation for MLS0720+17 is labelled as Day 0 and the following observations are labelled with respect to Day 0.

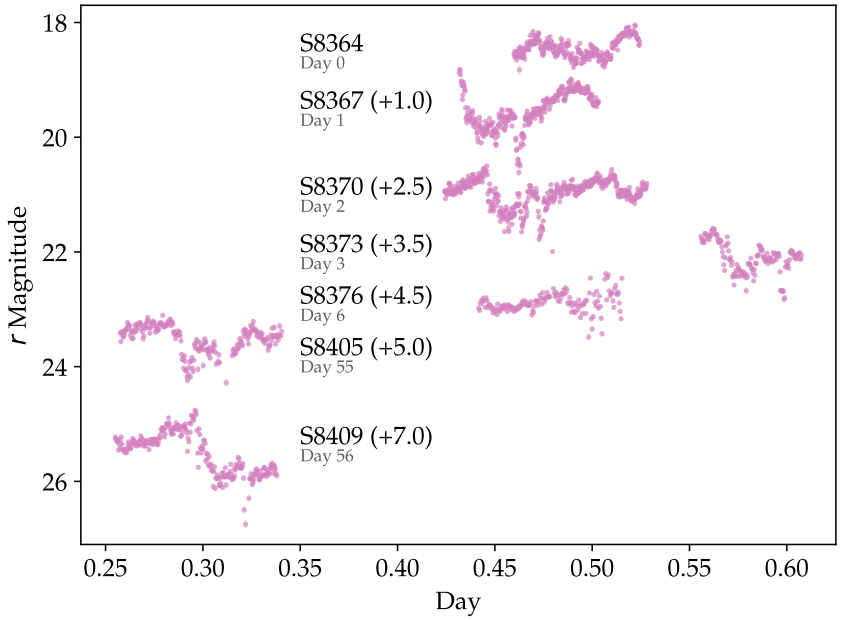

FIGURE D.1.6 – SHOC observations of CSS0812+04 over different nights. The observing run numbers are indicated next to the corresponding light curve. Vertical offsets, indicated by parentheses, are applied to some light curves for visual convenience. The first observation for CSS0812+04 is labelled as Day 0 and the following observations are labelled with respect to Day 0.

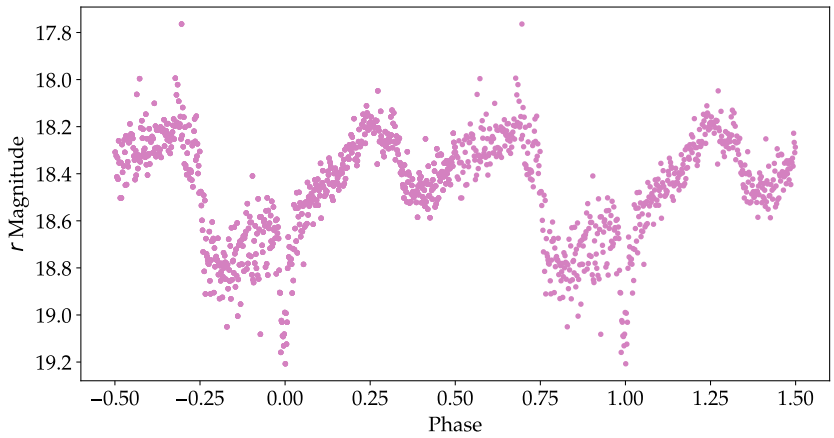

FIGURE D.1.7 – Average phase-folded light curve of CSS0812+04.

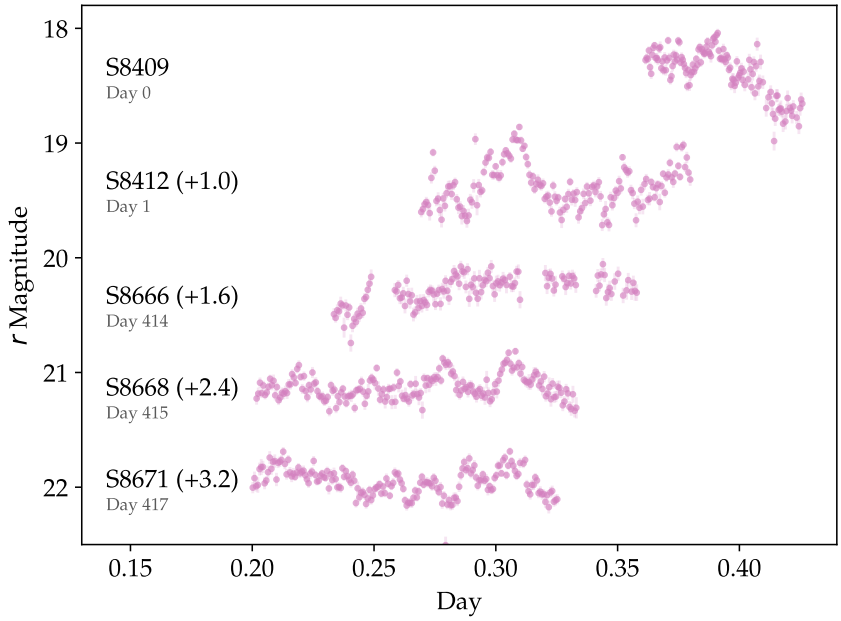

FIGURE D.1.8 – SHOC observations of CSS0910+16 over different nights. The observing run numbers are indicated next to the corresponding light curve. Vertical offsets, indicated by parentheses, are applied to some light curves for visual convenience. The first observation for CSS0910+16 is labelled as Day 0 and the following observations are labelled with respect to Day 0.

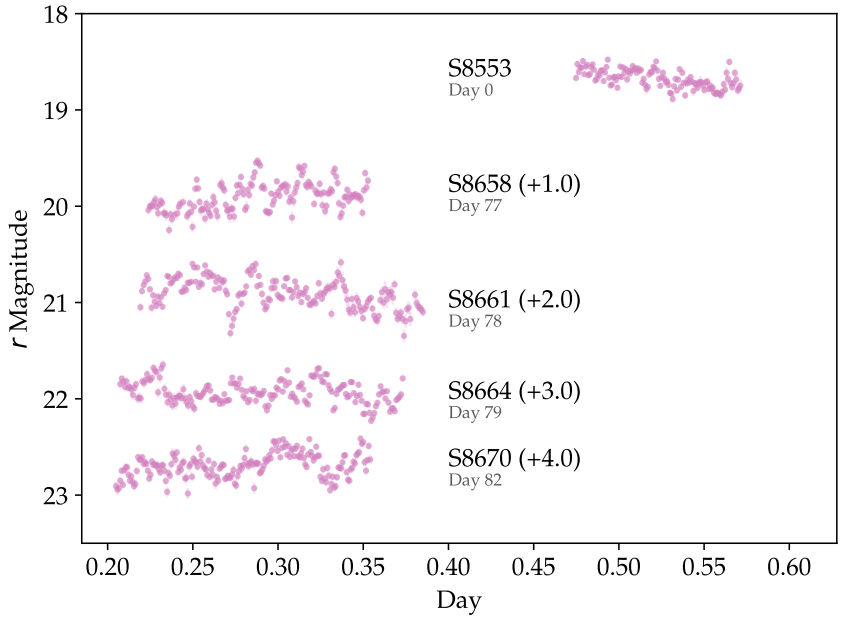

FIGURE D.1.9 – SHOC observations of SSS1012-18 over different nights. The observing run numbers are indicated next to the corresponding light curve. Vertical offsets, indicated by parentheses, are applied to some light curves for visual convenience. The first observation for SSS1012-18 is labelled as Day 0 and the following observations are labelled with respect to Day 0.

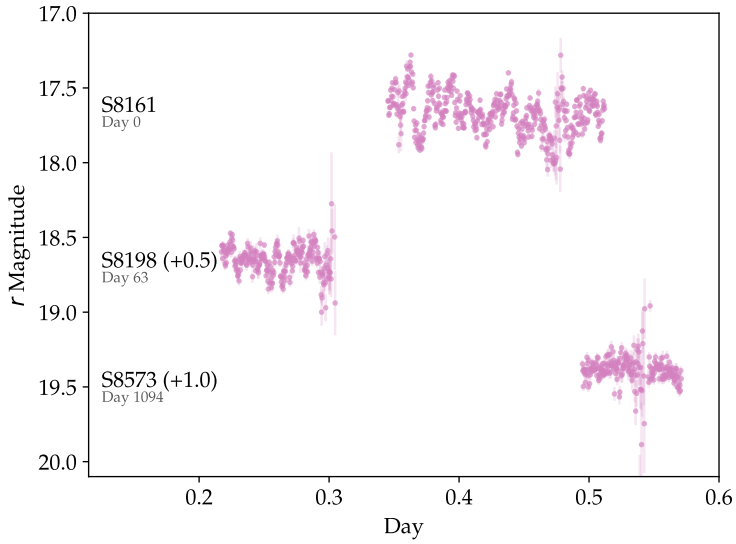

FIGURE D.1.10 – SHOC observations of SSS1020-33 over different nights. The observing run numbers are indicated next to the corresponding light curve. Vertical offsets, indicated by parentheses, are applied to some light curves for visual convenience. The first observation for SSS1020-33 is labelled as Day 0 and the following observations are labelled with respect to Day 0.

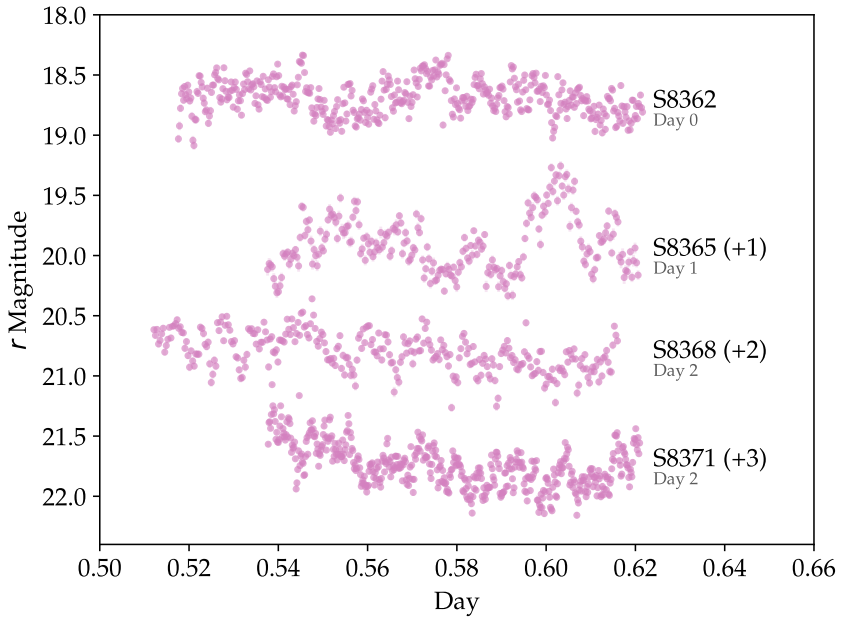

FIGURE D.1.11 – SHOC observations of CSS1127-05 over different nights. The observing run numbers are indicated next to the corresponding light curve. Vertical offsets, indicated by parentheses, are applied to some light curves for visual convenience. The first observation for CSS1127-05 is labelled as Day 0 and the following observations are labelled with respect to Day 0.

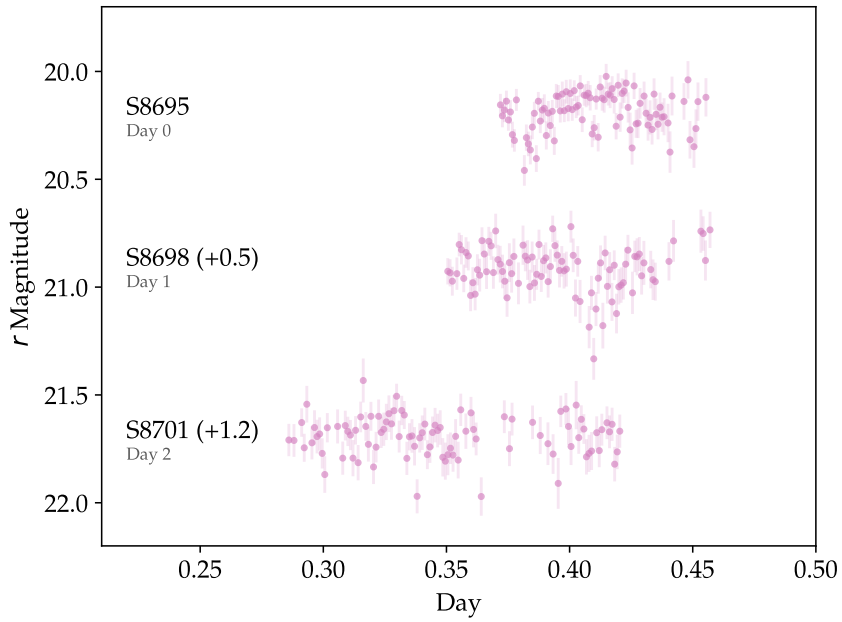

FIGURE D.1.12 – SHOC observations of CSS1455-11 over different nights. The observing run numbers are indicated next to the corresponding light curve. Vertical offsets, indicated by parentheses, are applied to some light curves for visual convenience. The first observation for CSS1455-11 is labelled as Day 0 and the following observations are labelled with respect to Day 0.

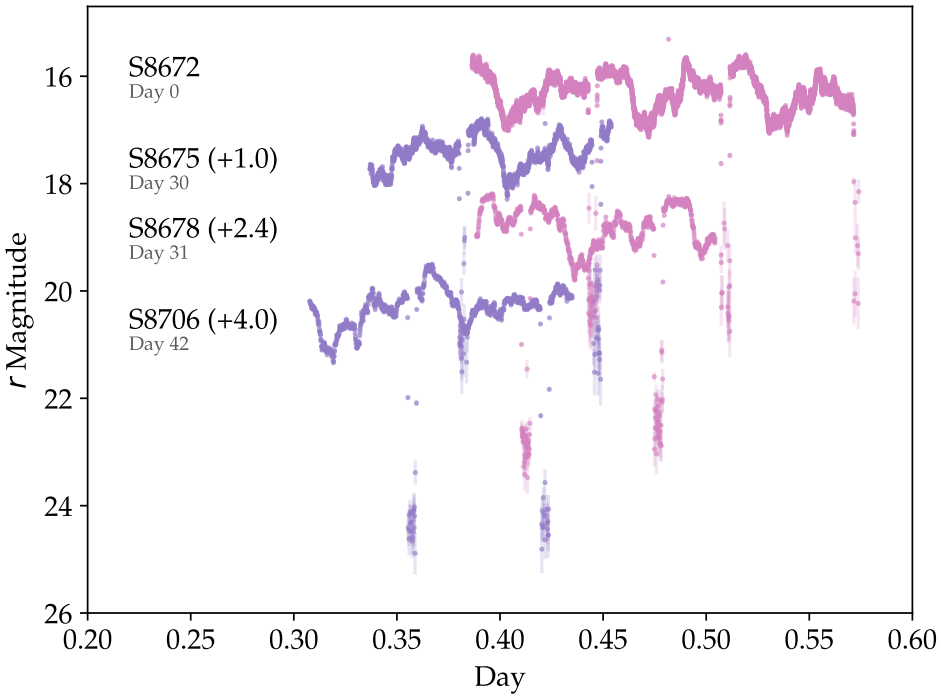

FIGURE D.1.13 – SHOC observations of MLS1525-03 over different nights. The observing run numbers are indicated next to the corresponding light curve. Vertical offsets, indicated by parentheses, are applied to some light curves for visual convenience. The first observation for MLS1525-03 is labelled as Day 0 and the following observations are labelled with respect to Day 0.

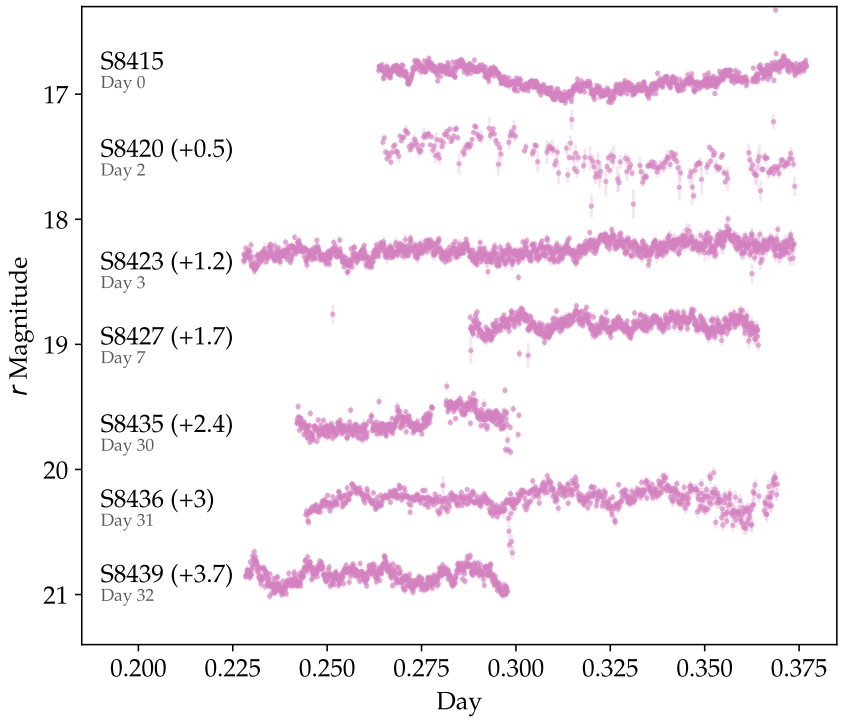

FIGURE D.1.14 – SHOC observations of CSS1619+13 over different nights. The observing run numbers are indicated next to the corresponding light curve. Vertical offsets, indicated by parentheses, are applied to some light curves for visual convenience. The first observation for CSS1619+13 is labelled as Day 0 and the following observations are labelled with respect to Day 0.

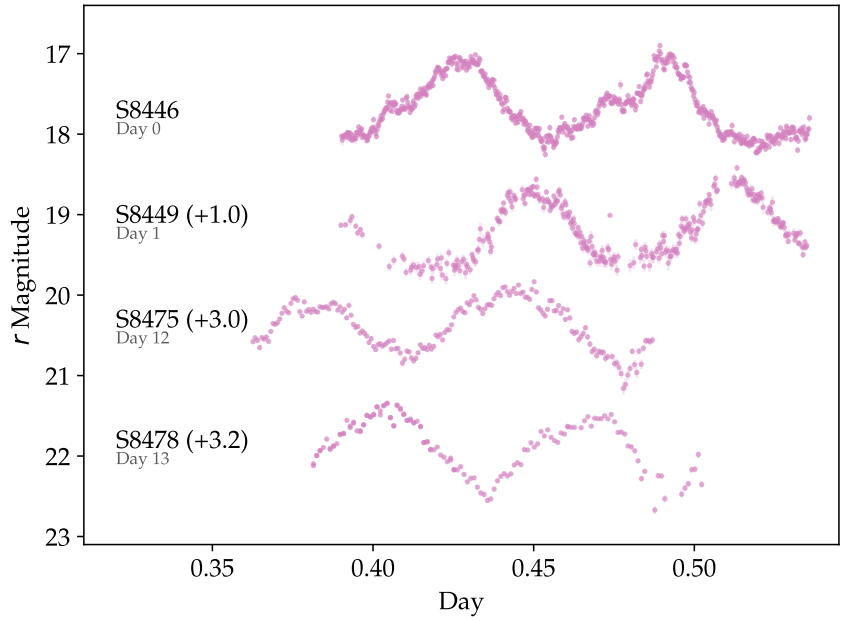

FIGURE D.1.15 – SHOC observations of SSS1944-42 over different nights. The observing run numbers are indicated next to the corresponding light curve. Vertical offsets, indicated by parentheses, are applied to some light curves for visual convenience. The first observation for SSS1944-42 is labelled as Day 0 and the following observations are labelled with respect to Day 0.

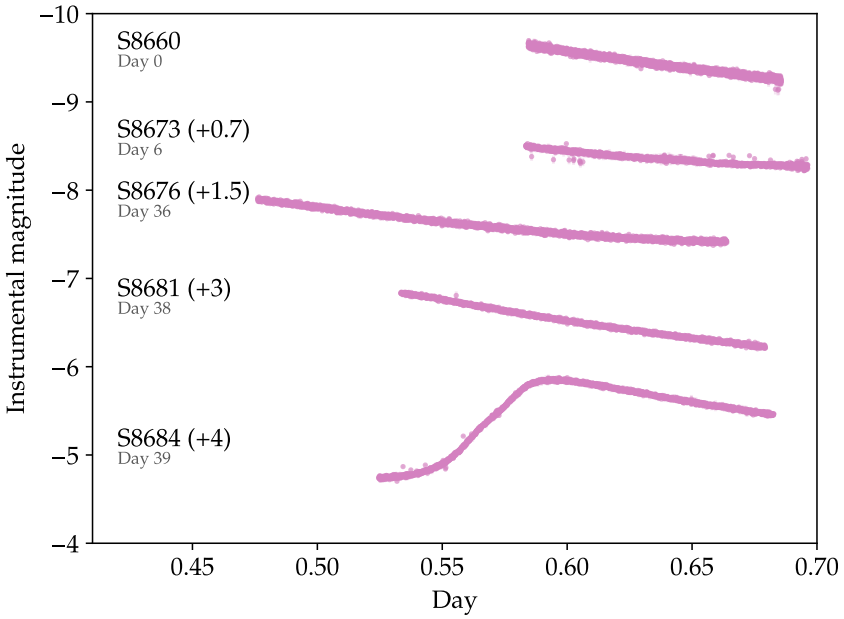

FIGURE D.1.16 – SHOC observations of MLS2044-16 over different nights. The observing run numbers are indicated next to the corresponding light curve. Vertical offsets, indicated by parentheses, are applied to some light curves for visual convenience. The first observation for MLS2044-16 is labelled as Day 0 and the following observations are labelled with respect to Day 0.

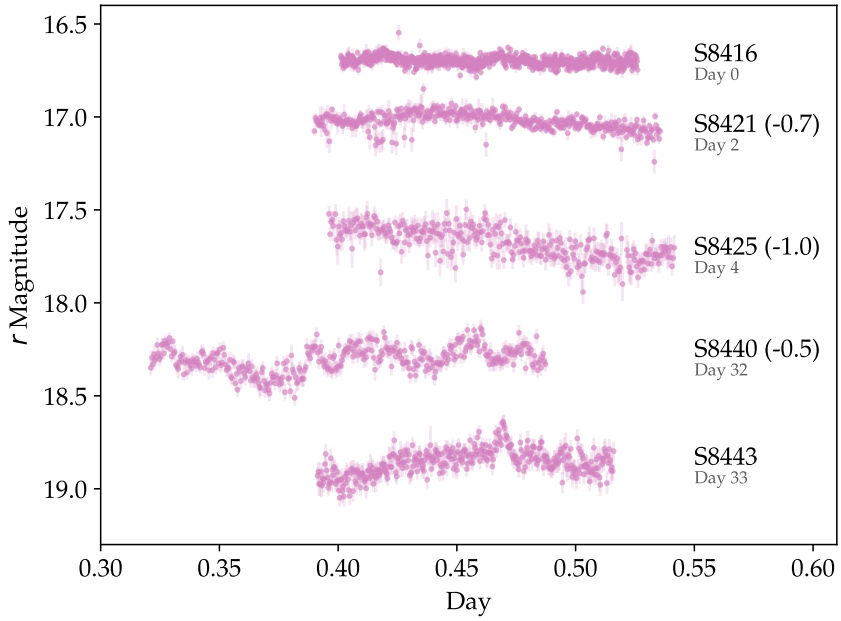

FIGURE D.1.17 – SHOC observations of SSS1935-53 over different nights. The observing run numbers are indicated next to the corresponding light curve. Vertical offsets, indicated by parentheses, are applied to some light curves for visual convenience. The first observation for SSS1935-53 is labelled as Day 0 and the following observations are labelled with respect to Day 0.

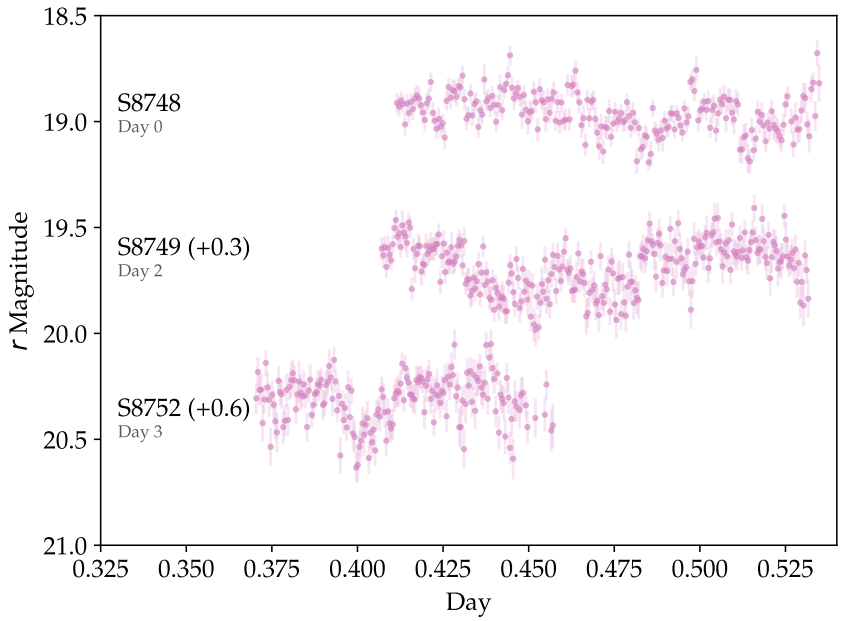

FIGURE D.1.18 – SHOC observations of CSS2042-09 over different nights. The observing run numbers are indicated next to the corresponding light curve. Vertical offsets, indicated by parentheses, are applied to some light curves for visual convenience. The first observation for CSS2042-09 is labelled as Day 0 and the following observations are labelled with respect to Day 0.

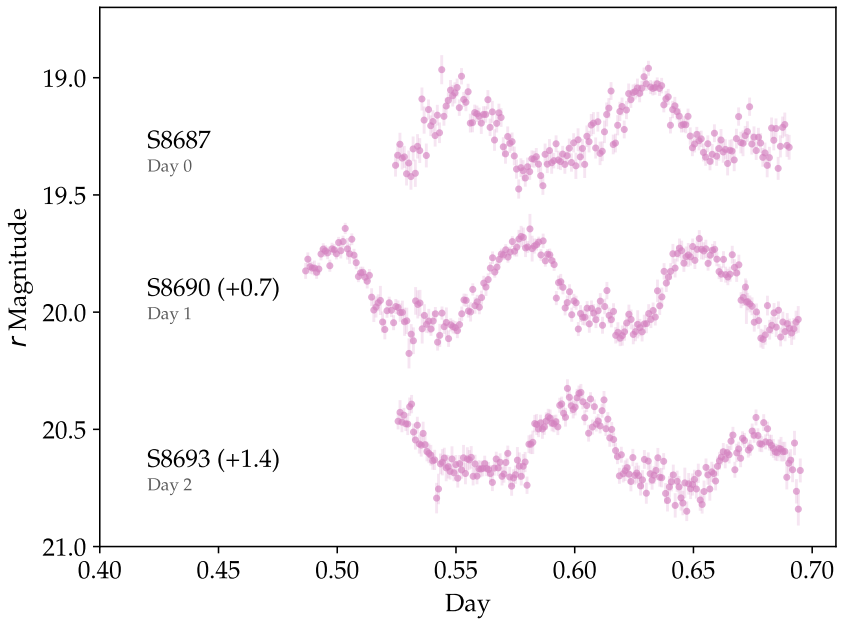

FIGURE D.1.19 – SHOC observations of SSS2046-31 over different nights. The observing run numbers are indicated next to the corresponding light curve. Vertical offsets, indicated by parentheses, are applied to some light curves for visual convenience. The first observation for SSS2046-31 is labelled as Day 0 and the following observations are labelled with respect to Day 0.

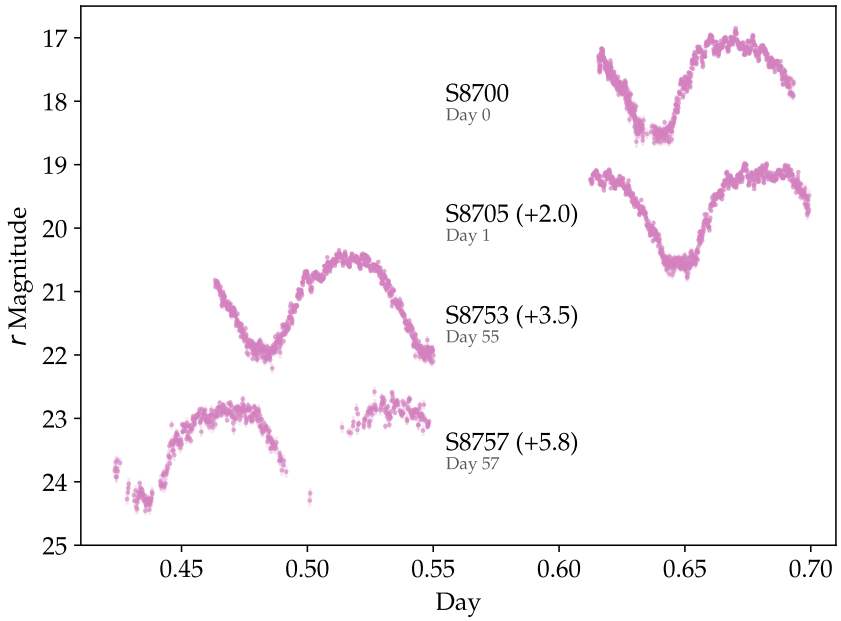

FIGURE D.1.20 – SHOC observations of CSS2154+15 over different nights. The observing run numbers are indicated next to the corresponding light curve. Vertical offsets, indicated by parentheses, are applied to some light curves for visual convenience. The first observation for CSS2154+15 is labelled as Day 0 and the following observations are labelled with respect to Day 0.

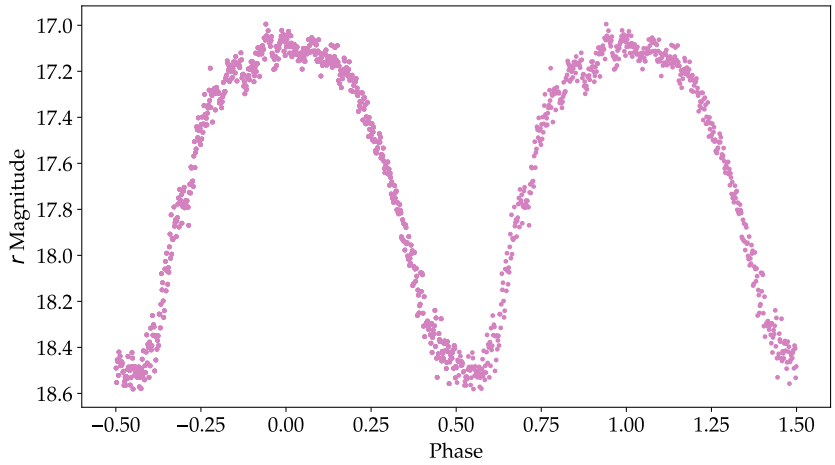

FIGURE D.1.21 – Average phase-folded light curve of CSS2154+15.

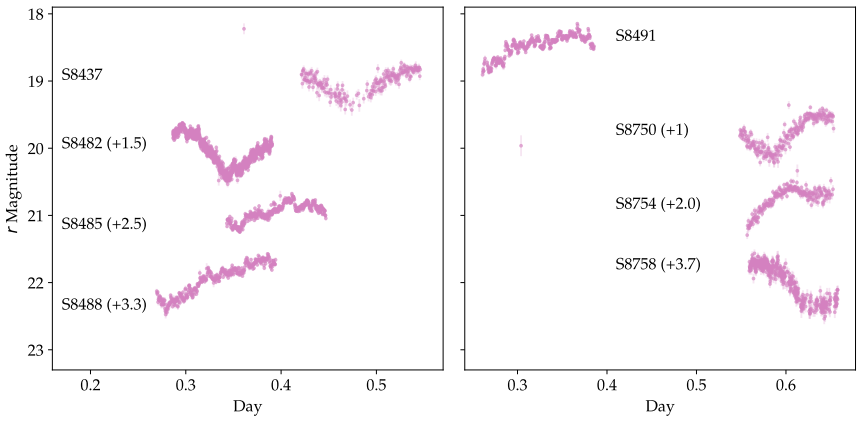

FIGURE D.1.22 – SHOC observations of CSS2335+12 over different nights. The observing run numbers are indicated next to the corresponding light curve. Vertical offsets, indicated by parentheses, are applied to some light curves for visual convenience. The first observation for CSS2335+12 is labelled as Day 0 and the following observations are labelled with respect to Day 0.

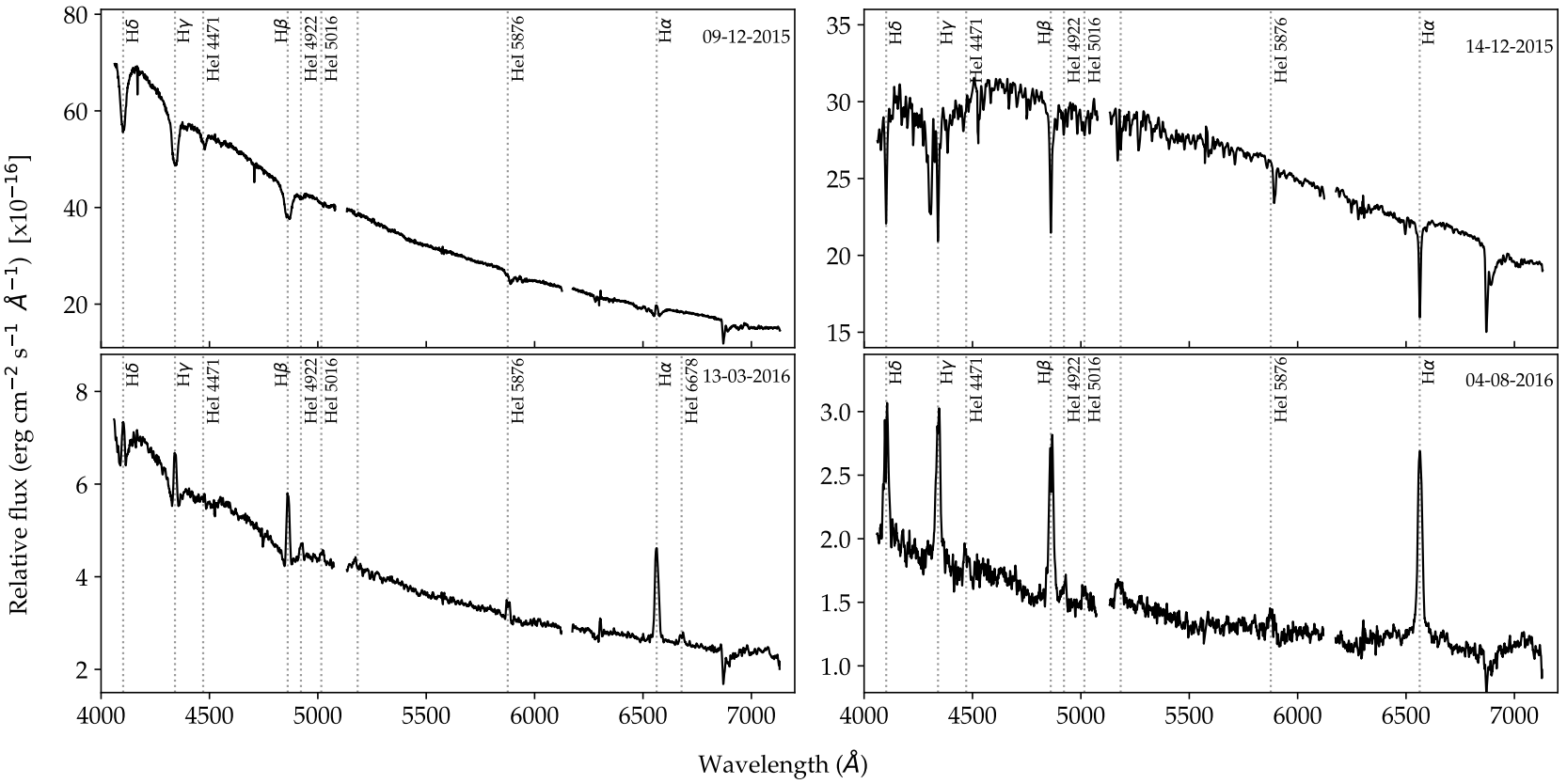

FIGURE D.2.1 – SALT spectra of SSS0617-36 taken over multiple nights. The dates of observations are indicated at the top of each spectrum. Identifiable emission lines are indicated by grey dotted lines.

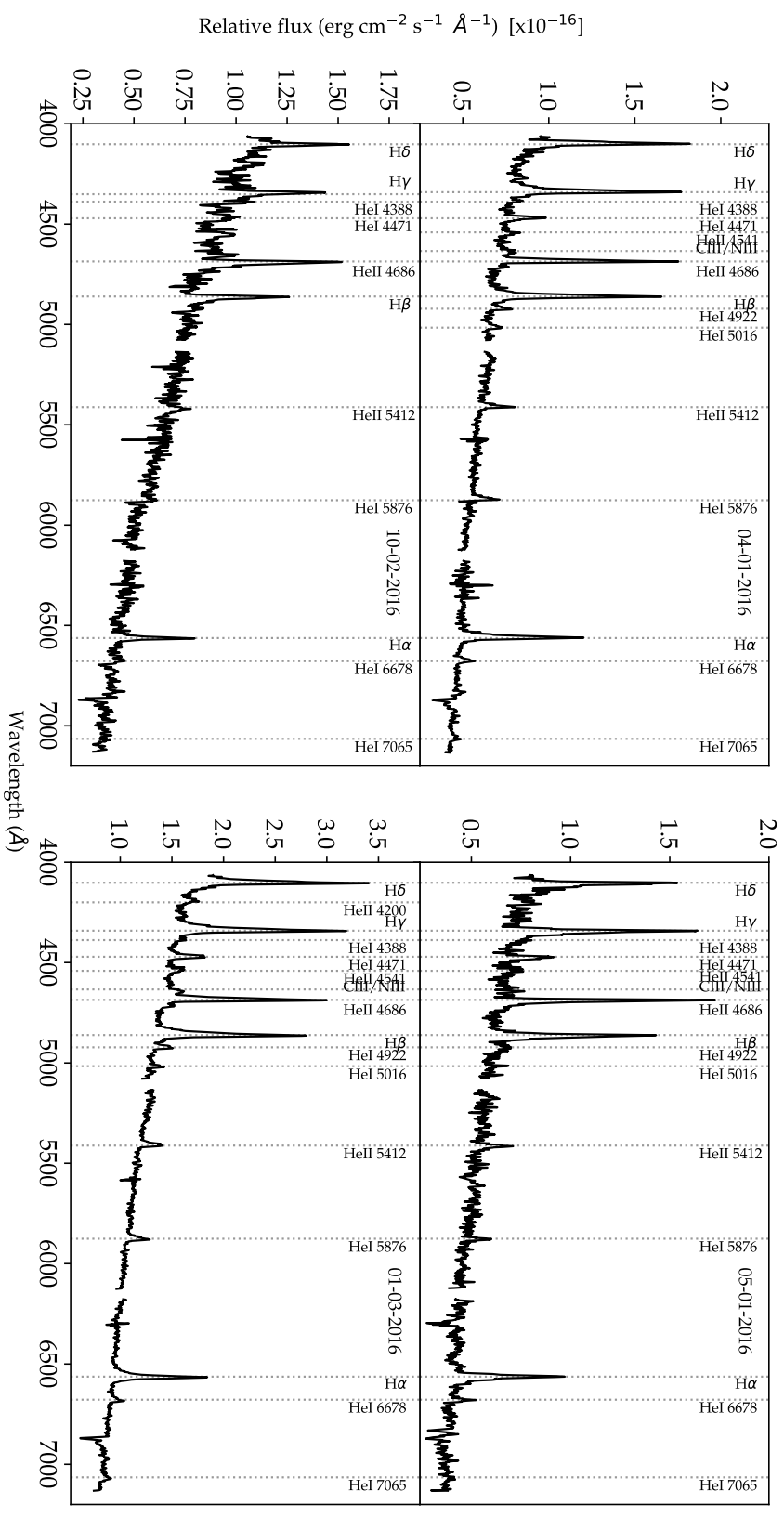

FIGURE D.2.2 – SALT spectra of CSS0812+04 taken over multiple nights. The dates of observations are indicated at the top of each spectrum. Identifiable emission lines are indicated by grey dotted lines.

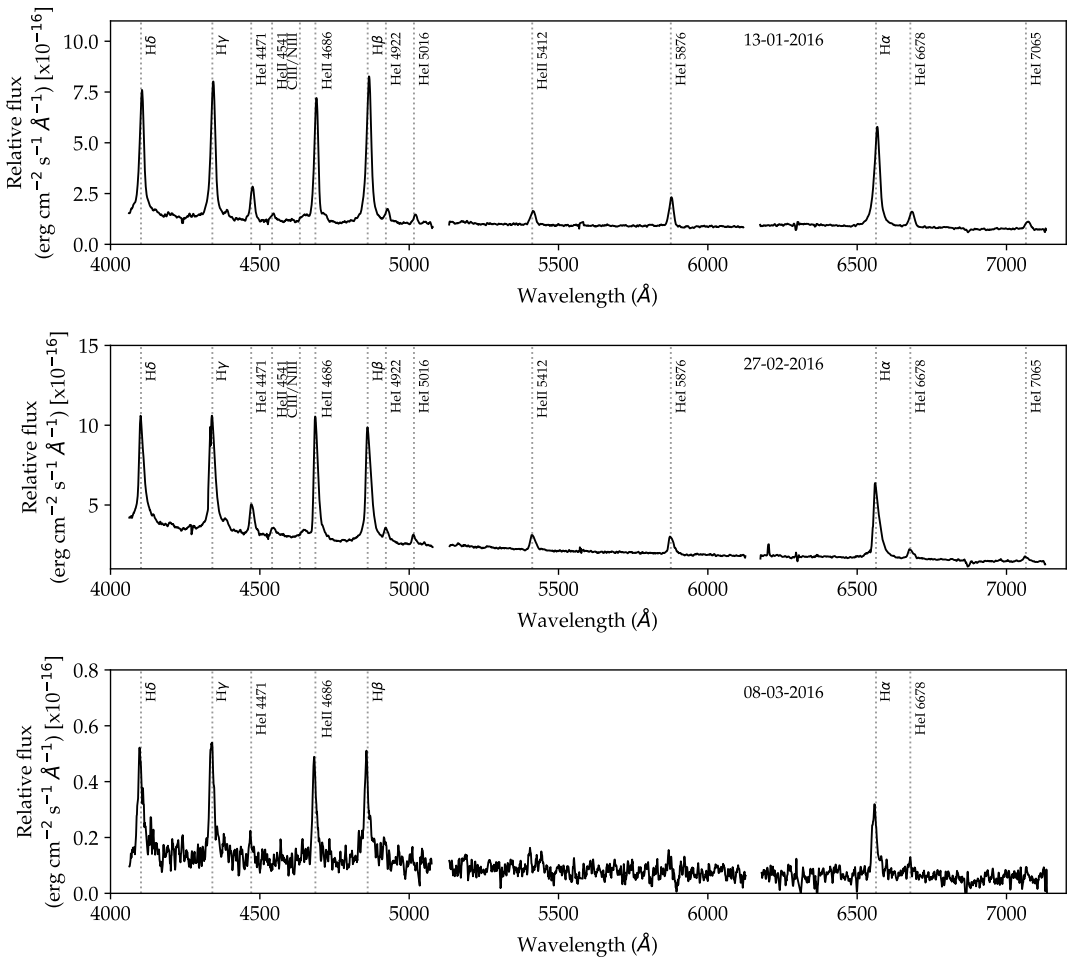

FIGURE D.2.3 – SALT spectra of CSS0812+04 taken over multiple nights. The dates of observations are indicated at the top of each spectrum. Identifiable emission lines are indicated by grey dotted lines.

Bibliography

Abbott, T. M. C., Robinson, E. L., Hill, G. J., and Haswell, C. A. (1992). Two Unusual Cataclysmic Variables at High Galactic Latitude: CP Eridani and AL Comae. ApJ, 399:680.

Achilleos, N., Wickramasinghe, D. T., and Wu, K. (1992). The accretion halo in AM Herculis systems. MNRAS, 256:80–96.

Anderson, S. F., Becker, A. C., Haggard, D., Prieto, J. L., Knapp, G. R., Sako, M., Halford, K. E., Jha, S., Martin, B., Holtzman, J., Frieman, J. A., Garnavich, P. M., Hayward, S., Ivezić, Ž., Mukadam, A. S., Sesar, B., Szkody, P., Malanushenko, V., Richmond, M. W., Schneider, D. P., and York, D. G. (2008). Two More Candidate AM Canum Venaticorum (am CVn) Binaries from the Sloan Digital Sky Survey. AJ, 135:2108–2113.

Anderson, S. F., Haggard, D., Homer, L., Joshi, N. R., Margon, B., Silvestri, N. M., Szkody, P., Wolfe, M. A., Agol, E., Becker, A. C., Henden, A., Hall, P. B., Knapp, G. R., Richmond, M. W., Schneider, D. P., Stinson, G., Barentine, J. C., Brewington, H. J., Brinkmann, J., Harvanek, M., Kleinman, S. J., Krzesinski, J., Long, D., Neilsen, Jr., E. H., Nitta, A., and Snedden, S. A. (2005). Ultracompact AM Canum Venaticorum Binaries from the Sloan Digital Sky Survey: Three Candidates Plus the First Confirmed Eclipsing System. AJ, 130:2230–2236.

Artusi, E., Conselvan, G., Tegon, A., and Zardin, D. (2016). Crowded Fields Photometry with DAOPHOT. Journal of the American Association of Variable Star Observers (JAAVSO), 44:149.

Aydi, E., Strader, J., Chomiuk, L., Kawash, A., Sokolovsky, K. V., Stanek, K. Z., Kochanek, C. S., and Shappee, B. J. (2021). SOAR spectroscopic follow up of ASASSN-21br - a possible AM CVn outburst? The Astronomer's Telegram, 14405:1.

Balbus, S. A. and Hawley, J. F. (1991). A Powerful Local Shear Instability in Weakly Magnetized Disks. I. Linear Analysis. ApJ, 376:214.

Balbus, S. A. and Hawley, J. F. (1998). Instability, turbulence, and enhanced transport in accretion disks. Reviews of Modern Physics, 70(1):1–53.

Balman, Ş. and Revnivtsev, M. (2012). X-ray variations in the inner accretion flow of dwarf novae. A&A, 546:A112.

Barwig, H., Ritter, H., and Barnbantner, O. (1994). 1H1752+081: a new eclipsing probable AM Herculis-type binary. A&A, 288:204–212.

Bellm, E. C., Kulkarni, S. R., Graham, M. J., Dekany, R., Smith, R. M., Riddle, R., Masci, F. J., Helou, G., Prince, T. A., Adams, S. M., Barbarino, C., Barlow, T., Bauer, J., Beck, R., Belicki, J., Biswas, R., Blagorodnova, N., Bodewits, D., Bolin, B., Brinnel, V., Brooke, T., Bue, B., Bulla, M., Burruss, R., Cenko, S. B., Chang, C.-K., Connolly, A., Coughlin, M., Cromer, J., Cunningham, V., De, K., Delacroix, A., Desai, V., Duev, D. A., Eadie, G., Farnham, T. L., Feeney, M., Feindt, U., Flynn, D., Franckowiak, A., Frederick, S., Fremling, C., Gal-Yam, A., Gezari, S., Giomi, M., Goldstein, D. A., Golkhou, V. Z., Goobar, A., Groom, S., Hacopians, E., Hale, D., Henning, J., Ho, A. Y. Q., Hover, D., Howell, J., Hung, T., Huppenkothen, D., Imel, D., Ip, W.-H., Ivezić, Ž., Jackson, E., Jones, L., Juric, M., Kasliwal, M. M., Kaspi, S., Kaye, S., Kelley, M. S. P., Kowalski, M., Kramer, E., Kupfer, T., Landry, W., Laher, R. R., Lee, C.-D., Lin, H. W., Lin, Z.-Y., Lunnan, R., Giomi, M., Mahabal, A., Mao, P., Miller, A. A., Monkewitz, S., Murphy, P., Ngeow, C.-C., Nordin, J., Nugent, P., Ofek, E., Patterson, M. T., Penprase, B., Porter, M., Rauch, L., Rebbapragada, U., Reiley, D., Rigault, M., Rodriguez, H., van Roestel, J., Rusholme, B., van Santen, J., Schulze, S., Shupe, D. L., Singer, L. P., Soumagnac, M. T., Stein, R., Surace, J., Sollerman, J., Szkody, P., Taddia, F., Terek, S., Van Sistine, A., van Velzen, S., Vestrand, W. T., Walters, R., Ward, C., Ye, Q.-Z., Yu, P.-C., Yan, L., and Zolkower, J. (2019). The Zwicky Transient Facility: System Overview, Performance, and First Results. PASP, 131(995):018002.

Belloni, D. and Schreiber, M. R. (2020). Are white dwarf magnetic fields in close binaries generated during common-envelope evolution? MNRAS, 492(1):1523–1529.

Bernardini, F., de Martino, D., Mukai, K., and Falanga, M. (2014). Swift J2218.4+1925: a new hard-X-ray-selected polar observed with XMM-Newton. MNRAS, 445(2):1403–1411.

Bernardini, F., de Martino, D., Mukai, K., Russell, D. M., Falanga, M., Masetti, N., Ferrigno, C., and Israel, G. (2017). Broad-band characteristics of seven new hard X-ray selected cataclysmic variables. MNRAS, 470(4):4815–4837.

Beuermann, K., Burwitz, V., Reinsch, K., Schwope, A., and Thomas, H. C. (2020). Neglected X-ray discovered polars. II. The peculiar eclipsing binary HY Eridani. A&A, 634:A91.

Beuermann, K., Diese, J., Paik, S., Ploch, A., Zachmann, J., Schwope, A. D., and Hessman, F. V. (2009). A long-term optical and X-ray ephemeris of the polar EK Ursae Majoris. A&A, 507(1):385–388.

Beuermann, K., Euchner, F., Reinsch, K., Jordan, S., and Gänsicke, B. T. (2007). Zeeman tomography of magnetic white dwarfs. IV. The complex field structure of the polars EF Eridani, BL Hydri and CP Tucanae. A&A, 463(2):647–655.

Beuermann, K. and Schwope, A. D. (1994). AM Herculis Binaries. In Shafter, A. W., editor, Interacting Binary Stars, volume 56 of Astronomical Society of the Pacific Conference Series, page 119.

Beuermann, K., Stella, L., and Patterson, J. (1987). Einstein Observations of EF Eridani (2A 0311-227), The Textbook Example of AM Herculis–Type Systems. ApJ, 316:360.

Beuermann, K. and Thomas, H. C. (1993). The ROSAT view of the cataclysmic variable sky. Advances in Space Research, 13(12):115–124.

Bianco, F. B., Ivezić, Ž., Jones, R. L., Graham, M. L., Marshall, P., Saha, A., Strauss, M. A., Yoachim, P., Ribeiro, T., Anguita, T., Bauer, A. E., Bauer, F. E., Bellm, E. C., Blum, R. D., Brandt, W. N., Brough, S., Catelan, M., Clarkson, W. I., Connolly, A. J., Gawiser, E., Gizis, J. E., Hložek, R., Kaviraj, S., Liu, C. T., Lochner, M., Mahabal, A. A., Mandelbaum, R., McGehee, P., Neilsen, Eric H., J., Olsen, K. A. G., Peiris, H. V., Rhodes, J., Richards, G. T., Ridgway, S., Schwamb, M. E., Scolnic, D., Shemmer, O., Slater, C. T., Slosar, A., Smartt, S. J., Strader, J., Street, R., Trilling, D. E., Verma, A., Vivas, A. K., Wechsler, R. H., and Willman, B. (2022). Optimization of the Observing Cadence for the Rubin Observatory Legacy Survey of Space and Time: A Pioneering Process of Community-focused Experimental Design. ApJS, 258(1):1.

Bildsten, L., Shen, K. J., Weinberg, N. N., and Nelemans, G. (2007). Faint Thermonuclear Supernovae from AM Canum Venaticorum Binaries. ApJ, 662(2):L95–L98.

Bildsten, L., Townsley, D. M., Deloye, C. J., and Nelemans, G. (2006). The Thermal State of the Accreting White Dwarf in AM Canum Venaticorum Binaries. ApJ, 640(1):466–473.

Bąkowska, K., Marsh, T. R., Steeghs, D., Nelemans, G., and Groot, P. J. (2021). Spectroscopy of the helium-rich binary ES Ceti reveals accretion via a disc and evidence of eclipses. A&A, 645:A114.

Bonnardeau, M. (2012). V1432 Aql: 5 more years of observations. Open European Journal on Variable Stars, 153:1–9.

Borisov, N. V., Gabdeev, M. M., Shimansky, V. V., Katysheva, N. A., Kolbin, A. I., Shugarov, S. Y., and Goranskij, V. P. (2016). Photometric and spectral studies of the eclipsing polar CRTS CSS081231 J071126+440405. Astrophysical Bulletin, 71(1):101–113.

Borisov, N. V., Gabdeev, M. M., Shimansky, V. V., Katysheva, N. A., and Shugarov, S. Y. (2017). Spectral and photometric studies of polar CRTS CSS 130604 J 215427+155714. Astrophysical Bulletin, 72:184–190.

Breedt, E. (2015). An update on the AM CVn family. In The Golden Age of Cataclysmic Variables and Related Objects - III (Golden2015), page 25.

Breedt, E., Gänsicke, B. T., Drake, A. J., Rodríguez-Gil, P., Parsons, S. G., Marsh, T. R., Szkody, P., Schreiber, M. R., and Djorgovski, S. G. (2014). 1000 cataclysmic variables from the Catalina Real-time Transient Survey. MNRAS, 443:3174–3207.

Breedt, E., Gänsicke, B. T., Girven, J., Drake, A. J., Copperwheat, C. M., Parsons, S. G., and Marsh, T. R. (2012a). The evolutionary state of short-period magnetic white dwarf binaries. MNRAS, 423(2):1437–1449.

Breedt, E., Gänsicke, B. T., Marsh, T. R., Steeghs, D., Drake, A. J., and Copperwheat, C. M. (2012b). CSS100603:112253-111037: a helium-rich dwarf nova with a 65 min orbital period. MNRAS, 425:2548–2556.

Breytenbach, H., Buckley, D. A. H., Hakala, P., Thorstensen, J. R., Kniazev, A. Y., Motsoaledi, M., Woudt, P. A., Potter, S. B., Lipunov, V., Gorbovskoy, E., Balanutsa, P., and Tyurina, N. (2019). Discovery, observations, and modelling of a new eclipsing polar: MASTER OT J061451.70-272535.5. MNRAS, 484(3):3831–3845.

Bridge, C. M., Cropper, M., Ramsay, G., de Bruijne, J. H. J., Reynolds, A. P., and Perryman, M. A. C. (2003). Variability of the accretion stream in the eclipsing polar EP Dra. MNRAS, 341(3):863–869.

Bridge, C. M., Cropper, M., Ramsay, G., Perryman, M. A. C., de Bruijne, J. H. J., Favata, F., Peacock, A., Rando, N., and Reynolds, A. P. (2002). STJ observations of the eclipsing polar HU Aqr. MNRAS, 336(4):1129–1138.

Buat-Ménard, V. and Hameury, J. M. (2002). Superoutbursts, superhumps and the tidal-thermal instability model. A&A, 386:891–898.

Buat-Ménard, V., Hameury, J. M., and Lasota, J. P. (2001). The nature of dwarf nova outbursts. A&A, 366:612–622.

Buckley, D., Breytenbach, H., Kniazev, A., Kotze, M. M., Motsoaledi, M., Potter, S., Woudt, P. A., Lipunov, V., and Gorbovskoy, E. (2015). MASTER-SAAO transient detections: new Cataclysmic Variable discoveries. In The Golden Age of Cataclysmic Variables and Related Objects - III (Golden2015), page 27.

Buckley, D. A., O'Donoghue, D., Hassall, B. J. M., Kellett, B. J., Mason, K. O., Sekiguchi, K., Watson, M. G., Wheatley, P. J., and Chen, A. (1993). Discovery of an EUV-bright polar in the period gap from the ROSAT Wide Field Camera sky survey. MNRAS, 262:93–108.

Buckley, D. A. H., Andreoni, I., Barway, S., Cooke, J., Crawford, S. M., Gorbovskoy, E., Gromadzki, M., Lipunov, V., Mao, J., Potter, S. B., Pretorius, M. L., Pritchard, T. A., Romero-Colmenero, E., Shara, M. M., Väisänen, P., and Williams, T. B. (2018). A comparison between SALT/SAAO observations and kilonova models for AT 2017gfo: the first electromagnetic counterpart of a gravitational wave transient - GW170817. MNRAS, 474(1):L71–L75.

Buckley, D. A. H., Ferrario, L., Wickramasinghe, D. T., and Bailey, J. A. (1998). Polarimetry of the eclipsing polar RX J0929.1-2404. MNRAS, 295(4):899–906.

Buckley, D. A. H. and Shafter, A. W. (1995). Polarimetry of the exceptionally long-period eclipsing polar RX J0515.6+0105. MNRAS, 275(4):L61–L66.

Burbidge, E. M. and Strittmatter, P. A. (1971). G61 - 29, a Helium Emission-Line Star. ApJ, 170:L39.

Burgh, E. B., Nordsieck, K. H., Kobulnicky, H. A., Williams, T. B., O'Donoghue, D., Smith, M. P., and Percival, J. W. (2003). Prime Focus Imaging Spectrograph for the Southern African Large Telescope: optical design. In Iye, M. and Moorwood, A. F. M., editors,

Instrument Design and Performance for Optical/Infrared Ground-based Telescopes, volume 4841 of Proc. SPIE, pages 1463–1471.

Burwitz, V. and Reinsch, K. (2001). ROSAT discovered soft x-ray intermediate polars: UU Col and RX J0806.3+1527. X-ray Astronomy: Stellar Endpoints, AGN, and the Diffuse X-ray Background, 599:522–525.

Burwitz, V., Reinsch, K., Beuermann, K., and Thomas, H.-C. (1999). RX J0501.7-0359: a new ROSAT discovered eclipsing polar in the period gap. In Hellier, C. and Mukai, K., editors, Annapolis Workshop on Magnetic Cataclysmic Variables, volume 157 of Astronomical Society of the Pacific Conference Series, page 127.

Burwitz, V., Reinsch, K., Schwope, A. D., Beuermann, K., Thomas, H. C., and Greiner, J. (1996). X-ray and optical observations of a new ROSAT discovered polar: RX J0453.4-4213. A&A, 305:507.

Camilleri, P., McNaught, R. H., Gilmore, A. C., and Kilmartin, P. M. (1992). Nova Puppis 1991. IAU Circ., 5422:1.

Campbell, H. C., Marsh, T. R., Fraser, M., Hodgkin, S. T., de Miguel, E., Gänsicke, B. T., Steeghs, D., Hourihane, A., Breedt, E., Littlefair, S. P., Koposov, S. E., Wyrzykowski, Ł., Altavilla, G., Blagorodnova, N., Clementini, G., Damljanovic, G., Delgado, A., Dennefeld, M., Drake, A. J., Fernández-Hernández, J., Gilmore, G., Gualandi, R., Hamanowicz, A., Handzlik, B., Hardy, L. K., Harrison, D. L., Iłkiewicz, K., Jonker, P. G., Kochanek, C. S., Kołaczkowski, Z., Kostrzewa-Rutkowska, Z., Kotak, R., van Leeuwen, G., Leto, G., Ochner, P., Pawlak, M., Palaversa, L., Rixon, G., Rybicki, K., Shappee, B. J., Smartt, S. J., Torres, M. A. P., Tomasella, L., Turatto, M., Ulaczyk, K., van Velzen, S., Vince, O., Walton, N. A., Wielgórski, P., Wevers, T., Whitelock, P., Yoldas, A., De Angeli, F., Burgess, P., Busso, G., Busuttil, R., Butterley, T., Chambers, K. C., Copperwheat, C., Danilet, A. B., Dhillon, V. S., Evans, D. W., Eyer, L., Froebrich, D., Gomboc, A., Holland, G., Holoien, T. W.-S., Jarvis, J. F., Kaiser, N., Kann, D. A., Koester, D., Kolb, U., Komossa, S., Magnier, E. A., Mahabal, A., Polshaw, J., Prieto, J. L., Prusti, T., Riello, M., Scholz, A., Simonian, G., Stanek, K. Z., Szabados, L., Waters, C., and Wilson, R. W. (2015). Total eclipse of the heart: the AM CVn Gaia14aae/ASSASN-14cn. MNRAS, 452:1060–1067.

Cannizzo, J. K. (2001a). The 2001 Superoutburst of WZ Sagittae: A Clue to the Dynamics of Accretion Disks. ApJ, 561(2):L175–L178.

Cannizzo, J. K. (2001b). The V-EUV Delay for Dwarf Nova Outbursts: A Case Study for VW Hydri, U Geminorum, and SS Cygni. ApJ, 556(2):847–857.

Cannizzo, J. K., Ghosh, P., and Wheeler, J. C. (1982). Convective accretion disks and the onset of dwarf nova outbursts. ApJ, 260:L83–L86.

Cannizzo, J. K., Shafter, A. W., and Wheeler, J. C. (1988). On the Outburst Recurrence Time for the Accretion Disk Limit Cycle Mechanism in Dwarf Novae. ApJ, 333:227.

Carter, P. J., Gänsicke, B. T., Steeghs, D., Marsh, T. R., Breedt, E., Kupfer, T., Gentile Fusillo, N. P., Groot, P. J., and Nelemans, G. (2014a). Two new AM Canum Venaticorum binaries from the Sloan Digital Sky Survey III. MNRAS, 439:2848–2853.

Carter, P. J., Marsh, T. R., Steeghs, D., Groot, P. J., Nelemans, G., Levitan, D., Rau, A., Copperwheat, C. M., Kupfer, T., and Roelofs, G. H. A. (2013a). A search for the hidden population of AM CVn binaries in the Sloan Digital Sky Survey. MNRAS, 429:2143–2160.

Carter, P. J., Steeghs, D., de Miguel, E., Goff, W., Koff, R. A., Krajci, T., Marsh, T. R., Gänsicke, B. T., Breedt, E., Groot, P. J., Nelemans, G., Roelofs, G. H. A., Rau, A., Koester, D., and Kupfer, T. (2013b). The helium-rich cataclysmic variable SBSS 1108+574. MNRAS, 431(1):372–382.

Carter, P. J., Steeghs, D., Marsh, T. R., Kupfer, T., Copperwheat, C. M., Groot, P. J., and Nelemans, G. (2014b). The AM Canum Venaticorum binary SDSS J173047.59+554518.5. MNRAS, 437:2894–2900.

Cartier, R., Gutierrez, C. P., Smith, M., Frohmaier, C., Inserra, C., Lyman, J., Kankare, E., Maguire, K., Smartt, S. J., Smith, K. W., Sullivan, M., Valenti, S., Yaron, O., Young, D., Manulis, I., Tonry, J., Stalder, B., Denneau, L., Heinze, A., Weiland, H., Rest, A., Wright, D., Chambers, K. C., Flewelling, H., Huber, M., Magnier, T. L. E., Schulz, A., Waters, C., Wainscoat, R. J., and Wilman, M. (2017). ePESSTO spectroscopic classification of optical transients. The Astronomer's Telegram, 10334.

Chornock, R. and Filippenko, A. V. (2003). No supernova 2003aw. IAU Circ., 8084:3.

Coleman, M. S. B., Kotko, I., Blaes, O., Lasota, J. P., and Hirose, S. (2016). Dwarf nova outbursts with magnetorotational turbulence. MNRAS, 462(4):3710–3726.

Collier Cameron, A., Duncan, D. K., Ehrenfreund, P., Foing, B. H., Kuntz, K. D., Penston, M. V., Robinson, R. D., and Soderblom, D. R. (1990). Fast Spectroscopic Variations on Rapidly Rotating Cool Dwarfs - Part Three - Masses of Circumstellar Absorbing Clouds on Ab-Doradus. MNRAS, 247:415.

Collier Cameron, A. and Woods, J. A. (1992). Prominence activity in G dwarfs of the Alpha Persei cluster. MNRAS, 258:360–370.

Coppejans, D. L., Körding, E. G., Knigge, C., Pretorius, M. L., Woudt, P. A., Groot, P. J., Van Eck, C. L., and Drake, A. J. (2016a). Statistical properties of dwarf novae-type cataclysmic variables: the outburst catalogue. MNRAS, 456(4):4441–4454.

Coppejans, D. L., Körding, E. G., Miller-Jones, J. C. A., Rupen, M. P., Sivakoff, G. R., Knigge, C., Groot, P. J., Woudt, P. A., Waagen, E. O., and Templeton, M. (2016b). Dwarf nova-type cataclysmic variable stars are significant radio emitters. MNRAS, 463:2229–2241.

Coppejans, D. L., Woudt, P. A., Warner, B., Körding, E., Macfarlane, S. A., Schurch, M. P. E., Kotze, M. M., Breytenbach, H. B., Gulbis, A. A. S., and Coppejans, R. (2014). High-speed photometry of faint cataclysmic variables - VIII. Targets from the Catalina Real-Time Transient Survey. MNRAS, 437(1):510–523.

Coppejans, R., Gulbis, A. A. S., Kotze, M. M., Coppejans, D. L., Worters, H. L., Woudt, P. A., Whittal, H., Cloete, J., and Fourie, P. (2013). Characterizing and Commissioning the Sutherland High-Speed Optical Cameras (SHOC). PASP, 125:976.

Copperwheat, C. M., Marsh, T. R., Littlefair, S. P., Dhillon, V. S., Ramsay, G., Drake, A. J., Gänsicke, B. T., Groot, P. J., Hakala, P., Koester, D., Nelemans, G., Roelofs, G., Southworth, J., Steeghs, D., and Tulloch, S. (2011). SDSS J0926+3624: the shortest period eclipsing binary star. MNRAS, 410(2):1113–1129.

Córdova, F. A., Chester, T. J., Tuohy, I. R., and Garmire, G. P. (1980). Soft X-ray pulsations from SS Cyg. ApJ, 235:163–176.

Cowley, A. P. and Crampton, D. (1977). A preliminary model for the X-ray binary AM Herculis. ApJ, 212:L121–L124.

Crawford, S. M., Still, M., Schellart, P., Balona, L., Buckley, D. A. H., Dugmore, G., Gulbis, A. A. S., Kniazev, A., Kotze, M., Loaring, N., Nordsieck, K. H., Pickering, T. E., Potter, S., Romero Colmenero, E., Vaisanen, P., Williams, T., and Zietsman, E. (2010). PySALT: the SALT science pipeline. In Silva, D. R., Peck, A. B., and Soifer, B. T., editors, Observatory Operations: Strategies, Processes, and Systems III, volume 7737 of Society of Photo-Optical Instrumentation Engineers (SPIE) Conference Series, page 773725.

Croom, S. M., Smith, R. J., Boyle, B. J., Shanks, T., Miller, L., Outram, P. J., and Loaring, N. S. (2004). The 2dF QSO Redshift Survey - XII. The spectroscopic catalogue and luminosity function. MNRAS, 349:1397–1418.

Cropper, M. (1986). Polarization observations of DQ HER stars and other cataclysmic variables. MNRAS, 222:225–233.

Cropper, M. (1989). The accretion region in AM HER systems : insights from polarimetry ofV834 Cen. MNRAS, 236:935–957.

Cropper, M. (1990). The Polars. Space Sci. Rev., 54:195–295.

Cropper, M., Harrop-Allin, M. K., Mason, K. O., Mittaz, J. P. D., Potter, S. B., and Ramsay, G. (1998). RX J1914.4+2456 - The first double-degenerate polar? MNRAS, 293:L57–L60.

Cropper, M., Ramsay, G., Hellier, C., Mukai, K., Mauche, C., and Pandel, D. (2002). X-ray observations of accreting white-dwarf systems. Philosophical Transactions of the Royal Society of London Series A, 360:1951.

Cropper, M. and Wickramasinghe, D. T. (1993). Cyclotron humps in AM HER systems - V. Two poles in DP Leo. MNRAS, 260:696–704.

Dall'Osso, S., Israel, G. L., and Stella, L. (2007). Unipolar inductor model coupled to GW emission: energy budget and model application to RX J0806+15 and RX J1914+24. A&A, 464:417–427.

Deloye, C. J., Taam, R. E., Winisdoerffer, C., and Chabrier, G. (2007a). The thermal evolution of the donors in AM Canum Venaticorum binaries. MNRAS, 381:525–542.

Deloye, C. J., Taam, R. E., Winisdoerffer, C., and Chabrier, G. (2007b). Thermal Evolution of AM CVn Binary Donors. In Napiwotzki, R. and Burleigh, M. R., editors, 15th European Workshop on White Dwarfs, volume 372 of Astronomical Society of the Pacific Conference Series, page 447.

Denisenko, D., Lipunov, V., Gorbovskoy, E., Tiurina, N., Balanutsa, P., Kornilov, V., Shatskiy, N., Chazov, V., Kuznetsov, A., Vladimirov, V., Ivanov, K., Yazev, S., Budnev, N., Konstantinov, E., Chuvalaev, O., Poleshchuk, V., Gress, O., Krushinsky, V., Zalozhnih, I., Popov, A., Bourdanov, A., Tlatov, A., Dormidontov, D., Senik, V., Parkhomenko, A., Yurkov, V., Gabovich, A., Sergienko, Y., Sinyakov, E., Shumkov, V., and Shurpakov, S. (2014). MASTER Archival Observations of the Very Bright Cataclysmic Variable ASASSN-14mv. The Astronomer's Telegram, 6857.

Dillon, M., Gänsicke, B. T., Aungwerojwit, A., Rodríguez-Gil, P., Marsh, T. R., Barros, S. C. C., Szkody, P., Brady, S., Krajci, T., and Oksanen, A. (2008). Orbital periods of cataclysmic variables identified by the SDSS - III. Time-series photometry obtained during the 2004/5 International Time Project on La Palma. MNRAS, 386(3):1568–1578.

Drake, A. J., Djorgovski, S. G., Mahabal, A., Beshore, E., Larson, S., Graham, M. J., Williams, R., Christensen, E., Catelan, M., Boattini, A., Gibbs, A., Hill, R., and Kowalski, R. (2009). First Results from the Catalina Real-Time Transient Survey. ApJ, 696:870–884.

Drake, A. J., Djorgovski, S. G., Mahabal, A. A., Graham, M. J., Williams, R., Prieto, J., Catelan, M., Christensen, E., and Larson, S. M. (2012). A candidate AM CVn system from CRTS. The Astronomer's Telegram, 4678.

Drake, A. J., Gänsicke, B. T., Djorgovski, S. G., Wils, P., Mahabal, A. A., Graham, M. J., Yang, T.-C., Williams, R., Catelan, M., Prieto, J. L., Donalek, C., Larson, S., and Christensen, E. (2014). Cataclysmic variables from the Catalina Real-time Transient Survey. MNRAS, 441:1186–1200.

Duffy, C., Ramsay, G., Wu, K., Mason, P. A., Hakala, P., Steeghs, D., and Wood, M. A. (2022). Short-duration accretion states of Polars as seen in TESS and ZTF data. MNRAS, 516(3):3144–3158.

Eisenstein, D. J., Annis, J., Gunn, J. E., Szalay, A. S., Connolly, A. J., Nichol, R. C., Bahcall, N. A., Bernardi, M., Burles, S., Castander, F. J., Fukugita, M., Hogg, D. W., Ivezić, Ž., Knapp, G. R., Lupton, R. H., Narayanan, V., Postman, M., Reichart, D. E., Richmond, M., Schneider, D. P., Schlegel, D. J., Strauss, M. A., SubbaRao, M., Tucker, D. L., Vanden Berk, D., Vogeley, M. S., Weinberg, D. H., and Yanny, B. (2001). Spectroscopic Target Selection for the Sloan Digital Sky Survey: The Luminous Red Galaxy Sample. AJ, 122:2267–2280.

Eisenstein, D. J., Weinberg, D. H., Agol, E., Aihara, H., Allende Prieto, C., Anderson, S. F., Arns, J. A., Aubourg, É., Bailey, S., Balbinot, E., and et al. (2011). SDSS-III: Massive Spectroscopic Surveys of the Distant Universe, the Milky Way, and Extra-Solar Planetary Systems. AJ, 142:72.

Elvius, A. (1975). Variable blur object with a peculiar spectrum. A&A, 44:117–121.

Ergma, E. V. and Fedorova, A. V. (1990). Evolution of a binary system consisting of a helium star and a white dwarf. Ap&SS, 163:143–152.

Espaillat, C., Patterson, J., Warner, B., and Woudt, P. (2005). The Helium-rich Cataclysmic Variable ES Ceti. PASP, 117(828):189–198.

Falanga, M., de Martino, D., Bernardini, F., and Mukai, K. (2019). Magnetic cataclysmic variables discovered in hard X-rays. Mem. Soc. Astron. Italiana, 90:126.

Faulkner, J., Flannery, B. P., and Warner, B. (1972). Ultrashort-Period Binaries. II. HZ 29 (=AM CVn): a Double-White Semidetached Postcataclysmic Nova? ApJ, 175:L79.

Ferrario, L., de Martino, D., and Gänsicke, B. T. (2015). Magnetic White Dwarfs. Space Sci. Rev., 191:111–169.

Ferrario, L., Wickramasinghe, D., Bailey, J., and Buckley, D. (1995). 1H 1752+08: the lowest field AM Herculis system? MNRAS, 273(1):17–24.

Ferrario, L., Wickramasinghe, D. T., Bailey, J., Hough, J. H., and Tuohy, I. R. (1992). Detection of photospheric Zeeman features and cyclotron emission lines in V834 CEN in a low state. MNRAS, 256:252–260.

Ferrario, L., Wickramasinghe, D. T., and Schmidt, G. (2002). Polarized line emission from magnetized accretion flows. MNRAS, 331:736–744.

Ferrario, L., Wickramasinghe, D. T., and Tuohy, I. R. (1989). An emission-line model for AM Herculis systems. ApJ, 341:327–339.

Fontaine, G., Brassard, P., Green, E. M., Charpinet, S., Dufour, P., Hubeny, I., Steeghs, D., Aerts, C., Randall, S. K., Bergeron, P., Guvenen, B., O'Malley, C. J., Van Grootel, V., Østensen, R. H., Bloemen, S., Silvotti, R., Howell, S. B., Baran, A., Kepler, S. O., Marsh, T. R., Montgomery, M. H., Oreiro, R., Provencal, J., Telting, J., Winget, D. E., Zima, W., Christensen-Dalsgaard, J., and Kjeldsen, H. (2011). Discovery of a New AM CVn System with the Kepler Satellite. ApJ, 726:92.

Frank, J., King, A., and Raine, D. J. (2002). Accretion Power in Astrophysics: Third Edition. Cambridge University Press.

Fuchs, J. T., Dunlap, B. H., Dennihy, E., O'Donoghue, D., Clemens, J. C., Reichart, D. E., Moore, J. P., LaCluyze, A. P., Haislip, J. B., and Ivarsen, K. V. (2016). The magnetic cataclysmic variable LSQ1725-64. MNRAS, 462(3):2382–2395.

Fujimoto, M. Y. and Sugimoto, D. (1982). Helium shell flashes and evolution of accreting white dwarfs. ApJ, 257:291–302.

Gabdeev, M. M. (2015). Photometric monitoring of polar candidates. Astrophysical Bulletin, 70(4):460–465.

Gabdeev, M. M., Fatkhullin, T. A., and Borisov, N. V. (2020). On the Possibility of Using Mid-Band Filters to Search for Polar Candidates. Astrophysical Bulletin, 75(3):320–324.

Gabdeev, M. M., Shimansky, V. V., Borisov, N. V., Bikmaev, I. F., Moskvitin, A. S., and Kolbin, A. I. (2019). Spectroscopic and Photometric Study of the Polar 1RXS J152506.9-032647. Astrophysical Bulletin, 74(3):308–315.

Gänsicke, B. T., Dillon, M., Southworth, J., Thorstensen, J. R., Rodríguez-Gil, P., Aungwerojwit, A., Marsh, T. R., Szkody, P., Barros, S. C. C., Casares, J., de Martino, D., Groot, P. J., Hakala, P., Kolb, U., Littlefair, S. P., Martínez-Pais, I. G., Nelemans, G., and Schreiber, M. R. (2009). SDSS unveils a population of intrinsically faint cataclysmic variables at the minimum orbital period. MNRAS, 397(4):2170–2188.

Gänsicke, B. T., Hoard, D. W., Beuermann, K., Sion, E. M., and Szkody, P. (1998). HST/GHRS observations of AM Herculis. A&A, 338:933–946.

García-Berro, E., Lorén-Aguilar, P., Aznar-Siguán, G., Torres, S., Camacho, J., Althaus, L. G., Córsico, A. H., Külebi, B., and Isern, J. (2012). Double Degenerate Mergers as Progenitors of High-field Magnetic White Dwarfs. ApJ, 749(1):25.

Garnavich, P. M., Szkody, P., Robb, R. M., Zurek, D. R., and Hoard, D. W. (1994). RJ 051542+0104.7: A New Magnetic, Eclipsing, Cataclysmic Variable. ApJ, 435:L141.

Geckeler, R. D. and Staubert, R. (1997). Periodic changes of the accretion geometry in the nearly-synchronous polar RX J1940.1-1025. A&A, 325:1070–1076.

Gokhale, V., Peng, X. M., and Frank, J. (2007). Evolution of Close White Dwarf Binaries. ApJ, 655:1010–1024.

Graham, M. J., Kulkarni, S. R., Bellm, E. C., Adams, S. M., Barbarino, C., Blagorodnova, N., Bodewits, D., Bolin, B., Brady, P. R., Cenko, S. B., Chang, C.-K., Coughlin, M. W., De, K., Eadie, G., Farnham, T. L., Feindt, U., Franckowiak, A., Fremling, C., Gezari, S., Ghosh, S., Goldstein, D. A., Golkhou, V. Z., Goobar, A., Ho, A. Y. Q., Huppenkothen, D., Ivezić, Ž., Jones, R. L., Juric, M., Kaplan, D. L., Kasliwal, M. M., Kelley, M. S. P., Kupfer, T., Lee, C.-D., Lin, H. W., Lunnan, R., Mahabal, A. A., Miller, A. A., Ngeow, C.-C., Nugent, P., Ofek, E. O., Prince, T. A., Rauch, L., van Roestel, J., Schulze, S., Singer, L. P., Sollerman, J., Taddia, F., Yan, L., Ye, Q.-Z., Yu, P.-C., Barlow, T., Bauer, J., Beck, R., Belicki, J., Biswas, R., Brinnel, V., Brooke, T., Bue, B., Bulla, M., Burruss, R., Connolly, A., Cromer, J., Cunningham, V., Dekany, R., Delacroix, A., Desai, V., Duev, D. A., Feeney, M., Flynn, D., Frederick, S., Gal-Yam, A., Giomi, M., Groom, S., Hacopians, E., Hale, D., Helou, G., Henning, J., Hover, D., Hillenbrand, L. A., Howell, J., Hung, T., Imel, D., Ip, W.-H., Jackson, E., Kaspi, S., Kaye, S., Kowalski, M., Kramer, E., Kuhn, M., Landry, W., Laher, R. R., Mao, P., Masci, F. J., Monkewitz, S., Murphy, P., Nordin, J., Patterson, M. T., Penprase, B., Porter, M., Rebbapragada, U., Reiley, D., Riddle, R., Rigault, M., Rodriguez, H., Rusholme, B., van Santen, J., Shupe, D. L., Smith, R. M., Soumagnac, M. T., Stein, R., Surace, J., Szkody, P., Terek, S., Van Sistine, A., van Velzen, S., Vestrand, W. T., Walters, R., Ward, C., Zhang, C., and Zolkower, J. (2019). The Zwicky Transient Facility: Science Objectives. PASP, 131(1001):078001.

Green, M. J., Hermes, J. J., Marsh, T. R., Steeghs, D. T. H., Bell, K. J., Littlefair, S. P., Parsons, S. G., Dennihy, E., Fuchs, J. T., Reding, J. S., Kaiser, B. C., Ashley, R. P., Breedt, E., Dhillon, V. S., Gentile Fusillo, N. P., Kerry, P., and Sahman, D. I. (2018a). A 15.7-minAM CVn binary discovered in K2. MNRAS, 477(4):5646–5656.

Green, M. J., Marsh, T. R., Carter, P. J., Steeghs, D., Breedt, E., Dhillon, V. S., Littlefair, S. P., Parsons, S. G., Kerry, P., Gentile Fusillo, N. P., Ashley, R. P., Bours, M. C. P., Cunningham, T., Dyer, M. J., Gänsicke, B. T., Izquierdo, P., Pala, A. F., Pattama, C., Outmani, S., Sahman, D. I., Sukaum, B., and Wild, J. (2020). Spectroscopic and

photometric periods of six ultracompact accreting binaries. MNRAS, 496(2):1243–1261.

Green, M. J., Marsh, T. R., Steeghs, D. T. H., Kupfer, T., Ashley, R. P., Bloemen, S., Breedt, E., Campbell, H. C., Chakpor, A., Copperwheat, C. M., Dhillon, V. S., Hallinan, G., Hardy, L. K., Hermes, J. J., Kerry, P., Littlefair, S. P., Milburn, J., Parsons, S. G., Prasert, N., van Roestel, J., Sahman, D. I., and Singh, N. (2018b). High-speed photometry of Gaia14aae: an eclipsing AM CVn that challenges formation models. MNRAS, 476(2):1663–1679.

Gulbis, A. A. S., O'Donoghue, D., Fourie, P., Rust, M., Sass, C., and Stoffels, J. (2011). SHOC: Sutherland High-speed Optical Cameras. In EPSC-DPS Joint Meeting 2011, page 1173.

Gunn, J. E., Carr, M., Rockosi, C., Sekiguchi, M., Berry, K., Elms, B., de Haas, E., Ivezić, Ž., Knapp, G., Lupton, R., Pauls, G., Simcoe, R., Hirsch, R., Sanford, D., Wang, S., York, D., Harris, F., Annis, J., Bartozek, L., Boroski, W., Bakken, J., Haldeman, M., Kent, S., Holm, S., Holmgren, D., Petravick, D., Prosapio, A., Rechenmacher, R., Doi, M., Fukugita, M., Shimasaku, K., Okada, N., Hull, C., Siegmund, W., Mannery, E., Blouke, M., Heidtman, D., Schneider, D., Lucinio, R., and Brinkman, J. (1998). The Sloan Digital Sky Survey Photometric Camera. AJ, 116:3040–3081.

Gunn, J. E., Siegmund, W. A., Mannery, E. J., Owen, R. E., Hull, C. L., Leger, R. F., Carey, L. N., Knapp, G. R., York, D. G., Boroski, W. N., Kent, S. M., Lupton, R. H., Rockosi, C. M., Evans, M. L., Waddell, P., Anderson, J. E., Annis, J., Barentine, J. C., Bartoszek, L. M., Bastian, S., Bracker, S. B., Brewington, H. J., Briegel, C. I., Brinkmann, J., Brown, Y. J., Carr, M. A., Czarapata, P. C., Drennan, C. C., Dombeck, T., Federwitz, G. R., Gillespie, B. A., Gonzales, C., Hansen, S. U., Harvanek, M., Hayes, J., Jordan, W., Kinney, E., Klaene, M., Kleinman, S. J., Kron, R. G., Kresinski, J., Lee, G., Limmongkol, S., Lindenmeyer, C. W., Long, D. C., Loomis, C. L., McGehee, P. M., Mantsch, P. M., Neilsen, Jr., E. H., Neswold, R. M., Newman, P. R., Nitta, A., Peoples, Jr., J., Pier, J. R., Prieto, P. S., Prosapio, A., Rivetta, C., Schneider, D. P., Snedden, S., and Wang, S.-i. (2006). The 2.5 m Telescope of the Sloan Digital Sky Survey. AJ, 131:2332–2359.

Hakala, P., Parsons, S. G., Marsh, T. R., Gänsicke, B. T., Ramsay, G., Schwope, A., and Hermes, J. J. (2022). Circular polarimetry of suspect wind-accreting magnetic prepolars. MNRAS, 513(3):3858–3870.

Hakala, P. J. (1995). Accretion stream mapping in eclipsing polars. an application of MEM and genetic optimisation. A&A, 296:164.

Hakala, P. J., Watson, M. G., Vilhu, O., Hassall, B. J. M., Kellett, B. J., Mason, K. O., and Piirola, V. (1993). The discovery of a new bright eclipsing AM HER system. MNRAS, 263:61–68.

Hameury, J.-M., Lasota, J.-P., and Warner, B. (2000). The zoo of dwarf novae: illumination, evaporation and disc radius variation. A&A, 353:244–252.

Hampel, F. R. (1974). The influence curve and its role in robust estimation. Journal of the American Statistical Association, 69(346):383–393.

Hardy, L. K., McAllister, M. J., Dhillon, V. S., Littlefair, S. P., Bours, M. C. P., Breedt, E., Butterley, T., Chakpor, A., Irawati, P., Kerry, P., Marsh, T. R., Parsons, S. G., Savoury, C. D. J., Wilson, R. W., and Woudt, P. A. (2017). Hunting for eclipses: high-speed observations of cataclysmic variables. MNRAS, 465:4968–4984.

Harrop-Allin, M. K., Cropper, M., Hakala, P. J., Hellier, C., and Ramseyer, T. (1999). Indirect imaging of the accretion stream in eclipsing polars - II. HU Aquarii. MNRAS, 308(3):807–817.

Harrop-Allin, M. K., Cropper, M., Potter, S. B., Dhillon, V. S., and Howell, S. B. (1997). Infrared spectroscopy of the long-period polar RX J0515.6+0105. MNRAS, 288(4):1033–1040.

Hawley, J. F. and Balbus, S. A. (1991). A Powerful Local Shear Instability in Weakly Magnetized Disks. II. Nonlinear Evolution. ApJ, 376:223.

Heerlein, C., Horne, K., and Schwope, A. D. (1999). Modelling of the magnetic accretion flow in HU Aquarii. MNRAS, 304(1):145–154.

Heise, J., Brinkman, A. C., Gronenschild, E., Watson, M., King, A. R., Stella, L., and Kieboom, K. (1985). An X-ray study of AM Herculis. I - Discovery of a new mode of soft X-ray emission. A&A, 148:L14–L16.

Hessman, F. V. (2000). The symptoms and causes of CV low-states. New A Rev., 44:155–160.

Hessman, F. V., Gänsicke, B. T., and Mattei, J. A. (2000). The history and source of mass-transfer variations in AM Herculis. A&A, 361:952–958.

Hirose, M. and Osaki, Y. (1990). Hydrodynamic Simulations of Accretion Disks in Cataclysmic Variables: Superhump Phenomenon in SU UMa Stars. PASJ, 42:135–163.

Hirose, S., Blaes, O., and Krolik, J. H. (2009). Turbulent Stresses in Local Simulations of Radiation-dominated Accretion Disks, and the Possibility of the Lightman-Eardley Instability. ApJ, 704(1):781–788.

Hložek, R., Ponder, K. A., Malz, A. I., Dai, M., Narayan, G., Ishida, E. E. O., Allam, T., J., Bahmanyar, A., Biswas, R., Galbany, L., Jha, S. W., Jones, D. O., Kessler, R., Lochner, M., Mahabal, A. A., Mandel, K. S., Martínez-Galarza, J. R., McEwen, J. D., Muthukrishna, D., Peiris, H. V., Peters, C. M., and Setzer, C. N. (2020). Results of the Photometric LSST Astronomical Time-series Classification Challenge (PLAsTiCC). arXiv e-prints, page arXiv:2012.12392.

Holoien, T. W.-S., Stanek, K. Z., Kochanek, C. S., Shappee, B. J., Prieto, J. L., Brimacombe, J., Bersier, D., Bishop, D. W., Dong, S., Brown, J. S., Danilet, A. B., Simonian, G. V., Basu, U., Beacom, J. F., Falco, E., Pojmanski, G., Skowron, D. M., Woźniak, P. R., Ávila, C. G., Conseil, E., Contreras, C., Cruz, I., Fernández, J. M., Koff, R. A., Guo, Z., Herczeg, G. J., Hissong, J., Hsiao, E. Y., Jose, J., Kiyota, S., Long, F., Monard, L. A. G., Nicholls, B., Nicolas, J., and Wiethoff, W. S. (2017). The ASAS-SN bright supernova catalogue - I. 2013-2014. MNRAS, 464:2672–2686.

Homer, L., Szkody, P., Chen, B., Henden, A., Schmidt, G. D., Fraser, O. J., Saloma, K., Silvestri, N. M., Taylor, H., and Brinkmann, J. (2005). XMM-Newton and Optical Follow-up Observations of Three New Polars from the Sloan Digital Sky Survey. ApJ, 620(2):929–937.

Honda, M., Osawa, K., Osada, K., Ito, S., Hashimoto, N., Shugarov, S. Y., Kohoutek, L., Richter, G., Gotz, W., Lefevre, J., Shefer, Y., Schippers, J. W., Madlow, E., Schnitz, M., Durkefalden, M., Callus, R., Marx, M. H., Trumpp, H. J., Jones, R., Cernis, K., Garnavich, P., Lemay, D., Seykora, E. J., Thompson, A. C., Kuhns, J. L., Kelley, G. W., Kirby, G., Stone, J. F., Dodds, E. F., Johnson, R., Duke, D., Miller, H. L., Edwards, T. W., Lockett, A., Maim, R., Cannon, J., Gates, W., Prentice, J., Wallace, D., Maloney, P., Upgren, A. R., Dillon, W. G., Gunnerson, R., Richardson, C., Stanton, R. H., King, F., Keen, R. A., Povenmire, H., Fellers, D., Talent, D., Tyson, C., Sampson, R., Weisberg, J., Decaria, M. D., Machholz, D., Wooten, J. W., Rather, J., Conquest, E., Hickson, E. B., Lightfoot, D., Howell, A., Kemble, L., Bergbusch, P., Wallentine, D., Cooperman, S., de Vegt, C., Gehuch, U. K., Debehogne, H., Samus, N. N., Martynov, D. Y., Tempesti, P., Shenavrin, V. I., Purton, C. R., Clark, P., Schroder, Baranowski, Garbacz, and de Terwagne (1975). Nova Cygni 1975. IAU Circ., 2826:1.

Hong, J., van den Berg, M., Grindlay, J. E., Servillat, M., and Zhao, P. (2012). Discovery of a Significant Magnetic Cataclysmic Variable Population in the Limiting Window. ApJ, 746(2):165.

Hōshi, R. (1973). X-Ray Emission from White Dwarfs in Close Binary Systems. Progress of Theoretical Physics, 49(3):776–789.

Hōshi, R. (1979). Accretion Model for Outbursts of Dwarf Nova. Progress of Theoretical Physics, 61(5):1307–1319.

Huber, P. J. (1981). Robust statistics.

Iben, Jr., I. and Tutukov, A. V. (1987). Evolutionary scenarios for intermediate-mass stars in close binaries. ApJ, 313:727–742.

Iben, Jr., I. and Tutukov, A. V. (1991). Helium star cataclysmics. ApJ, 370:615–629.

Iben, Icko, J. and Livio, M. (1993). Common Envelopes in Binary Star Evolution. PASP, 105:1373.

Iben, Icko, J. and Tutukov, A. V. (1986). On the Formation and Evolution of a Helium Degenerate Dwarf in a Close Binary. ApJ, 311:742.

Inogamov, N. A. and Sunyaev, R. A. (1999). Spread of matter over a neutron-star surface during disk accretion. Astronomy Letters, 25(5):269–293.

Isern, J., García-Berro, E., Külebi, B., and Lorén-Aguilar, P. (2017). A Common Origin of Magnetism from Planets to White Dwarfs. ApJ, 836(2):L28.

Isogai, K., Kato, T., Monard, B., Hambsch, F.-J., Myers, G., Starr, P., Cook, L. M., and Nogami, D. (2019). NSV 1440: first WZ Sge-type object in AM CVn stars and candidates. PASJ, 71(2):48.

Isogai, K., Kato, T., Nogami, D., Ohshima, T., and Imada, A. (2015). Research on AM CVn stars: ASASSN-14ei and CR Boo. In The Golden Age of Cataclysmic Variables and Related Objects - III (Golden2015), page 49.

Isogai, K., Tampo, Y., Kojiguchi, N., Taguchi, K., Itoh, J., Shibata, M., Kato, T., Itoh, H., and Kubotera, K. (2021). Spectroscopic and photometric confirmation of ASASSN-21au = ZTF20acyxwzf as the best candidate for a long-orbital period AM CVn star. The Astronomer's Telegram, 14390:1.

Israel, G. L., Panzera, M. R., Campana, S., Lazzati, D., Covino, S., Tagliaferri, G., and Stella, L. (1999). The discovery of 321 S pulsations in the ROSAT HRI light curves of 1BMW J080622.8+152732 = RX J0806.3+1527. A&A, 349:L1–L4.

Ivanova, N., Justham, S., Chen, X., De Marco, O., Fryer, C. L., Gaburov, E., Ge, H., Glebbeek, E., Han, Z., Li, X. D., Lu, G., Marsh, T., Podsiadlowski, P., Potter, A., Soker, N., Taam, R., Tauris, T. M., van den Heuvel, E. P. J., and Webbink, R. F. (2013). Common envelope evolution: where we stand and how we can move forward. A&A Rev., 21:59.

Ivezić, Ž., Kahn, S. M., Tyson, J. A., Abel, B., Acosta, E., Allsman, R., Alonso, D., AlSayyad, Y., Anderson, S. F., Andrew, J., Angel, J. R. P., Angeli, G. Z., Ansari, R., Antilogus, P., Araujo, C., Armstrong, R., Arndt, K. T., Astier, P., Aubourg, É., Auza, N., Axelrod, T. S., Bard, D. J., Barr, J. D., Barrau, A., Bartlett, J. G., Bauer, A. E., Bauman, B. J., Baumont, S., Bechtol, E., Bechtol, K., Becker, A. C., Becla, J., Beldica, C., Bellavia, S., Bianco, F. B., Biswas, R., Blanc, G., Blazek, J., Blandford, R. D., Bloom, J. S., Bogart, J., Bond, T. W., Booth, M. T., Borgland, A. W., Borne, K., Bosch, J. F., Boutigny, D., Brackett, C. A., Bradshaw, A., Brandt, W. N., Brown, M. E., Bullock, J. S., Burchat, P., Burke, D. L., Cagnoli, G., Calabrese, D., Callahan, S., Callen, A. L., Carlin, J. L., Carlson, E. L., Chandrasekharan, S., Charles-Emerson, G., Chesley, S., Cheu, E. C., Chiang, H.-F., Chiang, J., Chirino, C., Chow, D., Ciardi, D. R., Claver, C. F., Cohen-Tanugi, J., Cockrum, J. J., Coles, R., Connolly, A. J., Cook, K. H., Cooray, A., Covey, K. R., Cribbs, C., Cui, W., Cutri, R., Daly, P. N., Daniel, S. F., Daruich, F., Daubard, G., Daues, G., Dawson, W., Delgado, F., Dellapenna, A., de Peyster, R., de Val-Borro, M., Digel, S. W., Doherty, P., Dubois, R., Dubois-Felsmann, G. P., Durech, J., Economou, F., Eifler, T., Eracleous, M., Emmons, B. L., Fausti Neto, A., Ferguson, H., Figueroa, E., Fisher-Levine, M., Focke, W., Foss, M. D., Frank, J., Freemon, M. D., Gangler, E., Gawiser, E., Geary, J. C., Gee, P., Geha, M., Gessner, C. J. B., Gibson, R. R., Gilmore, D. K., Glanzman, T., Glick, W., Goldina, T., Goldstein, D. A., Goodenow, I., Graham, M. L., Gressler, W. J., Gris, P., Guy, L. P., Guyonnet, A., Haller, G., Harris, R., Hascall, P. A., Haupt, J., Hernandez, F., Herrmann, S., Hileman, E., Hoblitt, J., Hodgson, J. A., Hogan, C., Howard, J. D., Huang, D., Huffer, M. E., Ingraham, P., Innes, W. R., Jacoby, S. H., Jain, B., Jammes, F., Jee, M. J., Jenness, T., Jernigan, G., Jevremović, D., Johns, K., Johnson, A. S., Johnson, M. W. G., Jones, R. L., Juramy-Gilles, C., Jurić, M., Kalirai, J. S., Kallivayalil, N. J., Kalmbach, B., Kantor, J. P., Karst, P., Kasliwal, M. M., Kelly, H., Kessler, R., Kinnison, V., Kirkby, D., Knox, L., Kotov, I. V., Krabbendam, V. L., Krughoff, K. S., Kubánek, P., Kuczewski, J., Kulkarni, S., Ku, J., Kurita, N. R., Lage, C. S., Lambert, R., Lange, T., Langton, J. B., Le Guillou, L., Levine, D., Liang, M., Lim, K.-T., Lintott, C. J., Long, K. E., Lopez, M., Lotz, P. J., Lupton, R. H., Lust, N. B., MacArthur, L. A., Mahabal, A., Mandelbaum, R., Markiewicz, T. W., Marsh, D. S., Marshall, P. J., Marshall, S., May, M., McKercher, R., McQueen, M., Meyers,

J., Migliore, M., Miller, M., Mills, D. J., Miraval, C., Moeyens, J., Moolekamp, F. E., Monet, D. G., Moniez, M., Monkewitz, S., Montgomery, C., Morrison, C. B., Mueller, F., Muller, G. P., Muñoz Arancibia, F., Neill, D. R., Newbry, S. P., Nief, J.-Y., Nomerotski, A., Nordby, M., O'Connor, P., Oliver, J., Olivier, S. S., Olsen, K., O'Mullane, W., Ortiz, S., Osier, S., Owen, R. E., Pain, R., Palecek, P. E., Parejko, J. K., Parsons, J. B., Pease, N. M., Peterson, J. M., Peterson, J. R., Petravick, D. L., Libby Petrick, M. E., Petry, C. E., Pierfederici, F., Pietrowicz, S., Pike, R., Pinto, P. A., Plante, R., Plate, S., Plutchak, J. P., Price, P. A., Prouza, M., Radeka, V., Rajagopal, J., Rasmussen, A. P., Regnault, N., Reil, K. A., Reiss, D. J., Reuter, M. A., Ridgway, S. T., Riot, V. J., Ritz, S., Robinson, S., Roby, W., Roodman, A., Rosing, W., Roucelle, C., Rumore, M. R., Russo, S., Saha, A., Sassolas, B., Schalk, T. L., Schellart, P., Schindler, R. H., Schmidt, S., Schneider, D. P., Schneider, M. D., Schoening, W., Schumacher, G., Schwamb, M. E., Sebag, J., Selvy, B., Sembroski, G. H., Seppala, L. G., Serio, A., Serrano, E., Shaw, R. A., Shipsey, I., Sick, J., Silvestri, N., Slater, C. T., Smith, J. A., Smith, R. C., Sobhani, S., Soldahl, C., Storrie-Lombardi, L., Stover, E., Strauss, M. A., Street, R. A., Stubbs, C. W., Sullivan, I. S., Sweeney, D., Swinbank, J. D., Szalay, A., Takacs, P., Tether, S. A., Thaler, J. J., Thayer, J. G., Thomas, S., Thornton, A. J., Thukral, V., Tice, J., Trilling, D. E., Turri, M., Van Berg, R., Vanden Berk, D., Vetter, K., Virieux, F., Vucina, T., Wahl, W., Walkowicz, L., Walsh, B., Walter, C. W., Wang, D. L., Wang, S.-Y., Warner, M., Wiecha, O., Willman, B., Winters, S. E., Wittman, D., Wolff, S. C., Wood-Vasey, W. M., Wu, X., Xin, B., Yoachim, P., and Zhan, H. (2019). LSST: From Science Drivers to Reference Design and Anticipated Data Products. ApJ, 873(2):111.

Jayasinghe, T., Kochanek, C. S., Stanek, K. Z., Shappee, B. J., Holoien, T. W.-S., Thompson, T. A., Prieto, J. L., Dong, S., Pawlak, M., Shields, J. V., Pojmanski, G., Otero, S., Britt, C. A., and Will, D. (2018). The ASAS-SN catalogue of variable stars I: The Serendipitous Survey. MNRAS, 477:3145–3163.

Jester, S., Schneider, D. P., Richards, G. T., Green, R. F., Schmidt, M., Hall, P. B., Strauss, M. A., Vanden Berk, D. E., Stoughton, C., Gunn, J. E., Brinkmann, J., Kent, S. M., Smith, J. A., Tucker, D. L., and Yanny, B. (2005). The Sloan Digital Sky Survey View of the Palomar-Green Bright Quasar Survey. AJ, 130:873–895.

Jones, L., Yoachim, P., Ivezic, Z., Eric H. Neilsen, J., and Ribeiro, T. (2021). lsst-pst/pstn-051: v1.2.1.

Jones, M. H. and Watson, M. G. (1992). The EXOSAT obseravtions of SS Cygni. MNRAS, 257:633–649.

Jonker, P. G., Bassa, C. G., Nelemans, G., Steeghs, D., Torres, M. A. P., Maccarone, T. J., Hynes, R. I., Greiss, S., Clem, J., Dieball, A., Mikles, V. J., Britt, C. T., Gossen, L., Collazzi, A. C., Wijnands, R., In't Zand, J. J. M., Méndez, M., Rea, N., Kuulkers, E., Ratti, E. M., van Haaften, L. M., Heinke, C., Özel, F., Groot, P. J., and Verbunt, F. (2011). The Galactic Bulge Survey: Outline and X-ray Observations. ApJS, 194:18.

Jonker, P. G., Torres, M. A. P., Hynes, R. I., Maccarone, T. J., Steeghs, D., Greiss, S., Britt, C. T., Wu, J., Johnson, C. B., Nelemans, G., and Heinke, C. (2014). The Galactic Bulge Survey: Completion of the X-Ray Survey Observations. ApJS, 210:18.

Joye, W. A. and Mandel, E. (2003). New Features of SAOImage DS9. In Payne, H. E., Jedrzejewski, R. I., and Hook, R. N., editors, Astronomical Data Analysis Software

and Systems XII, volume 295 of Astronomical Society of the Pacific Conference Series, page 489.

Kafka, S., Ribeiro, T., Baptista, R., Honeycutt, R. K., and Robertson, J. W. (2008). New Complexities in the Low-State Line Profiles of AM Herculis. ApJ, 688:1302–1314.

Kafka, S., Tappert, C., Ribeiro, T., Honeycutt, R. K., Hoard, D. W., and Saar, S. (2010). Low-state Magnetic Structures in Polars: Nature or Nurture? ApJ, 721:1714–1724.

Kato, T. (2013). . vsnet-alert 15803.

Kato, T. (2022). Gaia22ayj: outburst from a deeply eclipsing 9.36-min binary? arXiv e-prints, page arXiv:2203.13975.

Kato, T. (2023). MGAB-V240: 23-min AM CVn star showing both 12-d supercycle and standstills. arXiv e-prints, page arXiv:2302.11148.

Kato, T., Dubovsky, P. A., Kudzej, I., Hambsch, F.-J., Miller, I., Ohshima, T., Nakata, C., Kawabata, M., Nishino, H., Masumoto, K., Mizoguchi, S., Yamanaka, M., Matsumoto, K., Sakai, D., Fukushima, D., Matsuura, M., Bouno, G., Takenaka, M., Nakagawa, S., Noguchi, R., Iino, E., Pickard, R. D., Maeda, Y., Henden, A., Kasai, K., Kiyota, S., Akazawa, H., Imamura, K., de Miguel, E., Maehara, H., Monard, B., Pavlenko, E. P., Antonyuk, K., Pit, N., Antonyuk, O. I., Baklanov, A. V., Ruiz, J., Richmond, M., Oksanen, A., Harlingten, C., Shugarov, S. Y., Chochol, D., Masi, G., Nocentini, F., Schmeer, P., Bolt, G., Nelson, P., Ulowetz, J., Sabo, R., Goff, W. N., Stein, W., Michel, R., Dvorak, S., Voloshina, I. B., Metlov, V., Katysheva, N., Neustroev, V. V., Sjoberg, G., Littlefield, C., Dębski, B., Sowicka, P., Klimaszewski, M., Curyło, M., Morelle, E., Curtis, I. A., Iwamatsu, H., Butterworth, N. D., Andreev, M. V., Parakhin, N., Sklyanov, A., Shiokawa, K., Novák, R., Irsmambetova, T. R., Itoh, H., Ito, Y., Hirosawa, K., Denisenko, D., Kochanek, C. S., Shappee, B., Stanek, K. Z., Prieto, J. L., Itagaki, K.-i., Stubbings, R., Ripero, J., Muyllaert, E., and Poyner, G. (2014a). Survey of period variations of superhumps in SU UMa-type dwarf novae. VI. The sixth year (2013-2014). PASJ, 66(5):90.

Kato, T., Hambsch, F.-J., and Monard, B. (2015). ASASSN-14cc: A likely helium analog of RZ Leonis Minoris. PASJ, 67:L2.

Kato, T., Hambsch, F.-J., Monard, B., Vanmunster, T., Maeda, Y., Miller, I., Itoh, H., Kiyota, S., Isogai, K., Kimura, M., Imada, A., Tordai, T., Akazawa, H., Tanabe, K., Otani, N., Ogi, M., Ando, K., Takigawa, N., Dubovsky, P. A., Kudzej, I., Shugarov, S. Y., Katysheva, N., Golysheva, P., Gladilina, N., Chochol, D., Starr, P., Kasai, K., Pickard, R. D., de Miguel, E., Kojiguchi, N., Sugiura, Y., Fukushima, D., Yamada, E., Uto, Y., Kamibetsunawa, T., Tatsumi, T., Takeda, N., Matsumoto, K., Cook, L. M., Pavlenko, E. P., Babina, J. V., Pit, N. V., Antonyuk, O. I., Antonyuk, K. A., Sosnovskij, A. A., Baklanov, A. V., Kafka, S., Stein, W., Voloshina, I. B., Ruiz, J., Sabo, R., Dvorak, S., Stone, G., Andreev, M. V., Antipin, S. V., Zubareva, A. M., Zaostrojnykh, A. M., Richmond, M., Shears, J., Dubois, F., Logie, L., Rau, S., Vanaverbeke, S., Simon, A., Oksanen, A., Goff, W. N., Bolt, G., Dębski, B., Kochanek, C. S., Shappee, B., Stanek, K. Z., Prieto, J. L., Stubbings, R., Muyllaert, E., Hiraga, M., Horie, T., Schmeer, P., and Hirosawa, K. (2016). Survey of period variations of superhumps in SU UMa-type dwarf novae. VIII. The eighth year (2015-2016). PASJ, 68(4):65.

Kato, T., Imada, A., Uemura, M., Nogami, D., Maehara, H., Ishioka, R., Baba, H., Matsumoto, K., Iwamatsu, H., Kubota, K., Sugiyasu, K., Soejima, Y., Moritani, Y., Ohshima, T., Ohashi, H., Tanaka, J., Sasada, M., Arai, A., Nakajima, K., Kiyota, S., Tanabe, K., Imamura, K., Kunitomi, N., Kunihiro, K., Taguchi, H., Koizumi, M., Yamada, N., Nishi, Y., Kida, M., Tanaka, S., Ueoka, R., Yasui, H., Maruoka, K., Henden, A., Oksanen, A., Moilanen, M., Tikkanen, P., Aho, M., Monard, B., Itoh, H., Dubovsky, P. A., Kudzej, I., Dancikova, R., Vanmunster, T., Pietz, J., Bolt, G., Boyd, D., Nelson, P., Krajci, T., Cook, L. M., Torii, K., Starkey, D. R., Shears, J., Jensen, L.-T., Masi, G., Hynek, T., Novák, R., Kocián, R., Král, L., Kučáková, H., Kolasa, M., Šťastný, P., Staels, B., Miller, I., Sano, Y., Ponthière, P. d., Miyashita, A., Crawford, T., Brady, S., Santallo, R., Richards, T., Martin, B., Buczynski, D., Richmond, M., Kern, J., Davis, S., Crabtree, D., Beaulieu, K., Davis, T., Aggleton, M., Morelle, E., Pavlenko, E. P., Andreev, M., Baklanov, A., Koppelman, M. D., Billings, G., Urbančok, L., Ögmen, Y., Heathcote, B., Gomez, T. L., Voloshina, I., Retter, A., Mularczyk, K., Złoczewski, K., Olech, A., Kedzierski, P., Pickard, R. D., Stockdale, C., Virtanen, J., Morikawa, K., Hambsch, F.-J., Garradd, G., Gualdoni, C., Geary, K., Omodaka, T., Sakai, N., Michel, R., Cárdenas, A. A., Gazeas, K. D., Niarchos, P. G., Yushchenko, A. V., Mallia, F., Fiaschi, M., Good, G. A., Walker, S., James, N., Douzu, K.-i., Julian, W. M., Butterworth, N. D., Shugarov, S. Y., Volkov, I., Chochol, D., Katysheva, N., Rosenbush, A. E., Khramtsova, M., Kehusmaa, P., Reszelski, M., Bedient, J., Liller, W., Pojmański, G., Simonsen, M., Stubbings, R., Schmeer, P., Muyllaert, E., Kinnunen, T., Poyner, G., Ripero, J., and Kriebel, W. (2009). Survey of Period Variations of Superhumps in SU UMa-Type Dwarf Novae. PASJ, 61:S395–S616.

Kato, T., Isogai, K., Hambsch, F.-J., Vanmunster, T., Itoh, H., Monard, B., Tordai, T., Kimura, M., Wakamatsu, Y., Kiyota, S., Miller, I., Starr, P., Kasai, K., Shugarov, S. Y., Chochol, D., Katysheva, N., Zaostrojnykh, A. M., Sekeráš, M., Kuznyetsova, Y. G., Kalinicheva, E. S., Golysheva, P., Krushevska, V., Maeda, Y., Dubovsky, P. A., Kudzej, I., Pavlenko, E. P., Antonyuk, K. A., Pit, N. V., Sosnovskij, A. A., Antonyuk, O. I., Baklanov, A. V., Pickard, R. D., Kojiguchi, N., Sugiura, Y., Tei, S., Yamamura, K., Matsumoto, K., Ruiz, J., Stone, G., Cook, L. M., de Miguel, E., Akazawa, H., Goff, W. N., Morelle, E., Kafka, S., Littlefield, C., Bolt, G., Dubois, F., Brincat, S. M., Maehara, H., Sakanoi, T., Kagitani, M., Imada, A., Voloshina, I. B., Andreev, M. V., Sabo, R., Richmond, M., Rodda, T., Nelson, P., Nazarov, S., Mishevskiy, N., Myers, G., Denisenko, D., Stanek, K. Z., Shields, J. V., Kochanek, C. S., Holoien, T. W. S., Shappee, B., Prieto, J. L., Itagaki, K.-i., Nishiyama, K., Kabashima, F., Stubbings, R., Schmeer, P., Muyllaert, E., Horie, T., Shears, J., Poyner, G., and Moriyama, M. (2017). Survey of period variations of superhumps in SU UMa-type dwarf novae. IX. The ninth year (2016-2017). PASJ, 69(5):75.

Kato, T. and Kojiguchi, N. (2021). New candidates for AM Canum Venaticorum stars among ASAS-SN transients. PASJ, 73(5):1375–1381.

Kato, T., Maehara, H., Miller, I., Ohshima, T., de Miguel, E., Tanabe, K., Imamura, K., Akazawa, H., Kunitomi, N., Takagi, R., Nose, M., Hambsch, F.-J., Kiyota, S., Pavlenko, E. P., Baklanov, A. V., Antonyuk, O. I., Samsonov, D., Sosnovskij, A., Antonyuk, K., Andreev, M. V., Morelle, E., Dubovsky, P. A., Kudzej, I., Oksanen, A., Masi, G., Krajci, T., Pickard, R. D., Sabo, R., Itoh, H., Stein, W., Dvorak, S., Henden, A., Nakagawa, S., Noguchi, R., Iino, E., Matsumoto, K., Nishitani, H., Aoki, T., Kobayashi,

H., Akasaka, C., Bolt, G., Shears, J., Ruiz, J., Shugarov, S. Y., Chochol, D., Parakhin, N. A., Monard, B., Shiokawa, K., Kasai, K., Staels, B., Miyashita, A., Starkey, D. R., Ögmen, Y., Littlefield, C., Katysheva, N., Sergey, I. M., Denisenko, D., Tordai, T., Fidrich, R., Goranskij, V. P., Virtanen, J., Crawford, T., Pietz, J., Koff, R. A., Boyd, D., Brady, S., James, N., Goff, W. N., Itagaki, K.-I., Nishimura, H., Nakashima, Y., Yoshida, S., Stubbings, R., Poyner, G., Maeda, Y., Korotkiy, S. A., Sokolovsky, K. V., and Ueda, S. (2012a). Survey of Period Variations of Superhumps in SU UMa-Type Dwarf Novae. III. The Third Year (2010-2011). PASJ, 64:21.

Kato, T., Maehara, H., and Uemura, M. (2012b). Characterization of Dwarf Novae Using SDSS Colors. PASJ, 64:63.

Kato, T., Ohshima, T., Denisenko, D., Dubovsky, P. A., Kudzej, I., Stein, W., de Miguel, E., Henden, A., Miller, I., Antonyuk, K., Antonyuk, O., Pit, N., Sosnovskij, A., Baklanov, A., Babina, J., Pavlenko, E. P., Matsumoto, K., Fukushima, D., Takenaka, M., Kawabata, M., Sakai, D., Maeda, K., Matsuda, R., Matsumoto, K., Littlefield, C., Oksanen, A., Itoh, H., Masi, G., Nocentini, F., Schmeer, P., Pickard, R. D., Kiyota, S., Dvorak, S., Ulowetz, J., Maeda, Y., Michel, R., Shugarov, S. Y., Chochol, D., and Novák, R. (2014b). Superoutburst of SDSS J090221.35+381941.9: First measurement of mass ratio in an AM CVn-type object using growing superhumps. PASJ, 66:L7.

Kato, T. and Osaki, Y. (2013a). Analysis of Three SU UMa-Type Dwarf Novae in the Kepler Field. PASJ, 65:97.

Kato, T. and Osaki, Y. (2013b). New Method of Estimating Binary's Mass Ratios by Using Superhumps. PASJ, 65:115.

Kent, B. J., Reading, D. H., Swinyard, B. M., Spurrett, P. H., and Graper, E. B. (1990). EUV band pass filters for the ROSAT Wide Field Camera. In Hudson, H. S. and Siegmund, O. H., editors, EUV, X-ray, and Gamma-ray instrumentation for astronomy, volume 1344 of Society of Photo-Optical Instrumentation Engineers (SPIE) Conference Series, pages 255–266.

Kepler, S. O., Pelisoli, I., Koester, D., Ourique, G., Kleinman, S. J., Romero, A. D., Nitta, A., Eisenstein, D. J., Costa, J. E. S., Külebi, B., Jordan, S., Dufour, P., Giommi, P., and Rebassa-Mansergas, A. (2015). New white dwarf stars in the Sloan Digital Sky Survey Data Release 10. MNRAS, 446(4):4078–4087.

Kessler, R., Bassett, B., Belov, P., Bhatnagar, V., Campbell, H., Conley, A., Frieman, J. A., Glazov, A., González-Gaitán, S., Hlozek, R., Jha, S., Kuhlmann, S., Kunz, M., Lampeitl, H., Mahabal, A., Newling, J., Nichol, R. C., Parkinson, D., Sajeeth Philip, N., Poznanski, D., Richards, J. W., Rodney, S. A., Sako, M., Schneider, D. P., Smith, M., Stritzinger, M., and Varughese, M. (2010). Results from the Supernova Photometric Classification Challenge. PASP, 122(898):1415.

Kloppenborg, B. K. (2023). Observations from the AAVSO International Database. https://www.aavso.org.

Knigge, C. (2006). The donor stars of cataclysmic variables. MNRAS, 373(2):484–502.

Knigge, C., Baraffe, I., and Patterson, J. (2011). The Evolution of Cataclysmic Variables as Revealed by Their Donor Stars. ApJS, 194(2):28.

Kobulnicky, H. A., Nordsieck, K. H., Burgh, E. B., Smith, M. P., Percival, J. W., Williams, T. B., and O'Donoghue, D. (2003). Prime focus imaging spectrograph for the Southern African large telescope: operational modes. In Iye, M. and Moorwood, A. F. M., editors, Instrument Design and Performance for Optical/Infrared Ground-based Telescopes, volume 4841 of Proc. SPIE, pages 1634–1644.

Kochanek, C. S., Shappee, B. J., Stanek, K. Z., Holoien, T. W.-S., Thompson, T. A., Prieto, J. L., Dong, S., Shields, J. V., Will, D., Britt, C., Perzanowski, D., and Pojmański, G. (2017). The All-Sky Automated Survey for Supernovae (ASAS-SN) Light Curve Server v1.0. PASP, 129(10):104502.

Koen, C. and O'Donoghue, D. (1995). Observations of Some Little-studied Cataclysmic Variables. ApJS, 101:347.

Kolb, U. and Baraffe, I. (1999). Brown dwarfs and the cataclysmic variable period minimum. MNRAS, 309(4):1034–1042.

Kolbin, A. I., Borisov, N. V., Burenkov, A. N., Spiridonova, O. I., Bikmaev, I. F., and Suslikov, M. V. (2023). Optical Study of the Polar BM CrB in a Low State. Astronomy Letters, 49(3):129–140.

Kolbin, A. I., Serebryakova, N. A., Gabdeev, M. M., and Borisov, N. V. (2019). Analysis of the Optical Cyclotron Emission of Polar CRTS CSS081231 J071126+440405. Astrophysical Bulletin, 74(1):80–92.

Kong, X., Luo, A. L., Li, X.-R., Wang, Y.-F., Li, Y.-B., and Zhao, J.-K. (2018). Spectral Feature Extraction for DB White Dwarfs Through Machine Learning Applied to New Discoveries in the Sdss DR12 and DR14. PASP, 130(990):084203.

Kornilov, V. G., Lipunov, V. M., Gorbovskoy, E. S., Belinski, A. A., Kuvshinov, D. A., Tyurina, N. V., Shatsky, N. I., Sankovich, A. V., Krylov, A. V., Balanutsa, P. V., Chazov, V. V., Kuznetsov, A. S., Zimnuhov, D. S., Senik, V. A., Tlatov, A. G., Parkhomenko, A. V., Dormidontov, D. V., Krushinsky, V. V., Zalozhnyh, I. S., Popov, A. A., Yazev, S. A., Budnev, N. M., Ivanov, K. I., Konstantinov, E. N., Gress, O. A., Chvalaev, O. V., Yurkov, V. V., Sergienko, Y. P., and Kudelina, I. P. (2012). Robotic optical telescopes global network MASTER II. Equipment, structure, algorithms. Experimental Astronomy, 33(1):173–196.

Kotko, I. and Lasota, J. P. (2012). The viscosity parameter α and the properties of accretion disc outbursts in close binaries. A&A, 545:A115.

Kotko, I., Lasota, J.-P., and Dubus, G. (2010). The outburst properties of AM CVn stars. Astronomische Nachrichten, 331:231.

Kotko, I., Lasota, J.-P., Dubus, G., and Hameury, J.-M. (2012). Models of AM Canum Venaticorum star outbursts. A&A, 544:A13.

Kotze, E. J., Potter, S. B., and McBride, V. A. (2015). Exploring inside-out Doppler tomography: non-magnetic cataclysmic variables. A&A, 579:A77.

Krishnan, S., Samudravijaya, K., and Rao, P. V. S. (1996). Feature selection for pattern classification with Gaussian mixture models: A new objective criterion. Pattern Recognition Letters, 17(8):803–809.

Kuijpers, J. and Pringle, J. E. (1982). Comments on radial white dwarf accretion. A&A, 114:L4–L6.

Kupfer, T., Breedt, E., Ramsay, G., Hodgkin, S., and Marsh, T. (2019). Detection of a photometric period during outburst in the AMCVn binary SDSS J080710.33+485259.6. The Astronomer's Telegram, 12558:1.

Kupfer, T., Groot, P. J., Bloemen, S., Levitan, D., Steeghs, D., Marsh, T. R., Rutten, R. G. M., Nelemans, G., Prince, T. A., Fürst, F., and Geier, S. (2015). Phase-resolved spectroscopy and Kepler photometry of the ultracompact AM CVn binary SDSS J190817.07+394036.4. MNRAS, 453:483–496.

Kupfer, T., Groot, P. J., Levitan, D., Steeghs, D., Marsh, T. R., Rutten, R. G. M., and Nelemans, G. (2013). Orbital periods and accretion disc structure of four AM CVn systems. MNRAS, 432:2048–2060.

Kupfer, T., Ramsay, G., van Roestel, J., Brooks, J., MacFarlane, S. A., Toma, R., Groot, P. J., Woudt, P. A., Bildsten, L., Marsh, T. R., Green, M. J., Breedt, E., Kilkenny, D., Freudenthal, J., Geier, S., Heber, U., Bagnulo, S., Blagorodnova, N., Buckley, D. A. H., Dhillon, V. S., Kulkarni, S. R., Lunnan, R., and Prince, T. A. (2017). The OmegaWhite Survey for Short-period Variable Stars. V. Discovery of an Ultracompact Hot Subdwarf Binary with a Compact Companion in a 44-minute Orbit. ApJ, 851(1):28.

Kurtz, M. J. and Mink, D. J. (1998). RVSAO 2.0: Digital Redshifts and Radial Velocities. PASP, 110(750):934–977.

Lamb, D. Q. (1985). Recent developments in the theory of am her and dq her stars. In Lamb, D. Q. and Patterson, J., editors, Cataclysmic Variables and Low-Mass X-Ray Binaries, pages 179–218, Dordrecht. Springer Netherlands.

Lamb, D. Q. and Masters, A. R. (1979). X and UV radiation from accreting magnetic degenerate dwarfs. ApJ, 234:L117–L122.

Lasota, J.-P., Dubus, G., and Kruk, K. (2008). Stability of helium accretion discs in ultracompact binaries. A&A, 486:523–528.

Lasota, J. P., Hameury, J. M., and Hure, J. M. (1995). Dwarf novae at low mass transfer rates. A&A, 302:L29.

Law, N. M., Kulkarni, S. R., Dekany, R. G., Ofek, E. O., Quimby, R. M., Nugent, P. E., Surace, J., Grillmair, C. C., Bloom, J. S., Kasliwal, M. M., Bildsten, L., Brown, T., Cenko, S. B., Ciardi, D., Croner, E., Djorgovski, S. G., van Eyken, J., Filippenko, A. V., Fox, D. B., Gal-Yam, A., Hale, D., Hamam, N., Helou, G., Henning, J., Howell, D. A., Jacobsen, J., Laher, R., Mattingly, S., McKenna, D., Pickles, A., Poznanski, D., Rahmer, G., Rau, A., Rosing, W., Shara, M., Smith, R., Starr, D., Sullivan, M., Velur, V., Walters, R., and Zolkower, J. (2009). The Palomar Transient Factory: System Overview, Performance, and First Results. PASP, 121:1395.

Levitan, D., Fulton, B. J., Groot, P. J., Kulkarni, S. R., Ofek, E. O., Prince, T. A., Shporer, A., Bloom, J. S., Cenko, S. B., Kasliwal, M. M., Law, N. M., Nugent, P. E., Poznanski, D., Quimby, R. M., Horesh, A., Sesar, B., and Sternberg, A. (2011). PTF1

J071912.13+485834.0: An Outbursting AM CVn System Discovered by a Synoptic Survey. ApJ, 739:68.

Levitan, D., Groot, P. J., Prince, T. A., Kulkarni, S. R., Laher, R., Ofek, E. O., Sesar, B., and Surace, J. (2015). Long-term photometric behaviour of outbursting AM CVn systems. MNRAS, 446:391–410.

Levitan, D., Kupfer, T., Groot, P. J., Kulkarni, S. R., Prince, T. A., Simonian, G. V., Arcavi, I., Bloom, J. S., Laher, R., Nugent, P. E., Ofek, E. O., Sesar, B., and Surace, J. (2013). Five new outbursting AM CVn systems discovered by the Palomar Transient Factory. MNRAS, 430:996–1007.

Levitan, D., Kupfer, T., Groot, P. J., Margon, B., Prince, T. A., Kulkarni, S. R., Hallinan, G., Harding, L. K., Kyne, G., Laher, R., Ofek, E. O., Rutten, R. G. M., Sesar, B., and Surace, J. (2014). PTF1 J191905.19+481506.2—a Partially Eclipsing AM CVn System Discovered in the Palomar Transient Factory. ApJ, 785:114.

Li, Z., Van Roestel, J., Kulkarni, S., Rich, R., Caiazzo, I., and ZTF Team (2022). A Systematic Search for Short Orbital Period Cataclysmic Variables Using the Zwicky Transient Facility. In American Astronomical Society Meeting Abstracts, volume 54 of American Astronomical Society Meeting Abstracts, page 346.03.

Linnell, A. P., Szkody, P., Plotkin, R. M., Holtzman, J., Seibert, M., Harrison, T. E., and Howell, S. B. (2010). GALEX and Optical Light Curves of WX LMi, SDSSJ103100.5+202832.2, and SDSSJ121209.31+013627.7. ApJ, 713(2):1183–1191.

Lipunov, V., Kornilov, V., Gorbovskoy, E., Shatskij, N., Kuvshinov, D., Tyurina, N., Belinski, A., Krylov, A., Balanutsa, P., Chazov, V., Kuznetsov, A., Kortunov, P., Sankovich, A., Tlatov, A., Parkhomenko, A., Krushinsky, V., Zalozhnyh, I., Popov, A., Kopytova, T., Ivanov, K., Yazev, S., and Yurkov, V. (2010). Master Robotic Net. Advances in Astronomy, 2010:349171.

Littlefield, C., Garnavich, P., Hoyt, T. J., and Kennedy, M. (2018). MASTER OT J132104.04+560957.8: A Polar with Absorption-Emission Line Reversals. AJ, 155(1):18.

Littlefield, C., Mukai, K., Mumme, R., Cain, R., Magno, K. C., Corpuz, T., Sandefur, D., Boyd, D., Cook, M., Ulowetz, J., and Martinez, L. (2015). Periodic eclipse variations in asynchronous polar V1432 Aql: evidence of a shifting threading region. MNRAS, 449(3):3107–3120.

Livio, M. and Pringle, J. E. (1994). Star spots and the period gap in cataclysmic variables. ApJ, 427:956–960.

Lomb, N. R. (1976). Least-Squares Frequency Analysis of Unequally Spaced Data. Ap&SS, 39(2):447–462.

LSST Science Collaboration, Abell, P. A., Allison, J., Anderson, S. F., Andrew, J. R., Angel, J. R. P., Armus, L., Arnett, D., Asztalos, S. J., Axelrod, T. S., Bailey, S., Ballantyne, D. R., Bankert, J. R., Barkhouse, W. A., Barr, J. D., Barrientos, L. F., Barth, A. J., Bartlett, J. G., Becker, A. C., Becla, J., Beers, T. C., Bernstein, J. P., Biswas, R., Blanton, M. R., Bloom, J. S., Bochanski, J. J., Boeshaar, P., Borne, K. D., Bradac, M., Brandt, W. N.,

Bridge, C. R., Brown, M. E., Brunner, R. J., Bullock, J. S., Burgasser, A. J., Burge, J. H., Burke, D. L., Cargile, P. A., Chandrasekharan, S., Chartas, G., Chesley, S. R., Chu, Y.-H., Cinabro, D., Claire, M. W., Claver, C. F., Clowe, D., Connolly, A. J., Cook, K. H., Cooke, J., Cooray, A., Covey, K. R., Culliton, C. S., de Jong, R., de Vries, W. H., Debattista, V. P., Delgado, F., Dell'Antonio, I. P., Dhital, S., Di Stefano, R., Dickinson, M., Dilday, B., Djorgovski, S. G., Dobler, G., Donalek, C., Dubois-Felsmann, G., Durech, J., Eliasdottir, A., Eracleous, M., Eyer, L., Falco, E. E., Fan, X., Fassnacht, C. D., Ferguson, H. C., Fernandez, Y. R., Fields, B. D., Finkbeiner, D., Figueroa, E. E., Fox, D. B., Francke, H., Frank, J. S., Frieman, J., Fromenteau, S., Furqan, M., Galaz, G., Gal-Yam, A., Garnavich, P., Gawiser, E., Geary, J., Gee, P., Gibson, R. R., Gilmore, K., Grace, E. A., Green, R. F., Gressler, W. J., Grillmair, C. J., Habib, S., Haggerty, J. S., Hamuy, M., Harris, A. W., Hawley, S. L., Heavens, A. F., Hebb, L., Henry, T. J., Hileman, E., Hilton, E. J., Hoadley, K., Holberg, J. B., Holman, M. J., Howell, S. B., Infante, L., Ivezic, Z., Jacoby, S. H., Jain, B., R, Jedicke, Jee, M. J., Garrett Jernigan, J., Jha, S. W., Johnston, K. V., Jones, R. L., Juric, M., Kaasalainen, M., Styliani, Kafka, Kahn, S. M., Kaib, N. A., Kalirai, J., Kantor, J., Kasliwal, M. M., Keeton, C. R., Kessler, R., Knezevic, Z., Kowalski, A., Krabbendam, V. L., Krughoff, K. S., Kulkarni, S., Kuhlman, S., Lacy, M., Lepine, S., Liang, M., Lien, A., Lira, P., Long, K. S., Lorenz, S., Lotz, J. M., Lupton, R. H., Lutz, J., Macri, L. M., Mahabal, A. A., Mandelbaum, R., Marshall, P., May, M., McGehee, P. M., Meadows, B. T., Meert, A., Milani, A., Miller, C. J., Miller, M., Mills, D., Minniti, D., Monet, D., Mukadam, A. S., Nakar, E., Neill, D. R., Newman, J. A., Nikolaev, S., Nordby, M., O'Connor, P., Oguri, M., Oliver, J., Olivier, S. S., Olsen, J. K., Olsen, K., Olszewski, E. W., Oluseyi, H., Padilla, N. D., Parker, A., Pepper, J., Peterson, J. R., Petry, C., Pinto, P. A., Pizagno, J. L., Popescu, B., Prsa, A., Radcka, V., Raddick, M. J., Rasmussen, A., Rau, A., Rho, J., Rhoads, J. E., Richards, G. T., Ridgway, S. T., Robertson, B. E., Roskar, R., Saha, A., Sarajedini, A., Scannapieco, E., Schalk, T., Schindler, R., Schmidt, S., Schmidt, S., Schneider, D. P., Schumacher, G., Scranton, R., Sebag, J., Seppala, L. G., Shemmer, O., Simon, J. D., Sivertz, M., Smith, H. A., Allyn Smith, J., Smith, N., Spitz, A. H., Stanford, A., Stassun, K. G., Strader, J., Strauss, M. A., Stubbs, C. W., Sweeney, D. W., Szalay, A., Szkody, P., Takada, M., Thorman, P., Trilling, D. E., Trimble, V., Tyson, A., Van Berg, R., Vanden Berk, D., VanderPlas, J., Verde, L., Vrsnak, B., Walkowicz, L. M., Wandelt, B. D., Wang, S., Wang, Y., Warner, M., Wechsler, R. H., West, A. A., Wiecha, O., Williams, B. F., Willman, B., Wittman, D., Wolff, S. C., Wood-Vasey, W. M., Wozniak, P., Young, P., Zentner, A., and Zhan, H. (2009). LSST Science Book, Version 2.0. arXiv e-prints, page arXiv:0912.0201.

Lubow, S. H. and Shu, F. H. (1975). Gas dynamics of semidetached binaries. ApJ, 198:383–405.

Lynden-Bell, D. and Pringle, J. E. (1974). The evolution of viscous discs and the origin of the nebular variables. MNRAS, 168:603–637.

Maccarone, T. J., Kupfer, T., Najera Casarrubias, E., Rivera Sandoval, L., Shaw, A., Britt, C., van Roestel, J., and Zurek, D. (2023). Strongly magnetized accretion in ultracompact binary systems. arXiv e-prints, page arXiv:2302.12318.

Macfarlane, S. A., Toma, R., Ramsay, G., Groot, P. J., Woudt, P. A., Drew, J. E., Barentsen, G., and Eislöffel, J. (2015). The OmegaWhite survey for short-period variable stars - I. Overview and first results. MNRAS, 454(1):507–530.

Macfarlane, S. A., Woudt, P. A., Dufour, P., Ramsay, G., Groot, P. J., Toma, R., Warner, B., Paterson, K., Kupfer, T., van Roestel, J., Berdnikov, L., Dagne, T., and Hardy, F. (2017). The OmegaWhite Survey for short-period variable stars - IV. Discovery of the warm DQ white dwarf OW J175358.85-310728.9. MNRAS, 470(1):732–741.

Mahabal, A. A., Djorgovski, S. G., Drake, A. J., Donalek, C., Graham, M. J., Williams, R. D., Chen, Y., Moghaddam, B., Turmon, M., Beshore, E., and Larson, S. (2011). Discovery, classification, and scientific exploration of transient events from the Catalina Real-time Transient Survey. Bulletin of the Astronomical Society of India, 39:387–408.

Marsh, T., Parsons, S., and Dhillon, V. (2017). ASASSN 17-fp shows 51-minute periodic variations. The Astronomer's Telegram, 10354.

Marsh, T. R. (1999). Kinematics of the helium accretor GP COM. MNRAS, 304(2):443–450.

Marsh, T. R. (2001). Doppler Tomography. In Boffin, H. M. J., Steeghs, D., and Cuypers, J., editors, Astrotomography, Indirect Imaging Methods in Observational Astronomy, volume 573 of Lecture Notes in Physics, Berlin Springer Verlag, page 1.

Marsh, T. R. and Horne, K. (1988). Images of accretion discs. II - Doppler tomography. MNRAS, 235:269–286.

Marsh, T. R. and Steeghs, D. (2002). V407 Vul: a direct impact accretor. MNRAS, 331:L7–L11.

Martin, R. G., Nixon, C. J., Pringle, J. E., and Livio, M. (2019). On the physical nature of accretion disc viscosity. New A, 70:7–11.

Mason, P. A., Wells, N. K., Motsoaledi, M., Szkody, P., and Gonzalez, E. (2019). CRTS J035010.7 + 323230, a new eclipsing polar in the cataclysmic variable period gap. MNRAS, 488(2):2881–2891.

Masters, A. R. (1978). The binary system containing the pulsar PSR 1913+16 and ultra-violet and X-rad PhD thesis, University of Illinois, Urbana-Champaign.

Mazeh, T., Kieboom, K., and Heise, J. (1986). A photometric study of AM Herculis in the normal and reversed soft X-ray modes. MNRAS, 221:513–521.

Meggitt, S. M. A. and Wickramasinghe, D. T. (1989). Two-pole emission in AM Herculis-type systems. MNRAS, 236:31–45.

Merloni, A., Predehl, P., Becker, W., Böhringer, H., Boller, T., Brunner, H., Brusa, M., Dennerl, K., Freyberg, M., Friedrich, P., Georgakakis, A., Haberl, F., Hasinger, G., Meidinger, N., Mohr, J., Nandra, K., Rau, A., Reiprich, T. H., Robrade, J., Salvato, M., Santangelo, A., Sasaki, M., Schwope, A., Wilms, J., and German eROSITA Consortium, t. (2012). eROSITA Science Book: Mapping the Structure of the Energetic Universe. arXiv e-prints, page arXiv:1209.3114.

Meyer, F. and Meyer-Hofmeister, E. (1981). On the elusive cause of cataclysmic variable outbursts. A&A, 104:L10–L12.

Meyer, F. and Meyer-Hofmeister, E. (1984). Outbursts in dwarf novae accretion disks. A&A, 132:143–150.

Miceli, A., Rest, A., Stubbs, C. W., Hawley, S. L., Cook, K. H., Magnier, E. A., Krisciunas, K., Bowell, E., and Koehn, B. (2008). Evidence for Distinct Components of the Galactic Stellar Halo from 838 RR Lyrae Stars Discovered in the LONEOS-I Survey. ApJ, 678(2):865–887.

Mineshige, S. and Osaki, Y. (1985). Disk-instability model for outbursts of dwarf novae. II Full-disk calculations. PASJ, 37(1):1–18.

Morales-Rueda, L., Marsh, T. R., Steeghs, D., Unda-Sanzana, E., Wood, J. H., and North, R. C. (2003). New results on GP Com. A&A, 405:249–261.

Motch, C. and Haberl, F. (1995). New Soft and hard X-ray IPs from the ROSAT Galactic Plane Survey. In Buckley, D. A. H. and Warner, B., editors, Magnetic Cataclysmic Variables, volume 85 of Astronomical Society of the Pacific Conference Series, page 109.

Motch, C., Haberl, F., Guillout, P., Pakull, M., Reinsch, K., and Krautter, J. (1996). New cataclysmic variables from the ROSAT All-Sky Survey. A&A, 307:459–469.

Motsoaledi, M., Aydi, E., Buckley, D. A. H., Strader, J., Chomiuk, L., Kawash, A., Sokolovsky, K. V., Woudt, P. A., Stanek, K. Z., Kochanek, C. S., and Shappee, B. J. (2021). Spectroscopic and photometric confirmation of ASASSN-21br as an AM CVn system. The Astronomer's Telegram, 14421:1.

Mukai, K. (1988). Accretion streams in AM HER type systems. MNRAS, 232:175–197.

Mukai, K., Hellier, C., Madejski, G., Patterson, J., and Skillman, D. R. (2003). X-Ray Variability of the Magnetic Cataclysmic Variable V1432 Aquilae and the Seyfert Galaxy NGC 6814. ApJ, 597(1):479–493.

Muno, M. P., Baganoff, F. K., Bautz, M. W., Brandt, W. N., Garmire, G. P., and Ricker, G. R. (2003). X-Ray Sources with Periodic Variability in a Deep Chandra Image of the Galactic Center. ApJ, 599(1):465–474.

Myers, G., Patterson, J., de Miguel, E., Hambsch, F.-J., Monard, B., Bolt, G., McCormick, J., Rea, R., and Allen, W. (2017). Resynchronization of the Asynchronous Polar CD Ind. PASP, 129(974):044204.

Narayan, G., Zaidi, T., Soraisam, M. D., Wang, Z., Lochner, M., Matheson, T., Saha, A., Yang, S., Zhao, Z., Kececioglu, J., Scheidegger, C., Snodgrass, R. T., Axelrod, T., Jenness, T., Maier, R. S., Ridgway, S. T., Seaman, R. L., Evans, E. M., Singh, N., Taylor, C., Toeniskoetter, J., Welch, E., Zhu, S., and ANTARES Collaboration (2018). Machine-learning-based Brokers for Real-time Classification of the LSST Alert Stream. ApJS, 236(1):9.

Narayan, R. and Popham, R. (1993). Hard X-rays from accretion disk boundary layers. Nature, 362(6423):820–822.

Nather, R. E., Robinson, E. L., and Stover, R. J. (1981). The twin-degenerate interacting binary G 61-29. ApJ, 244:269–279.

Nelemans, G. (2005). AM CVn stars. In Hameury, J.-M. and Lasota, J.-P., editors, The Astrophysics of Cataclysmic Variables and Related Objects, volume 330 of Astronomical Society of the Pacific Conference Series, page 27.

Nelemans, G., Portegies Zwart, S. F., Verbunt, F., and Yungelson, L. R. (2001). Population synthesis for double white dwarfs. II. Semi-detached systems: AM CVn stars. A&A, 368:939–949.

Nelemans, G., Yungelson, L. R., and Portegies Zwart, S. F. (2004). Short-period AM CVn systems as optical, X-ray and gravitational-wave sources. MNRAS, 349:181–192.

Nelemans, G., Yungelson, L. R., van der Sluys, M. V., and Tout, C. A. (2010). The chemical composition of donors in AM CVn stars and ultracompact X-ray binaries: observational tests of their formation. MNRAS, 401:1347–1359.

Nemec, J. and Nemec, A. F. L. (1991). Mixture models for studying stellar populations. In Janes, K., editor, The Formation and Evolution of Star Clusters, volume 13 of Astronomical Society of the Pacific Conference Series, pages 512–531.

O'Donoghue, D. (1986). The radius of the accretion disc in Z Cha between outbursts. MNRAS, 220:23P–26.

O'Donoghue, D. (1995). High Speed CCD Photometry. Baltic Astronomy, 4:519–526.

O'Donoghue, D., Buckley, D. A. H., Balona, L. A., Bester, D., Botha, L., Brink, J., Carter, D. B., Charles, P. A., Christians, A., Ebrahim, F., Emmerich, R., Esterhuyse, W., Evans, G. P., Fourie, C., Fourie, P., Gajjar, H., Gordon, M., Gumede, C., de Kock, M., Koeslag, A., Koorts, W. P., Kriel, H., Marang, F., Meiring, J. G., Menzies, J. W., Menzies, P., Metcalfe, D., Meyer, B., Nel, L., O'Connor, J., Osman, F., Du Plessis, C., Rall, H., Riddick, A., Romero-Colmenero, E., Potter, S. B., Sass, C., Schalekamp, H., Sessions, N., Siyengo, S., Sopela, V., Steyn, H., Stoffels, J., Scholtz, J., Swart, G., Swat, A., Swiegers, J., Tiheli, T., Vaisanen, P., Whittaker, W., and van Wyk, F. (2006). First science with the Southern African Large Telescope: peering at the accreting polar caps of the eclipsing polar SDSS J015543.40+002807.2. MNRAS, 372(1):151–162.

O'Donoghue, D., Kilkenny, D., Chen, A., Stobie, R. S., Koen, C., Warner, B., and Lawson, W. A. (1994). EC15330-1403 and the AM CVn stars. MNRAS, 271:910–918.

O'Donoghue, D., Menzies, J. W., and Hill, P. W. (1987). Photometry and spectroscopy of the interacting binary white dwarf V803 CEN (AE-1). MNRAS, 227:347–359.

Oliveira, A. S., Rodrigues, C. V., Cieslinski, D., Jablonski, F. J., Silva, K. M. G., Almeida, L. A., Rodríguez-Ardila, A., and Palhares, M. S. (2017). Exploratory Spectroscopy of Magnetic Cataclysmic Variables Candidates and Other Variable Objects. AJ, 153(4):144.

Oliveira, A. S., Rodrigues, C. V., Martins, M., Palhares, M. S., Silva, K. M. G., Lima, I. J., and Jablonski, F. J. (2020). Exploratory Spectroscopy of Magnetic Cataclysmic Variables Candidates and Other Variable Objects. II. AJ, 159(3):114.

Osaki, Y. (1974). An Accretion Model for the Outbursts of U Geminorum Stars. PASJ, 26:429.

Osaki, Y. (1985). Irradiation-induced mass-overflow instability as a possible cause of superoutbursts in SU UMa stars. A&A, 144:369–380.

Osaki, Y. (1989). A model for the superoutburst phenomenon of SU Ursae Majoris stars. PASJ, 41:1005–1033.

Osaki, Y. and Kato, T. (2013). The Cause of the Superoutburst in SU UMa Stars is Finally Revealed by Kepler Light Curve of V1504 Cygni. PASJ, 65:50.

Paczyński, B. (1967). Gravitational Waves and the Evolution of Close Binaries. Acta Astron., 17:287.

Paczynski, B. (1976). Common Envelope Binaries. In Eggleton, P., Mitton, S., and Whelan, J., editors, Structure and Evolution of Close Binary Systems, volume 73, page 75.

Paczynski, B. and Sienkiewicz, R. (1981). Gravitational radiation and the evolution of cataclysmic binaries. ApJ, 248:L27–L30.

Pandel, D., Córdova, F. A., and Howell, S. B. (2003). X-ray and ultraviolet observations of the dwarf nova VW Hyi in quiescence. MNRAS, 346(4):1231–1241.

Pandel, D., Córdova, F. A., Mason, K. O., and Priedhorsky, W. C. (2005). X-Ray Observations of the Boundary Layer in Dwarf Novae at Low Accretion Rates. ApJ, 626(1):396–410.

Pandel, D., Cordova, F. A., Shirey, R. E., Ramsay, G., Cropper, M., Mason, K. O., Much, R., and Kilkenny, D. (2002). First XMM-Newton observations of strongly magnetic cataclysmic variables - II. Timing studies of DP Leo and WW Hor. MNRAS, 332(1):116–126.

Paterson, K., Woudt, P. A., Warner, B., Breytenbach, H., Gilligan, C. K., Motsoaledi, M., Thorstensen, J. R., and Worters, H. L. (2019). High-speed photometry of faint cataclysmic variables - IX. Targets from multiple transient surveys. MNRAS, 486(2):2422–2434.

Patterson, J., Skillman, D. R., Thorstensen, J., and Hellier, C. (1995). The Remarkable Eclipsing Asynchronous AM Herculis Binary RX J19402-1025. PASP, 107:307.

Patterson, J., Williams, G., and Hiltner, W. A. (1981). The amazing X-ray light curve of 2A 0311-22.7. ApJ, 245:618–623.

Pavlenko, E. P., Mason, P. A., Sosnovskij, A. A., Shugarov, S. Y., Babina, J. V., Antonyuk, K. A., Andreev, M. V., Pit, N. V., Antonyuk, O. I., and Baklanov, A. V. (2018). Asynchronous polar V1500 Cyg: orbital, spin, and beat periods. MNRAS, 479(1):341–347.

Philippov, A. A., Rafikov, R. R., and Stone, J. M. (2016). Spreading Layers in Accreting Objects: Role of Acoustic Waves for Angular Momentum Transport, Mixing, and Thermodynamics. ApJ, 817(1):62.

Phillips, M., Prieto, J. L., Shappee, B. J., Dong, S., and Stanek, K. (2016). ASASSN-16mj: a candidate AM CVn system. The Astronomer's Telegram, 9692:1.

Pichardo Marcano, M., Rivera Sandoval, L. E., Maccarone, T. J., and Scaringi, S. (2021). TACOS: TESS AM CVn Outbursts Survey. MNRAS, 508(3):3275–3289.

Piirola, V., Coyne, G. V., and Reiz, A. (1990). Simultaneous UBVRI polarimetry of VV Puppis during an active phase. A&A, 235(1-2):245–254.

Piro, A. L. and Bildsten, L. (2004). Spreading of Accreted Material on White Dwarfs. ApJ, 610(2):977–990.

Podsiadlowski, P., Han, Z., and Rappaport, S. (2003). Cataclysmic variables with evolved secondaries and the progenitors of AM CVn stars. MNRAS, 340:1214–1228.

Popham, R. and Narayan, R. (1995). Accretion Disk Boundary Layers in Cataclysmic Variables. I. Optically Thick Boundary Layers. ApJ, 442:337.

Prieto, J. L. (2016). Errata for ATel #9692. The Astronomer's Telegram, 9693:1.

Prieto, J. L., Morrell, N., Grupe, D., Stanek, K. Z., Kochanek, C. S., Holoien, T. W.-S., Davis, A. B., Basu, U., Beacom, J. F., Bersier, D., Shappee, B. J., Brimacombe, J., Szczygiel, D., and Pojmanski, G. (2014a). Follow-up of ASASSN-14ei show He lines in the spectra and Swift/XRT X-ray detection. The Astronomer's Telegram, 6475.

Prieto, J. L., Stanek, K. Z., Kochanek, C. S., Holoien, T. W.-S., Shappee, B. J., Davis, A. B., Jencson, J., Basu, U., Beacom, J. F., Bersier, D., Brimacombe, J., Szczygiel, D., and Pojmanski, G. (2014b). ASAS-SN Discovery of an Unusual Outburst from USNO-B1.0 0421-0026203. The Astronomer's Telegram, 6340.

Ramsay, G., Barclay, T., Steeghs, D., Wheatley, P. J., Hakala, P., Kotko, I., and Rosen, S. (2012). The long-term optical behaviour of helium-accreting AM CVn binaries. MNRAS, 419:2836–2843.

Ramsay, G. and Cropper, M. (2002a). First X-ray observations of the polar CE Gru. MNRAS, 335:918–922.

Ramsay, G. and Cropper, M. (2002b). XMM-Newton observations of the asynchronous polar BY Cam. MNRAS, 334:805–810.

Ramsay, G. and Cropper, M. (2004a). The energy balance of polars revisited. MNRAS, 347:497–507.

Ramsay, G. and Cropper, M. (2004b). The XMM-Newton-MSSL survey of Polars. In Vrielmann, S. and Cropper, M., editors, IAU Colloq. 190: Magnetic Cataclysmic Variables, volume 315 of Astronomical Society of the Pacific Conference Series, page 106.

Ramsay, G. and Cropper, M. (2007). XMM-Newton observations of the eclipsing polar V2301 Oph. MNRAS, 379(3):1209–1216.

Ramsay, G., Cropper, M., Wu, K., Mason, K. O., Córdova, F. A., and Priedhorsky, W. (2004). XMM-Newton observations of polars in low accretion states. MNRAS, 350:1373–1384.

Ramsay, G., Green, M. J., Marsh, T. R., Kupfer, T., Breedt, E., Korol, V., Groot, P. J., Knigge, C., Nelemans, G., Steeghs, D., Woudt, P., and Aungwerojwit, A. (2018). Physical properties of AM CVn stars: New insights from Gaia DR2. A&A, 620:A141.

Ramsay, G., Mason, K. O., Cropper, M., Watson, M. G., and Clayton, K. L. (1994). ROSAT Observations of An-Ursae and Mr-Serpentis - the Status of the Soft X-Ray Excess in Am-Herculis Stars. MNRAS, 270:692.

Ramsay, G., Rosen, S., Hakala, P., and Barclay, T. (2009). 2XMMiJ225036.9+573154 - a new eclipsing AMHer binary discovered using XMM-Newton. MNRAS, 395(1):416–421.

Ramsay, G. and Wheatley, P. J. (1998). Spectroscopic observations of the eclipsing polar MN Hya (RX J0929-24). MNRAS, 301(1):95–100.

Rau, A., Kulkarni, S. R., Law, N. M., Bloom, J. S., Ciardi, D., Djorgovski, G. S., Fox, D. B., Gal-Yam, A., Grillmair, C. C., Kasliwal, M. M., Nugent, P. E., Ofek, E. O., Quimby, R. M., Reach, W. T., Shara, M., Bildsten, L., Cenko, S. B., Drake, A. J., Filippenko, A. V., Helfand, D. J., Helou, G., Howell, D. A., Poznanski, D., and Sullivan, M. (2009). Exploring the Optical Transient Sky with the Palomar Transient Factory. PASP, 121:1334.

Rau, A., Roelofs, G. H. A., Groot, P. J., Marsh, T. R., Nelemans, G., Steeghs, D., Salvato, M., and Kasliwal, M. M. (2010). A Census of AM CVn Stars: Three New Candidates and One Confirmed 48.3-Minute Binary. ApJ, 708:456–461.

Reimers, D. and Hagen, H. J. (2000). HS0922+1333: another low accretion rate polar with a pronounced cyclotron line spectrum. A&A, 358:L45–L48.

Richards, G. T., Fan, X., Newberg, H. J., Strauss, M. A., Vanden Berk, D. E., Schneider, D. P., Yanny, B., Boucher, A., Burles, S., Frieman, J. A., Gunn, J. E., Hall, P. B., Ivezić, Ž., Kent, S., Loveday, J., Lupton, R. H., Rockosi, C. M., Schlegel, D. J., Stoughton, C., SubbaRao, M., and York, D. G. (2002). Spectroscopic Target Selection in the Sloan Digital Sky Survey: The Quasar Sample. AJ, 123:2945–2975.

Ricker, G. R., Winn, J. N., Vanderspek, R., Latham, D. W., Bakos, G. Á., Bean, J. L., Berta-Thompson, Z. K., Brown, T. M., Buchhave, L., Butler, N. R., Butler, R. P., Chaplin, W. J., Charbonneau, D., Christensen-Dalsgaard, J., Clampin, M., Deming, D., Doty, J., De Lee, N., Dressing, C., Dunham, E. W., Endl, M., Fressin, F., Ge, J., Henning, T., Holman, M. J., Howard, A. W., Ida, S., Jenkins, J. M., Jernigan, G., Johnson, J. A., Kaltenegger, L., Kawai, N., Kjeldsen, H., Laughlin, G., Levine, A. M., Lin, D., Lissauer, J. J., MacQueen, P., Marcy, G., McCullough, P. R., Morton, T. D., Narita, N., Paegert, M., Palle, E., Pepe, F., Pepper, J., Quirrenbach, A., Rinehart, S. A., Sasselov, D., Sato, B., Seager, S., Sozzetti, A., Stassun, K. G., Sullivan, P., Szentgyorgyi, A., Torres, G., Udry, S., and Villasenor, J. (2015). Transiting Exoplanet Survey Satellite (TESS). Journal of Astronomical Telescopes, Instruments, and Systems, 1:014003.

Ritter, H. and Kolb, U. (2003). Catalogue of cataclysmic binaries, low-mass X-ray binaries and related objects (Seventh edition). A&A, 404:301–303.

Rivera Sandoval, L. E., Heinke, C. O., Hameury, J. M., Cavecchi, Y., Vanmunster, T., Tordai, T., and Romanov, F. D. (2022). The Fast Evolving, Tremendous Blue Superoutburst in ASASSN-21au Reveals a Dichotomy in the Outbursts of Long-period AM CVns. ApJ, 926(1):10.

Rivera Sandoval, L. E., Maccarone, T. J., Cavecchi, Y., Britt, C., and Zurek, D. (2021). The outburst of a 60 min AM CVn reveals peculiar colour evolution: implications for outbursts in long-period double white dwarfs. MNRAS, 505(1):215–222.

Rodriguez, A. C., Galiullin, I., Gilfanov, M., Kulkarni, S. R., Khamitov, I., Bikmaev, I., van Roestel, J., Yungelson, L., El-Badry, K., Sunayev, R., Prince, T. A., Buntov, M., Caiazzo, I., Drake, A., Gorbachev, M., Graham, M. J., Gumerov, R., Irtuganov, E., Laher, R. R., Masci, F. J., Medvedev, P., Purdum, J., Sakhibullin, N., Sklyanov, A., Smith, R., Szkody, P., and Vanderbosch, Z. P. (2023). SRGeJ045359.9+622444: A 55 Minute Period Eclipsing AM Canum Venaticorum Star Discovered from a Joint SRG/eROSITA + ZTF Search. ApJ, 954(1):63.

Rodriguez, A. C., Kulkarni, S. R., Prince, T. A., Szkody, P., Burdge, K. B., Caiazzo, I., van Roestel, J., Vanderbosch, Z. P., El-Badry, K., Bellm, E. C., Gänsicke, B. T., Graham, M. J., Mahabal, A. A., Masci, F. J., Mróz, P., Riddle, R., and Rusholme, B. (2022). Discovery of Two Polars from a Crossmatch of ZTF and the SRG/eFEDS X-ray Catalog. arXiv e-prints, page arXiv:2206.04714.

Rodríguez-Gil, P., Martínez-Pais, I. G., and de la Cruz Rodríguez, J. (2009). The magnetic SW Sextantis star RXJ1643.7+3402. MNRAS, 395(2):973–978.

Roelofs, G. H. A., Groot, P. J., Marsh, T. R., Steeghs, D., Barros, S. C. C., and Nelemans, G. (2005). SDSS J124058.03-015919.2: a new AM CVn star with a 37-min orbital period. MNRAS, 361:487–494.

Roelofs, G. H. A., Groot, P. J., Nelemans, G., Marsh, T. R., and Steeghs, D. (2006). Kinematics of the ultracompact helium accretor AM Canum Venaticorum. MNRAS, 371(3):1231–1242.

Roelofs, G. H. A., Groot, P. J., Nelemans, G., Marsh, T. R., and Steeghs, D. (2007a). On the orbital periods of the AM CVn stars HP Librae and V803 Centauri. MNRAS, 379(1):176–182.

Roelofs, G. H. A., Groot, P. J., Steeghs, D., Marsh, T. R., and Nelemans, G. (2007b). The long-period AM CVn star SDSS J155252.48+320150.9. MNRAS, 382:1643–1647.

Roelofs, G. H. A., Groot, P. J., Steeghs, D., Rau, A., de Groot, E., Marsh, T. R., Nelemans, G., Liebert, J., and Woudt, P. (2009). SDSSJ080449.49+161624.8: a peculiar AM CVn star from a colour-selected sample of candidates. MNRAS, 394:367–374.

Roelofs, G. H. A., Nelemans, G., and Groot, P. J. (2007c). The population of AM CVn stars from the Sloan Digital Sky Survey. MNRAS, 382:685–692.

Roelofs, G. H. A., Rau, A., Marsh, T. R., Steeghs, D., Groot, P. J., and Nelemans, G. (2010). Spectroscopic Evidence for a 5.4 Minute Orbital Period in HM Cancri. ApJ, 711:L138–L142.

Rosen, S. R., Mason, K. O., and Cordova, F. A. (1987). Phase-resolved optical spectroscopy of the AM HER system E 1405-451. MNRAS, 224:987–1006.

Rosen, S. R., Mittaz, J. P. D., Buckley, D. A., Layden, A. C., Clayton, K. L., McCain, C., Wynn, G. A., Sirk, M. M., Osborne, J. P., and Watson, M. G. (1996). Accretion mode changes in QS Tel (RE 1938-461): EUVE, ROSAT and optical observations. MNRAS, 280(4):1121–1142.

Rosen, S. R., Rainger, J. F., Burleigh, M. R., Mittaz, J. P. D., Buckley, D. A. H., Sirk, M. M., Lieu, R., Howell, S. B., and de Martino, D. (2001). Multiwavelength monitoring of QS Tel. MNRAS, 322(3):631–642.

Ruiz, M. T., Rojo, P. M., Garay, G., and Maza, J. (2001). CE 315: A New Interacting Double-Degenerate Binary Star. ApJ, 552(2):679–684.

Savonije, G. J., de Kool, M., and van den Heuvel, E. P. J. (1986). The minimum orbital period for ultra-compact binaries with helium burning secondaries. A&A, 155:51–57.

Scargle, J. D. (1982). Studies in astronomical time series analysis. II. Statistical aspects of spectral analysis of unevenly spaced data. ApJ, 263:835–853.

Schmidt, G. D., Ferrario, L., Wickramasinghe, D. T., and Smith, P. S. (2001). The Cyclotron Fundamental Exposed in the High-Field Magnetic Variable V884 Herculis. ApJ, 553(2):823–831.

Schmidt, G. D., Liebert, J., and Stockman, H. S. (1995). Detection of the Hot White Dwarf in the Magnetic Nova V1500 Cygni with the Hubble Space Telescope. ApJ, 441:414.

Schmidt, G. D., Smith, P. S., Szkody, P., and Anderson, S. F. (2008). New Magnetic Cataclysmic Variables from the Sloan Digital Sky Survey. PASP, 120(864):160.

Schmidt, G. D., Szkody, P., Homer, L., Smith, P. S., Chen, B., Henden, A., Solheim, J.-E., Wolfe, M. A., and Greimel, R. (2005a). Unraveling the Puzzle of the Eclipsing Polar SDSS J015543.40+002807.2 with XMM and Optical Photometry/Spectropolarimetry. ApJ, 620(1):422–431.

Schmidt, G. D., Szkody, P., Smith, P. S., Silber, A., Tovmassian, G., Hoard, D. W., Gänsicke, B. T., and de Martino, D. (1996). AR Ursae Majoris: The First High-Field Magnetic Cataclysmic Variable. ApJ, 473:483.

Schmidt, G. D., Szkody, P., Vanlandingham, K. M., Anderson, S. F., Barentine, J. C., Brewington, H. J., Hall, P. B., Harvanek, M., Kleinman, S. J., Krzesinski, J., Long, D., Margon, B., Neilsen, Eric H., J., Newman, P. R., Nitta, A., Schneider, D. P., and Snedden, S. A. (2005b). New Low Accretion Rate Magnetic Binary Systems and their Significance for the Evolution of Cataclysmic Variables. ApJ, 630(2):1037–1053.

Schreiber, M. R., Belloni, D., Gänsicke, B. T., Parsons, S. G., and Zorotovic, M. (2021). The origin and evolution of magnetic white dwarfs in close binary stars. Nature Astronomy, 5:648–654.

Schreiber, M. R., Hameury, J. M., and Lasota, J. P. (2004). Delays in dwarf novae II: VW Hyi, the tidal instability and enhanced mass transfer models. A&A, 427:621–635.

Schwarz, R., Greiner, J., Tovmassian, G. H., Zharikov, S. V., and Wenzel, W. (2002). A new two-pole accretion polar: RX J1846.9+5538. A&A, 392:505–514.

Schwope, A. (2012). CV surveys with eROSITA. Mem. Soc. Astron. Italiana, 83:844.

Schwope, A. D. and Beuermann, K. (1990). Cyclotron and Zeeman spectroscopy of V 834 Centauri. A&A, 238:173.

Schwope, A. D., Beuermann, K., Buckley, D. A. H., Ciardi, D., Cropper, M., Horne, K., Howell, S., Mantel, K. H., Metzner, A., O'Brien, K., Schwarz, R., Sirk, M., Steeghs, D., Still, M., and Thomas, H. C. (1998). Polars - multisite emission - multiwavelength observation. In Howell, S., Kuulkers, E., and Woodward, C., editors, Wild Stars in the Old West, volume 137 of Astronomical Society of the Pacific Conference Series, page 44.

Schwope, A. D., Beuermann, K., and Jordan, S. (1995). Magnetism in the polar BL Hydri. A&A, 301:447.

Schwope, A. D., Beuermann, K., and Thomas, H.-C. (1990). Cyclotron radiation in UZ Fornacis (=EXO033319 - 2554.2) in a low state of accretion. A&A, 230:120–126.

Schwope, A. D., Brunner, H., Buckley, D., Greiner, J., Heyden, K. v. d., Neizvestny, S., Potter, S., and Schwarz, R. (2002a). The census of cataclysmic variables in the ROSAT Bright Survey. A&A, 396:895–910.

Schwope, A. D., Brunner, H., Hambaryan, V., and Schwarz, R. (2002b). LARPs – Low-accretion rate polars. In Gänsicke, B. T., Beuermann, K., and Reinsch, K., editors, The Physics of Cataclysmic Variables and Related Objects, volume 261 of Astronomical Society of the Pacific Conference Series, page 102.

Schwope, A. D., Buckley, D. A. H., O'Donoghue, D., Hasinger, G., Truemper, J., and Voges, W. (1997a). RX J2115.7-5840: a short-period, asynchronous polar. A&A, 326:195–202.

Schwope, A. D., Hambaryan, V., Schwarz, R., Kanbach, G., and Gänsicke, B. T. (2002c). A multiwavelength timing analysis of the eclipsing polar DP Leo. A&A, 392:541–551.

Schwope, A. D., Horne, K., Steeghs, D., and Still, M. (2011). Dissecting the donor star in the eclipsing polar HU Aquarii. A&A, 531:A34.

Schwope, A. D., Mackebrandt, F., Thinius, B. D., Littlefield, C., Garnavich, P., Oksanen, A., and Granzer, T. (2015). Multi-epoch time-resolved photometry of the eclipsing polar CSS081231:071126+440405. Astronomische Nachrichten, 336(2):115.

Schwope, A. D., Mantel, K. H., and Horne, K. (1997b). Phase-resolved high-resolution spectrophotometry of the eclipsing polar HU Aquarii. A&A, 319:894–908.

Schwope, A. D. and Thinius, B. (2012). CSS091109:035759+102943: A candidate polar. Astronomische Nachrichten, 333(8):717.

Schwope, A. D., Thomas, H. C., and Beuermann, K. (1993). Discovery of the bright eclipsing polar RXJ 2107.9-0518. A&A, 271:L25–L28.

Schwope, A. D., Thomas, H. C., Mante, K. H., Haefner, R., and Staude, A. (2003). Cyclotron spectroscopy of HU Aquarii. A&A, 402:201–209.

Schwope, A. D., Worpel, H., Traulsen, I., and Sablowski, D. (2020). The various accretion modes of AM Herculis: Clues from multi-wavelength observations in high accretion states. A&A, 642:A134.

Semeniuk, I. (1980). Photometry of V436 CEN during superoutburst in May 1978. A&AS, 39:29–33.

Shafter, A. W., Davenport, J. R. A., Güth, T., Kattner, S., Marin, E., and Sreenivasamurthy, N. (2008). Time-Resolved Photometry of the Optical Counterpart of Swift J2319.4+2619. PASP, 120(866):374.

Shafter, A. W., Reinsch, K., Beuermann, K., Misselt, K. A., Buckley, D. A. H., Burwitz, V., and Schwope, A. D. (1995). RX J0515.6+0105: an Unusual, Eclipsing, Magnetic Cataclysmic Variable. ApJ, 443:319.

Shakura, N. I. and Sunyaev, R. A. (1973). Black holes in binary systems. Observational appearance. A&A, 24:337–355.

Shappee, B. J., Prieto, J. L., Grupe, D., Kochanek, C. S., Stanek, K. Z., De Rosa, G., Mathur, S., Zu, Y., Peterson, B. M., Pogge, R. W., Komossa, S., Im, M., Jencson, J., Holoien, T. W.-S., Basu, U., Beacom, J. F., Szczygieł, D. M., Brimacombe, J., Adams, S., Campillay, A., Choi, C., Contreras, C., Dietrich, M., Dubberley, M., Elphick, M., Foale, S., Giustini, M., Gonzalez, C., Hawkins, E., Howell, D. A., Hsiao, E. Y., Koss, M., Leighly, K. M., Morrell, N., Mudd, D., Mullins, D., Nugent, J. M., Parrent, J., Phillips, M. M., Pojmanski, G., Rosing, W., Ross, R., Sand, D., Terndrup, D. M., Valenti, S., Walker, Z., and Yoon, Y. (2014). The Man behind the Curtain: X-Rays Drive the UV through NIR Variability in the 2013 Active Galactic Nucleus Outburst in NGC 2617. ApJ, 788:48.

Shears, J. (2017). Amateur astronomers and the new golden age of cataclysmic variable star astronomy. ArXiv e-prints.

Silber, A. D., Remillard, R. A., Horne, K., and Bradt, H. V. (1994). 1H 1752+081: an Eclipsing Cataclysmic Variable with a Small Accretion Disk. ApJ, 424:955.

Singh, K. P., Szkody, P., Barrett, P., White, N. E., Fierce, E., Silber, A., Hoard, D. W., Hakala, P. J., Piirola, V., and Sohl, K. (1995). A New Magnetic Cataclysmic Variable: WGA J1047.1+6335. ApJ, 453:L95.

Sirk, M. M. and Howell, S. B. (1998). The Three-dimensional Structure of Extreme-Ultraviolet Accretion Regions in AM Herculis Stars: Modeling of Extreme-Ultraviolet Photometric and Spectroscopic Observations. ApJ, 506(2):824–841.

Smak, J. (1967). Light variability of HZ 29. Acta Astron., 17:255.

Smak, J. (1971). Eruptive Binaries. II. U Geminorum. Acta Astron., 21:15.

Smak, J. (1982). Accretion in cataclysmic binaries. I - Modified alpha-disks with convection. Acta Astron., 32(3-4):199–211.

Smak, J. (1983). Accretion in cataclysmic binaries. III - Helium binaries. Acta Astron., 33:333–337.

Smak, J. (1984a). Accretion in cataclysmic binaries. IV. Accretion disks in dwarf novae. Acta Astron., 34:161–189.

Smak, J. (1984b). Eruptive binaries. XI. Disk-radius variations un U Gem. Acta Astron., 34:93–96.

Smak, J. (1984c). Outbursts of dwarf novae. PASP, 96:5–18.

Smak, J. (1996). Dwarf nova outbursts and superoutbursts. In Evans, A. and Wood, J. H., editors, IAU Colloq. 158: Cataclysmic Variables and Related Objects, volume 208 of Astrophysics and Space Science Library, page 45.

Smak, J. (1999). Dwarf Nova Outbursts. III. The Viscosity Parameter alpha. Acta Astron., 49:391–401.

Smak, J. (2000). Unsolved problems of dwarf nova outbursts. New A Rev., 44(1-2):171–175.

Smak, J. (2008). Superoutbursts of Z Cha and their Interpretation. Acta Astron., 58:55–64.

Smak, J. (2009a). Are Disks in Dwarf Novae during their Superoutbursts Really Eccentric? Acta Astron., 59:89–101.

Smak, J. (2009b). New Interpretation of Superhumps. Acta Astron., 59:121–130.

Smak, J. (2009c). On the Amplitudes of Superhumps. Acta Astron., 59(1):103–107.

Smak, J. (2009d). On the Origin of Tilted Disks and Negative Superhumps. Acta Astron., 59:419–430.

Smak, J. (2013). On the Periods of Negative Superhumps and the Nature of Superhumps. Acta Astron., 63(1):109–114.

Smak, J. I. (1998). Dwarf Nova Outbursts. I. The UV Delay. Acta Astron., 48:677–693.

Smartt, S. J., Valenti, S., Fraser, M., Inserra, C., Young, D. R., Sullivan, M., Pastorello, A., Benetti, S., Gal-Yam, A., Knapic, C., Molinaro, M., Smareglia, R., Smith, K. W., Taubenberger, S., Yaron, O., Anderson, J. P., Ashall, C., Balland, C., Baltay, C., Barbarino, C., Bauer, F. E., Baumont, S., Bersier, D., Blagorodnova, N., Bongard, S., Botticella, M. T., Bufano, F., Bulla, M., Cappellaro, E., Campbell, H., Cellier-Holzem, F., Chen, T.-W., Childress, M. J., Clocchiatti, A., Contreras, C., Dall'Ora, M., Danziger, J., de Jaeger, T., De Cia, A., Della Valle, M., Dennefeld, M., Elias-Rosa, N., Elman, N., Feindt, U., Fleury, M., Gall, E., Gonzalez-Gaitan, S., Galbany, L., Morales Garoffolo, A., Greggio, L., Guillou, L. L., Hachinger, S., Hadjiyska, E., Hage, P. E., Hillebrandt, W., Hodgkin, S., Hsiao, E. Y., James, P. A., Jerkstrand, A., Kangas, T., Kankare, E., Kotak, R., Kromer, M., Kuncarayakti, H., Leloudas, G., Lundqvist, P., Lyman, J. D., Hook, I. M., Maguire, K., Manulis, I., Margheim, S. J., Mattila, S., Maund, J. R., Mazzali, P. A., McCrum, M., McKinnon, R., Moreno-Raya, M. E., Nicholl, M., Nugent, P., Pain, R., Pignata, G., Phillips, M. M., Polshaw, J., Pumo, M. L., Rabinowitz, D., Reilly, E., Romero-Cañizales,

C., Scalzo, R., Schmidt, B., Schulze, S., Sim, S., Sollerman, J., Taddia, F., Tartaglia, L., Terreran, G., Tomasella, L., Turatto, M., Walker, E., Walton, N. A., Wyrzykowski, L., Yuan, F., and Zampieri, L. (2015). PESSTO: survey description and products from the first data release by the Public ESO Spectroscopic Survey of Transient Objects. A&A, 579:A40.

Smee, S. A., Gunn, J. E., Uomoto, A., Roe, N., Schlegel, D., Rockosi, C. M., Carr, M. A., Leger, F., Dawson, K. S., Olmstead, M. D., Brinkmann, J., Owen, R., Barkhouser, R. H., Honscheid, K., Harding, P., Long, D., Lupton, R. H., Loomis, C., Anderson, L., Annis, J., Bernardi, M., Bhardwaj, V., Bizyaev, D., Bolton, A. S., Brewington, H., Briggs, J. W., Burles, S., Burns, J. G., Castander, F. J., Connolly, A., Davenport, J. R. A., Ebelke, G., Epps, H., Feldman, P. D., Friedman, S. D., Frieman, J., Heckman, T., Hull, C. L., Knapp, G. R., Lawrence, D. M., Loveday, J., Mannery, E. J., Malanushenko, E., Malanushenko, V., Merrelli, A. J., Muna, D., Newman, P. R., Nichol, R. C., Oravetz, D., Pan, K., Pope, A. C., Ricketts, P. G., Shelden, A., Sandford, D., Siegmund, W., Simmons, A., Smith, D. S., Snedden, S., Schneider, D. P., SubbaRao, M., Tremonti, C., Waddell, P., and York, D. G. (2013). The Multi-object, Fiber-fed Spectrographs for the Sloan Digital Sky Survey and the Baryon Oscillation Spectroscopic Survey. AJ, 146(2):32.

Smith, M. P., Nordsieck, K. H., Burgh, E. B., Percival, J. W., Williams, T. B., O'Donohue, D., O'Connor, J., and Schier, J. A. (2006). The prime focus imaging spectrograph for the Southern African Large Telescope: structural and mechanical design and commissioning. In Society of Photo-Optical Instrumentation Engineers (SPIE) Conference Series, volume 6269 of Proc. SPIE, page 62692A.

Solheim, J.-E. (2010). AM CVn Stars: Status and Challenges. PASP, 122:1133.

Staubert, R., Friedrich, S., Pottschmidt, K., Benlloch, S., Schuh, S. L., Kroll, P., Splittgerber, E., and Rothschild, R. (2003). The near-synchronous polar <ASTROBJ>V1432 Aql</ASTROBJ> (<ASTROBJ>RX J1940.1-1025</ASTROBJ>): Accretion geometry and synchronization time scale. A&A, 407:987–998.

Steeghs, D., Horne, K., Marsh, T. R., and Donati, J. F. (1996). Slingshot prominences during dwarf nova outbursts? MNRAS, 281:626–636.

Stella, L., Beuermann, K., and Patterson, J. (1986). Uncorrelated Soft and Hard X-Ray Short-Term Variations from AM Herculis. ApJ, 306:225.

Stellingwerf, R. F. (1978). Period determination using phase dispersion minimization. ApJ, 224:953–960.

Stetson, P. B. (1987). DAOPHOT - A computer program for crowded-field stellar photometry. PASP, 99:191–222.

Stetson, P. B. (1990). On the growth-curve method for calibrating stellar photometry with CCDs. PASP, 102:932–948.

Stockman, H. S. and Lubenow, A. F. (1987). The Energy Distributions of Magnetic Variables - the Effects of Inhomogeneous Accretion Columns. Ap&SS, 131(1-2):607–611.

Stockman, H. S., Schmidt, G. D., Liebert, J., and Holberg, J. B. (1994). Eclipse Mapping of the Accreting Magnetic White Dwarf in DP Leonis with HST. ApJ, 430:323.

Strauss, M. A., Weinberg, D. H., Lupton, R. H., Narayanan, V. K., Annis, J., Bernardi, M., Blanton, M., Burles, S., Connolly, A. J., Dalcanton, J., Doi, M., Eisenstein, D., Frieman, J. A., Fukugita, M., Gunn, J. E., Ivezić, Ž., Kent, S., Kim, R. S. J., Knapp, G. R., Kron, R. G., Munn, J. A., Newberg, H. J., Nichol, R. C., Okamura, S., Quinn, T. R., Richmond, M. W., Schlegel, D. J., Shimasaku, K., SubbaRao, M., Szalay, A. S., Vanden Berk, D., Vogeley, M. S., Yanny, B., Yasuda, N., York, D. G., and Zehavi, I. (2002). Spectroscopic Target Selection in the Sloan Digital Sky Survey: The Main Galaxy Sample. AJ, 124:1810–1824.

Suleimanov, V., Hertfelder, M., Werner, K., and Kley, W. (2014). Modeling the EUV spectra of optically thick boundary layers of dwarf novae in outburst. A&A, 571:A55.

Sunyaev, R. A. and Shakura, N. I. (1986). Disk Accretion onto a Weak Field Neutron Star - Boundary Layer Disk Luminosity Ratio. Soviet Astronomy Letters, 12:117–120.

Szkody, P. (1981). IUE observations of eight dwarf novae : a study of the outburst cyclefrom 0.12 to 3.5 microns. ApJ, 247:577–589.

Szkody, P., Anderson, S. F., Agüeros, M., Covarrubias, R., Bentz, M., Hawley, S., Margon, B., Voges, W., Henden, A., Knapp, G. R., Vanden Berk, D. E., Rest, A., Miknaitis, G., Magnier, E., Brinkmann, J., Csabai, I., Harvanek, M., Hindsley, R., Hennessy, G., Ivezic, Z., Kleinman, S. J., Lamb, D. Q., Long, D., Newman, P. R., Neilsen, E. H., Nichol, R. C., Nitta, A., Schneider, D. P., Snedden, S. A., and York, D. G. (2002). Cataclysmic Variables from The Sloan Digital Sky Survey. I. The First Results. AJ, 123:430–442.

Szkody, P., Anderson, S. F., Brooks, K., Gänsicke, B. T., Kronberg, M., Riecken, T., Ross, N. P., Schmidt, G. D., Schneider, D. P., Agüeros, M. A., Gomez-Moran, A. N., Knapp, G. R., Schreiber, M. R., and Schwope, A. D. (2011). Cataclysmic Variables from the Sloan Digital Sky Survey. VIII. The Final Year (2007-2008). AJ, 142:181.

Szkody, P., Anderson, S. F., Hayden, M., Kronberg, M., McGurk, R., Riecken, T., Schmidt, G. D., West, A. A., Gänsicke, B. T., Nebot Gomez-Moran, A., Schneider, D. P., Schreiber, M. R., and Schwope, A. D. (2009). Cataclysmic Variables from SDSS. VII. The Seventh Year (2006). AJ, 137:4011–4019.

Szkody, P., Anderson, S. F., Schmidt, G., Hall, P. B., Margon, B., Miceli, A., SubbaRao, M., Frith, J., Harris, H., Hawley, S., Lawton, B., Covarrubias, R., Covey, K., Fan, X., Murphy, T., Narayanan, V., Raymond, S., Rest, A., Strauss, M. A., Stubbs, C., Turner, E., Voges, W., Bauer, A., Brinkmann, J., Knapp, G. R., and Schneider, D. P. (2003a). Two Rare Magnetic Cataclysmic Variables with Extreme Cyclotron Features Identified in the Sloan Digital Sky Survey. ApJ, 583(2):902–906.

Szkody, P., Cordova, F. A., Tuohy, I. R., Stockman, H. S., Angel, J. R. P., and Wisniewski, W. (1980). AM HER : Simultaneous X-ray, optical and near IR coverage. ApJ, 241:1070–1076.

Szkody, P., Dicenzo, B., Ho, A. Y. Q., Hillenbrand, L. A., van Roestel, J., Ridder, M., DeJesus Lima, I., Graham, M. L., Bellm, E. C., Burdge, K., Kupfer, T., Prince, T. A.,

Masci, F. J., Mróz, P. J., Golkhou, V. Z., Coughlin, M., Cunningham, V. A., Dekany, R., Graham, M. J., Hale, D., Kaplan, D., Kasliwal, M. M., Miller, A. A., Neill, J. D., Patterson, M. T., Riddle, R., Smith, R., and Soumagnac, M. T. (2020). Cataclysmic Variables in the First Year of the Zwicky Transient Facility. AJ, 159(5):198.

Szkody, P., Everett, M. E., Dai, Z., and Serna-Grey, D. (2018). Follow-up Observations of SDSS and CRTS Candidate Cataclysmic Variables II. AJ, 155(1):28.

Szkody, P., Everett, M. E., Howell, S. B., Landolt, A. U., Bond, H. E., Silva, D. R., and Vasquez-Soltero, S. (2014). Follow up Observations of SDSS and CRTS Candidate Cataclysmic Variables. AJ, 148(4):63.

Szkody, P., Fraser, O., Silvestri, N., Henden, A., Anderson, S. F., Frith, J., Lawton, B., Owens, E., Raymond, S., Schmidt, G., Wolfe, M., Bochanski, J., Covey, K., Harris, H., Hawley, S., Knapp, G. R., Margon, B., Voges, W., Walkowicz, L., Brinkmann, J., and Lamb, D. Q. (2003b). Cataclysmic Variables from the Sloan Digital Sky Survey. II. The Second Year. AJ, 126:1499–1514.

Szkody, P., Henden, A., Fraser, O., Silvestri, N., Bochanski, J., Wolfe, M. A., Agüeros, M., Warner, B., Woudt, P., Tramposch, J., Homer, L., Schmidt, G., Knapp, G. R., Anderson, S. F., Covey, K., Harris, H., Hawley, S., Schneider, D. P., Voges, W., and Brinkmann, J. (2004). Cataclysmic Variables from the Sloan Digital Sky Survey. III. The Third Year. AJ, 128:1882–1893.

Szkody, P., Henden, A., Fraser, O. J., Silvestri, N. M., Schmidt, G. D., Bochanski, J. J., Wolfe, M. A., Agüeros, M., Anderson, S. F., Mannikko, L., Downes, R. A., Schneider, D. P., and Brinkmann, J. (2005). Cataclysmic Variables from Sloan Digital Sky Survey. IV. The Fourth Year (2003). AJ, 129:2386–2399.

Szkody, P., Henden, A., Mannikko, L., Mukadam, A., Schmidt, G. D., Bochanski, J. J., Agüeros, M., Anderson, S. F., Silvestri, N. M., Dahab, W. E., Oguri, M., Schneider, D. P., Shin, M.-S., Strauss, M. A., Knapp, G. R., and West, A. A. (2007). Cataclysmic Variables from Sloan Digital Sky Survey. VI. The Sixth Year (2005). AJ, 134(1):185–194.

Szkody, P., Linnell, A. P., Campbell, R. K., Plotkin, R. M., Harrison, T. E., Holtzman, J., Seibert, M., and Howell, S. B. (2008). GALEX, Optical, and Infrared Light Curves of MQ Dra: UV Excesses at Low Accretion Rates. ApJ, 683(2):967–977.

Szkody, P., Vennes, S., Schmidt, G. D., Wagner, R. M., Fried, R., Shafter, A. W., and Fierce, E. (1999). ASCA, RXTE, EUVE, and Optical Observations of the High Magnetic Field Cataclysmic Variable AR Ursae Majoris. ApJ, 520(2):841–848.

Taam, R. E. (1980). Helium runaways in white dwarfs. ApJ, 237:142–147.

Taam, R. E. and Sandquist, E. L. (2000). Common Envelope Evolution of Massive Binary Stars. ARA&A, 38:113–141.

Takeo, M., Hayashi, T., Ishida, M., Nakaniwa, N., and Maeda, Y. (2021). Spatial distribution of the X-ray-emitting plasma of U Geminorum in quiescence and outburst. PASJ, 73(1):143–153.

Thomas, H. C., Beuermann, K., Reinsch, K., Schwope, A. D., and Burwitz, V. (2012). The high-field polar RX J1007.5-2017. A&A, 546:A104.

Thomas, H. C., Beuermann, K., Schwope, A. D., and Burwitz, V. (1996). RX J1957.1-5738: a new low-field polar discovered with ROSAT. A&A, 313:833–840.

Thorstensen, J. R., Alper, E. H., and Weil, K. E. (2016). A Trip to the Cataclysmic Binary Zoo: Detailed Follow-up of 35 Recently Discovered Systems. AJ, 152:226.

Thorstensen, J. R. and Halpern, J. (2013). Optical and X-Ray Studies of 10 X-Ray-selected Cataclysmic Binaries. AJ, 146(5):107.

Thorstensen, J. R., Motsoaledi, M., Woudt, P. A., Buckley, D. A. H., and Warner, B. (2020). Optical Studies of Eight AM Herculis-type Cataclysmic Variable Stars. AJ, 160(2):70.

Thorstensen, J. R. and Skinner, J. N. (2012). Spectroscopy and Photometry of Cataclysmic Variable Candidates from the Catalina Real Time Survey. AJ, 144:81.

Thorstensen, J. R. and Taylor, C. J. (2001). Spectroscopy and orbital periods of four cataclysmic variable stars. MNRAS, 326(4):1235–1242.

Thorstensen, J. R., Taylor, C. J., Peters, C. S., Skinner, J. N., Southworth, J., and Gänsicke, B. T. (2015). Spectroscopic Orbital Periods for 29 Cataclysmic Variables from the Sloan Digital Sky Survey. AJ, 149(4):128.

Tody, D. (1986). The IRAF Data Reduction and Analysis System. In Crawford, D. L., editor, Instrumentation in astronomy VI, volume 627 of Proc. SPIE, page 733.

Tonry, J. L., Denneau, L., Flewelling, H., Heinze, A. N., Onken, C. A., Smartt, S. J., Stalder, B., Weiland, H. J., and Wolf, C. (2018a). The ATLAS All-Sky Stellar Reference Catalog. ApJ, 867(2):105.

Tonry, J. L., Denneau, L., Heinze, A. N., Stalder, B., Smith, K. W., Smartt, S. J., Stubbs, C. W., Weiland, H. J., and Rest, A. (2018b). ATLAS: A High-cadence All-sky Survey System. PASP, 130(988):064505.

Tout, C. A., Wickramasinghe, D. T., and Ferrario, L. (2004). Magnetic fields in white dwarfs and stellar evolution. MNRAS, 355(3):L13–L16.

Tovmassian, G. H. and Zharikov, S. V. (2007). On the orbital period of the magnetic cataclysmic variable HS 0922+1333. A&A, 468(2):643–647.

Traulsen, I., Reinsch, K., Schwope, A. D., Schwarz, R., Walter, F. M., and Burwitz, V. (2014). Phase-resolved X-ray spectroscopy and spectral energy distribution of the X-ray soft polar RS Caeli. A&A, 562:A42.

Truemper, J. (1982). The ROSAT mission. Advances in Space Research, 2(4):241–249.

Tsugawa, M. and Osaki, Y. (1997). Disk Instability Model for the AM Canum Venaticorum Stars. PASJ, 49:75–84.

Tuohy, I. R., Mason, K. O., Garmire, G. P., and Lamb, F. K. (1981). Pointed soft X-ray observations of AM Her. ApJ, 245:183–194.

Tutukov, A. and Yungelson, L. (1996). Double-degenerate semidetached binaries with helium secondaries: cataclysmic variables, supersoft X-ray sources, supernovae and accretion-induced collapses. MNRAS, 280:1035–1045.

Tutukov, A. V. and Fedorova, A. V. (1989). Formation and Evolution of Close Binary Stars Containing Helium Donors. Soviet Ast., 33:606.

Tutukov, A. V., Fedorova, A. V., Ergma, E. V., and Yungelson, L. R. (1985). Evolution of Low-Mass Close Binaries - the Minimum Orbital Period. Soviet Astronomy Letters, 11:52–56.

van der Sluys, M. V., Verbunt, F., and Pols, O. R. (2005). Reduced magnetic braking and the magnetic capture model for the formation of ultra-compact binaries. A&A, 440:973–979.

van Dokkum, P. G. (2001). Cosmic-Ray Rejection by Laplacian Edge Detection. Publications of the Astronomical Society of the Pacific, 113(789):1420.

van Roestel, J., Creter, L., Kupfer, T., Szkody, P., Fuller, J., Green, M. J., Rich, R. M., Sepikas, J., Burdge, K., Caiazzo, I., Mróz, P., Prince, T. A., Duev, D. A., Graham, M. J., Shupe, D. L., Laher, R. R., Mahabal, A. A., and Masci, F. J. (2021). A Systematic Search for Outbursting AM CVn Systems with the Zwicky Transient Facility. AJ, 162(3):113.

van Roestel, J., Kupfer, T., Green, M. J., Wong, T. L. S., Bildsten, L., Burdge, K., Prince, T., Marsh, T. R., Szkody, P., Fremling, C., Graham, M. J., Dhillon, V. S., Littlefair, S. P., Bellm, E. C., Coughlin, M., Duev, D. A., Goldstein, D. A., Laher, R. R., Rusholme, B., Riddle, R., Dekany, R., and Kulkarni, S. R. (2022). Discovery and characterization of five new eclipsing AM CVn systems. MNRAS, 512(4):5440–5461.

VanderPlas, J. T. and Ivezić, Ž. (2015). Periodograms for Multiband Astronomical Time Series. ApJ, 812(1):18.

Vennes, S., Wickramasinghe, D. T., Thorstensen, J. R., Christian, D. J., and Bessell, M. S. (1996). On the Orbital Period of the New Cataclysmic Variable EUVE J2115-586. AJ, 112:2254.

Verbunt, F. (1982). Accretion Disks in Stellar X-Ray Sources. Space Sci. Rev., 32(4):379–404.

Verbunt, F. and Zwaan, C. (1981). Magnetic braking in low-mass X-ray binaries. A&A, 100:L7–L9.

Vogel, J., Byckling, K., Schwope, A., Osborne, J. P., Schwarz, R., and Watson, M. G. (2008). The serendipituous discovery of a short-period eclipsing polar in 2XMMp. A&A, 485(3):787–795.

Vogel, J., Schwope, A. D., and Schwarz, R. (2011). XMM-Newton observations of the pre-polar HS0922+1333. A&A, 530:A117.

Voges, W., Aschenbach, B., Boller, T., Bräuninger, H., Briel, U., Burkert, W., Dennerl, K., Englhauser, J., Gruber, R., Haberl, F., Hartner, G., Hasinger, G., Kürster, M., Pfeffermann, E., Pietsch, W., Predehl, P., Rosso, C., Schmitt, J. H. M. M., Trümper, J.,

and Zimmermann, H. U. (1999). The ROSAT all-sky survey bright source catalogue. A&A, 349:389–405.

Vogt, N. (1974). Photometric study of the dwarf nova VW Hydri. A&A, 36:369–378.

Waagen, E. O. (2017). ASASSN-17fp rebrightening event and ongoing monitoring. AAVSO Alert Notice, 580.

Wagner, R. M., Kaur, A., Porter, A., Wilber, A., Woodward, C. E., Starrfield, S. G., Hartmann, D. H., Davis, A. B., Holoien, T. W. S., Simonian, G., Stanek, K. Z., Kochanek, C. S., Shappee, B. J., and Prieto, J. L. (2014). Identification of a New Candidate Outbursting AM CVn System from ASAS-SN. The Astronomer's Telegram, 6669:1.

Wang, Q.-S., Qian, S.-B., Han, Z.-T., Zejda, M., Fernández-Lajus, E., and Zhu, L.-Y. (2018). Photometric analysis of the eclipsing polar MN Hya. Research in Astronomy and Astrophysics, 18(7):075.

Wang, Q.-S., Qian, S.-B., and Zhu, L.-Y. (2021). Revisiting the X-ray emission of the asynchronous polar V1432 Aql. Research in Astronomy and Astrophysics, 21(12):315.

Warner, B. (1975). Observations of rapid blue variables - XV. VW Hydri. MNRAS, 170:219–228.

Warner, B. (1995a). Cataclysmic variable stars. Cambridge Astrophysics Series, 28.

Warner, B. (1995b). The AM Canum Venaticorum Stars. Ap&SS, 225:249–270.

Warner, B. (1999). Low States in Cataclysmic Variables. In Hellier, C. and Mukai, K., editors, Annapolis Workshop on Magnetic Cataclysmic Variables, volume 157 of Astronomical Society of the Pacific Conference Series, page 63.

Warner, B. (2015). Aspects of observations and evolution of AM CVn stars. Mem. Soc. Astron. Italiana, 86:129.

Warner, B. and Robinson, E. L. (1972). Observations of rapid variables - IX. AM CVn (HZ 29). MNRAS, 159:101–111.

Warner, B. and Woudt, P. A. (2002). KUV 01584-0939: A Helium-transferring Cataclysmic Variable with an Orbital Period of 10 Minutes. PASP, 114:129–131.

Watson, M. G., King, A. R., and Williams, G. A. (1987). X-ray and optical flickering in EF Eri. MNRAS, 226:867–878.

Watson, M. G., Schröder, A. C., Fyfe, D., Page, C. G., Lamer, G., Mateos, S., Pye, J., Sakano, M., Rosen, S., Ballet, J., Barcons, X., Barret, D., Boller, T., Brunner, H., Brusa, M., Caccianiga, A., Carrera, F. J., Ceballos, M., Della Ceca, R., Denby, M., Denkinson, G., Dupuy, S., Farrell, S., Fraschetti, F., Freyberg, M. J., Guillout, P., Hambaryan, V., Maccacaro, T., Mathiesen, B., McMahon, R., Michel, L., Motch, C., Osborne, J. P., Page, M., Pakull, M. W., Pietsch, W., Saxton, R., Schwope, A., Severgnini, P., Simpson, M., Sironi, G., Stewart, G., Stewart, I. M., Stobbart, A. M., Tedds, J., Warwick, R., Webb, N., West, R., Worrall, D., and Yuan, W. (2009). The XMM-Newton serendipitous survey. V. The Second XMM-Newton serendipitous source catalogue. A&A, 493(1):339–373.

Webb, N. A., Schwope, A., Zolotukhin, I., Lin, D., and Rosen, S. R. (2018). Two new magnetic cataclysmic variables discovered in the 3XMM catalogue. A&A, 615:A133.

Webbink, R. F. and Wickramasinghe, D. T. (2005). A Model for Low Accretion Rate Polars. In Hameury, J. M. and Lasota, J. P., editors, The Astrophysics of Cataclysmic Variables and Related Objects, volume 330 of Astronomical Society of the Pacific Conference Series, page 137.

Wevers, T., Hodgkin, S. T., Jonker, P. G., Bassa, C., Nelemans, G., van Grunsven, T., Gonzalez-Solares, E. A., Torres, M. A. P., Heinke, C., Steeghs, D., Maccarone, T. J., Britt, C., Hynes, R. I., Johnson, C., and Wu, J. (2016a). The Chandra Galactic Bulge Survey: optical catalogue and point-source counterparts to X-ray sources. MNRAS, 458:4530–4546.

Wevers, T., Torres, M. A. P., Jonker, P. G., Wetuski, J. D., Nelemans, G., Steeghs, D., Maccarone, T. J., Heinke, C., Hynes, R. I., Udalski, A., Kostrzewa-Rutkowska, Z., Groot, P. J., Gazer, R., Szymański, M. K., Britt, C. T., Wyrzykowski, Ł., and Poleski, R. (2016b). Discovery of a high state AM CVn binary in the Galactic Bulge Survey. MNRAS, 462:L106–L110.

Whitehurst, R. (1988). Numerical simulations of accretion discs - I. Superhumps : a tidal phenomenon of accretion discs. MNRAS, 232:35–51.

Wickramasinghe, D. T. and Ferrario, L. (1988). Cyclotron Emission from Inhomogeneous Shocks in AM Herculis–Type Systems. ApJ, 334:412.

Wickramasinghe, D. T. and Ferrario, L. (2005). The origin of the magnetic fields in white dwarfs. MNRAS, 356(4):1576–1582.

Wickramasinghe, D. T., Ferrario, L., and Bailey, J. (1989). A 56 MG field at the second pole in VV Puppis. ApJ, 342:L35–L38.

Wickramasinghe, D. T. and Martin, B. (1985). The magnetic field of AM Herculis. MNRAS, 212:353–358.

Wickramasinghe, D. T. and Wu, K. (1991). An interpretation of the field alignment in AM Herculis type systems. MNRAS, 253:11P–15P.

Wiehahn, M., Potter, S. B., Warner, B., and Woudt, P. A. (2004). Photometric and polarimetric observations of the eclipsing polar SDSS J015543.40+002807.2. MNRAS, 355(3):689–693.

Williams, R. E. and Ferguson, D. H. (1982). He I line emission and the helium abundance in cataclysmic variables. ApJ, 257:672–685.

Wils, P., Gänsicke, B. T., Drake, A. J., and Southworth, J. (2010). Data mining for dwarf novae in SDSS, GALEX and astrometric catalogues. MNRAS, 402:436–446.

Wong, T. L. S. and Bildsten, L. (2021). Mass Transfer and Stellar Evolution of the White Dwarfs in AM CVn Binaries. ApJ, 923(1):125.

Wood, M. A., Casey, M. J., Garnavich, P. M., and Haag, B. (2002). Superhumps in the helium dwarf nova KL Draconis. MNRAS, 334(1):87–93.

Wood, M. A., Winget, D. E., Nather, R. E., Hessman, F. V., Liebert, J., Kurtz, D. W., Wesemael, F., and Wegner, G. (1987). The Exotic Helium Variable PG 1346+082. ApJ, 313:757.

Wood-Vasey, W. M., Aldering, G., Nugent, P., and Li, K. (2003). Supernovae 2003av and 2003aw. IAU Circ., 8077:1.

Worpel, H. and Schwope, A. D. (2015). XMM-Newton and optical observations of the eclipsing polar CSS081231:071126+440405. A&A, 583:A130.

Worpel, H., Schwope, A. D., Granzer, T., Reinsch, K., Schwarz, R., and Traulsen, I. (2016). X-ray and optical observations of four polars. A&A, 592:A114.

Woudt, P. A. and Warner, B. (2001). High-speed photometry of faint cataclysmic variables - I. V359 Cen, XZ Eri, HY Lup, V351 Pup, V630 Sgr, YY Tel, CQ Vel and CE-315. MNRAS, 328(1):159–166.

Woudt, P. A. and Warner, B. (2003). The new AM CVn star in Hydra. MNRAS, 345(4):1266–1270.

Woudt, P. A. and Warner, B. (2011). CSS233313-155744: an eclipsing dwarf nova with a 61.7-min orbital period. The Astronomer's Telegram, 3705.

Woudt, P. A., Warner, B., and de Budé, D. (2012a). Orbital Period Distribution of Cataclysmic Variables in the Catalina Real-Time Transient Survey. African Skies, 16:141.

Woudt, P. A., Warner, B., de Budé, D., Macfarlane, S., Schurch, M. P. E., and Zietsman, E. (2012b). High-speed photometry of faint cataclysmic variables - VII. Targets selected from the Sloan Digital Sky Survey and the Catalina Real-time Transient Survey. MNRAS, 421:2414–2429.

Woudt, P. A., Warner, B., and Motsoaledi, M. (2013). CSS121123:045020-093113: A WZ Sge-type dwarf nova amongst the AM CVn systems. The Astronomer's Telegram, 4726.

Woudt, P. A., Warner, B., and Rykoff, E. (2005). 2QZ J142701.6-012310. IAU Circ., 8531:3.

Wu, K. and Chanmugam, G. (1988). Cyclotron Spectra from Inhomogeneous Accretion Columns. ApJ, 331:861.

Wu, K., Cropper, M., Ramsay, G., and Sekiguchi, K. (2002). An electrically powered binary star? MNRAS, 331:221–227.

York, D. G., Adelman, J., Anderson, Jr., J. E., Anderson, S. F., Annis, J., Bahcall, N. A., Bakken, J. A., Barkhouser, R., Bastian, S., Berman, E., Boroski, W. N., Bracker, S., Briegel, C., Briggs, J. W., Brinkmann, J., Brunner, R., Burles, S., Carey, L., Carr, M. A., Castander, F. J., Chen, B., Colestock, P. L., Connolly, A. J., Crocker, J. H., Csabai, I., Czarapata, P. C., Davis, J. E., Doi, M., Dombeck, T., Eisenstein, D., Ellman, N., Elms, B. R., Evans, M. L., Fan, X., Federwitz, G. R., Fiscelli, L., Friedman, S., Frieman, J. A., Fukugita, M., Gillespie, B., Gunn, J. E., Gurbani, V. K., de Haas, E., Haldeman, M.,

Harris, F. H., Hayes, J., Heckman, T. M., Hennessy, G. S., Hindsley, R. B., Holm, S., Holmgren, D. J., Huang, C.-h., Hull, C., Husby, D., Ichikawa, S.-I., Ichikawa, T., Ivezić, Ž., Kent, S., Kim, R. S. J., Kinney, E., Klaene, M., Kleinman, A. N., Kleinman, S., Knapp, G. R., Korienek, J., Kron, R. G., Kunszt, P. Z., Lamb, D. Q., Lee, B., Leger, R. F., Limmongkol, S., Lindenmeyer, C., Long, D. C., Loomis, C., Loveday, J., Lucinio, R., Lupton, R. H., MacKinnon, B., Mannery, E. J., Mantsch, P. M., Margon, B., McGehee, P., McKay, T. A., Meiksin, A., Merelli, A., Monet, D. G., Munn, J. A., Narayanan, V. K., Nash, T., Neilsen, E., Neswold, R., Newberg, H. J., Nichol, R. C., Nicinski, T., Nonino, M., Okada, N., Okamura, S., Ostriker, J. P., Owen, R., Pauls, A. G., Peoples, J., Peterson, R. L., Petravick, D., Pier, J. R., Pope, A., Pordes, R., Prosapio, A., Rechenmacher, R., Quinn, T. R., Richards, G. T., Richmond, M. W., Rivetta, C. H., Rockosi, C. M., Ruthmansdorfer, K., Sandford, D., Schlegel, D. J., Schneider, D. P., Sekiguchi, M., Sergey, G., Shimasaku, K., Siegmund, W. A., Smee, S., Smith, J. A., Snedden, S., Stone, R., Stoughton, C., Strauss, M. A., Stubbs, C., SubbaRao, M., Szalay, A. S., Szapudi, I., Szokoly, G. P., Thakar, A. R., Tremonti, C., Tucker, D. L., Uomoto, A., Vanden Berk, D., Vogeley, M. S., Waddell, P., Wang, S.-i., Watanabe, M., Weinberg, D. H., Yanny, B., Yasuda, N., and SDSS Collaboration (2000). The Sloan Digital Sky Survey: Technical Summary. AJ, 120:1579–1587.

Yungelson, L. R., Nelemans, G., and van den Heuvel, E. P. J. (2002). On the formation of neon-enriched donor stars in ultracompact X-ray binaries. A&A, 388:546–551.

Zhang, X.-F., Liu, J.-Z., Jeffery, C. S., Hall, P. D., and Bi, S.-L. (2018). The double helium-white dwarf channel for the formation of AM CVn binaries. Research in Astronomy and Astrophysics, 18(1):009.